LANDSLIDE HAZARDS IN ALPINE REGION: MECHANICS AND MITIGATION

EDITED BY: Yun Zheng, Dongri Song, Fei Meng, Yongtao Yang, Tingting Liu and Xuewei Liu

PUBLISHED IN: Frontiers in Earth Science

frontiers Research Topics

frontiers

ISSN 1664-8714
ISBN 978-2-83250-343-0
DOI 10.3389/978-2-83250-343-0

About Frontiers

Frontiers is more than just an open-access publisher of scholarly articles: it is a pioneering approach to the world of academia, radically improving the way scholarly research is managed. The grand vision of Frontiers is a world where all people have an equal opportunity to seek, share and generate knowledge. Frontiers provides immediate and permanent online open access to all its publications, but this alone is not enough to realize our grand goals.

Frontiers Journal Series

The Frontiers Journal Series is a multi-tier and interdisciplinary set of open-access, online journals, promising a paradigm shift from the current review, selection and dissemination processes in academic publishing. All Frontiers journals are driven by researchers for researchers; therefore, they constitute a service to the scholarly community. At the same time, the Frontiers Journal Series operates on a revolutionary invention, the tiered publishing system, initially addressing specific communities of scholars, and gradually climbing up to broader public understanding, thus serving the interests of the lay society, too.

Dedication to Quality

Each Frontiers article is a landmark of the highest quality, thanks to genuinely collaborative interactions between authors and review editors, who include some of the world's best academicians. Research must be certified by peers before entering a stream of knowledge that may eventually reach the public - and shape society; therefore, Frontiers only applies the most rigorous and unbiased reviews.
Frontiers revolutionizes research publishing by freely delivering the most outstanding research, evaluated with no bias from both the academic and social point of view. By applying the most advanced information technologies, Frontiers is catapulting scholarly publishing into a new generation.

What are Frontiers Research Topics?

Frontiers Research Topics are very popular trademarks of the Frontiers Journals Series: they are collections of at least ten articles, all centered on a particular subject. With their unique mix of varied contributions from Original Research to Review Articles, Frontiers Research Topics unify the most influential researchers, the latest key findings and historical advances in a hot research area! Find out more on how to host your own Frontiers Research Topic or contribute to one as an author by contacting the Frontiers Editorial Office: frontiersin.org/about/contact

LANDSLIDE HAZARDS IN ALPINE REGION: MECHANICS AND MITIGATION

Topic Editors:
Yun Zheng, Institute of Rock and Soil Mechanics, Chinese Academy of Sciences (CAS), China
Dongri Song, Institute of Mountain Hazards and Environment, Chinese Academy of Sciences (CAS), China
Fei Meng, Swinburne University of Technology, Australia
Yongtao Yang, Institute of Rock and Soil Mechanics, Chinese Academy of Sciences (CAS), China
Tingting Liu, Wuhan University of Technology, China
Xuewei Liu, Institute of Rock and Soil Mechanics, Chinese Academy of Sciences (CAS), China

Citation: Zheng, Y., Song, D., Meng, F., Yang, Y., Liu, T., Liu, X., eds. (2022). Landslide Hazards in Alpine Region: Mechanics and Mitigation. Lausanne: Frontiers Media SA. doi: 10.3389/978-2-83250-343-0

Table of Contents

frontiers | Frontiers in Earth Science

TYPE Editorial
PUBLISHED 13 September 2022
DOI 10.3389/feart.2022.978930

OPEN ACCESS

EDITED BY
Chong Xu,
Ministry of Emergency Management, China

REVIEWED BY
Naveen James,
Indian Institute of Technology Ropar, India
Aiguo Xing,
Shanghai Jiao Tong University, China
Zizheng Guo,
Hebei University of Technology, China

*CORRESPONDENCE
Dongri Song,
drsong@imde.ac.cn

SPECIALTY SECTION
This article was submitted to Geohazards and Georisks, a section of the journal Frontiers in Earth Science

RECEIVED 27 June 2022
ACCEPTED 19 August 2022
PUBLISHED 13 September 2022

CITATION
Zheng Y, Song D, Meng F, Liu T, Yang Y and Liu X (2022), Editorial: Landslide hazards in alpine region: Mechanics and mitigation.
Front. Earth Sci. 10:978930.
doi: 10.3389/feart.2022.978930

Editorial: Landslide hazards in alpine region: Mechanics and mitigation

Yun Zheng[1], Dongri Song[2]*, Fei Meng[1,3], Tingting Liu[1,3], Yongtao Yang[1] and Xuewei Liu[1]

[1]State Key Laboratory of Geomechanics and Geotechnical Engineering, Institute of Rock and Soil Mechanics, Chinese Academy of Sciences, Wuhan, China, [2]Key Laboratory of Mountain Hazards and Earth Surface Process, Institute of Mountain Hazards and Environment, Chinese Academy of Sciences, Chengdu, China, [3]School of Civil Engineering and Architecture, Wuhan University of Technology, Wuhan, China

KEYWORDS

alpine regions, landslide, debris flow, stability, earthquake, hazard mitigation

Editorial on the Research Topic
Landslide hazards in alpine region: Mechanics and mitigation

Alpine regions refer to mountainous areas with high altitudes, cool climates and large differences in day and night temperatures, which can only be adapted to grow more cold-tolerant crops. The Qinghai-Tibet Plateau is a typical alpine region. Comparing to the low altitude areas, the engineering geological conditions in alpine regions are much more complicated. These include steep mountain slopes (Figure 1), complex geotechnical structures, and severe environmental conditions such as strong earthquakes, drastic change in temperature (for example, the temperature difference between day and night can be up to 50 degrees, in the Qinghai-Tibet Plateau), and extreme precipitation. Besides, the disturbance from human being is also noticeable, like blasting excavation, vegetation destruction, and vehicle loads, etc. The coupling of these unfavorable factors leads to frequent landslides (slope instability and landslide dam, avalanche, and debris flow, etc.), which seriously threaten lives and the safe construction and operation of infrastructures. The Research Topic is to present the recent advances in engineering geological features, landslide mechanisms, and mitigation technologies in alpine regions. This will help us to prevent and control landslide hazards that may be encountered in hydropower projects, highways, railways, and open-pit mining.

Due to strong tectonic movement, earthquake is one of the most common triggers of landslide hazards in alpine regions. For example, in the Qinghai-Tibet Plateau, a total of 5,185 earthquakes of M ≧ 3 occurred from 1971 to 2021, including 56 strong earthquakes with M ≧ 6 (Liu, 2021). This Research Topic includes two articles on evaluating methods for earthquake-induced landslides. Li et al. examine the critical acceleration for regional seismic landslide hazard assessments by finite element limit analysis. The proposed model improves previous mechanical models for regional seismic landslide hazard assessments. Zhang et al. discuss the upper bound analysis of the stability of 3D slopes in the saturated

FIGURE 1
Steep mountain slopes in alpine regions.

soft clay subjected to seismic loading. It is suggested that the effects of horizontal and vertical seismic forces must be considered simultaneously in the seismic design of saturated soft clay slopes.

Drastic change in temperature is the natural environment often faced by the rock and soil mass in alpine regions. This can lead to deterioration of the physical and mechanical properties of the rock and soil mass, which is detrimental to slope stability. As global warming accelerates the rate of glacial retreat, factors such as thawing rock formations and glacial meltwater weaken the stability of slopes. Then, in the event of a strong earthquake, the chances of an avalanche landslide disaster would be very high, such as the Khumbu glacier landslide (Ding et al., 2018). In this Research Topic, An et al. focus on the shear strength and microstructure of granite residual soil under an extremely low temperature. Fu et al. carry out systematic research on mechanical properties of frozen glacial tills due to short periods of thawing. They find that the difference between peak and critical resistances decreases with increasing thawing time and reflects changes in shear behavior. Zhang et al. note that the stress-strain curves of embankment clay changed from strain hardening or stabilization to softening during freeze-thaw cycles.

Precipitation, especially Extreme Precipitation Events, is commonly believed to be the most important factor triggering landslides, and there is no exception in alpine regions. Extreme Precipitation Events refers to instances during which the amount of rain or snow experienced in a location substantially exceeds what is normal. What constitutes a period of extreme precipitation varies according to location and season. From 1961 to 2017, the annual precipitation of Qinghai-Tibet Plateau showed an upward trend, with a rate of 8.06 mm/10 a, and the average annual precipitation reached 472.36 mm. At the same time, there has been a marked increase in the number of Extreme Precipitation Events (Ma et al., 2020). This Research Topic includes three articles on the assessing method of landslides caused by precipitation. Fu et al. propose an innovative strength parameter estimation method for soil-rock mixture for evaluating the deposit slope stability under rainfall. Zhou et al. describe a predisposed geological emergence of a rainfall-induced soil-rock mixture landslide at Chongqing City, China. Bao et al. note that the slope creeping is a dynamic development process, from stable deformation to unstable failure, and rainfall can accelerate this process. The effect of the disturbance from human being on the stability of slope is also noticeable, *i.e.*, the blasting excavation, as discussed in the articles by Wang et al. and Wu et al.

Due to the development of rivers and the large differences in terrain, a large numbers of hydropower stations are built in alpine regions. Landslide dams are massive blockages of river channels resulting from massive earth movements, which is a special kind of landslide hazard in alpine regions. In this Research Topic, Xie et al. describe the accumulation characteristics and mechanism of landslide debris dam based on physical model tests. The damming process and accumulation mechanism of the landslide dam are found to be changed with slope conditions. Zhou et al. present an experimental investigation of the outburst discharge of landslide dam overtopping failure. They suggest that hydrographs of the breaching flow and outburst flood can be divided into three stages where each stage is separated by inflection points and peak

discharges. Also in this Research Topic, Yang et al. note that the excavation of a spillway can effectively reduce the peak breach discharge, therefore delay the time to peak.

Anchoring frame beam is a very common form of support for reinforced slopes and centrifugal tests have been proved to be an intuitive and effective means for investigating the working mechanism of frame beams. This Research Topic concludes an article by Zhang et al. that explores the application of multi-channel selector in centrifuge model test of anchoring slope by frame beam. They find that multi-channel selector can be successfully applied in varying environments, saving time and reducing the cost of obtaining a single set of data.

Author contributions

All authors listed have made a substantial, direct, and intellectual contribution to the work and approved it for publication.

Acknowledgments

We are grateful to all the contributors to this Research Topic.

Conflict of interest

The authors declare that the research was conducted in the absence of any commercial or financial relationships that could be construed as a potential conflict of interest.

Publisher's note

All claims expressed in this article are solely those of the authors and do not necessarily represent those of their affiliated organizations, or those of the publisher, the editors and the reviewers. Any product that may be evaluated in this article, or claim that may be made by its manufacturer, is not guaranteed or endorsed by the publisher.

References

Ding, C., Feng, G. C., Zhou, Y. S., Wang, H. Q., Du, Y. N., and Chen, C. Y. (2018). Nepal earthquake triggered landslides recognition and deformation analysis of avalanches' region. *Geomatics Inf. Sci. Wuhan Univ.* 43 (6), 847–852. doi:10.13203/j.whugis20160031

Liu, J. (2021). *Earthquake distribution data on the Qinghai-Tibet Plateau (1971-2021, M≥3)*. Beijing: National Tibetan plateau data center. CSTR: 18406.11.SolidEar.tpdc.271929. (Download the reference: RIS | Bibtex). doi:10.11888/SolidEar.tpdc.271929

Ma, W. D., Liu, F. G., Zhou, Q., Chen, Q., Liu, F., and Chen, Y. P. (2020). Characteristics of extreme precipitation over the Qinghai-Tibet Plateau from 1961 to 2017. *J. Nat. Resour.* 35, 3039–3050. doi:10.31497/zrzyxb.20201218

frontiers in Earth Science

ORIGINAL RESEARCH
published: 20 September 2021
doi: 10.3389/feart.2021.757724

Research on Application of Multi-Channel Selector in Centrifugal Model Test of Anchoring Slope by Frame Beam

Junhui Zhang[1], Feng Li[1], Shiping Zhang[1], Jiankun Zhou[2] and Houming Wu[3]*

[1]National Engineering Laboratory of Highway Maintenance Technology, Changsha University of Science and Technology, Changsha, China, [2]Guangzhou Chengan Testing LTD. of Highway and Bridge, Guangzhou, China, [3]Guangxi Communications Investment Group Corporation Ltd., Nanning, China

An anchoring frame beam is a very common form of support for reinforced slopes, especially in alpine regions. Centrifugal tests have proved to be an intuitive and effective means of investigating the mechanism of action of frame beams. However, the data acquisition system of the geotechnical centrifuge in service has the problem of a small number of acquisition channels. A multi-channel selector based on the existing acquisition system was proposed, designed, processed, and manufactured, and it was debugged, tested, and applied in a no-load centrifugal test, static pressure model test, and centrifugal model test. The results show that the acquisition mode of the multi-channel selector connected with a maximum of 288 sensors has been changed from "one-to-one" to "one-to-many". Its influence on various sensor signals is negligible. The multi-channel selector can work normally, which communicates and feeds back with the remote controller in the 1–120 g no-load centrifugal test. In the static load model test, 162 sensor signals were well collected through it. And only 51 channels were used to effectively obtain the signals of 187 sensors in a 70 g centrifugal model test of an anchoring slope with a frame beam. The multi-channel selector can be successfully applied in different use environments, saving time and reducing the cost of obtaining a single set of data.

Keywords: multi-channel selector, data acquisition system, centrifuge model test, anchoring slope, frame beam

OPEN ACCESS

Edited by:
Yun Zheng,
Institute of Rock and Soil Mechanics (CAS), China

Reviewed by:
Zhi-feng Wang,
Chang'an University, China
Chaoyi Sun,
Institute of Rock and Soil Mechanics (CAS), China

****Correspondence:***
Shiping Zhang
zhangshipingwy@126.com

Specialty section:
This article was submitted to Geohazards and Georisks, a section of the journal Frontiers in Earth Science

Received: *12 August 2021*
Accepted: *06 September 2021*
Published: *20 September 2021*

Citation:
Zhang J, Li F, Zhang S, Zhou J and Wu H (2021) Research on Application of Multi-Channel Selector in Centrifugal Model Test of Anchoring Slope by Frame Beam. Front. Earth Sci. 9:757724. doi: 10.3389/feart.2021.757724

INTRODUCTION

Landslides (Amato et al., 2019; Carlà et al., 2019; Kreczmer et al., 2021) occur every year around the world, especially in alpine regions (Zhang J. et al., 2021; Zheng et al., 2018; Zhou et al., 2021). An anchoring frame beam is a very common form of support for reinforced slopes (Lin et al., 2017; Shi et al., 2019; Zheng et al., 2021b). Various research methods, such as theoretical analysis (Wang et al., 2020; Zeghal et al., 2018; Zhang S. et al., 2021; Zheng et al., 2021a), laboratory tests (Pan et al., 2020; Yao et al., 2020; Zhang et al., 2020b), numerical simulations (Ge et al., 2017), and on-site monitoring (Zhang et al., 2020a; Zhao et al., 2020) were used to study the mechanism and prevention of landslides. The physical model test is the most commonly used entity research method (Ghandil et al., 2016), which is widely used in many disciplines such as geotechnical, hydraulic, structure, etc. (Lin et al., 2018). Among them, the geotechnical centrifugal model test is becoming more and more popular with researchers, because it uses the super-gravity field to make the test object obtain the internal stress state of its weight similar to the prototype, thereby effectively ensuring that the static/

dynamic response, stress path, deformation, and failure mechanism of the test body are highly consistent with the prototype (El Sawwaf et al., 2006; Chen et al., 2018; Weng et al., 2020). It is generally recognized by international engineering and academic circles. With the continuous advancement of centrifuge construction technology and the substantial expansion of the scope of test applications, most of the geotechnical centrifuge equipment has basically improved the technology in the simulation of static/dynamic conditions. It is well known that the construction and maintenance costs of geotechnical centrifuges are enormous, leading to high costs for each centrifugal model test, so it is desirable to collect as much test data as possible. However, a static and dynamic data acquisition system with many geotechnical centrifuges in service is usually equipped, which carries tens or hundreds of channels for connecting various sensors in a "one-to-one" manner. As a result, the number of data obtained in many centrifugal model tests cannot exceed the number of channels of the data acquisition system, which inevitably causes the data of each channel to be expensive. Therefore, it is very meaningful to obtain more data based on the number of channels of the existing acquisition system to reduce the cost of a single dataset in a centrifugal model test.

Many scholars have carried out centrifugal model tests and obtained a large amount of test data (Ng et al., 2004; Thusyanthan et al., 2007). However, all were limited by the number of channels in the data acquisition system, and the number of sensors used in a test was relatively small (Li et al., 2019; Shen et al., 2020). Viswanadham et al. (2009) studied geotextile-reinforced slopes subjected to differential settlements during centrifuge at 40 g, and five datasets of Linearly Variable Differential Transformer (LVDT) were collected. Chortis et al. (2020) researched the influence of scour depth and type for monopiles in sand under monotonic lateral loading by geotechnical centrifuge. Twenty strain gauges were embedded at different depths on the left and right sides of the model pile. Sabagh et al. (2020) used seven sensors (five found surface settlement LVDT, two tunnel displacement LVDT) and one camera to study the response to a continuous shallow tunnel crossing an active normal fault. Liu et al. (2011) carried out the centrifugal model test of the deformation mode of the geosynthetic structure-reinforced soil wall under seismic load during service life and reinforcement load. A total of thirty-six sensors including eight LVDTs, sixteen strain gauges, and twelve accelerometers were installed. In the centrifugal model test of Rotta et al. (Rotta Loria et al., 2015), ten strain gauges were attached to each of the three energy piles in order to obtain the energy of thermo-mechanical loads that the piles were subjected to in saturated sand. Ueda et al. (2019) researched a pile model which they embedded in an inclined ground and subjected to liquefaction-induced lateral spreading using four different centrifugal accelerations from 13 to 50 g, and six pore water pressure transducers, six accelerometers, twelve strain gauges, four laser-displace sensors, and one thermocouple were obtained. The research of Wang et al. (2019) and Yang et al. (2019) were about the performance and load-bearing characteristics of the single friction wheel foundation of offshore wind turbines under lateral moment loads and the vertical performance in the sand, and only one LVDT was used in their tests. Some researchers (Kutter et al., 2018; Sahare et al., 2020) carried out Liquefaction Experiments and Analysis Projects (LEAP). The centrifugal models were equipped with 14 accelerometers and 10 pore pressure transducers, and 20 data acquisition channels were utilized.

In addition, other measurement technologies such as cameras, optical fibers, wireless transmission (Bluetooth, radio, 4G, etc.) were also used in the centrifugal model test (Gourc et al., 2010; Herbert et al., 2011; Kuang et al., 2011). It was an effective supplement to the data acquisition system that comes with the existing centrifuge. However, many problems in the test process (untimely test data acquisition, too much invalid data, poor synchronization, etc.) increased the risk of test failure. Cao et al. (2018) tested a method for estimating soil moisture using an active heating fiber Bragg grating (FBG) sensor. Among them, a FBG acquisition instrument was fixed on the rotating arm of the centrifuge, and it rotated with the rotating arm during the test. At this time, the collected test data could not be viewed. Broekman et al. (2020) developed a linear drive system that provides closed-loop control in cyclic, monotonic, or static load or displacement control, and CCTV cameras were used in the centrifuge.

Thus, the objective of this paper was to propose a multi-channel selector design and successfully use it for centrifugal model testing of an anchoring slope with a frame beam to achieve the purpose of reducing the cost of a single data test. This study was organized as follows. First, the multi-channel selector was designed and manufactured, and its workflow was introduced. Then, a set of sensors such as earth pressure gauges, laser displacement gauges, strain gauges, etc., were selected to be connected to the multi-channel selector and then connected to the data acquisition system and compared with the directly connected data acquisition system. Finally, the multi-channel selector was applied in a centrifugal model test of an anchoring slope with a frame beam, and 187 sets of data were successfully obtained and analyzed.

WORKING PRINCIPLE AND MANUFACTURE OF THE MULTI-CHANNEL SELECTOR

The multi-channel selector was designed based on the dynamic data acquisition system supporting the geotechnical centrifuge of Changsha University of Science and Technology. The system could collect 64 sets of channel data at one time, including 32 sets of voltage data, 16 sets of electron current data, and 16 sets of strain data.

Working Principle of the Multi-Channel Selector

The hardware of the current data acquisition system was connected by the data acquisition computer, the terminal next to the model box, and various sensors as shown in **Figure 1A**. Their connection method was that one terminal can only connect to one sensor, which can be called one-to-one. Therefore, the

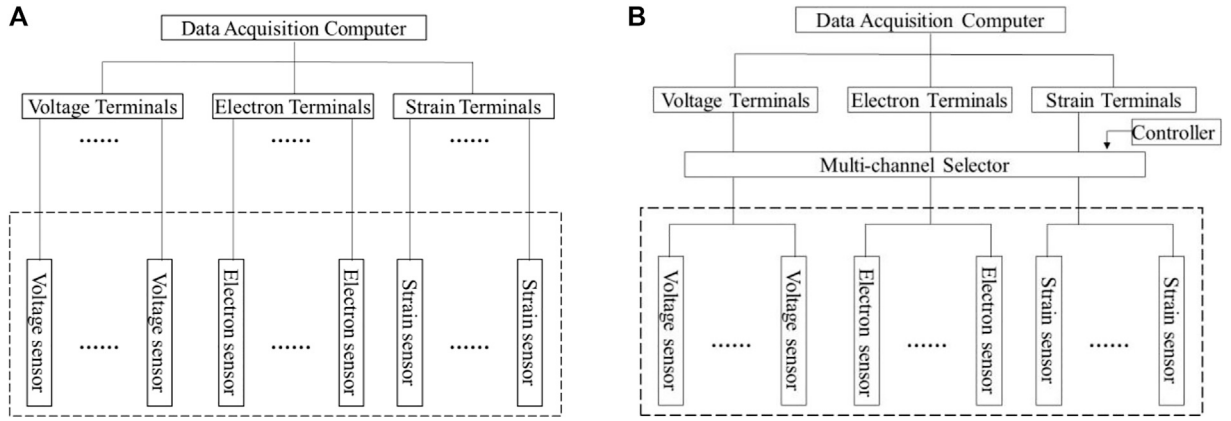

FIGURE 1 | Hardware connection diagram: **(A)** current connection; **(B)** added multi-channel selector.

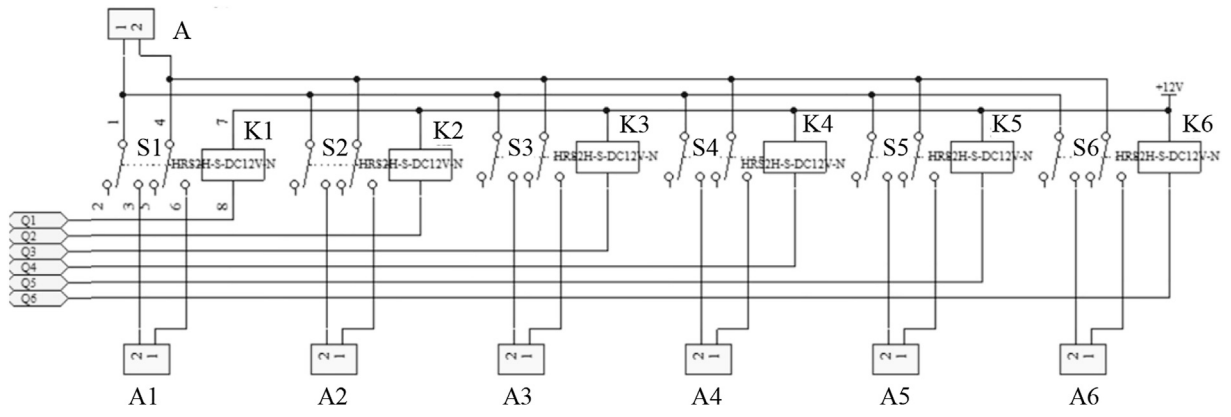

FIGURE 2 | Multi-channel selector connection diagram.

geotechnical centrifuge data acquisition system was equipped with a panel containing 64 terminals next to the model box, and only 64 sensors can be connected at most. The multi-channel selector was set between the original terminal and the sensor, and was connected to them with a shielded cable, as shown in **Figure 1B**.

Taking the voltage connection terminals numbered A in **Figure 2** as an example, the working principle of the multi-channel selector can be introduced in detail as follows. It contained one total output port (A), six input ports (A1~A6), and six dual control switches (S1~ S6). Generally, all switches were open, and port A had no voltage. When the control angle was energized so that the control switch NO.S1 was closed and the remaining switches were open, the circuit between the input terminal A1 and the output terminal A was connected. Then, two-core shielded cables that transmit signals "+" and "-" were used to connect the terminal block and the multi-channel selector. At this time, the hardware connection between the sensor signal connected to the input terminal A1 and the data acquisition computer was realized, and its signals using the current acquisition software were collected, stored, and displayed. Similarly, when the control switch NO.S2 was closed when the remaining switches were open, the sensor signal connected to input port A2 was collected, stored, and displayed. By analogy, the signals of the six input ports could be collected, stored, and displayed. Thereby, multiple sensor signals were obtained using one terminal, which can be called "one-to-many". Each channel terminal was extended to connect six sensors. And taking eight terminals as a group in our centrifuge, if eight terminals were connected to a multi-channel selector, forty-eight sensors could be expanded, as shown in **Figure 3**. The connection mode was changed from "one-to-one" to "one-to-many", so that more sensor signals were collected, stored, and displayed.

Module Design and Process of the Multi-Channel Selector

In order to achieve the above purpose, a circuit diagram and circuit board were designed and processed, as shown in **Figure 4**.

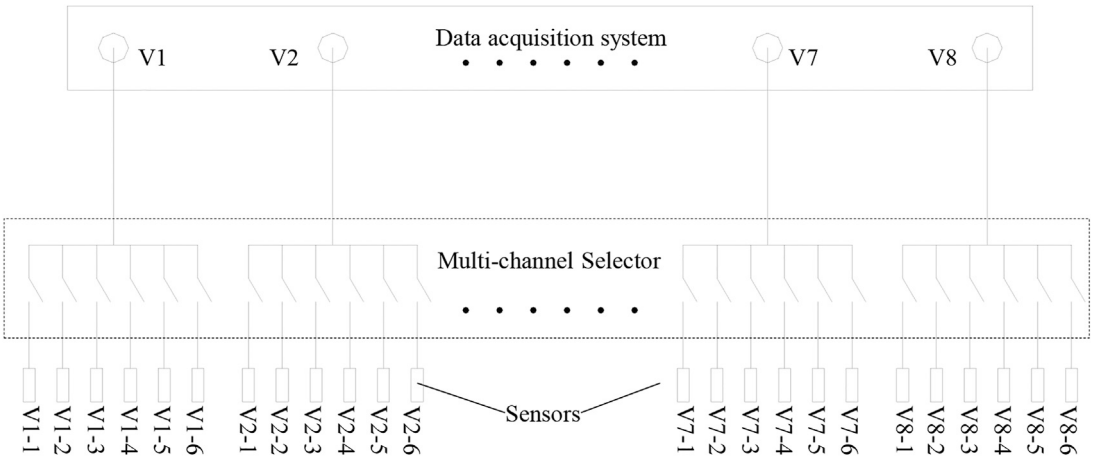

FIGURE 3 | Multi-channel selector connection diagram.

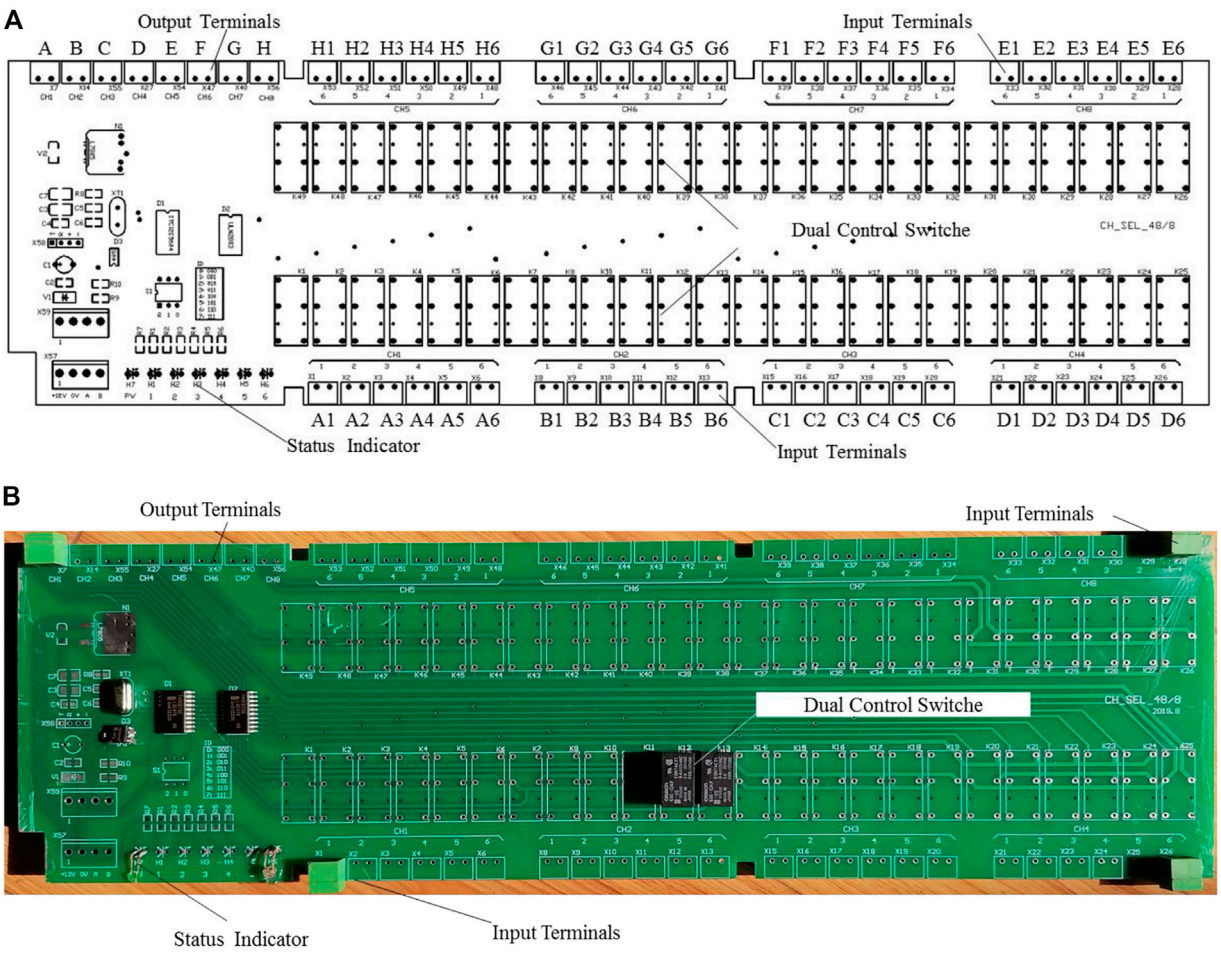

FIGURE 4 | Circuit diagram and circuit board of multi-channel selection module.

One set of sixteen-pin output plugs, eight sets of twelve-pin input plugs, and one row of light-emitting diodes were installed on both sides of the multi-channel selection board. In addition, forty-eight dual-control switches, one eight-to-one analog switch, one single-chip microcomputer, one dial switch, and one RS485 signal transceiver were welded on the front. The input and output terminals were used to connect sensors and the data acquisition system, respectively. The forty-eight dual-control switches were divided into six groups, eight groups were set to control the connection of input and output terminals. The functions of each part were: one eight-to-one analog switch was used to control which group of dual control switches work, one single-chip microcomputer was to send work instructions, one dial switch was to display the current working status, and one RS485 signal transceiver was to accept remote control commands and feed back the results of execution to the remote control. According to the size of various parts and the line interval, the size of each circuit board was 350 × 100 mm (length × width).

The single-chip microcomputer according to **Table 1** sent out the binary signal command "000″ to indicate that A1 was turned on. At this time, the 1# pin of the eight-to-one analog switch was energized, and the power was supplied to the control site of the K1 switch of the dual-control analog switch. The K1 switch was closed to make the A1 plug in the input plug and the A plug in the output plug realize the physical connection. The other switches (K2~K6) connected to the A plug of the output plug were not powered and in the disconnected state, which would not affect the signal of the A plug of the output plug, so that the data acquisition server could realize A1 signal collection, storage, and display of the sensor connected with the plug. Then according to the wireless remote control box, it sent out binary signal instructions 001, 010, 011, 100, and 101 in turn, which means to connect the A2, A3, A4, A5, A6 sensors plugged into the input plug, and the eight-to-one analog switch sequentially simulates the dual control. The control sites of K2, K3, K4, K5, and K6 were powered, so that the K2, K3, K4, K5, and K6 switches were closed, and the A2, A3, A4, A5, and A6 sensors inserted in the input plug were connected to the output. The signal connection of the A plug in the plug could realize the signal collection, storage, and display of all sensors connected to the A2, A3, A4, A5, and A6 plugs by using the existing data acquisition server in turn.

Each multi-channel selected the 1–6 switches in the controller to switch synchronously, and up to six sensors could be controlled simultaneously per signal command. For example, the input plug of A1~A6, B1~B6, C1~C6, D1~D6, E1~E6, F1~F6, G1~G6, and H1~H6 were respectively connected to the corresponding sensors. If the "000" command was issued, when the first sensor was selected to be collected, the A1, B1, C1, D1, E1, F1, G1, and H1 terminals of the input plug were powered by the K1 switch control angle of the dual-control analog switch, and connected to the output plug of A to H, thus realizing the connection of the signal. In order to clearly observe the working condition of the multi-channel selection controller, the 1# light of the light-emitting diode was always on. By analogy, if the "001" command was issued, it meant that when the second sensor was selected, the A2, B2, C2, D2, E2, F2, G2, and H2 terminals of the input plug were powered by the K2 switch control angle of the two-open and double-close analog switch. Respectively, signal connection with the A, B, C, D, E, F, G, and H plugs of the output plug was realized. At this time, the 2# light of the light-emitting diode of the multi-channel selection controller was always on.

Manufacture of Multi-Channel Selector

According to the centrifugal data collection experience, six modules numbered M1~M6 were assembled into a multi-channel selector, as shown in **Figure 5**. Its external dimensions were 358 mm × 291 mm × 102 mm (length × width × height), and it was a box body formed by cutting and welding a steel plate with a thickness of 1 mm. In addition, a 102 mm × 30 mm ×2 mm (length × width × thickness) angle steel with two screw holes was welded on the bottom of the left and right sides of the box to fix the instrument on the centrifuge to avoid it falling off during the rotation. Through the use of a multi-meter test, all channels on the multi-channel selector were connected and disconnected in compliance with the design requirements, indicating that this device was feasible.

The centrifuge test process continuously rotated around the central axis (without stopping), and the existing centrifuge cable channels had all been used up, making it impossible to control the multi-channel selector through wired methods. Therefore, a wireless method was selected for control signal transmission and reception. The operating instructions are shown in **Table 2**. An unloaded centrifugal test was carried out in advance, all doors and covers were closed, consistent with the centrifuge test state. The results show that the multi-channel selector operates well under the condition of 120 g centrifugation, indicating that it can be used in centrifugal tests.

To test the influence of the multi-channel selector on the voltage and electron signals, five kinds of voltage signals (1, 2, 3, 4, 5 V) and five kinds of electron signals (4, 8, 12, 16, 20 mA) were collected. **Figure 6** shows that no matter whether the multi-channel selector was connected or not, the collected signals were the same, indicating that the multi-channel selector had no influence on signal acquisition, or its influence could be ignored.

APPLICATION OF MULTI-CHANNEL SELECTOR IN STATIC PRESSURE MODEL TEST OF AN ANCHORING SLOPE BY FRAME BEAM

After the previous test, the multi-channel selector could be remotely controlled and connected to the line. The actual effect of it was compared through a static pressure model test.

Static Pressure Model Test Plan

A static pressure model of a cubic soil block was designed, in which we placed the soil block model, the loading steel plate, the

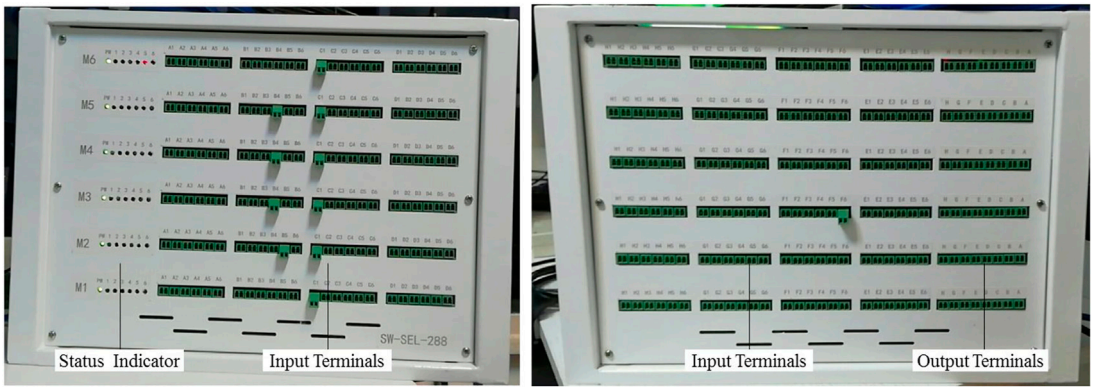

FIGURE 5 | Picture of multi-channel selector.

dynamometer, the jack, and the measuring sensors from bottom to top in the reaction frame, as shown **Figure 7**. The size of the soil block was 150 mm × 150 mm × 150 mm, which was compacted layer by layer by means of tamping. The front and back sides and top of the soil block model were used to place the frame beam model and the loading steel plate, and the rest were restrained by a U-shaped steel plate to limit the deformation of the soil block.

In order to obtain the actual use effect of the multi-channel selector, many sensors were installed in the model test. The detailed installation was as follows:

The nine axial force sensors (voltage sensor) were buried inside the soil block.

The three earth pressure sensors (voltage sensor) were loaded between the steel plate and soil block, soil block and U-shaped plate.

TABLE 1 | Signal numbering code.

J_2	J_1	J_0	EN	ON	J_2	J_1	J_0	EN	ON
0	0	0	1	1	1	0	0	1	5
0	0	1	1	2	1	0	1	1	6
0	1	0	1	3	1	1	0	1	7
0	1	1	1	4	X	X	X	0	None

TABLE 2 | Operational order.

NO.	Send command	Backtrack	Comment
1	XX 10 0064 0001 02 0000 CRC	XX 10 0064 0001 CRC	Closed
2	XX 10 0064 0001 02 0001 CRC	XX 10 0064 0001 CRC	1 Channel open
3	XX 10 0064 0001 02 0002 CRC	XX 10 0064 0001 CRC	2 Channel open
4	XX 10 0064 0001 02 0003 CRC	XX 10 0064 0001 CRC	3 Channel open
5	XX 10 0064 0001 02 0004 CRC	XX 10 0064 0001 CRC	4 Channel open
6	XX 10 0064 0001 02 0005 CRC	XX 10 0064 0001 CRC	5 Channel open
7	XX 10 0064 0001 02 0006 CRC	XX 10 0064 0001 CRC	6 Channel open
8		XX 90 YY CRC	Error

Note: 1. XX is the ID address of the module (01–06); 2. CRC is the communication data check code.

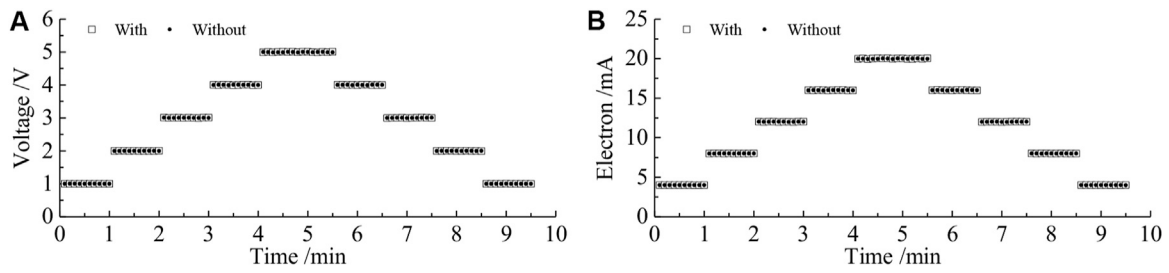

FIGURE 6 | Comparison of **(A)** voltage and **(B)** electron signals with or without a multi-channel selector.

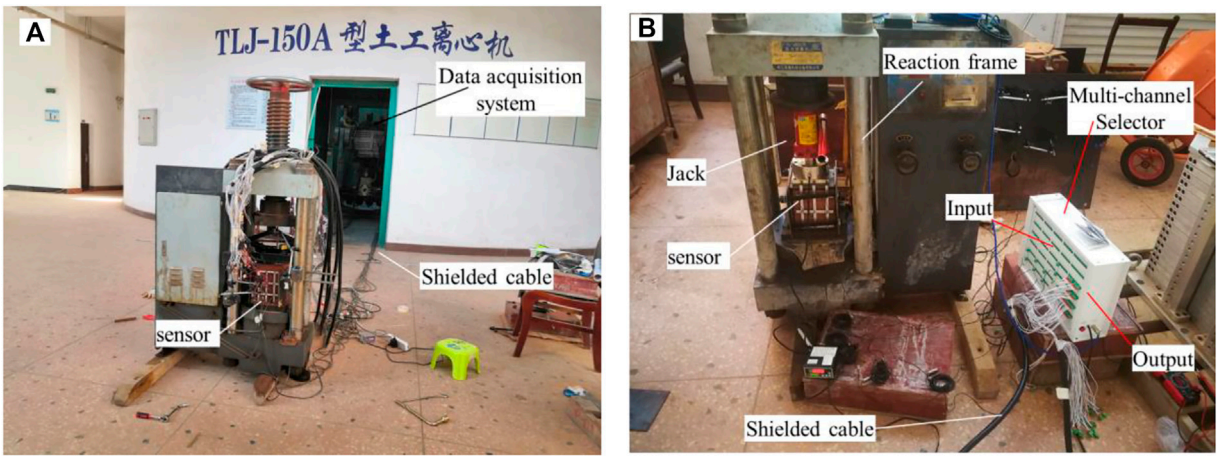

FIGURE 7 | Cable connection diagram for the static pressure model test.

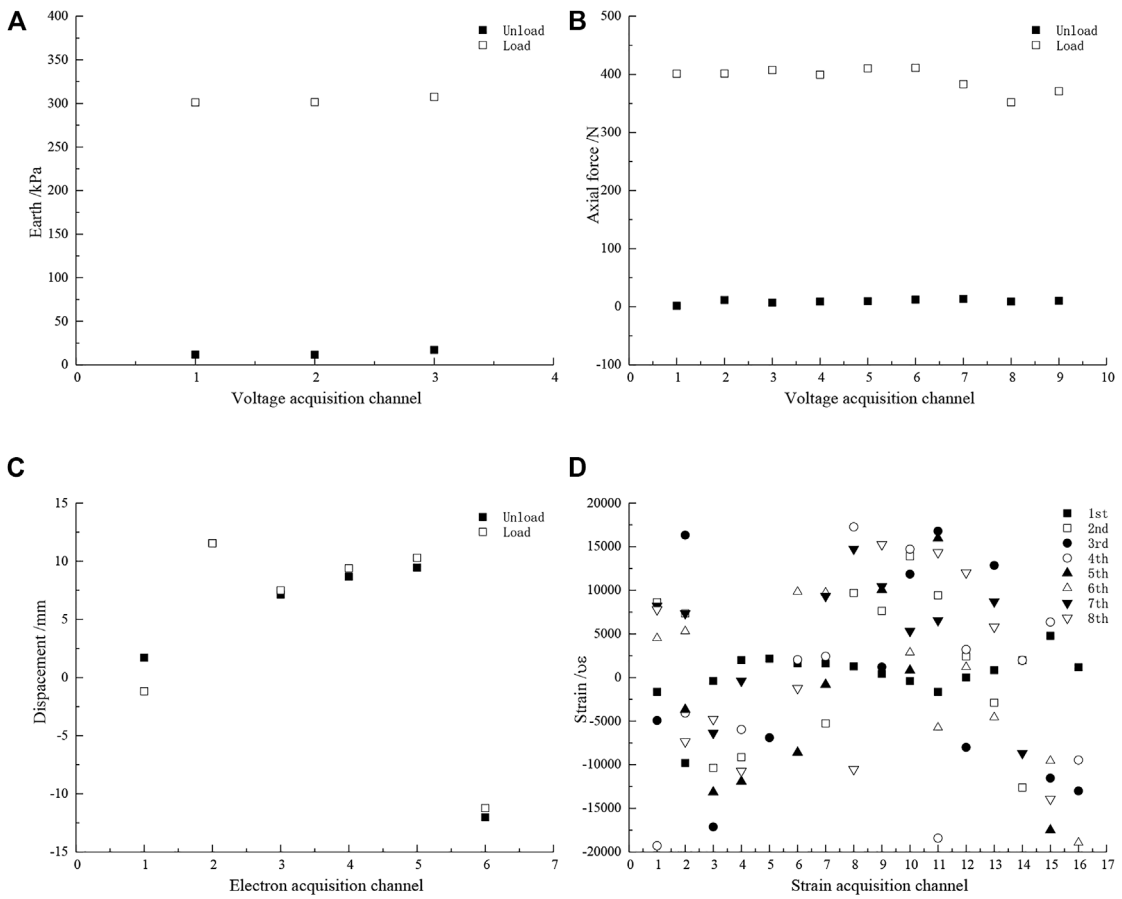

FIGURE 8 | Data of static pressure model test: **(A)** earth pressure, **(B)** axial force, **(C)** displacement, and **(D)** strain.

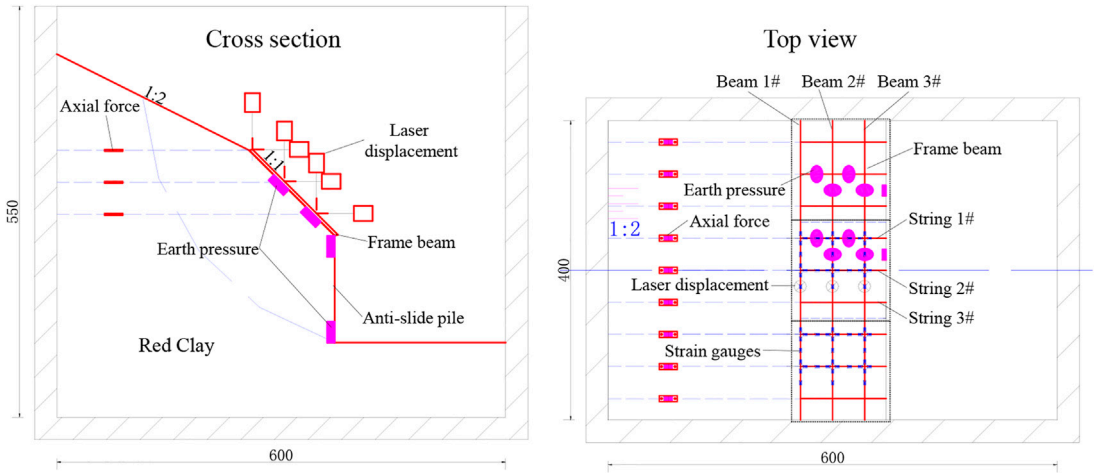

FIGURE 9 | Design drawing of the centrifugal model test.

TABLE 3 | Number of sensors and grouping acquisition scheme.

NO.	Axial force	Earth pressure	Laser displacement	Strain gauges
Total	27	10	6	144
1	9a	10	6	16a
2	9b	10	6	16b
3	9c	10	6	16c
4	9a	10	6	16d
5	9b	10	6	16e
6	9c	10	6	16f
7	9a	10	6	16g
8	9b	10	6	16h
9	9c	10	6	16l

The six laser displacement sensors (electron sensor) were used to measure the deformation of frame beams, longitudinal beams, and soil blocks.

A total of 144 strain gauges (strain sensor) were pasted on the frame beam model.

After the model was made and the sensors were installed, the cables of all sensors were inserted into the input end of the multi-channel selector, and the output end was connected to the data acquisition system. The actual effect of the cable connection is shown in **Figure 7**.

Analysis of Static Pressure Model Test

The twelve voltage channels, six electron current channels, and sixteen strain channels of the data acquisition system were collected from the soil pressure sensors, axial force sensors, displacement sensors, and strain sensors on the unloaded and loaded plates, as shown in **Figure 8**. A total of 162 sets of data were obtained.

Figure 8A displays the result of the earth pressure data. It shows that the earth pressure after loading increased to 300 kPa, which is consistent with the load applied by the loaded steel plate. Similarly, the axial force meters in nine groups of soil bodies were obtained, and the average value of the axial force loaded was 400 N in **Figure 8B** . In addition, the laser displacement data were within the range of −15–15 mm in **Figure 8C**, and the measured value was consistent with the display of the sensor. The displacement change before and after loading was relatively small, and its value was 1–2 mm. The focus of this model test was the collection of the strain data. The data of 144 strain gauges were collected in nine groups, as shown in **Figure 8D**. Its strain value was −20,000 με to 20,000 με, which corresponds to the change in resistance value measured by a multi-meter.

Through the static pressure model test, it was found that when the multi-channel selector works normally it is easy to operate, and connects quickly. It only takes 1–2 s to switch once using the multi-channel selector, and it takes 30 s to 1 min to select manual operation for this step. The installation of the multi-channel selector and the sensor and data acquisition system can break through the limit of the number of centrifuge acquisition channels and achieve more sensor data acquisition tasks. Another new discovery is that the multi-channel selector can also be used for data collection in conventional model tests, which can effectively shorten the

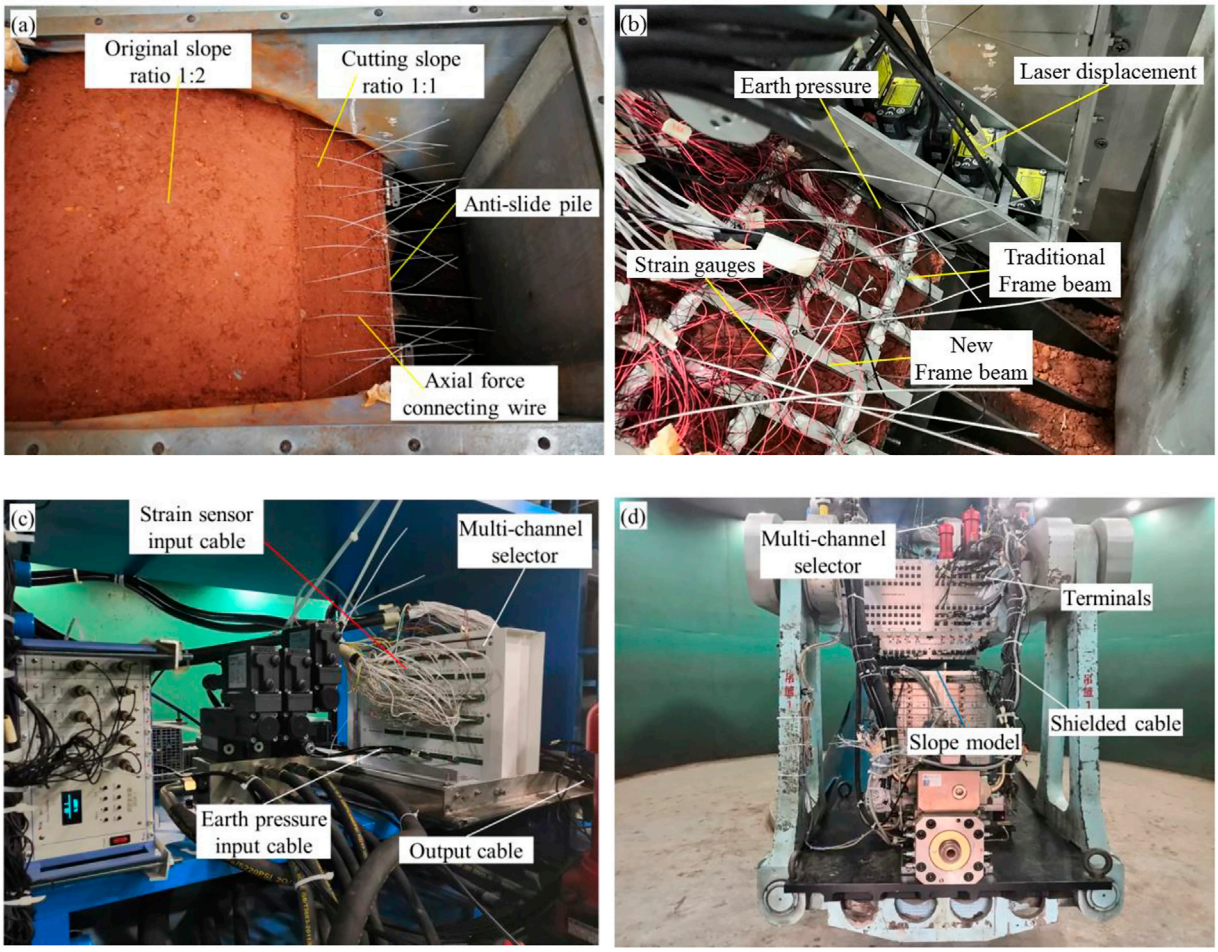

FIGURE 10 | Process photos of the centrifugal model test: **(A)** slope forming and axial installation; **(B)** frame beam and sensor installation; **(C)** connection of various cables and multi-channel acquisition instrument; **(D)** all cable connection renderings.

time for manually disassembling the cable between the sensor and the collector.

APPLICATION OF MULTI-CHANNEL SELECTOR IN CENTRIFUGAL MODEL TEST OF AN ANCHORING SLOPE BY FRAME BEAM

Although the multi-channel acquisition instrument had been well applied in the static pressure model test, its purpose was to expand the data acquisition channel of the existing centrifuge, so it needed to be applied in the centrifuge model test.

Design and Production of Centrifugal Model Test

The purpose was to test the application effect of the multi-channel selector through the centrifugal model test of reinforced cut slopes by anchoring frame beams. The original slope ratio was 1:2, and the first level adopted anti-slide piles with a height of 10 m; the second level slope was supported by anchor cable frame beams with a slope height of 8 m and a slope ratio of 1:1. The surface layer of the slope was red clay with a thickness of 11–18 m. The frame beam was a reinforced concrete structure with a size of 0.6 × 0.6 m (width × height). The spacing between its strings and beams was 3 m, and the length was 9 m as a unit.

Combining various constraints, the scale of this centrifugal model was $n = 70$. The slope model and anchoring frame beam were designed, manufactured, and installed according to **Figure 9**. The model was embedded with 27 axial forces (voltage sensor), 10 earth pressures (voltage sensor), six laser displacements (electron sensor), and 144 strain gauges (strain sensor). And a total of 187 sets of data needed to be collected.

Although the data acquisition system was configured with 64 channels, each channel could only collect the sensor signal of the corresponding signal category, not any signal. For example, if an electron current sensor or strain sensor was plugged into a voltage

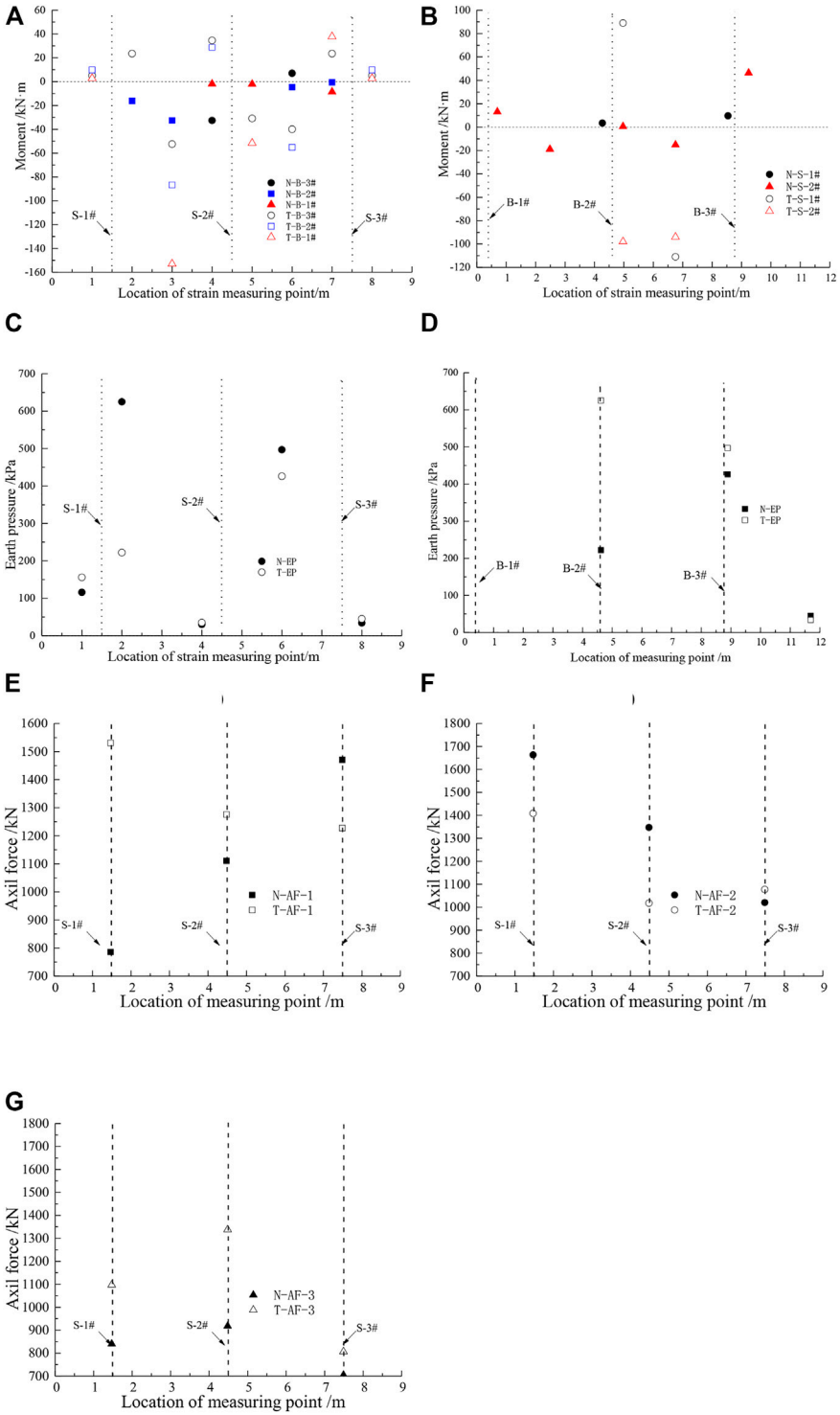

FIGURE 11 | Moment of frame beam: **(A)** beams, **(B)** strings; earth pressure: the bottom of the **(C)** beam, **(D)** string and axial force of the anchor cable: **(E)** 1#, **(F)** 2#; **(G)** 3#.

channel, the signal data obtained was wrong. According to the number and type of sensors, the number of times to collect data of axial force, earth pressure, displacement, and strain was three, one, one, and nine, respectively. In order to obtain all sensor data, it was determined that the maximum number of data collection was nine. The number of sensors and the group collection scheme

are shown in **Table 3**. Therefore, the signals of 187 sensors were connected to the data acquisition system through a multi-channel selector. The model making, sensor installation, and cable connection are shown in **Figure 10**.

Analysis of Centrifugal Model Test

When the centrifuge rotated to the target acceleration of 70 g, the sensor signal data were collected according to the above-mentioned collection scheme. As the laser displacement gauge exceeded the measurement range and some strain gauges were disconnected, the data for 21 axial forces, 10 earth pressures, and 103 strain gauges were obtained. **Figure 11** shows the moment of the frame beam, the earth pressure at the bottom of the beam, and the axial force of the anchor cable.

The results of the centrifugal test model for the moment of the frame beams in **Figures 11A,B** show that the moment in the length direction of the entire beam cannot be described intuitively and accurately, due to varying degrees of damage and abnormality at the measuring points on the beams in the test. However, the strain gauges on the frame beams are arranged symmetrically, and the distribution of the moment along the length of the beam can be described intuitively and accurately based on the existing test results of the measuring points. Beam 1# between the two adjacent anchor cables, that is, the beam at the mid-span section of the beam body is subjected to a greater negative moment than beams 2# and 3#, which is expressed as beam 1#> 2#> 3#. The moment of the frame beams gradually decreases along with the increase in the height of the slope, that is, the top of the frame beam is the smallest and the bottom is the largest. In the moments of the transverse and longitudinal beam sections of the hinged fabricated anchor cable frame beams and the moments of the transverse and longitudinal beam sections of the traditional frame beams, it is found that the positive and negative moments on each section of the traditional frame beams are greater than those of the hinged fabricated anchor cable frame beams. It means that the new structure can use smaller size or reinforcement to achieve the same supporting effect as the traditional structure.

Similarly, **Figures 11C,D** are the results of the distribution of the bottom soil pressure data of the hinged-type fabricated anchor cable frame beam and the traditional frame beam cross beam and longitudinal beam. It can be seen from **Figure 11C** that at the same horizontal longitudinal beam position, the soil pressure in the middle section of the beam is expressed as: the soil pressure at the bottom of the traditional frame beam is greater than the bottom soil pressure of the hinged-type fabricated anchor frame beam, and the soil pressure is located in the upper middle of the frame beam longitudinal beam. The pressure is greater than the bottom soil pressure in the middle span of the frame beam longitudinal beam. The soil pressure at the bottom of the beam at the mid-span section of the same horizontal beam is greater than that of the traditional structure. In addition, because there are fewer earth pressure gauges arranged, the data obtained are more discrete, and it is difficult to concretely and accurately reflect the influence of the frame beams on the distribution of earth pressure at the bottom of the beam when the two frame beams support slopes.

The comparison diagram of the axial force of the two structures is shown in **Figures 11E–G**. From the overall trend, it can be concluded that the axial force of the anchor cable of the traditional structure is greater than that of the new structure. The main performance is: beam 1#> beam 2#> beam 3#, that is, the axial force of the anchor cable on the frame beam shows a non-linear decrease along the slope height, with the smallest slope at the top and the largest at the bottom. This is slightly different from the uniform or simple linear distribution of the anchor cable axial force assumed in the design of the frame beam. The actual situation encountered during the centrifugal model test must be considered, especially the difference between the left and right anchor cable axial force changes. It may be caused by the boundary effect. On the other hand, during the centrifugal model test, the structural characteristics of the frame beam, the degree of compaction, the flatness of the slope, the frame beam material, and the specifications of the axial force sensor will have a greater impact on the accuracy of the test data.

CONCLUSIONS

The existing centrifugal data acquisition system had a limited number of channels, and it was impossible to collect test data exceeding the number of channels in a centrifugal model test of an anchoring slope by frame beam. In view of the above shortcomings, the multi-channel selector was proposed, and it was debugged in the centrifugal no-load pre-test, and it was applied in the static pressure model and centrifugal model test. The main findings of this study are summarized as follows.

1) A multi-channel selection module is processed and manufactured through principle design, purchase of components and processing circuit boards, and assembled into a multi-channel selector. It can transform the existing “one-to-one” collection mode into “one-to-many”.
2) In the no-load test of different centrifugal fields of 1–120 g, the multi-channel selector operates stably, and realizes good wireless connection and communication with the remote controller.
3) In the static pressure model test, various sensors were connected to a multi-channel selector and then connected to a data acquisition system. The signals of 162 sensors were collected, stored, and displayed.
4) The multi-channel selector was successful in a 70 g centrifugal model test of an anchoring slope by frame beam. Only 51 channels were used to effectively obtain the signals of 187 sensors. And after the comparative analysis of the measured data, it is concluded that the force of the new structure is better than the traditional structure.

DATA AVAILABILITY STATEMENT

The original contributions presented in the study are included in the article/Supplementary Material, further inquiries can be directed to the corresponding author.

AUTHOR CONTRIBUTIONS

All authors listed have made a substantial, direct, and intellectual contribution to the work and approved it for publication.

FUNDING

National Natural Science Foundation of China (52025085, 51927814, 51878078, 51908070), Training Program for High-level Technical Personnel in Transportation Industry (2018-025), Design Theory, Method and Demonstration of Durability Asphalt Pavement on Heavy-duty Traffic Conditions in Shanghai Area (CTKY-PTRC-2018-003), Science and Technology Innovation Program of Hunan Province (2020RC4048), and the Hunan Provincial Innovation Foundation for Postgraduate (CX 2018B527).

REFERENCES

Amato, G., Eisank, C., Castro-Camilo, D., and Lombardo, L. (2019). Accounting for Covariate Distributions in Slope-Unit-Based Landslide Susceptibility Models. A Case Study in the alpine Environment. *Eng. Geology.* 260, 105237. doi:10.1016/j.enggeo.2019.105237

Broekman, A., Willem Jacobsz, S., Louw, H., Kearsley, E., Gaspar, T., and Da Silva Burke, T. S. (2020). Fly-by-Pi: Open Source Closed-Loop Control for Geotechnical Centrifuge Testing Applications. *HardwareX* 8, e00151. doi:10.1016/j.ohx.2020.e00151

Cao, D.-F., Shi, B., Zhu, H.-H., Inyang, H. I., Wei, G.-Q., and Duan, C.-Z. (2018). A Soil Moisture Estimation Method Using Actively Heated Fiber Bragg Grating Sensors. *Eng. Geology.* 242, 142–149. doi:10.1016/j.enggeo.2018.05.024

Carlà, T., Tofani, V., Lombardi, L., Raspini, F., Bianchini, S., Bertolo, D., et al. (2019). Combination of GNSS, Satellite InSAR, and GBInSAR Remote Sensing Monitoring to Improve the Understanding of a Large Landslide in High alpine Environment. *Geomorphology* 335, 62–75. doi:10.1016/j.geomorph.2019.03.014

Chen, R., Yin, X., Tang, L., and Chen, Y. (2018). Centrifugal Model Tests on Face Failure of Earth Pressure Balance Shield Induced by Steady State Seepage in Saturated sandy silt Ground. *Tunnelling Underground Space Technol.* 81, 315–325. doi:10.1016/j.tust.2018.06.031

Chortis, G., Askarinejad, A., Prendergast, L. J., Li, Q., and Gavin, K. (2020). Influence of Scour Depth and Type on P-Y Curves for Monopiles in Sand under Monotonic Lateral Loading in a Geotechnical Centrifuge. *Ocean Eng.* 197, 106838. doi:10.1016/j.oceaneng.2019.106838

El Sawwaf, M., and Nazir, A. (2006). The Effect of Soil Reinforcement on Pullout Resistance of an Existing Vertical Anchor Plate in Sand. *Comput. Geotechnics* 33, 167–176. doi:10.1016/j.compgeo.2006.04.001

Ge, S., Zu-yu, C., Yuan, L., Ming-shou, Z., and Jian-yu, W. (2017). Experimental and Numerical Investigation of the Centrifugal Model for Underwater Explosion Shock Wave and Bubble Pulsation. *Ocean Eng.* 142, 523–531. doi:10.1016/j.oceaneng.2017.04.035

Ghandil, M., Behnamfar, F., and Vafaeian, M. (2016). Dynamic Responses of Structure-Soil-Structure Systems with an Extension of the Equivalent Linear Soil Modeling. *Soil Dyn. Earthquake Eng.* 80, 149–162. doi:10.1016/j.soildyn.2015.10.014

Gourc, J. P., Camp, S., Viswanadham, B. V. S., and Rajesh, S. (2010). Deformation Behavior of clay Cap Barriers of Hazardous Waste Containment Systems: Full-Scale and Centrifuge Tests. *Geotextiles and Geomembranes* 28, 281–291. doi:10.1016/j.geotexmem.2009.09.014

Herbert, D. M., Gardner, D. R., Harbottle, M., Thomas, J., and Hughes, T. G. (2011). The Development of a New Method for Testing the Lateral Load Capacity of Small-Scale Masonry walls Using a Centrifuge and Digital Image Correlation. *Construction Building Mater.* 25, 4465–4476. doi:10.1016/j.conbuildmat.2011.02.002

Hongze, Z., Dongyu, W., Ming, M., and Kaihui, Z. (2020). Parameter Inversion and Location Determination of Evolutionary Weak Layer for Open-Pit Mine Slope. *Int. J. Coal Sci. Technol.* 7, 714–724. doi:10.1007/s40789-020-00337-w

Kreczmer, K., Dąbski, M., and Zmarz, A. (2021). Terrestrial Signature of a Recently-Tidewater Glacier and Adjacent Periglaciation, Windy Glacier (South Shetland Islands, Antarctic). *Front. Earth Sci.* 9. doi:10.3389/feart.2021.671985

Kuang, K. S. C., Tan, C. Y., Chew, S. H., and Quek, S. T. (2011). Monitoring of Large Strains in Submerged Geotextile Tubes Using Plastic Optical Fibre Sensors. *Sensors Actuators A: Phys.* 167, 338–346. doi:10.1016/j.sna.2011.03.013

Kutter, B. L., Carey, T. J., Hashimoto, T., Zeghal, M., Abdoun, T., Kokkali, P., et al. (2018). LEAP-GWU-2015 Experiment Specifications, Results, and Comparisons. *Soil Dyn. Earthquake Eng.* 113, 616–628. doi:10.1016/j.soildyn.2017.05.018

Li, J., Wang, X., Guo, Y., and Yu, X. (2019). Vertical Bearing Capacity of the Pile Foundation with Restriction Plate via Centrifuge Modelling. *Ocean Eng.* 181, 109–120. doi:10.1016/j.oceaneng.2019.04.026

Lin, Y.-L., Li, Y.-X., Yang, G.-L., and Li, Y. (2017). Experimental and Numerical Study on the Seismic Behavior of Anchoring Frame Beam Supporting Soil Slope on Rock Mass. *Soil Dyn. Earthquake Eng.* 98, 12–23. doi:10.1016/j.soildyn.2017.04.008

Lin, Y.-L., Cheng, X.-M., Yang, G.-L., and Li, Y. (2018). Seismic Response of a Sheet-Pile Wall with Anchoring Frame Beam by Numerical Simulation and Shaking Table Test. *Soil Dyn. Earthquake Eng.* 115, 352–364. doi:10.1016/j.soildyn.2018.07.028

Liu, H., Wang, X., and Song, E. (2011). Reinforcement Load and Deformation Mode of Geosynthetic-Reinforced Soil Walls Subject to Seismic Loading during Service Life. *Geotextiles and Geomembranes* 29, 1–16. doi:10.1016/j.geotexmem.2010.06.003

Ng, C. W. W., Li, X. S., Van Laak, P. A., and Hou, D. Y. J. (2004). Centrifuge Modeling of Loose Fill Embankment Subjected to Uni-Axial and Bi-Axial Earthquakes. *Soil Dyn. Earthquake Eng.* 24, 305–318. doi:10.1016/j.soildyn.2003.12.002

Pan, W., Pan, W., Luo, J., Fan, L., Li, S., and Erdenebileg, U. (2020). Slope Stability of Increasing Height and Expanding Capacity of South Dumping Site of Hesgoula Coal Mine: A Case Study. *Int. J. Coal Sci. Technol.* 8, 427–440. doi:10.1007/s40789-020-00335-y

Rotta Loria, A. F., Gunawan, A., Shi, C., Laloui, L., and Ng, C. W. W. (2015). Numerical Modelling of Energy Piles in Saturated Sand Subjected to Thermo-Mechanical Loads. *Geomechanics Energ. Environ.* 1, 1–15. doi:10.1016/j.gete.2015.03.002

Sabagh, M., and Ghalandarzadeh, A. (2020). Centrifugal Modeling of Continuous Shallow Tunnels at Active Normal Faults Intersection. *Transportation Geotechnics* 22, 100325. doi:10.1016/j.trgeo.2020.100325

Sahare, A., Tanaka, Y., and Ueda, K. (2020). Numerical Study on the Effect of Rotation Radius of Geotechnical Centrifuge on the Dynamic Behavior of Liquefiable Sloping Ground. *Soil Dyn. Earthquake Eng.* 138, 106339. doi:10.1016/j.soildyn.2020.106339

Shen, C., Bo, J., Qi, W., Zhang, X., Huang, J., and Qiao, F. (2020). Analysis of the Surface Rupture Process of Strong Earthquakes Based on Centrifuge Tests. *Soil Dyn. Earthquake Eng.* 136, 106239. doi:10.1016/j.soildyn.2020.106239

Shi, K., Wu, X., Liu, Z., and Dai, S. (2019). Coupled Calculation Model for Anchoring Force Loss in a Slope Reinforced by a Frame Beam and Anchor Cables. *Eng. Geology.* 260, 105245. doi:10.1016/j.enggeo.2019.105245

Thusyanthan, N. I., Madabhushi, S. P. G., and Singh, S. (2007). Tension in Geomembranes on Landfill Slopes Under Static and Earthquake Loading-Centrifuge Study. *Geotextiles and Geomembranes* 25, 78–95. doi:10.1016/j.geotexmem.2006.07.002

Ueda, K., Sawada, K., Wada, T., Tobita, T., and Iai, S. (2019). Applicability of the Generalized Scaling Law to a Pile-Inclined Ground System Subject to Liquefaction-Induced Lateral Spreading. *Soils and Foundations* 59, 1260–1279. doi:10.1016/j.sandf.2019.05.005

Viswanadham, B. V. S., and König, D. (2009). Centrifuge Modeling of Geotextile-Reinforced Slopes Subjected to Differential Settlements. *Geotextiles and Geomembranes* 27, 77–88. doi:10.1016/j.geotexmem.2008.09.008

Wang, X., Zeng, X., and Li, J. (2019). Vertical Performance of Suction Bucket Foundation for Offshore Wind Turbines in Sand. *Ocean Eng.* 180, 40–48. doi:10.1016/j.oceaneng.2019.03.049

Wang, Z.-F., Shen, S.-L., Modoni, G., and Zhou, A. (2020). Excess Pore Water Pressure Caused by the Installation of Jet Grouting Columns in clay. *Comput. Geotechnics* 125, 103667. doi:10.1016/j.compgeo.2020.103667

Weng, X., Sun, Y., Yan, B., Niu, H., Lin, R., and Zhou, S. (2020). Centrifuge Testing and Numerical Modeling of Tunnel Face Stability Considering Longitudinal Slope Angle and Steady State Seepage in Soft Clay. *Tunnelling Underground Space Technol.* 101, 103406. doi:10.1016/j.tust.2020.103406

Yang, X., Zeng, X., Wang, X., Berrila, J., and Li, X. (2019). Performance and Bearing Behavior of Monopile-Friction Wheel Foundations under Lateral-Moment Loading for Offshore Wind Turbines. *Ocean Eng.* 184, 159–172. doi:10.1016/j.oceaneng.2019.05.043

Yao, Y., Ni, J., and Li, J. (2021). Stress-dependent Water Retention of Granite Residual Soil and its Implications for Ground Settlement. *Comput. Geotechnics* 129, 103835. doi:10.1016/j.compgeo.2020.103835

Zeghal, M., Goswami, N., Kutter, B. L., Manzari, M. T., Abdoun, T., Arduino, P., et al. (2018). Stress-strain Response of the LEAP-2015 Centrifuge Tests and Numerical Predictions. *Soil Dyn. Earthquake Eng.* 113, 804–818. doi:10.1016/j.soildyn.2017.10.014

Zhang, J., Li, F., Zeng, L., Peng, J., and Li, J. (2020a). Numerical Simulation of the Moisture Migration of Unsaturated clay Embankments in Southern China Considering Stress State. *Bull. Eng. Geol. Environ.* 80, 11–24. doi:10.1007/s10064-020-01916-6

Zhang, J., Peng, J., Zhang, A., and Li, J. (2020b). Prediction of Permanent Deformation for Subgrade Soils Under Traffic Loading in Southern China. *Int. J. Pavement Eng.*, 1–10. doi:10.1080/10298436.2020.1765244

Zhang, J., Zhang, A., Huang, C., Yu, H., and Zhou, C. (2021). Characterising the Resilient Behaviour of Pavement Subgrade with Construction and Demolition Waste under Freeze-Thaw Cycles. *J. Clean. Prod.* 300, 126702. doi:10.1016/j.jclepro.2021.126702

Zhang, S., Ronald, P., and Zhang, J. (2021). Three-dimensional frequency-domain Green's functions of a finite fluid-saturated soil layer underlain by rigid bedrock to interior loadings. *Int. J. Geomech.* doi:10.1061/(ASCE)GM.1943-5622.0002235

Zheng, Y., Chen, C., Liu, T., Zhang, H., Xia, K., and Liu, F. (2018). Study on the Mechanisms of Flexural Toppling Failure in Anti-inclined Rock Slopes Using Numerical and Limit Equilibrium Models. *Eng. Geology.* 237, 116–128. doi:10.1016/j.enggeo.2018.02.006

Zheng, Y., Chen, C., Liu, T., and Ren, Z. (2021a). A New Method of Assessing the Stability of Anti-Dip Bedding Rock Slopes Subjected to Earthquake. *Bull. Eng. Geol. Environ.* 80, 3693–3710. doi:10.1007/s10064-021-02188-4

Zheng, Y., Wang, R., Chen, C., Sun, C., Ren, Z., and Zhang, W. (2021b). Dynamic Analysis of Anti-Dip Bedding Rock Slopes Reinforced by Pre-stressed Cables Using Discrete Element Method. *Eng. Anal. Boundary Elem.* 130, 79–93. doi:10.1016/j.enganabound.2021.05.014

Zhou, X., Wei, P., Fu, X., Li, L., and Xue, X. (2021). Dynamic Process and Mechanism of the Catastrophic Taihongcun Landslide Triggered by the 2008 Wenchuan Earthquake Based on Field Investigations and Discrete Element Method Simulations. *Front. Earth Sci.* 9, 710031. doi:10.3389/feart.2021.710031

Conflict of Interest: Author JZ and HW were employed by Changsha University of Science and Technology in 2017 to 2020. They declare that the research was conducted in the absence of any commercial or financial relationships.

The remaining authors declare that the research was conducted in the absence of any commercial or financial relationships that could be construed as a potential conflict of interest.

Publisher's Note: All claims expressed in this article are solely those of the authors and do not necessarily represent those of their affiliated organizations, or those of the publisher, the editors and the reviewers. Any product that may be evaluated in this article, or claim that may be made by its manufacturer, is not guaranteed or endorsed by the publisher.

frontiers in Earth Science

ORIGINAL RESEARCH
published: 12 October 2021
doi: 10.3389/feart.2021.766524

Experimental Investigation of the Outburst Discharge of Landslide Dam Overtopping Failure

Mingjun Zhou[1,2], *Zhenming Shi*[1,2], *Gordon G. D. Zhou*[3,4], *Kahlil Fredrick E. Cui*[3,4]* and *Ming Peng*[1,2]

[1]Key Laboratory of Geotechnical and Underground Engineering of Ministry of Education, Tongji University, Shanghai, China, [2]Department of Geotechnical Engineering, College of Civil Engineering, Tongji University, Shanghai, China, [3]Key Laboratory of Mountain Hazards and Earth Surface Process, Institute of Mountain Hazards and Environment, Chinese Academy of Sciences, Chengdu, China, [4]University of Chinese Academy of Sciences, Beijing, China

Research on the factors and mechanisms that influence outburst floods are essential for estimating outflow hydrographs and the resulting inundation. In this study, large flume tests are conducted to investigate the effects of the upstream inflow and the presence of loose erodible deposits on the breaching flow and the subsequent outburst floods. Experimental results reveal that hydrographs of the breaching flow and outburst flood can be divided into three stages where each stage is separated by inflection points and peak discharges. It is found that the larger the inflow discharge, the larger the peak discharge of the outburst flood and the shorter the time needed to reach the peak and inflection discharges of the outburst flood. The breaching flow decreases along the longitudinal direction at rates that increase with the inflow discharge. The ratio between the length of the upstream dam shoulder and the dam width is inversely related to the ratio of the outburst discharge to inflow discharge. We also show that the presence of loose deposits at the dam toe can amplify the peak discharge of outburst flood by increasing the solids content of the water flow.

Keywords: landslide dam, overtopping failure, inflow discharge, loose deposits, breaching flow, outburst discharge

OPEN ACCESS

Edited by:
Yun Zheng,
Institute of Rock and Soil Mechanics (CAS), China

Reviewed by:
Qiming Zhong,
Nanjing Hydraulic Research Institute, China
Tingkai Nian,
Dalian University of Technology, China

***Correspondence:**
Kahlil Fredrick E. Cui
kfcui@imde.ac.cn

Specialty section:
This article was submitted to Geohazards and Georisks, a section of the journal Frontiers in Earth Science

Received: *29 August 2021*
Accepted: *23 September 2021*
Published: *12 October 2021*

Citation:
Zhou M, Shi Z, Zhou GGD, Cui KFE and Peng M (2021) Experimental Investigation of the Outburst Discharge of Landslide Dam Overtopping Failure. Front. Earth Sci. 9:766524. doi: 10.3389/feart.2021.766524

INTRODUCTION

Landslide dams are massive blockages of river channels resulting from mass Earth movements (Costa and Schuster, 1988; Casagli et al., 2003) including earthquakes (Zheng H et al., 2021). The structural failure of these dams, oftentimes due to overtopping (Shen et al., 2020a; Shen et al., 2020b; Zheng Y et al., 2021), result to flooding that can lead to casualties and destroy downstream infrastructures (King et al., 1989; Cui et al., 2013; Zhou et al., 2013; Xiong et al., 2020). Outburst flooding events are also agents of large-scale geomorphic change (Fan et al., 2019; Liu et al., 2019; Fan et al., 2020) that influence river evolution over timescales of 10^4–10^5 years in mountain terrains, e.g., Baimakou landslide dam (Korup, 2006; Korup et al., 2010; Walsh et al., 2012; van Gorp et al., 2016; Liu et al., 2018). A better understanding of the flooding induced by landslide dam failure is important for the prediction and mitigation this mountain disaster.

Previous statistical analysis have found that the outburst discharge of landslide dam failure is a function of the dam geometry (dam height) and dammed lake properties (water level, lake volume) (e.g., Kirkpatrick, 1977; Singh and Snorrason, 1984; Costa, 1985; Webby, 1996; Pierce et al., 2010; Peng and Zhang, 2012; Liu et al., 2019). However, landslide dam failure events often occur in

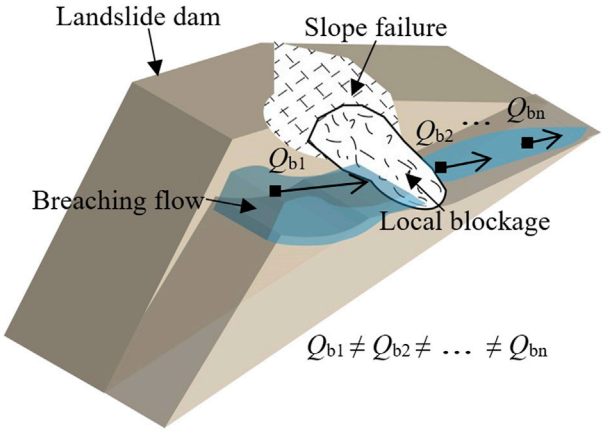

FIGURE 1 | The sketch of the variation of dam breaching discharge along the longitudinal direction during side slope failures.

mountainous areas where field measurement data are difficult to obtain. This is why predictions of outburst flood discharge in the downstream area by statistical analysis significantly deviate (at times in orders of hundreds) from measured data (Zhou M.J. et al., 2019). In order to supplement our knowledge on the mechanisms of landslide dam breaching and its outburst flooding, well-controlled experiments of landslide dam breaching are conducted to understand the effects of the dam geometry (e.g., Davies et al., 2007; Cao et al., 2011; Chen et al., 2012; Walder et al., 2015; Yang et al., 2015; Jiang and Wei, 2020; Zhu et al., 2020), soil material characteristics (e.g., Cao et al., 2011; Jiang et al., 2018b; Xiong et al., 2018; Zhu et al., 2020), initial moisture content (e.g., Chen S.C. et al., 2015; Jiang et al., 2020) and river channel slopes (e.g., Jiang et al., 2020; Zhu et al., 2020). Recently, external boundary effects such as seismic perturbations (e.g., Shi et al., 2014), surging (e.g., Peng et al., 2019) and cascading failures (e.g., Zhou et al., 2013; Shi et al., 2015; Zhou et al., 2015), etc. on landslide dam outburst have also been investigated. However, despite the recent advances in the research of landslide dam breaching, our understanding of the influence of parameters such as the upstream inflow and the presence of loose deposit (Zhou G.G.D. et al., 2019; Zhou M.J. et al., 2019; Jiang et al., 2020) remain incomplete. Field evidence from the Hsialin landslide dam failure (Dong et al., 2011; Li et al., 2011) and Zhouqu landslide dam cascading failure (Cui et al., 2013) suggest that both of the abovementioned parameters may have important impacts on the peak discharge in the downstream area.

The influence of inflow discharge on the outburst flood cannot be separated from the breaching flow. Breaching flow refers to the water flow at the top of the dam and along the dam's surface while the outburst flood is the flow that reaches the downstream area of the dam. In previous studies, the breaching flow is assumed to be uniform and steady so as to facilitate the rapid assessment of landslide dam disasters (e.g., Chang and Zhang, 2010; Wu, 2013; Chen Z.Y. et al., 2015; Zhong et al., 2018; Zhang et al., 2020; Zhong et al., 2020). In such cases, the change in the flow rate in the dammed reservoir is equivalent to the outburst flood and it will not change along the dam longitudinal direction. In reality however, local blockages resulting from dam surface instabilities may hinder the upstream flow to proceed further downstream (**Figure 1**). This consequently results to inhomogeneous discharge measurements at different points along the dam surface. Furthermore, recent field observations and physical modelling tests also reveal that dam breaching flow are not steady but are turbulent and unsteady (Jiang et al., 2017; Jiang et al., 2020). These observations indicate that the overtopping flow cannot be consistent throughout the entire dam body. Therefore, it is still unclear how the upstream inflow affects the spatial evolution of the breaching discharge as well as the downstream outburst flood.

The flooding further downstream can also be affected by the presence of loose deposits behind the dam. There are two main ideas on the influence of loose deposit on the outburst discharge. One of which suggests that the loose deposits behind landslide dams serve as a rough contact surface which dissipates the kinetic energy of the water flow, effectively providing resistance to the flow motion thereby slowing it down (Bellos et al., 1992; Wu, 2007; Wu, 2013). Another reasoning is that the entrained loose granular materials increase the flood volume and potential energy, consequently improving the mobility of the solid-fluid mixture flow (Fannin and Wise, 2001; Wang et al., 2003; Breien et al., 2008). Although, bed-sediment entrainment by dry granular avalanches are often accompanied by increased flow-front speeds and further run-out distances (Mangeney et al., 2007), they have limited relevance to sediment flows (Iverson et al., 1997; Iverson et al., 2010) and outburst floods from landslide dam failures. Therefore, it is still unclear how loose deposits behind the dam affects the resulting outburst flood.

In this work, a series of large flume tests are conducted to give a comprehensive perspective of the outburst discharge of landslide dams due to overtopping failure. Specifically, we aim to 1) study the longitudinal evolution of the breach discharge and 2) investigate the effects of different upstream inflows and the presence of loose deposits on the outburst floods. In the succeeding sections, we first detail our experimental set-up, using which we are able to capture a three stage evolution of landslide dam failure. We then present the mechanisms in which the inflow discharge affects the evolution of the breaching flow as well as the influence of the presence of loose deposits, located at the dam toe, on the outburst floods. Results of this work are expected to improve the estimation of outflow hydrographs which are useful for early warning and risk mitigation in mountainous areas.

MATERIALS AND METHODS

Experimental Setup and Instrumentation

Experimental landslide dams are constructed in a large flume in the Dongchuan Debris Flow Observation and Research Station (DDFORS), Dongchuan District, Yunnan Province, China (N 26°14′30″, E103°08′11″). Two sets of tests are conducted: in the first group the inflow discharge is varied from 2.0 $\times 10^{-3}$ m^3/s to 6.9 $\times 10^{-3}$ m^3/s. The main purpose of this group is to evaluate the effects of different initial inflow discharge on the subsequent flow

TABLE 1 | Test program.

Test ID	Upstream inflow Q_{in}($\times 10^{-3}$ m^3/s)	Downstream condition (U/E)
U-Q2.0	2.0	Unerodible bed
U-Q3.0	3.0	
U-Q5.3	5.3	
U-Q6.9	6.9	
E-Q2.0	2.0	Erodible bed
E-Q3.0	3.0	
E-Q5.3	5.3	

evolution and dam failure. The effects of installing an erodible bed on the outburst discharge is studied in the second set of tests in which the inflow discharge is varied from 2.0 $\times 10^{-3}$ m^3/s to 5.3 $\times 10^{-3}$ m^3/s. The details for each modeling test are summarized in **Table 1**.

The flume is a straight concrete channel, inclined at 12° from the horizontal (**Figure 2A**) At one side of the dam, a glass window is installed that allows the observation of the longitudinal dam breach evolution (**Figure 2B**). The glass window is divided into sections with 6 reference lines labelled I, J, K, L, M and N

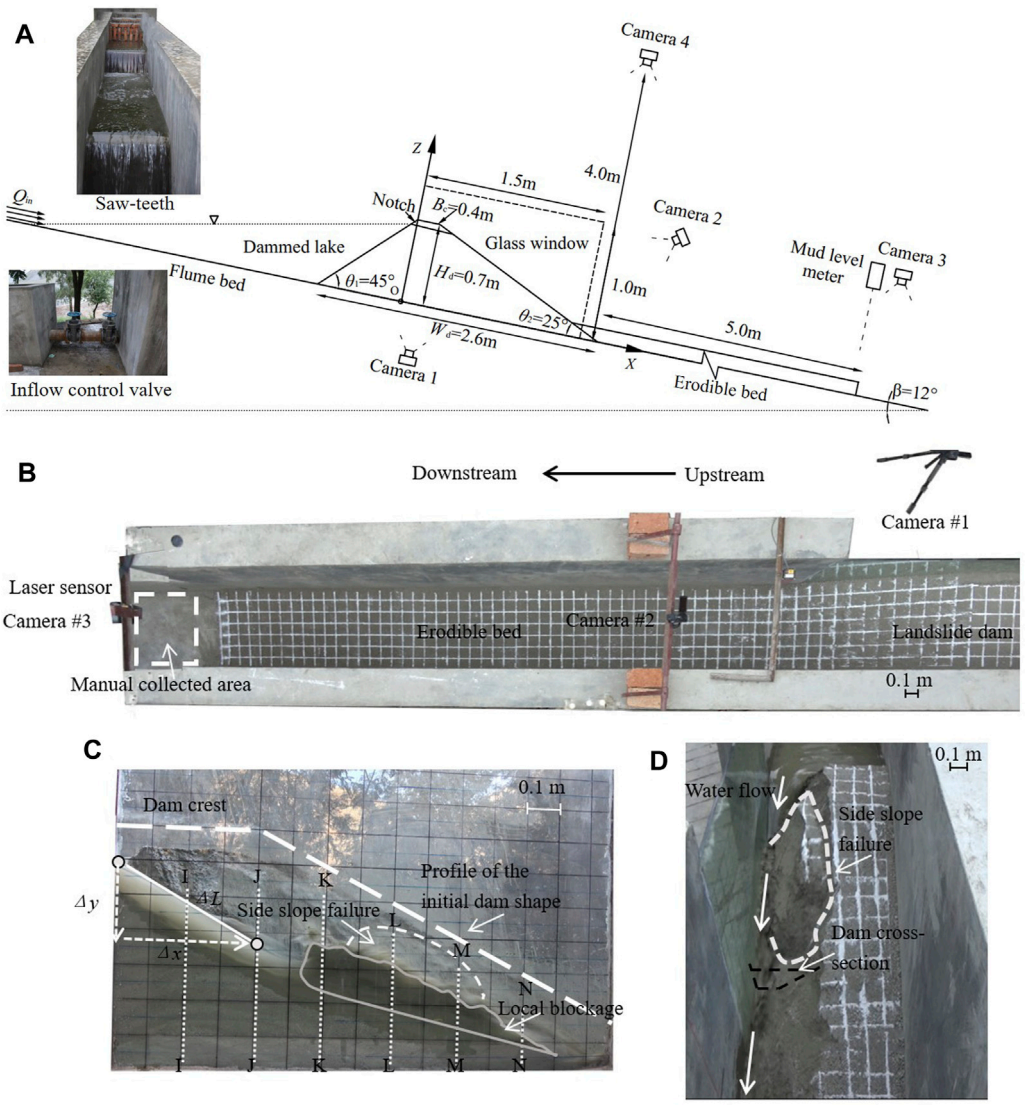

FIGURE 2 | (A) Schematic diagram of the model dam with the exact dimensions **(B)** an illustration of the large debris flow flume in DDFORS (10 m long, 0.7 m wide and 1.4 m deep, inclined at 12° to the horizontal) as viewed from camera #4 **(C)** a side-view from of the model dam as viewed from the side region of the flume from the vantage point of camera #1 **(D)** A front view of the model dam as viewed from the downstream region of the flume by camera #2. The dam, which is built on a concrete floor, is confined by walls 0.7 m apart and 1.4 m high. In erodible bed tests, a 0.2 m thick, 5 m long flat pile is connected to the dam toe.

(**Figure 2C**) where *Introduction* Section is 0.2 m away from the upstream dam crest. Each subsequent section is 0.2 m away from the previous section. At the lower end of the flume is a manual collection area which is 5 m away from downstream dam toe (**Figure 2A**). A water container, with a capacity of 12 m^3, is connected to the top of the flume through a channel with rows of saw-teeth which serve to minimize turbulence and provide steady inflow for the tests (**Figure 2A**).

To capture the landslide dam breaching and outburst process, four digital video cameras (SONY FDR-AX40, 1440 × 1080 pixels, 25 fps) and a laser sensor (Leuze, ODSL 30/V-3V0 M-S12) with a resolution of ±1 mm are installed above the channel. The velocity of a tracer particle is measured as the total distance it has travelled within a pre-defined frame of reference (Δx) divided by the total time it takes to span the said of reference frame (**Figure 2C**). Camera 1 is positioned on the free side of the glass panel, set to record the velocity v_b and flow depth d_b of the breaching flow (**Figure 2C**). Camera 2 is used to capture the cross-sectional evolution of the landslide dam by monitoring the change of the cross-sectional width w_b (**Figure 2D**). Camera 3 is installed to record the motion of tracer particles and calculate the velocity v_{out} of the outburst flood (**Figure 2A**). Camera 4 is placed 4 m above the flume base and records the whole dam failure process (result as shown in **Figure 2B**). A laser sensor, located 5 m away from the downstream dam toe, is used to measure the depth d_{out} of the outburst flood (method reference from Gregoretti et al., 2010; Pickert et al., 2011). The discharge of the breaching flow and outburst flood is calculated from the measured flow depth, velocity and channel width as:

$$Q_i = v_i d_i w_i \quad (1)$$

where the subscript $i = out$ represents outburst flood while $i = b$ denotes breaching flow.

Model Design

Scaling laws play a crucial role in designing physical model tests (Iverson, 2015). For better understanding of the landslide dam failure process which involves grain-fluid mixtures, Peng and Zhang (2012) proposed a set of dimensionless numbers - $\frac{H_d}{W_d}$, $\frac{V_d^{1/3}}{H_d}$ and $\frac{V_l^{1/3}}{H_d}$ - that consider the influence of the dammed lake volume (V_l) (Costa and Schuster, 1988), the landslide dam height (H_d) and the volume of the landslide dam (V_d) (Korup, 2004). The validity of these dimensionless parameters has been verified by Zhou M.J. et al. (2019). The ratio of the dam height to its width $\frac{H_d}{W_d}$ defines the average slope erosion. The ratio between the cubic root of the dam volume and height, $\frac{V_d^{1/3}}{H_d}$ is known as the dam shape coefficient and reflects the amount of granular material that can be entrained. The lake shape coefficient is the ratio between the cube root of the water volume and the dam height $\frac{V_l^{1/3}}{H_d}$ and defines the potential lake volume. **Table 2** shows that the geometry of the modeled landslide dam fall within the acceptable range of values estimated from natural landslide dams. The last column of **Table 2** lists specific landslide dam cases whose dimensionless constants are close to those obtained for the experimental dams (Diexi landslide dam (1936); Xiaogangjian landslide dam (2008); Donghekou landslide dam (2008)). It can therefore be said that the geometry of these modelled dams can be considered to represent real landslide dams.

TABLE 2 | Geometric characteristics of the model landslide dams.

Parameter	Value	Real case range	Geometrically identical cases
H_d/W_d	0.269	0.002–3.000	Diexi landslide dam (0.196) Donghekou landslide dam (0.267)
$V_d^{1/3}/H_d$	1.289	1.074–39.782	Xiaogangjian landslide dam (1.260) Huoshigou landslide dam (1.116)
$V_l^{1/3}/H_d$	1.228	0.934–30.039	Macaotan landslide dam (1.400) Huoshigou landslide dam (0.954)

Note: Data collected from Costa and Schuster, 1988; Korup, 2004; Xu et al., 2009; Yin et al., 2009; Peng and Zhang, 2012.

Granular Material Used in Flume Model Test

To emulate the poorly-sorted soils of natural landslide dams, the granular materials in the Jiangjia Ravine near DDFORS, are used to construct the modeled landslide dams. Particles with diameters larger than 20 mm are removed in all tests (**Figure 3**). The diameters of fine particles (< 0.25 mm) are measured using a Malvern Mastersizer 2000. This device is designed to measure the size of small particles and the distribution of these sizes within a sample using laser diffraction and on known particle size distribution statistics (Malvern Instruments Ltd, 2007). Sediment samples in all experimental sets have mean grain diameters of d_{50} = 0.85 mm (**Figure 3**). The spread of the grain-size distribution is measured to be $\sigma_g = \frac{d_{84}}{d_{16}} = 75$ (Walder,

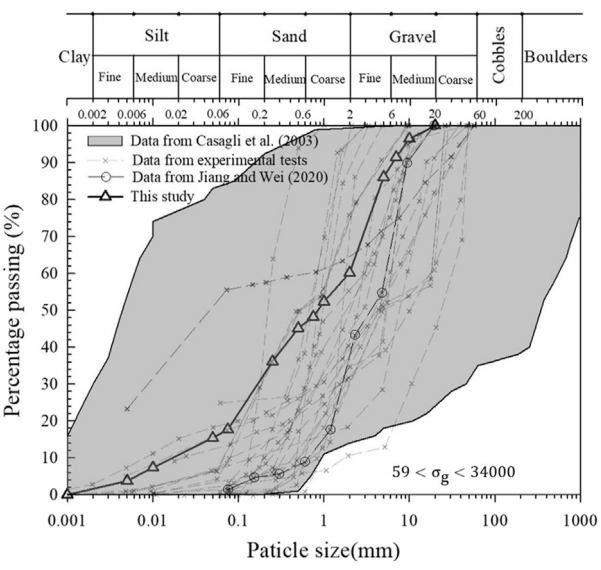

FIGURE 3 | The shaded region is the cumulative grain size distribution of 42 landslide dams in the Northern Apennines (Casagli et al., 2003) and the data points marked as crosses are data from the experimental tests of Yan and Cao, 2009; Cao et al., 2011; Xu et al., 2013; Shi et al., 2014; Yang et al., 2015; Zhou et al., 2015; Jiang et al., 2017; Jiang et al., 2018a; Jiang et al., 2018b; Xiong et al., 2018; Jiang and Wei, 2020; Jiang et al., 2020; Zhu et al., 2020. The solid line represents the grain-size distribution of the modeled landslide dams.

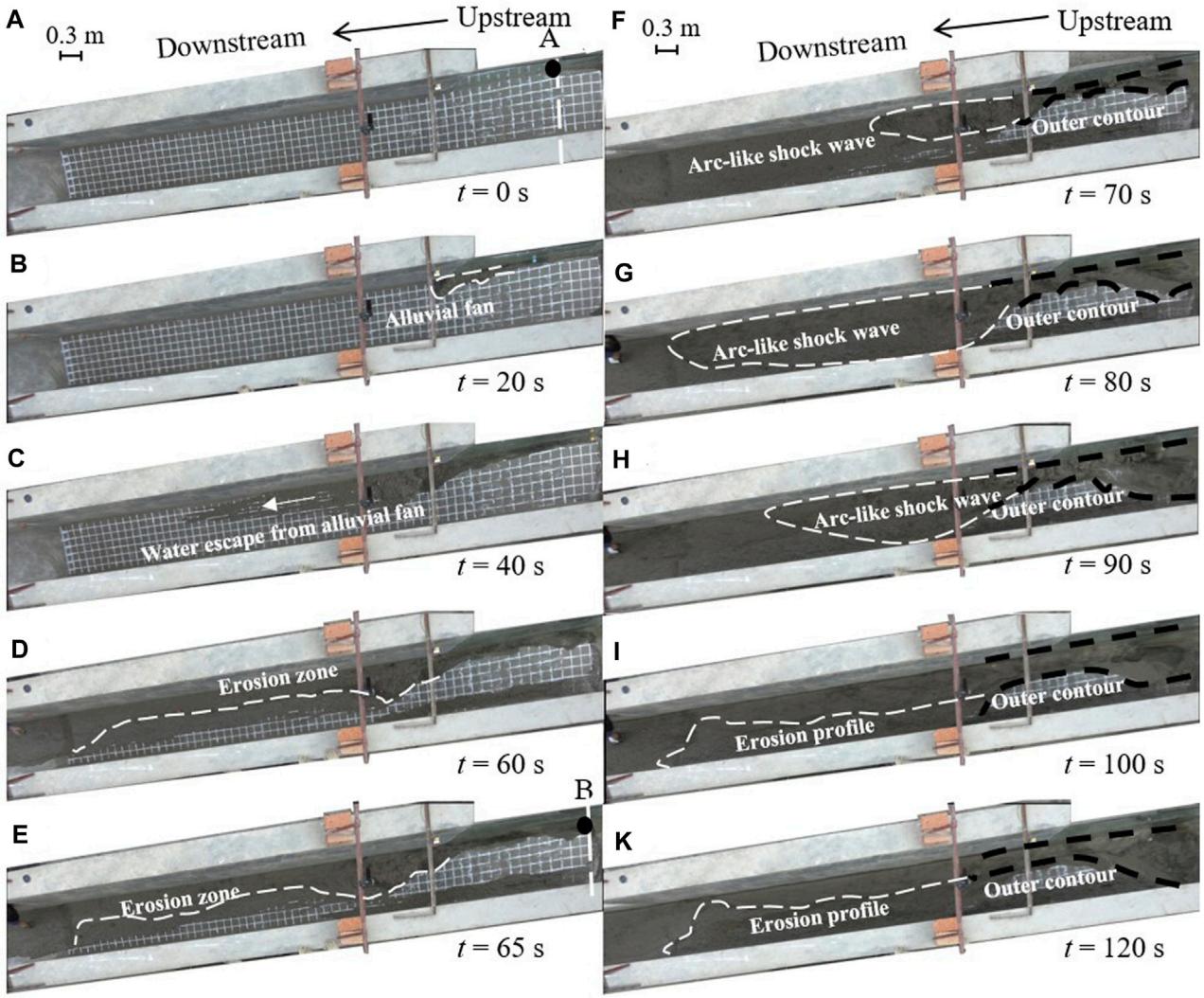

FIGURE 4 | Snapshots of the dam-breaching process (Test No. E-Q3.0). t_0 = 0 s is the moment when water starts to travel along the initial notch and eventually reaches the downstream crest. The grid is 0.1 m × 0.1 m. The dashed lines mark the surface profile of the dam geometry.

2016), which falls between the range (59 and 34,000) obtained for granular materials in real landslide dams (Casagli et al., 2003). The unit weight and friction angle of the solid materials are measured to be ρ_s = 2650 kg/m^3 and φ = 30°respectively, and the initial water content is 6% (Zhou and Ng, 2010). **Figure 3** shows that the grain-size distributions of the modeled landslide dams coincide with those measured from natural dams (Casagli et al., 2003) and other experimental dams used in previous studies (Yan and Cao, 2009; Cao et al., 2011; Xu et al., 2013; Shi et al., 2014; Yang et al., 2015; Zhou et al., 2015; Jiang et al., 2017; Jiang et al., 2018a; Jiang et al., 2018b; Xiong et al., 2018; Jiang and Wei, 2020; Jiang et al., 2020; Zhu et al., 2020).

Dam Construction

The landslide dams are constructed as follows: granular materials are well-mixed and poured from the same height onto the sloping channel. Manual compaction is done to ensure that the void ratio (0.79–0.82) of each layer is consistent with field conditions which are usually in the range of 0.59–1.11 (Chang and Zhang, 2010; Chang et al., 2011). This process is repeated until the desired dam geometry is achieved. The same material, construction process and void ratio are employed for the erodible bed which is 0.2 m thick. After the dam crest was smoothed and leveled, a rectangular notch ($h_0 \times w_0$ = 0.05 m × 0.1 m) is excavated on the dam crest, adjacent to the glass side-wall. This ensures that the overtopping failure starts at the same place every time, guaranteeing the repeatability of the experiments (Hakimzadeh et al., 2014).

A gridded pattern (0.1 m × 0.1 m) is drawn on the dam body using white powder (**Figure 2A**) which helps quantify the development of breaching, downstream erosion and deposition. After dam construction, all the instruments are simultaneously switched on. The water valve is opened and the upstream flow enters the dammed lake. To reduce the effects of seepage or piping on the dam failure process, the water in the reservoir is filled rapidly.

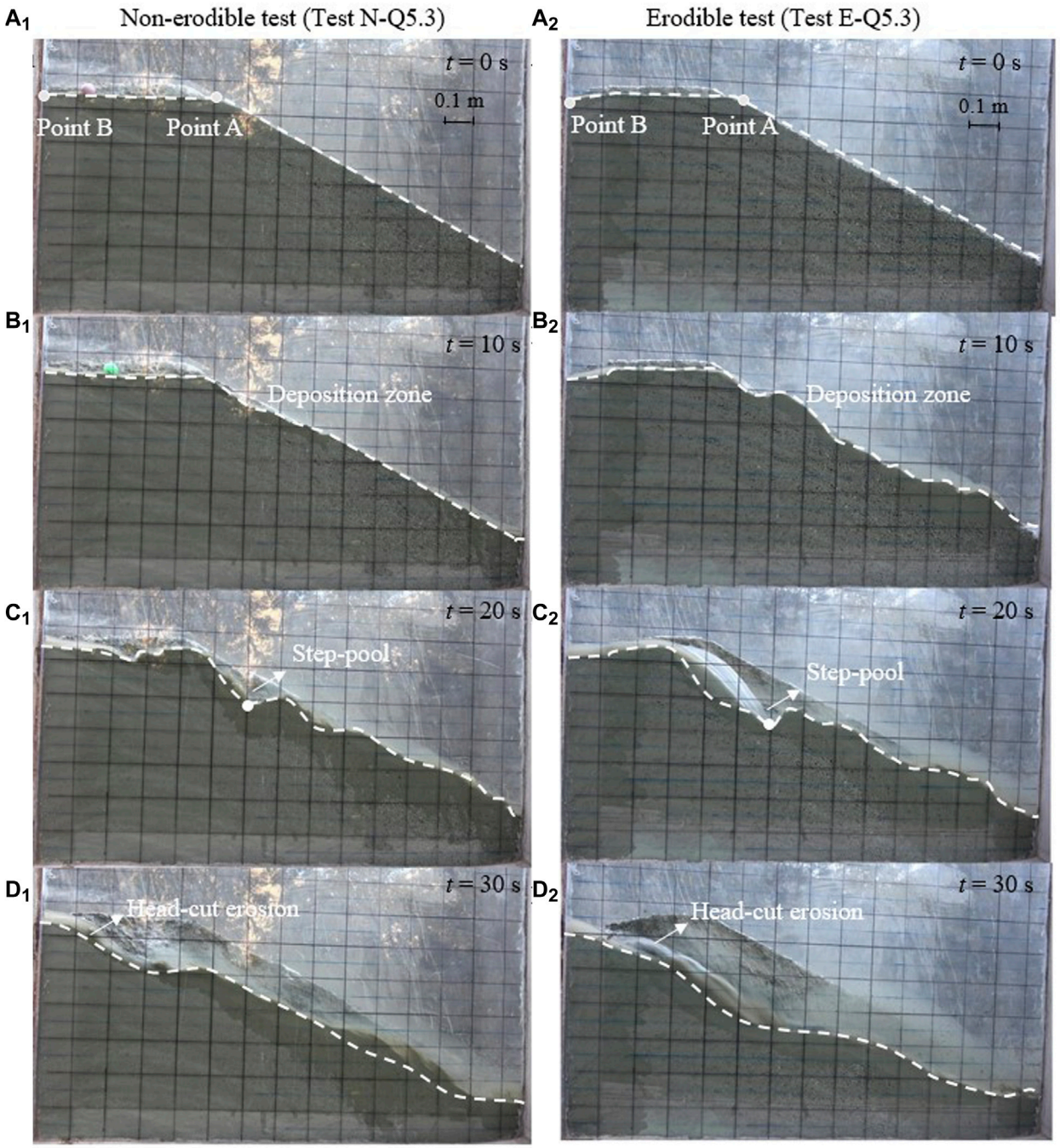

FIGURE 5 | Longitudinal snapshots of the dam-breaching process (Test Nos. N-Q5.3 **left** side and E-Q5.3 **right** side). The grid size on the window is 0.1 m × 0.1 m.

After it is filled to the crest, the inflow is adjusted to a fixed discharge value. As the water starts to flow over the dam crest, tracer particles are dropped into the dammed lake reservoir, throughout the entire failure process, to capture the velocity of the outburst flood as well as the breaching flow. In addition, continuous sampling was adopted during the tests to calculate the changes of the outburst flood density. The density is calculated from the weight and volume of the sampled outburst floods.

RESULTS

General Observations

The rapid change of the hydrodynamic conditions during landslide dam breach makes the process of dam failure very complex. **Figure 4** shows a series of aerial views of test No. E-Q3.0 from Camera 4. The initial time of dam breaching $t = 0$ s is when water starts to travel along the initial notch and

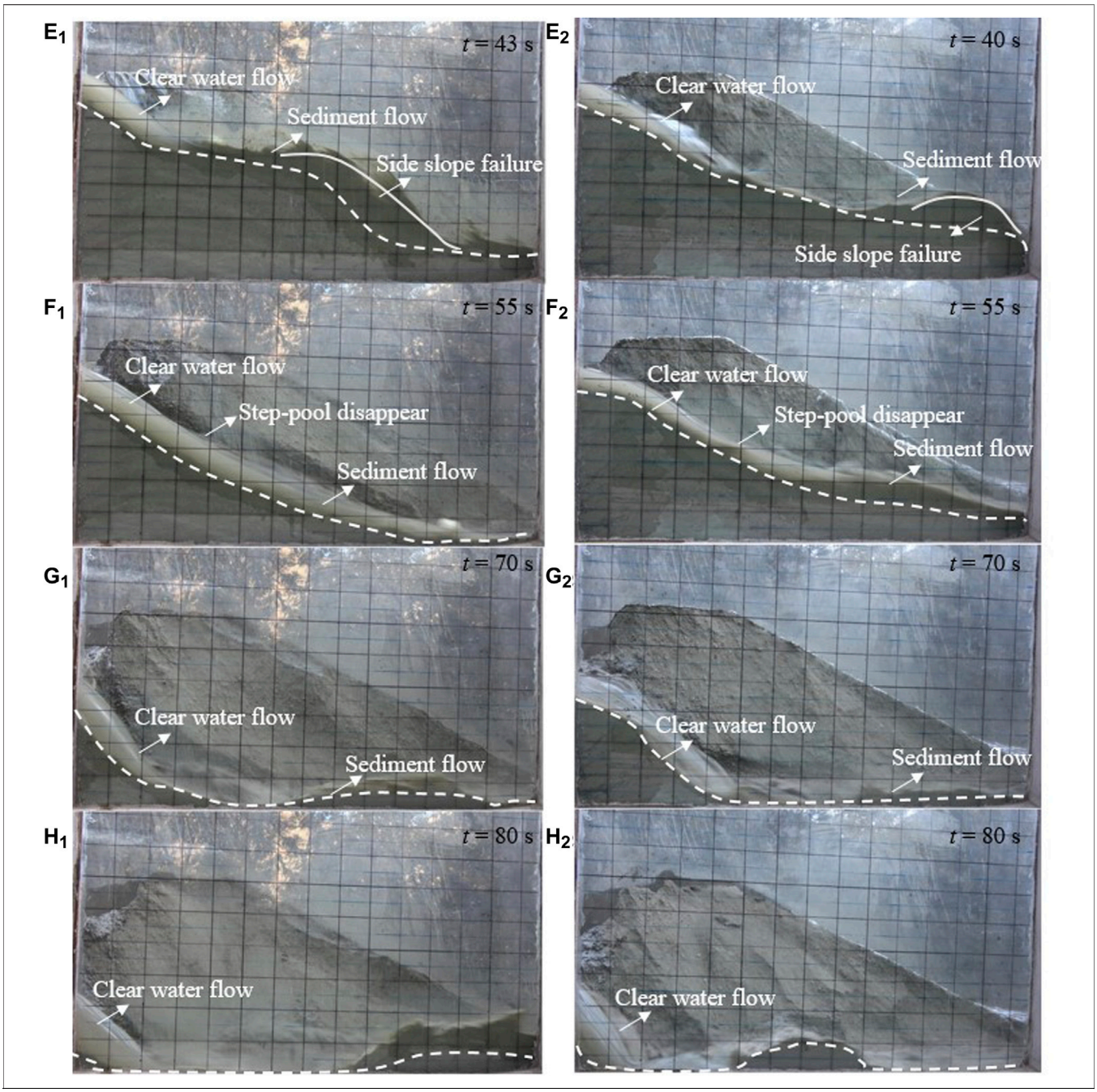

eventually reaches the downstream dam shoulder, Point A (**Figure 4A**). This is where the overtopping failure of the landslide dam initially occurs. At this stage, the water flow is insufficient to erode the soil and most of the sediment are transported only up to the downstream dam slope face, developing into an alluvial fan that advances toward the toe of the dam (**Figure 4B**). The stream eventually incises the alluvial fan, forming a narrow channel which allows the incoming water to flow through fan (**Figure 4C**). Due to the continuous supply upstream, the water flow gradually increases, eroding the loose downstream deposits (**Figure 4D**). **Figure 4E**, shows the erosion of the upstream dam shoulder, point B. In this stage, the outburst flood increases rapidly and non-uniform, arc-like shock waves are frequently observed (**Figures 4F–H**). These turbulent and unsteady flows induce frequent, albeit temporary, localized blockages that effectively widen the dam breach width (**Figures 4F–H**). This indicates that the flow discharge can hardly remain constant along the longitudinal direction. The outer lateral contour of the dam is shaped like an hour glass, wherein the ends are wide and the mid-section is

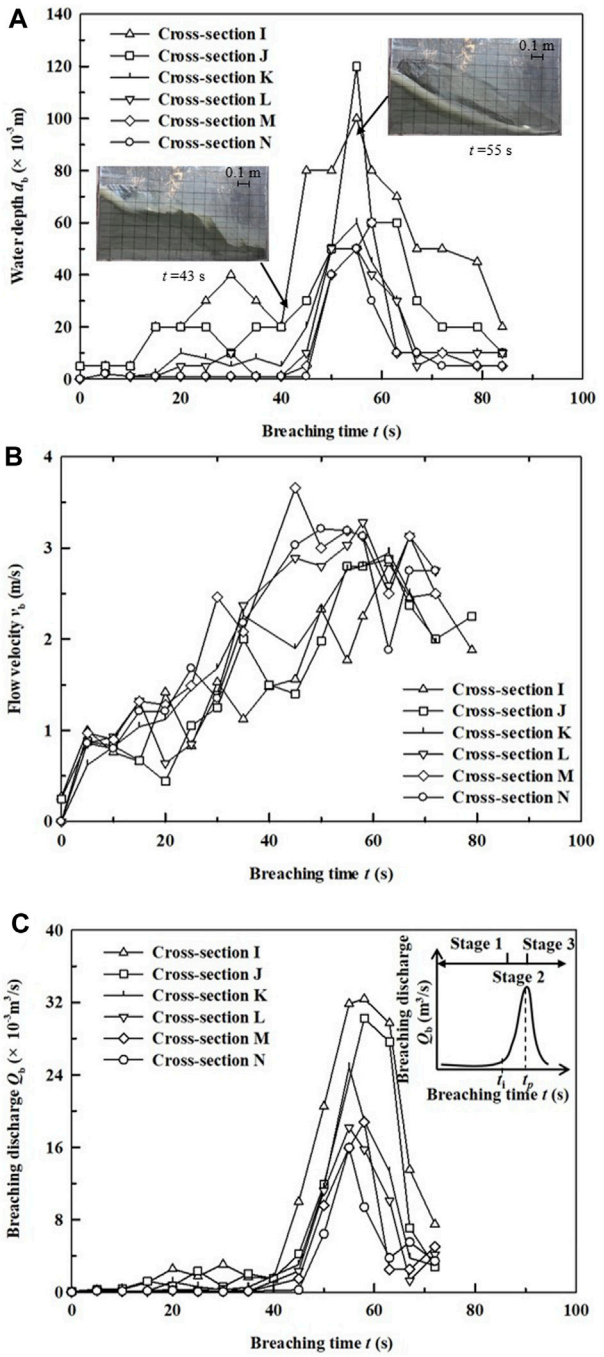

FIGURE 6 | The evolution of the **(A)** depth **(B)** velocity and **(C)** discharge of breaching flow at different dam sections.

narrow (**Figures 4F–K** black line). This is quite different from existing models that assume that the outer contour is linear (Chang and Zhang, 2010; Zhong et al., 2018). Large scale erosion of the downstream loose deposits are also recorded in these stages (**Figures 4F–H**). Finally, the dam breaching process ends when clear water is observed downstream and the breach side slope remains stable (**Figure 4K**).

Longitudinal Evolution of Dam Breaching

Figure 5 (A_1,A_2) show snapshots of the longitudinal dam breach process at t = 0 s of test N-Q5.3 (left side) which has no erodible bed behind the dam and test E-Q5.3 (right side) which has an erodible bed behind the dam respectively. At the initial stage, since the breaching discharge is small, most of the sediment transport is still confined to the area immediately below dam the crest, Point A (**Figure 5**) (B_1,B_2). At around t = 20 s, the formation of erosional step pools (Parker and Izumi, 2000; Walder et al., 2015) is observed in the two set ups at the same location (x = 0.6 m) (**Figure 5**) (C_1,C_2). The upstream migration of these shallow pools, which coalesce into a headcut, lead to the establishment of hydraulic control at the breach crest, an erosional feature that functions as a weir (**Figure 5**) (D_1,D_2). As the upstream inflow continues to supply flowing water, the fine particles are more easily eroded and entrained into the outburst floods, resulting in an increase of suspended particles in the water.

When the erosion point reaches the upstream dam shoulder Point B [t = 43 s in N-Q5.3, and at t = 40 s in test No. E-Q5.3 (**Figure 5**) (E_1, E_2)], the dam crest completely collapses and the water level of the dammed lake quickly decreases as larger amounts of water are released downstream. From this stage, the water flow at the overtopped dam crest is clear but becomes murky and sediment-laden near the dam toe as it entrains soil particles along its path. The step-pools gradually disappear (**Figure 5**) (F_1, F_2) accelerating the erosion process along the dam surface, promoting further side slope failure. The depth of the water starts to decline and the geometry of the sloping bed begins to smoothen out as a result of its exposure to the rapid water flows. This decline in depth continues until the water level in the reservoir is close to the residual dam height (**Figure 5**) (H_1, H_2). At this point, no further side slope failure and erosion occurs. Finally, an almost identical final dam breaching morphology is observed in both sets of experiments (**Figure 5**) (H_1, H_2).

Hydrological Evolution of Dam Breaching Flow

Figure 6 shows representative temporal profiles (test N-Q5.3) of the water depth d_b, flow velocity v_b and breaching discharge Q_b at different sections of the dam. Initially, the breaching flow has not reached the downstream dam slope, so the cross-section of the water depth at the downstream dam slope is close to zero (**Figure 6A**). At later times, d_b at different cross-sections begin to gradually increase. Sudden increase in the values of d_b, similar to that in **section 1** at t = 30 s, are due to the short-term formation of step-pools (**Figure 5**) (D_1). At around t = 43 s the upstream shoulder is eroded [refer to **Figure 5** (E_1)] resulting in the rapid increase of d_b. At t = 55 s, the water depth at different sections reach peak values (**Figure 6A**). Thereafter, the flow height rapidly declines prior to finally stabilizing at a steady, shallow water depth. **Figure 6B** shows that $v_b$at the different dam sections rapidly increase, reaching values greater than 3 m/s. At early stages, the velocity difference between the different sections is noticeably small. The discrepancies of v_b at the different sections is greatest when v_b is maximum.

Figure 6C shows the evolution of discharge of the breaching flow. The trend of the breaching discharge is identical to that of the water depth: the flow initially increases slowly from zero, followed by a rapid increase up to a peak discharge value before decreasing. The temporal evolution of the discharge can be divided into three stages separated by inflection points, i.e. abrupt changes in the values of Q_b. The first

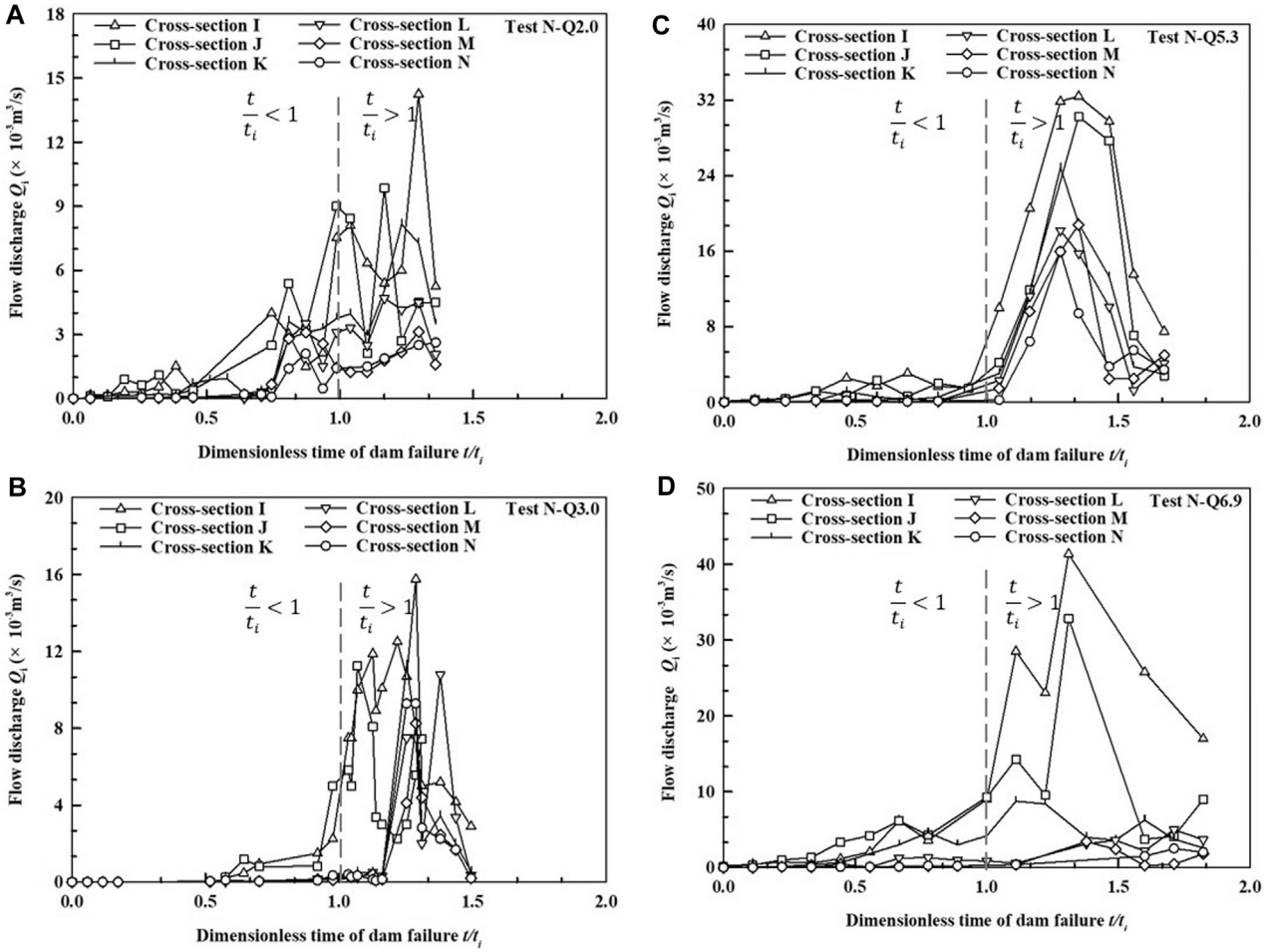

FIGURE 7 | Hydrographs of the dam-breaching flow discharge at different dam sections for different inflow discharges **(A)** Q_{in} = 2.0 × 10^{-3} m^3/s **(B)** Q_{in} = 3.0 × 10^{-3} m^3/s **(C)** Q_{in} = 5.3 × 10^{-3} m^3/s **(D)** Q_{in} = 6.9 × 10^{-3} m^3/s.

inflection point t_i, at the different sections, is at ~ 43 s equivalent to the time at which the upstream shoulder is eroded (refer to **Figure 5**). The second inflection point is the time at which the peak discharge t_p is measured t ~ 55 s. This three-stage evolution model is consistent with the observations of Zhou G.G.D. et al. (2019) on the outburst flood evolution measured downstream of the landslide dam. Stage 1 is characterized by the rapid increase of the breaching flow velocity and the slow but steady increase of the water depth and discharge. In Stage 2 the breaching flow depth and discharge rapidly increase up until the peak value. In Stage 3, the breaching flow and discharge diminish whereas the flow velocity is maintained at a constant large value.

Hydrological Evolution of Breaching Flow Along Longitudinal Direction

Hydrological Evolution of Breaching Flow

Figure 7 shows the breaching hydrological evolution of landslide dam overtopping failure process, in dimensionless time (t/t_i) without an erodible bed. The value of breaching discharge at different cross-section is different especially during rapid stages (Stages 2 and 3). The evolution of both the breaching flow is consistent at the different sections wherein values gently increase first in Stage 1 (before t/t_i = 1) followed by a sudden positive change in Stage 2 (after t/t_i = 1), and thereafter the outburst flood attenuates in Stage 3. Note that, because side slope instabilities mainly occur after Stage 2, the change of the whole overtopping flow rate fluctuates greatly from during this stage in all tests (**Figure 7**). In addition, the maximum overtopping breaching discharge is usually obtained at the front of the dam body under different Q_{in} (**Figure 7**). Moreover, the peak breaching discharge increases from 14.3 × 10^{-3} m^3/s to 41.3 × 10^{-3} m^3/s as the upstream inflow is also increased from 2.0 × 10^{-3} m^3/s to 6.9 × 10^{-3} m^3/s (**Figure 7**). It can be seen in **Figure 6A**, that the breaching discharge significantly varies along the flow direction due to the influence of the local topography, consequently resulting in a constantly changing streamline. The different breaching flows measured at different cross-sections of the dam all support the theory that the overtopping flow discharge is not even along the flow body (e.g., Jiang et al., 2017; Jiang et al., 2020), which is different

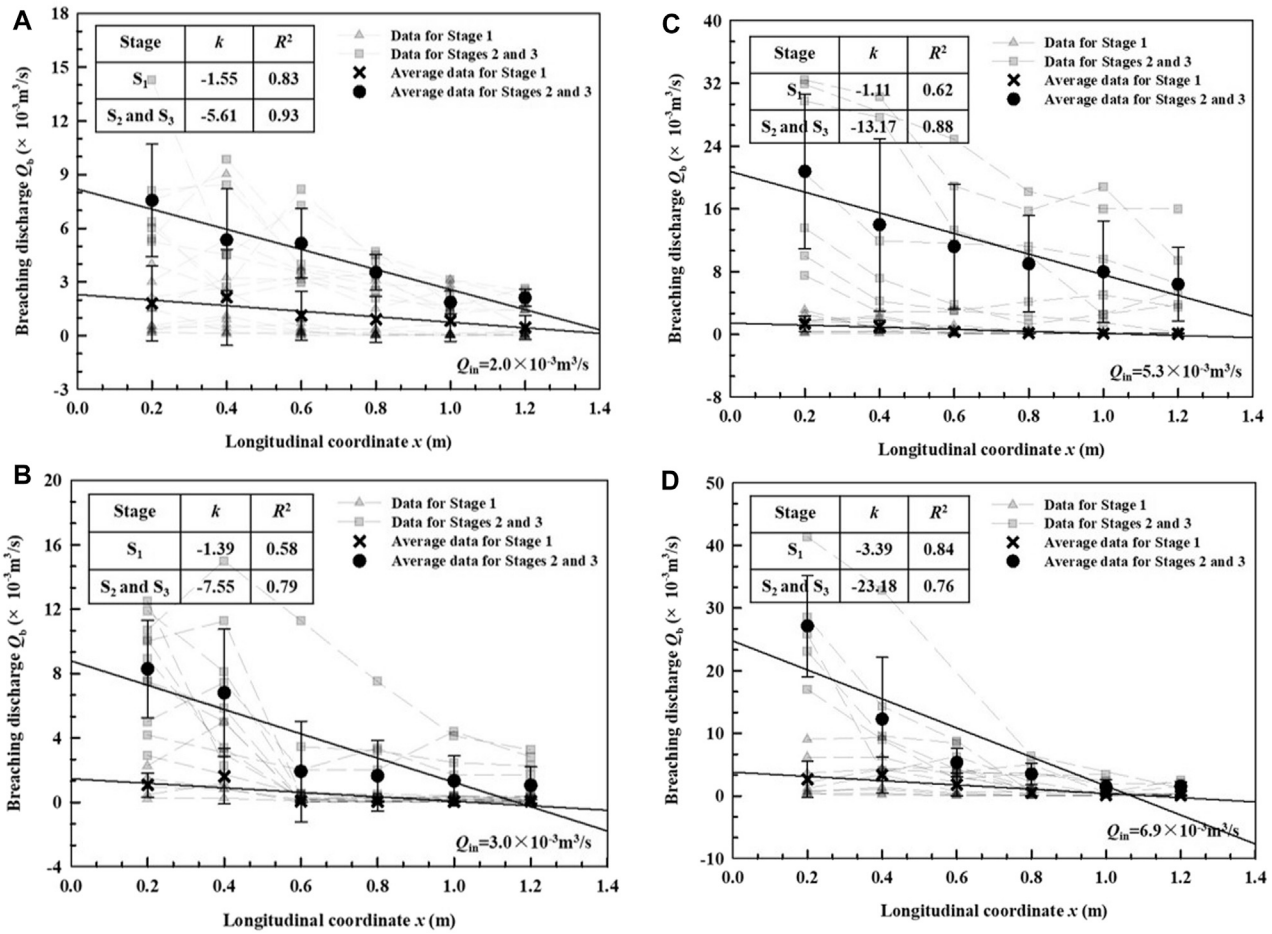

FIGURE 8 | The evolution of average breaching flow discharge along the longitudinal direction during different Stage 1 and Stages 2 and 3 **(A)** Q_{in} = 2.0 × 10^{-3} m^3/s **(B)** Q_{in} = 3.0 × 10^{-3} m^3/s **(C)** Q_{in} = 5.3 × 10^{-3} m^3/s **(D)** Q_{in} = 6.9 × 10^{-3} m^3/s.

from many assumptions used in rapid assessment models (e.g., Chang and Zhang, 2010; Wu, 2013; Chen Z.Y. et al., 2015; Zhong et al., 2018; Zhang et al., 2020; Zhong et al., 2020).

Breaching Flow Attenuation Along the Longitudinal Direction

Figure 8 shows the breaching discharge evolution along longitudinal direction at different inflow discharges. Considering that Stages 2 and 3 are the main stages of outburst flow evolution wherein peak discharges are obtained and Stage 1 is small and basically unchanged (**Figure 7**), we separate the two parts when studying the change of the breaching discharge along the flow direction. The triangular (gray) markers represent the breaching discharge at different cross sections and at different points in time during Stage 1, while the rectangular (gray) markers represent the measured discharges during Stages 2 and 3. The breaching flow above the dam decreases along the longitudinal direction and averaging across the different points in each stage (cross black marks for Stage 1, and circles black for Stages 2 and 3), one can observe a clear linear decline. The slope of this decline k is steeper for points in Stages 2 and 3 than it is for Stage 1. Values for the slope k and R^2 are provided in the table in the upper left corner of the figure.

This decreasing trend is related to the local blockages resulting from the collapse of loose dam soils, particularly in Stages 2 and 3, which affect the water flow (**Figure 1**). Energy of the water flow is consumed to wash away or overcome the local blockages, which effectively reduces the discharge of the breaching flow. Although the collapses are random and do not occur consistently at the same place, the breaching discharge at the rear of dam is most affected by the collapses due to the lower dam heights in this region. Similar trends are observed for different upstream inflow discharges, although the magnitude of the slopes noticeably increase with Q_{in} (**Figure 8**). Due to the increase of the upstream inflow, the water level of the dam body always maintains a high breach water level, leading to stronger flows. The greater the flow disturbance, the more likely for collapses to occur along the path that can further decrease the discharge.

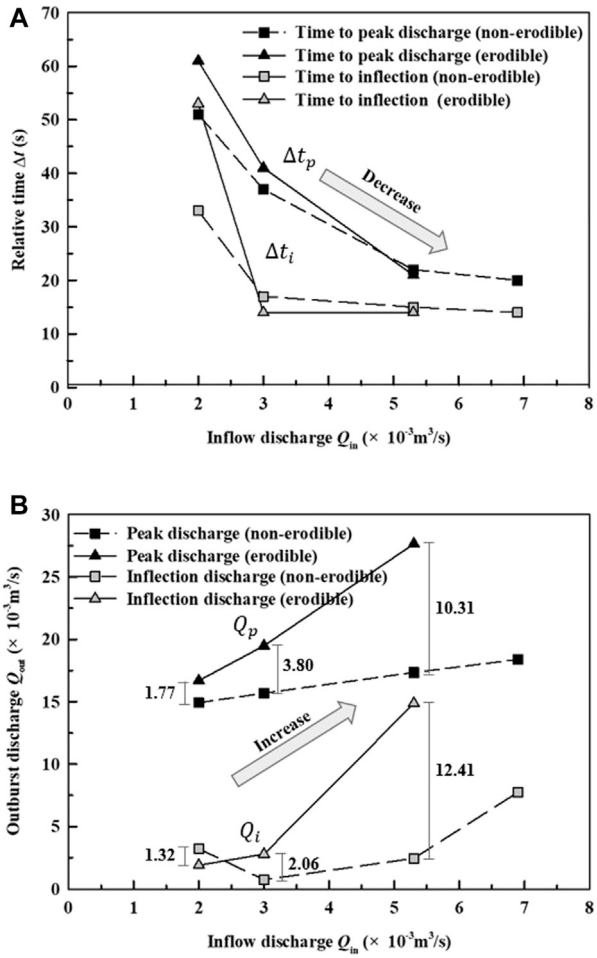

FIGURE 9 | Influence of upstream flow discharge on **(A)** the time to inflection discharge and peak discharge and **(B)** the outburst discharge of dams with erodible beds (Test Nos. E-Q2.0, E-Q3.0, E-Q5.3) and those with non-erodible beds (Test Nos. N-Q2.0, N-Q3.0, N-Q5.3, N-Q6.9).

Analysis on Influencing Factors of Outburst Flood

Figure 9A shows the influence of inflow discharge and loose deposit on the time to inflection flow discharge and the time to peak flow discharge. The relative time (Δt) is the actual time minus the time at which the first flow reaches the collection area.

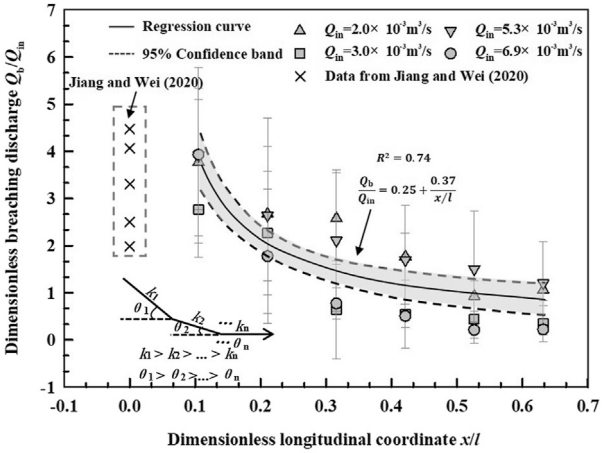

FIGURE 10 | The magnification coefficient of the breaching flow varies along the dimensionless longitudinal coordinate.

All the data related to timescales relevant to the breaching process are summarized in **Table 3**. Both the time to inflection discharge (Δt_i) and peak discharge (Δt_p) tend to decrease with the increase of upstream inflow. It is also observed that the Δt of the erodible-bed test group and the non-erodible bed group are nearly identical and becomes more so with the increase of the upstream inflow. In addition, it is observed that Δt_i no longer changes when the upstream flow discharge is greater than 5.3 × 10^{-3} m^3/s, which means the influence of the inflow discharge of the landslide dam on the outburst flood is limited (**Figure 9A**).

Figure 9B shows the influence of upstream inflow discharge Q_{in} on the inflection flow discharge Q_i and peak flow discharge Q_p of outburst floods for dams with and without erodible beds. From **Figure 9B**, it is observed that both Q_i and Q_p increase with Q_{in} regardless of whether there is loose accumulation of soils behind the dam or not. This is different from the findings of previous non-erodible bed experiments which conclude that the upstream inflow has little effect on the peak flow discharge (Cao et al., 2011; Xu et al., 2013). Furthermore, the increase in the upstream inflow increases the difference of the Q_{out} of dams with and without erodible beds (**Figure 9B**). This indicates that the dams having erodible beds more strongly influenced by upstream inflows compare to dams without erodible beds.

TABLE 3 | Characteristic timescales and discharges for each test.

Test ID	Time to first flow arrive t_f(s)	Time to inflection t_i(s)	Time to peak discharge t_p(s)	Inflection discharge Q_i(× 10^{-3} m^3/s)	Peak discharge Q_p(× 10^{-3} m^3/s)
U-Q2.0	46	79	97	3.2	14.9
U-Q3.0	54	71	91	0.7	15.7
U-Q5.3	32	47	54	2.5	17.3
U-Q6.9	30	44	50	7.7	18.4
E-Q2.0	66	119	127	1.90	16.7
E-Q3.0	55	69	96	2.80	19.5
E-Q5.3	27	41	48	14.9	27.7

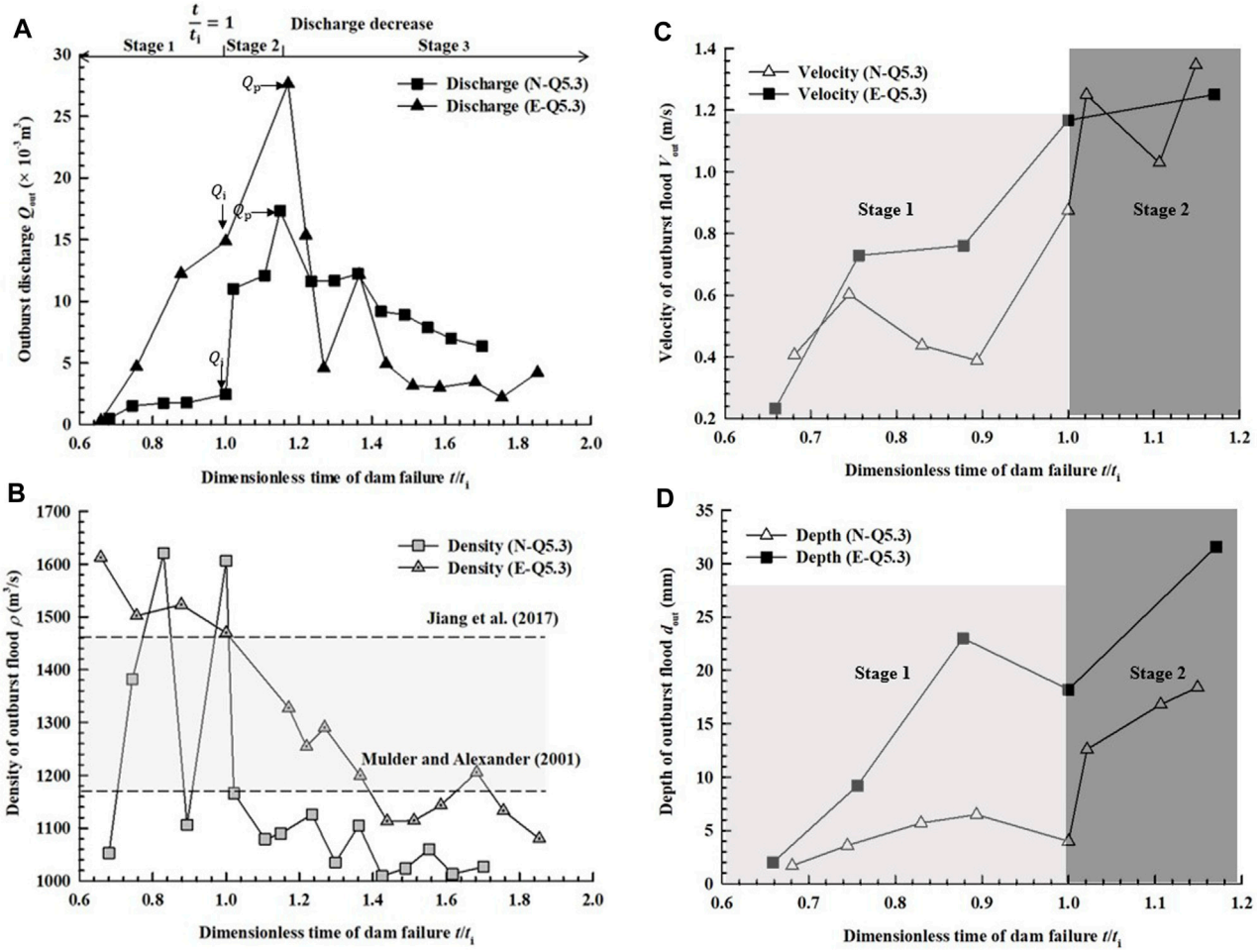

FIGURE 11 | The **(A)** discharge of the outburst floods and **(B)** density of the outburst flood in tests N-Q5.3 and E-Q5.3. The **(C)** velocity and **(D)** water depth of outburst floods in Stages 1 and 2.

DISCUSSION

Effects of the Upstream Inflow on the Mechanisms of Outburst Flooding

Figure 10 shows the change of the normalized breaching discharge $\left(\frac{Q_b}{Q_{in}}\right)$ along the dimensionless longitudinal coordinate x/l in Stages 2 and 3 for different Q_{in}. The ratio $\frac{Q_b}{Q_{in}}$ can also be considered as an amplification coefficient. The l is the length from the upstream dam shoulder to downstream dam toe. The solid line represents the best fit to the measured data with an $R^2 = 0.74$. The shaded area bounded by the dotted lines represent the 95% confidence band. The change of $\frac{Q_b}{Q_{in}}$ along the dam surface can be defined by an inverse proportional relationship of the form: $\frac{Q_b}{Q_{in}} = 0.25 + \frac{0.37}{x/l}$. This shows that the amplification coefficient of the breach discharge decreases gradually along the dam body in a non-linear fashion. A schematic diagram in the inset of **Figure 10** illustrates the geometric mechanisms behind this behavior. The $\frac{Q_b}{Q_{in}}$ values of the experimental data of Jiang and Wei (2020) falls between 2-5 at the upstream dam shoulder ($x/l = 0$), reasonably falling within the range of values obtained in this study (**Figure 10**). In addition, the amplification factor is asymptotic to 0.62, i.e. the average of breaching flow discharge of Stages 2 and 3 above the dam cannot be less than 0.62 times of the inflow discharge. Therefore, with the increase of the upstream inflow, the flow at the outlet increases, which leads to the larger downstream outburst floods.

Influence of Loose Deposits Behind the Dam on the Mechanism of Outburst Flood

Another phenomenon is that the peak flow of dams with erodible beds are higher than those without erodible beds (**Table 3**). This means that the loose deposits have a magnifying effect on the outburst floods. The enhancement effect of the loose deposits in the fluid is often observed in debris flow experiments involving movable beds. Iverson et al. (2010) argued that the amplification effect of debris flows can be

attributed to the influence of excess pore water pressures in erodible bed due to load process. However, the water content of the loose deposit in this study is almost zero, therefore it is still not clear what the amplification effect is.

Figure 1A shows the outburst hydrographs of tests N-Q5.3 and E-Q5.3 where the three stages detailed in the previous sections can still be observed. In order to compare outburst discharge at different Stages of those two sets of downstream conditions, the hydrographs are projected in dimensionless time (t/t_i), where t is the time of flow and t_i is the time of inflection discharge. In **Figure 11A** it can be noticed that prior to the peak discharge (Stages 1 and 2), there is a period of time in which the flow front still travels from the dam toe to the measurement location (5 m away), in which no discharge data is recorded. After which, the outburst discharge begins to gently increase, marking the arrival of the initial minor surges. A sudden positive change in the discharge trend–an inflection point–is observed at $\frac{t}{t_i} = 1$, marking the occurrence of outburst flooding. This steep rise in the inflection discharge ends when the peak discharge is achieved.

Figure 11B shows the density of the outburst floods of tests N-Q5.3 and E-Q5.3. The density of flows steadily decrease in two tests. Before the peak discharge, during the early stages of the dam failure, the flood density is relatively high in both conditions (Jiang et al., 2017) (**Figure 11B**). The transition to the lower densities corresponds to the time at which the inflection discharges are recorded. The density of the discharge of dams with erodible beds are noticeably larger than those without. The outburst floods in test N-Q5.3 are comparable to low-density turbidity currents (Middleton and Hampton, 1973; Mulder and Alexander, 2001) (with densities lower than 1165 kg/m^3), while the flows in test E-Q5.3 can be likened to sediment flows (with densities more than 1165 kg/m^3 and less than 1460 kg/m^3) or even debris flows (more than 1460 kg/m^3). Once the material starts to move down the slope, it will once again increase the momentum of the outburst flood and further increase the flow velocity of outburst flood (**Figure 11C**). The erosion of loose deposits in the erodible bed increases the sediment concentration and hence the flow depth (**Figure 11D**). Thus the increased outburst flood discharge of dams with erodible beds behind them are mainly due to increased flow height which results from the increased sediment concentration in the entraining flows.

CONCLUSION

By using flume modelling tests, the effects of upstream inflow discharge and downstream bed erodibility on the breaching flow and outburst flooding induced by landslide dam overtopping failure are investigated. The spatial-temporal evolution of breaching flows on different overtopping failure stages are presented in detail. In addition, the mechanisms underlying the enlargement of outburst flood discharge due to the presence of erodible beds behind landslide dams are discussed. The key conclusions drawn are as follows:

1) The breaching flow develops consistently with the downstream outburst. It can be divided into three stages where each stage is defined by distinct discharge dynamics. The definition of these stages are unaffected by the presence of an erodible base behind the dam. Furthermore, the maximum value of breach discharge increases with the increase of upstream inflow.
2) The breaching flow above the dam gradually decreases along the longitudinal direction. The average value of the outburst discharge at different sections during the different stages gradually decrease. The rate of decline of the breaching flow discharge in rapid failure stages (Stages 2 and 3) is higher than that of Stage 1. In addition, the larger the upstream inflow, the faster the dam breaching discharge decreases in Stages 2 and 3.
3) The scale amplification of the breaching flow decreases along the dam surface. An inverse equation is proposed to define the spatial evolution of the scale amplification (Stages 2 and 3). The rate of decline is asymptotic to a limit $\frac{Q_b}{Q_{in}} = 0.62$ at the downstream dam toe.
4) The larger the inflow, the larger the peak discharges, and the shorter the time it takes to reach the said discharge. The dependence of peak discharge and inflection discharge on inflow is stronger when an erodible bed exists behind the dam. The replenishment of loose deposits behind the dam is an important reason for the significant increase of its peak outburst discharge.

The failure process of a landslide dam is a complex process which involves geotechnical and hydro-dynamic concepts. As a simplification, we only consider the evolution of overtopping flow of a dam body with one shape. The void ratio of the dam is kept uniform along the depth to imitate a naturally loose accumulation. Although the influence of inflow discharge on the peak outburst flood discharge is also affected by storage capacity, water content, and the density and gradation of the loose deposits behind the dam, these variables are not considered in this study. These items will be the focus of our future work, along with the consideration of the interactions between the scale amplification and breaching flow during the landslide dam failure.

DATA AVAILABILITY STATEMENT

The original contributions presented in the study are included in the article/Supplementary Material, further inquiries can be directed to the corresponding author.

AUTHOR CONTRIBUTIONS

MZ finished data collection and this manuscipt. ZS contributed to the conceptualization, supervision and funding acquisition. GZ reviewed and edited the manuscript. KC contributed to the conceptualization and reviewed and polised the manuscript. MP reviewed and edited the manuscript.

ACKNOWLEDGMENTS

The authors acknowledge the financial support from the National Natural Science Foundation of China (Grant Nos. 41731283, 42007252, 41877234).

REFERENCES

Bellos, C. V., Soulis, V., and Sakkas, J. G. (1992). Experimental Investigation of Two-Dimensional Dam-Break Induced Flows. *J. Hydraulic Res.* 30 (1), 47–63. doi:10.1080/00221689209498946

Breien, H., De Blasio, F. V., Elverhøi, A., and Høeg, K. (2008). Erosion and Morphology of a Debris Flow Caused by a Glacial lake Outburst Flood, Western Norway. *Landslides* 5, 271–280. doi:10.1007/s10346-008-0118-3

Cao, Z., Yue, Z., and Pender, G. (2011). Landslide Dam Failure and Flood Hydraulics. Part I: Experimental Investigation. *Nat. Hazards* 59 (2), 1003–1019. doi:10.1007/s11069-011-9814-8

Casagli, N., Ermini, L., and Rosati, G. (2003). Determining Grain Size Distribution of Material Composing Landslide Dams in the Northern Apennine: Sampling and Processing Methods. *Eng. Geol.* 69 (1), 83–97. doi:10.1016/s0013-7952(02)00249-1

Chang, D. S., and Zhang, L. M. (2010). Simulation of the Erosion Process of Landslide Dams Due to Overtopping Considering Variations in Soil Erodibility along Depth. *Nat. Hazards Earth Syst. Sci.* 10 (4), 933–946. doi:10.5194/nhess-10-933-2010

Chang, D. S., Zhang, L. M., Xu, Y., and Huang, R. Q. (2011). Field Testing of Erodibility of Two Landslide Dams Triggered by the 12 May Wenchuan Earthquake. *Landslides* 8 (3), 321–332. doi:10.1007/s10346-011-025610.1007/s10346-011-0256-x

Chen, S.-C., Lin, T.-W., and Chen, C.-Y. (2015). Modeling of Natural Dam Failure Modes and Downstream Riverbed Morphological Changes with Different Dam Materials in a Flume Test. *Eng. Geology.* 188, 148–158. doi:10.1016/j.enggeo.2015.01.016

Chen, S. S., Xu, G. M., Zhong, Q. M., and Gu, X. W. (2012). Development and Application of Centrifugal Model Test System for Break of Earth-Rock Dams. *J. Hydraul. Eng.* 43 (2), 241–245. in Chinese. doi:10.13243/j.cnki.slxb.2012.02.006

Chen, Z. Y., Ma, L. Q., Yu, S., Chen, S. J., Zhou, X. B., Sun, P., et al. (2015). Back Analysis of the Draining Process of the Tangjiashan Barrier lake. *J. Hydraul. Eng.* 141 (4), 1–14. doi:10.1061/(asce)hy.1943-7900.0000965

Costa, J. E. (1985). *Floods from Dam Failures. U.S. Geological Survey, U.S. Geological Survey Open-File Report*. Reston, VA: U.S. Geological Survey, 85–560.

Costa, J. E., and Schuster, R. L. (1988). The Formation and Failure of Natural Dam. *Geol. Soc. Am. Bull.* 100, 1054–1068. doi:10.1130/0016-7606(1988)100<1054:tfafon>2.3.co;2

Cui, P., Zhou, G. G. D., Zhu, X. H., and Zhang, J. Q. (2013). Scale Amplification of Natural Debris Flows Caused by Cascading Landslide Dam Failures. *Geomorphology* 182 (427), 173–189. doi:10.1016/j.geomorph.2012.11.009

Davies, T. R., Manville, V., Kunz, M., and Donadini, L. (2007). Modeling Landslide Dambreak Flood Magnitudes: Case Study. *J. Hydraul. Eng.* 133 (7), 713–720. doi:10.1061/(asce)0733-9429(2007)133:7(713)

Dong, J.-J., Li, Y.-S., Kuo, C.-Y., Sung, R.-T., Li, M.-H., Lee, C.-T., et al. (2011). The Formation and Breach of a Short-Lived Landslide Dam at Hsiaolin Village, Taiwan - Part I: Post-event Reconstruction of Dam Geometry. *Eng. Geology.* 123, 40–59. doi:10.1016/j.enggeo.2011.04.001

Fan, X., Dufresne, A., Siva Subramanian, S., Strom, A., Hermanns, R., Tacconi Stefanelli, C., et al. (2020). The Formation and Impact of Landslide Dams - State of the Art. *Earth-Science Rev.* 203, 103116. doi:10.1016/j.earscirev.2020.103116

Fan, X., Scaringi, G., Korup, O., West, A. J., Westen, C. J., Tanyas, H., et al. (2019). Earthquake-Induced Chains of Geologic Hazards: Patterns, Mechanisms, and Impacts. *Rev. Geophys.* 57 (2), 421–503. doi:10.1029/2018RG000626

Fannin, R. J., and Wise, M. P. (2001). An Empirical-Statistical Model for Debris Flow Travel Distance. *Can. Geotech. J.* 38 (5), 982–994. doi:10.1139/t01-030

Gregoretti, C., Maltauro, A., and Lanzoni, S. (2010). Laboratory Experiments on the Failure of Coarse Homogeneous Sediment Natural Dams on a Sloping Bed. *J. Hydraul. Eng.* 136 (11), 868–879. doi:10.1061/(asce)hy.1943-7900.0000259

Hakimzadeh, H., Nourani, V., and Amini, A. B. (2014). Genetic Programming Simulation of Dam Breach Hydrograph and Peak Outflow Discharge. *J. Hydrol. Eng.* 19 (4), 757–768. doi:10.1061/(asce)he.1943-5584.0000849

Iverson, R. M., Reid, M. E., and LaHusen, R. G. (1997). Debris-flow Mobilization from Landslides. *Annu. Rev. Earth Planet. Sci.* 25, 85–138. doi:10.1146/annurev.earth.25.1.85

Iverson, R. M., Reid, M. E., Logan, M., LaHusen, R. G., Godt, J. W., Griswold, J. P., et al. (2010). Positive Feedback and Momentum Growth during Debris-Flow Entrainment of Wet Bed Sediment. *Nat. Geosci* 4 (2), 116–121. doi:10.1038/ngeo1040

Iverson, R. M. (2015). Scaling and Design of Landslide and Debris-Flow Experiments. *Geomorphology* 244, 9–20. doi:10.1016/j.geomorph.2015.02.033

Jiang, X., and Wei, Y. (2020). Erosion Characteristics of Outburst Floods on Channel Beds under the Conditions of Different Natural Dam Downstream Slope Angles. *Landslides* 17, 1823–1834. doi:10.1007/s10346-020-01381-y

Jiang, X., Wei, Y., Wu, L., and Lei, Y. (2018a). Experimental Investigation of Failure Modes and Breaching Characteristics of Natural Dams. *Geomatics, Nat. Hazards Risk* 9 (1), 33–48. doi:10.1080/19475705.2017.1407367

Jiang, X., Wörman, A., Chen, P., Huang, Q., and Chen, H. (2020). Mechanism of the Progressive Failure of Non-cohesive Natural Dam Slopes. *Geomorphology* 363, 107198. doi:10.1016/j.geomorph.2020.107198

King, J., Loveday, I., and Schuster, R. L. (1989). The 1985 Bairaman Landslide Dam and Resulting Debris Flow, Papua New Guinea. *Q. J. Eng. Geology. Hydrogeology* 22 (4), 257–270. doi:10.1144/gsl.qjeg.1989.022.04.02

Kirkpatrick, G. W. (1977). "Evaluation Guidelines for Spillway Adequacy. Evaluation of Dam Safety," in Proceedings of the Engineering Foundation Conference, Zurich, 395–414.

Korup, O. (2004). Geomorphometric Characteristics of New Zealand Landslide Dams. *Eng. Geology.* 73 (1), 13–35. doi:10.1016/j.enggeo.2003.11.003

Korup, O., Montgomery, D. R., and Hewitt, K. (2010). Glacier and Landslide Feedbacks to Topographic Relief in the Himalayan Syntaxes. *Proc. Natl. Acad. Sci.* 107 (12), 5317–5322. doi:10.1073/pnas.0907531107

Korup, O. (2006). Rock-slope Failure and the River Long Profile. *Geol* 34 (1), 45–48. doi:10.1130/g21959.1

Li, M.-H., Sung, R.-T., Dong, J.-J., Lee, C.-T., and Chen, C.-C. (2011). The Formation and Breaching of a Short-Lived Landslide Dam at Hsiaolin Village, Taiwan - Part II: Simulation of Debris Flow with Landslide Dam Breach. *Eng. Geology.* 123, 60–71. doi:10.1016/j.enggeo.2011.05.002

Liu, W., Carling, P. A., Hu, K., Wang, H., Zhou, Z., Zhou, L., et al. (2019). Outburst Floods in China: A Review. *Earth-Science Rev.* 197, 102895. doi:10.1016/j.earscirev.2019.102895

Liu, W., Hu, K., Carling, P. A., Lai, Z., Cheng, T., and Xu, Y. (2018). The Establishment and Influence of Baimakou Paleo-Dam in an Upstream Reach of the Yangtze River, southeastern Margin of the Tibetan Plateau. *Geomorphology* 321, 167–173. doi:10.1016/j.geomorph.2018.08.028

Malvern Instruments Ltd (2007). *MAN0384-1.0 Mastersizer 2000 User Manual*.

Mangeney, A., Tsimring, L. S., Volfson, D., Aranson, I. S., and Bouchut, F. (2007). Avalanche Mobility Induced by the Presence of an Erodible Bed and Associated Entrainment. *Geophys. Res. Lett.* 34 (22), 22401. doi:10.1029/2007gl031348

Middleton, G. V., and Hampton, M. A. (1973). "Sediment Gravity Flows: Mechanics of Flow and Deposition," in *Turbidity and Deep Water Sedimentation* (Pacific Section: SEPM), 1–38.

Mulder, T., and Alexander, J. (2001). The Physical Character of Subaqueous Sedimentary Density Flows and Their Deposits. *Sedimentology* 48 (2), 269–299. doi:10.1046/j.1365-3091.2001.00360.x

Parker, G., and Izumi, N. (2000). Purely Erosional Cyclic and Solitary Steps Created by Flow over a Cohesive Bed. *J. Fluid Mech.* 419, 203–238. doi:10.1017/S0022112000001403

Peng, M., Jiang, Q.-L., Zhang, Q.-Z., Hong, Y., Jiang, M.-z., Shi, Z.-M., et al. (2019). Stability Analysis of Landslide Dams under Surge Action Based on Large-Scale Flume Experiments. *Eng. Geology.* 259, 105191. doi:10.1016/j.enggeo.2019.105191

Peng, M., and Zhang, L. M. (2012). Breaching Parameters of Landslide Dams. *Landslides* 9 (1), 13–31. doi:10.1007/s10346-011-0271-y

Pickert, G., Weitbrecht, V., and Bieberstein, A. (2011). Breaching of Overtopped River Embankments Controlled by Apparent Cohesion. *J. Hydraulic Res.* 49 (2), 143–156. doi:10.1080/00221686.2011.552468

Pierce, M. W., Thornton, C. I., and Abt, S. R. (2010). Predicting Peak Outflow from Breached Embankment Dams. *J. Hydrol. Eng.* 15 (5), 338–349. doi:10.1061/(asce)he.1943-5584.0000197

Shen, D., Shi, Z., Peng, M., Zhang, L., and Jiang, M. (2020a). Longevity Analysis of Landslide Dams. *Landslides* 17, 1797–1821. doi:10.1007/s10346-020-01386-7

Shen, D., Shi, Z., Peng, M., Zhang, L., and Zhu, Y. (2020b). Preliminary Analysis of a Rainfall-Induced Landslide hazard Chain in Enshi City, Hubei Province, China in July 2020. *Landslides* 18, 509–512. doi:10.1007/s10346-020-01553-w

Shi, Z. M., Guan, S. G., Peng, M., Zhang, L. M., Zhu, Y., and Cai, Q. P. (2015). Cascading Breaching of the Tangjiashan Landslide Dam and Two Smaller Downstream Landslide Dams. *Eng. Geology.* 193 (2), 445–458. doi:10.1016/j.enggeo.2015.05.021

Shi, Z. M., Wang, Y. Q., Peng, M., Chen, J. F., and Ji, Y. (2014). Characteristics of the Landslide Dams Induced by the 2008 Wenchuan Earthquake and Dynamic Behavior Analysis Using Large-Scale Shaking Table Tests. *Eng. Geol.* 194, 25–37. doi:10.1016/j.enggeo.2014.10.009

Singh, K. P., and Snorrason, A. (1984). Sensitivity of Outflow Peaks and Flood Stages to the Selection of Dam Breach Parameters and Simulation Models. *J. Hydrol.* 68 (1), 295–310. doi:10.1016/0022-1694(84)90217-8

van Gorp, W., Schoorl, J. M., Temme, A. J. A. M., Reimann, T., Wijbrans, J. R., Maddy, D., et al. (2016). Catchment Response to Lava Damming: Integrating Field Observation, Geochronology and Landscape Evolution Modelling. *Earth Surf. Process. Landforms* 41 (11), 1629–1644. doi:10.1002/esp.3981

Walder, J. S. (2016). Dimensionless Erosion Laws for Cohesive Sediment. *J. Hydraul. Eng.* 142 (2), 04015047. doi:10.1061/(asce)hy.1943-7900.0001068

Walder, J. S., Iverson, R. M., Godt, J. W., Logan, M., and Solovitz, S. A. (2015). Controls on the Breach Geometry and Flood Hydrograph during Overtopping of Noncohesive Earthen Dams. *Water Resour. Res.* 51 (8), 6701–6724. doi:10.1002/2014wr016620

Walsh, L. S., Martin, A. J., Ojha, T. P., and Fedenczuk, T. (2012). Correlations of Fluvial Knickzones with Landslide Dams, Lithologic Contacts, and Faults in the Southwestern Annapurna Range, central Nepalese Himalaya. *J. Geophys. Res.* 117, a–n. doi:10.1029/2011JF001984

Wang, G. H., Sassa, K., and Fukuoka, H. (2003). Downslope Volume Enlargement of a Debris Slide–Debris Flow in the 1999 Hiroshima, Japan, Rainstorm. *Eng. Geol.* 69 (3), 309–330. doi:10.1016/s0013-7952(02)00289-2

Webby, M. G. (1996). Discussion of "Peak Outflow from Breached Embankment Dam" by David C. Froehlich. *J. Water Resour. Plann. Manage.* 122 (4), 316–317. doi:10.1061/(asce)0733-9496(1996)122:4(316)

Wu, W. M. (2007). *Computational River Dynamics*. London: Taylor and Francis Press.

Wu, W. (2013). Simplified Physically Based Model of Earthen Embankment Breaching. *J. Hydraul. Eng.* 139 (8), 837–851. doi:10.1061(asce)hy.1943-7900.000074110.1061/(asce)hy.1943-7900.0000741

Xiangang, J., Jiahua, H., Yunwei, W., Zhipan, N., Fenghui, C., Zuyin, Z., et al. (2018b). The Influence of Materials on the Breaching Process of Natural Dams. *Landslides* 15, 243–255. doi:10.1007/s10346-017-0877-9

Xiangang, J., Peng, C., Huayong, C., and Yayong, G. (2017). Formation Conditions of Outburst Debris Flow Triggered by Overtopped Natural Dam Failure. *Landslides* 14 (3), 821–831. doi:10.1007/s10346-016-0751-1

Xiong, X., Shi, Z. M., Guan, S. G., and Zhang, F. (2018). Failure Mechanism of Unsaturated Landslide Dam under Seepage Loading - Model Tests and Corresponding Numerical Simulations. *Soils and Foundations* 58, 1133–1152. doi:10.1016/j.sandf.2018.05.012

Xiong, Z., Feng, G., Feng, Z., Miao, L., Wang, Y., Yang, D., et al. (2020). Pre- and post-failure Spatial-Temporal Deformation Pattern of the Baige Landslide Retrieved from Multiple Radar and Optical Satellite Images. *Eng. Geology.* 279, 105880. doi:10.1016/j.enggeo.2020.105880

Xu, F.-g., Yang, X.-g., Zhou, J.-w., and Hao, M.-h. (2013). Experimental Research on the Dam-Break Mechanisms of the Jiadanwan Landslide Dam Triggered by the Wenchuan Earthquake in China. *Scientific World J.* 2013, 1–13. doi:10.1155/2013/272363

Xu, Q., Fan, X.-M., Huang, R.-Q., and Westen, C. V. (2009). Landslide Dams Triggered by the Wenchuan Earthquake, Sichuan Province, South West China. *Bull. Eng. Geol. Environ.* 68 (3), 373–386. doi:10.1007/s10064-009-0214-1

Yan, J., Cao, Z.-x., Liu, H.-h., and Chen, L. (2009). Experimental Study of Landslide Dam-Break Flood over Erodible Bed in Open Channels. *J. Hydrodyn.* 21 (1), 124–130. doi:10.1016/S1001-6058(08)60127-4

Yang, Y., Cao, S.-y., Yang, K.-j., and Li, W.-p. (2015). Experimental Study of Breach Process of Landslide Dams by Overtopping and its Initiation Mechanisms. *J. Hydrodyn.* 27 (6), 872–883. doi:10.1016/S1001-6058(15)60550-9

Yin, Y., Wang, F., and Sun, P. (2009). Landslide Hazards Triggered by the 2008 Wenchuan Earthquake, Sichuan, China. *Landslides* 6 (2), 139–152. doi:10.1007/s10346-009-0148-5

Zhang, L., Xiao, T., He, J., and Chen, C. (2019). Erosion-based Analysis of Breaching of Baige Landslide Dams on the Jinsha River, China, in 2018. *Landslides* 16, 1965–1979. doi:10.1007/s10346-019-01247-y

Zheng, H., Shi, Z., Shen, D., Peng, M., Hanley, K. J., Ma, C., et al. (2021). Recent Advances in Stability and Failure Mechanisms of Landslide Dams. *Front. Earth Sci.* 9, 659935. doi:10.3389/feart.2021.659935

Zheng, Y., Chen, C., Liu, T., and Ren, Z. (2021). A New Method of Assessing the Stability of Anti-dip Bedding Rock Slopes Subjected to Earthquake. *Bull. Eng. Geol. Environ.* 80, 3693–3710. doi:10.1007/s10064-021-02188-4

Zhong, Q., Chen, S., and Shan, Y. (2020). Prediction of the Overtopping-Induced Breach Process of the Landslide Dam. *Eng. Geology.* 274, 105709. doi:10.1016/j.enggeo.2020.105709

Zhong, Q. M., Chen, S. S., Mei, S. A., and Cao, W. (2018). Numerical Simulation of Landslide Dam Breaching Due to Overtopping. *Landslides* 15 (6), 1183–1192. doi:10.1007/s10346-017-0935-3

Zhou, G. G. D., Cui, P., Chen, H. Y., Zhu, X. H., Tang, J. B., and Sun, Q. C. (2013). Experimental Study on Cascading Landslide Dam Failures by Upstream Flows. *Landslides* 10 (5), 633–643. doi:10.1007/s10346-012-0352-6

Zhou, G. G. D., Cui, P., Tang, J. B., Chen, H. Y., Zou, Q., and Sun, Q. C. (2015). Experimental Study on the Triggering Mechanisms and Kinematic Properties of Large Debris Flows in Wenjia Gully. *Eng. Geology.* 194, 52–61. doi:10.1016/j.enggeo.2014.10.021

Zhou, G. G. D., and Ng, C. W. W. (2010). Dimensional Analysis of Natural Debris Flows. *Can. Geotech. J.* 47 (7), 719–729. doi:10.1139/t09-134

Zhou, G. G. D., Zhou, M., Shrestha, M. S., Song, D., Choi, C. E., Cui, K. F. E., et al. (2019). Experimental Investigation on the Longitudinal Evolution of Landslide Dam Breaching and Outburst Floods. *Geomorphology* 334, 29–43. doi:10.1016/j.geomorph.2019.02.035

Zhou, M.-j., Zhou, G. G. D., Cui, K. F. E., Song, D.-r., and Lu, X.-q. (2019). Influence of Inflow Discharge and Bed Erodibility on Outburst Flood of Landslide Dam. *J. Mt. Sci.* 16 (4), 778–792. doi:10.1007/s11629-018-5312-8

Zhu, X., Peng, J., Liu, B., Jiang, C., and Guo, J. (2020). Influence of Textural Properties on the Failure Mode and Process of Landslide Dams. *Eng. Geology.* 271, 105613. doi:10.1016/j.enggeo.2020.105613

Conflict of Interest: The authors declare that the research was conducted in the absence of any commercial or financial relationships that could be construed as a potential conflict of interest.

Publisher's Note: All claims expressed in this article are solely those of the authors and do not necessarily represent those of their affiliated organizations, or those of the publisher, the editors and the reviewers. Any product that may be evaluated in this article, or claim that may be made by its manufacturer, is not guaranteed or endorsed by the publisher.

frontiers in Earth Science

ORIGINAL RESEARCH
published: 13 October 2021
doi: 10.3389/feart.2021.772459

Artificial Ground Freezing Impact on Shear Strength and Microstructure of Granite Residual Soil Under an Extremely Low Temperature

Ran An[1], Xianwei Zhang[2,3], Lingwei Kong[2,3], Jianwu Gong[1] and Xuewen Lei[4]*

[1]Wuhan University of Science and Technology, Wuhan, China, [2]Chinese Academy of Sciences (CAS), Beijing, China, [3]Institute of Rock and Soil Mechanics (CAS), Wuhan, China, [4]School of Health Sciences, Wuhan University, Wuhan, China

The Artificial Ground Freezing (AGF) method, which is widely used in tunnel excavations, significantly affects the properties of geotechnical materials in frozen walls under extremely low temperatures. In order to simulate the AGF process, the freezing treatment with a temperature of –30°C and thawing treatment temperature of 25°C were performed on natural specimens of granite residual soil (GRS). Subsequently, triaxial (TRX) tests were conducted to evaluate mechanical properties and Nuclear Magnetic Resonance Image (NMRI) tests were applied to detect pore distributions of GRS. To clarify variations of microstructure after freezing-thawing, the relaxation time (T_2) distribution curves and T_2-weighted images from NMRI results were thoroughly analyzed from the perspective of quantization and visualization. Results show that the shear strength as well as the cohesion of GRS are reduced sharply by the AGF process, while the internal friction angle decreases gently. The pore size distribution (PSD) converted from the T_2 curve is constituted of two different peaks, corresponding to micro-pores with diameters from 0.1 to 10 μm and macro-pores with diameters from 10 to 1,000 μm. Under the AGF impact, the expansion in macro-pores and shrinkage in micro-pores simultaneously exist in the specimen, which was verified from a visualized perspective by T_2-weighted images. The frost heaving damage on shear strength is attributed to the microstructural disturbance caused by the presence of large-scale pores and uneven deformations in GRS, which is subjected to the AGF impact under an extremely low temperature.

Keywords: artificial ground freezing method, granite residual soil, frost heaving damage, pore size distribution, shear strength

OPEN ACCESS

Edited by:
Fei Meng,
Swinburne University of Technology, Australia

Reviewed by:
Zhongqiong Zhang,
Northwest Institute of Eco-Environment and Resources (CAS), China
Yin Song,
Zhongyuan University of Technology, China

****Correspondence:***
Ran An
anran@wust.edu.cn

Specialty section:
This article was submitted to Geohazards and Georisks, a section of the journal Frontiers in Earth Science

Received: *08 September 2021*
Accepted: *27 September 2021*
Published: *13 October 2021*

Citation:
An R, Zhang X, Kong L, Gong J and Lei X (2021) Artificial Ground Freezing Impact on Shear Strength and Microstructure of Granite Residual Soil Under an Extremely Low Temperature. Front. Earth Sci. 9:772459. doi: 10.3389/feart.2021.772459

INTRODUCTION

For decades, a growing number of metro engineering projects have been under construction in large and medium-sized cities in China, as a result of rapid developments of urbanizations (Fang et al., 2011; Chen et al., 2015; Liu et al., 2021). Meanwhile, urban environments and geotechnical properties have been inevitably influenced by subway tunnel excavations at a varying degree during construction and operation periods (Fu et al., 2014). Currently, the artificial ground freezing (AGF) method is widely used in tunnel excavations due to its advantages of broad applicability, high strength performance, seepage prevention, and environmental protections (Lackner et al., 2008; Liu et al., 2017). Although the AGF method has great advantages, the frost heaving damage and

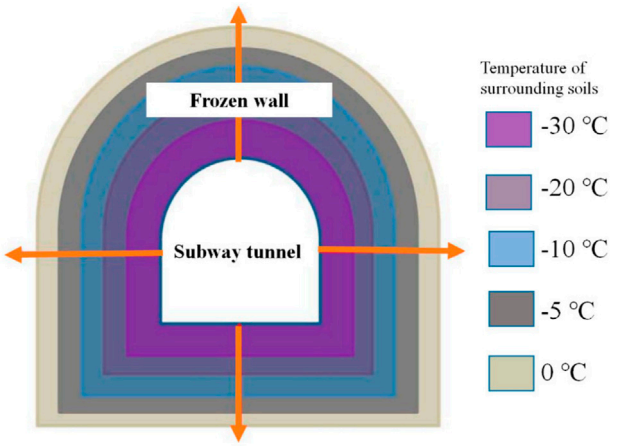

FIGURE 1 | Diagram of the AFG method applied to tunnel constructions.

thaw-induced deformations of geotechnical materials during construction adversely affects the stability of underground structures (Vitel et al., 2015). As the AGF method in tunnel constructions is used more frequently, it is evident that our knowledge about the mechanical behaviors and microstructure of soils is insufficient at this stage (Pimentel et al., 2012).

Granite residual soil (GRS), which is considered as a kind of problematic soil, is extensively distributed in the southeast areas of China (An et al., 2019). The GRS that contain montmorillonite, illite, and other hydrophilic minerals are easily affected by the environmental changes they experience (Toll and Ong 2015). Presently in China, the distributed regions of granitic regolith generally create engineering problems for infrastructure constructions (He et al., 2020). Due to inferior properties, such as high permeability, high compressibility, low strength, and easily-disturbed characteristics of GRS, the AGF method serves as an important constructing technique of metro tunnels and cross passages in the formations (Fonseca et al., 2006). Under the influence of freezing-thawing (F-T) process, the mechanical characteristics of soils are severely degraded by frost heave and cracking propagation (Konrad and Morgenstern, 1980). Therefore, the structural damage of GRS caused by F-T process induces potential dangers to the safe operation of subway tunnels, increasing the probability of losing stability control during excavations.

A substantial amount of findings in the field of frost heave on soils have been made in the past decades, particularly in the frozen earth regions (Black and Tice 1989; Bronfenbrener and Bronfenbrener, 2010; Cécile et al., 2016; Bai et al., 2018). During AGF constructions, the frost heaving effect kept the soils around tunnel pipes at negative temperatures (Zhou and Tang 2015). Generally, the temperature of the interfaces between tunnel pipes and geomaterials can reach an extremely low value of −30°C (Han et al., 2016). In addition, an increasing distance between the soil and pipes results in a rise in the temperature of soil, as presented in **Figure 1**. Recently, the impacts of AGF method on soils in frozen walls has become of increasing concern. Pichler and Lackner (2003) concluded that the micromechanical performance of soils was reduced remarkably after performing artificial freezing method, resulting in uneven deformations of the ground under dynamic loads. Cui and Zhang (2015) found that the pore structure in geomaterials exhibited uneven expansions after freezing-thawing. An et al. (2020) found the microstructure in residual soil showed a significant variation after the AGF treatment by performing NMR and SEM tests. It is generally believed that the F-T process affects not only physical characteristics such as porosity, dry density, and hydraulic conductivity, but also mechanical behaviors, such as the stress-strain relation, elastic modulus, and shear strength parameters of soils (Shoop and Bigl, 1997; Lai et al., 2010; Tian et al., 2018). Additionally, it has been well-documented that extremely low temperatures applied to soils significantly affects their microstructural characteristics (Pichler et al., 2003; Zhou and Tang 2018). However, there have been rare reports of correlations between mechanical and microstructural parameters of GRS. Even though some researchers have recently become aware of microstructural effects on mechanical properties, their concerns mostly focused on natural frozen soil, instead of soils in artificially frozen walls.

Over the past decades, non-destructive detecting methods, such as Nuclear Magnetic Resonance (NMR) and Computed Tomography (CT), have become increasingly prevalent to analyze the pore distributions in rocks and soils (Kong et al., 2017; Li et al., 2020). The NMRI technique offers an effective and reliable method to identify the microstructure in a tested material from a visual and quantitative perspective (An et al., 2020b). The NMRI scan also provides a rapid and convenient testing procedure which saves measuring time for investigating the pore-water distributions during the freezing process (Nakashima et al., 2011). Acknowledging the most functional potential of NMRI technique in measuring pore water in specimens, a set of studies have been performed on soils affected by the F-T damage (Watanabe and Wake 2009; Kong et al., 2020). Nevertheless, the relationship between macroscopic mechanical behavior and microstructure of GRS requires further exploration.

In this paper, the shear strength and pore distributions of granite residual soil under the AGF process has been focused on. In order to simulate the environmental impact of AGF construction on actual soils, undisturbed specimens of GRS were frozen at a negative temperature of −30°C and then thawed at 25°C. A set of triaxial loading tests with different confining pressures and NMRI scanning were performed to study mechanical and microstructural properties of GRS. This study contributes to the cognization of geotechnical problems involving the AGF method in tunnel constructions.

MATERIALS AND METHODS

Materials

The material studied in this paper was undisturbed GRS collected from a natural slope located in Xiamen, Southeast China. The physical properties, including the dry density ρ_d, moisture content w, specific gravity G_s, hydraulic coefficient K, and

TABLE 1 | Physical and mineralogic properties of GRS.

ρ_d/g·cm^{-3}	W/%	K/cm·s^{-1}	Void ratio	G_s	Atterberg limits		Mineral composition/%			
					w_L	w_p	kaolinite	illite	quartz	hematite
1.37	26.03	1.15×10^{-7}	0.63	2.71	65.6	25.9	38.5	5.2	53.6	2.5

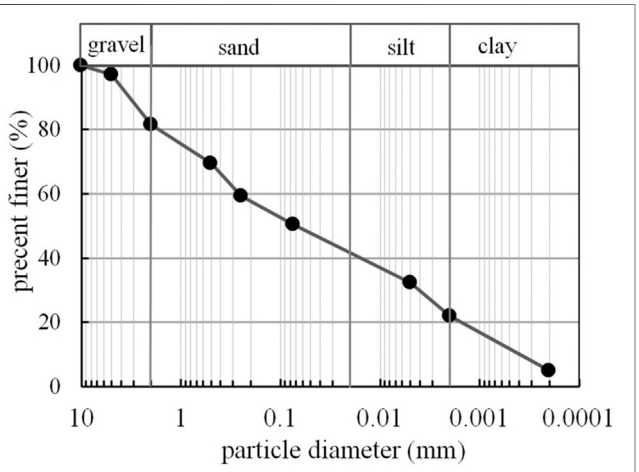

FIGURE 2 | The grain size distribution of GRS.

Atterberg limit (I_l and I_p), were tested by referring to the standard GB/T 50123 (National Standard for the People's Republic of China, 1999). The mineral composition was quantitatively acquired from XRD tests by referring to the "ASTM D4926-2015." Basic physical parameters and the mineral composition of GRS are summarized in **Table 1**. The grain size distribution of GRS was measured by referring to ASTM D422-63 (2002). As presented in **Figure 2**, the grain distribution curve of GRS shows that fine and coarse particles both have a high proportion while intermediate-size particles have a low proportion, which is the most prominent fabric characteristic of granite residual soils.

Sample Preparation

The undisturbed specimens of GRS were collected by using the exploratory trench sampling technique at the surface of an excavation slope. Firstly, the cubic soil blocks (30 cm × 30 cm × 30 cm) were carefully cut in the sampling field. Then, plastic films were wrapped on the surface of the soil blocks and packed into the wooden boxes which were filled with foamed materials. Eventually, the wooden boxes were fixed and transported to the laboratory. The cylinder columns with a diameter of 50 mm and a height of 100 mm were elaborately prepared from cubic blocks of soil. In order to simulate the freezing-thawing process in AGF method by laboratory tests, the prepared specimens of GRS were frozen up to a negative temperature of −30°C and kept cool for 48 h in a programmable cryogenic freezer. Subsequently, these specimens were defrosted at room temperature of 25°C for 24 h and fully saturated by using a vacuum saturation device for 72 h. After the process of freezing and thawing, these samples were placed carefully in the constant temperature chamber.

Test Methods

1) Triaxial loading tests

The shear strength and stress-strain curves of GRS were measured by a set of triaxial loading tests under consolidated-undrained (CU) states, by referring to ASTM D4767-11. Standard cylinder specimens with a diameter of 50 mm and a height of 100 mm were coated with a rubber film and placed in the pressure chamber for backpressure saturations. Then, the saturated specimens were subjected to confining pressures of 100, 200, and 300 kPa. Finally, the shear process was started with the displacement increasing rate set as 0.015 mm/min. During the test, the shear process was stopped when the axial strain reached nearly 20%.

2) Nuclear Magnetic Resonance Image (NMRI) scans

Before the NMRI tests, the specimen was vacuumed and then saturated by distilled water for 24 h to remove the air in pores to ensure a fully saturated state. The AniMR-150 NMR imaging system was applied to obtain the relaxation time T_2 spectrums and pseudo-color images of pore water through Carr Purcell Meiboom-Gill (CPMG) sequence. To generate a uniform and stable magnetic field, the testing temperature of the device was controlled to be about 25°C. Each NMRI test takes about 30 min for scanning. The amplitude of NMR signal intensity (T_2) indicates the present protons in pore water and provides information of pore distributions. After the T_2 distribution curves which provided information of pore distributions were obtained, the pseudo-color images of pore water in specimens were captured by the imaging function pf NMRI system.

RESULTS AND ANALYSIS

Stress-Strain Behavior and Shear Strength

The deviatoric stress versus axial strain curves of GRS before and after F-T process were measured by triaxial loading tests, as illustrated in **Figure 3**. It is evident that the stress-strain curves of undisturbed specimens of GRS under different confining pressures exhibit a strain-softening feature. Under the consolidation-undrainage condition, the deviatoric stress of soils increases rapidly when the axial strain reached 5%. Then, the stress descended after reaching the peak stress (see in **Figure 3A**). For soil columns under the cooling temperature

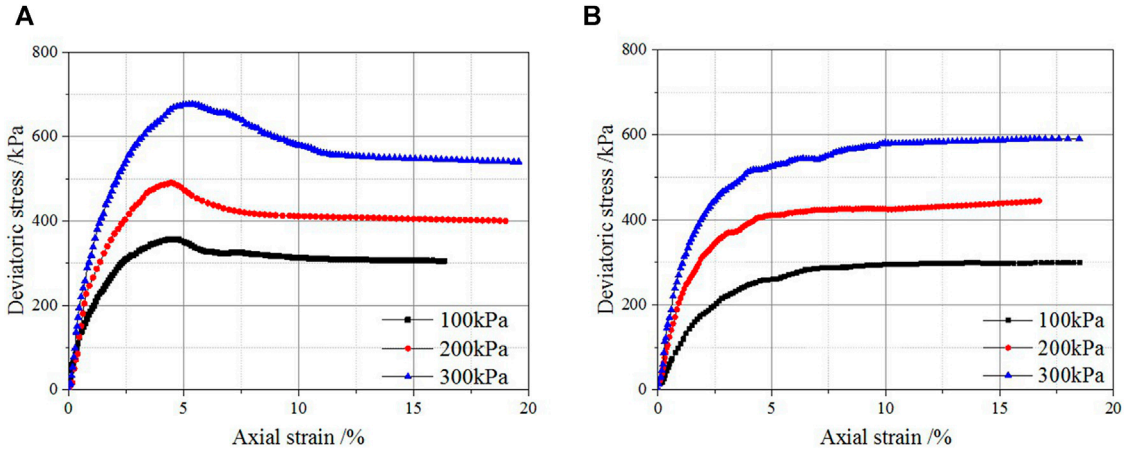

FIGURE 3 | Stress-strain curves at different confining pressures: **(A)** original specimens; **(B)** F-T specimens.

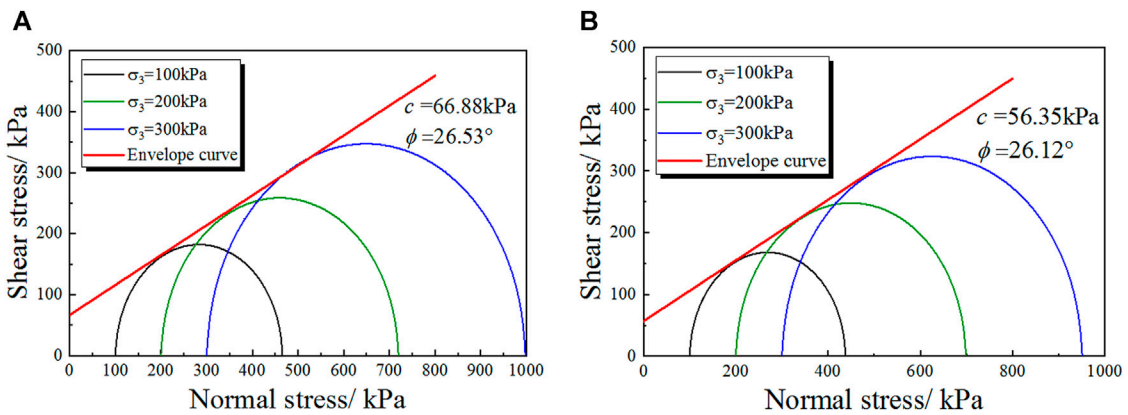

FIGURE 4 | Mohr-Coulomb failure envelope curves: **(A)** original specimens; **(B)** F-T specimens.

of -30°C, the deviatoric stress rose at first and remained stable afterwards as the axial strain increases, which is characterized as a strain-hardening type (see in **Figure 3B**). Besides, the soil columns exhibit more brittle behavior at different confining pressures and great reductions in peak stress after freezing-thawing. This phenomenon is attributed to the pressure caused by ice lens formation increasing the friability of GRS, leading to a reduction of peak stress when large deformation occurs to the specimen (He et al., 2020).

Further, the stress-strain curves of GRS before and after freezing-thawing both increase with the increasement of confining pressures, as a result of an enhancement in the elastic modulus. The relationship between the axial stress σ_1 and confining pressure σ_3 from TRX results can be interpreted according to the Mohr-Coulomb criterion (Zhang et al., 2017):

$$\sigma_1 = \frac{2c \cdot \cos\varphi}{1 - \sin\varphi} + \frac{1 + \sin\varphi}{1 - \sin\varphi}\sigma_3, \quad (1)$$

Where, c denotes the cohesion (kPa) and φ denotes the internal friction angle (°).

The failure envelopes from the triaxial results are given in **Figure 4.** The linear relationship between the normal stress and shear strength is easy to be observed for the original and F-T specimens of GRS. After the F-T process, the envelope curves exhibit a decreasing trend along the shear stress axis, as well as the slope of the linear function (He et al., 2020). The shear parameters (cohesion c and internal friction angle φ) of GRS before and after F-T process are obtained by the More-Coulomb criterion, as **Figure 5** illustrated. Through calculating, the cohesion of GRS is reduced by about 15.7% while the internal friction angle is only reduced about 1.5%. It is easily recognizable that the decreasing extent of cohesion of GRS is much higher than that of internal friction angle due to AGF effects. This phenomenon can be ascribed to the cracking behavior of GRS due to negative temperatures that mainly weaken the original cohesive force of clay aggregates rather than the friction force between the grains (Zeng et al., 2018).

Pore Size Distributions

The NMRI measurements have been widely used to evaluate the pore size distributions of porous medias for decades (Yao et al.,

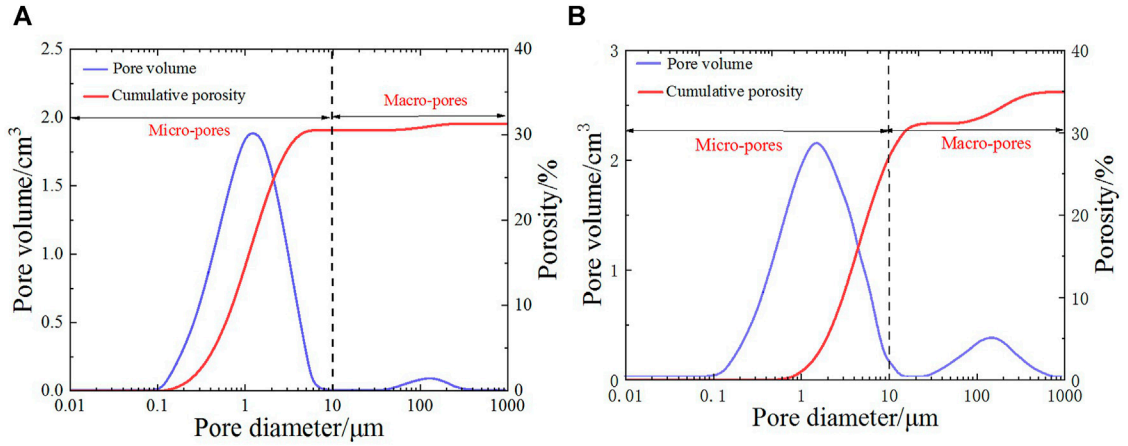

FIGURE 5 | Pore volume distributions of GRS: **(A)** original specimen, **(B)** F-T specimen.

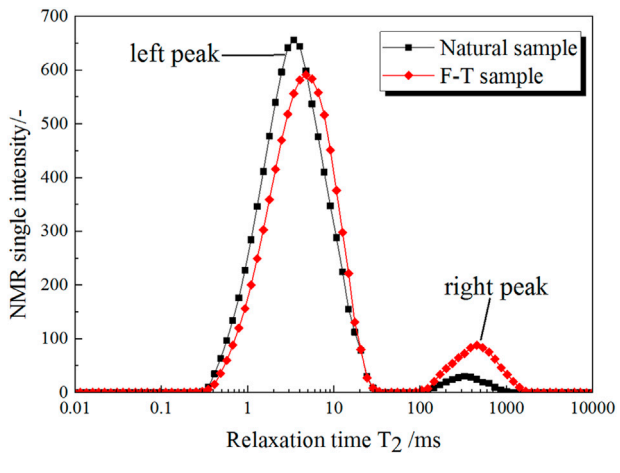

FIGURE 6 | T_2 distribution curves from NMR tests.

2021). For the saturated specimens of soils, the porosity is mainly determined by initial moisture contents. It is concluded that the measured T_2 distribution curves are used to characterize the pore distributions in soils, where the abscissa is the relaxation time T_2 representing the pore size and the ordinate is the NMR signal intensity reflecting the pore-water volume with the current size. In this present section, the T_2 curves of the GRS exhibit two different peaks, as plotted in **Figure 6**. It is clear that the amplitudes of left peaks are significantly higher than those of right peaks in T_2 distribution curves. After the A-T process, the left and right peak in the T_2 distribution curve of the original specimen both shifted rightward along the X-coordinate, representing a rise in pore diameters of GRS. Moreover, the NMR signal intensity and the spectrum area of the right peak in the T_2 distribution curve significantly increase under the AGF impact. (ASTMD422-63,2002); ASTMD4926,2015.

The relaxation time T_2 is complex since it is regulated by three relaxation mechanisms: bulk, surface, and diffusion relaxations. To simplify, the T_2 values of porous mediums ascertained from NMRI tests are primarily regulated by the surface relaxation effect, which can be expressed as **Eq. 2** (Watanabe and Wake 2009).

$$\frac{1}{T_2} = \rho_2 \frac{S}{V}, \tag{2}$$

where, ρ_2 denotes the surface relaxation coefficient, which is a parameter of magnetic interactions at the fluid-solid interface. $\frac{S}{V}$ denotes the ratio of the surface area S to the pore volume V.

$$\frac{S}{V} = \frac{F_s}{D}, \tag{3}$$

Where, F_s denotes the geometric factor of pore (6 for the spherical pored and 4 for cylindrical pores) and D denotes the pore diameters.

Kong et al. (2017) proved that the cylindrical model is suitable to represent pores in soil, and **Eq. 2** can be expressed as:

$$\frac{1}{T_2} = \frac{4\rho_2}{D} \tag{4}$$

Accordingly, the relaxation time T_2 is linearly proportional to the pore diameter. It is viable to estimate the pore diameter by using the T_2 distribution curves based on the surface relaxation coefficient ρ_2. It is worth noting that ρ_2 is normally assumed to be a constant for a specific sample when interpreting NMR results. The ρ_2 value depends on the paramagnetic impurities on the grain surfaces interacting with hydrogen nuclei in pore water and the imposing of additional relaxations (Lyu et al., 2018). The ρ_2 is also related to the combination of pore fluid and mineral grain and pore fluid for interpreting NMR results (Kong et al., 2020). In this study, the ρ_2 value was determined as 0.258 μm/s based on the Schlumberger-Doll Research (SDR) equation (Daigle and Dugan 2009).

In addition, the pore volume V_i of GRS at the current diameter of D is expressed as:

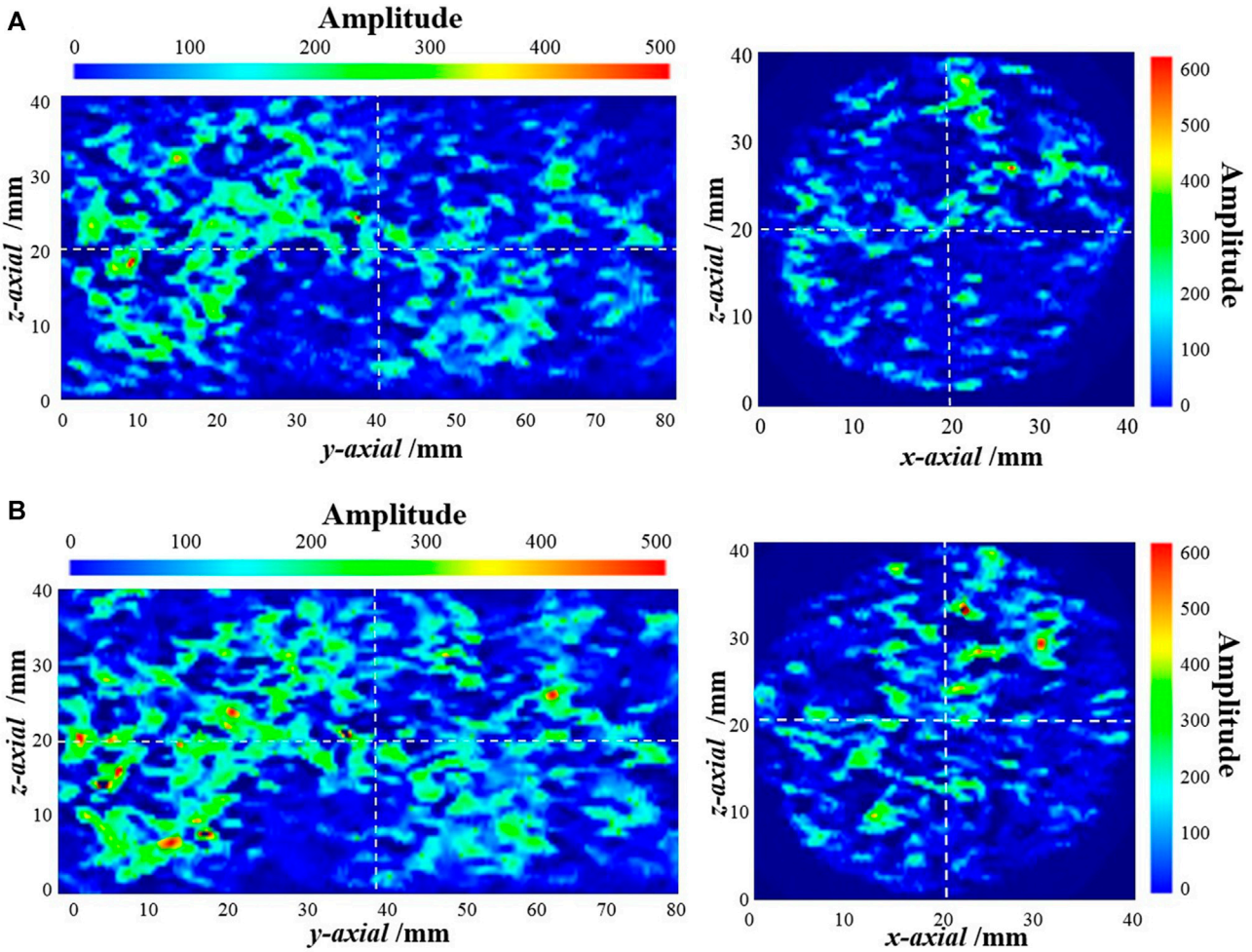

FIGURE 7 | T_2-weighted images of GRS: **(A)** Original specimen, **(B)** F-T specimen.

$$V_i = \frac{A_i}{\sum A_i} \cdot \frac{m_w}{\rho_w} = \frac{A_i}{\sum A_i} \cdot \frac{m_s - m_d}{\rho_w}, \quad (5)$$

where A_i denotes the amplitude of NMR signal, m_w denotes the mass of water, m_s denotes total mass of, m_d denotes the mass of thoroughly dried specimens, and ρ_w is water density.

According to the principle of NMR tests, the volume of pore water in fully saturated samples with different sizes are in fact equal to the corresponding pore volume. Accordingly, the amounts and volumes of pore in the tested samples can be calculated by using the T_2 spectras and the conversion coefficient ρ_2 (Kong et al., 2018). Based on the PSD results of original specimens of GRS (see in **Figure 5A**), the quantified pores that have diameters less than 1 μm account for over 40% of the total pores, while more than 90% of the pores have a diameter less than 10 μm. Further, we divided the pores into micro-pores with the equivalent diameter $D < 10$ μm and macro-pores with the equivalent $D > 10$ μm. The volumes of pores were calculated considering all pores in the samples, according to the study from Tian et al. (2018). The curves of PSD and cumulative porosity of the GRS after F-T process are given in **Figure 5B**. The pore size distributions (PSD) of original and F-T specimens are both constituted of two peaks, corresponding to micro-pores with diameters from 0.01 to 10 μm and macro-pores with diameters from 10 to 1,000 μm. After freezing and thawing, the pore volume of the left peak declines while the right peak moves upward, suggesting that the pore size distribution of GRS significantly changed. According to the pore size distribution curves, the macro-pore volume increases sharply, the micro-pore volume decreases slightly, and the total porosity increases by nearly 11.1%, as a result of the AGF impact at the extremely low temperature.

To further analyze the microstructural variations, the pore characteristics of the GRS were obtained based on the imaging features of NMRI tests, as given in **Figure 7**. The pore water distributed zones in the specimen is visually discerned with T_2-weighted images. In this paper, the T_2-weighted profile and cross-sectional images were obtained to observe the pore variations of GRS after the F-T process. From **Figure 7A**, it is obvious that the number of large-scale pores in the original specimen is relatively

few. The pseudo-color images of GRS after freezing-thawing were presented in **Figure 7B**, which shows that the AGF impact reinforced the expansion of pores. Besides, the heterogeneous degree of the microstructure is also increased by F-T process, which is proven by the pores in GRS becoming more anisotropic for both profiles and cross-sections. Thus, the change in pore size distributions can be verified from a visualized perspective, according to the results of T_2-weighted images. He et al.,2020.

DISCUSSION

According to the classical theory of soil mechanics, three components exist in natural soils: the soil skeleton, pore, and water filled in pores (Terzaghi 1943). For granite residual soils in the F-T state, the soil skeleton is composed of coarse and fine particles, the pore is characterized by a binary distribution, and the water exists in solid and liquid forms. The shear strength reduction is attributed to the microstructural disturbance of GRS under the AGF impact. During the freezing-thawing process, the expansive pressures induced by formations of ice lens increase the friability of soil specimens, reducing the off-peak stress in large deformations. Moreover, the thawing procedure of ice lens accumulates the cracking process in GRS, which contributes to the structural failure of the specimen.

When the GRS is at an extremely low temperature, the effect of expansion and shrinkage of soils due to AGF method controls the trend of volume change together (Villar and Lloret 2015). As the distance between soil particles increased, the cohesion force of clay aggregates and sandy particles declined significantly. In addition, the negative pressures in unfrozen areas in the specimens squeezed the clay particles to become more rigid, thereby reducing the decreasing amplitude of the internal friction angle. Accordingly, the frost heaving effect results in an obvious degradation in the cohesion instead of internal friction angle of the specimen. As the freezing front moves, the formation of ice lens in frozen areas and the moisture migration under negative pressures in unfrozen areas both exist, contributing to uneven deformations in the GRS. As a result, the frost heaving and thawing effect causes a disturbance in mechanical behaviors due to AGF constructions (Wang et al., 2020). On this basis, the shear strength decreases synchronously with the pore enlargement of GRS during the AGF process.

CONCLUSION

Based on this experimental study, the following conclusions are drawn:

1) The process of freezing-thawing on the shear strength of GRS under an extremely low temperature was investigated by performing triaxial loading tests. The stress-strain curves of the original specimen display a strain-softening feature while exhibiting a strain-hardening feature after the F-T process. The cohesion is reduced by about 15.7% while the internal friction angle was only reduced about 1.5%, due to the AGF impact.
2) Based on the results of NMRI tests, two peaks in the T_2 distribution curve of the original specimen shift to the right after the AGF process. Meanwhile, the NMR signal intensity of the right peak increases dramatically. With the assistance of the surface relaxation coefficient (ρ_2), the T_2 distribution curve could be converted to the pore size distribution curve. Under the AGF impact, micropores are squeezed under negative pressures in unfrozen areas and macro-pores are enlarged due to the formation of ice lens.
3) The discussion on frost heaving mechanism demonstrates that the mechanical property is closely related to the pore size distribution. The variation of large pores can be attributed to the formation of ice lens, negative pressures in unfrozen areas, as well as the accumulation of uneven deformations. Therefore, the microstructural disturbance in soil weakened the original cohesive force among grains, directly resulting in a reduction of shear strength. The discussion on pore size distributions primarily interprets the phenomenon of frost heaving damage on mechanical behaviors of GRS under AGF constructions. (Lu et al.,2019; He et al.,2020; Li et al.,2021)

DATA AVAILABILITY STATEMENT

The raw data supporting the conclusion of this article will be made available by the authors, without undue reservation.

AUTHOR CONTRIBUTIONS

RA performed the tests and wrote the manuscript. LK designed the tests. XZ processed part of the data. All authors contributed extensively to the review and revision of this manuscript.

FUNDING

The present study had the financial support of the National Natural Science Foundation of China (Grant Number: 12102312 and 42177148) and Open Fund of State Key Laboratory of Geohazard Prevention and Geoenvironment Protection (Grant Number: SKLGP2021K011).

REFERENCES

An, R., Kong, L., Guo, A., and Zhang, X. (2019). A Proposed Method to Determine *In-Situ* Shear Modulus and Shear Strain Decay Curves in Different Structured Soil. *E3s Web Conf.* 92 (5), 18004. doi:10.1051/e3sconf/20199218004

An, R., Kong, L., and Li, C. (2020). Pore Distribution Characteristics of Thawed Residual Soils in Artificial Frozen-wall Using NMRI and MIP Measurements. *Appl. Sci.* 10, 544. doi:10.3390/app10020544

An, R., Kong, L. W., and Li, C. S. (2020). Strength Attenuation and Microstructure Damage of Granite Residual Soils under Hot and Rainy Weather. *Chin. J. Rock Mech. Eng.* 39 (9), 1902–1911. doi:10.13722/j.cnki.jrme.2020.0073

ASTM D422-63 (2002). *Standard Test Method for Consolidated Undrained Triaxial Compression Test for Cohesive Soils*. West Conshohocken, PA: ASTM International.

ASTM D4926 (2015). *Standard Standard Test Method for Gamma Alumina Content in Catalysts and Catalyst Carriers Containing Silica and Alumina by X-ray Powder Diffraction*. West Conshohocken, PA: ASTM International.

Bai, R., Lai, Y., Zhang, M., and Yu, F. (2018). Theory and Application of a Novel Soil Freezing Characteristic Curve. *Appl. Therm. Eng.* 129, 1106–1114. doi:10.1016/j.applthermaleng.2017.10.121

Black, P. B., and Tice, A. R. (1989). Comparison of Soil Freezing Curve and Soil Water Curve Data for Windsor sandy Loam. *Water Resour. Res.* 25, 2205–2210. doi:10.1029/wr025i010p02205

Bronfenbrener, L., and Bronfenbrener, R. (2010). Frost Heave and Phase Front Instability in Freezing Soils. *Cold Regions Sci. Tech.* 64 (1), 19–38. doi:10.1016/j.coldregions.2010.07.001

Chen, R. P., Li, Z. C., Chen, Y. M., Ou, C. Y., Hu, Q., and Rao, M. (2015). Failure Investigation at a Collapsed Deep Excavation in Very Sensitive Organic Soft clay. *Jc Performc Constr. Fac.* 2015 (040140783). doi:10.1061/(asce)cf.1943-5509.0000557

Cui, Z.-D., and Zhang, Z.-L. (2015). Comparison of Dynamic Characteristics of the Silty clay before and after Freezing and Thawing under the Subway Vibration Loading. *Cold Regions Sci. Tech.* 119, 29–36. doi:10.1016/j.coldregions.2015.07.004

Daigle, H., and Dugan, B. (2009). Extending Nmr Data for Permeability Estimation in fine-grained Sediments. *Mar. Pet. Geology.* 26 (8), 1419–1427. doi:10.1016/j.marpetgeo.2009.02.008

Fang, Q., Zhang, D., and Wong, L. N. Y. (2011). Environmental Risk Management for a Cross Interchange Subway Station Construction in china. *Tunnelling Underground Space Tech.* 26 (6), 750–763. doi:10.1016/j.tust.2011.05.003

Fonseca, A. V. D., Carvalho, J., Ferreira, C., Santos, J. A., Almeida, F., Pereira, E., et al. (2006). Characterization of a Profile of Residual Soil from Granite Combining Geological, Geophysical and Mechanical Testing Techniques. *Geotech Geol. Eng.* 24 (5), 1307–1348. doi:10.1007/s10706-005-2023-z

Fu, J., Yang, J., Zhang, X., Klapperich, H., and Abbas, S. M. (2014). Response of the Ground and Adjacent Buildings Due to Tunnelling in Completely Weathered Granitic Soil. *Tunnelling Underground Space Tech.* 43, 377–388. doi:10.1016/j.tust.2014.05.022

Han, L., Ye, G.-l., Li, Y.-h., Xia, X.-h., and Wang, J.-h. (2016). *In Situ* monitoring of Frost Heave Pressure during Cross Passage Construction Using Ground-Freezing Method. *Can. Geotech. J.* 53, 530–539. doi:10.1139/cgj-2014-0486

He, X.-C., Xu, Y.-S., Shen, S.-L., and Zhou, A.-N. (2020). Geological Environment Problems during Metro Shield Tunnelling in Shenzhen, China. *Arab. J. Geosci.* 13 (2). doi:10.1007/s12517-020-5071-z

He, Z., Xiang, D., and Liu, Y. (2020). Triaxial Creep Test and Particle Flow Simulation of Coarse-Grained Soil Embankment Filler. *Front. Earth Sci.* 8. doi:10.3389/feart.2020.00062

Kong, L., Sayem, H. M., and Tian, H. (2018). Influence of Drying-Wetting Cycles on Soil-Water Characteristic Curve of Undisturbed Granite Residual Soils and Microstructure Mechanism by Nuclear Magnetic Resonance (NMR) Spin-Spin Relaxation Time (T2) Relaxometry. *Can. Geotech. J.* 55, 208–216. doi:10.1139/cgj-2016-0614

Kong, L., Wang, Y., Sun, W., and Qi, J. (2020). Influence of Plasticity on Unfrozen Water Content of Frozen Soils as Determined by Nuclear Magnetic Resonance. *Cold Regions Sci. Tech.* 172, 102993. doi:10.1016/j.coldregions.2020.102993

Konrad, J.-M., and Morgenstern, N. R. (1980). A Mechanistic Theory of Ice Lens Formation in fine-grained Soils. *Can. Geotech. J.* 17, 473–486. doi:10.1139/t80-056

Lackner, R., Pichler, C., and Kloiber, A. (2008). Artificial Ground Freezing of Fully Saturated Soil: Viscoelastic Behavior. *J. Eng. Mech.* 134134, 1–11. doi:10.1061/(ASCE)0733-939910.1061/(asce)0733-9399(2008)134:1(1)

Li, C., Kong, L., Shu, R., An, R., and Jia, H. (2020). Dynamic Three-Dimensional Imaging and Digital Volume Correlation Analysis to Quantify Shear Bands in grus. *Mech. Mater.* 151, 103646. doi:10.1016/j.mechmat.2020.103646

Li, T., Kong, L., and Guo, A. (2021). The Deformation and Microstructure Characteristics of Expansive Soil under Freeze-Thaw Cycles with Loads. *Cold Regions Sci. Tech.* 192, 103393. doi:10.1016/j.coldregions.2021.103393

Liu, X., Hu, C., Liu, Q., and He, J. (2021). Grout Penetration Process Simulation and Grouting Parameters Analysis in Fractured Rock Mass Using Numerical Manifold Method. *Eng. Anal. Boundary Elem.* 123, 93–106. doi:10.1016/j.enganabound.2020.11.008

Liu, Y., Hu, J., Xiao, H., and Chen, E. J. (2017). Effects of Material and Drilling Uncertainties on Artificial Ground Freezing of Cement-Admixed Soils. *Can. Geotech. J.* 54, 1659–1671. doi:10.1139/cgj-2016-0707

Lu, Z., Xian, S., Yao, H., Fang, R., and She, J. (2019). Influence of Freeze-Thaw Cycles in the Presence of a Supplementary Water Supply on Mechanical Properties of Compacted Soil. *Cold Regions Sci. Tech.* 157, 42–52. doi:10.1016/j.coldregions.2018.09.009

Lyu, C., Ning, Z., Wang, Q., and Chen, M. (2018). Application of NMR T2 to Pore Size Distribution and Movable Fluid Distribution in Tight Sandstones. *Energy Fuels* 32, 1395–1405. doi:10.1021/acs.energyfuels.7b03431

Nakashima, Y., Mitsuhata, Y., Nishiwaki, J., Kawabe, Y., Utsuzawa, S., and Jinguuji, M. (2011). Non-destructive Analysis of Oil-Contaminated Soil Core Samples by X-ray Computed Tomography and Low-Field Nuclear Magnetic Resonance Relaxometry: a Case Study. *Water Air Soil Pollut.* 214, 681–698. doi:10.1007/s11270-010-0473-2

Pellet, C., Hilbich, C., Marmy, A., and Hauck, C. (2016). Soil Moisture Data for the Validation of Permafrost Models Using Direct and Indirect Measurement Approaches at Three alpine Sites. *Front. Earth Sci.* 3 (91). doi:10.3389/feart.2015.00091

Pichler, C., Lackner, R., and Mang, H. A. (2003). Continuum-micromechanics Approach for Determination of Frost Heave in Artificial Ground Freezing. *Comput. Fluid Solid Mech.*, 128. 578–581. doi:10.1016/B978-008044046-0.50142-1

Pimentel, E., Papakonstantinou, S., and Anagnostou, G. (2012). Numerical Interpretation of Temperature Distributions from Three Ground Freezing Applications in Urban Tunnelling. *Tunnelling Underground Space Tech.* 28, 57–69. doi:10.1016/j.tust.2011.09.005

Shoop, S. A., and Bigl, S. R. (1997). Moisture Migration during Freeze and Thaw of Unsaturated Soils: Modeling and Large Scale Experiments. *Cold Regions Sci. Tech.* 25 (1), 33–45. doi:10.1016/s0165-232x(96)00015-8

Terzaghi, K. T. (1943). *Theoretical Soil Mechanics*. J. Wiley and Sons, inc.

Tian, H., Wei, C., and Tan, L. (2019). Effect of Freezing-Thawing Cycles on the Microstructure of Soils: A Two-Dimensional NMR Relaxation Analysis. *Cold Regions Sci. Tech.* 158, 106–116. doi:10.1016/j.coldregions.2018.11.014

Toll, D. G., and Ong, B. H. (2015). Critical-state Parameters for an Unsaturated Residual sandy clay. *Géotechnique* 53 (1), 93–104.

Villar, M. V., and Lloret, A. (2004). Influence of Temperature on the Hydro-Mechanical Behaviour of a Compacted Bentonite. *Appl. Clay Sci.* 26 (1-4), 337–350. doi:10.1016/j.clay.2003.12.026

Vitel, M., Rouabhi, A., Tijani, M., and Guérin, F. (2015). Modeling Heat Transfer between a Freeze Pipe and the Surrounding Ground during Artificial Ground Freezing Activities. *Comput. Geotechnics* 63 (jan), 99–111. doi:10.1016/j.compgeo.2014.08.004

Wang, S., Yang, P., Dai, D., Xue, K., and Li, D. (2020). A Study on Micro-pore Characteristics of clay Due to Freeze-Thaw and Compression by Mercury Intrusion Porosimetry. *Front. Earth Sci.* 7, 344. doi:10.3389/feart.2019.00344

Watanabe, K., and Wake, T. (2009). Measurement of Unfrozen Water Content and Relative Permittivity of Frozen Unsaturated Soil Using NMR and TDR. *Cold Regions Sci. Tech.* 59, 34–41. doi:10.1016/j.coldregions.2009.05.011

Yao, C., Wei, C., Ma, T., Chen, P., and Tian, H. (2021). Experimental Investigation on the Influence of Thermochemical Effect on the Pore-Water Status in Expansive Soil. *Int. J. Geomech.* 21 (6), 04021080. doi:10.1061/(ASCE)GM.1943-5622.0002020

Yuanming, L., Zhihua, G., Shujuan, Z., and Xiaoxiao, C. (2010). Stress-Strain Relationships and Nonlinear Mohr Strength Criteria of Frozen Sandy Clay. *Soils and Foundations* 50 (1), 45–53. doi:10.3208/sandf.50.45

Zeng, Z., Kong, L., Wang, M., and Sayem, H. M. (2018). Assessment of Engineering Behaviour of an Intensely Weathered Swelling Mudstone under Full Range of Seasonal Variation and the Relationships Among Measured Parameters. *Can. Geotech. J.* 55, 1837–1849. doi:10.1139/cgj-2017-0582

Zhang, X. W., Kong, L. W., Yin, S., and Chen, C. (2017). Engineering Geology of Basaltic Residual Soil in Leiqiong, Southern China. *Eng. Geology.* 220, 196–207. doi:10.1016/j.enggeo.2017.02.002

Zhou, J., and Tang, Y. (2015). Centrifuge Experimental Study of Thaw Settlement Characteristics of Mucky clay after Artificial Ground Freezing. *Eng. Geology.* 190, 98–108. doi:10.1016/j.enggeo.2015.03.002

Zhou, J., and Tang, Y. (2018). Practical Model of Deformation Prediction in Soft clay after Artificial Ground Freezing under Subway Low-Level Cyclic Loading. *Tunnelling Underground Space Tech.* 76, 30–42. doi:10.1016/j.tust.2018.03.003

Conflict of Interest: The authors declare that the research was conducted in the absence of any commercial or financial relationships that could be construed as a potential conflict of interest.

Publisher's Note: All claims expressed in this article are solely those of the authors and do not necessarily represent those of their affiliated organizations, or those of the publisher, the editors and the reviewers. Any product that may be evaluated in this article, or claim that may be made by its manufacturer, is not guaranteed or endorsed by the publisher.

frontiers in Earth Science

ORIGINAL RESEARCH
published: 19 October 2021
doi: 10.3389/feart.2021.768757

Applications of an Innovative Strength Parameter Estimation Method of the SoilRock Mixture in Evaluating the Deposit Slope Stability Under Rainfall

Xiaodong Fu[1,2], *Zhenping Zhang*[3]*, *Qian Sheng*[1,2], *Yongqiang Zhou*[1,2], *Juehao Huang*[1,2], *Zhe Wu*[4,5] *and Mingyang Liu*[4,5]

[1]State Key Laboratory of Geomechanics and Geotechnical Engineering, Institute of Rock and Soil Mechanics, Chinese Academy of Sciences, Wuhan, China, [2]School of Engineering Science, University of Chinese Academy of Sciences, Beijing, China, [3]School of Architecture and Civil Engineering, Shenyang University of Technology, Shenyang, China, [4]China State Construction International Holdings Limited, Hong Kong, Hong Kong, SAR China, [5]China State Construction International Investments (Hubei) Limited, Wuhan, China

OPEN ACCESS

Edited by:
Fei Meng,
Swinburne University of Technology, Australia

Reviewed by:
Shaobo Chai,
Chang'an University, China
Rong Lifan,
Shijiazhuang Tiedao University, China
Xiaocheng Huang,
Hunan University of Science and Technology, China

***Correspondence:**
Zhenping Zhang
zhangzhenping16@mails.ucas.edu.cn

Specialty section:
This article was submitted to Geohazards and Georisks, a section of the journal Frontiers in Earth Science

Received: *01 September 2021*
Accepted: *09 September 2021*
Published: *19 October 2021*

Citation:
Fu X, Zhang Z, Sheng Q, Zhou Y, Huang J, Wu Z and Liu M (2021) Applications of an Innovative Strength Parameter Estimation Method of the SoilRock Mixture in Evaluating the Deposit Slope Stability Under Rainfall. Front. Earth Sci. 9:768757. doi: 10.3389/feart.2021.768757

Deposit landslides are one of the most representative geological hazards around the world, and the poor understanding of the mechanical characteristics of the soilrock mixture (S-RM) increases the difficulties in evaluating the stability of the deposit slope subjected to rainfall. This study attempted to propose an innovative strength parameter estimation method of the S-RM based on the concept and format of the generalized HoekBrown criterion. The system of "rock blocks–soil–contact surface" was considered the main source providing resistance to the external force, and the effect of the soil matrix, rock blocks, and the contact surface between them was taken into account. The verification of the estimation method was proved based on the abundant test data. A typical deposit slope located in the Taoyuan region of Yunnan Province, China, was selected as a case study, and the estimation method was applied to provide the shear parameters of the S-RM. The slope stability subjected to different types of rainfall was analyzed considering the parameter deteriorations, and the results show that the deposit landslide is more prone to the wave-type rainfall, which shows a deeper response depth of pore water pressure and a smaller safety factor. The present study suggests a simple estimation method for the shear parameters of the S-RM using a few parameters for the engineers and provides an understanding of the deposit slope stability during the rainfall process.

Keywords: deposit slope, soilrock mixture, strength parameter, Hoek-brown criterion, rainfall

INTRODUCTION

Worldwide, a large number of deep and loose deposits such as moraine, alluvial, and fluviallacustrine sediments are formed under dynamic actions such as tectonic uplift, river erosion, earthquake, and glaciation. Under the disturbance of the natural and artificial processes, it is commonly found that the occurrence of the deposit slope hazard with the characteristics of huge scale and quantity, such as collapse, landslide, and debris flow (Fu et al., 2020a; Zheng et al., 2021). The deposit slope hazard has been intensely studied in the last two decades due to its high risk and serious damage, and the results indicate that rainfall is a great threat to the deposit slopes in the mountainous region and even leads to deposit landslide and debris flow (Cascini et al., 2010; Fiorillo et al., 2013; Fu et al., 2020b;

Pantaleone et al., 2018; Shang et al., 2003; Xiao et al., 2020; Wang et al., 2015). Many deposit slope hazards induced by rainfall have been reported in recent years, which have posed a serious threat to the safety and property of the local human and infrastructure constructions. Therefore, the stability of the deposit slope in the mountainous area is an important research subject.

The soilrock mixture (S-RM) is the main component of the deposit slope. As a typical multi-phase geomaterial, it possesses the characteristics of anisotropy, discontinuity, and scale effect. Compared with soil and rock, the research on the mechanical properties of the S-RM is not comprehensive enough. So far, studies on the mechanical properties of the S-RM are in progress, employing mechanical tests predominantly, and the large-scale apparatuses are more preferred to avoid the constraints on the motions of rock fragments inside because of the equipment boundary. The numerical simulation methods on the S-RM could be divided into continuous and discontinuous medium simulations (Ding et al., 2010; Fu et al., 2017; Fu et al., 2019; Liu et al., 2020; Liu et al., 2021; Meng et al., 2018; Qi et al., 2021; Yang et al., 2020; Zou et al., 2011). The test and simulation results show that the mechanical properties are affected by several influencing factors such as rock block proportion, water content, compactness, and granulometric composition, and the rock block proportion plays an important role in the mechanical properties (Afifipour and Moarefvand, 2014; Monkul and Ozden, 2007; Xu et al., 2011; Yang Y. et al., 2016; Chang and Phantachang, 2016; Xu et al., 2019). Several test results show that the strength parameters of the S-RM present a complex variation law as the rock block proportion increases, and the turning points of the parameters could be observed in a relatively low and high rock block proportion, which presents considerable challenges in the determination of the shear parameters of the natural S-RM. These results provide important inspiration for the discussion of the relationship between the strength characteristics of the natural S-RM and the rock block proportion. The determination methods of the shear parameters widely used make attempts to treat the S-RM as the coarse-grained soil or completely strongly weathered rock equivalently, which lacks the discussions about the strength of the contact surfaces and the roles rock blocks and soil matrix play in the overall strength (He et al., 2018; Lü et al., 2019; Miščević and Vlastelica, 2014; Wörman, 1993; Zhang et al., 2019). Furthermore, the influence of water content on the mechanical properties of S-RM also deserves careful study. The strength parameters are fragile to water and show obvious deteriorations as water content increases, which is responsible for the failure of the deposit slope during rainfall (Duong et al., 2013; Deng, 2016; Huang, 2016; Qi, 2016; Zhou et al., 2016; Wei et al., 2019). However, the variabilities in the mechanical characteristics of the S-RM in different regions and the limitations of the simulation software result that the shear parameter deteriorations are difficult to take into account in the deposit slope assessments.

This study aims to investigate the strength characteristics of the natural S-RM and propose an innovative strength parameter estimation method to obtain the strength parameters. Given the similarities between the natural S-RM and rock masses, the relative concepts and variables in the generalized H-B criterion are taken as references for the determination and calculation of the strength parameters of the S-RM. The rock block proportion and strength of contact surface between rock blocks and soil matrix were chosen as key influence factors of the overall strength based on the test data. The nonlinear strength criterion to estimate strength was proposed, and the verification of the estimated method was performed based on a series of test data. The strength deterioration due to the effect of water was also taken into consideration. A typical deposit slope near the site of the Taoyuan Jinsha River suspension bridge in Yunnan Province, China, was selected as the case study. The slope stability was evaluated considering the shear parameter deteriorations subjected to different types of rainfall.

EXPRESSIONS OF THE NONLINEAR STRENGTH CRITERION

The HoekBrown Criterion

In the past decades, as one of the most famous and commonly used nonlinear strength criteria, the HoekBrown (H-B) criterion proposed by Hoek and Brown (1980), has been applied successfully in describing rock failure mechanisms, and the accuracy has been improved in rock engineering and rock mechanics. The original H-B criterion is a nonlinear strength criterion, which is based on several conventional rock laboratory and *in situ* test data, and the expression is as follows:

$$\sigma_1 = \sigma_3 + \sigma_c\left(m\frac{\sigma_3}{\sigma_c} + s\right)^{0.5}, \tag{1}$$

where σ_1 and σ_3 are the maximum and minimum principal stresses, respectively; σ_c is the unconfined compressive strength of the rock; m is a dimensionless empirical parameter of the rock, which is utilized to describe the degree of hardness of the rock; s is a dimensionless empirical parameter reflecting the degree of integrity of the rock mass, for intact rock $s = 1$.

The criterion was modified later by Hoek et al. (1992) to the generalized version as follows:

$$\sigma_1 = \sigma_3 + \sigma_c\left(m_b\frac{\sigma_3}{\sigma_c} + s\right)^{a} \tag{2}$$

where parameter a can be estimated from the geological strength index (GSI) as follows:

$$a = 0.5 + \frac{1}{6}\left[\exp\left(-GSI/15\right) - \exp\left(-20/3\right)\right]. \tag{3}$$

The parameters m_b and s could be obtained based on GSI, which characterizes the quality of the rock masses. The GSI depends on the structure of the rock sample and the surface condition of the joints. The parameters m_b and s are defined by Hoek et al. (1992) as follows:

$$m_b = m_i \exp\left(\frac{GSI - 100}{28 - 14D}\right), \tag{4}$$

$$s = \exp\left(\frac{GSI - 100}{9 - 3D}\right), \tag{5}$$

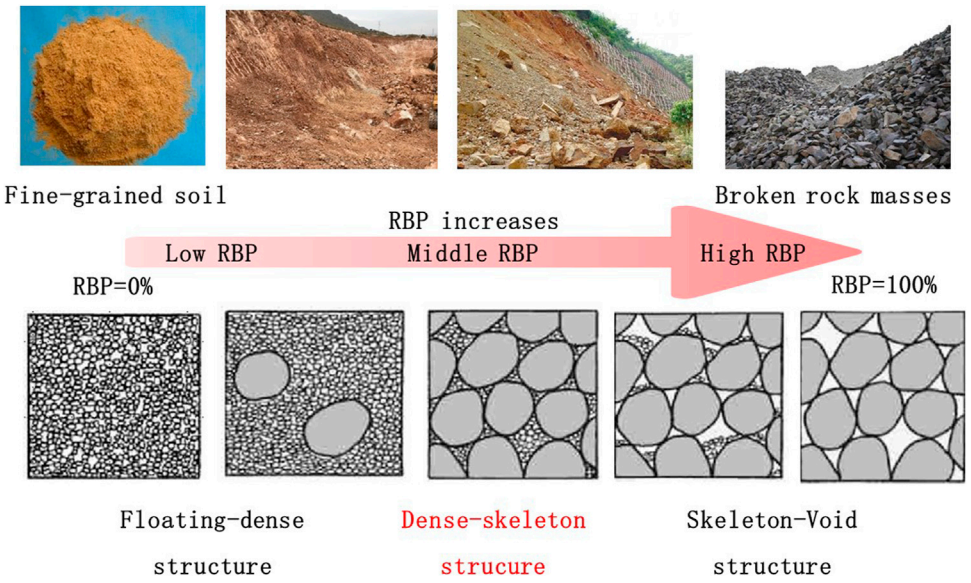

FIGURE 1 | Sketch map of the structural transformation of the soilrock mixture.

where D is proposed as a disturbance coefficient, which varies from 0.0 for the undisturbed *in situ* rock masses to 1.0 for very disturbed rock masses; m_b is the value for m for intact rock and can be obtained from experiments. Considering the case without available test data, Hoek et al. (2002) and Marinos and Hoek (2001) also provided an approximate value range of m_i for different types of rock as reference.

In the practical engineering construction, to estimate the safety of the deposit slope, the MohrCoulomb (M-C) criterion strength parameters, cohesion and friction angle, of geomaterials are commonly used. Therefore, many attempts have been made to derive the equivalent M-C parameters from the nonlinear strength criterion. Hoek and Brown (1997) proposed a nonlinear shear strength relationship based on the generalized H-B criterion and a series of test values, and the equation is defined as follows:

$$\tau = A\sigma_c\left(\frac{\sigma_n}{\sigma_c} - T\right)^B, \tag{6}$$

where τ and σ_n are the shear and normal stresses, respectively; A and B are materials constants, and the parameter T is defined as follows:

$$T = \left(m_b - \sqrt{m_b^2 + 4s}/2\right), \tag{7}$$

where the meaning of parameters m_b and s are shown above, and the calculation equation of the parameters are **Eqs 4**, **5**.

Strength Characteristics of the Natural SoilRock Mixture

Natural S-RM is composed of the soil matrix with different sizes of rock blocks mixed up. There are huge differences in the mechanical properties of the individual components, which thus leads to the complex strength characteristics of the geomaterial. **Figure 1** shows the features and transformation of the structure of the S-RM with different rock block proportions. The results show that the spatial feature of the rock blocks inside changes from floating in the soil matrix to a dense state and finally in a skeleton state as the rock block proportion increases. During the process, the main source of the overall S-RM strength also changes from the soil-matrix to rock blocks-soil-contact surface and rock blocks. The effect of the contact surface between the soil matrix and rock blocks is crucial for the resistance of S-RM to the external force, as well as the individual components.

The Nonlinear Strength Criterion for the SoilRock Mixture

In fact, the components of the natural S-RM are similar to the strongly weathered rock, and both are formed by the rock fragments with various sizes, fine-grained soil, and pores. The structure and surface conditions are chosen as the important factors for the strength of the rock in the H-B criterion. Similarly, the structure and strength of the contact surface between rock blocks and soil matrix (short as "contact surface") also play the dominant role in the strength of the S-RM. Thus, the concept and format of the nonlinear shear strength criterion proposed by Hoek and Brown (1997) could be used as the reference, and the format of the nonlinear strength criterion for the S-RM is defined as follows:

$$\tau = f(\sigma_n, \sigma_{c\text{-}SRM}, T_s, n\ldots). \tag{8}$$

Based on the expression of the nonlinear shear strength criterion shown in **Eq. 6** and the influence factors as shown in

Eq. 8, a power-law nonlinear strength criterion of the S-RM is proposed and is defined as follows:

$$\tau = A_s \sigma_{c-SRM} \left(\frac{\sigma_n}{\sigma_{c-SRM}} - T_s \right)^n, \tag{9}$$

where $\sigma_{c\text{-}SRM}$ is the unconfined compressive strength of the S-RM, which is utilized to describe the strength of the contact surface; A_s is a nonlinear strength constant of the power-law criterion, and n is the nonlinearity coefficient; parameter T_s is a material constant, which is related to the rock block proportion, and strength of fine-grained soil and rock blocks.

INNOVATIVE STRENGTH PARAMETER ESTIMATION METHOD OF THE SOILROCK MIXTURE

Shear Parameter Estimation Method of the SoilRock Mixture

The unconfined confined strength (UCS) $\sigma_{c\text{-}SRM}$ is used in the power-law criterion to describe the strength of the contact surface inside the S-RM. Several studies have shown that the value of UCS decreases compared with the soil sample as the rock block proportion increases (Afifipour and Moarefvand, 2014; Hu, 2014; Zhang et al., 2020). There is a lot of evidence that the emergence of the contact surface with low strength is responsible for the decreasing trend. Thus, the UCS of the S-RM is chosen to describe the strength of the contact surface indirectly, and the expression proposed by Kalender et al. (2014) for the value is utilized as follows:

$$\sigma_{c-SRM} / \sigma_c = \frac{A - A^{\eta}}{A - 1}, \tag{10}$$

where σ_c is the UCS value of the soil matrix; characteristic parameter A is a strength constant, which represents the contact strength between the soil and rock blocks, and it could be determined based on the value diagram using σ_c and the internal friction angle or the roughness of the rock blocks; η is the volume ratio of the rock blocks.

In order to obtain the required constant parameters in the nonlinear strength criterion, more than 140 groups of direct shear test data were collected as the shear parameter database of the natural S-RM (Avşar et al., 2015; Chang and Cheng, 2014; Chang and Phantachang, 2016; Deng, 2016; Deng et al., 2013; Deng, 2014; Liu et al., 2017; Ma et al., 2019; Monkul and Ozden, 2007; Qi, 2016; Rahardjo et al., 2008; Sun et al., 2014; Tang et al., 2018; Wang et al., 2016; Wang, 2011; Wang et al., 2013; Wei et al., 2008; Wu, 2015; Wu et al., 2017; Xu et al., 2019; Xu et al., 2011; Xue et al., 2014; Yang JH. et al., 2016; Yang et al., 2010; Zhang et al., 2016). Considering the limitations of the test data and the object of the study, the scope of application of the estimation method in this study must meet three conditions.

1) Based on the rock block proportion threshold in the previous literature, a range of rock block proportion was set as 30–90%.
2) The particle diameter range of the rock block of the geomaterial for the nonlinear strength criterion should be also set to no more than 60 mm.
3) The normal stress range of 0–1200 kPa was set as the applicable range

With the guide of the expressions in the nonlinear shear strength criterion, the quantitative expressions of the constant parameters are proposed based on test data after a lot of trials and nonlinear fitting.

The expression of T_s is similar to the equation of the parameter T of the H-B criterion as shown in **Eq. 7** and is presented as follows:

$$T = \left(m_s - \sqrt{m_s + 4 s_R} / 2 \right), \tag{11}$$

where m_s is a dimensionless constant that is related to the rock block proportion and the strength of the contact surface. The expression of m_s is defined as follows:

$$m_s = m_{Ri} \frac{100}{G} \left(\exp\left(26.21\gamma^3 - 49.83\gamma^2 + 32.48\gamma - 8.81\right) \right) \quad 0.3 \le \gamma \le 0.9, \tag{12}$$

where γ is the mass ratio of the rock block in the S-RM; the parameter m_{Ri} is a dimensionless constant which is utilized to describe the fragment degree of the geomaterial, and the expression is defined as follows:

$$m_{Ri} = 25 \exp\left(0.25 - \gamma\right) \quad 0.3 \le \gamma \le 0.9, \tag{13}$$

As the rock block proportion increases, the S-RM turns from the fine-grained soil matrix into the mixture of rock blocks and soil in a dense state and finally converts into the heavily broken masses with the void structure as shown in **Figure 1**, where the RBP is the abbreviation of rock block proportion. Compared to the soil matrix, the fragment degree of the geomaterial increases as the rock block proportion increases, and the value of the parameter m_{Ri} keeps decrease.

The parameter G in **Eq. 12** is defined as the geological parameter of the S-RM with the guide of GSI in the generalized H-B criterion, and the value is related to the friction effect provided by the contact surface inside the geomaterials. The strength of the contact surface could be divided into the cohesive and internal friction effects. The former one is mainly controlled by the strength of the soil matrix and the roughness of the rock blocks, which has been considered by introducing the parameter $\sigma_{c\text{-}SRM}$ and characteristic parameter A into the criterion. The latter one is mainly controlled by the number of contact surfaces and the roughness of the rock blocks. **Figure 1** shows that the larger the rock block proportion is, the more the contact surface is and the more obvious the internal friction effect provided by the contact surface is. Thus, based on the test data, the expression of G is shown as follows:

$$G = 30.45 \ln\left(100\gamma\right) - 44.19 \quad 0.3 \le \gamma \le 0.9, \tag{14}$$

The undetermined parameters A_s and n in the strength criterion of the S-RM could be obtained based on the test data using the nonlinear fitting. To improve the engineering

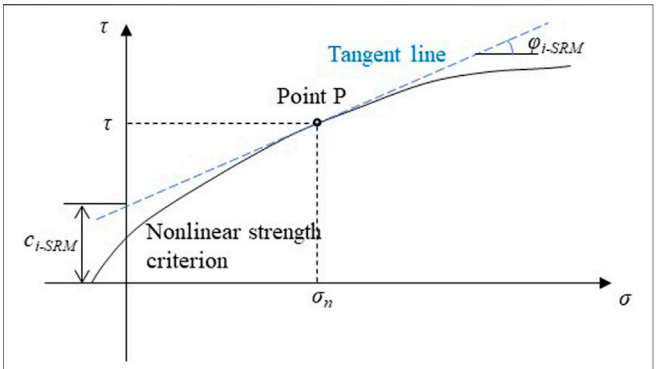

FIGURE 2 | Nonlinear strength envelope and the tangent line.

applicability and extend the scope of the application for the estimation of the shear parameters, the relationships between A_s or n and rock block proportion were also proposed based on the database, respectively, and the expressions are defined as follows:

$$A_s = \begin{cases} (-3.315\gamma + 3.305)\gamma & 0.3 \le \gamma \le 0.6 \\ (-3.353\gamma^2 + 4.156\gamma + 0.104\gamma)\gamma & 0.6 < \gamma \le 0.9 \end{cases}, \quad (15)$$

$$n = \begin{cases} -8.291\gamma^2 + 7.046\gamma - 0.594 & 0.3 \le \gamma \le 0.6 \\ -5.2\gamma^2 + 8.367\gamma - 2.478 & 0.6 < \gamma \le 0.9 \end{cases}. \quad (16)$$

To bring the nonlinear strength criterion into evaluating the stability of the deposit slope, the tangential method was applied to calculate the equivalent M-C parameters for the S-RM with the nonlinear strength envelope. As illustrated in **Figure 2**, a tangent line could be made through one-point P on the nonlinear strength envelope, and the tangent line could replace the nonlinear relationship with the form of the equivalent M-C strength parameters. Taking the stress status at point P as an example, the expression of the tangent line could be represented as follows:

$$\tau = c_{i-SRM} + \sigma_n \tan \varphi_{i-SRM}, \quad (17)$$

where the parameters $c_{i\text{-}SRM}$ and $\varphi_{i\text{-}SRM}$ are the equivalent M-C shear parameters. According to **Figure 2**, the gradient of the tangent line at the point P could be derived from **Eq. 9** as **Eq. 18** shown. The equivalent cohesion could be obtained with the combination of **Eqs 18** and **Eq. 19**. The expressions of the equivalent M-C shear parameters based on the nonlinear strength criterion are as follows:

$$\varphi_{i-SRM} = \arctan\left[A_s n \sigma_{i-SRM}\left(\frac{\sigma_n}{\sigma_{i-SRM}} - T_s\right)^{n-1}\right], \quad (18)$$

$$c_{i-SRM} = \tau - \sigma_n \tan \varphi_{i-SRM} \quad (19)$$

The Shear Parameters Estimation Method Considering the Effect of Water

Many researchers have employed mechanical experiments to focus on the mechanical properties of the natural S-RM subjected to various water contents, and results show that the shear parameters are sensitive to water, which should be focused on in the evaluation of the deposit slope (Al-Shayea, 2001; Al Aqtash and Bandini, 2015; Malizia and Shakoor, 2018; Zhou et al., 2020). Several types of fitting curves between the shear parameters and the water content have been proposed to represent the deterioration trends of the mechanical properties based on the test data, such as the exponential, power, linear, and parabola function. However, this type of fitting function barely describes the deterioration trend based on the test data and is only suitable for the material from one region, which could not be utilized widely as a reference.

In this study, the empirical approaches proposed by Zhang et al. (2021) are used to estimate the shear parameters considering water softening, which were proposed by test data to describe a more general deterioration feature. The expressions are as follows:

$$c = c_0 a^{-0.089\left(a^2 - 5.93a + 12.56\right)}, \quad (20)$$

$$\varphi = \varphi_0\left[\sqrt{e^{(1-\gamma)(a-1)/a}} - 0.49\log_{10} a\right], \quad (21)$$

where a is the water content variation ratio, c_0 is the reference cohesion, and φ_0 is the reference friction angle of the S-RM sample with natural water content.

VERIFICATION OF THE STRENGTH ESTIMATION METHOD BASED ON TEST DATA

To verify the accuracy of the proposed nonlinear strength criterion of the S-RM, the large-scale direct test data in the database were utilized as the standard values, and the comparisons between the standard and the estimated values of shear strength calculated by the nonlinear strength criterion were made as shown in **Figure 3**. The results show that the estimated and test shear strength values are concentrated on both sides of the line of $y = x$, and the relationship between the estimated and test values is $y = 0.9515x$, with the coefficient of determination as 0.9082. The data points located under the $y = x$ are more than the ones above the blue line. The area of error range ±50 kPa and ±100 kPa is marked as the dark and light blue areas, respectively. Most of the estimated values are distributed in the dark blue area, which means the absolute error of the estimated values is around ±50 kPa. A few estimated values located outside the blue area are ±100 kPa larger than the measured values. Although the estimated values are overall smaller than the test values, the error between the estimated and test values is acceptable. The results prove that the nonlinear strength criterion of the S-RM proposed in this study could be utilized for the shear parameter estimations.

BACKGROUND AND MODELING OF A CASE

Background

The engineering application of the nonlinear strength criterion of the S-RM was performed using a typical deposit slope in the

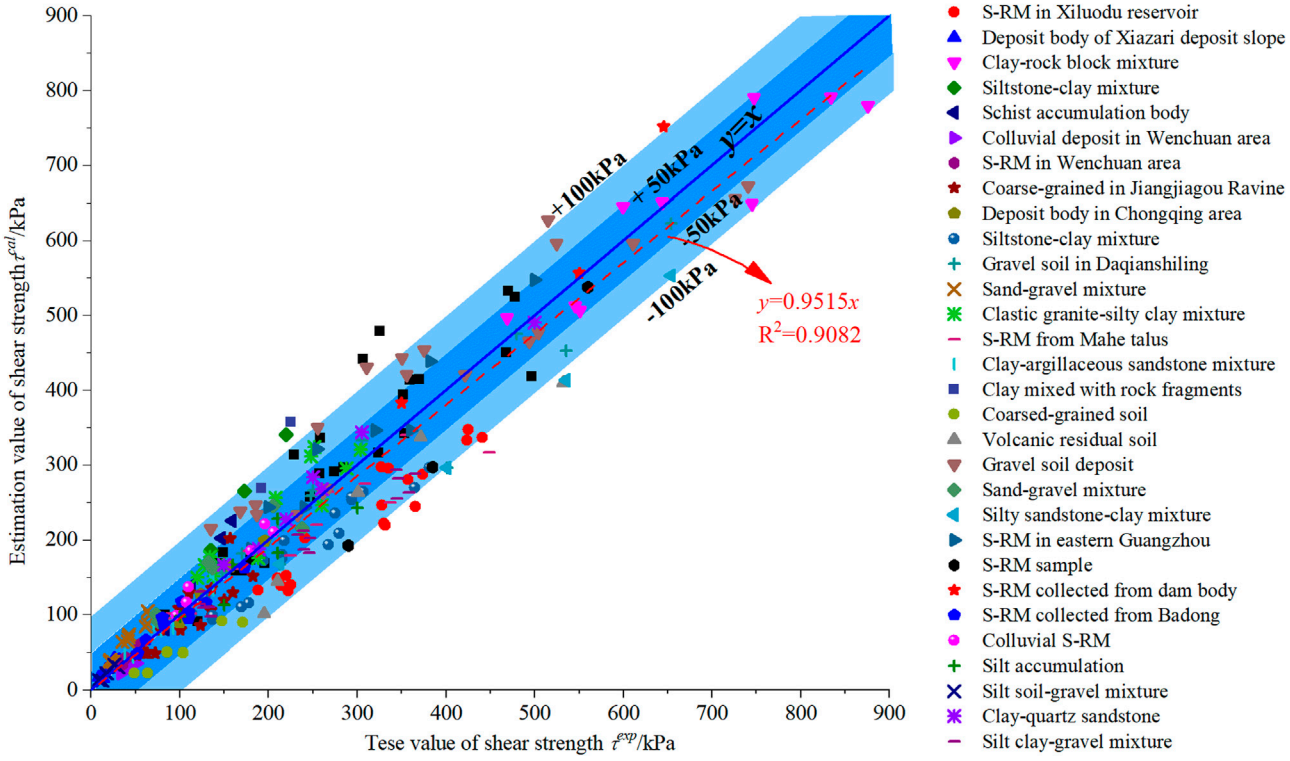

FIGURE 3 | Comparison between the estimated and test shear strength values.

following. The slope is located near the Taoyuan Jinsha River suspension bridge site in Yunnan Province, China (**Figure 4A**). The Taoyuan Jinsha River suspension bridge is located in the K76 along the Dali-Yongsheng expressway, which spans the reservoir area 21 km upstream of Ludila hydropower station. The rock of the North Bank of the suspension bridge (Yongsheng bank) is mainly moderately weathered limestone with good rock mass stability. However, at the South Bank of the suspension bridge (Dali bank), in the long-term geological evolution process, including strong crustal movement, river undercutting erosion, and historical landslide, deep and loose deposits were formed. The suspension bridge adopts the gravity anchor foundation as the bearing structure. The anchor foundation construction needs large-scale excavation, with an excavation area of more than 3000 m^2.

The 3D model based on tilt photography using an unmanned aerial vehicle shows the excavated boundary of the foundation pit of gravity anchorage (**Figure 4B**). During the construction of the gravity anchorage, the disturbance shows a negative impact on the stability of the east slope. In addition, the climatic condition of the Taoyuan region is complex, and the annual rainfall is about 750 mm. The stability of the excavation slope subjected to different types of rainfall is important for anchorage construction. Therefore, the deposit slope was selected as a case study as the application of the nonlinear strength criterion, and the stability assessment of the slope considering parameter deterioration was performed to better understand the influence of rainfall on the slope failure.

Geological and Numerical Model

As shown in **Figure 4B**, a typical profile of deposit slope is selected, and the geological and numerical models are shown in **Figure 5**. The slope included about five parts according to the survey data: the first one was the S-RM with small size gravels in a slightly dense state, the second one was the S-RM with large size gravels in the dense state, the third one was the dense silt-semi-rock layer, the fourth layer was the dense silt soil, and the fifth one was comprised of the moderately weathered limestone. The height of the model was about 235 m, and the width was set to 360 m. In the numerical model, the number of the grid points was 11,439, and the number of the triangle-quadrilateral zone was 11,384.

Determination of the Shear Parameters of the S-RM

As shown in **Figure 5**, the emergence stratum consists of the Quaternary Holocene colluvium layer, the Quaternary Pleistocene alluvial layer, and the Devonian stratum. Among these, the Quaternary Holocene colluvium and Pleistocene alluvial layer consist of clay, silt, and limestone fragments of various sizes, which could be classified as the typical S-RM. The field investigation shows that the maximum particle diameter of

A Taoyuan Jinsha River suspension bridge

B Excavated boundary of foundation pit of gravity anchorage

FIGURE 4 | Site investigation of the case. **(A)** Taoyuan Jinsha River suspension bridge. **(B)** Excavated boundary of foundation pit of gravity anchorage.

the gravels in the shallow region is about 60 mm due to the weathering effect, while the maximum diameter of the gravel in the deeper layers lies in the range of 60–90 mm. Therefore, the colluvial type S-RM in the shallow region is suitable for the nonlinear strength criterion, and the shear parameters of the material are determined as follows:

1) Determination of the rock block proportion. Several groups of the natural S-RM samples were collected from the deposit slope, and the particle size test was performed. The cumulative curve of the particle size of the S-RM sample from the east slope is shown in **Figure 6**. The soil-rock threshold was set as 2 mm, and the rock block proportion of the S-RM on the east slope is 62%.
2) Determination of the parameter of the nonlinear strength criterion. The UCS value of the soil matrix is obtained as 812.67 kPa based on the uniaxial compressive test. Geological data show that the gravels in the S-RM commonly assume in the angularsubangular shape. The characteristic parameter A was determined as 0.5 utilizing the value chart proposed by Kalender et al. (2014) taking the UCS value of the soil matrix and the roughness of the gravel into account.
3) Determination of the shear parameters of the S-RM. On the basis of the rock block proportion and UCS value of the S-RM, the nonlinear strength envelope of the S-RM with 68% rock block proportion was drawn as shown in **Figure 7**. The cohesion and friction angle of the geomaterial could be obtained using the tangential method, and the shear parameters have the following values: c = 89.85 kPa, φ = 23.33°.

Material Parameter of the Deposit Slope

The mechanical parameters of the S-RM located in the shallow region of the deposit slope have been obtained based on the nonlinear strength criterion. The mechanical parameters of the geomaterial in other strata were determined according to

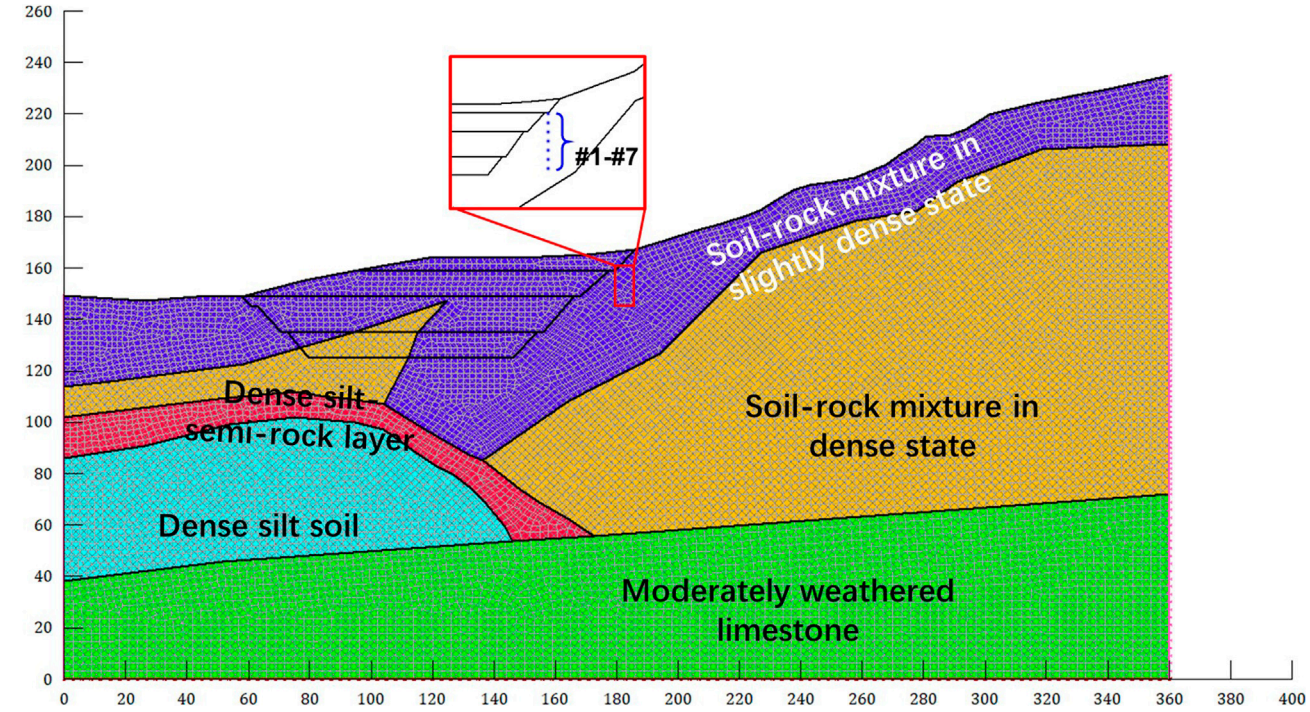

FIGURE 5 | Geological and numerical model of the deposit slope.

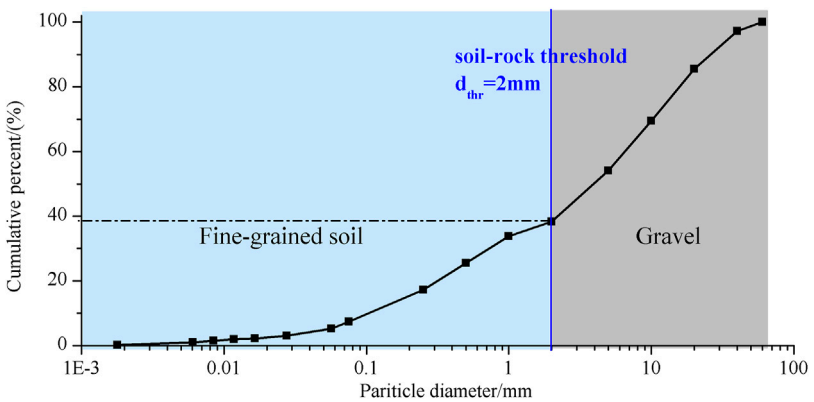

FIGURE 6 | Cumulative curve of the particle diameter of the soilrock mixture.

the prospecting data and experience reduction. The physical and mechanical parameters of geomaterials are listed in **Table 1**.

The assessment of the deposit slope under different types of rainfall was performed using the SEEP/W module of Geo-studio software. The module takes full advantage of the saturatedunsaturated seepage calculation in the rainfall numerical simulation, which fully considers the influence of the negative pore-water pressure (matrix suction) on the slope stability. In the unsaturated seepage process, the water content and permeability coefficient of the geomaterial are not fixed values, which are related to the change of the matrix suction. Therefore, the hydraulic curves of the S-RM in the slightly dense and dense state were set as shown in **Figure 8**.

STABILITY ASSESSMENTS OF THE DEPOSIT SLOPE UNDER EXCAVATION AND RAINFALL

Simulation Schemes

The numerical scheme of the stability evaluation of the deposit slope is divided into two parts: first, the deposit

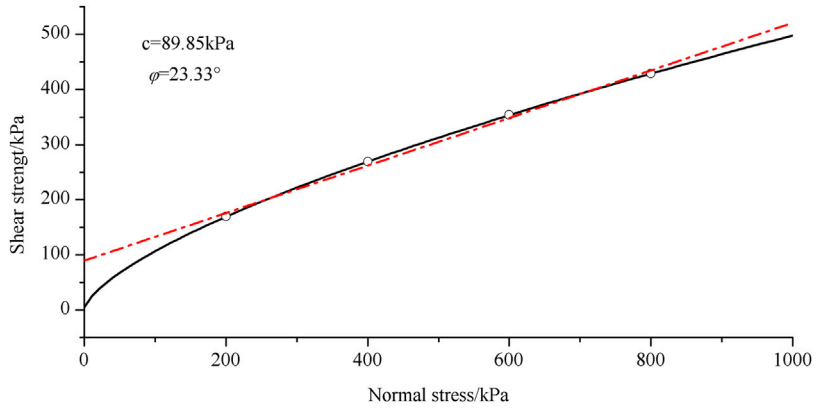

FIGURE 7 | Strength envelope of the soilrock mixture of the case.

TABLE 1 | Physical and mechanical parameters of the geomaterials.

Material	Modulus of Elasticity/MPa	Cohesion/kPa	Friction angle/(°)	Bulk density/(kN/m^3)	Possion ratio
Slightly dense soilrock mixture	242	89.85	23.33	19	0.3
Dense soilrock mixture	250	106.1	31.6	20.5	0.31
Dense silt-semi-rock	514	150	25	19.5	0.26
Dense silt soil	600	200	25	19.5	0.26
Moderately weathered limestone	35,000	22,000	50	21.5	0.22

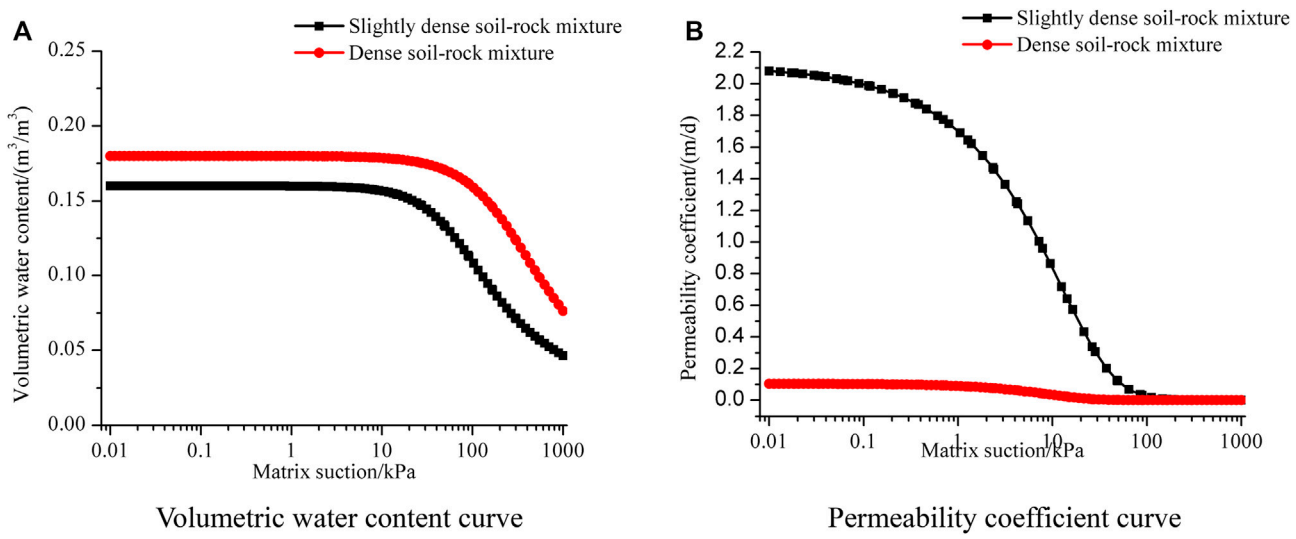

FIGURE 8 | Curves of hydraulic parameters with pore water pressure of the material in the layer of deposit. **(A)** Volumetric water content curve. **(B)** Permeability coefficient curve.

slope was excavated in four steps according to the design plan for the construction, and then, two types of rainfall were performed on the excavation slope to analyze the stability considering parameter deteriorations. The SIGMA module in the Geo-studio software was adopted to present the excavation process, and the SEEP/W module was utilized for the seepage analyses during the rainfall. Then, the SLOPE module was embedded used to obtain the potential sliding surfaces along with their safety factors based on the limit equilibrium theory of the deposit slope under rainfall.

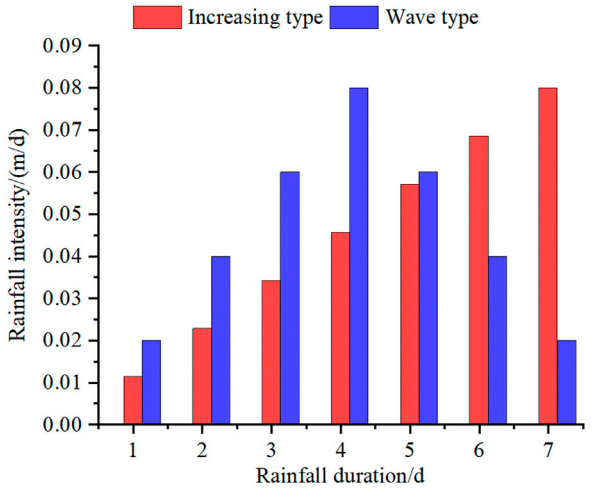

FIGURE 9 | Distributions of two types of rainfall intensities.

The rainfall in the Taoyuan region is concentrated from June to September, and the total rainfall is relatively small. The rainfall types of the rainfall events in the Taoyuan region could be divided into two types: increasing and wave type. The total rainfall for the numerical model was set as 280mm, and the rainfall duration for the two types was the same as 7 days. The daily rainfall of two rainfall types was shown in **Figure 9**.

Stability Evaluations

Figure 10A shows that the potential sliding surface of the slope before excavation is located nearly the top of the slope, and the bottom of the surface has reached the dense S-RM layer. The safety factor of the potential surface is 2.842, which is within the corresponding range of the stable slope.

Figure 10B shows the location of the potential sliding surface along with its safety factor after excavation. Compared with the location of the potential sliding surface before excavation, the potential sliding surface changed from the top to the nearby excavation area, which indicates that the stability of the slope has been controlled by the stress status due to excavation disturbance. The safety factor of the potential sliding surface was decreased from 2.842 to 2.052, and the slope was still in a stable state. There was no obvious local destroy observed in the excavation slope based on the field survey, which is consistent with the numerical result.

To analyze the influence of rainfall type on the seepage and stability of the deposit slope, the increasing and wave types of rainfall were performed under the same rainfall and rainfall duration considering the parameter deterioration. As shown in **Figure 5**, to quantitatively describe the variations of the hydraulic parameters due to rainfall infiltration, seven monitor points were set in the layer of the slightly dense S-RM. **Figure 11** shows the variations of the pore water pressure in different depths during the rainfall. The pore water pressure of #1 point near the surface responded immediately since the rainfall started, and the pore pressure water increased from −541.58 kPa to −423.18 kPa and −359.97 kPa under the effect of the increasing (**Figure 11A**) and wave-type (**Figure 11B**) rainfall, respectively. According to the rainfall intensity variations (**Figure 9**), the intensity of the wave type is larger than the increasing type in the first five days of rainfall. The pore water pressure of #1 under the wave-type rainfall has reached −133.68 kPa after five days of rainfall while the value is still less than −150 kPa under the increasing type. The pore water pressure of #5 with the height of 144 m has shown an increase after five wave-type rainy days, which indicates that the deepest pore-water pressure response depth of the wave-type rainfall in **Figure 11B** has reached 20 m below the surface. Under the same rainfall duration, the rainfall influence depth is much shallower subjected to the increasing type of rainfall, and the pore water pressure #4 has just shown an increasing trend after five rainy days. The rainfall intensity of the wave-type rainfall starts to decrease after the fifth day, which also leads to the decrease of pore water pressure of points #1 and 2# in the last two days of rainfall. In contrast, the intensity of the increasing type increases monotonically, and the pore water pressure in the shallow region keeps increasing in the whole rainfall process. Under the same total rainfall and rainfall duration, the deepest response depth of pore water pressure of the increasing type is still under 25 m, while the obvious increase of the pore water pressure at the same depth under the wave-type rainfall has been observed at the end of rainfall.

As shown in **Figures 12A,B**, a similar phenomenon also appeared in the variation of the water content of the monitor points. The values of the points located near the surface are more sensitive to the variation of rainfall intensity; the water content of the #1 and #2 decreases after the fifth rainy day in **Figure 12B**, which is attributed to the reduction of rainfall intensity in the wave-type rainfall. The water content of point #7 has shown an increasing trend compared to the initial state, which means the rainfall infiltration has reached that depth and supply. In summary, the wave-type rainfall has a deeper infiltration depth and a larger influence area on the pore water pressure and water content than the increasing type rainfall, which could be seen as the dangerous rainfall type for slope stability.

The stabilities of the deposit slope subjected to two types of rainfall considered parameter deterioration were carried out. **Figure 13** presents the variations of the safety factor of the potential sliding surfaces during the two different types of rainfall. The results show that the safety factor of the potential sliding surface is closely related to the rainfall intensity. During the first five days of the rainfall, the intensity of the wave type is much larger than that of the increasing type, which leads to a faster decrease in the safety factor after the same rainfall duration. During the last two days of rainfall, the intensity of the increasing type rainfall has been greater than the wave type, and the decrease of the safety factor of the deposit slope is also larger than that under the wave type, the former about 0.068, from 1.789 to 1.721, while the latter one is only 0.048. The largest intensity of the two types of rainfall appears at the fifth and the end day of rainfall, respectively, and an obvious decrease could be observed after the peak rainfall intensity, which is attributed to the hysteresis due to rainfall infiltration. After the same rainfall duration, the safety factor of the wave type is smaller than the increasing type.

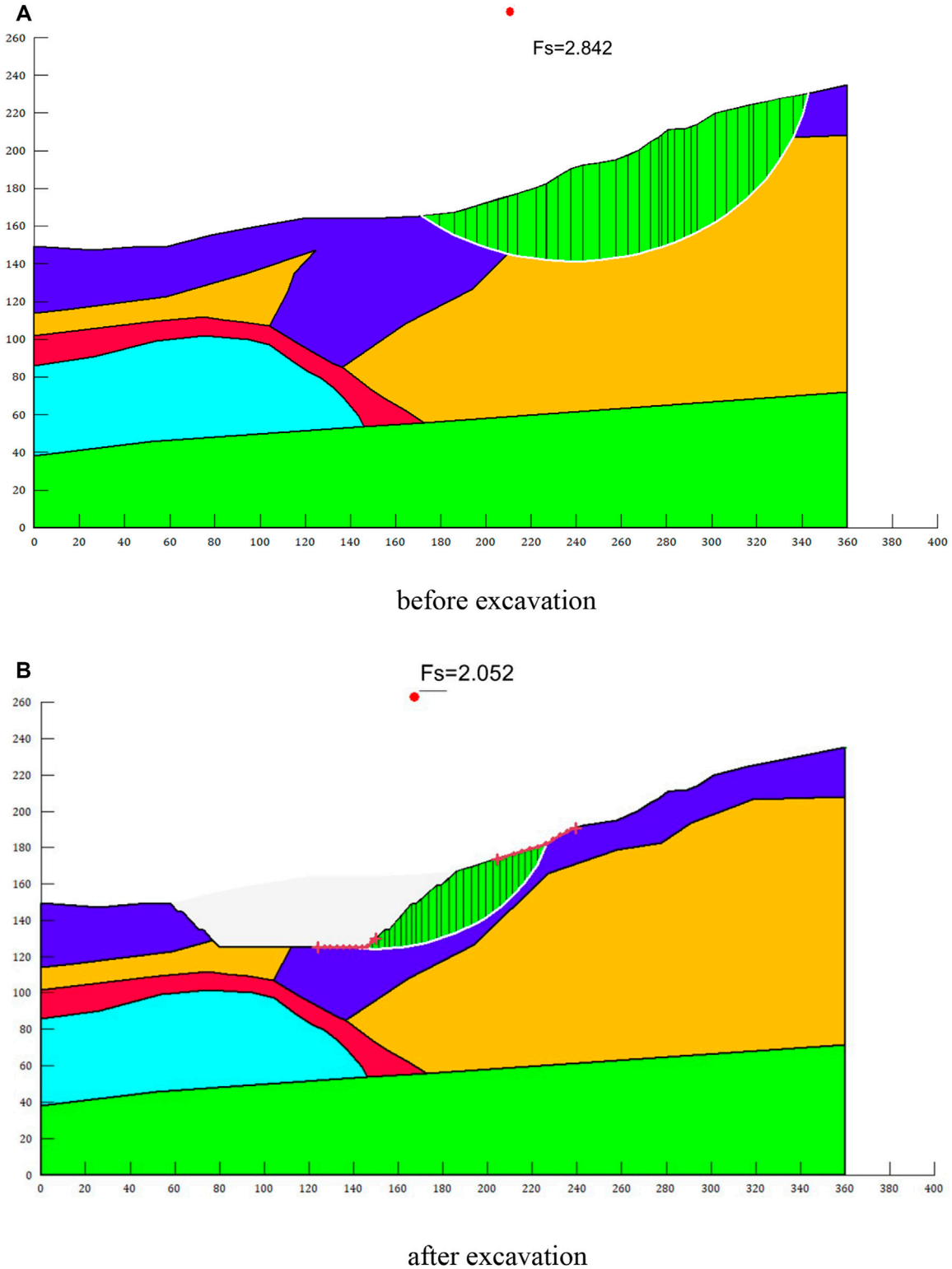

FIGURE 10 | Safety factors and potential sliding surface of the deposit slope. **(A)** before excavation. **(B)** after excavation.

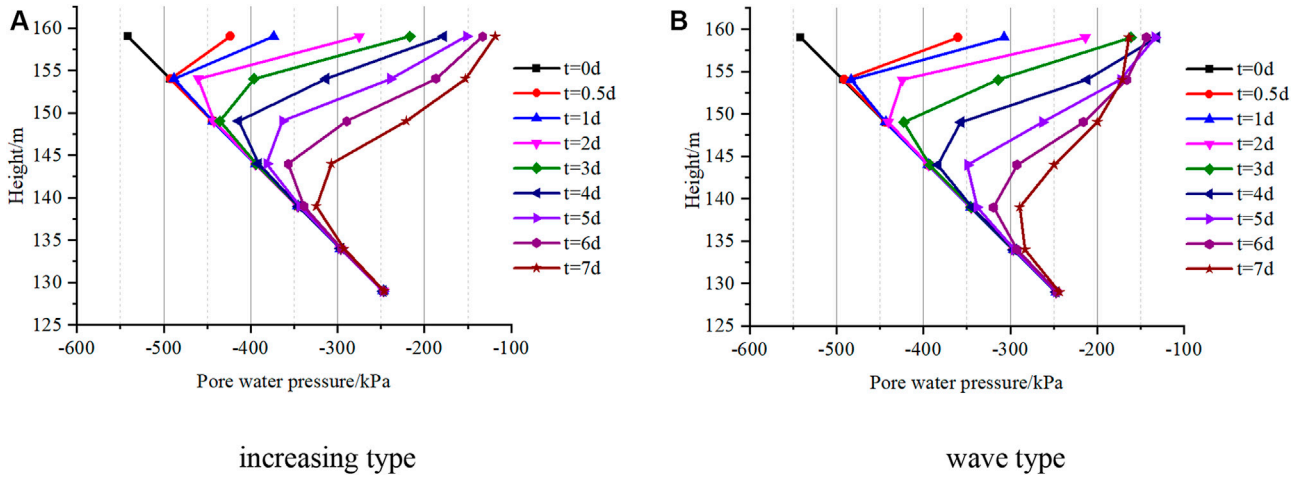

FIGURE 11 | Pore water pressure of monitor points under different rainfall conditions. **(A)** increasing type. **(B)** wave type.

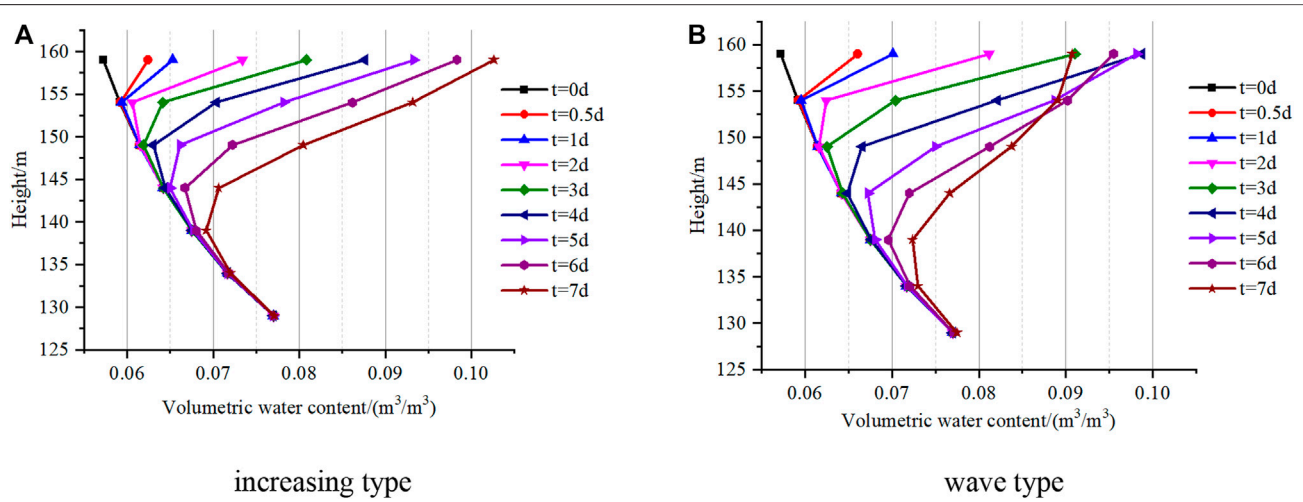

FIGURE 12 | Water content of monitor points under different rainfall conditions. **(A)** increasing type. **(B)** wave type.

Figure 14 shows the locations of the potential sliding surfaces of the deposit slope after the increasing and wave type of rainfall. Compared to the simulation result before excavation in **Figure 10B**, the location of the potential sliding surface is much shallower. The parameter deterioration was considered in the calculation of the safety factor, which is related to the increase of pore water pressure. Therefore, the location of the potential sliding surface is controlled by the variable region of the pore water pressure is near the surface, which shows very good agreement with the common shallow retrogressive landslides due to rainfall.

CONCLUSION

S-RM is one of the most common geological materials and presents considerable challenges due to its complex mechanical characteristics and compositions. An innovative shear parameter estimation method was proposed in this study, and its application for the deposit slope with the parameter deterioration was discussed subjected to different types of rainfall. The following conclusions and recommendations could be derived:

1) The empirical nonlinear strength criterion of the S-RM and the shear parameter estimation method were proposed. Based on the similarities between the natural S-RM and the rock masses, the generalized H-B was utilized as the reference format of the expression of the nonlinear strength criterion, and the rock block proportion and the strength of the contact surface were chosen as the vital influence factors. The scope of the estimation method was given considering the test conditions, and the influence of water on the shear parameters was also discussed.

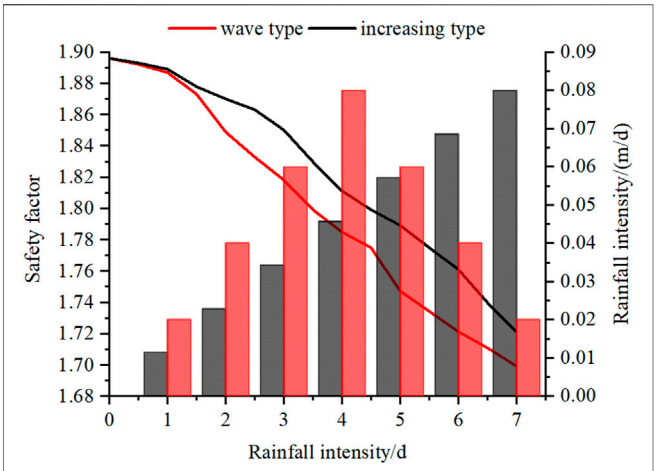

FIGURE 13 | Safety factors of the deposit slope under different rainfall conditions.

2) A series of large-scale direct test data were collected to build the database of the natural S-RM, which was utilized as the reference for the verification of the nonlinear strength criterion. In addition, the natural S-RM located in the deposit slope in Taoyuan, Yunnan Province, China, was selected as the research object, and its mechanical parameters were determined using the estimation method proposed in this study.
3) The numerical case study was performed to study the influence of rainfall type on the seepage field and stability considering the parameter deterioration. The results from the numerical study indicate that the pore water pressure and water content are related to the rainfall intensity, and the wave-type rainfall presents a larger infiltration area. The same situation was also observed in the variation of the safety factor, and the wave-type rainfall shows a more serious impact on the slope stability.

DATA AVAILABILITY STATEMENT

The raw data supporting the conclusions of this article will be made available by the authors, without undue reservation.

ETHICS STATEMENT

Written informed consent was obtained from relevant individuals for the publication of any potentially identifiable images or data included in this article.

AUTHOR CONTRIBUTIONS

ZZ and QS were involved in the final development of the project and manuscript preparation. XF wrote the manuscript draft. YZ and JH analyzed the data. ZW and ML carried out the field investigation. All authors: corrections, modifications, and final acceptance.

FUNDING

The work reported in this paper was financially supported by the Youth Innovation Promotion Association CAS (No.2021325), the National Natural Science Foundation of China (No. 51779250), and the International Partnership Program of Chinese Academy of Sciences (Grant No. 131551KYSB20180042).

ACKNOWLEDGMENTS

We would like to acknowledge the reviewers and the editors for their comments and suggestions.

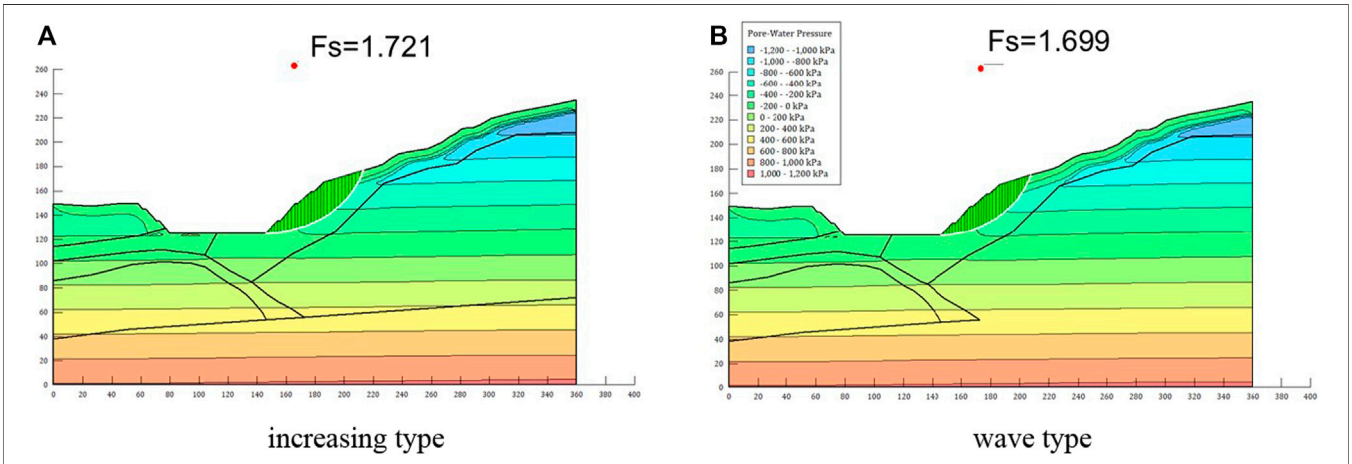

FIGURE 14 | Safety factors and potential sliding surface of the deposit slope after different rainfall conditions. **(A)** increasing type. **(B)** wave type.

REFERENCES

Afifipour, M., and Moarefvand, P. (2014). Mechanical Behavior of Bimrocks Having High Rock Block Proportion. *Int. J. Rock Mech. Mining Sci.* 65, 40–48. doi:10.1016/j.ijrmms.2013.11.008

Al Aqtash, U., and Bandini, P. (2015). Prediction of Unsaturated Shear Strength of an Adobe Soil from the Soil-Water Characteristic Curve. *Construction Building Mater.* 98, 892–899. doi:10.1016/j.conbuildmat.2015.07.188

Al-Shayea, N. A. (2001). The Combined Effect of clay and Moisture Content on the Behavior of Remolded Unsaturated Soils. *Eng. Geology.* 62 (4), 319–342. doi:10.1016/s0013-7952(01)00032-1

Avşar, E., Ulusay, R., and Mutlutürk, M. (2015). An Experimental Investigation of the Mechanical Behavior and Microstructural Features of a Volcanic Soil (Isparta, Turkey) and Stability of Cut Slopes in This Soil. *Eng. Geology.* 189, 68–83.

Cascini, L., Cuomo, S., Pastor, M., and Sorbino, G. (2010). Modeling of Rainfall-Induced Shallow Landslides of the Flow-type. *J. Geotech. Geoenviron. Eng.* 136 (1), 85–98. doi:10.1061/(asce)gt.1943-5606.0000182

Chang, K.-T., and Cheng, M.-C. (2014). Estimation of the Shear Strength of Gravel Deposits Based on Field Investigated Geological Factors. *Eng. Geology.* 171, 70–80. doi:10.1016/j.enggeo.2013.12.014

Chang, W.-J., and Phantachang, T. (2016). Effects of Gravel Content on Shear Resistance of Gravelly Soils. *Eng. Geology.* 207, 78–90. doi:10.1016/j.enggeo.2016.04.015

Deng, H. F. (2016). "Test Research on the Shear Strength Characteristics of Rock-Soil Aggregate Mixture," (Fuzhou: East China University of Technology). M.Sc.

Deng, H. F., Yuan, X. F., Li, J. L., Li, J. L., Luo, Q., and Zhu, M. (2013). Research on Failure Characteristics and Determination Method for Shear Strength of Earth-Rock Aggregate in Direct Shear Tests. *Chin. J. Rock Mech. Eng.* 32 (S2), 4065–4072. doi:10.3969/j.issn.1000-6915.2013.z2.133

Deng, X. C. (2014). "The Tunnel Excavation and its Slope Stability in the Accumulation Body," (Chongqing: Chongqing Jiaotong University). M.Sc.

Ding, X. L., Li, Y. X., and Wang, X. (2010). Particle Flow Modeling Mechanical Properties of Soil and Rock Mixtures Based on Digital Image. *Chin. J. Rock Mech. Eng.* 29 (3), 477–484. doi:10.1360/972008-2552

Duong, T. V., Tang, A. M., Cui, Y.-J., Trinh, V. N., Dupla, J.-C., Calon, N., et al. (2013). Effects of Fines and Water Contents on the Mechanical Behavior of Interlayer Soil in Ancient Railway Sub-structure. *Soils and Foundations* 53 (6), 868–878. doi:10.1016/j.sandf.2013.10.006

Fiorillo, F., Esposito, L., Grelle, G., Revellino, P., and Guadagno, F. M. (2013). Further Hydrological Analyses on Landslide Initiation in the Sarno Area (Italy). *Ital. J. Geosciences* 132, 341–349. doi:10.3301/ijg.2012.43

Fu, X. D., Sheng, Q., Du, W. J., Mei, H. R., Chen, H., and Du, Y. X. (2020a). Evaluation of dynamic stability and analysis of reinforcement measures of a landslide under seismic action: a case study on the Yanyangcun landslide. *Bulletin of Engineering Geology and the Environment.* 79, 2847–2862.

Fu, X. D., Sheng, Q., Zhang, Y. H., Chen, J., Zhang, S. K., and Zhang, Z. P. (2017). Computation of the safety factor for slope stability using discontinuous deformation analysis and the vector sum method. *Computers and Geotechnics* 92, 68–76.

Fu, X. D., Sheng, Q., Tang, H., Chen, J., Du, Y. X., Zhang, Z. P., and Mei, H. R. (2019). Seismic stability analysis of a rock block using the block theory and Newmark method. *International Journal for Numerical and Analytical Methods in Geomechanics* 43(7), 1392–1409.

Fu, X. D., Sheng, Q., Li, G., Zang, Z. P., Zhou, Y. Q., and Du, Y. X. (2020b). Analysis of landslide stability under seismic action and subsequent rainfall: a case study on the Ganjiazhai giant landslide along the Zhaotong-Qiaojia road during the 2014 Ludian earthquake, Yunnan, China. *Bulletin of Engineering Geology and the Environment.* 79, 5229–5248.

He, Z.-M., Tang, H.-l., and Deng, X. (2018). Effect of Seepage Force on Stability of High Embankment with Coarse-Grained Soil during Rainfall. *J. Highw. Transp. Res. Dev. (English Ed.)* 12 (1), 44–52. doi:10.1061/jhtrcq.0000609

Hoek, E., Carranza-Torres, C., and Corkum, B. (2002). "Hoek-Brown Failure Criterion-2002 Edition," in Proc. NARMS-TAC Conference, Volume 1: Toronto, 267–273.

Hoek, E., Wood, D., and Shah, S. (1992). "A Modified Hoek–Brown Failure Criterion for Jointed Rock Masses," in Proceedings Rock Characterization: ISRM Symposium, Eurock'92, Chester, UK, 14–17 September 1992 (Thomas Telford Publishing), 209–214.

Hoek, E., and Brown, E. T. (1980). Empirical Strength Criterion for Rock Masses. *J. Geotech. Engrg. Div.* 106 (9), 1013–1035. doi:10.1061/ajgeb6.0001029

Hoek, E., and Brown, E. T. (1997). Practical Estimates of Rock Mass Strength. *Int. J. Rock Mech. Mining Sci.* 34 (8), 1165–1186. doi:10.1016/s1365-1609(97)80069-x

Hu, W. (2014). "Experimental Study on Shear Strength of Soil-Rock Mixture in Xiluodu Reservior," (Wuhan: Institute of Rock and Soil Mechanics, Chinese Academy of Sciences). Ph.D.

Huang, J. H. (2016). "Study on the Strength Characteristics of Glacial deposit Body in Taoping, Li County, Sichuan Province," (Chengdu: Chengdu University of Technology). M.Sc.

Kalender, A., Sonmez, H., Medley, E., Tunusluoglu, C., and Kasapoglu, K. E. (2014). An Approach to Predicting the Overall Strengths of Unwelded Bimrocks and Bimsoils. *Eng. Geology.* 183, 65–79. doi:10.1016/j.enggeo.2014.10.007

Liu, X. R., Tu, Y. L., Wang, P., Zhong, Z-L., Tang, W. B., and Du, L. B. (2017). Particle Breakage of Soil-Rock Aggregate Based on Large-Scale Direct Shear Tests. *Chin. J. Geotechnical Eng.* 39 (08), 1425–1434. doi:10.11779/CJGE201708009

Liu, Z. Y., Su, L. J., Zhang, C. L., Iqbal, J., Hu, B. L., and Dong, Z. B. (2020). Investigation of the dynamic process of the Xinmo landslide using the discrete element method. *Computers and Geotechnics* 123, 103561.

Lü, Q., Chen, P., Kim, B., Zheng, J., and Ji, J. (2019). Probabilistic Assessment of Seismic Stability of a Rock Slope by Combining the Simulation of Stochastic Ground Motion with Permanent Displacement Analysis. *Eng. Geology.* 260, 105210. doi:10.1016/j.enggeo.2019.105210

Ma, C., Zhan, H., Zhang, T., and Yao, W. (2019). Investigation on Shear Behavior of Soft Interlayers by Ring Shear Tests. *Eng. Geology.* 254, 34–42. doi:10.1016/j.enggeo.2019.04.002

Malizia, J. P., and Shakoor, A. (2018). Effect of Water Content and Density on Strength and Deformation Behavior of clay Soils. *Eng. Geology.* 244, 125–131. doi:10.1016/j.enggeo.2018.07.028

Marinos, P., and Hoek, E. (2001). Estimating the Geotechnical Properties of Heterogeneous Rock Masses Such as Flysch. *Bull. Eng. Geology. Environ.* 60 (2), 85–92. doi:10.1007/s100640000090

Meng, Y. W., Wang, Y., Shao, Y. Z., Yan, Z., and Chen, F. (2018). "Numerical Analysis of Excavation Stability of Loose deposit on Highway High Slope," in APCIM & ICTTE 2018: Proceedings of the Asia-Pacific Conference on Intelligent Medical 2018 & International Conference on Transportation and Traffic Engineering 2018, December 2018, in Beijing, China, 59–62. doi:10.1145/3321619.3321648

Miščević, P., and Vlastelica, G. (2014). Impact of Weathering on Slope Stability in Soft Rock Mass. *J. Rock Mech. Geotechnical Eng.* 6 (3), 240–250. doi:10.1016/j.jrmge.2014.03.006

Monkul, M. M., and Ozden, G. (2007). Compressional Behavior of Clayey Sand and Transition Fines Content. *Eng. Geology.* 89 (3), 195–205. doi:10.1016/j.enggeo.2006.10.001

Pantaleone, D. V., Francesco, F., Rita, T., and Delia, C. (2018). Seasonal and Event-Based Hydrological and Slope Stability Modeling of Pyroclastic Fall Deposits Covering Slopes in Campania (Southern Italy). *Water* 10 (9), 1140. doi:10.3390/w10091140

Qi, C., Li, L., Li, R., Gan, F., Zhang, W., and Han, H. (2021). Stability Mechanism Recognition and Failure Risk Assessment on a High Slope by Synthesizing Different Analysis Methods. *Nat. Hazards* 108 (2), 1569–1584. doi:10.1007/s11069-021-04745-2

Qi, D. (2016). "Experimental Study on the Mechanical Properties of Soil-Rock Mixture," (Zhengzhou: North China University of Water Resources and Electric power). M.Sc.

Rahardjo, H., Indrawan, I. G. B., Leong, E. C., and Yong, W. K. (2008). Effects of Coarse-Grained Material on Hydraulic Properties and Shear Strength of Top Soil. *Eng. Geology.* 101 (3), 165–173. doi:10.1016/j.enggeo.2008.05.001

Shang, Y. J., Yang, Z. F., Li, L. H., Liua, D., Liaoa, Q., and Wang, Y. (2003). A Super-large Landslide in Tibet in 2000: Background, Occurrence, Disaster, and Origin. *Geomorphology* 54 (3), 225–243. doi:10.1016/s0169-555x(02)00358-6

Sun, S. R., Peng Lei, X., Ji Min, W., Wengan, F., Jin, L. J., and Kanungo, D. P. (2014). Strength Parameter Identification and Application of Soil–Rock Mixture for Steep-Walled Talus Slopes in Southwestern China. *Bull. Eng. Geology. Environ.* 73 (1), 123–140. doi:10.1007/s10064-013-0524-1

Tang, J., Xu, D., and Liu, H. (2018). Effect of Gravel Content on Shear Behavior of Sand-Gravel Mixture. *Rock Soil Mech.* 39 (01), 93–102. doi:10.16285/j.rsm.2017.1527

Wang, C. D., Shen, Q., Wu, R., Wu, R., Fu, M., and Yang, C. G. (2016). Experimental Study on Effect of Stone Content on Engineering Performance of Crushed Stone Soil. *Railway Eng.* 02, 97–101. doi:10.36012/etr.v2i10.2804

Wang, J. C. (2011). "Experimental Research on Shear Parameter of High Cut Slope Gravel Soil in Badong and its Engineering Application," (Yichang: China Three Gorges University). M.Sc.

Wang, X., Pedrycz, W., and Niu, R. (2015). Spatio-temporal Analysis of Quaternary deposit Landslides in the Three Gorges. *Nat. Hazards* 75 (3), 2793–2813. doi:10.1007/s11069-014-1462-3

Wang, Z. G., Hu, R. L., Zhang, R., and Xu, W. (2013). Study of Geotechnical Mechanical Characteristics of a Large Soil-Rock Mixture in a Hydropower Project. *Chin. J. Rock Mech. Eng.* 32 (S2), 3836–3843. doi:10.21656/1000-0887.400225

Wei, H. Z., Wang, R., Hu, M. J., and Zhao, H.-Y. (2008). Strength Behaviour of Gravelly Soil with Different Coarse-Grained Contents in Jiangjiagou Ravine. *Rock Soil Mech.* 01, 48–51+57. doi:10.12677/hjce.2020.911127

Wei, Y., Wu, X., Xia, J., Miller, G. A., Cai, C., Guo, Z., et al. (2019). The Effect of Water Content on the Shear Strength Characteristics of Granitic Soils in South China. *Soil Tillage Res.* 187, 50–59. doi:10.1016/j.still.2018.11.013

Wörman, A. (1993). Seepage-Induced Mass Wasting in Coarse Soil Slopes. *J. Hydraulic Eng.* 119 (10), 1155–1168. doi:10.1061/(asce)0733-9429(1993)119:10(1155)

Wu, R. (2015). "Study on the Strength experiment of Gravel Soil in the Slope of Daqianshiling Tunnel," (Wuhan: China university of Geosciences). Ms.c.

Wu, R. A., Zhang, Y. S., Wang, X. L., Yao, X. L., Yang, Z. H., Du, G. L., et al. (2017). *In Situ* direct Shearing Test on Landslide Accumulation Body Intensity of Wenchuan Earthquake Region. *J. Geomechanics* 23 (01), 105–114. doi:10.5194/nhess-2016-193-rc1

Xiao, S. Y., Su, L. J., Jiang, Y. J., Qu, X., Xu, M., Hu, X. B., et al. (2020). Experimental investigation on the impact force of the dry granular flow against a flexible barrier. *Landslides* 17, 1465–1483.

Xu, D.-S., Tang, J.-Y., Zou, Y., Rui, R., and Liu, H.-B. (2019). Macro and Micro Investigation of Gravel Content on Simple Shear Behavior of Sand-Gravel Mixture. *Construction Building Mater.* 221, 730–744. doi:10.1016/j.conbuildmat.2019.06.091

Xu, W. J., Xu, Q., and Hu, R. L. (2011). Study on the Shear Strength of Soil–Rock Mixture by Large Scale Direct Shear Test. *Int. J. Rock Mech. Mining Sci.* 48 (8), 1235–1247. doi:10.1016/j.ijrmms.2011.09.018

Xue, Y. D., Liu, Z. Q., and Wu, J. (2014). Direct Shear Tests and PFC2D Numerical Simulation of Colluvial Mixture. *Rock Soil Mech.* 35 (S2), 587–592. doi:10.1007/978-94-015-9285-7_25

Yang, J. H., Dong, J. Y., Huang, Z. Q., Zheng, H. G., Qi, D., et al. (2016a). Large-scale Direct Shear Tests on Accumulation Body with Different Stone Contents. *Chin. J. Geotechnical Eng.* 38 (S2), 161–166. doi:10.18400/tekderg.606816

Yang, J. H., Dong, J. Y., Liu, H. D., Huang, Z. Q., Jiang, T., et al. (2010). *In Situ* direct Shear Tests of the Large-Scale Accumulation Body and Three-Dimensional Stability Analysis of the Slope. *J. China Coal Soc.* 35 (03), 392–396. doi:10.4028/www.scientific.net/amm.170-173.1124

Yang, Y., Sun, G., Zheng, H., and Fu, X. (2016b). A Four-Node Quadrilateral Element Fitted to Numerical Manifold Method with Continuous Nodal Stress for Crack Analysis. *Comput. Structures* 177, 69–82. doi:10.1016/j.compstruc.2016.08.008

Yang, Y. T., Xu, D. D., Liu, F., and Zheng, H. (2020). Modeling the entire progressive failure process of rock slopes using a strength-based criterion. *Computers and Geotechnics* 126, 103726.

Zhang, Z.-L., Xu, W.-J., Xia, W., and Zhang, H.-Y. (2016). Large-scale *In-Situ* Test for Mechanical Characterization of Soil-Rock Mixture Used in an Embankment Dam. *Int. J. Rock Mech. Mining Sci.* 86, 317–322. doi:10.1016/j.ijrmms.2015.04.001

Zhang, Z. P., Fu, X. D., Sheng, Q., and Du, Y. (2021). Stability of Cracking Deposit Slope Considering Parameter Deterioration Subjected to Rainfall. *Int. J. Geomechanics* 21 (7), 05021001. doi:10.1061/(asce)gm.1943-5622.0002045

Zhang, Z. P., Sheng, Q., Fu, X. D., and Du, Y. X. (2019). An approach to predicting the shear strength of soil-rock mixture based on rock block proportion. *Bulletin of Engineering Geology and the Environment* 79(1), 2423–2437.

Zhang, Z., Sheng, Q., Fu, X., Zhou, Y., Huang, J., and Du, Y. (2020). An Approach to Predicting the Shear Strength of Soil-Rock Mixture Based on Rock Block Proportion. *Bull. Eng. Geol. Environ.* 79 (5), 2423–2437. doi:10.1007/s10064-019-01658-0

Zheng, Y., Wang, R. Q., Chen, C. X., Sun, C. Y., Ren, Z. H., and Zhang, W. (2021). Dynamic analysis of anti-dip bedding rock slopes reinforced by pre-stressed cables using discrete element method. *Engineering Analysis with Boundary Elements* 130(4), 79–93.

Zhou, J. W., Cui, P., and Yang, X. G. (2016). Effects of Material Composition and Water Content on the Mechanical Properties of Landslide Deposits Triggered by the Wenchuan Earthquake. *Acta Geologica Sinica (English Edition)* 90 (1), 242–257. doi:10.1111/acgs.2016.90.issue-5

Zhou, Z., Liu, Z.-z., Yang, H., Gao, W.-y., and Zhang, C.-c. (2020). Freeze-thaw Damage Mechanism of Elastic Modulus of Soil-Rock Mixtures at Different Confining Pressures. *J. Cent. South. Univ.* 27 (2), 554–565. doi:10.1007/s11771-020-4316-z

Zou, L. F., Xu, W. Y., and Shi, C. (2011). Three Dimensional Numerical Analysis of Deformation and Stability of Zone II of Xiazanri Slope deposit. *Appl. Mech. Mater.* 90-93, 2372–2379. doi:10.4028/www.scientific.net/amm.90-93.2372

Conflict of Interest: ZW and ML are employed by China State Construction International Holdings Limited and China State Construction International Investments (Hubei) Limited.

The remaining authors declare that the research was conducted in the absence of any commercial or financial relationships that could be construed as a potential conflict of interest.

frontiers in Earth Science

ORIGINAL RESEARCH
published: 16 November 2021
doi: 10.3389/feart.2021.773872

Study on Blasting Technology for Open-Pit Layering of Complex Mine Adjacent to High and Steep Slope

Menglai Wang[1], Xiaoshaung Li[2,3,4], Qihang Li[5], Yunjin Hu[3]*, Qiusong Chen[6] and Song Jiang[7]*

[1]Yunnan Phosphate Group Co. Ltd., Kunming, China, [2]School of Civil Engineering, Shaoxing University, Shaoxing, China, [3]Key Laboratory of Rock Mechanics and Geohazards of Zhejiang Province, Shaoxing University, Shaoxing, China, [4]College of Civil Engineering, Qilu Institute of Technology, Jinan, China, [5]School of Resources and Environmental Engineering, Jiangxi University of Science and Technology, Ganzhou, China, [6]School of Resources and Safety Engineering, Central South University, Changsha, China, [7]School of Resources Engineering, Xi'an University of Architecture and Technology, Xi'an, China

In China, mining blasting vibration has seriously threatened the safety and stability of high and steep rock slopes. In this paper, taking the east mining area of Jianshan Phosphorus Mine as the research background, combined with field survey, field blasting test, numerical simulation and theoretical analysis, we systematically studied the adjacent high-steep rock slope and the layered blasting technology of complex ore. Based on wide hole spacing blasting numerical simulation and field tests, the use of 8 × 4 m hole network parameters, oblique line hole-by-hole initiation method, detonator delay using 35 ms between holes, 65 ms between rows and 500 ms within the holes, the rock mass rate was reduced and the drilling workload was decreased. In addition, regression analysis was carried out on a large amount of vibration test data, and the attenuation law and propagation law of blasting vibration of adjacent high and steep slopes were predicted, which provided a reference for mine production blasting. By establishing a mathematical model of cumulative damage of rock mass blasting, it shows that the depth of impact of mining blasting on the slope of Jianshan open-pit was 0–3.6m, but the blasting did not cause overall damage to the adjacent high and steep slopes. In the future, this model can be used to predict rock damage caused by subsequent blasting.

Keywords: open-pit mine, high and steep slope, blasting technology, blasting vibration, numerical simulation

OPEN ACCESS

Edited by:
Yun Zheng,
Institute of Rock and Soil Mechanics (CAS), China

Reviewed by:
Longlong Chen,
Politecnico di Milano, Italy
Chunyang Zhang,
Wuhan University of Technology, China

****Correspondence:***
Qihang Li
qihangli0325@126.com
Yunjin Hu
huyunjin@tsinghua.org.cn

Specialty section:
This article was submitted to Geohazards and Georisks, a section of the journal Frontiers in Earth Science

Received: *10 September 2021*
Accepted: *04 October 2021*
Published: *16 November 2021*

Citation:
Wang M, Li X, Li Q, Hu Y, Chen Q and Jiang S (2021) Study on Blasting Technology for Open-Pit Layering of Complex Mine Adjacent to High and Steep Slope. Front. Earth Sci. 9:773872. doi: 10.3389/feart.2021.773872

INTRODUCTION

In recent years, with the mining of China's mineral resources, the mineral economy has promoted the rapid development of the social economy. On the contrary, it has caused pollution and damage to the surrounding environment of the mines (Liu et al., 2021). In detail, most of the forms of mining are blasting. Due to the violent vibration caused by explosives during blasting, it will have a serious impact on the surrounding buildings and the lives of residents near the open-pit mine, especially the stability of the high and steep slope near the mine edge, causing the loosening and disintegration of the slope structure of the mine (Sazid. 2017; Umrao et al., 2017). In addition, because of the complexity, instantaneity, uncertainty and differences of blasting media and blasting conditions, the prediction of blasting vibration velocity has always been a major technical problem to be solved urgently (Wang et al., 2019). There are two main reasons for the instability of the high and steep slope of the mine. One is determined by the characteristics of the geological structure of the mine's high and steep slopes, mainly induced by local hydrogeological conditions. The other is due to changes in

the topography of the surrounding high and steep slopes after the mine goes out, such as the instability of the slope caused by the vibration of the impact of blasting. Regardless of the factor, changes in geological structure will cause serious landslides, mudslides under the conditions of blasting vibration and heavy rain, causing immeasurable losses to society (Ramin et al., 2020). Therefore, it is necessary to develop blasting technology and blasting vibration for the open-pit of Jianshan Phosphorus Mine, which can ensure the safety of rock slopes and provide guidance for subsequent mining and blasting.

With the increase in demand for rock mining by blasting in mines, many scholars have carried out in-depth research in theoretical analysis, field tests and numerical simulations (Aldas and Ecevitoglu. 2008; Ren et al., 2014; Wang et al., 2021). Guo et al. analyzed the response of different types of slopes to blasting vibration (Guo et al., 2001). Zhang et al. used the field test method of blasting vibration to carry out an experimental study on the propagation law of blasting vibration under the influence of elevation factors (Zhang et al., 2017). Wang et al. proposed a calculation formula for dynamic time history stability coefficient of bedding high-steep rock slopes driven by underground blasting for the common high-steep bedding rock slopes in engineering (Wang. 2018). Narayan et al. proposed a novel directional controlled blasting technology for unstable highway slopes, which effectively improved the stability of the slope after blasting (Narayan et al., 2020). Wu et al. evaluated the stability of high and steep slopes driven by repeated blasting of the fault zone by combining shaking table tests, limit equilibrium theory, and least squares method (Wu et al., 2020). On the basis of previous research results, Deng and Chen comprehensively discussed the blasting excavation and stability control technology of ultra-high and steep rock slopes in China's hydropower projects, and discussed its research progress and limitations (Deng and Chen. 2021). On the other hand, Ma et al. studied the weakening of slope stability under the dual effects of rainfall infiltration and blasting vibration (Ma et al., 2021). However, these methods only conduct experiments and theoretical analysis on the stability of the slope after blasting, and have no effective verification and are limited.

In the past 20 years, computer technology has developed rapidly, and numerical simulation has become an important research method (Li et al., 2021; Li et al., 2021). Among them, a series of numerical simulation verification studies have been carried out in the mine blasting process. Xie et al. used SLIDE software to simulate the actual slope model of the open-pit mine, and proposed a slope stability criterion based on the safety factor (Xie et al., 2015). Gui et al. established a numerical simulation considering the geological characteristics of the site by means of the finite difference method, and concluded that the propagation of the explosion wave in the free field is significantly controlled by the geological conditions of the site (Gui et al., 2017). Jiang et al. used the dynamic finite element method to analyze the characteristics of the explosive load, and produced three-dimensional numerical models of open-pit mines and underground mines (Jiang et al., 2018). Chen et al. used the tensile and compression damage model to simulate the entire process of blasting and excavation of a typical bedrock slope, and through parameter analysis, the stability of the slope under the blasting load was ensured (Chen et al., 2019). Li et al. used a comprehensive study method combining theoretical analysis, field testing, and numerical simulation to develop a collaborative blasting technology for high and steep slopes and underground tunnels (Li et al., 2019).

In short, the above methods did not consider the influence of blasting vibration on the stability of adjacent high-steep slopes during the blasting process of open-pit minesand there is no systematic discussion on the mechanical stability and cumulative damage of rock slopes. In the numerical simulation part, most methods use a single finite difference method to simulate and verify the mine blasting process, which has certain limitations. In addition, the propagation and superposition process of the explosion equivalent stress is a major difficulty in studying the mechanical stability of adjacent high-steep slopes under blasting vibration.

Against these challenges, the east mining area of Jianshan Phosphate Mine in Yunnan Province is taken as the research object. Combined with on-site investigation, on-site blasting tests, numerical simulation and theoretical analysis, the open-pit layered blasting technology of complex ore near high and steep slopes was systematically studied. Based on the numerical simulation of wide hole spacing blasting, the method of using 8 × 4 hole network parameters and oblique line hole-by-hole initiation was proposed, which greatly reduced the lump rate of the rock mass and improved the stability of the slope. On the other hand, a detailed analysis of the equivalent stress propagation and equivalent superposition process of blasting vibration was carried out. In addition, the attenuation law and propagation law of blasting vibration on high and steep slopes were predicted, and the cumulative damage model of slope rock mass blasting was established to ensure the safety of adjacent high and steep slopes, thereby promoting the progress of scientific research on blasting in mines.

ENGINEERING BACKGROUND

Geological Profile

As shown in **Figure 1**, the Jianshan Phosphate Mine is located near Haikou Town, Xishan District, Kunming City, Yunnan Province, China, with well-developed land and water transportation. The longitude of the study area is 102°06′09″-102°49′56″ and the latitude is 24°08′24″-24°17′35″. In addition, Haikou Town is a heavy industrial zone in Kunming City, with abundant natural resources, convenient transportation and well industrial foundation. The Jianshan Phosphate Mine is located in the middle of the Jianshan mining area.and the northern slope of Jianshan is the exposed part of the bottom rock of the stope. The topography is characterized by alpine topography, with the characteristics of gentle south and steep north. The topography of the foothills is roughly the same as the tilt direction of the rock formations. The peak elevation of the

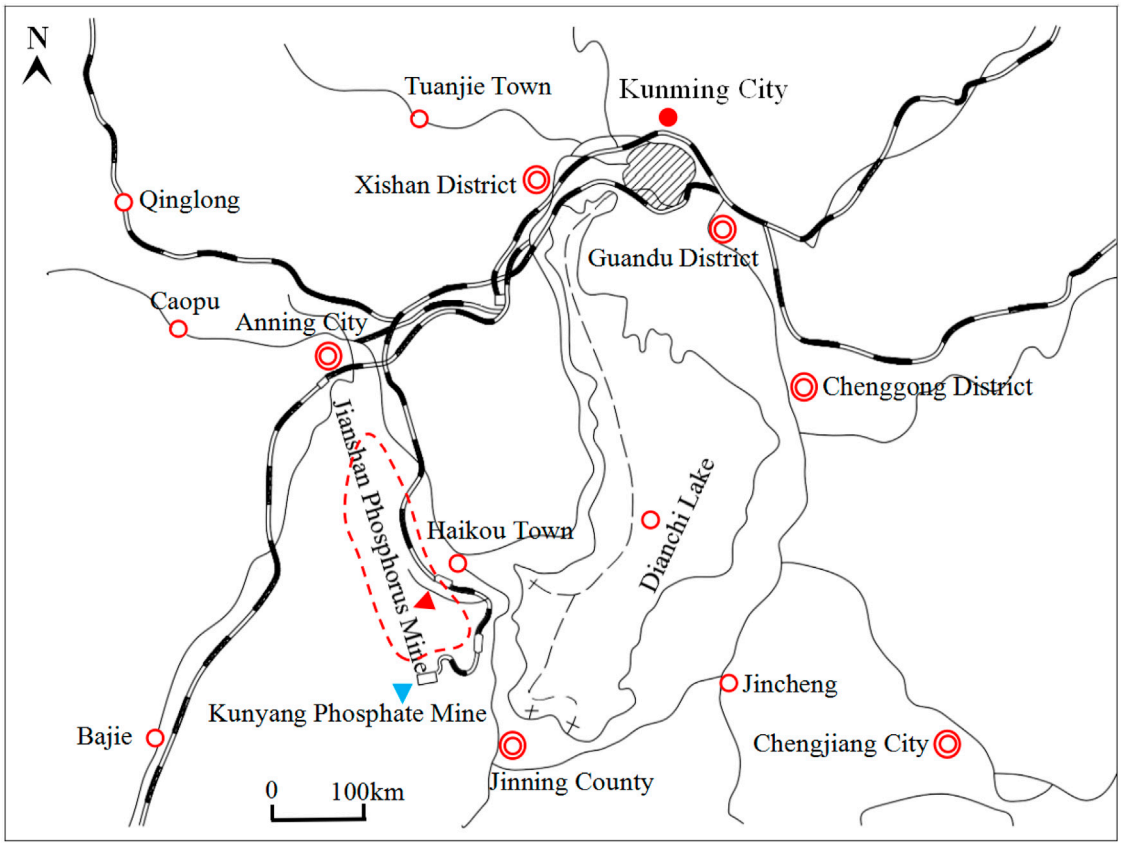

FIGURE 1 | Location map of Jianshan Phosphate Mine.

highest peak in the mining area is 2,205.75 m, and the slope has north-south rain fissures and gully cuts, and the lowest erosion base elevation is 1,883.15 m. Over 20 perennial rivers in the surface water system converge into Dianchi Lake, the river at the exit of Dianchi Lake is Haikou River. It flows from east to west through the northern edge of the mining area, the highest water level is 1,886.86 m, and the lowest water level is 1,883.15 m. The annual average rainfall is 886.99 mm and the evaporation is 1,903.8 mm. In addition, there will be frost from December to February, with an average annual frost period of 64–75 days.

Mining Area Structure

The mining area is located in the eastern section of the north wing of the Xiangtiao Village anticline, and the stratum is inclined to the north, in a monoclinic form, with a relatively simple structure and no faults with a drop of more than 30 m. The eastern strata strikes nearly east-west, with steep dips to upright. There are two reverse faults parallel to the axis of the Xiangtiao Village anticline in the southern part of the middle section of the mining area. It pushes the deep strata upwards and makes the ore strata overlap, and the force to the west is weaker than the east. Correspondingly, there are some small axially along strike and inclined wide and gentle fold groups, and vertical fractures with tensile characteristics and small normal faults.

Common folds in the mining area are generally of two types: one is the wide and gentle folds along the inclined direction and strike in the west of the mining area; the other is the traction folds produced by the strong compression in the east of the mining area. The fault structure in the area is not well developed, with only one strike reverse fault group (F_1) and one strike normal fault group (F_2), which are mainly manifested as duplication or lack of ore layers. In addition, the reverse fault group (F_{1-1}, F_{1-2}) has a certain influence on the northern ore body in the east mining area of Jianshan Phosphorus Mine.

1) F_{1-1} reverse fault: The F_{1-1} reverse fault is the main fault in the mining area. The overall strike is close to east-west, with an inclination of 330°–20°, a length of 1,420 m, and the dip angle of the fault plane is steep from the east to the west. The north plate rises, pushing the deep ore layer to the shallower, causing the ore layer to be repeated, and the repeated fault distance is less than 17 m.
2) F_{1-2} reverse fault: The F_{1-2} reverse fault is a reverse fault roughly parallel to F_{1-1}. It strikes east-west, with a dip of 340°–360°, a dip angle of 49–60°, and a length of 1,020 m. The

north plate rises, the ore layers are repeated, and the vertical fault distance is nearly 30 m.

BLASTING TEST IN JIANSHAN STOPE

Blasting Status and Blasting Plan

Currently, with the continuous decrease of mining depth, the east mining area of Jianshan Phosphorus Mine has formed a high-steep slope with a step height of 30 m, a slope surface of 42–51°, and a slope height of more than 200 m. Since the Jianshan stope is close to the high and steep slopes of Jianshan, and the production operations are more frequent, it is particularly important to avoid the high and steep slopes from being affected by blasting vibration. The production of Jianshan Phosphate Mine adopts the deep-hole step blasting method, and the designed step height is 10 m. The drilling equipment is the Atlas φ152 drilling rig of Jianshan Phosphate Mine and the Atlas φ145 (φ130, φ120, φ115, φ90) drilling rig of the engineering company. Blasting mainly uses 1# rock emulsion explosive and rock expanded ammonium nitrate explosive (the diameter of the roll is 70 mm, 1.5 kg/cylinder).

In this study, the hole mesh parameters used by the mine (5.5 m × 5 m for φ152 drilling rigs, 5 m × 4.5 m for φ145 drilling rigs) are generally acceptable from the field test results. However, when the isosceles triangle is used to arrange the holes and the blast hole density coefficient m = 1.155, the resistance lines of the blast holes in different directions are the most uniform, which is the most effective for increasing the blasting volume of the blast hole and improving the blasting crushing quality (Li et al., 2021; Li et al., 2021). The blasting parameters are designed as follows:

1) Chassis Resistance Line (The horizontal distance from the center of the bottom of the blast hole to the foot of the step):

$$W_d = (25 \sim 40)D = 3.625 \sim 5.8m. \quad (1)$$

In the formula: D-Drilling diameter (0.145 m).

2) Super deep:

$$h_1 = (0.1 \sim 0.35)W_d = 0.45 \sim 1.575m. \quad (2)$$

3) Drilling length:

$$L = H + h_1 = 10 + 0.5 = 10.5m. \quad (3)$$

4) Hole distance:

$$a = mW_d = 1.15W_d = 1.15 \times 4.5 = 5.2m. \quad (4)$$

In the formula: m-Blast hole density factor (1.155).

5) Row spacing:

$$b = (0.6 \sim 1)W_d = 2.7 \sim 4.5m. \quad (5)$$

6) Explosive unit consumption:

$$q = \frac{0.29kg}{m^3}. \quad (6)$$

7) Explosive charge:

$$Q = qV = 0.29 \times 5.2 \times 4.5 \times 10 = 69kg. \quad (7)$$

8) Length of explosive charge:

$$L_1 = Q/q_1 = 6.9m \quad (8)$$

In the formula: q_1 -Line charge density (about 10 kg/m).

9) Length of blockage:

$$L_2 = L - L_1 = 10.5 - 6.9 = 3.6m. \quad (9)$$

Based on the empirical formula $L_2 \geq (0.7–0.8)\ W_d \geq 3.15–3.6m$, the designed packing length of 3.6 m is feasible.

As shown in **Figure 2**, a diagonal hole-by-hole detonation network was used in the field test. Among them, the blasting direction of the blast hole is toward the side of the steps and the steep slope, and the line of the deep holes that are detonated at the same time obliquely intersects the eyebrow line of the steps at an angle (generally 45°) (Geng et al., 2021; Li et al., 2021). The advantage is that the actual distance between the blast holes increases, and the blast hole density coefficient increases, which is beneficial to improve the fragmentation of blasting and reduce the vibration at high and steep slopes. In addition, appropriately increasing the delay interval between holes can increase the frequency of blasting vibration, thereby reducing the impact on adjacent slopes.

Optimization of Blasting Parameters and Field Test

To further improve the blasting effect and increase mine production efficiency we optimized the plan, considering the implementation of a wide hole spacing and small resistance line blasting plan. In order to reduce the on-site test workload, a numerical simulation model was established to provide technical guidance for the optimization plan (Li et al., 2021).

The 1# rock emulsion explosive is used for medium-wave mining and blasting of dolomite and sandy dolomite in Jianshan Phosphate Mine. After investigation, it is found that the reasonable delay time between holes in Jianshan Phosphate Mine is 15–50 ms, and the delay time between rows is 40–80 ms. In addition, combined with the surface delay of the existing plastic detonator network detonator series, it is preliminarily determined that the delay time between the holes is 17 ms/42 ms, 35 ms/65 ms, 25 ms/42 ms, 42 ms/65 ms. In order to better complete geometric solid modeling and dynamic response analysis, ANSYS/LS-DYNA software is used to numerically calculate 16 combinations of wide hole spacing and small resistance line blasting schemes (4 kinds of hole mesh parameters and the delay time between four groups of holes and rows) (Peng. 2005).

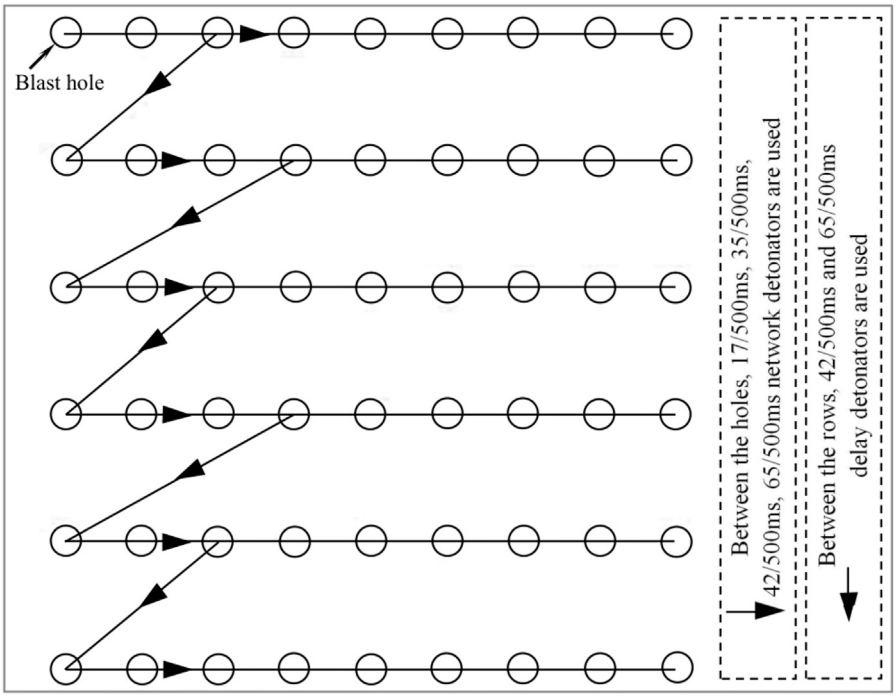

FIGURE 2 | Slash hole-by-hole detonation network diagram.

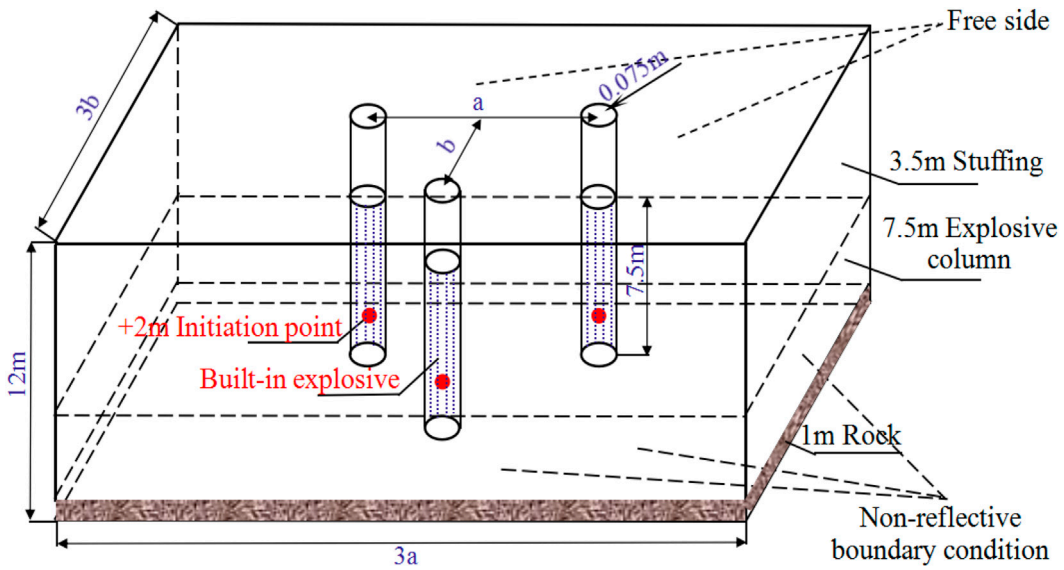

FIGURE 3 | Model size and blasthole layout drawing.

Establishment of 3D Numerical Model

The assumptions before the numerical simulation using ANSYS/LS-DYNA are: 1) The rock material is considered an ideal elastoplastic body, and the initial damage such as joints and fissures inside the rock is not considered. 2) The expansion of the detonation product is an adiabatic process, and the seepage effect of the detonation gas is not considered. 3) The shape of the explosive is uniformly distributed in a cylinder, that is, the explosive stress acting on the wall of the blast hole is evenly distributed. 4) The effect of gravity is very small compared to the explosion stress, and the influence of gravity on the charge is not considered.

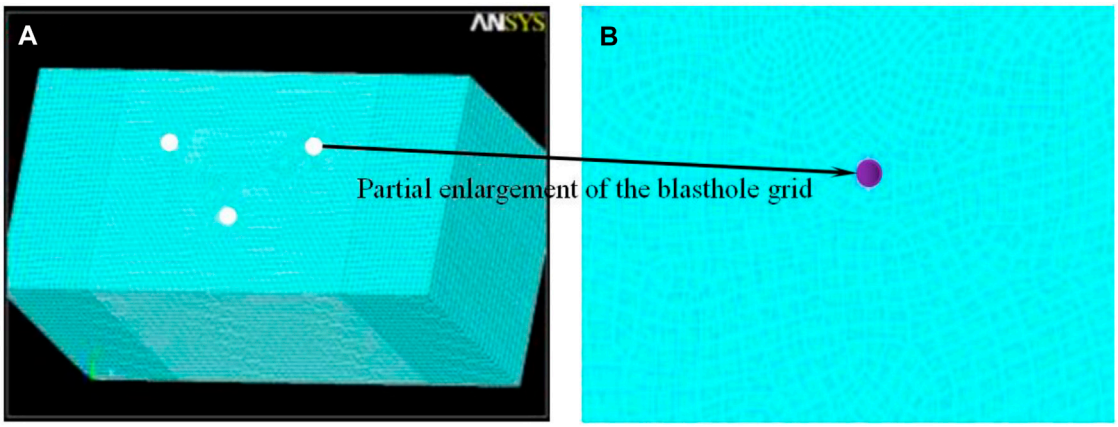

FIGURE 4 | Blasting model meshing diagram. **(A)** Wide hole spacing model meshing diagram; **(B)** Partial enlarged view of blasthole grid.

TABLE 1 | Numerical simulation scheme.

Model number	Blasthole density coefficient (m)	Single hole burden area (S/m^2)	Hole distance (a/m)	Row spacing (b/m)	Postponement time	
					Between holes	Between rows
1-1	1.5	24	6	4	17	42
1-2					35	65
1-3					25	42
1-4					42	65
2-1	2.0	24.5	7	3.5	17	42
2-2					35	65
2-3					25	42
2-4					42	65
3-1	2.0	32	8	4	17	42
3-2					35	65
3-3					25	42
3-4					42	65
4-1	3.0	27	9	3	17	42
4-2					35	65
4-3					25	42
4-4					42	65

In the numerical simulation, the 3D solid164 element type is used, and the overall model is established with three times the hole spacing and row spacing (3a × 3b) of the blast hole. There are three blast holes in the model, the blast holes are arranged in a triangle, and the height of the model is 12 m. The free surface from the top to the bottom of the blast hole are respectively: packing material (3.5 m), grain height (7.5 m) and reserved rock bottom (1 m). In addition, the detonation point is set at +2 m, and the model size and blast hole layout are as shown in **Figure 3**.

Numerical Simulation Process

As shown in **Figure 4A**, the numerical model adopts a meshing method that combines mapping and sweeping to reduce calculation time while ensuring calculation accuracy. In addition, the mesh size near the blasthole is smaller, and the mesh size far away from the blasthole is larger. After the mesh is divided, the number of units in each group of models is between 180 and 220,000. A partial enlarged view of the blasthole grid is shown in **Figure 4B**. When initiating hole by hole, the front and above the explosion zone are free surfaces. In this order value simulation, the top and front of the model are defined as free surfaces, and the remaining surfaces of the model are set as non-reflective boundary conditions to avoid stress wave reflection at the boundary (**Figure 3**). Choosing the ALE (Arbitrary Lagrangian Eulerian) algorithm will realize the fluid-solid coupling dynamic analysis to overcome the numerical calculation difficulties caused by the element distortion (Kenamond et al., 2021). In this number value simulation, the total initiation time of each

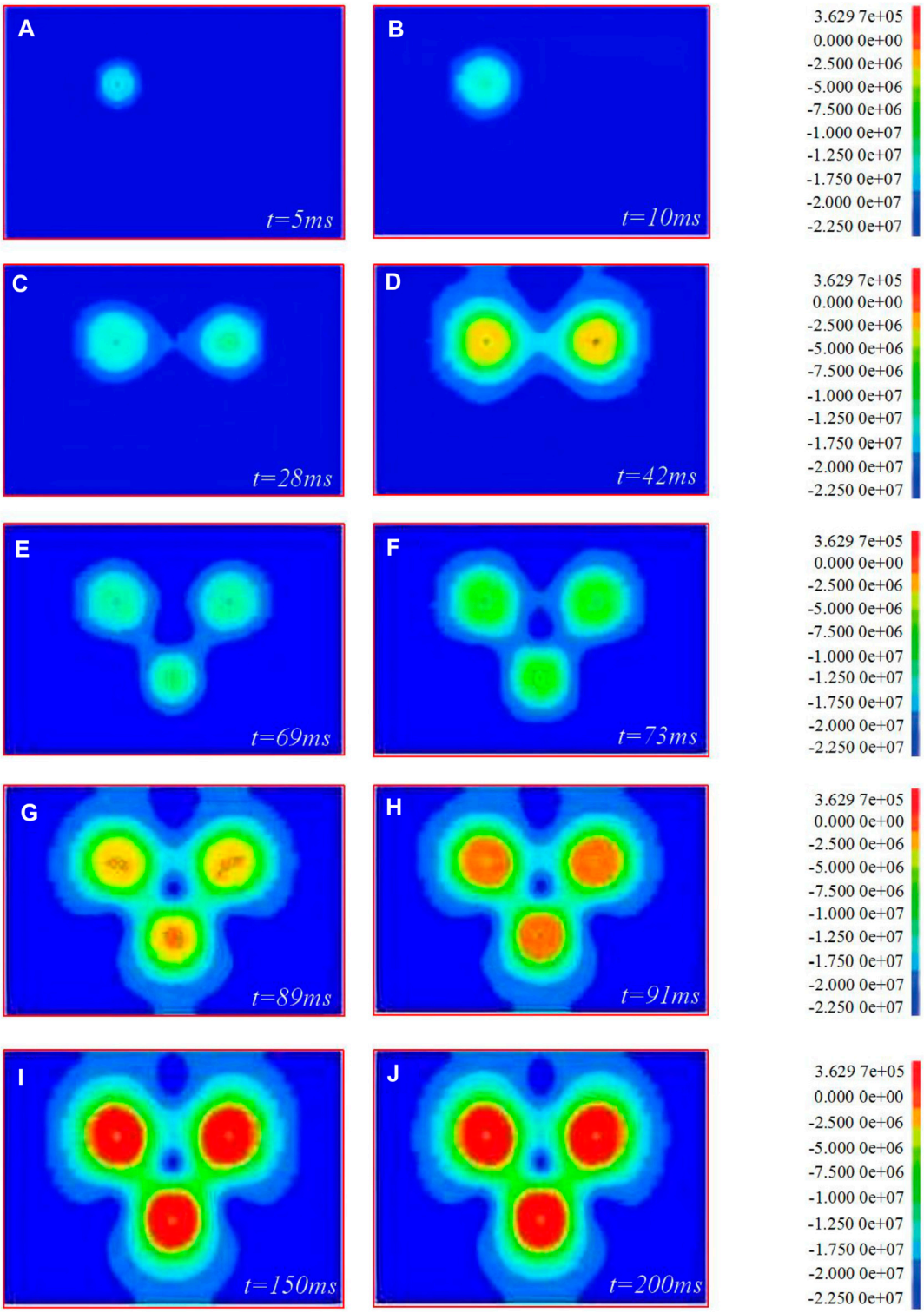

FIGURE 5 | The propagation process of stress wave in wide hole spacing blasting. **(A–J)** are stresses wave propagation effect of t = 5 ms, t = 10 ms, t = 28 ms, t = 42 ms, t = 69 ms, t = 73 ms, t = 89 ms, t = 91 ms, t = 150 ms and t = 200 ms, respectively.

group of calculation models is less than 120 ms. In order to be able to collect the complete element equivalent stress value, the solution time of this simulation is 200 ms, and the calculation step is 1 ms.

Numerical Simulation Results

Through the numerical calculation of 16 groups of blasting plans, the propagation process of the equivalent stress between the holes and the superposition of the equivalent stress of each group of plans are analyzed to determine the optimal blasting plan. The model scheme is as shown in **Table 1**.

Analysis of Equivalent Stress Propagation Process

To analyze the rock fragmentation after blasting, here, we take the 1-1 model as the analysis object to illustrate the stress wave propagation process of this group of models at different times.

As shown in **Figure 5**, the first blasthole detonated at 5 ms and +2 m, and the stress wave propagated outward in a circular shape (**Figures 5A,B**). The second blasthole detonated at 28 ms, and the equivalent stress of the first and second blastholes was superimposed at the line connecting the center of the blasthole at 28 ms (**Figure 5C**). At 42 ms, the equivalent stress is reflected from the free surface, forming a reflected tensile wave to break the rock (**Figure 5D**). The second row of blastholes detonated at 69 ms, and the equivalent stress began to be superimposed between the rows at 69 ms (**Figure 5E**). At 73 ms, the equivalent stress starts to be superimposed between the holes and between the rows (**Figure 5F**). At 89–91 ms, the equivalent stress superimposed between holes and rows is obvious. There are stress weakening areas between the center line of the first row of blastholes and the second row of blastholes and between the first row of blastholes and the free surface (Emad et al., 2018; Gao et al., 2021). There is a strong stress concentration phenomenon at the center of the hole (**Figures 5G,H**). In addition, the stress superposition between rows is more obvious at 150 ms, but the equivalent stress peak value is gradually decreasing (**Figure 5I**). At 200 ms, the superposition process of equivalent stress between holes and rows gradually stabilizes (**Figure 5J**).

Analysis of Equivalent Stress Superposition

It can be seen from **Figures 6–9** that when the hole spacing and row spacing are the same, although the delayed initiation time of each blast hole is different, the superposition of equivalent stress between holes and rows is basically the same. With the increase of hole density coefficient, the superposition of equivalent stress between holes and rows changes greatly. Among them, the stacking between holes is weakened and the stacking between rows is enhanced. In detail, when m = 1.5, the superposition of equivalent stress at the midpoint of blast hole connection is obvious. The equivalent stress first reaches the dynamic tensile strength of rock and causes it to be damaged, and even prone to over broken rock. In addition, the fissures between holes generate a stress wave that diffuses around, resulting in the reduction of the equivalent stress value of the surrounding rocks. A certain range of stress weakening zone is formed between the two rows of blastholes, which inhibits the development of fractures in other directions (Averbeck and Kerscher, 2017). When m = 2, the superposition of equivalent stress between holes and rows is weak. During blasting, it is similar to forming two independent blasting funnels, and it is easy to form large or triangular spine shaped rock ridges between holes. When m = 2.7–3, the superposition of equivalent stress between rows increases. The stress weakening zone moves towards the free surface from the center line of the first row of blastholes to the second row of blastholes, far away from the blasting action range. On the other hand, the fracture angle generated by the small resistance line increases, resulting in the increase of the corresponding free surface and the reflected tensile wave, which is conducive to the fracture of rocks between holes and rows. In summary, during the blasting of dolomite and sandy dolomite in Jianshan phosphate mine, scheme 8 × 4 should be selected to achieve the dynamic tensile strength of rock, ensure rock fragmentation and avoid serious blasting harmful effects.

Field Test Results

Based on the optimized combination of blasting parameters, blast hole network parameters, and delay interval, an 8 × 4 scheme is selected for field testand the mine's existing detonator with a combination of 35 and 65 ms delay interval is used. A diagonal hole-by-hole detonation network is adopted. The blastholes in the same row are connected with the same delay between the holes. When the rows are connected, the second blasthole in the first row is connected to the second row with an interrow delay detonator. A blast hole is connected in the same way for each row in the back row.

Compared with the large block rate of the mine before the test, the large block rate of the three tests using the 8 × 4 scheme has been reduced by 10.4, 16.7, and 15.6% respectively, and the maximum size of the block has been reduced. It shows that with the increase of the blast hole density coefficient, the distance between the rows decreases and the stress superposition between the rows increases, which makes the rock fragmentation more uniform (Miao et al., 2021). In the process of blasting, the influence of flying rocks on the surroundings can be better controlled (Li et al., 2021). After the resumption of mining in the east mining area of Jianshan Phosphorus Mine, by accelerating the slope unloading speed, the slope change rate was effectively slowed down, which provided a guarantee for the continuous mining work below (Li et al., 2021). At the same time, the technology effectively protects the slope surface, makes the entire slope surface smooth and flat, improves production efficiency, and speeds up the slope cutting progress.

BLASTING VIBRATION MONITORING

Blasting Vibration Monitoring of High Slope

As shown in **Figure 10A**, in order to study the seismic effect of blasting vibration on high slopes and to determine whether the high slopes are within the safe allowable range, we have arranged

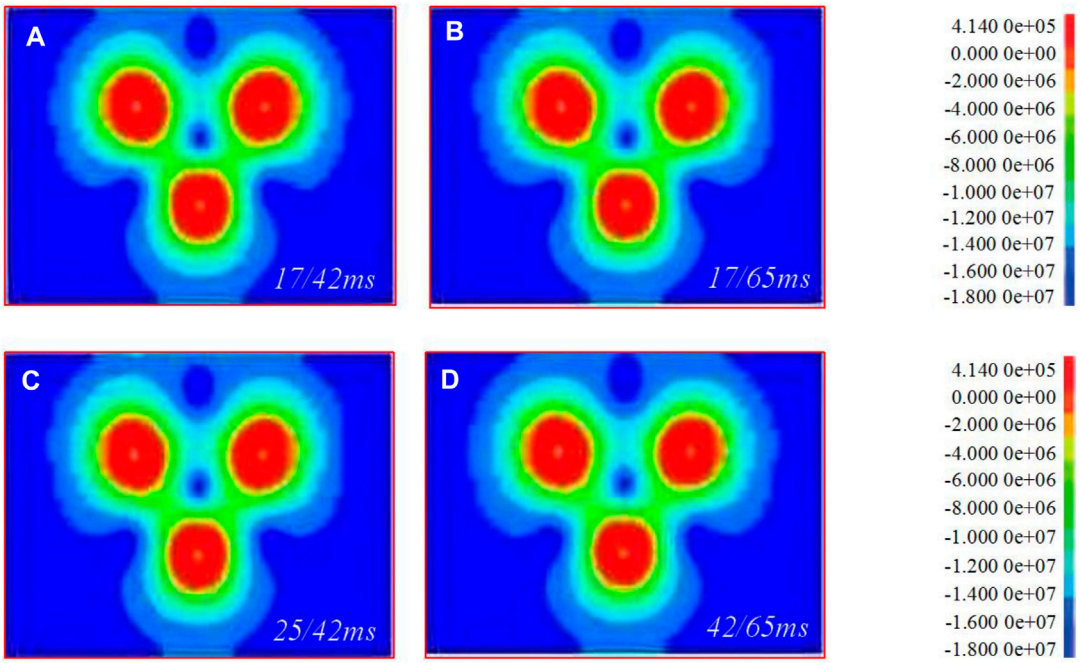

FIGURE 6 | 6 × 4 model 200 ms equivalent stress superposition. **(A–D)** are the superposition of equivalent stresses of 17/42 ms, 17/65 ms, 25/42 ms and 42/65 ms, respectively.

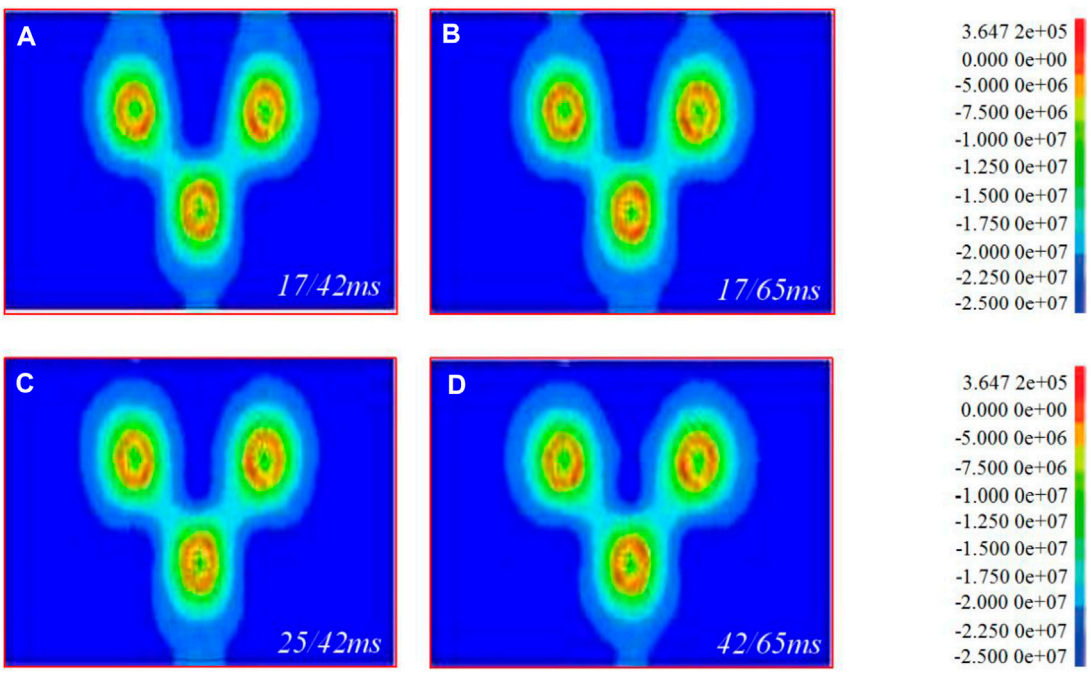

FIGURE 7 | 7 × 3.5 model 200 ms equivalent stress superposition. **(A–D)** are the superposition of equivalent stresses of 17/42 ms, 17/65 ms, 25/42 ms and 42/65 ms, respectively.

denser measuring points in areas where the slopes are severely deformed. According to the actual situation of blasting in Jianshan Phosphorus Mine, monitoring points were arranged on the high slope of Jianshan stope (Chen et al., 2020). **Figure 10B** which shows the time history curve of the vibration velocity of the measuring point at the 2,070 m

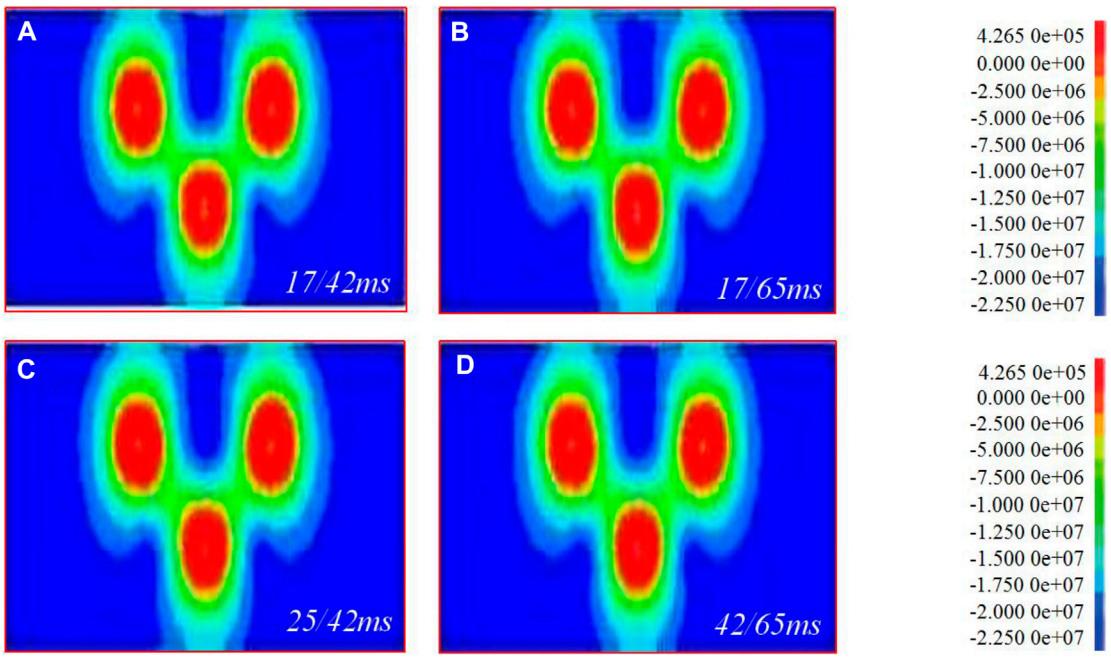

FIGURE 8 | 8 × 4 model 200 ms equivalent stress superposition. **(A–D)** are the superposition of equivalent stresses of 17/42 ms, 17/65 ms, 25/42 ms and 42/65 ms, respectively.

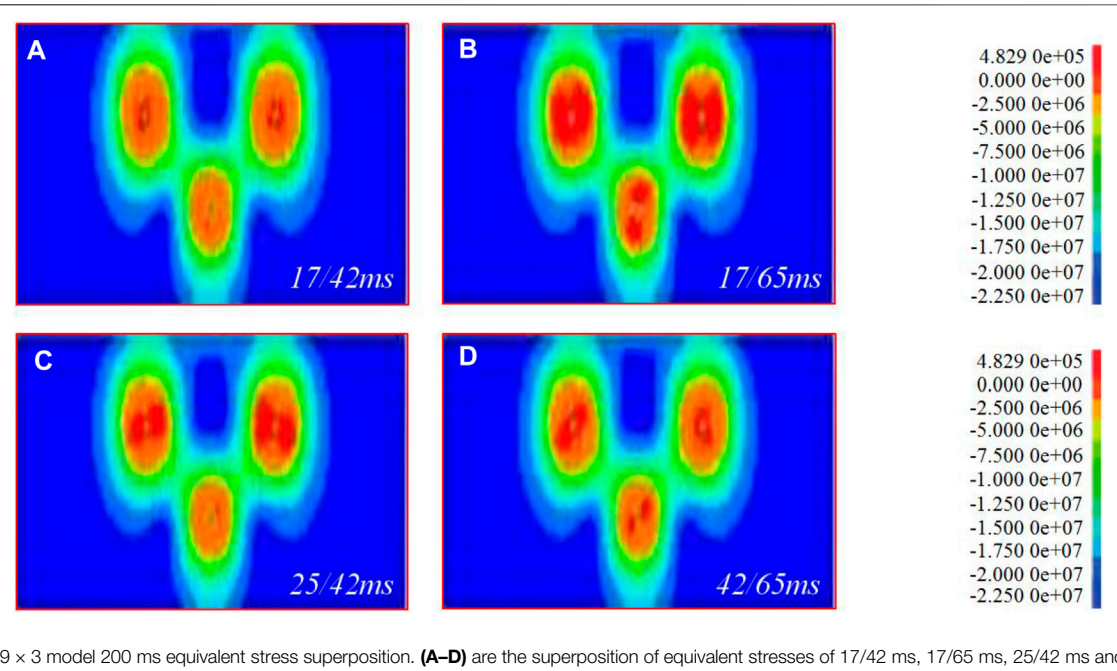

FIGURE 9 | 9 × 3 model 200 ms equivalent stress superposition. **(A–D)** are the superposition of equivalent stresses of 17/42 ms, 17/65 ms, 25/42 ms and 42/65 ms, respectively.

platform on the east side of the Jianshan slope. During the mining blasting process, more than 20 vibration monitoring tasks were carried out. Among them, several groups of data measured on high slopes are selected for comparison and analysis (**Table 2**). The comparison results show that: 1) According to the safety allowable vibration speed standard for permanent rock high slopes, the on-site slope vibration speed standard control is determined to be 5 cm/s. However,

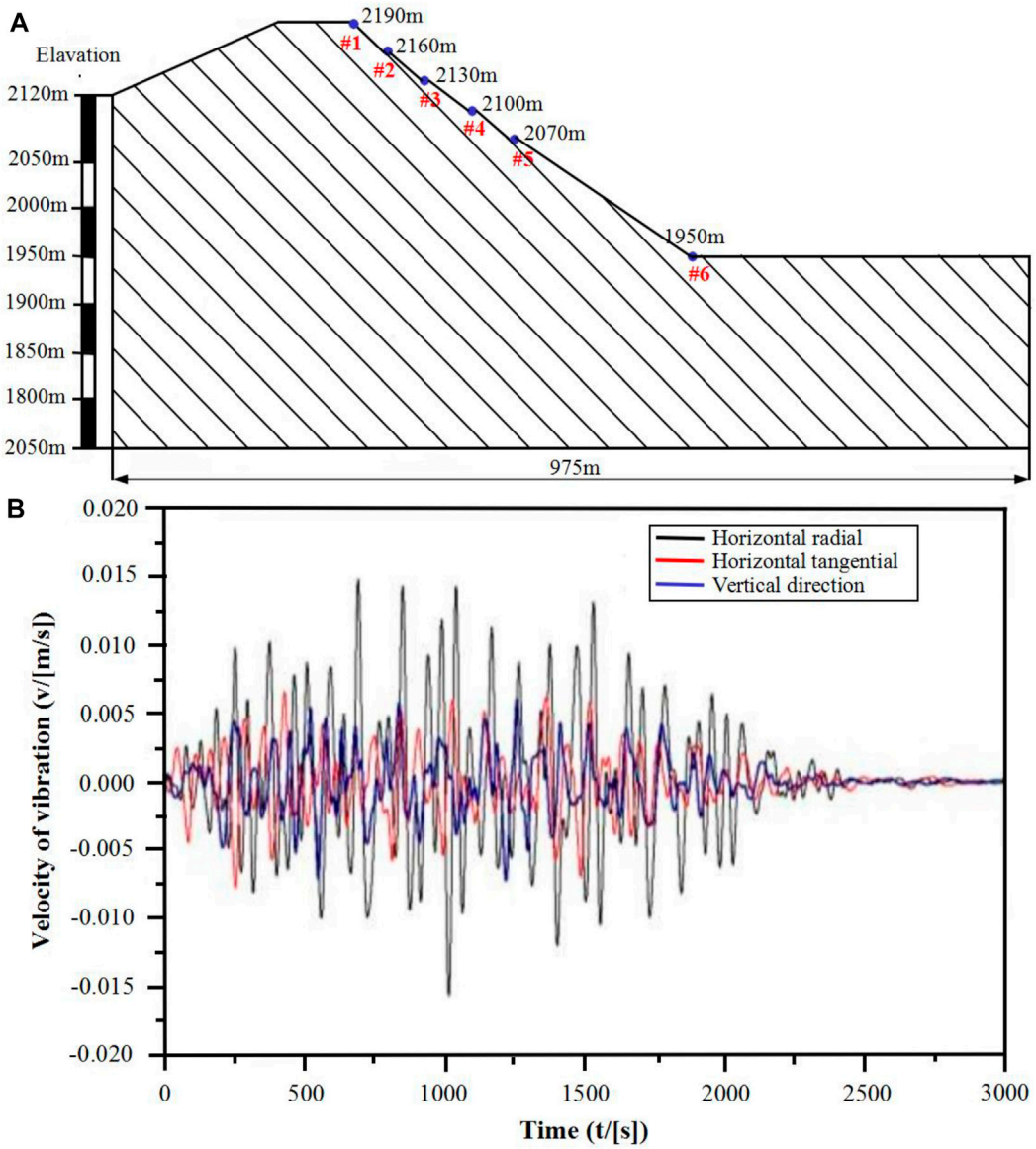

FIGURE 10 | Blasting monitoring of high and steep slopes. **(A)** Layout of high slope monitoring points; **(B)** Time-history curve of the vibration velocity of the measuring point at the 2070 platform on the east side of the Jianshan slope.

the peak vibration velocity of the measuring point on the high slope of Jianshan mountain is less than this standard. 2) As shown in **Table 2**, when the maximum single shot charge is the same, the blasting vibration speed basically decreases with the increase of the blasting center distance. Among them, the elevation amplification effect appeared in 7–12 blasts. This is because the nature of the rock mass, the integrity of the rock mass, the slope and the thickness of the slope and the mountain mass affect the elevation effect. In addition, the slope will affect the intensity and frequency of the blasting vibration wave. Therefore, the degree of elevation magnification effect is different (Chen et al., 2020).

Propagation Law of Blasting Vibration on High Slope

Considering the elevation effect of blasting vibration wave propagation, regression analysis is carried out on the measured

TABLE 2 | Typical vibration data statistics table.

Vibration measurement sequence	Maximum single shot dose (kg)	R (horizontal distance m)	Maximum vibration speed (cm/s)			Measuring point position (m)
			(X axis)	(Y axis)	(Z axis)	
1	68	181	0.81297	0.91690	1.02708	2,040
2	68	204	0.95276	0.57948	0.81892	2,070
3	68	257	0.39402	0.37856	0.52117	2,100
4	68	245	0.34240	0.36117	0.41472	2,040
5	68	268	0.50395	0.48517	0.22429	2070
6	68	290	0.37563	0.26169	0.18477	2,100
7	68	184	0.45802	0.35448	0.36015	2,040
8	68	304	0.43470	0.35239	0.38911	2,070
9	68	395	0.24226	0.34963	0.41585	2,100
10	69	316	0.28700	0.23558	0.17683	2,040
11	69	379	0.31565	0.25781	0.13977	2,070
12	69	449	0.43220	0.34333	0.28921	2,100
13	69	173	0.76787	0.74798	0.66574	2,040
14	69	239	0.55729	0.36768	0.43232	2,070
15	69	284	0.44222	0.30748	0.26959	2,100

data in **Table 2**. The following formula is used to predict the attenuation law and propagation law of blasting vibration on high slopes (Shi et al., 2015):

$$v = k\left[\frac{\sqrt[3]{Q}}{D}\right]^{\alpha}\left[\frac{\sqrt[3]{Q}}{H}\right]^{\beta}. \tag{10}$$

In the formula: D-Explosion center distance (Horizontal distance, m); Q-Explosive charge; H-Design step height.

The logarithms on both sides of **Formula 10** are:

$$\lg v = \lg k + \alpha \lg\left[\frac{\sqrt[3]{Q}}{D}\right] + \beta \lg\left[\frac{\sqrt[3]{Q}}{H}\right]. \tag{11}$$

In **Formula 11**, let $Y = \lg v$, $X_1 = \lg[\frac{\sqrt[3]{Q}}{R}]$, $X_2 = \lg[\frac{\sqrt[3]{Q}}{H}]$, then:

$$Y = \lg k + \alpha X_1 + \beta X_2. \tag{12}$$

Since **Formula 11** can be transformed into a binary linear relationship, use the binary linear regression Matlab program to find the values of k, α, β.

1) Regression analysis of X-axis vibration data

According to **Formula 12**, using MATLAB software regression analysis, the result is shown in **Figure 11A**, the calculation can be: k = 29.7235, a = 1.5243, β = -0.5152.

Thus, the X-axis propagation law of blasting vibration on the high slope of Jianshan Phosphorus Mine:

$$v = 29.7235\left[\frac{\sqrt[3]{Q}}{D}\right]^{1.5243}\left[\frac{\sqrt[3]{Q}}{H}\right]^{-0.5152}. \tag{13}$$

Meanwhile, the maximum amount of medicine Q_{max} for slope safety can be deduced as follows:

$$Q_{max} \le \left[\frac{V}{29.7235}\right]^{2.9729} \cdot D^{4.5316} \cdot H^{-1.5316}. \tag{14}$$

2) Regression analysis of Y-axis vibration data

According to **Formula 12**, the result is shown in **Figure 11B**, the calculation can be: k = 19.3108, a = 0.8960, β = 0.0350.

Thus, the Y-axis propagation law of blasting vibration on the high slope of Jianshan Phosphorus Mine:

$$v = 19.3108\left[\frac{\sqrt[3]{Q}}{D}\right]^{0.8960}\left[\frac{\sqrt[3]{Q}}{H}\right]^{0.0350}. \tag{15}$$

Meanwhile, the maximum amount of medicine Q_{max} for slope safety can be deduced as follows:

$$Q_{max} \le \left[\frac{V}{19.3108}\right]^{3.2223} \cdot D^{2.8872} \cdot H^{0.1128}. \tag{16}$$

3) Regression analysis of Z-axis vibration data

According to **Formula 12**, the result is shown in **Figure 11C**, the calculation can be: k = 1430.54, a = 1.9255, β = 0.0701.

Therefore, the Z-axis propagation law of blasting vibration on the high slope of Jianshan Phosphorus Mine:

$$v = 1430.54\left[\frac{\sqrt[3]{Q}}{D}\right]^{1.9255}\left[\frac{\sqrt[3]{Q}}{H}\right]^{0.0701}. \tag{17}$$

At the same time, the maximum amount of medicine Q_{max} for slope safety can be deduced as follows:

$$Q_{max} \le \left[\frac{V}{1430.54}\right]^{1.5033} \cdot D^{2.8946} \cdot H^{0.1054}. \tag{18}$$

DISCUSSIONS

In order to study the damage of the rock in the slope under the action of blasting vibration, based on the acoustic test of the slope rock mass before and after blasting, the study on the cumulative

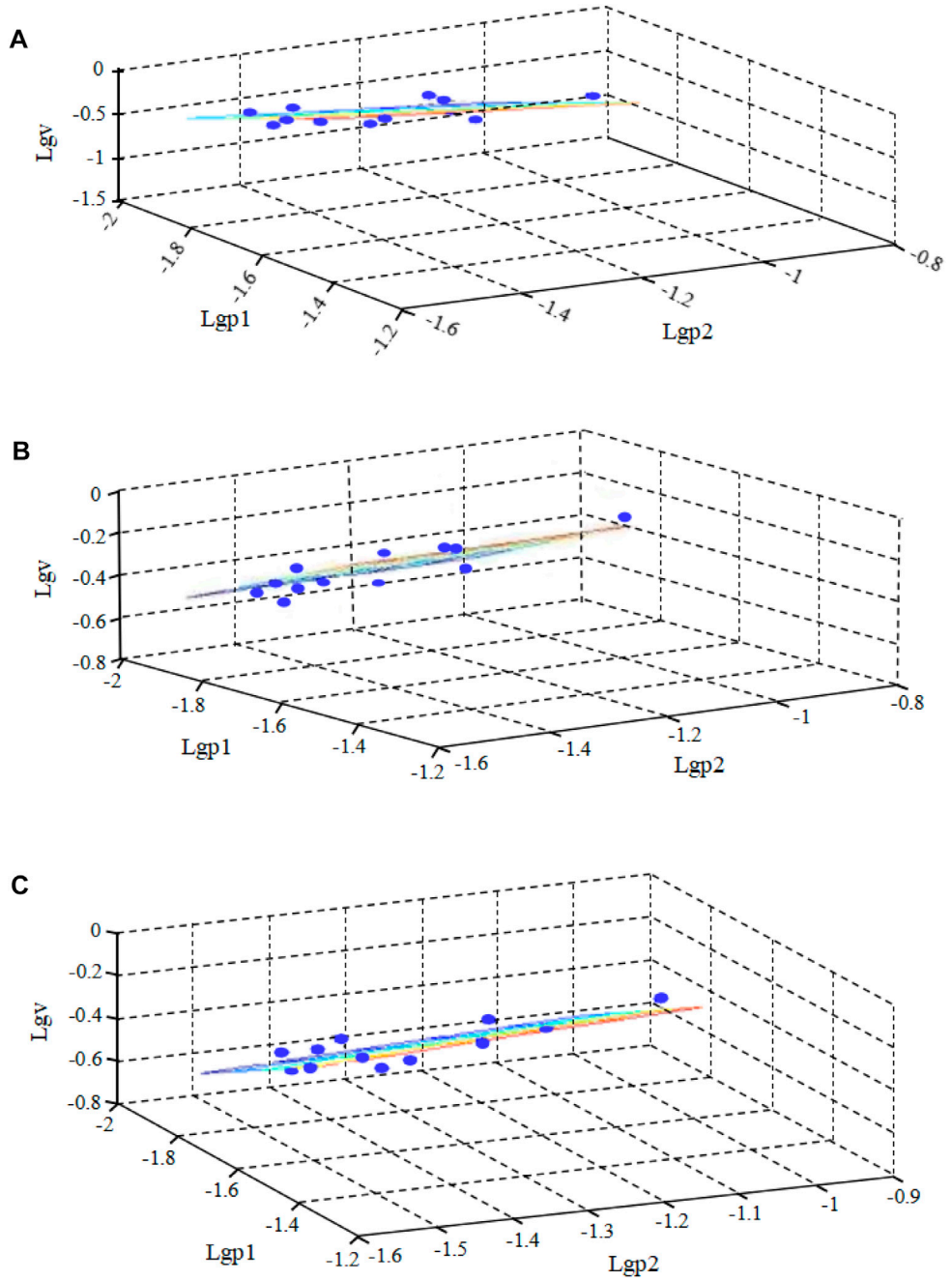

FIGURE 11 | Regression analysis results of vibration data of different coordinate axes. **(A)** *X*-axis vibration data regression analysis results; **(B)** *Y*-axis vibration data regression analysis results; **(C)** *Z*-axis vibration data regression analysis results.

damage of the slope rock mass under the action of blasting vibration was carried out, and the expansion model of the cumulative damage effect of rock mass blasting was established (Yan. 2007).

Sonic Test and Result Analysis

The sound wave test method before and after blasting is used to judge the quality damage of the slope of Jianshan open-pit mine caused by blasting. Specifically, by testing the post-blast wave velocity Cp2 and the pre-blast wave velocity Cp1 of the rock mass at the same part of the slope of the Jianshan open-pit stope, and calculating the sound wave change rate $\Delta Cp=(1-Cp2/Cp1)$ of the rock mass at the same part before and after the explosion. If ΔCp is greater than 10%, it is judged that the blasting has destroyed the rock mass. If ΔCp is less than or equal to 10%, it is judged that the blasting is safe and the rock mass is not damaged. In our study, blasting tests were carried

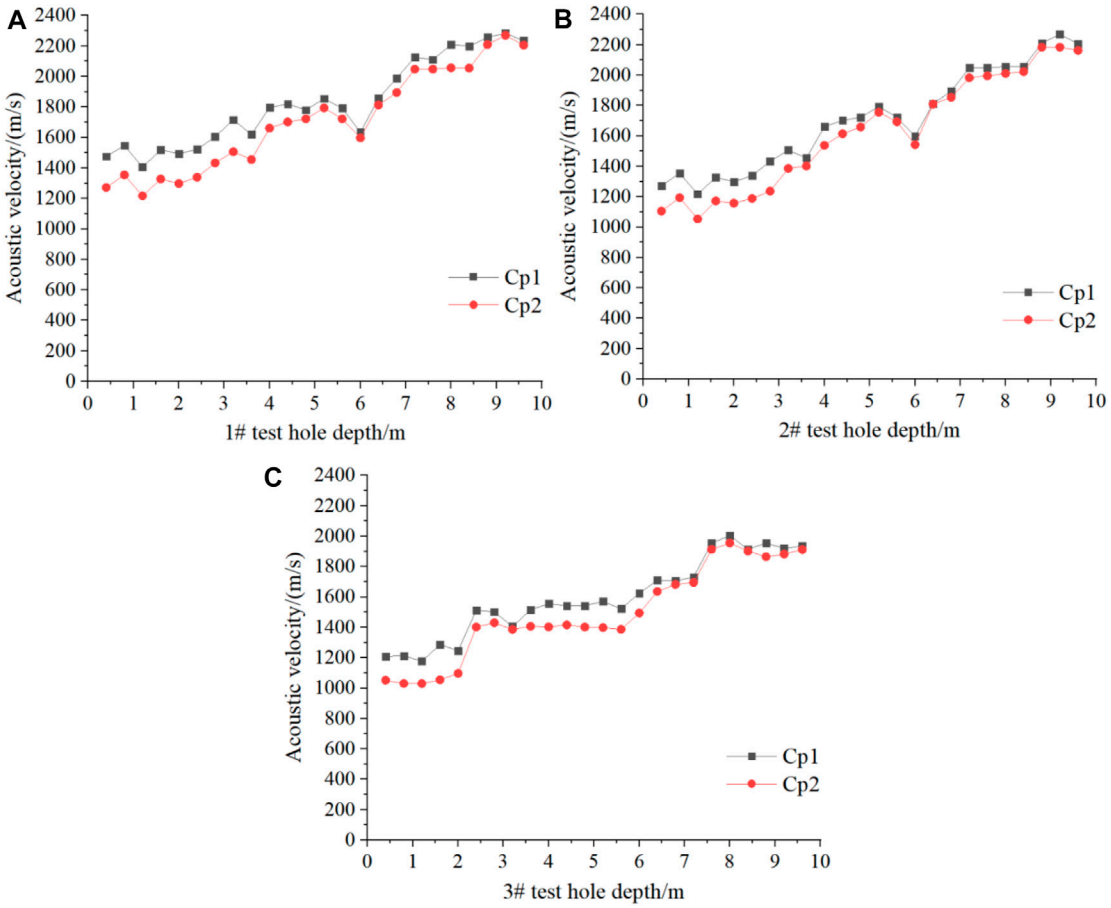

FIGURE 12 | Comparison of sonic (longitudinal wave) wave speeds before and after the explosion of different test holes. **(A)** Comparison of the sonic wave velocity before and after the explosion of the 1# test hole; **(B)** Comparison of the sonic wave velocity before and after the explosion of the 2# test hole; **(C)** Comparison of the sonic wave velocity before and after the explosion of the 3# test hole.

out on holes 1#, 2# and 3# respectively, and the wave velocity Cp1 before blasting and the wave velocity Cp2 after blasting of holes 1#-3# were calculated and analyzed. **Figures 12A–C** are the comparison diagrams of the pre-blast wave velocity Cp1 and post-blast wave velocity Cp2 of the tested holes #1, #2 and #3, respectively.

As shown in **Figure 12**, the depth of the impact of blasting on the slope of the Jianshan open-pit is in the range of 0–3.6 m. And according to the sonic test results before and after blasting, the blasting has almost no damage to the deeper rock mass (Xu et al., 2012; Zhang et al., 2020). Thus, the blasting will not cause damage to the adjacent high and steep slopes as a whole.

Establishment of a Cumulative Damage Model for Slope Rock Mass Blasting

The fatigue damage of a material refers to the ratio of the number of active load cycles that the current material can withstand to the number of active load cycles that the material can withstand when it is destroyed (Xu et al., 2021). Generally speaking, the damage to the rock mass caused by blasting excavation will cause the original joint fissures of the rock mass to open, expand, or generate new fissures, resulting in the decrease of the mechanical parameters of the rock mass. The damage degree of rock mass can be expressed as:

$$D = 1 - \frac{E}{E_0} = 1 - \left[\frac{v}{v_0}\right]^2 = 1 - K = 1 - (1 - \eta)^2. \quad (19)$$

In **Formula 19**, D-damage degree of rock mass; E-the elastic modulus of the rock mass before blasting; E_0-the equivalent elastic modulus of the rock mass after blasting; v-sonic wave velocity before rock blasting; v_0-sonic wave velocity after rock blasting; K-rock mass integrity factor; η-sonic wave velocity reduction rate.

Rock damage should include two parts: one part is the initial damage D_0 caused by geological defects such as natural joints, fissures, and micro-cavities in the rock; the other part is the blasting damage ΔD caused by crack propagation caused by blasting stress waves. Therefore, the rock mass damage D after blasting can be expressed as follows:

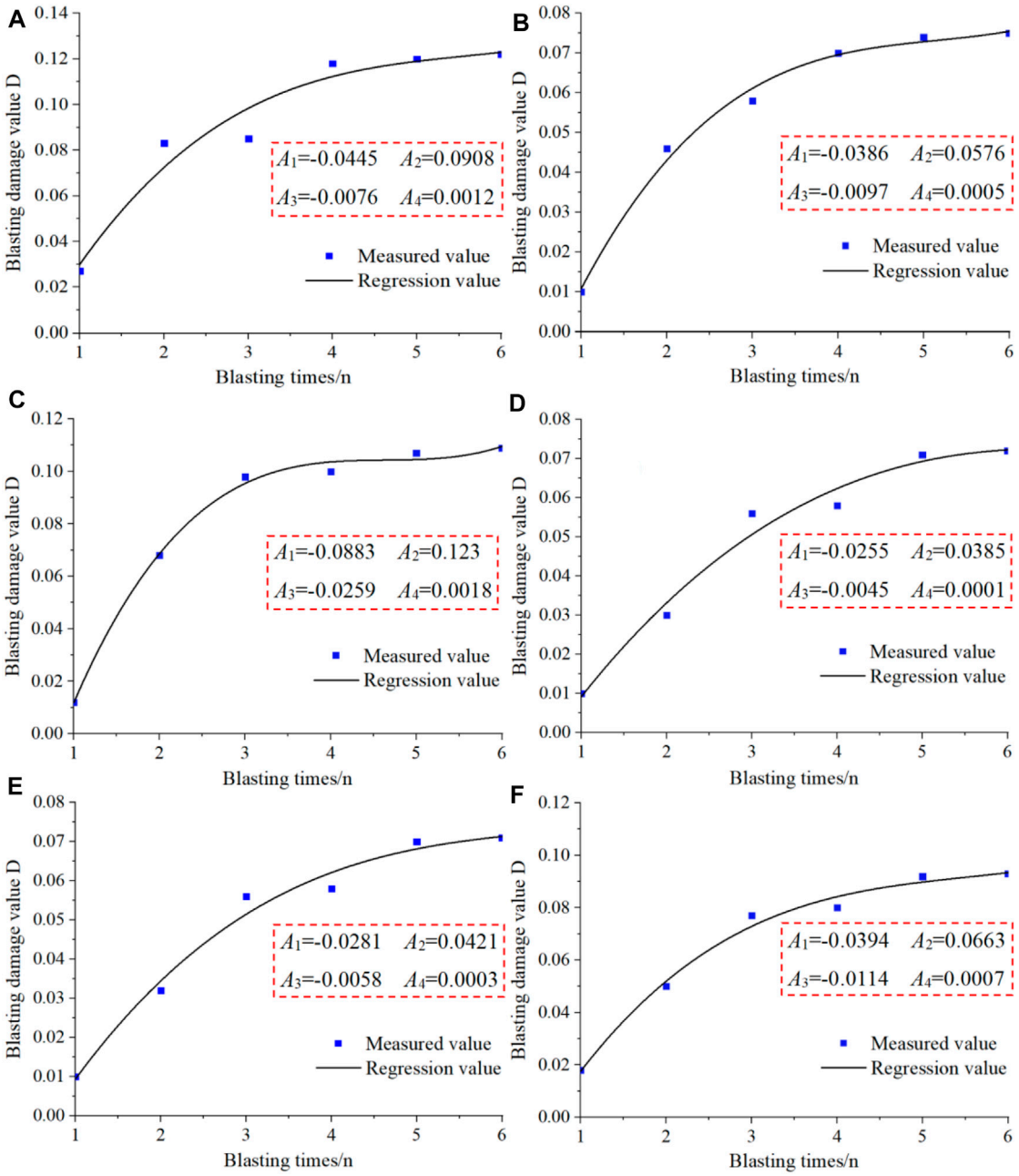

FIGURE 13 | Cumulative damage evolution curve. **(A)** 1# Non-linear cumulative damage evolution curve at 2.4 m of borehole; **(B)** 1# Non-linear cumulative damage evolution curve at 4.0 m of borehole; **(C)** 2# Non-linear cumulative damage evolution curve at 2.4 m of borehole; **(D)** 2# Non-linear cumulative damage evolution curve at 4.0 m of borehole; **(E)** 3# Non-linear cumulative damage evolution curve at 2.4 m of borehole; **(F)** 3# Non-linear cumulative damage evolution curve at 4.0 m of borehole.

$$D = D_0 + \Delta D. \tag{20}$$

Simultaneous **Formulas 19**, **20** can be obtained:

$$D_0 = 1 - \left[\frac{v_m}{v_0}\right]^2 = 1 - \left[\frac{v_0 - \Delta v_0}{v_0}\right]^2 = 1 - (1 - \eta_0)^2. \tag{21}$$

In **Formula 21**, v_m-sonic velocity of the rock mass; v_0-sonic velocity of the rock mass; Δv_0-the difference between the sound velocity of the rock mass and the sound velocity of the rock mass; $\eta 0$-the initial sound velocity reduction rate of the rock mass before blasting.

After the blasting stress wave acts, the rock mass blasting damage appears, and the total damage increases. Based on the change of sound velocity, the damage ΔD of rock mass blasting can be defined as:

$$\Delta D = 1 - \left[\frac{v}{v_m}\right]^2 = 1 - \left[1 - \frac{\Delta v}{v_m}\right]^2 = 1 - (1 - \eta)^2. \tag{22}$$

In **Formula 22**, v-sonic wave velocity of rock mass after blasting; Δv-sonic wave velocity of rock mass before and after blasting.

Under the influence of blasting for a long period of time, rock mass blasting damage continues to accumulate. Each blasting damage can be expressed by the sonic velocity reduction rate ΔD, therefore:

$$\Delta D_n = 1 - \left[\frac{v_n}{v_m}\right]^2 = 1 - \left[1 - \frac{\Delta v_n}{v_m}\right]^2 = 1 - \left(1 - \eta_n\right)^2. \quad (23)$$

The formula for cumulative damage of rock mass under blasting action is:

$$D = D_0 + \Delta D_n = 1 - \left(1 - \eta_0\right)^2 + 1 - \left(1 - \eta_n\right)^2 = 2\left(\eta_0 + \eta_n\right)^2 - \eta_0^2 - \eta_n^2, \quad (24)$$

$$D = A_1 + A_2 n + A_3 n^2 + A_4 n^3. \quad (25)$$

In **Formula 25**, D-damage degree of rock mass; n-the number of blasting; A_1, A_2, A_3 and A_4-the undetermined constants of the regression curve, respectively.

The cumulative damage expansion model of rock mass blasting characterized by the reference quantity of rock mass sound velocity reduction rate is shown in **Formula 24**. Under the action of multiple blasting, the damage of the rock mass continues to accumulate. When the accumulation of damage reaches a certain level, it will cause the rock mass instability and destruction. In **Figure 13**, with the hole depth 2.4 and 4.0 m as the research object of cumulative damage of blasting, a third degree polynomial is used to fit the degree of cumulative damage of rock mass, and the mathematical model of non-linear cumulative damage of rock mass under the action of six blasting is analyzed.

New Prospects of Research on Mine Blasting Technology

Currently, our method adopts the 8 × 4 m hole network parameters and the slash hole-by-hole initiation method, and the detonator delay time adopts 35 ms between holes, 65 ms between rows, and 500 ms within holes to achieve a better blasting effect. In detail, the blasting fragmentation is relatively uniform, the block rate is reduced, and it will not affect the adjacent high and steep rock slopes. In addition, by establishing a mathematical model of cumulative damage of rock mass blasting, it shows that blasting vibration will not cause damage to the slope as a whole. In the future, we will widely apply this technology in the field of mine blasting. And try to test the blasting methods of 17/42, 25/42, 25/65, 42/65 and other forms of detonators outside the hole with extended time to find a best blasting plan. In addition, since the initial joints and fissures in the rock are not considered in the numerical simulation of blasting in our study, we will consider these factors in the selection of the best blasting plan in future studies. On the other hand, the mathematical model of cumulative damage of rock mass blasting can be used to predict the rock mass damage caused by subsequent blasting, which provides a reference for mine production blasting.

CONCLUSION

Combined with field survey, field blasting test, numerical simulation and theoretical analysis, this paper systematically studies the open-pit layered blasting technology of a complex mine adjacent to high and steep slope. By monitoring the blasting vibration of high and steep slopes, the attenuation law and propagation law of blasting vibration are predicted. The following conclusions were drawn.

1) Based on the numerical simulation of wide hole spacing blasting and field tests, a scheme using 8 × 4 m hole network parameters, diagonal line-by-hole initiation method, and detonator delay time of 35 ms between holes, 65 ms between rows, and 500 ms within holes is proposed. It reduces the workload of drilling, decreases the cost of drilling, and does not affect the adjacent high and steep slopes.
2) Regression analysis of a large number of blasting vibration test data, obtained the blasting vibration propagation law in the Jianshan stope, and predicted the attenuation law and propagation law of blasting vibration on high and steep slopes, which provided a reference for mine production blasting.
3) A mathematical model for cumulative damage of rock mass blasting is established. The research results show that the impact depth of mining blasting in the Jianshan open-pit on the adjacent high and steep slope is 0–3.6 m, but the blasting has almost no damage to the deeper rock mass, thus, the blasting will not cause damage to the slope as a whole. In the future, this model can be used to predict rock damage caused by subsequent blasting.

DATA AVAILABILITY STATEMENT

The raw data supporting the conclusion of this article will be made available by the authors, without undue reservation.

AUTHOR CONTRIBUTIONS

MW and QL wrote the original draft and performed the calculation and analysis. XL contributed to the conceptualization, supervision, methodology, and funding acquisition. YH was responsible for the writing of the original draft and funding acquisition. QC and SJ contributed to the conceptualization and obtaining the resources and reviewed and edited the manuscript.

FUNDING

This work was supported by National Natural Science Foundation of China (No.41867033) and Postdoctoral Science Foundation of China (No. 2019M650144) and State Key Laboratory of Safety and Health for Metal Mines (zdsys 2019-005). The authors wish to acknowledge these supports.

REFERENCES

Aldas, G. G. U., and Ecevitoglu, B. (2008). Waveform Analysis in Mitigation of Blast-Induced Vibrations. *J. Appl. Geophys.* 66 (1), 25–30. doi:10.1016/j.jappgeo.2008.08.004

Averbeck, S., and Kerscher, E. (2017). Critical Plane Analysis of Multiaxial Fatigue Experiments Leading to White Etching Crack Formation. *J. Phys. Conf. Ser.* 843 (1), 012028–012370. doi:10.1088/1742-6596/843/1/012028

Chen, L., Zhang, W., Gao, X., Wang, L., Li, Z., Böhlke, T., et al. (2020a). Design Charts for Reliability Assessment of Rock Bedding Slopes Stability against Bi-planar Sliding: SRLEM and BPNN Approaches. *Georisk: Assess. Manage. Risk Engineered Syst. Geohazards* 2020, 1–16. doi:10.1080/17499518.2020.1815215

Chen, L., Zhang, W., Zheng, Y., Gu, D., and Wang, L. (2020b). Stability Analysis and Design Charts for Over-dip Rock Slope against Bi-planar Sliding. *Eng. Geology.* 275, 105732. doi:10.1016/j.enggeo.2020.105732

Chen, Y., Xu, J., Huo, X., Wang, J., and Younesian, D. (2019). Numerical Simulation of Dynamic Damage and Stability of a Bedding Rock Slope under Blasting Load. *Shock and Vibration* 2019, 1–13. doi:10.1155/2019/9616859

Deng, K., and Chen, M. (2021). Blasting Excavation and Stability Control Technology for Ultra-high Steep Rock Slope of Hydropower Engineering in China: a Review. *Eur. J. Remote Sensing* 54 (2), 92–106. doi:10.1080/22797254.2020.1752811

Dokht, R. M. H., Smith, B., Kao, H., Visser, R., and Hutchinson, J. (2020). Reactivation of an Intraplate Fault by Mine-Blasting Events: Implications to Regional Seismic Hazard in Western Canada. *J. Geophys. Res. Solid Earth* 125 (6), 1–15. doi:10.1029/2020JB019933

Emad, M. Z., Mitri, H., and Kelly, C. (2018). Dynamic Model Validation Using Blast Vibration Monitoring in Mine Backfill. *Int. J. Rock Mech. Mining Sci.* 107, 48–54. doi:10.1016/j.ijrmms.2018.04.047

Gao, H., Gao, Y., Wang, J., Fu, Q., Qiao, B., Wei, X., et al. (2021). Study on Bidirectional Blasting Technology for Composite Sandstone Roof in Gob-Side Entry-Retaining Mining Method. *Appl. Sci.* 11 (7524), 7524. doi:10.3390/app11167524

Geng, J., Li, Q., Li, X., Zhou, T., Liu, Z., and Xie, Y. (2021). Research on the Evolution Characteristics of Rock Mass Response from Open-Pit to Underground Mining. *Adv. Mater. Sci. Eng.* 2021, 1–15. doi:10.1155/2021/3200906

Gui, Y. L., Zhao, Z. Y., Zhou, H. Y., Goh, A. T. C., and Jayasinghe, L. B. (2017). Numerical Simulation of Rock Blasting Induced Free Field Vibration. *Proced. Eng.* 191, 451–457. doi:10.1016/j.proeng.2017.05.203

Guo, X. B., Xiao, Z. X., and Zhang, Z. C. (2001). Slope Effect of Blasting Vibration. *Chin. J. Rock Mech. Eng.* 20 (1), 83–87. doi:10.3321/j.issn:1000-6915.2001.01.019

Jiang, N., Zhou, C., Lu, S., and Zhang, Z. (2018). Effect of Underground Mine Blast Vibrations on Overlaying Open Pit Slopes: A Case Study for Daye Iron Mine in China. *Geotech Geol. Eng.* 36 (3), 1475–1489. doi:10.1007/s10706-017-0402-x

Kenamond, M., Kuzmin, D., and Shashkov, M. (2021). A Positivity-Preserving and Conservative Intersection-Distribution-Based Remapping Algorithm for Staggered ALE Hydrodynamics on Arbitrary Meshes. *J. Comput. Phys.* 435, 110254. doi:10.1016/J.JCP.2021.110254

Li, B., Wang, E., Li, Z., Niu, Y., Li, N., and Li, X. (2021a). Discrimination of Different Blasting and Mine Microseismic Waveforms Using FFT, SPWVD and Multifractal Method. *Environ. Earth Sci.* 80 (1), 1–16. doi:10.1007/S12665-020-09330-7

Li, L., Zhang, J., and Wu, L. (2019). Construction Technology of Cooperative Blasting in High-Steep Slope and Underground Tunnel in Offshore Oil Depot. *J. Coastal Res.* 98 (sp1), 1–5. doi:10.2112/SI98-001.1

Li, X., Geng, J., Li, Q., Tian, W., and Zhou, T. (2021b). Behaviors and Overlying Strata Failure Law for Underground Filling of a Gently Inclined Medium-Thick Phosphate Deposit. *Adv. Civil Eng.* 2021, 1–17. doi:10.1155/2021/3275525

Li, X., Liu, Z., and Yang, S. (2021c). Similar Physical Modeling of Roof Stress and Subsidence in Room and Pillar Mining of a Gently Inclined Medium-Thick Phosphate Rock. *Adv. Civil Eng.* 2021, 1–17. doi:10.1155/2021/6686981

Li, X., Peng, K., Peng, J., and Hou, D. (2021e). Experimental Investigation of Cyclic Wetting-Drying Effect on Mechanical Behavior of a Medium-Grained sandstone. *Eng. Geology.* 293, 106335. doi:10.1016/j.enggeo.2021.106335

Li, X., Peng, K., Peng, J., and Xu, H. (2021f). Effect of Cyclic Wetting-Drying Treatment on Strength and Failure Behavior of Two Quartz-Rich Sandstones under Direct Shear. *Rock Mech. Rock Eng.* 54 (7), 1–16. doi:10.1007/s00603-021-02583-z

Li, X. S., Peng, K., Peng, J., and Hou, D. (2021d). Effect of thermal Damage on Mechanical Behavior of a fine-grained sandstone. *Arabian J. Geosciences* 14 (13), 1–16. doi:10.1007/s12517-021-07607-0

Li, X., Wang, Y., Yang, S., Xiong, J., and Zhao, K. (2021g). Research Progress in the Mining Technology of the Slowly Inclined, Thin to Medium Thick Phosphate Rock Transition from Open-Pit to Underground Mine. *Appl. Maths. Nonlinear Sci.* 6 (1), 319–334. doi:10.2478/AMNS.2021.2.00017

Li, X., Yang, S., Wang, Y., Nie, W., and Liu, Z. (2021h). Macro-micro Response Characteristics of Surrounding Rock and Overlying Strata towards the Transition from Open-Pit to Underground Mining. *Geofluids* 2021, 1–18. doi:10.1155/2021/5582218

Liu, B., Tian, K., Huang, B., Zhang, X., Bian, Z., Mao, Z., et al. (2021). Pollution Characteristics and Risk Assessment of Potential Toxic Elements in a Tin-Polymetallic Mine Area Southwest China: Environmental Implications by Multi-Medium Analysis. *Bull. Environ. Contam. Toxicol.* 2021, 1–11. doi:10.1007/S00128-021-03314-4

Ma, C., Wu, L., Sun, M., and Lei, D. (2021). Failure Mechanism and Stability Analysis of Bank Slope Deformation under the Synergistic Effect of Heavy Rainfall and Blasting Vibration. *Geotech Geol. Eng.* 2021, 1–14. doi:10.1007/S10706-021-01868-Y

Miao, Y., Zhang, Y., Wu, D., Li, K., Yan, X., and Lin, J. (2021). Rock Fragmentation Size Distribution Prediction and Blasting Parameter Optimization Based on the Muck-Pile Model. *Mining, Metall. Exploration* 38, 1071–1080. doi:10.1007/S42461-021-00384-0

Narayan, K. B., Arvind, K. M., Singh, M. M., Aditya, R., and Singh, P. K. (2020). Directional Controlled Blasting Technique for Excavation of Unstable Slopes along the Konkan Railway Route. *Mining Eng.* 72 (7), 106–107.

Peng, D. H. (2005). Analysis of Dynamic Response on Blasting Vibration about Excavated Slope in a Surface Mine. *J. China Coal Soc.* 30 (6), 705–709. doi:10.3321/j.issn:0253-9993.2005.06.006

Sazid, M. (2017). Effect of Underground Blasting on Surface Slope Stability: A Numerical Approach. *Am. J. Mining Metall.* 4 (1), 32–36. doi:10.12691/ajmm-4-1-2

Shi, J. J., Xue, L., Zhang, Q., and Meng, H. L. (2015). Vibration Propagation Law in Different Areas of Tunnel Face Caused by Blasting. *Amm* 744-746, 1005–1009. doi:10.4028/www.scientific.net/AMM.744-746.1005

Umrao, R. K., Singh, R., Sharma, L. K., and Singh, T. N. (2017). Soil Slope Instability along a Strategic Road Corridor in Meghalaya, north-eastern India. *Arab J. Geosci.* 10 (12), 1–10. doi:10.1007/s12517-017-3043-8

Wang, G. (2018). Stability Analysis of Steep and High Bedding Rock Slopes under the Action of Underground Blasting Vibration. *J. China Foreign Highw.* 2018 (3), 24–28. doi:10.14048/j.issn.1671-2579.2018.03.006

Wang, J. M., Chen, Z. H., Zhou, Z. H., Zhang, L. F., and Zhang, X. D. (2019). Study on Instability Mechanism of Rock Slope with Trailing Edge Cracks Induced by Blasting and Rainfall. *J. Saf. Sci. Technol.* 15 (1), 62–68. doi:10.11731/j.issn.1673-193x.2019.01.010

Wang, W., Wei, Y., Guo, M., Li, Y., and Wang, G. D. (2021). Coupling Technology of Deep-Hole Presplitting Blasting and Hydraulic Fracturing Enhance Permeability Technology in Low-Permeability and Gas Outburst Coal Seam: A Case Study in the No. 8 mine of Pingdingshan, China. *Adv. Civil Eng.* 2021, 1–12. doi:10.1155/2021/5569678

Wu, T., Zhou, C., Jiang, N., Xia, Y., and Zhang, Y. (2020). Stability Analysis for High-Steep Slope Subjected to Repeated Blasting Vibration. *Arab J. Geosci.* 13 (17), 7207–7227. doi:10.1007/s12517-020-05857-y

Xiang, R., Rong, Z., Qiujing, L., and Xingming, C. (2014). Study on Blasting Safety Technology Applied in Karst Limestone Mine. *Proced. Eng.* 84, 873–878. doi:10.1016/j.proeng.2014.10.509

Xie, Z. H., Xie, R. Y., and Lu, X. Y. (2015). Stability Analysis on High and Steep Slope of Open-Pit Based on Limit Equilibrium Method. *Amm* 777, 106–111. doi:10.4028/www.scientific.net/AMM.777.106

Xu, S., Li, Y. H., An, L., and Yang, Y. J. (2012). Study on High and Steep Slope Stability in Condition of Underground Mining Disturbance. *J. Mining Saf. Eng.* 29 (6), 888–893.

Xu, T., Fu, M., Yang, S.-q., Heap, M. J., and Zhou, G.-l. (2021). A Numerical Meso-Scale Elasto-Plastic Damage Model for Modeling the Deformation and Fracturing of Sandstone under Cyclic Loading. *Rock Mech. Rock Eng.* 54, 4569–4591. doi:10.1007/S00603-021-02556-2

Yan, C.-b. (2007). Blasting Cumulative Damage Effects of Underground Engineering Rock Mass Based on Sonic Wave Measurement. *J. Cent. South. Univ. Technol.* 14 (2), 230–235. doi:10.1007/s11771-007-0046-8

Zhang, S., Gao, W., Yan, L., Liu, J., and Liu, L. (2020). The Characteristics of Blasting Vibration Frequency Bands in Jointed Rock Mass Slope. *Environ. Earth Sci.* 79 (23), 1–16. doi:10.1007/s12665-020-09267-x

Zhang, X. L., Yi, H. B., Xin, G. S., and Yang, H. T. (2017). Influence of Elevation on the Blasting Vibration Law in the Slope of an Open-Pit Mine. *Metal Mine* 2017 (7), 55–59.

Conflict of Interest: Author MW was employed by the company Yunnan Phosphate Group Co., Ltd.

The remaining authors declare that the research was conducted in the absence of any commercial or financial relationships that could be construed as a potential conflict of interest.

Publisher's Note: All claims expressed in this article are solely those of the authors and do not necessarily represent those of their affiliated organizations, or those of the publisher, the editors and the reviewers. Any product that may be evaluated in this article, or claim that may be made by its manufacturer, is not guaranteed or endorsed by the publisher.

frontiers in Earth Science

ORIGINAL RESEARCH
published: 25 November 2021
doi: 10.3389/feart.2021.774200

Emergency Survey and Stability Analysis of a Rainfall-Induced Soil-Rock Mixture Landslide at Chongqing City, China

Chang Zhou[1], Dong Ai[2], Wei Huang[2], Huiyuan Xu[2], Liwen Ma[2], Lichuan Chen[3] and Luqi Wang[4]*

[1]School of Resources and Geosciences, China University of Mining and Technology, Xuzhou, China, [2]The Seventh Geological Brigade of Hubei Geological Bureau, Yichang, China, [3]Chongqing Engineering Research Center of Automatic for Geological Hazards, Chongqing Institute of Geology and Mineral Resources, Chongqing, China, [4]School of Civil Engineering, Chongqing University, Chongqing, China

The stability analysis of damaged landslides and unstable debris is important for rescue work and emergency operations. This paper investigates a predisposed geological emergence, inducing the factors and deformation processes of the Zhongbao landslide, which happened on July 25, 2020. The stability of the landslide debris was evaluated by an integrated monitoring system consisting of ground-based radar, unmanned aerial vehicles, airborne Lidar, thermal infrared temperature monitoring, GNSS displacement monitoring, deep displacement monitoring, and rainfall monitoring. The strata and weak layer controlled the landslide failure, and topography defined the boundary of the failed rock mass. A continually intensive rainfall caused the deformation and accelerated failure of the landslide. The shallow and steep deposit (Part I) firstly slid at a high velocity, and then pushed the rear part of the landslide (Part II) to deform, forming numerous cracks, which accelerated the rainfall infiltrating into the rock mass. The moisture content increase could decrease the strength of the shale rock within the bedding planes. Finally, with the rock and soil mass sliding along the weak layer, a barrier dam and a barrier lake were formed. The monitoring and numerical simulation results showed that after the landslide failure, there was still local collapse and deformation occurrences which threatened rescue work and barrier lake excavation, and the stability of the accumulation area gradually decreased as the rainfall increased. Therefore, the barrier dam was not excavated until the accumulation rate gradually stabilized on July 28. Moreover, most of the reactivated deposits still accumulated in the transportation and source areas. Thus, in August, the displacement of the landslide debris gradually accelerated in a stepwise manner, and responded strongly to rainfall, especially in the accumulation area, so that it was inferred that the damaged landslide could slide again and cause a more threatening and severe failure. The analysis results of the study area can provide references for the failure mechanism of a rainfall-induced landslide and the stability evaluation of a damaged landslide.

Keywords: damaged landslide, emergency monitoring, rainfall, failure mechanism, thermal infrared temperature

OPEN ACCESS

Edited by:
Yun Zheng,
Institute of Rock and Soil Mechanics (CAS), China

Reviewed by:
Wu Wenan,
Beijing University of Technology, China
Longlong Chen,
Politecnico di Milano, Italy

****Correspondence:***
Wei Huang
huangwei@cug.edu.cn

Specialty section:
This article was submitted to Geohazards and Georisks, a section of the journal Frontiers in Earth Science

Received: *11 September 2021*
Accepted: *19 October 2021*
Published: *25 November 2021*

Citation:
Zhou C, Ai D, Huang W, Xu H, Ma L, Chen L and Wang L (2021) Emergency Survey and Stability Analysis of a Rainfall-Induced Soil-Rock Mixture Landslide at Chongqing City, China. Front. Earth Sci. 9:774200. doi: 10.3389/feart.2021.774200

INTRODUCTION

Rainfall-induced landslides are widely distributed in the world, for example, over 2,500 landslide events were reported between 1950 and 2005 (Tohari, 2018). Rainfall increases the weight of the sliding mass, decreases the shear strength of the soil, and groundwater level change could cause dynamic and static pore pressure inside landslide (Tsai, 2008; Li et al., 2018a). As one of the most catastrophic types of landslide, the affected bedding rock has a strong sensitivity to water, because a weak structural layer is widely developed in the rock strata (Gu, 1979; Huang, 2007; Yin, 2011; Tang et al., 2019; Wang et al., 2019; Chen et al., 2020), such as in the 2008 Jiweishan landslide (Yin et al., 2011; Tang et al., 2015; Zhang et al., 2018a), 2006 Leyte landslide (Evans et al., 2007; Guthrie et al., 2009), and so on. Therefore, it is necessary to study the deformation characteristics and failure mechanism of affected bedding rock slopes triggered by rainfall.

Multi-field information is very important in understanding the deformation characteristics of a landslide. Over the last decade, some new technologies have been developed to monitor landslide deformation, such as GB-InSAR, TLS, IRT, digital photogrammetry (DP), and so on (Nicola et al., 2010; Del Ventisette et al., 2011; Bardi et al., 2014; Crosetto et al., 2016; Zin et al., 2016; Casagli et al., 2017; Li et al., 2020; Zhou et al., 2020), and have achieved remarkable achievements in monitoring, prediction, and early warning of the landslides (Xu et al., 2016; Piciullo et al., 2018; Ouyang et al., 2019). Those technologies are characterized by more efficient operation and higher accuracy of monitoring data, compared with traditional monitoring sensors: offering high-resolution image data acquisition, data diversity, device portability, and easy and fast data processing (Casagli et al., 2017). Those devices can systematically and easily update their data. However, there are few reports about using these technologies to monitor damaged landslide debris, where local deformations or further collapse can still occur and threaten rescue and emergency work.

A catastrophic landslide occurred in Chongqing, China, during July 23–27, 2020. A total of 520 persons were evacuated and two roads were damaged. A barrier lake formed and threatened the safety of over 8,500 residents downstream at the Quantang Hydropower Station and Canggou Township. Chen et al., 2021 analyzed the deformation characteristics of this landslide and believed it to be an accumulation landslide, sliding along the bedrock interface. However, new research found that three weakened layers can be observed within the landslide debris, and the deeper internal weakened layer is the sliding zone, which means that this landslide has completely different deformation characteristics. In this paper, the new investigation and monitoring results are presented. The deformation mechanism and stability of the landslide are analyzed by using some advanced technologies and numerical simulation to provide information for the barrier lake excavation and the rescue work. Uniaxial compression tests of shale samples with different bedding planes and moisture content were taken.

MATERIALS AND METHODS

Description of the Zhongbao Landslide

The Zhongbao landslide is located on the north side of the Yancang river, about 59 km to the Wulong District, Chongqing, China (**Figure 1A**). In plan view, the shape of the Zhongbao landslide can be approximately likened a tongue, being 850 m in length and 200 m in width (**Figure 1B**). The thickness of the landslide is estimated to be 25–47 m, and its' volume approximately $4.6 \times 106\ m^3$ (**Figure 1C**). The slope of the landslide surface is 25°–45°. The main sliding direction is 210°, approximately perpendicular to the Yancang River. The Zhongbao landslide began to slide at 16:00 on July 23, 2020, accelerated and slid into the river on July 27, and destroyed three buildings and main roads. Over $1.0 \times 104\ m^3$ of soil and rock mass slipped into the river and formed a barrier lake.

The field investigation indicates that the main geologic units of the area are deposits and shales. The uppermost part of the surficial deposits are eluvial deposits (up to 0.5~3.5 m thick), whereas stratigraphically lower layers comprise mostly alluvial deposits and colluvial deposits. The eluvial deposits consist of clay and 10~45% of gravel clasts (**Figures 2A,B**). The diameter of the gravel clasts ranges from 50 to 300 mm. *In-situ* exposed outcrops over 10 m high (undisturbed by the landslide) crop out near the western limit of the depictions of the lithological structure (**Figure 2C**). Dominant pale-yellow shales, 0.2~0.5 m thick, are found in the pelitic structure with developed joints. The main component of shales is smectite and other clay minerals, which are easily weathered and softened by water. The rocks dip 25° toward 130°. Two dominant joints are found in the study area (**Figure 2D**). The first joint dips 75° toward 5°–15° with a width of 3~15 mm and a length of 1.5–4.9 m, and the joint spacing is 1.30–4.20 m. The second one dips 80° toward 210°–230° with a width of 2–12 mm and a length of over 10 m, and the joint spacing is 1.10–2.70 m. The joints are partially filled with clay.

Landslide Monitoring After Failure

Emergency Monitoring Systems

After landslide failure, emergency work and stability evaluation of the reactivated deposits are necessary, but conventional monitoring technologies are not equipped to monitor the damaged landslide, because of the instability of the landslide and debris. Therefore, some new methods are taken to monitor the deformation of the landslide (**Figure 3**):

1) Ground-based radar

HC-GBSAR1000 ground-based radar monitoring system uses Ground-based repeated orbit interferometric SAR technology, which accurately measures the displacement of the landslide's surface by comparing different pictures at different times based on the principle of phase interference. This technology has the technical advantages of being all-weather, high-precision, and a continuous measurement in time and space. Therefore, it was used in emergency monitoring of the landslide.

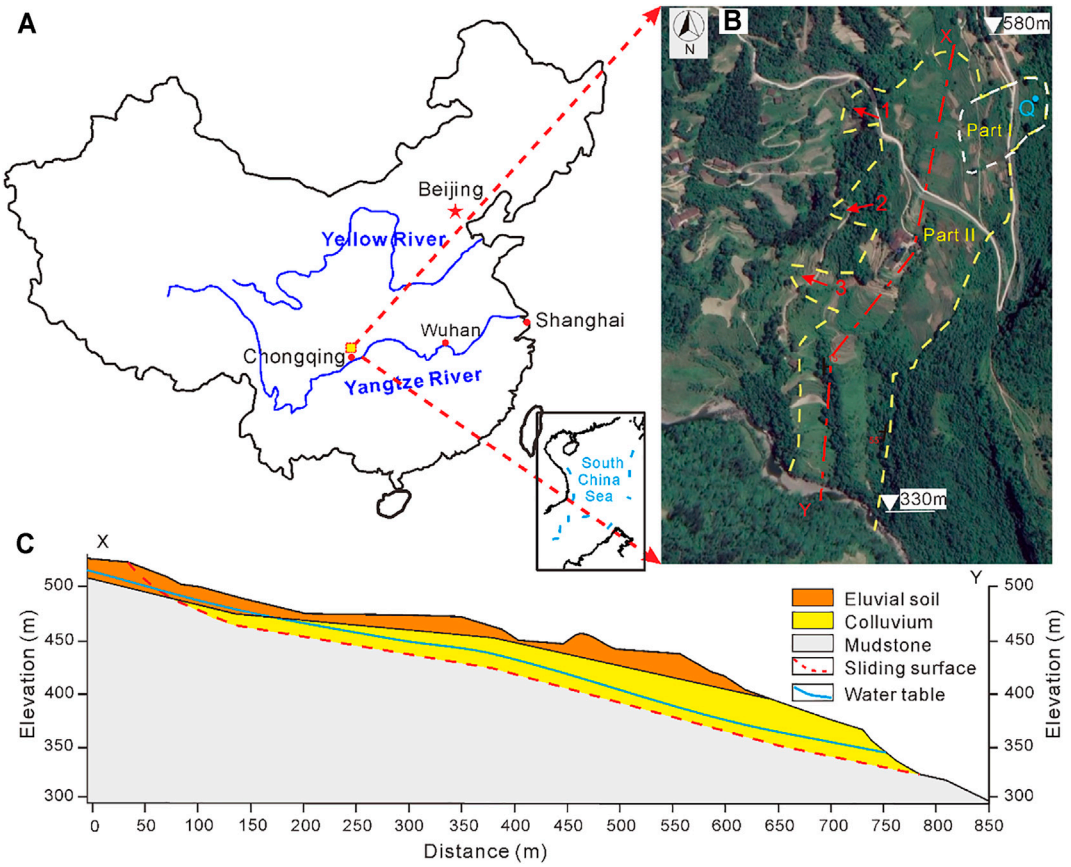

FIGURE 1 | Zhongbao landslide: **(A)** location of the landslide, **(B)** plane view and **(C)** vertical profile after landslide failure.

2) Unmanned Aerial Vehicle

Five sensors are equipped in the unmanned aerial vehicle to take pictures from five viewpoints. Meanwhile, the location of the vehicle during flight is recorded, including its height, speed, and flight direction. Based on the digital aerial stereo images, the image points and coordinates are automatically recognized, and the three-dimensional coordinate of the study objection is formed by using the analytical photogrammetry method. This technology could rapidly obtain a digital orthophoto, a digital elevation model, and high-resolution three-dimensional models, which provide fundamental data for the evaluation and monitoring of the landslide.

3) Airborne Lidar

The airborne Lidar integrates multiple technologies, such as laser, computers, high dynamic carrier attitude determination technology, and High-precision dynamic GNSS (Glogbal navigation satellite system) differential technology. This technology recognizes objects by laser technology and analyzes those data by computer technology. Airborne lidar is composed of a laser scanner system, a position and orientation system (POS) (GNSS), and a high-resolution camera system. The technology can avoid the effect of trees and obtain a high-resolution photograph and 3D point cloud data rapidly and accurately. Those data are used to analyze the deformation and the volume of the landslide.

4) Thermal infrared temperature monitoring

The thermal Infrared Camera FLIR X8400sc is a device that converts energy into an electrical signal. It has a precision of ±0.1°C, a temperature resolution of 0.04°C, a resolution of 1,280 × 1,024 pixels, and a spectral range of [1.5 5.1] μm. This equipment measures the temperature of the landslide surface so as to obtain the temperature of the field.

Conventional Monitoring Systems

Conventional monitoring equipment has been widely used in natural hazard monitoring because of its low cost, simple structure, and easy construction. In addition, they are applied for their wireless transmission of measurement data. In this paper, these monitoring technologies are used (**Figure 3**):

1) GNSS displacement monitoring

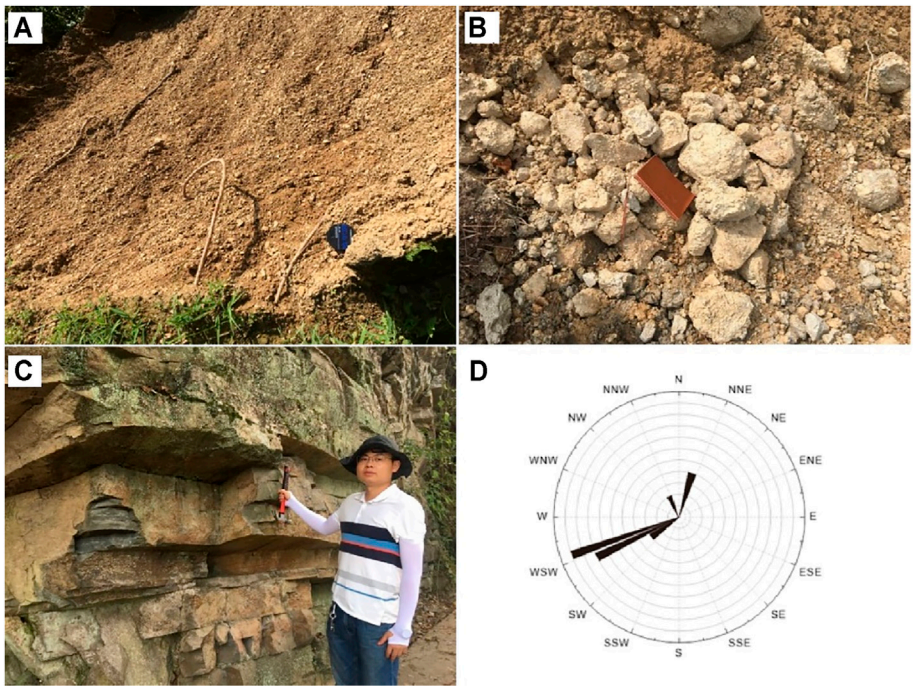

FIGURE 2 | (A) Eluvium, **(B)** gravel soil, **(C)** Hanjiadian Formation Shale (S1h), and **(D)** rose diagram of the joins.

The principle of GNSS monitoring is to determine the position of the GNSS receiver using the distance intersection method by measuring the distance between four or more satellites and receivers. The base station is constructed in a stable area, and monitoring stations are built in a deformation area. The displacements of the monitoring stations are calculated by comparing the location between the base and monitoring stations.

2) Displacement monitoring in depth

The flexible inclinometer probe, invented by Chongqing Engineering Research Center of Automatic Monitoring for Geological Hazards, measures its angle by three-dimensional micro-mechatronics measurement units (MEMS) to calculate horizontal displacement. The flexible probe monitoring system includes a flexible probe, controller, and PC software. One probe contains 80 measurement units and vertical spacing of 1.0 m. Unfortunately, the flexible probe did not work after being installed into the landslide.

3) Rainfall monitoring

A tipping bucket rain gauge was used to measure precipitation because it is characterized by real-time recording of rainfall with high accuracy and requiring almost no human factor. The measurable range of the equipment is 0.01 mm ~ 4 mm/min, and the precision is ±2%.

4) Sound and light alarm

The received data being collected and analyzed by the monitoring terminal is uploaded to a remote control terminal and then the alarm information is pushed to the sound and light warning terminal for an efficient and timely warning. Sound and light alarms are carried out in time to remind nearby vehicles and personnel to react to disasters.

RESULTS

Deformation of the Zhongbao Landslide

The Zhongbao landslide was first found to have deformed on July 22. Several cracks were recorded on the uphill side of the landslide after a continuous intense rainfall. As the landslide deformed, the eastern boundary of the landslide was generated, then a great many tension cracks formed at Part II while Part I gave way (**Figure 4B**). The uphill slope slid over 20 m, and the downhill slope suffered local deformation. On July 24, the sliding mass was transported to the middle and downhill slopes, causing the downhill slope to gradually collapse (**Figure 4C**). On July 25, there was a strong rainfall, the downslope had obvious deformation, and the sliding mass gradually slid into the Yancang River. The barrier lake and dam were formed (**Figures 4D,E**).

The steep Part I firstly deformed and collapsed, which destroyed the main road. The upstream portion of Part II gradually deformed and pushed the middle portion to slip. Due to the cliff at the east side of the landslide, the sliding direction of the landslide gradually changed from 165° in the

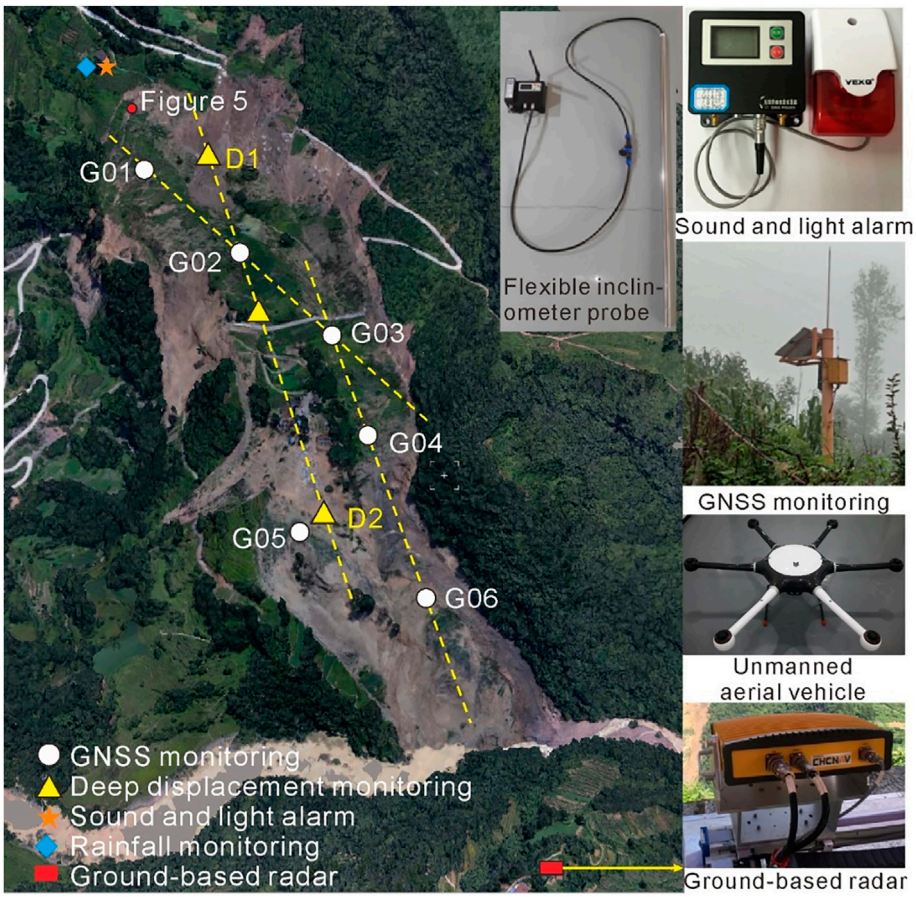

FIGURE 3 | Monitoring system of the failure landslide and photographs of the devices.

source area to 220° in the transportation area, and finally to 180° in the accumulation area. According to the deformation characteristics of the landslide, the landslide area could be divided into five areas (**Figure 9**):

Part I: This portion is located at the northeast side of the landslide (**Figure 5**). Reactivated deposits of Part I covered Part II. This part is 140–245 m wide and 230 m long, about 10 m thick with its largest elevation difference being 102 m. The deformation characteristics of the road showed that the accumulation moved with Part II, inferring that Part I failed before Part II. Due to the steep slope, engineering projection, and continual rainfall, Part I slipped with velocity and compressed Part II, which accelerated the movement of Part II. Therefore, the uplift area and puddle were found in part II.

Source area (**Figure 5**): The length and elevation difference of this area is approximately 207 and 46 m, respectively. Under the effect of rainfall and part I, the rear section of Part II gradually deformed and developed into scratch (**Figure 6A**) and tension cracks. Those cracks became an infiltration path for rainfall which damaged the yale structure and decreased the shear strength of the soil and rock. The rock became severely fragmented (**Figure 6B**). The deformation of the landslide thus accelerated. Many scarplets and cracks were found in this portion. Moreover, the boundary between the source area and the transportation area was an uplift zone with an average height of 3.0 m (**Figure 5**).

Transportation area (**Figure 7**): Owing to the rear section sliding and pushing the rock soil mass in the transportation area, some buildings and houses in the middle section only formed tension cracks but were not completely destroyed (**Figure 7**). Some parts were uplifted. In the plane view, this area had an approximately rectangular shape with a length of 340 m and an average width of 175 m. Some pools were found on the landslide. The road debris showed that it slid about 99 m but kept good continuity.

Accumulation area (**Figure 8**): The rear part became steep again, and the dip direction of the exposed rock was 15°. Thus, the sliding direction of the landslide changed. The sliding mass slipped and mobilized surficial deposits in the accumulation area by scraping, entraining, and pushing them downward. Finally, the reactivated deposits accumulated in the toe of the landslide and formed a barrier dam and barrier lake. The thermal infrared monitoring found that the temperature field appeared abnormal in the place where the groundwater was exposed. Moreover, the temperatures of the accumulation area were higher than in other areas.

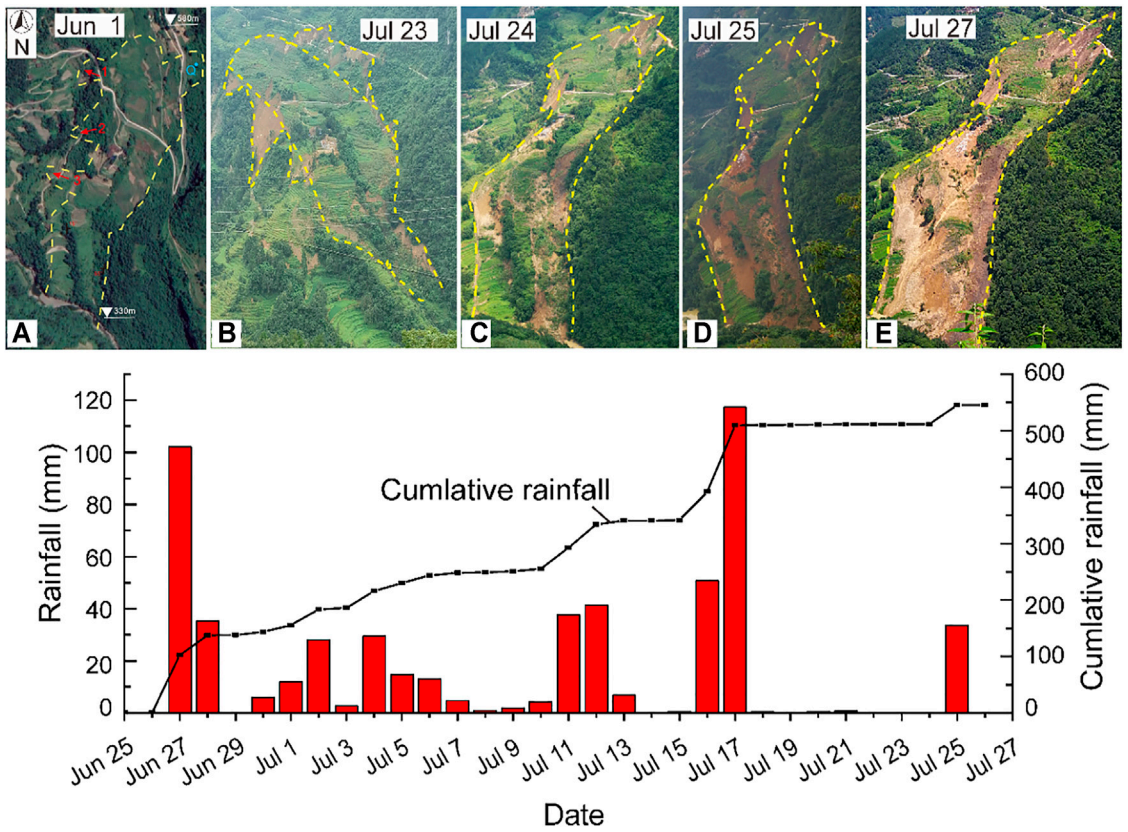

FIGURE 4 | Deformation characteristics and rainfall vs. time.

Secondary-landslide area: Three secondary-landslides (1–3# in **Figure 5**) were found at the west side of the landslide because of the V-shaped valley. No. 1 secondary-landslide was caused by the source area sliding along the direction of 230°. No. 2 is located on the cliff, so could be from the collapse of the sliding mass. No. 3, caused by a change in the sliding direction of Part II, occurred and buried a small road.

Stability of the Failure Landslide

1) Visual observation of surface deformation

The radar technology was used to evaluate the volume and deformation characteristics of the landslide because it can remove the trees on the landslide surface and obtain the rear geography of the landslide. **Figure 9** shows that Part I had an obvious boundary with 4.1 × 102 m^2. Its sliding mass accumulated in Part II and slipped to the transportation area of Part II. The downhill slope continued onto progressive retrogressive collapse and slid into the river. Thus, this landslide was still unstable. Moreover, a cliff was observed on the northeast side of the landslide with over 1 × 106 m^2 colluvial deposits where there was also the occurrence of Part I.

2) Surface displacement

An emergency monitoring was started from July 27 to Aug 2. Ground-based radar was 2.8 km away from the landslide (**Figure 3**). The surface deformation of the landslide was scanned from July 27 to October 2. Unfortunately, the monitoring was non-continuous due to the power issues and a change in the device location. Therefore, two periods are selected to analyze the deformation characteristics of the landslide debris.

Figure 10 is the monitoring results of the landslide surface from 16:00 July 27 to 06: 00 July 28. The uphill and middle of the landslide showed no obvious deformation, but the downhill section had large deformation with the largest displacement being 200 mm (**Figure 10A**). The displacements of four monitoring points in the downslope are shown in **Figure 10B**. It is observed that the displacement of P2 and P4 slowly increased and reached about 50 mm. However, the displacement at P1 and P3 had the largest values. The velocity of P1 gradually decreased after July 28. The displacement at P3 sharply increased at 22:00 July 27 and then tended to be stable. Moreover, local deformation was also found at the cliff on the northeast side of the downslope (approximately −50 mm).

Figure 11 shows the displacement of the landslide surface from 11:00 to 17:00 July 28. It was found that the largest

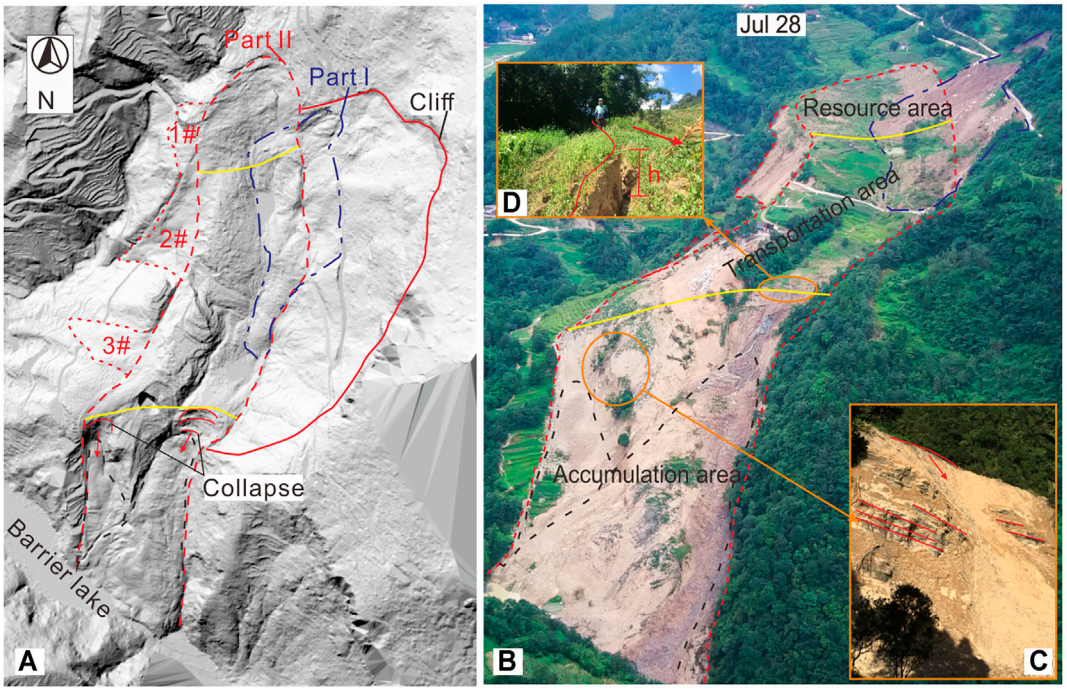

FIGURE 5 | The result of the Airborne Lidar after filtering out trees. Note the black dashed line is the secondary landslide in the accumulation area. Yellow lines separate the three parts (see text). Sub-photographs are the scarplet and local collapse, respectively.

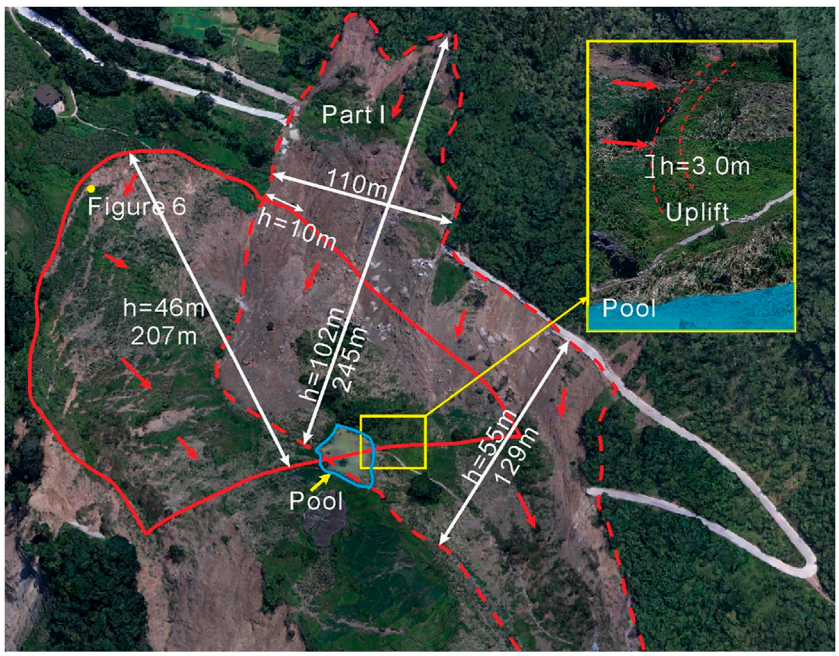

FIGURE 6 | Picture of the source area and Part I area. The sub-picture is the uplift zone between the source area (left) and the transportation area (right). Note, "h" represents the elevation difference of the landslide area.

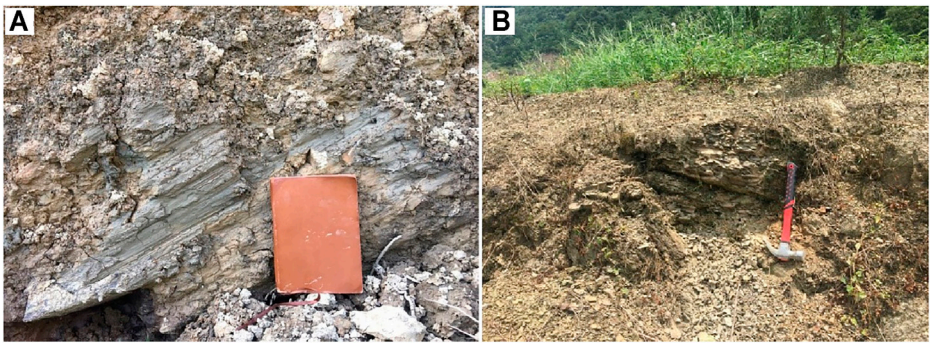

FIGURE 7 | (A) Scratch and **(B)** broken rock. See **Figure 3** for the locations of pictures.

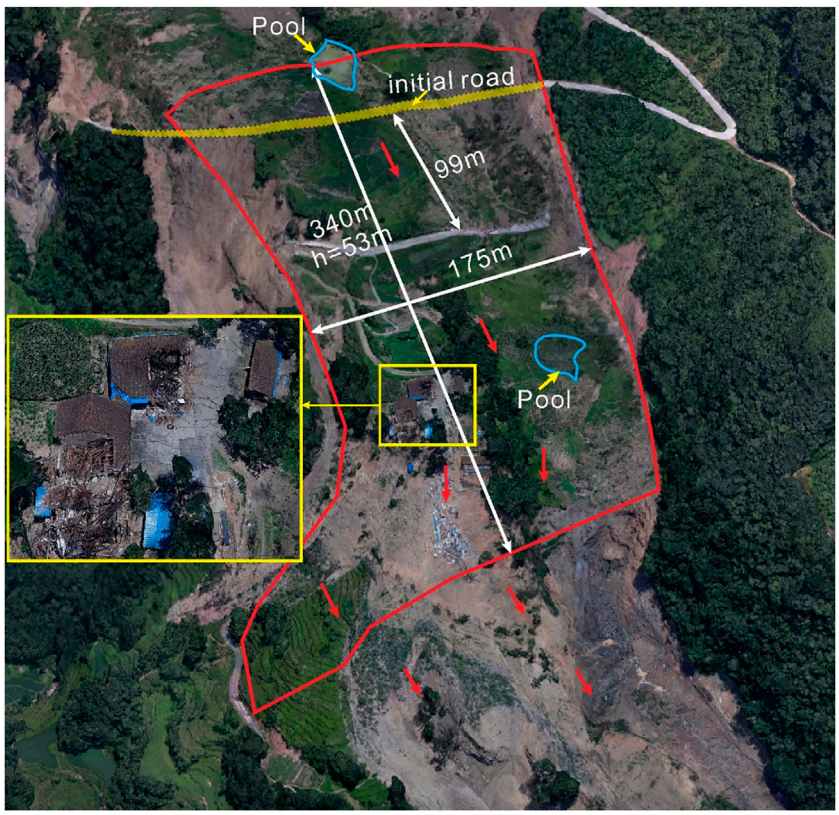

FIGURE 8 | Picture of transportation area. The sub-picture is the village which shows that most of those buildings maintain good integrity. The road also kept good continuity across two sides, even though it slid over 90 m. The blues line are pools.

displacement of the landslide is about 70 mm, which is clearly smaller than that in **Figure 10** (**Figure 11A**). The displacement of the point at P was monitored (**Figure 11B**). The displacement increases with a velocity of 12 mm/h, which indicated that local collapse was still occurring **Figure 11C** shows that the upslope also had small deformation (>40 mm) and the whole landslide was stable.

In consequence, after the landslide collapse, this landslide tended to be stable except for local collapses. The emergency works were taken in the source and transportation area before July 28, and then, the barrier dam was excavated on July 28. The traditional monitoring equipment was installed on the landslide surface.

In **Figure 12**, the rainfall and displacement from Aug 12 to Oct 1 was recorded. The second wet month (from September to October) was characterized by a 333 mm cumulative rainfall. The downhill slope (G05, G06) had large deformation with a velocity as high as 6 cm/day (G06). The increment displacement of the

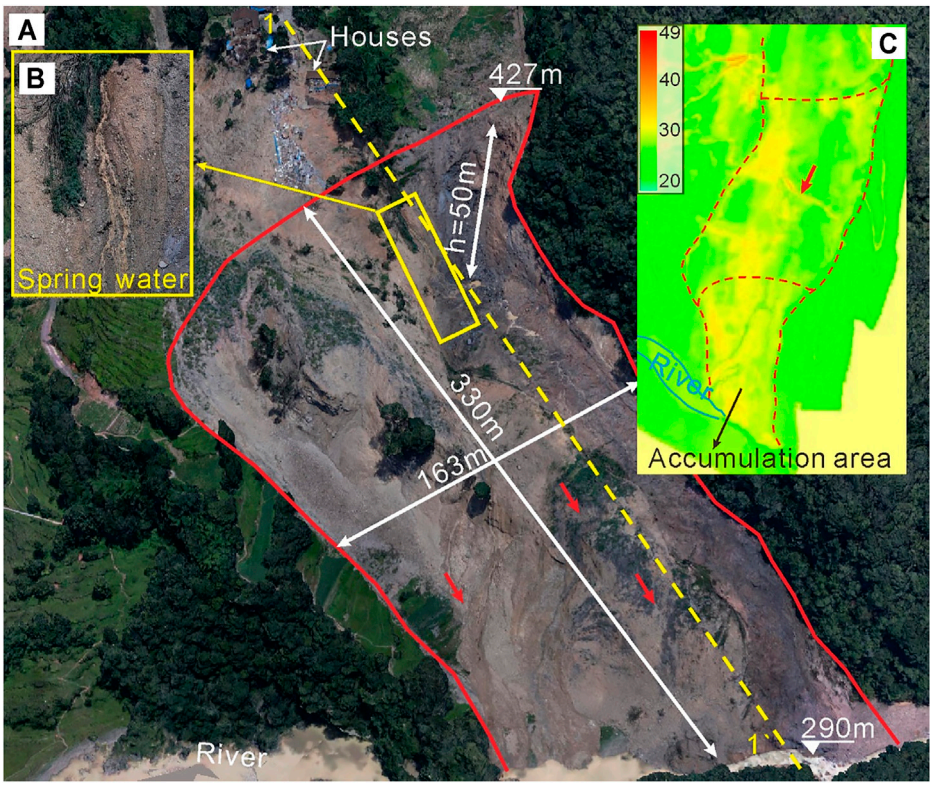

FIGURE 9 | Picture of accumulation area **(A)**, the spring water **(B)**, and the temperature of the landslide surface **(C)**.

G06 suddenly decreased tending to zero, but the G05 went on with a constant rate of 3.8 mm/day. Clearly, the rainfall reactivated the landslide. Moreover, the increase of the displacement at G06 and G05 generally lagged 1 day behind the rainfall. Another portion of the landslide had a smaller displacement (<30 mm/month), but also responded to the rainfall and gradually increased.

DISCUSSION

Failure Mechanism of the Zhongbao Landslide

Water has a significant effect on the strength of shale rock. The increase of the water content could lead to mineral particle dissolution and the increase of clay minerals. As a result, the shale structure becomes loose, the mic-cracks gradually increase, and finally, the rock degrades and softens (Feng and Ding, 2005; Cornelius et al., 2011; Zhu et al., 2015; Ling et al., 2016; Liu et al., 2016; Xue et al., 2018; Li et al., 2019). Moreover, a filed investigation found that the primary porosity of shale in the landslide area was well developed, and three sets of the superior fractures caused the loosening of the rock. Therefore, after a constant rainfall (July 15–18), the rainfall infiltrated into the landslide and decreased the shear strength of the rock. Further, underground water had a lubrication effect on the rock layers, so that the landslide began to deform on July 22. The displacement of the monitoring results also showed that the failure landslide had a large deformation after a strong rainfall (Sep 6). Moreover, the lag time of the landslide deformation after failure (about 1 day) was shorter than that of the landslide before failure response to rainfall (about 6 days), which could be because of the loose deposits after landslide collapse accelerated the rainfall infiltration. According to the deformation characteristics of the landslide, the deformation process could be divided into three stages:

Creep deformation stage: Rainfall caused a shallow landslide (Part I). A continuous rainfall lasted for almost 20 days and increased the groundwater level. As a result, the weight of the sliding mass was increased and the shear strength of the soil decreased. Moreover, the main road provided beneficial conditions for Part I failure. The reactivated deposit impacted and compressed the upslope of part II which accelerated the deformation of the landslide (**Figure 4B**). Besides, the gentle slope in the middle of the landslide is conducive to the accumulation of groundwater. Therefore, under the action of groundwater immersion, the landslide gradually moved. Thus, the scratch and shear cracks were generated at the uphill side of the landslide (**Figure 6**). The uphill section gradually generated obvious deformation. The deformation direction of part I is 230°.

Accelerated deformation stage: After the rear part of the landslide was initialized, it gradually slid along the sliding zone and compressed the middle section. Although there was no rainfall, the surface water continually infiltrated along these

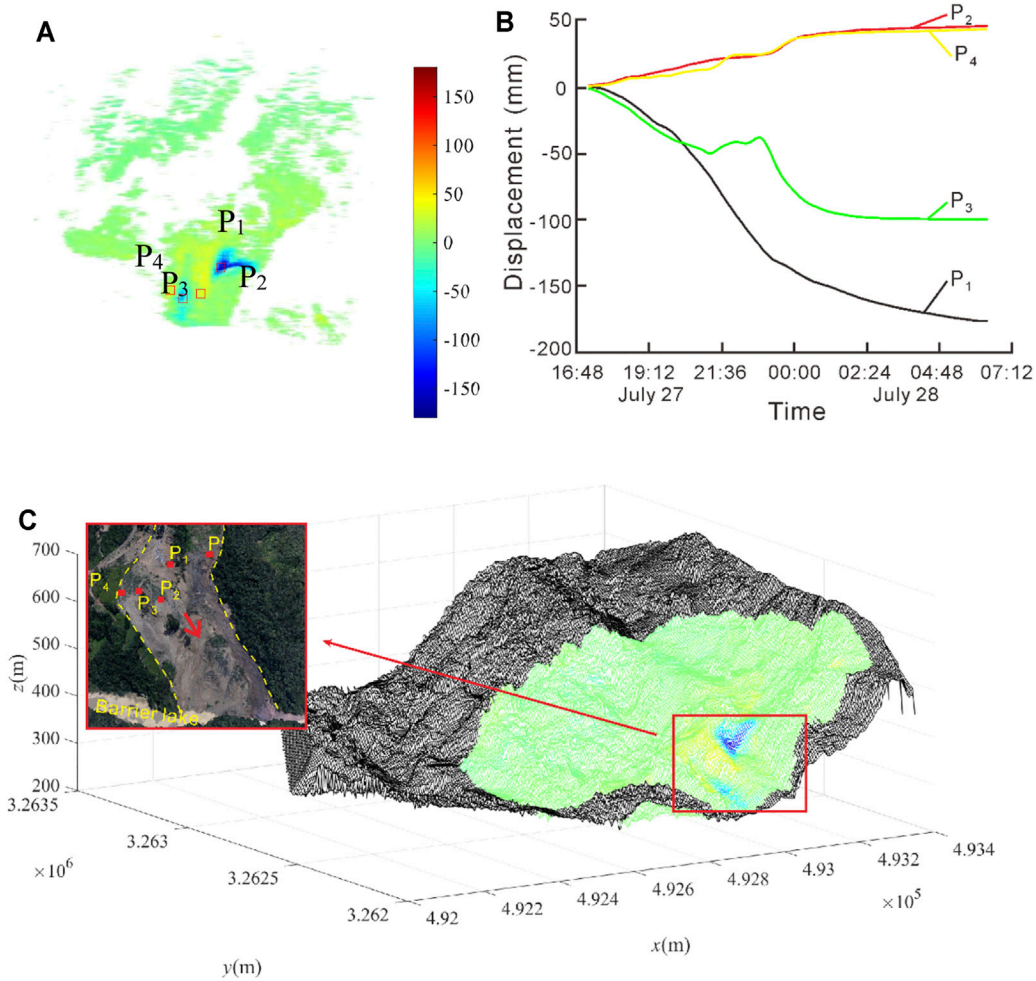

FIGURE 10 | Deformation of the Zhongbao landslide during July 27–28. **(A)** Accumulative displacement of the landslide surface; **(B)** the displacements of monitoring points vise time; **(C)** Three-dimensional topographic map. Note, the negative value of the displacement means that the point moves toward the Radar.

shear cracks, and the shear strength of the soil continually decreased under groundwater immersion. The sliding zone rapidly developed and the landslide slid over 90 m (**Figure 4C**). The sliding direction was 210°.

Accumulation stage: the landslide slides out from the steep ridge of the front edge and pushes and scrapes the shale (**Figure 4E**), which accumulates at the foot of the landslide and a barrier lake is formed. Moreover, the scarplet in front of the landslide led to the deposit mainly accumulating in the landslide toe and forming a secondary landslide (**Figure 9**) which still deformed after the landslide failure, especially when heavy rainfall occured.

The pale-yellow shale samples, with different water content and angles of bedding planes, were tested to obtain the compressive strength by uniaxial compression test (shown in **Figure 13**). All curves had the same shapes that as the water content increased, the compressive strength gradually decreased (Yang et al., 2007; Wei et al., 2015. The angle of bedding planes also had significant importance on the strength, because the clay minerals filled in the bedding plane, the content of which could be over 35% clay minerals (Fang et al., 2019), such as kaolinite, montmorillonite, illite, absorbed water and swelled, causing expansive pressure. As a result, the shale rock gradually split and disintegrated along the bedding plane (Rybacki et al., 2015; Rybacki et al., 2016; Teng et al., 2017), which also provided further seepage channels. Moreover, two clay layers (0.5–1.5 m thickness) were observed in the shale rock layer, one of which was the sliding surface. According to the other reports, the shear strength properties of the clay have a significant decrease when the moisture content increases (Dafalla, 2013; Li et al., 2018b; He et al., 2018), and are more sensitive than the rock. Therefore, after intense rainfall, the landslide slipped along the clay layer, and the shale rock was fragmented in the sliding mass.

After the landslide failed, the barrier lake formed in front of the landslide increased the groundwater level of the accumulation area (**Figure 14**). The reservoir impoundment could accelerate the landslide deformation and failure (Macfarlane, 2009; Huang et al., 2016; Li et al., 2018b; Wang et al., 2019). When the lake flooded the downhill portion of the deposit, the shear resistance was reduced (He et al., 2018), especially for the destroyed

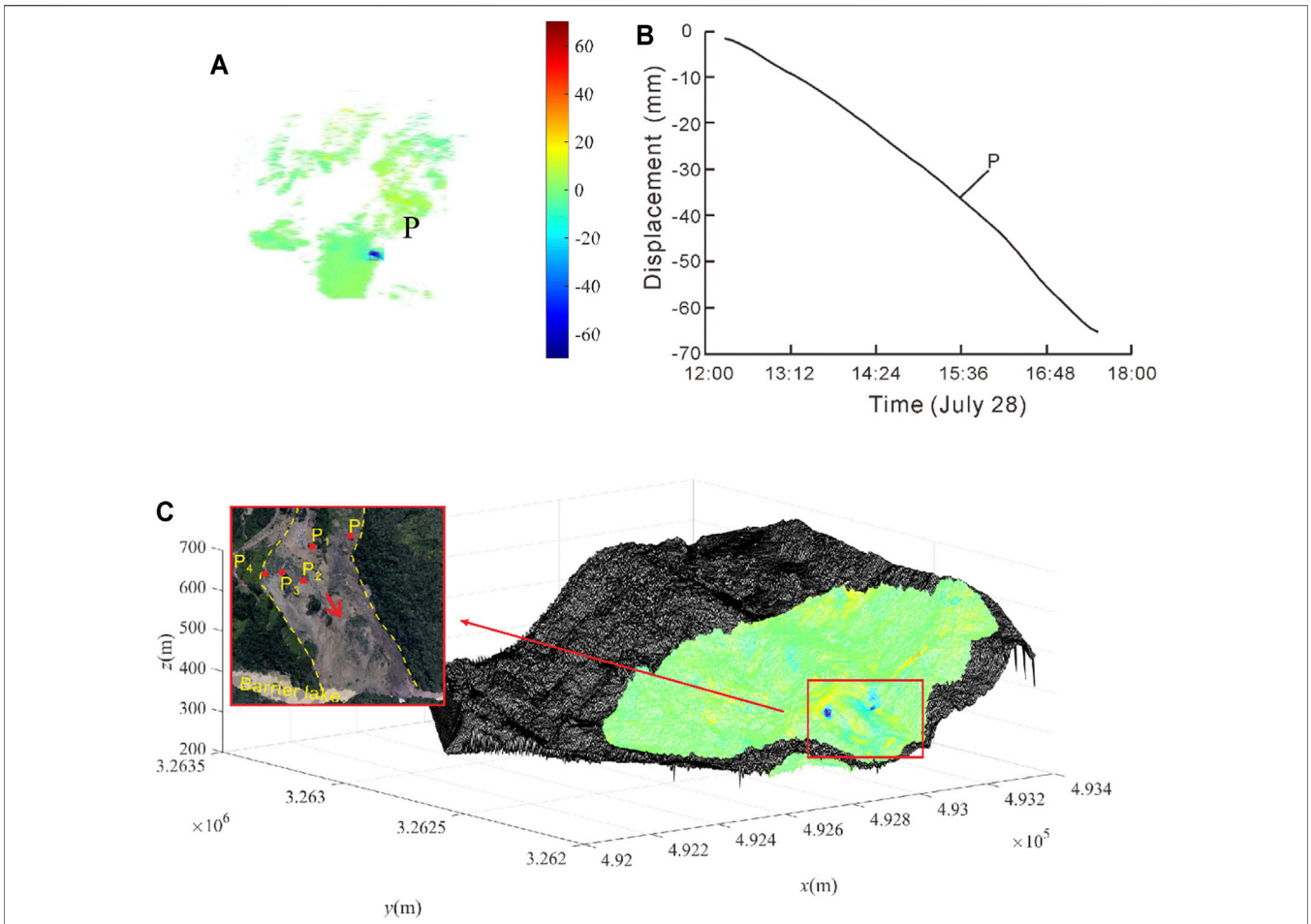

FIGURE 11 | Deformation of the Zhongbao landslide during July 28. **(A)** Accumulative displacement of the landslide surface; **(B)** the displacements of monitoring points vise time; **(C)** Three-dimensional topographic map.

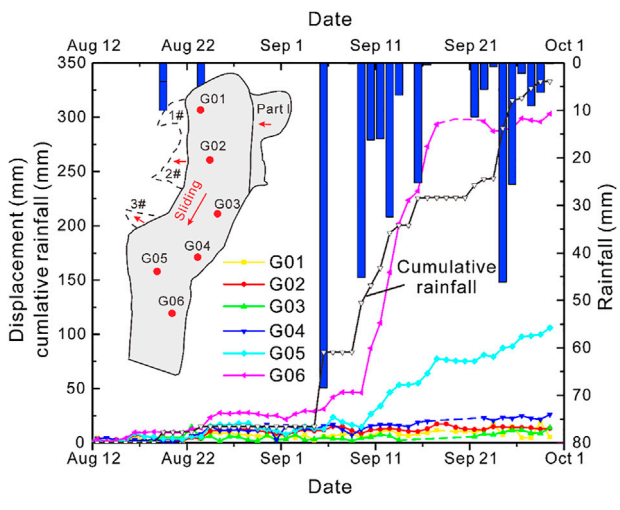

FIGURE 12 | Rainfall cumulative displacement of monitoring points and vs. time.

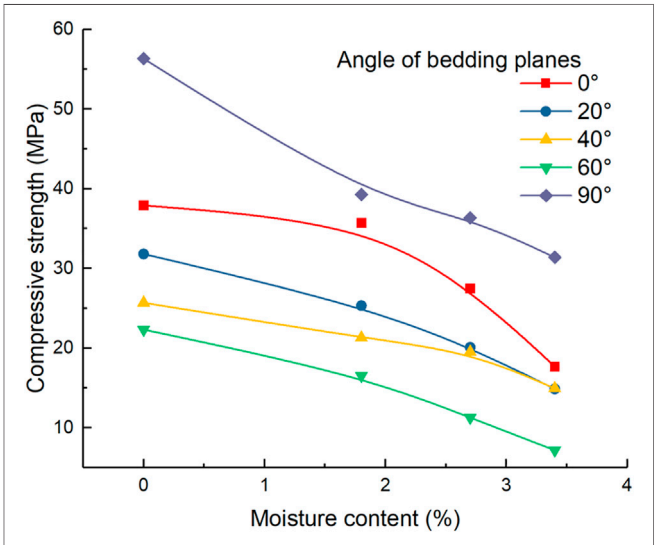

FIGURE 13 | Influence of moisture content on the compressive strength of the shales with different angles of bedding planes.

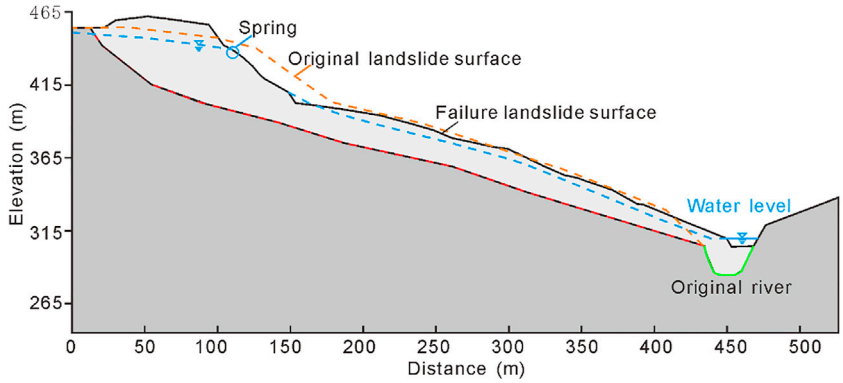

FIGURE 14 | Profile 1–1′ of the accumulation area (shown in **Figure 9**).

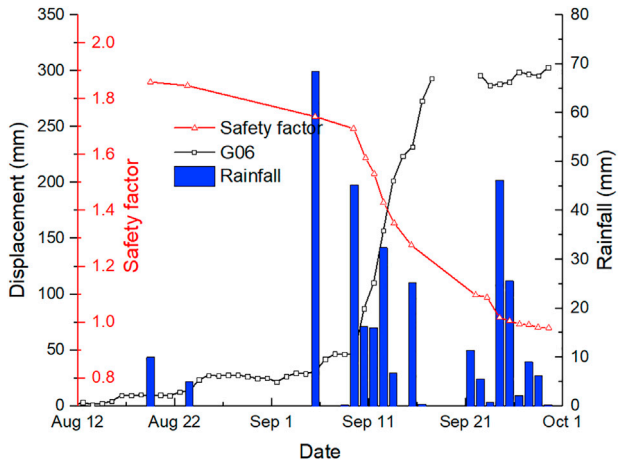

FIGURE 15 | Safety factor of the accumulation area.

deposits, so that the deposit still had a strong response to the rainfall. In the collapse at the shear outlet of the landslide, several springs with a flow velocity of 0.1–0.6 m^3/s indicated that the seepage field rapidly declined which could decrease the stability of the landslide (Berilgen, 2007; Della Seta et al., 2013; Hu et al., 2017; Sui and Zheng, 2017; Zhang et al., 2018b; Wu et al., 2020; Yang et al., 2020). The stability of the accumulation area was evaluated using Geo-slope software. Firstly, we evaluated the safety factor of the accumulation area under rainfalls (**Figure 15**). The safety factor of the accumulation area had a strong response to the rainfall and presented a certain linear change as the displacement increased. During an intensity continuous rainfall, the safety factor significantly decreases, because the groundwater level rapidly increases. If the dammed lake is excavated and drained during this stage, the landslide could slide again and form a larger barrier dam.

Emergency Monitoring System for the Damaged Landslide

After landslide failure, the re-activated deposit and the barrier lake could cause secondary economic losses (Fan et al., 2015; Gischig et al., 2016; Liu et al., 2020), so emergency engineering is necessary (Xiao et al., 2021). This paper constructed an integrated monitoring system for landslide failure. The monitoring equipment is non-contact measurements such as Ground-based radar, Unmanned Aerial Vehicles, Airborne Lidar, and thermal infrared temperature monitoring. These devices can scan the whole landslide surface and obtain point cloud data to evaluate the stability of the landslide debris in detail. The monitoring results found that deformation mainly occurred in the scarp at the uphill side of the landslide, and the deformation gradually tend to become stable after July 28. Those results provided guidance for rescue work and the excavation of barrier lakes. However, these devices are too expensive and difficult to operate if used for long-term monitoring of landslides, and also in addition only obtain deformation information of the landslide surface. Therefore, After landslide failure gradually stableizes, conventional sensors should be installed into the landslide to measure the displacement of the typical landslide profiles, such as GNSS, GPS, deep monitoring, and so on. Those devices can measure the multi-filed information of the landslide for a long time without interruption, which could provide information for reconstruction work. In this paper, the monitoring for the failing landslide shows that the failing landslide debris is still responsive to rainfall, especially at the front and middle parts of the landslide. Thus, engineering activities and human activity should be avoided as far as possible in the middle and front parts as the landslide could slip again and form a dammed lake. Moreover, over 1 × 106 m^2 of colluvial deposits on the northeast side of the landslide could be initialized and fail under the long-term effects of rainfall, which could cause extensive damage to the landslide. Therefore, the most effective monitoring method is non-contact devices, such as ground-based radar, unmanned air vehicles, three-dimensional laser scanners, and so on.

CONCLUSION

The Zhongbao landslide is a typical rainfall-induced landslide in the Yancang River area, situated in the Wulong District, Chongqing, China. It most likely originated catastrophically as a rockslide combined with a shallow landslide. The shallow soil slope, located in the uphill side of the landslide was triggered by continuous torrential rain, which pushed the rear part of the landslide to deform and accelerated rainfall infiltration into the landslide. The increase of the water content decreased the strength of the shale rock and made the rock more broken. The landslide gradually slid along the weak layer within the rock layer and formed a barrier lake. Moreover, the accumulation area was still deformed.

After the landslide failure, an emergency monitoring system with multiple monitoring devices was constructed to measure the deformation of the whole landslide surface. The monitoring results provided some advice for emergency engineering. The compromised landslide gradually became stable after July 28. Then, some conventional monitoring methods were installed into the landslide and the results found that the reactivated deposits still responded to rainfall.

DATA AVAILABILITY STATEMENT

The original contributions presented in the study are included in the article/Supplementary Material, further inquiries can be directed to the corresponding author.

ETHICS STATEMENT

Written informed consent was obtained from the relevant individuals for the publication of any potentially identifiable images or data included in this article.

AUTHOR CONTRIBUTIONS

The work was carried out in collaboration between all the authors. LC and LM designed the monitoring system and provided the monitoring data; WH, HX, LC taken the investigation; CZ wrote the original draft; CZ, HX, LW, and DA reviewed and edited the draft. All authors have read and agreed to the published version of the manuscript.

FUNDING

This study was financially supported by the National Key Research and Development Program of China (Grant No. 2017YFC1501303); Key Research and Development Program of Xinjiang Uygur Autonomous Region (Grant No. 2021B03004-3); Chongqing Technology Innovation and Application Development Special Key Projects (cstc2019jscx-tjsbX0015).

ACKNOWLEDGMENTS

The authors appreciate the work of the Chengdu University of Technology for providing the data of the thermal infrared temperature monitoring. All support is gratefully acknowledged.

REFERENCES

Bardi, F., Frodella, W., Ciampalini, A., Bianchini, S., Del Ventisette, C., Gigli, G., et al. (2014). Integration between Ground Based and Satellite SAR Data in Landslide Mapping: The San Fratello Case Study. *Geomorphology* 223, 45–60. doi:10.1016/j.geomorph.2014.06.025

Berilgen, M. M. (2007). Investigation of Stability of Slopes under Drawdown Conditions. *Comput. Geotechnics* 34, 81–91. doi:10.1016/j.compgeo.2006.10.004

Casagli, N., Tofani, V., Morelli, S., Frodella, W., Ciampalini, A., Raspini, F., et al. (2017). Remote Sensing Techniques in Landslide Mapping and Monitoring, Keynote Lecture. *Geoenvironmental Disasters* 4, 1–19. doi:10.1007/978-3-319-53487-9_1

Chen, L. C., Yang, H. Q., and Song, K. L. (2021). Failure Mechanisms and Characteristics of the Zhongbao Landslide at Liujing Village, Wulong, China[J]. *Landslides* 275, 1–30. doi:10.1007/s10346-020-01594-1

Chen, L., Zhang, W., Zheng, Y., Gu, D., and Wang, L. (2020). Stability Analysis and Design Charts for Over-dip Rock Slope against Bi-planar Sliding. *Eng. Geology.* 275, 105732. doi:10.1016/j.enggeo.2020.105732

Cornelius, F., Stephan, K., Wang, J. W., and Reiner, D. (2011). Weathering of Fruchtschiefer Building Stones: mineral Dissolution or Rock Disaggregation? [J]. *Environ. Earth Sci.* 63, 7–8. doi:10.1007/s12665-011-0986-z

Crosetto, M., Monserrat, O., Cuevas-González, M., Devanthéry, N., and Crippa, B. (2016). Persistent Scatterer Interferometry: A Review. *ISPRS J. Photogrammetry Remote Sensing* 115, 78–89. doi:10.1016/j.isprsjprs.2015.10.011

Dafalla, M. A. (20132013). Effects of Clay and Moisture Content on Direct Shear Tests for Clay-Sand Mixtures. *Adv. Mater. Sci. Eng.* 2013, 1–8. doi:10.1155/2013/562726

Del Ventisette, C., Intrieri, E., Luzi, G., Casagli, N., Fanti, R., and Leva, D. (2011). Using Ground Based Radar Interferometry during Emergency: the Case of the A3 Motorway (Calabria Region, Italy) Threatened by a Landslide. *Nat. Hazards Earth Syst. Sci.* 11, 2483–2495. doi:10.5194/nhess-11-2483-2011

Della Seta, M., Martino, S., and Scarascia Mugnozza, G. (2013). Quaternary Sea-Level Change and Slope Instability in Coastal Areas: Insights from the Vasto Landslide (Adriatic Coast, central Italy). *Geomorphology* 201, 462–478. doi:10.1016/j.geomorph.2013.07.019

Evans, S. G., Guthrie, R. H., Roberts, N. J., and Bishop, N. F. (2007). The Disastrous 17 February 2006 Rockslide-Debris Avalanche on Leyte Island, Philippines: a Catastrophic Landslide in Tropical Mountain Terrain. *Nat. Hazards Earth Syst. Sci.* 7, 89–101. doi:10.5194/nhess-7-89-2007

Fan, L., Lehmann, P., and Or, D. (2015). Effects of Hydromechanical Loading History and Antecedent Soil Mechanical Damage on Shallow Landslide Triggering. *J. Geophys. Res. Earth Surf.* 120, 1990–2015. doi:10.1002/2015jf003615

Fang, Z. W., Zhang, S. P., Liu, H. M., Teng, J. B., and Zhu, L. P. (2019). Bedding Structure Characteristics and the Storage Controlling Factors of Mud-Shale in Upper Es4 to Lower Es3 Members in Jiyang Depression [J]. *Pet. Geology. Recovery Efficiency* 26 (1), 101–108. doi:10.13673/j.cnki.cn37-1359/te.2019.01.011

Feng, X. T., and Ding, W. X. (2005). Meso-mechanical experiment of Micro-fracturing Process of Rock under Coupled Mechanical-Hydrological Chemical Environment[J]. *Chin. J. Rock Mech. Eng.* 24 (9), 1465–1473. doi:10.3321/j.issn:1000-6915.2005.09.002

Gischig, V., Preisig, G., and Eberhardt, E. (2016). Numerical Investigation of Seismically Induced Rock Mass Fatigue as a Mechanism Contributing to the Progressive Failure of Deep-Seated Landslides. *Rock Mech. Rock Eng.* 49, 2457–2478. doi:10.1007/s00603-015-0821-z

Gu, D. Z. (1979). *Foundation of Rock Mass Engineering geomechanics[M]*. Beijing: Science Press.

Guthrie, R. H., Evans, S. G., Catane, S. G., Zarco, M. A. H., and Saturay, R. M. (2009). The 17 February 2006 Rock Slide-Debris Avalanche at Guinsaugon Philippines: a Synthesis. *Bull. Eng. Geol. Environ.* 68, 201–213. doi:10.1007/s10064-009-0205-2

He, C., Hu, X., Tannant, D. D., Tan, F., Zhang, Y., and Zhang, H. (2018). Response of a Landslide to Reservoir Impoundment in Model Tests. *Eng. Geology.* 247, 84–93. doi:10.1016/j.enggeo.2018.10.021

Hu, X., Tan, F., Tang, H., Zhang, G., Su, A., Xu, C., et al. (2017). *In-situ* Monitoring Platform and Preliminary Analysis of Monitoring Data of Majiagou Landslide with Stabilizing Piles. *Eng. Geology.* 228, 323–336. doi:10.1016/j.enggeo.2017.09.001

Huang, Q. X., Wang, J. L., and Xue, X. (2016). Interpreting the Influence of Rainfall and Reservoir Infilling on a Landslide. *Landslide* 13, 1139–1149.

Huang, R. Q. (2007). Large-scale Landslides and Their Sliding Mechanisms in China since the 20th Century[J]. *China J. Rock Mech. Eng.* 26, 433–454.

Li, C., Wang, M., and Liu, K. (2018a). A Decadal Evolution of Landslides and Debris Flows after the Wenchuan Earthquake. *Geomorphology* 323, 1–12. doi:10.1016/j.geomorph.2018.09.010

Li, S., Sun, Q., Zhang, Z., and Luo, X. (2018b). Physical Modelling and Numerical Analysis of Slope Instability Subjected to Reservoir Impoundment of the Three Gorges. *Environ. Earth Sci.* 77 (4). doi:10.1007/s12665-018-7321-x

Li, Y. S., Jiao, Q. S., Hu, X. H., Li, Z. L., Li, B., Jingfa, Z., et al. (2020). Detecting the Slope Movement after the 2018 Baige Landslides Based on Ground-Based and Space-Borne Radar Observations[J]. *Eng. Geology.* 84, 1–12. doi:10.1016/j.enggeo.2017.09.001

Li, Z. B., Huang, T. M., Pang, Z. H., Xiong, D. M., Li, Y. M., Tian, J., et al. (2019). Study on Groundwater Baseline Quality, Monitoring Indicators and Contamination Tracing Methods Related to Shale Gas Development: a Case Study in the Fulling Gas Field in SW China[J]. *J. Eng. Geology.* 27 (1), 170–177. doi:10.13544/j.cnki.jeg.2019-056

Ling, S. X., Wu, X. Y., Sun, C. W., Liao, X., Ren, Y., and Li, X. N. (2016). Experimental Study of Chemical Damage and Mechanical Deterioration of Black Shale Due to Water-Rock Chemical Action[J]. *J. Exp. Mech.* 31 (4), 511–524. doi:10.7520/1001-4888-15-241

Liu, J., Xu, Q., Wang, S., Siva Subramanian, S., Wang, L., and Qi, X. (2020). Formation and Chemo-Mechanical Characteristics of Weak clay Interlayers between Alternative Mudstone and sandstone Sequence of Gently Inclined Landslides in Nanjiang, SW China. *Bull. Eng. Geol. Environ.* 79, 4701–4715. doi:10.1007/s10064-020-01859-y

Liu, X., Zeng, W., Liang, L., and Xiong, J. (2016). Experimental Study on Hydration Damage Mechanism of Shale from the Longmaxi Formation in Southern Sichuan Basin, China. *Petroleum* 2, 54–60. doi:10.1016/j.petlm.2016.01.002

Macfarlane, D. F. (2009). Observations and Predictions of the Behaviour of Large, Slow-Moving Landslides in Schist, Clyde Dam Reservoir, New Zealand. *Eng. Geology.* 109, 5–15. doi:10.1016/j.enggeo.2009.02.005

Nicola, C., Filippo, C., Chiara, D. V., and Guido, L. (2010). Monitoring, Prediction, and Early Warning Using Ground-Based Radar Interferometry[J]. *Landslides* 7, 291–301. doi:10.1007/s10346-010-0215-y

Ouyang, C., Zhao, W., An, H., Zhou, S., Wang, D., Xu, Q., et al. (2019). Early Identification and Dynamic Processes of ridge-top Rockslides: Implications from the Su Village Landslide in Suichang County, Zhejiang Province, China. *Landslides* 16, 799–813. doi:10.1007/s10346-018-01128-w

Piciullo, L., Calvello, M., and Cepeda, J. M. (2018). Territorial Early Warning Systems for Rainfall-Induced Landslides. *Earth-Science Rev.* 179, 228–247. doi:10.1016/j.earscirev.2018.02.013

Rybacki, E., Reinicke, A., Meier, T., Makasi, M., and Dresen, G. (2015). What Controls the Mechanical Properties of Shale Rocks? - Part I: Strength and Young's Modulus. *J. Pet. Sci. Eng.* 135, 702–722. doi:10.1016/j.petrol.2015.10.028

Rybacko, E., Meier, T., and Dresen, G. (2016). What Controls the Mechanical Properties of Shale Rocks[J]. *J. Pet. Sci. Eng.* 144, 39–58. doi:10.1016/j.petrol.2016.02.022

Sui, W., and Zheng, G. (2017). An Experimental Investigation on Slope Stability under Drawdown Conditions Using Transparent Soils. *Bull. Eng. Geol. Environ.* 77, 977–985. doi:10.1007/s10064-017-1082-8

Tang, H., Zou, Z., Xiong, C., Wu, Y., Hu, X., Wang, L., et al. (2015). An Evolution Model of Large Consequent Bedding Rockslides, with Particular Reference to the Jiweishan Rockslide in Southwest China. *Eng. Geology.* 186, 17–27. doi:10.1016/j.enggeo.2014.08.021

Tang, J., Dai, Z., Wang, Y., and Zhang, L. (2019). Fracture Failure of Consequent Bedding Rock Slopes after Underground Mining in Mountainous Area. *Rock Mech. Rock Eng.* 52, 2853–2870. doi:10.1007/s00603-019-01876-8

Teng, J. Y., Tang, J. X., Zhang, Y. N., Duan, J. C., and Wang, J. B. (2017). Damage Process and Characteristics of Layered Water-Bearing Shale under Uniaxial Compression [J]. *Rock and soil Mechanism* 38 (6), 1629–1638+1646. doi:10.16285/j.rsm.2017.06.011

Tohari, A. (2018). Study of Rainfall-Induced Landsldie: A Review. *IOP Conference Series: Earth and Environmental Science.* 118, 1–7. doi:10.1088/1755-1315/118/1/012036

Tsai, T.-L. (2008). The Influence of Rainstorm Pattern on Shallow Landslide. *Environ. Geol.* 53 (7), 1563–1569. doi:10.1007/s00254-007-0767-x

Wang, L. Q., Yin, Y. P., Huang, B. L., and Dai, Z. W. (2019). Damage Evolution and Stability Analysis of the Jianchuandong Dangerous Rock Mass in the Three Gorges Reservoir Area. *Eng. Geology.* 265, 105439.

Wu, W., Yang, Y., and Zheng, H. (2020). Hydro-mechanical Simulation of the Saturated and Semi-saturated Porous Soil-Rock Mixtures Using the Numerical Manifold Method. *Comp. Methods Appl. Mech. Eng.* 370, 113238. doi:10.1016/j.cma.2020.113238

Xiao, T., Huang, W., Deng, Y., Tian, W., and Sha, Y. (2021). Long-Term and Emergency Monitoring of Zhongbao Landslide Using Space-Borne and Ground-Based InSAR. *Remote Sensing* 13, 1578. doi:10.3390/rs13081578

Xu, Q., Liu, H., Ran, J., Li, W., and Sun, X. (2016). Field Monitoring of Groundwater Responses to Heavy Rainfalls and the Early Warning of the Kualiangzi Landslide in Sichuan Basin, Southwestern China. *Landslides* 13, 1555–1570. doi:10.1007/s10346-016-0717-3

Xue, H. Q., Zhou, S. W., Jiang, Y. L., Zhang, F., Dong, Z., and Guo, W. (2018). Effects of Hydration on the Microstructure and Physical Properties of Shale[J]. *Pet. Exploration Dev.* 45 (6), 1075–1081. doi:10.1016/s1876-3804(18)30118-6

Yang, C. H., Wang, Y. Y., Li, J. G., and Gao, F. (2007). Testing Study about the Effect of Different Water Content on Rock Creep Law[J]. *J. China Coal Soc.* 32 (7), 698–702. doi:10.7520/1001-4888-15-241

Yang, Y., Sun, G., Zheng, H., and Yan, C. (2020). An Improved Numerical Manifold Method with Multiple Layers of Mathematical Cover Systems for the Stability Analysis of Soil-Rock-Mixture Slopes. *Eng. Geology.* 264, 105373. doi:10.1016/j.enggeo.2019.105373

Yin, Y. (2011). Recent Catastrophic Landslides and Mitigation in China. *J. Rock Mech. Geotechnical Eng.* 3, 10–18. doi:10.3724/sp.j.1235.2011.00010

Yin, Y., Sun, P., Zhang, M., and Li, B. (2011). Mechanism on Apparent Dip Sliding of Oblique Inclined Bedding Rockslide at Jiweishan, Chongqing, China. *Landslides* 8, 49–65. doi:10.1007/s10346-010-0237-5

Wei, Y. L., Yang, C. H., Guo, Y., Liu, W., Wang, L., and Heng, S. (2015). Experimental Investigation on Deformation and Fracture Characteristics of Brittle Shale with Natural Cracks under Uniaxial Cyclic Loading[J]. *Rock Soil Mech.* 36 (6), 1649–1658. doi:10.16285/j.rsm.2015.06.017

Zhang, M., McSaveney, M., Shao, H., and Zhang, C. (2018a). The 2009 Jiweishan Rock Avalanche, Wulong, China: Precursor Conditions and Factors Leading to Failure. *Eng. Geology.* 233, 225–230. doi:10.1016/j.enggeo.2017.12.010

Zhang, Y., Hu, X., Tannant, D. D., Zhang, G., and Tan, F. (2018b). Field Monitoring and Deformation Characteristics of a Landslide with Piles in the Three Gorges Reservoir Area. *Landslides* 15 (3), 581–592. doi:10.1007/s10346-018-0945-9

Zhou, C., Ying, C., Hu, X., Xu, C., and Wang, Q. (2020). Thermal Infrared Imagery Integrated with Multi-Field Information for Characterization of Pile-Reinforced Landslide Deformation. *Sensors (Basel)* 20, 1–7. doi:10.3390/s20041170

Zhu, B. L., Li, X. N., Wu, X. Y., and Wang, Y. J. (2015). Experimental Study of Micro-characteristics of Selling for Black Shale under Influence of Water[J]. *Chin. J. Rock Mech. Eng.* 34 (Z2), 3896–3905. doi:10.13722/j.cnki.jrme.2014.1147

Zin, A., Hawari, K., Hawari, K., and Khamisan, N. (2016). Early Detection of Spots High Water Saturation for Landslide Prediction Using Thermal Imaging Analysis. *Ijesd* 7 (1), 41–45. doi:10.7763/ijesd.2016.v7.738

Conflict of Interest: The authors declare that the research was conducted in the absence of any commercial or financial relationships that could be construed as a potential conflict of interest.

frontiers in Earth Science

ORIGINAL RESEARCH
published: 29 November 2021
doi: 10.3389/feart.2021.783273

Soil-Water Characteristics and Creep Deformation of Unsaturated Expansive Subgrade Soil: Experimental Test and Simulation

Yongsheng Yao[1], *Jue Li*[1]*, *Ziqiong Xiao*[2] *and Hongbin Xiao*[3]

[1]College of Traffic and Transportation, Chongqing Jiaotong University, Chongqing, China, [2]School of Economics, Central South University of Forestry and Technology, Changsha, China, [3]School of Civil Engineering, Central South University of Forestry and Technology, Changsha, China

The creep deformation of expansive soil has been considered as a vital threat to the safety in engineering construction because it may cause serious slope diseases in geological engineering. Meanwhile, since expansive soil usually remains in unsaturated state, its mechanical property is significantly affected by the seasonal environment. Therefore, the nonlinear deformation of expansive soil has received increasing attention, especially the humidity-dependent creep properties. This study focused on the stability of the unsaturated expansive soil subgrade considering rainfall and the creep behavior. Pressure plate extractor and direct shear tests were performed to investigate the hydro-mechanical and creep characteristics of the unsaturated expansive soil. Both the Van-Genuchten and Burgers models were applied to analyze the test results and inserted into the numerical model of the slope under rainfall infiltration. Results show that the compaction degree and the stress state was closely related to the water holding capacity of the expansive soil. The nonlinearity of the creep behavior became increasingly obvious with the increase of time and the stress level. The safety factor of the slope decreased as the rainfall time increased, and the most dangerous slide of the slope moved toward the foot of the slope. Considering the long-term creep process, there was a period of rapid growth in horizontal displacement that is detrimental to the stability of the slope. Besides, the rainfall infiltration could accelerate the slope failure before and after this creep process.

Keywords: subgrade engineering, expansive soil, soil-water characteristics, creep behavior, numerical simulation

OPEN ACCESS

Edited by:
Yun Zheng,
Institute of Rock and Soil Mechanics (CAS), China

Reviewed by:
Runqing Wang,
Institute of Rock and Soil Mechanics (CAS), China
Wu Wenan,
Beijing University of Technology, China

***Correspondence:**
Jue Li
lijue1207@cqjtu.edu.cn

Specialty section:
This article was submitted to Geohazards and Georisks, a section of the journal Frontiers in Earth Science

Received: *25 September 2021*
Accepted: *08 November 2021*
Published: *29 November 2021*

Citation:
Yao Y, Li J, Xiao Z and Xiao H (2021) Soil-Water Characteristics and Creep Deformation of Unsaturated Expansive Subgrade Soil: Experimental Test and Simulation. Front. Earth Sci. 9:783273. doi: 10.3389/feart.2021.783273

1 INTRODUCTION

Disasters caused by expansive soil have received increasing attention with the development of engineering construction (Ikeagwuani and Nwonu, 2019). Expansive soil is a special kind of porous soil with moisture dependence and is rich in kaolinite, montmorillonite, illite, and other mineral components (Leng et al., 2018). The repeated swelling and shrinking behavior of expansive soil is caused by the change in natural environment (Soltani et al., 2018). For example, under the drying and wetting cycles, the overlying pavement with expansive soil will be prone to uneven settlement, leading to the destruction or instability of the engineering structure (Lu et al., 2019). This phenomenon presents significant challenges to road engineering in designing and building stable

pavement structures (Khan et al., 2020). Expansive soil is widely distributed in more than 40 countries and regions. In China, the annual economic loss caused by the geological disasters caused by expansive soil is as high as 15 billion. Current studies show that the expansive soil slope has the characteristics of shallow layer expansion and contraction and seasonality (Mehta et al., 2017). The soil–water characteristics of expansive soil are closely related to its strength. In pavement engineering, the most expansive soil subgrade structures are located above the groundwater level and remain in unsaturated state for a long time. Zhang et al. (2020) analyzed the water–air migration law of the subgrade structure through a series of numerical models and found that, considering the atmospheric environment, groundwater, and other factors, the water content of subgrade soil gradually increases during the operation period and reaches the equilibrium state in approximately 3 years. However, the current traditional framework used for pavement design and construction ignores the water migration law and its effect on unsaturated embankment soil.

The hydraulic characteristics of expansive soils are fully understood by the soil–water characteristic curve (SWCC). SWCC is an important testing tool to investigate the relationship between matric suction and water content of the unsaturated soil (Yao et al., 2019). Li et al. (2019) emphasized that it is necessary for subgrade design to establish the humidity field affecting the stiffness and deformation of the subgrade structure. It is widely accepted that matric suction plays an important role in mechanical properties of the unsaturated soil, including resilient modulus and shear strength (Yao et al., 2018). Pooni et al. (2021) applied the dewpoint potentiometer to measure the hydraulic behavior and the results showed the hydraulic variation has strong influence on the stabilization for an expansive subgrade. Therefore, the SWCC features of expansive soil must be investigated to scientifically and effectively evaluate the stability of the expansive soil slope (Dai et al., 2020). In general, matric suction can be measured directly or indirectly. Direct measurement can be performed using the tensiometer (Take and Bolton, 2003), axis-translation (Toll et al., 2013), and filter paper (Houston et al., 1994) methods. The pressure plate extractor has been widely utilized in assessing the SWCC of unsaturated soil on the basis of axial translation technology (Wang et al., 2015). A clay plate is used in this device with a high air intake value to isolate the gas and water phases in the soil to achieve precise suction control. Meanwhile, some mathematical models have been proposed by fitting the test data points into continuous functions to describe the SWCC behavior (Yang and Bai, 2019). Fredlund and Xing (1994), Van Genuchten (1980) and Gardener et al. (1970) have all made outstanding contributions in these models. Among them, the Van-Genuchten model is considered to have a good fitting effect and reliability and has been widely used to predict the permeability coefficient, strength, and pore water distribution of unsaturated soils.

In addition to the soil–water characteristics, the rheological property of the expansive soil is also considered in slope stability (Cong et al., 2020). The rheological behavior study mainly focuses on the creep deformation of expansive soil over time (Pawlik and Šamonil, 2018). In terms of the creep test, the research object covers a wide range, such as coarse–grained (Hou et al., 2018), marine sediment (Huang et al., 2020), and frozen (Li et al., 2017) soils. Given its high water content and compressibility, soft soil has an obvious creep characteristic (Zhou et al., 2021). Many studies have been conducted on the creep characteristics of soft soil. However, for hard clays, such as expansive soils, few studies have been conducted on the creep properties (Shan et al., 2021). As the key to solving the creep-related problems of expansive soil, a constitutive model of creep behavior is developed to discuss the relationship between deformation, stress, strength, and time (Liu et al., 2020). According to the experimental test data, some researchers established the theoretical creep model by using mechanical theory and element combination. Fan et al. (2011) carried out compression creep tests and compared the Burgers and K-H models by fitting the rheological properties of expansive soil. Peng et al. (2020) found that the nonlinear fractional derivative creep model could describe the creep characteristics of expansive soil well and established a shear creep constitutive equation and its parameters. Therefore, the creep mechanism of expansive soil must be explored, and the theoretical model must be introduced in practical engineering design to fundamentally control the disasters caused by expansive soil.

In previous research, the numerical method was usually applied to analyze the failure mechanism of slopes and was supported by experimental results (Zheng et al., 2018; Zheng et al., 2021). It is a responsible way to quickly predict the stability of slopes under different environmental and loading conditions. Therefore, the moisture distribution of an expansive soil slope in this study was calculated using the Geo-studio software and inserted into the FLAC3D model. The study aims to evaluate the stability of the unsaturated expansive soil subgrade using the rainfall infiltration model and consider the creep deformation. Thus, experimental tests were performed to investigate the hydro-mechanical characteristics of unsaturated expansive soil and survey the influences of compaction and stress on the SWCC results. Similarly, the creep behavior of expansive soils was studied using direct shear tests, and the results were fitted by the Burgers model. In the simulation, the non-linearity and time dependence of the shear properties were defined by the CVISC creep model.

TABLE 1 | Physical soil properties.

Index	Testing value
Natural moisture content (%)	26.5
Density (g/cm^3)	1.93
Void ratio	0.77
Specific gravity	2.70
Saturation (%)	92.9
Liquid limit (%)	61.4
Plastic limit (%)	22.8
Plasticity index (%)	38.6
Maximum dry density (g/cm^3)	1.89
Optimum moisture content (%)	15.8
Free expansion ration (%)	62.5

TABLE 2 | Mineral properties of expansive soil.

Mineral composition (%)	Expansive soil
Montmorillonite	10–15
Hydromica	15–25
Quartz	20–30

saturation or volume and water content in unsaturated soils. SWCC is commonly used to characterize the water holding capacity of unsaturated soils and is influenced by several factors, including mineral composition, grain size distribution, overlying stress, and dry density. Therefore, SWCC and its

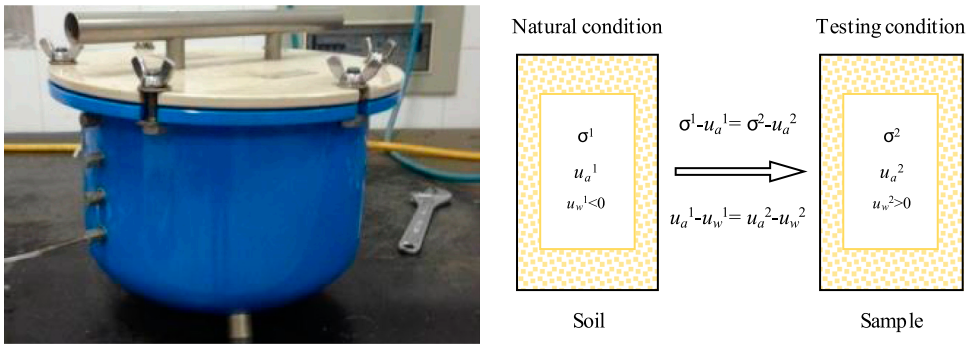

FIGURE 1 | Illustration of **(A)** pressure plate extractor and **(B)** its test principle.

2 MATERIALS AND METHODS

2.1 Materials

The soil samples were taken from Nanning, Guangxi, from alluvial expansive soil. Physical property and XRD diffraction tests were carried out on the soil samples. The basic physical property index and the mineral composition are shown in **Tables 1**, **2**.

The mineral composition and content are one of the important factors affecting the mechanical properties of expansive soil. Generally, the higher the content of strong hydrophilic minerals (such as montmorillonite hydromica) in the soil is, the greater the water absorption rate of the soil and the higher the plasticity index are. In particular, the relaxation rate of the soil samples and the significance of the creep characteristics of the test results increase with montmorillonite content. Quartz has little effect on stress relaxation.

Some studies show that the expansive soil in the subgrade slope gradually evolves into the sheet frame or stack structure after long-term compression (Jalal et al., 2020). The results show that the shear creep characteristic is obvious. In addition, after expansive soil absorbs water, the thickened structural water film on the surface of the soil particles increases the viscosity between the soil particles, which leads to the more obvious creep characteristics of expansive soil. Therefore, SWCC and direct shear creep tests must be performed on expansive soil to understand the engineering properties of the expansive soil subgrade.

2.2 Soil–Water Characteristic Curve Test

SWCC is a concept introduced by soil hydrodynamics and is defined as the curve of the relationship between suction and prediction model are among the natural characteristics of expansive soil.

The pressure plate extractor Model1600-15bar produced by the Soil Moisture Company of the United States was used in this test, as shown in **Figure 1A**. The test device adopts shaft translation technology to control the suction to avoid the gasification of water in the suction control system. The technique achieves a positive pore water pressure (u_w) by increasing the pore gas pressure (UA). As shown in **Figure 1B**, the total stress (σ^1), pore gas pressure (u_a^1), and pore water pressure (u_w^1) of unsaturated soil under natural conditions increased to σ^2, u_a^2, and u_w^2 during the process of compression. However, the net normal stress (σ-u_a) and matric suction (u_a-u_w) of the tested soil samples did not change. Consequently, the pressure plate meter enables the control of matric suction at high atmospheric pressures. Zhang et al. (2021) studied the water-holding performance of the typical subgrade soil, and their results show that the matric suction is generally in the range of 0–1,000 kPa. Given that the maximum control suction of the 15Bar clay plate reaches 1,500 kPa, this test meets the SWCC test requirements of unsaturated expansive soil. The main test procedures are as follows.

(1) The clay plate is fully saturated. The pressure chamber is filled with distilled water until the clay plate is submerged by 1–2 cm. The pressure chamber and valve are closed to apply a pressure of 5 kPa. The clay plate reaches saturation until the volumetric flask is free of bubbles.
(2) The saturated soil sample is installed in the pressure chamber. The ring knife sample of expansive soil reaches the saturation state through the vacuum method. A saturated

TABLE 3 | Scheme of direct shear test.

Vertical stress (kPa)	Shear stress (kPa)
50	8.5 → 25.5 → 42.5 → 93.5 → 161.5
100	8.5 → 25.5 → 42.5 → 93.5 → 161.5
200	8.5 → 25.5 → 42.5 → 127.5 → 204
300	8.5 → 25.5 → 42.5 → 127.5 → 204

soil sample is placed on a clay plate, and the pressure chamber is closed. The internal pressure is adjusted to 0.1 kPa for the soil sample to reach equilibrium. The balance of the soil sample is marked by the absence of change in mass or water flow from the drain.

(3) The water content of the soil sample is calculated using the mass method. The mass of the balanced soil sample is measured using an electronic balance (with an accuracy of 0.001 g).

(4) The above process is repeated to obtain the water content under different suction forces. The corresponding water content is tested under a series of suction conditions (1, 10, 20, 50, 100, 200, 400, 800, and 1,000 kPa), and the corresponding SWCC curve is drawn.

2.3 Direct Shear Creep Test

An improved stress-controlled direct shear instrument, made in Nanjing, China, was used for testing. This experiment aims to obtain the relationship between the strain and time of expansive soil under different stresses. Two kinds of loading methods can be used for the creep test on soil, including separate and graded loading. At present, the graded loading method is often used, that is, the same sample is tested under different stress levels. The method does not have significant differences in soil samples and instruments, thus ensuring a small dispersion in test data. Therefore, the hierarchical loading method was adopted in this study. Shear creep tests were carried out at four vertical stresses (50, 100, 200, and 300 kPa), and the test sequence is shown in **Table 3**. The test procedure is as follows.

(1) The specimen is unsaturated and consolidated under specified stresses. To prevent moisture evaporation in the soil samples during consolidation, a wet cloth covers the shear box.

(2) Rapid shear test is performed on the consolidated soil samples. The shear rate is 12 RPM, and the peak shear strength under different stresses is measured. As shown in **Table 3**, the maximum shear stress for each stage loading is determined.

(3) The shear strain is obtained by stepwise loading. According to the sequence in **Table 3**, horizontal shear stress is applied to the soil samples. The next load is applied after the strain stabilizes.

3 NUMERICAL MODELLING METHODOLOGY

Rainfall infiltration is a complex saturation-unsaturation seepage process. This process causes changes in the pore water pressure, volume, water content, and transient saturated zone of the expansive soil slope (Yao et al., 2021). These changes are detrimental to slope stability. Therefore, finite element analysis was carried out under rainfall conditions to capture the deformation behavior of unsaturated slopes to evaluate the effectiveness of stability, further illustrating the importance of SWCC for the structural design of subgrade soil. Meanwhile, the humidity of the subgrade also affects the creep characteristics of the expansive soil slope. In this paper, combined with the built-in CVISC constitutive model, the influence of the superposition effect of humidity and creep on the deformation of an expansive soil slope is discussed.

3.1 Slope Geometry and Parameters

A typical expressway slope in Nanning was selected for numerical modeling, as shown in **Figure 2**. The height of the clay slope is 10 m, and the slope ratio is 1:2.0. Geological exploration revealed that the shallow layer of the slope is expansive soil (0–2 m), and the lower layer is pluvial clay. The physical parameters of each layer of soil were assumed constant, and the contact of each layer is a fully connected. **Table 4** summarizes the material properties of each soil layer. The initial humidity of the slope is considered uniform and constant, and the water table is located 1.5 m above the bottom of the model. The hydraulic characteristics of the soil layer are discussed in the next section.

3.2 Numerical Simulation of Rainfall Process

Geo-studio was used for the numerical simulation of the slope to simulate the hydraulic response of expansive soil and the slope stability under the condition of rainfall. The SEEP/W module of this software accurately simulated the seepage process of saturated unsaturated soil through the Richards governing equation. To deal with the severe hydraulic response caused by water seepage at the boundary, the quadrilateral element with vertical joints was used to discretely treat the shallow expansive soil in the model. Other areas used the mixed regular quadrilateral and triangle elements. The surface of the

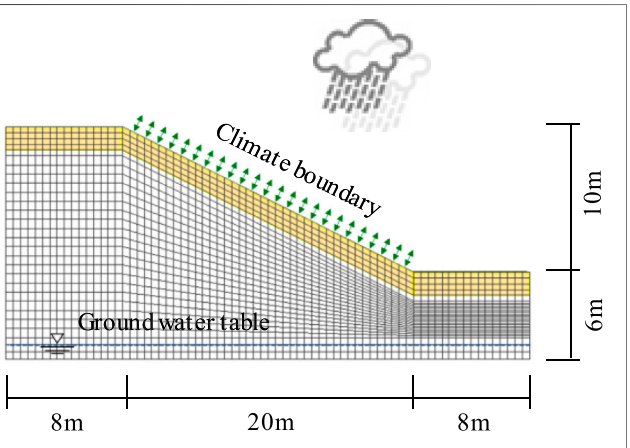

FIGURE 2 | Numerical model of a typical highway slope.

TABLE 4 | Material properties.

Layer	Unit weight (kN/m^3)	Young's modulus (MPa)	Poisson's ratio	Cohesion (kPa)	Friction angle (°)
Expansive soil	19.5	11	0.33	12	17
Clay	21	29	0.3	29	24

slope was set as a free permeable surface, while the bottom surface and the vertical surfaces on both sides of the model were set as impervious water surfaces.

The seepage characteristics of expansive soil slope under rainfall infiltration was calculated under the action of transient flow. For the initial hydraulic state, the model had a pressure head of 0 at the groundwater level. The pressure water head below the underground water level was calculated according to **Eq. 1** and linearly increased with the depth. The unsaturated zone above the underground waterline was evaluated according to the negative pressure head, which decreased linearly in the opposite direction of gravity. The initial water content was considered as the saturated water content below the groundwater level, and the water content in the unsaturated area above the groundwater level decreased gradually with the increase of elevation.

$$p = \gamma h \tag{1}$$

where p stands for the hydraulic head; γ stands for the unit weight of water; h stands for the liquid height.

The Van-Genuchten model is a commonly used model for predicting the soil water characteristic curve of expansive soil, as shown in **Eq. 2**. The model is widely used in the unsaturated seepage analysis of subgrade slope because its parameters are easy to obtain, and it's fitting accuracy is high. The permeability coefficient of expansive soil was measured by the double-loop water-permeation test. According to Darcy's law, permeability coefficient K was calculated using **Eq. 3**. Therefore, the permeability coefficient of the lower clay is 1.90×10^{-8} m/s, while that of expansive soil is 2.70×10^{-7} m/s.

$$\theta = \theta_r + \frac{\theta_s - \theta_r}{[1 + (au_w)^n]^m} \tag{2}$$

$$K = Q/AI \tag{3}$$

where θ, θ_s, and θ_r represent the volume water content, saturated volume water content, and residual volume water content, respectively; u_w represents the pore water pressure; a, n, and m are fitting parameters; K is the permeability coefficient; Q is the water flow of the steady seepage; A is the area of inner diameter of double ring; I represents the hydraulic gradient.

The seepage characteristics of an expansive soil slope under rainfall infiltration are closely related to rainfall intensity, rainfall duration, and rainfall type. According to the meteorological data, rainstorm generally occurs in Nanning from April to August, and the duration is usually 1–2 days. In addition, the duration of moderate rain is approximately 5 days, and its rainfall intensity is 10–25 mm/day. By conversion, the permeability coefficient of expansive soil is approximately 23 mm/day. Considering the boundary condition of rainfall, this study only analyzed the seepage condition of the slope under moderate rain. Therefore, the rainfall intensity was set to 10, 12.5, and 20 mm/day, and the rainfall duration was set to 5 days.

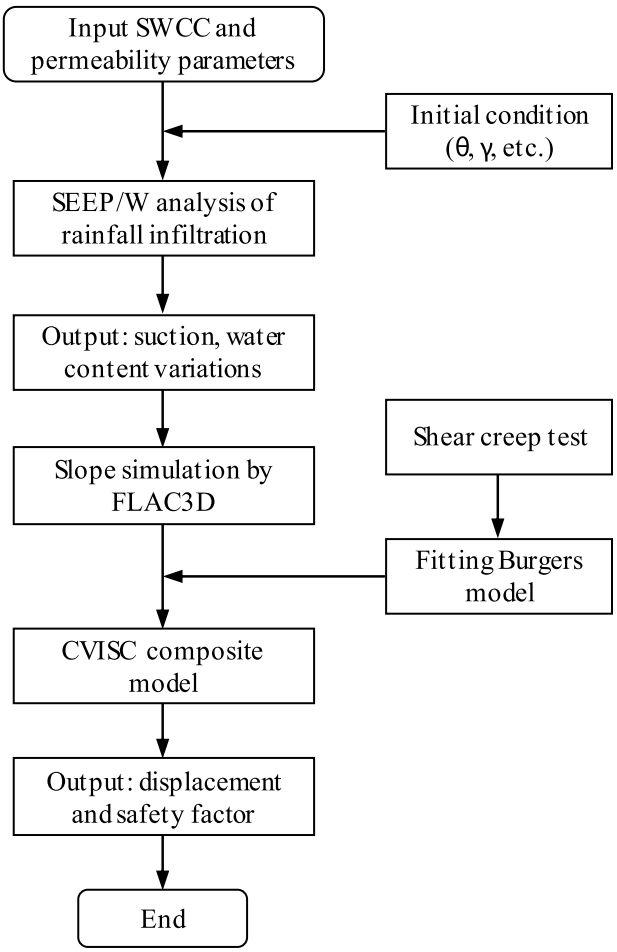

FIGURE 3 | Model calculation framework considering humidity and creep.

3.3 Analysis Plan of Slope Stability

Pore water and gas coexist in unsaturated soil, so the stress of soil is borne by the main framework, the pore water, and the pore gas. According to the extended Mohr-Coulomb criterion, the shear strength (τ_f) of unsaturated soil is expressed as **Eq. 4**. In unsaturated soils, the pore water pressure (u_w) increases, and the matric suction (u_a-u_w) decreases with the increase of the soil water content, and the shear strength (τ_f) of unsaturated soils finally decreases. The cohesion and internal friction angle of

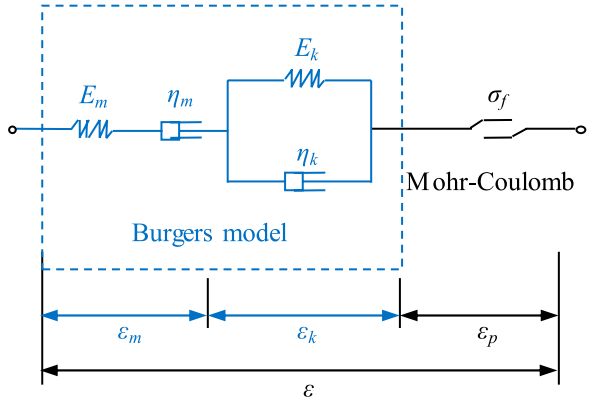

FIGURE 4 | Creep model of CVISC.

expansive soil in the saturated state were 8 kPa and 11°, respectively. The cohesive force and internal friction angle of the lower clay were 27 kPa and 23°, respectively. The matric suction of the unsaturated expansive soil slope changed constantly during rainfall. Therefore, the safety factor and sliding surface of the expansive soil slope also changed dynamically with time during the entire rainfall process.

$$\tau_f = c' + \left(\sigma_f - u_a\right)\tan\varphi' + \left(u_a - u_w\right)\tan\varphi^b \tag{4}$$

where c' and φ' stand for the effective cohesion and the effective friction angle when the matric suction is 0; σ_f is the yield stress; φ^b is the friction angle related to the matric suction.

To analyze the impact of rainfall conditions on slope stability, the pore water pressure at any moment of the Geo-Studio software was imported into the FLAC3D model in this study. With and without setting the CVISC creep model, the change of the sliding surface of the slope was simulated. Meanwhile, the strength reduction method was used to calculate the safety factor of the expansive soil slope during rainfall infiltration. The calculation flow chart of the stability analysis is shown in **Figure 3**.

The CVISC composite creep model is embedded in the FLAC3D software. This model combines the Burgers and Mohr–Coulomb models, as shown in **Figure 4**. The Burgers model can reflect the viscoelastic deformation of expansive soil well, and the corresponding constitutive relationship is shown in **Eq. 5**. On the basis of the direct shear creep test results and the regression analysis of the creep parameters of the Burgers model, the corresponding model parameters can be obtained.

$$\varepsilon = \frac{\tau}{E_m} + \frac{\tau}{\eta_m}t + \frac{\tau}{E_k}\left(1 - e^{-\frac{E_k}{\eta_k}}\right) \tag{5}$$

where E_m and η_m represent the elastic modulus and the viscosity coefficient of the Maxwell element; E_k and η_k stand for the elastic modulus and the viscosity coefficient of the Kelvin element; τ is the shear stress; ε is the strain; t is the time.

4 RESULTS AND DISCUSSION

The results and their applications are presented and discussed in this section. The Van-Genuchten model used to fit the SWCC of expansive soil is reported in this study, and the effects of stress and compactness on the SWCC of expansive soil were analyzed. Subsequently, the Burgers model was used to study the creep behavior of expansive soils to evaluate the effect of the stress states on the creep properties. Finally, the influence of the above test results on the stability of the expansive soil slope under rainfall conditions is described by numerical analysis.

4.1 SWCC and Fitting Model

To predict the SWCC law of unsaturated expansive soils, some mathematical equations are proposed to obtain the water content or matric suction of soil at any state. **Table 5** shows the fitting parameters of the Van-Genuchten model corresponding to each compaction degree and vertical stress condition, which can be used to understand the water holding capacity of expansive soil. The least square method achieved the best fit for each set of measurement data points and produced different parameter sets. The Van-Genuchten model used the residual water content as a fitting parameter ranging from 0.001 to 0.01. However, these values do not show a uniform trend with stress and density. Generally, the residual water content of the soil sample decreased with the increase of compactness because the high-density soil sample has few pores. Similar conclusions were drawn by Pooni et al. (2021). In addition, according to the results in **Table 5**, the sum of the residual squares of the fitted data is greater than 99%, indicating that the Van-Genuchten model can effectively predict the SWCC of expansive soil. The numerical simulation used 85% compacting degree and 0 kPa vertical pressure.

Figure 5 shows the SWCC test results in different states. The experimental results show that the SWCC of unsaturated expansive soil had an obvious turning point, which can clearly reflect the boundary effect and transition stages. When the matric suction was less than 50 kPa, the soil sample was in the boundary effect stage. In this stage, the water content of the soil sample decreased slowly with the increase of the matric suction, and the curve is gentle. The gas phase in the soil was suspended in the water as a closed bubble and flowed with water because the soil was near saturation. When the suction exceeded 50 kPa until the end of the test, the soil sample was in the transition stage. At this stage, the SWCC exhibited approximately linear changes. The water content of the soil samples decreased clearly with the increase of the matric suction. At this stage, the gas phase of the soil was partially connected with the internal pores, and the air began to enter the soil and occupy the large pore channels in the soil. Therefore, the saturation decreased rapidly with the increase of the suction, and the soil properties changed sharply. In practical engineering, this stage is characterized by unsaturated expansive soil.

Figure 5A shows the test results on expansive soil under no overburden pressure. Under the same matric suction conditions, the higher the dry density was, the lower the water content was; the effect of dry density on matric suction weakened when the matric suction increased gradually. This phenomenon occurred

TABLE 5 | Fitting parameters for SWCC.

Compaction degree (%)	Vertical stress (kPa)	*a* (kPa)	*n* (E)	*M*	θ_r (%)	R^2 (%)
85	0	1.196-2	1.851	0.460	1.84-3	99.75
	30	1.613-2	1.890	0.471	2.74-3	99.61
	60	1.541-2	1.978	0.494	1.77-3	99.56
	90	1.493-2	2.014	0.503	1.25-3	99.43
90	0	1.298-2	1.882	0.469	1.75-3	99.61
	30	1.196-2	1.924	0.480	2.25-3	99.56
	60	1.128-2	2.014	0.504	1.44-3	99.50
	90	1.139-2	2.053	0.513	1.04-3	99.55
98	0	1.107-2	2.011	0.503	1.60-3	99.54
	30	1.081-2	2.079	0.519	2.24-3	99.38
	60	1.056-2	2.184	0.542	4.85-3	99.48
	90	1.135-2	2.219	0.549	1.38-3	99.42

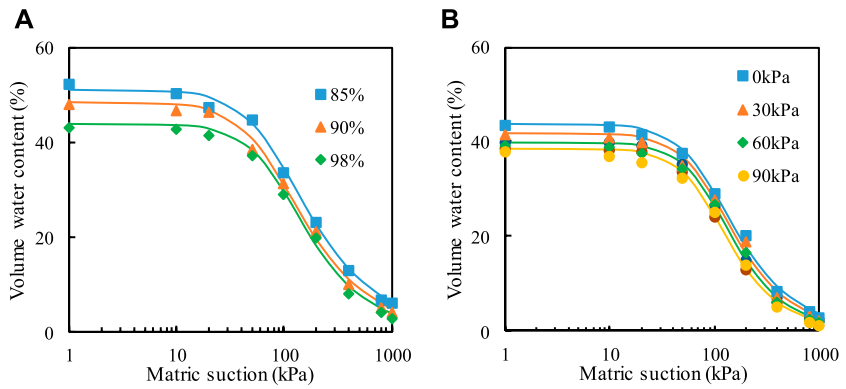

FIGURE 5 | SWCC results under different **(A)** compaction degrees and **(B)** stress conditions.

because the effect of dry density on the soil–water characteristic curve was mainly realized by changing the pore condition of the soil. When the dry density was small, the internal pores and pore size of the expansive soil were large, resulting in poor water holding capacity. **Figure 5B** shows the SWCC of the soil sample with 98% compaction degree. The results show that the air intake of the soil samples moved back, and the influence of suction on the water content weakened with the increase of vertical stress. Similarly, the greater the vertical stress was, the lesser the porosity of the soil sample and the greater the capillary suction of the soil were.

4.2 Direct Shear Creep Results

Figure 6 displays the shear strain time relationship curve of the graded loading. The compaction degree of the testing soil was 85%. The results under the vertical stress of 50 and 100 kPa show that when the deviator stress level was low, the strain of the expansive soil only included instantaneous strain and attenuated creep strain during the test duration; when the deviator stress increased to 93.5 kPa, the creep process of expansive soil experienced three complete stages during the test time, namely, attenuation creep, steady-state creep, and accelerated creep, and the expansive soil finally underwent creep failure; when horizontal shear stress was added to 161.5 kPa, the two soil samples were suddenly damaged, so the results are not shown in the figure. When the vertical stress was 200 and 300 kPa, the creep curve of soil showed the same change trend. When the horizontal shear stress was less than 42.5 kPa, attenuation creep was observed, the shear displacement was mainly instantaneous, and the creep tended to be stable within 2 days. The change process of the creep curve is consistent with the creep law when the vertical stress is 50 and 100 kPa.

Traditional rheological model theory regards the soil as a linear body and uses linear rheological theory to study the rheological problem of soil. The linear creep model shows a linear relationship between strain and stress when subjected to external stress. However, many studies now believe that the constitutive relationship of soil is different at different times and strain increases nonlinearly. For the nonlinear creep model, the stress–strain relationship is viscoelastic. On the basis of the direct shear creep test data, regression analysis was performed on the parameters of the Burgers model. The results in **Table 6** indicate that the fitting effect of the model is better under high vertical stress. In general, this model can be used to describe the nonlinear creep behavior of expansive soil under different stress states and has certain applicability.

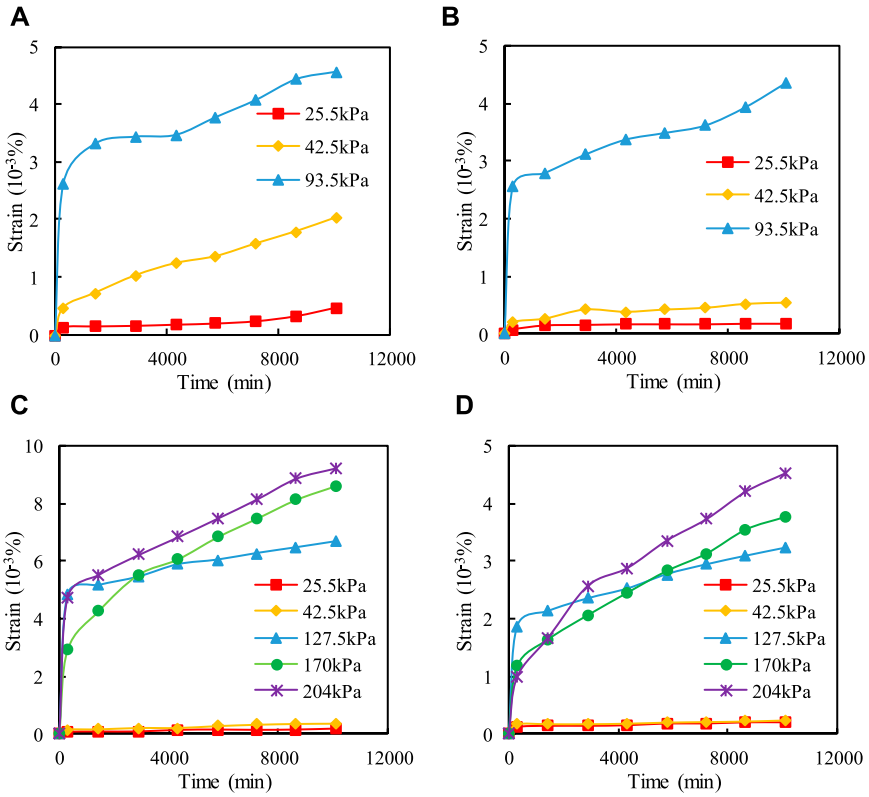

FIGURE 6 | Results of direct shear tests at the vertical stress: **(A)** 50 kPa; **(B)** 100 kPa; **(C)** 200 kPa; **(D)** 300 kPa.

TABLE 6 | Fitting parameters of Burgers model.

Vertical stress (kPa)	Shear stress (kPa)	E_m (kPa)	E_k (kPa)	η_m (kPa·min)	η_k (kPa·min)	R^2 (%)
50	25.5	2.80E + 05	1.50E + 05	4.56E + 09	1.63E + 08	88.54
	42.5	4.25E + 05	4.25E + 04	5.94E + 08	4.25E + 07	93.49
	93.5	9.35E + 05	9.35E + 04	2.22E + 08	9.35E + 07	80.23
100	25.5	2.98E + 08	1.77E + 05	9.59E + 09	8.25E + 07	99.84
	42.5	4.72E + 08	1.57E + 05	1.56E + 09	3.91E + 07	96.62
	93.5	1.04E + 09	3.62E + 04	5.70E + 08	3.02E + 06	99.60
200	25.5	2.83E + 08	5.26E + 05	2.63E + 09	4.43E + 07	93.53
	42.5	4.70E + 08	3.50E + 05	1.70E + 09	8.44E + 06	98.37
	127.5	1.45E + 09	2.60E + 04	6.89E + 08	4.37E + 05	99.82
	170	1.94E + 09	4.96E + 04	3.07E + 08	8.35E + 05	98.38
	204	2.33E + 09	4.25E + 04	4.43E + 08	7.15E + 05	99.83
300	25.5	2.82E + 08	2.26E + 05	3.12E + 09	2.22E + 07	98.87
	42.5	4.90E + 08	2.70E + 05	5.71E + 09	4.55E + 06	99.12
	127.5	1.45E + 09	6.67E + 04	9.26E + 08	1.12E + 06	99.72
	170	1.94E + 09	1.37E + 05	6.46E + 08	2.31E + 06	99.54
	204	2.33E + 09	1.67E + 05	5.86E + 08	2.80E + 06	98.24

4.3 Seepage Analysis Subjected to Rainfall Infiltration

The process of rainfall infiltration was simulated by the Geo-studio/Seep software. **Figure 7** shows the slope humidity field at different rainfall times, subjected by the rainfall intensity of 20 mm/day. In the model, the moisture content of the soil increased gradually with continuous rainfall. The shallower the depth was, the earlier the start of water content increase was. The influence of rainfall infiltration on the soil moisture content of the slope gradually developed from the surface soil to its depth. The

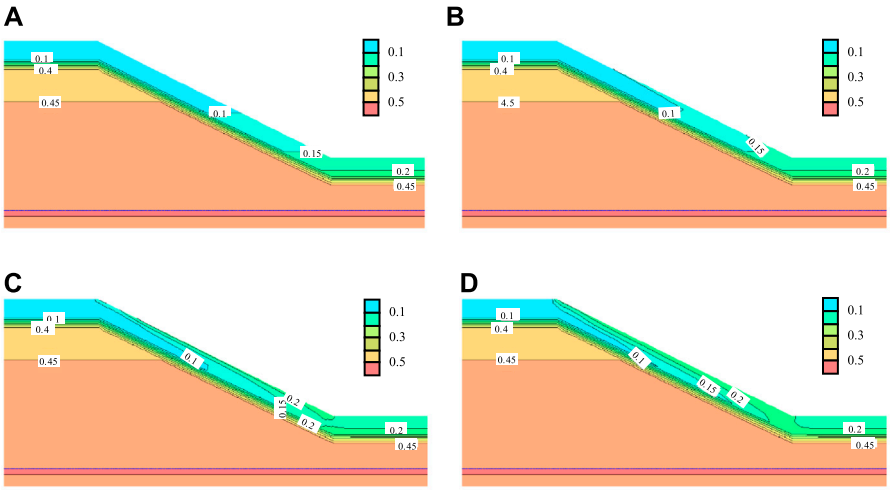

FIGURE 7 | Humidity field under the 20 mm/day rainfall at: **(A)** 1 day; **(B)** 2 days; **(C)** 3 days; **(D)** 5 days.

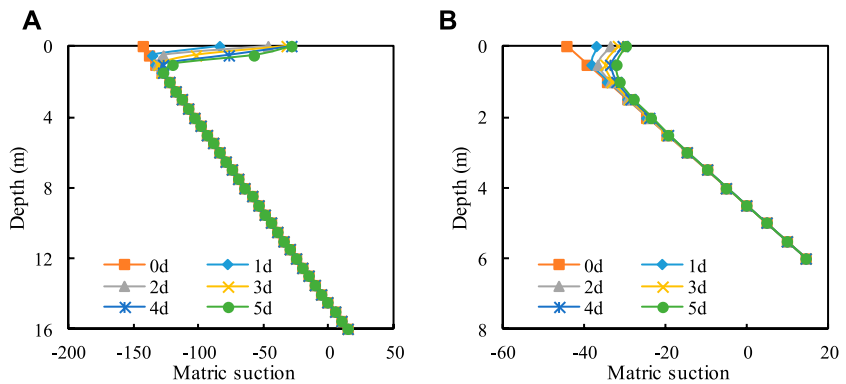

FIGURE 8 | Matric suction along the slope depth at: **(A)** the top and **(B)** the foot of the slope.

influence of the depth of rainfall infiltration gradually increased with the rainfall duration, and the nearer the slope was, the greater the increase in water content was. After the rainfall, the water content in the expansive soil was replenished by rain and infiltrated along the slope. Given the poor permeability of clay, the rainfall only gathered above the slope foot when the rainfall lasted for 3 days.

The unsaturated seepage process of expansive soil was accompanied by the change in matric suction. **Figure 8** shows the suction variation along the depth at the foot and top of the slope during rainfall, according to the above distribution of water content. The results show that the matric suction changes obviously in the expansive soil but has no effect on the ordinary clay. A positive correlation existed between the range of suction and the depth of rainfall infiltration because the rainfall intensity was greater than the soil infiltration capacity. Meanwhile, the matric suction of the expansive soil near the top of the slope was significantly higher than that near the foot of the slope.

4.4 Influence of Rainfall Infiltration on Slope Stability

The matric suction of soil changes constantly with rainfall, and also affects the shear properties of expansive soil slope. As it displayed in **Figure 3**, the computation results of the humidity were obtained by the Geo-studio model and were imported into the slope model in the FLAC3D. **Figures 9A**, **10A** are the distributions of pore water pressure before and after the rainfall. In the initial state, the pore water pressure presents gradient changes along the gravity direction. After the rainfall for 5 days, the pore water pressure increased within a certain region in the slope, which was related to the influence depth of rainfall infiltration.

The increase in humidity led to the strength softening of expansive soil, which affected the shear strain and displacement of the slope. **Figures 9B**, **10B** illustrate the effect of the rainfall infiltration on the slope stability. As the rain occurred, the maximum shear surface of the slope moved down and the sliding speed increased at the foot of the slope. Meanwhile, the

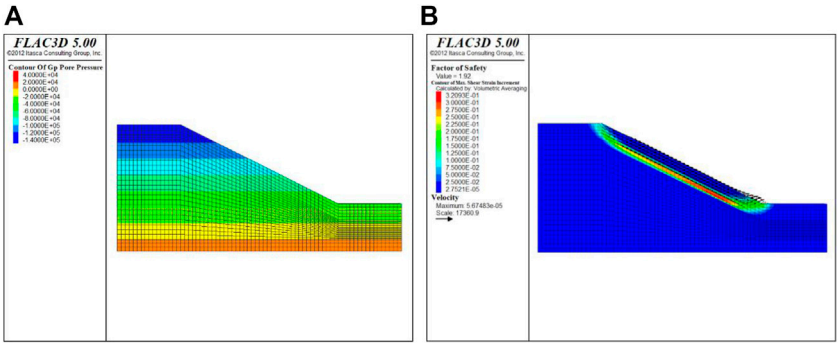

FIGURE 9 | Distribution of **(A)** pore water pressure and **(B)** shear strain after reduction (T = 0 days).

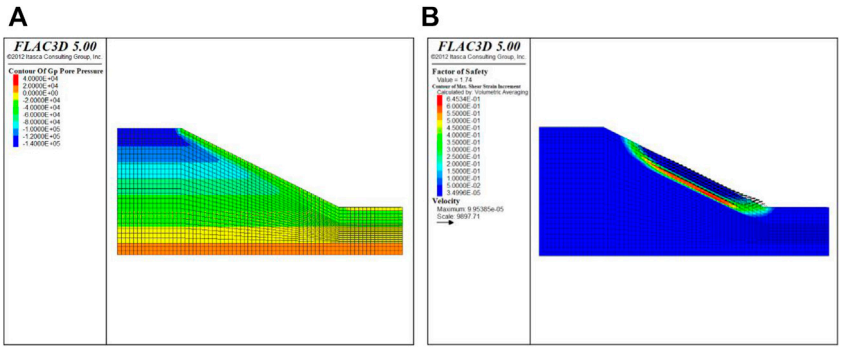

FIGURE 10 | Distribution of **(A)** pore water pressure and **(B)** shear strain after reduction (T = 5 days).

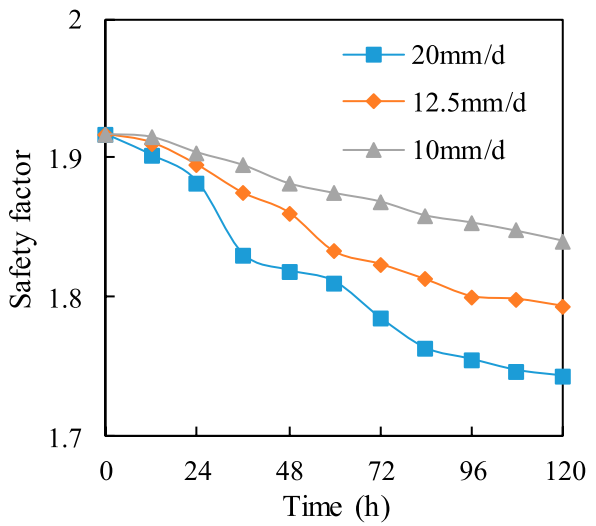

FIGURE 11 | Changes of safety factor with different rainfall conditions.

safety factor of stability analysis decreased from the initial value of 1.917 to 1.743. It was seen clearly that the seepage formed near the slope surface and flowed to the foot of the slope. As a result, the most dangerous sliding surface moved to the foot of the slope, and the slope was gradually losing stability. **Figure 11** shows the change in the safety factor of the expansive soil slope under different rainfall conditions. the higher the rainfall intensity was, the higher the rainfall infiltration rate and the deeper the rainfall infiltration were. With the increase of rainfall intensity under the same infiltration rate, the more water infiltrating the soil was, the faster the soil water content increase was.

4.5 Influence of Creep Behavior on Slope Stability

Furthermore, the long-term performance of the slope is related to the creep process of expansive soil, which may last for months or years. Based on the CVISC model, the viscoelastic-plastic deformation of the expansive slope was calculated in the above simulation. **Figure 12** shows the contours of the horizontal displacement during different creep times. The model was in a naturel water distribution, as shown in **Figure 9A**. On the one hand, the displacement of the slope increased obviously over time and the maximum displacement occurred at the foot of the slope. On the other hand, the deformation within the clay layer was at a low level with the time, due to no assignment of the creep model for it.

According to the stability analysis, the expansive soil slope can easily slip along the horizontal direction at the foot of the slope.

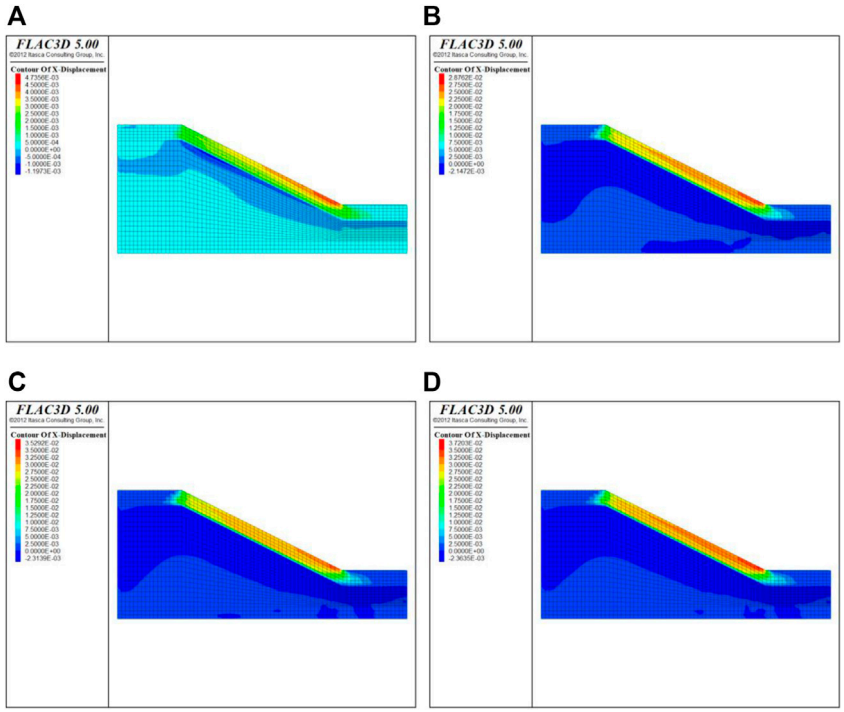

FIGURE 12 | Changes of x-displacement of slope at: **(A)** 1 year; **(B)** 3 years; **(C)** 5 years; **(D)** 7 years.

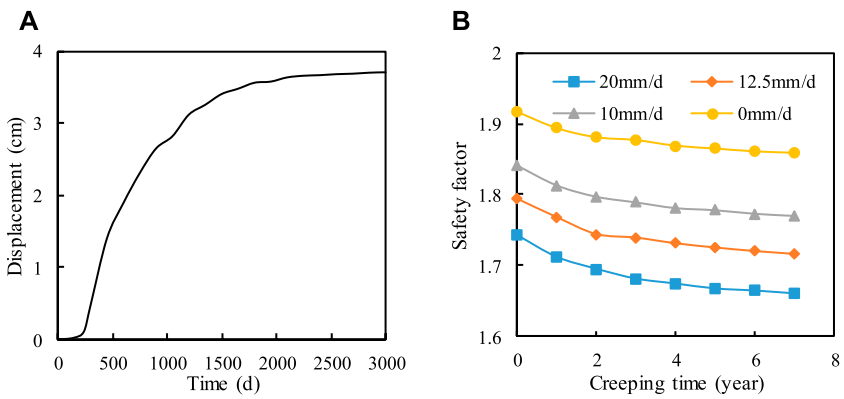

FIGURE 13 | Changes of **(A)** displacement of the slope foot and **(B)** safety factor of expansive soil slope.

Therefore, **Figure 13A** shows the change of horizontal displacement at the foot of the slope with time was measured in the above model. It did not take the rainfall into account. The test results show that the horizontal displacement of the slope foot gradually increased with the extension of time. The displacement increased greatly in 1–3 years, but the creep was stable after 7 years. The maximum displacement was approximately 3.69 cm. Meanwhile, the long-term creep behavior also led to slope stability attenuation. However, compared with the creep failure of the expansive soil, the rainfall infiltration is a rapid and significant effect on the stability of the slope. **Figure 13B** shows safety factors of the slope considering the rainfall of 5 days after the long-term creep process. The result in the absence of rainfall shows that the slope safety factor decreased from 1.917 to 1.859, while the time increased from 0 to 7 years. The occurrence of rainfall further accelerated the failure of the slope because the wetting of the slope reduced the maximum strength of the slope. For 5 days suffered by 20 mm/d rainfall, the safety factor reduced 0.083 over time. For no rainfall, the safety factor only decreased 0.058. It implies that the influence of the creep behavior on the slope stability was also enhanced with the increase of rainfall intensity.

4.6 Discussion

The analyses have shown that the rainfall and the creep behavior are significant over time that is related to the stability of the expansive soil slope. Previous studies suggested that the depth of rainfall infiltration ranged from 1.0 to 3.5 m, and it was possible to occur a passive failure within the softened soil layer at shallow depths (Zhan et al., 2007; Pei et al., 2020). The increase in water content was detrimental for the slope stability of the unsaturated soil, as it mentioned in **Eq. 4**. Furthermore, the creep deformation exacerbated the failure process of the unsaturated slope. In this study, the effects of the stress state on the SWCC and creep properties were obtained at laboratory. The corresponding models and parameters were assigned into the slope simulation. The ranges of matric suction were positively correlated with the depth of rainfall infiltration. This was consistent with the filed results reported by Wang et al. (2017), who found that the displacement of the slope was mainly along the horizontal direction and the deformation rate depended on the rainfall intensity and duration.

The numerical model was considering the long-term creep deformance of the slope. The result shows that there was a period of rapid growth in the horizontal displacement at the slope foot. Besides, the occurrence of rainfall may accelerate this failure of the slope. Therefore, the creep behavior of the expansive soil slope could be under-estimated in the slope design. Further study should be carried out to investigate the effect of the long-term creep on micro-cracks and hydraulic properties of the expansive soil. In addition, the current study only analyzed the effect of the rainfall on the slope stability before and after the creep process, and further study should consider both dry-wet cycles and creep time of this investigated soil on the slope deformation. At last, some treatment and modified soil should be applied to further consider the effects of rainfall and creep on SWCC and slope stability, including the soil-rock mixture (Yao et al., 2022).

5 CONCLUSION

This study investigated the effect of the rainfall infiltration on the stability of the expansive soil slope before and after long-term creep proceed. Experimental tests were performed to obtain the SWCC and creep behavior of the unsaturated expansive soil. A pressure plate apparatus was used to measure the SWCCs of different compaction degrees and stress conditions. Meanwhile, the Burgers model was applied to describe the creep behavior under different stress conditions. Both Geo-studio software and FLAC3D were combined to calculate the stability of the expansive soil slope under rainfall infiltration. The main findings of this paper were presented as following.

(1) The Van-Genuchten model had a good fitting effect with the results of SWCC. For the SWCC, there was an obvious turning point, distinguishing between the boundary effect stage and the transition stage. As the compaction degree or the vertical stress increased, it presents a general trend with a lower desorption rate in the SWCC.
(2) The nonlinearity of the creep behavior was affected by creep time and stress level on the expansive soil. The longer the creep time and the higher the stress level, the higher the nonlinear degree. The fitting results show that the Burgers model can be used to characterize the creep behavior of expansive soil.
(3) Rainfall infiltration has a great influence on the stability of the expansive soil slope. With the increase of rainfall time, the safety factor decreased gradually. Meanwhile, the most dangerous slide of the slope moves towards the foot of the slope.
(4) The preliminary analyses have shown that there was a period of rapid growth in the horizontal displacement at the slope foot, considering the long-term creep model. This phenomenon could reduce the slope stability. Besides, its influence on the safety factor was further enhanced with the increase of rainfall intensity.

DATA AVAILABILITY STATEMENT

The original contributions presented in the study are included in the article/supplementary material, further inquiries can be directed to the corresponding author.

AUTHOR CONTRIBUTIONS

All authors listed have made a substantial, direct, and intellectual contribution to the work and approved it for publication.

FUNDING

This research was funded by the National Natural Science Foundation of China, grant number 51908562; the Standardization Project of Hunan Province; the Research Foundation of Education Bureau of Hunan Province, China, grant number 19B581; the Natural Science Foundation of Hunan Province, China, grant number 2020JJ5987. The Natural Science Foundation of Chongqing, China, grant number cstc2018jcyjAX0640.

ACKNOWLEDGMENTS

We are grateful to the professor Jie Liu and his student Jianzheng Liu in Hebei University of Engineering for the support and advice of numerical modeling. We appreciate the software and data access provided by the Changsha University of Science and Technology. The editors and two reviewers are thanked for critical and constructive comments.

REFERENCES

Cong, S., Nie, Z., and Hu, Q. (2020). A Disturbed State Concept-Based Stress-Relaxation Model for Expansive Soil Exposed to Freeze-Thaw Cycling. *KSCE J. Civ Eng.* 24 (9), 2621–2630. doi:10.1007/s12205-020-2000-3

Dai, Z., Chen, S., and Li, J. (2020). Physical Model Test of Seepage and Deformation Characteristics of Shallow Expansive Soil Slope. *Bull. Eng. Geol. Environ.* 79 (8), 4063–4078. doi:10.1007/s10064-020-01811-0

Fan, Z., Xiao, H., and Tang, Y. (2011). Experimental Study on Creep Characteristics for Nanning Unsaturated Expansive Soils. *Highw. Eng.* 36 (6), 43–47. doi:10.3969/j.issn.1674-0610.2011.06.009

Fredlund, D. G., and Xing, A. (1994). Equations for the Soil-Water Characteristic Curve. *Can. Geotech. J.* 31 (4), 521–532. doi:10.1139/t94-061

Gardener, W., Hillel, D., and Benzamin, Y. (1970). Post Irrigation Movement of Soil Water: II. Simultaneous Redistribution and Evaporation. *Water Resour. Res.* 6 (4), 1148–1153.

Hou, F., Lai, Y., Liu, E., Luo, H., and Liu, X. (2018). A Creep Constitutive Model for Frozen Soils with Different Contents of Coarse Grains. *Cold Regions Sci. Tech.* 145, 119–126. doi:10.1016/j.coldregions.2017.10.013

Houston, S. L., Houston, W. N., and Wagner, A.-M. (1994). Laboratory Filter Paper Suction Measurements. *Geotechnical Test. J.* 17 (2), 185–194.

Huang, W., Wen, K., Deng, X., Li, J., Jiang, Z., Li, Y., et al. (2020). Constitutive Model of Lateral Unloading Creep of Soft Soil under Excess Pore Water Pressure. *Math. Probl. Eng.* 2020, 1-13. doi:10.1155/2020/5017546

Ikeagwuani, C. C., and Nwonu, D. C. (2019). Emerging Trends in Expansive Soil Stabilisation: A Review. *J. Rock Mech. Geotechnical Eng.* 11 (2), 423–440. doi:10.1016/j.jrmge.2018.08.013

Jalal, F. E., Xu, Y., Jamhiri, B., and Memon, S. A. (2020). On the Recent Trends in Expansive Soil Stabilization Using Calcium-Based Stabilizer Materials (CSMs): A Comprehensive Review. *Adv. Mater. Sci. Eng.* 2020, 1-23. doi:10.1155/2020/1510969

Khan, M. A., Wang, J. X., and Sarker, D. (2020). Development of Analytic Method for Computing Expansive Soil-Induced Stresses in Highway Pavement. *Int. J. Geomech.* 20 (2), 04019160. doi:10.1061/(asce)gm.1943-5622.0001511

Leng, T., Tang, C., Xu, D., Li, Y., Zhang, Y., Wang, K., et al. (2018). Advance on the Engineering Geological Characteristics of Expansive Soil. *J. Eng. Geology.* 26 (1), 112–128.

Li, D., Yang, X., and Chen, J. (2017). A Study of Triaxial Creep Test and Yield Criterion of Artificial Frozen Soil under Unloading Stress Paths. *Cold Regions Sci. Tech.* 141, 163–170. doi:10.1016/j.coldregions.2017.06.009

Li, J., Zheng, J., Yao, Y., Zhang, J., and Peng, J. (2019). Numerical Method of Flexible Pavement Considering Moisture and Stress Sensitivity of Subgrade Soils. *Adv. Civil Eng.* 2019, 1-10. doi:10.1155/2019/7091210

Liu, J., Jing, H., Meng, B., Wang, L., Yang, J., and Zhang, X. (2020). A Four-Element Fractional Creep Model of Weakly Cemented Soft Rock. *Bull. Eng. Geol. Environ.* 79 (10), 5569–5584. doi:10.1007/s10064-020-01869-w

Lu, Y., Liu, S., Alonso, E., Wang, L., Xu, L., Li, Z., et al. (2019). Volume Changes and Mechanical Degradation of a Compacted Expansive Soil under Freeze-Thaw Cycles. *Cold Regions Sci. Tech.* 157, 206–214. doi:10.1016/j.coldregions.2018.10.008

Mehta, B., Sachan, A., and Engineering, G. (2017). Effect of Mineralogical Properties of Expansive Soil on its Mechanical Behavior. *Geotech Geol. Eng.* 35 (6), 2923–2934. doi:10.1007/s10706-017-0289-6

Pawlik, Ł., and Šamonil, P. (2018). Soil Creep: The Driving Factors, Evidence and Significance for Biogeomorphic and Pedogenic Domains and Systems - A Critical Literature Review. *Earth-Science Rev.* 178, 257–278. doi:10.1016/j.earscirev.2018.01.008

Pei, P., Zhao, Y., Ni, P., and Mei, G. (2020). A Protective Measure for Expansive Soil Slopes Based on Moisture Content Control. *Eng. Geology.* 269, 105527. doi:10.1016/j.enggeo.2020.105527

Peng, R., Peng, W., Hua, Z., and Yin, T. (2020). Nonlinear Behavior of clay Creep and its Fractional Derivative Creep Model. *Eng. Mech.* 37 (9), 153–160. doi:10.6052/j.issn.1000-4750.2019.10.0624

Pooni, J., Robert, D., Giustozzi, F., Gunasekara, C., Setunge, S., and Venkatesan, S. (2021). Hydraulic Characteristics of Stabilised Expansive Subgrade Soils in Road Pavements. *Int. J. Pavement Eng.*, 1–18. doi:10.1080/10298436.2021.1883610

Shan, R.-l., Bai, Y., Ju, Y., Han, T.-y., Dou, H.-y., and Li, Z.-l. (2021). Study on the Triaxial Unloading Creep Mechanical Properties and Damage Constitutive Model of Red sandstone Containing a Single Ice-Filled Flaw. *Rock Mech. Rock Eng.* 54 (2), 833–855. doi:10.1007/s00603-020-02274-1

Soltani, A., Deng, A., and Taheri, A. (2018). Swell-compression Characteristics of a Fiber-Reinforced Expansive Soil. *Geotextiles and Geomembranes* 46 (2), 183–189. doi:10.1016/j.geotexmem.2017.11.009

Take, W. A., and Bolton, M. D. (2003). Tensiometer Saturation and the Reliable Measurement of Soil Suction. *Géotechnique* 53 (2), 159–172. doi:10.1680/geot.2003.53.2.159

Toll, D. G., Lourenço, S. D. N., and Mendes, J. (2013). Advances in Suction Measurements Using High Suction Tensiometers. *Eng. Geology.* 165, 29–37. doi:10.1016/j.enggeo.2012.04.013

Van Genuchten, M. T. (1980). A Closed-form Equation for Predicting the Hydraulic Conductivity of Unsaturated Soils. *Soil Sci. Soc. America J.* 44 (5), 892–898. doi:10.2136/sssaj1980.03615995004400050002x

Wang, J., Gu, T., and Xu, Y. (2017). Field Tests of Expansive Soil Embankment Slope Deformation under the Effect of the Rainfall Evaporation Cycle. *Appl. Ecol. Env Res.* 15 (3), 343–357. doi:10.15666/aeer/1503_343357

Wang, M., Kong, L., Zang, M., and Engineering, G. (2015). Effects of Sample Dimensions and Shapes on Measuring Soil-Water Characteristic Curves Using Pressure Plate. *J. Rock Mech. Geotechnical Eng.* 7 (4), 463–468. doi:10.1016/j.jrmge.2015.01.002

Yang, G., and Bai, B. (2019). Thermo-hydro-mechanical Model for Unsaturated clay Soils Based on Granular Solid Hydrodynamics Theory. *Int. J. Geomech.* 19 (10), 04019115. doi:10.1061/(asce)gm.1943-5622.0001498

Yao, Y., Li, J., Ni, J., Liang, C., and Zhang, A. (2022). Effects of Gravel Content and Shape on Shear Behaviour of Soil-Rock Mixture: Experiment and DEM Modelling. *Comput. Geotechnics* 141, 104476. doi:10.1016/j.compgeo.2021.104476

Yao, Y., Ni, J., and Li, J. (2021). Stress-dependent Water Retention of Granite Residual Soil and its Implications for Ground Settlement. *Comput. Geotechnics* 129, 103835. doi:10.1016/j.compgeo.2020.103835

Yao, Y., Qian, J., Li, J., Zhang, A., and Peng, J. (2019). Calculation and Control Methods for Equivalent Resilient Modulus of Subgrade Based on Nonuniform Distribution of Stress. *Adv. Civil Eng.* 2019, 1-11. doi:10.1155/2019/6809510

Yao, Y., Zheng, J., Zhang, J., Peng, J., and Li, J. (2018). Model for Predicting Resilient Modulus of Unsaturated Subgrade Soils in south China. *KSCE J. Civ Eng.* 22 (6), 2089–2098. doi:10.1007/s12205-018-1703-1

Zhan, T. L., Ng, C. W., and Fredlund, D. G. (2007). Field Study of Rainfall Infiltration into a Grassed Unsaturated Expansive Soil Slope. *Can. Geotech. J.* 44 (4), 392–408. doi:10.1139/t07-001

Zhang, J.-h., Li, F., Zeng, L., Zheng, J.-l., Zhang, A.-s., and Zhang, Y.-q. (2020). Effect of Cushion and Cover on Moisture Distribution in clay Embankments in Southern China. *J. Cent. South. Univ.* 27 (7), 1893–1906. doi:10.1007/s11771-020-4418-7

Zhang, J., Li, F., Zeng, L., Peng, J., and Li, J. (2021). Numerical Simulation of the Moisture Migration of Unsaturated clay Embankments in Southern China Considering Stress State. *Bull. Eng. Geol. Environ.* 80 (1), 11–24. doi:10.1007/s10064-020-01916-6

Zheng, Y., Chen, C., Liu, T., and Ren, Z. (2021). A New Method of Assessing the Stability of Anti-dip Bedding Rock Slopes Subjected to Earthquake. *Bull. Eng. Geol. Environ.* 80 (5), 3693–3710. doi:10.1007/s10064-021-02188-4

Zheng, Y., Chen, C., Liu, T., Zhang, H., Xia, K., and Liu, F. (2018). Study on the Mechanisms of Flexural Toppling Failure in Anti-inclined Rock Slopes Using Numerical and Limit Equilibrium Models. *Eng. Geology.* 237, 116–128. doi:10.1016/j.enggeo.2018.02.006

Zhou, F., Wang, L., and Liu, H. (2021). A Fractional Elasto-Viscoplastic Model for Describing Creep Behavior of Soft Soil. *Acta Geotech.* 16 (1), 67–76. doi:10.1007/s11440-020-01008-5

Conflict of Interest: The authors declare that the research was conducted in the absence of any commercial or financial relationships that could be construed as a potential conflict of interest.

Publisher's Note: All claims expressed in this article are solely those of the authors and do not necessarily represent those of their affiliated organizations or those of the publisher, the editors, and the reviewers. Any product that may be evaluated in this article, or claim that may be made by its manufacturer, is not guaranteed or endorsed by the publisher.

frontiers in Earth Science

ORIGINAL RESEARCH
published: 22 December 2021
doi: 10.3389/feart.2021.799467

Mechanical Properties of Frozen Glacial Tills due to Short Periods of Thawing

Yanju Fu[1,3], *Yao Jiang*[1,2,3]*, *Jiao Wang*[1,2]*, *Ziming Liu*[1,3] *and Xingsheng Lu*[1,3]

[1]Key Laboratory of Mountain Hazards and Earth Surface Process, Institute of Mountain Hazards and Environment, Chinese Academy of Sciences (CAS), Chengdu, China, [2]China-Pakistan Joint Research Center on Earth Sciences (CAS-HEC), Islamabad, Pakistan, [3]University of Chinese Academy of Sciences, Beijing, China

Due to the warming climate, glacier retreat has left massive glacial tills in steep gullies; ice in the soil is prone to change phase resulting in the decrease of the ice strength and bonding of soil particles; collapse of thawing tills can lead to debris flows with disastrous consequences for geotechnical infrastructures. To improve our understanding of the mechanics of thawing glacial tills, we conducted unconsolidated–undrained direct shear tests on glacial tills from Tianmo gully on the southeastern Tibetan Plateau. Control specimens were not subjected to freeze–thaw action. A total of 648 specimens with three different dry densities, three initial water contents, and 18 thawing times were tested. Peak shear strength, peak stress to displacement ratio (0.857), and cohesion were the highest in frozen specimens. After a thawing time of 0.25 h, there was a marked decline in shear strength; maximum friction was 2.58, which was far below the value of cohesive strength. For thawing times of 0.25–4 h, peak strength varied little with thawing time, but cohesion decreased and internal friction angle increased with increasing thawing time. Our results indicate that thawing of the solid ice in the till during the initial phase of till thawing is the key control of peak till strength; the effect of ice on cohesion is greater during the initial phase of thawing and in loose tills. Moreover, frequent sediment recharge of gullies may be explained by the decrease of cohesion with increasing thawing time caused by short-term destruction of ice bonding.

Keywords: glacial till, thawing process, shear behavior, strength properties, direct shear test

OPEN ACCESS

Edited by:
Tingting Liu,
Wuhan University of Technology, China

Reviewed by:
Mahya Roustaei,
University of Alberta, Canada
Xianwei Zhang,
Institute of Rock and Soil Mechanics (CAS), China

***Correspondence:**
Yao Jiang
yjiang@imde.ac.cn
Jiao Wang
wangjiao@imde.ac.cn

Specialty section:
This article was submitted to Volcanology, a section of the journal Frontiers in Earth Science

Received: *21 October 2021*
Accepted: *06 December 2021*
Published: *22 December 2021*

Citation:
Fu Y, Jiang Y, Wang J, Liu Z and Lu X (2021) Mechanical Properties of Frozen Glacial Tills due to Short Periods of Thawing. Front. Earth Sci. 9:799467. doi: 10.3389/feart.2021.799467

INTRODUCTION

Periglacial debris flow is an important surface process during deglaciation. Under a warming climate, Himalayan glaciers have decreased considerably in length and area, the largest are found in southeastern Tibet (Yao et al., 2012; Cui et al., 2018; Nie et al., 2021). Especially, climate warming affects not only accelerating the deglaciation processes but also increasing the mountain hazards risk. Climate waring induced a faster thawing process, where the amount of glacial meltwater can increase and then the catchments' hydrogeologic settings will be further changed. This thawing process is characterized by collapse and caving of glacial tills in steep alpine gullies, which can charge headwater catchments with loose sediments and become the source of labile materials for glacial debris flows (Huggel et al., 2012; Cossart et al., 2014; Wang et al., 2019). These sediments comprise mixtures of debris, ice, fluids, and other materials, and will deform and undergo a sudden loss of strength when subjected to freeze–thaw action (Viklander, 1998; Konrad, 2010;

Vanapalli and Han, 2016). The cause of frequent gully recharge remains unknown, although interactions between ice and soil particles should be taken as qualitative approximations of the soil mechanics of natural slopes.

There have been numerous studies on frozen permafrost. They propose that the presence of ice enhances soil mechanical properties, and ice debris mixtures deform little under low temperatures are generally more resistant than their components in alpine environments (Konrad and Morgenstern, 1980; Ting et al., 1983; Hivon and Sego, 1995). As temperature rises towards the thawing point, films of unfrozen water gradually form at the interface between ice and soil particles, glacial tills on the surface of steep slopes determines the evolution of slope collapse (Chamberlain et al., 1972; Zimmermann and Haeberli, 1992; Moore, 2014; Zhang et al., 2014). However, above findings are failure explain the conclusion that till provides the main source of materials for glacial debris flows.

Thawing can result in changes in internal friction angle and ice cohesion (Czurda and Hohmann, 1997; Lai et al., 2008). The decrease of cohesion with thawing is consistent with the exponential relationship between cohesion and ice content reported by Arenson and Springman (2005b). They focused on the effect of ice content on the cohesion of frozen soils at different temperatures, and did not study the effect of liquid water. However, after contact with water, glacial tills become extremely unstable and their compactness decreases (Vanapalli and Han, 2016). Both dry density and water content are key factors that affect till pore structure and particle distribution, which directly determine initial ice and water migration (Sayles and Carbee, 1981; Eskişar et al., 2015). Nevertheless, no consensus has been reached regarding the influence of thawing on soil mechanics; the relationship between ice phase transition and short-term soil instability remains unknown.

This study focuses on the shear and thawing processes, and further clarifies the contribution of ice bonding to shear strength. The objective of this study is to improve understanding of glacial debris flow initiation and sediment recharge in gullies by investigating the shear behavior and characteristics of frozen glacial tills after short periods of thawing. Glacial tills were collected from the headwater area of the Tianmo gully in Tibet. A total of 648 specimens with three different dry densities, three initial water contents, and 18 thawing times were subjected to conventional direct shear tests. Further, a quantitative assessment of the relationships among water content, dry density, total normal stress and thawing time were explored. More importantly, the potential relation between the ice particle characteristics and till strength to be discussed, and the mechanism variation of thawing on glacial till characteristics to be presented.

STUDY AREA AND SAMPLING LOCATION

Tianmo gully is in Parlung Tsangpo Basin on the southeastern Tibetan Plateau. The length of the main channel is approximately 5.1 km and the average gradient is 25.9% (King et al., 2016). The basin is wider upstream and narrower downstream. Tianmo gully is one of the tributaries of the Parlung Tsangpo River between the villages of Guxiang and Tongmai; the terrain is rugged and mountainous. Like most of the tributaries of the Parlung Tsangpo River in this area, Tianmo gully is short and steep; erosion rate is high and exceeds 5 mm per year (Wang et al., 2019). The headwater area of Tianmo gully is heavily glaciated (**Figures 1A,C,F** are the start and outlet points), and produces massive glacial tills at the front of the glaciers (Deng et al., 2017).

Assuming that the thickness of the ice debris cover is greater than that of the active layer of the permafrost, mass movement activity occurs only under specific topographic conditions and/or under the action of external meltwater sources or slope undercutting (Schomacker, 2008). However, there have been more than three large-scale debris flows took place in the Tianmo gully at July 25–31 (DF1) and September 5–8 (DF2) of 2010, September 4 of 2007 (DF3) (Ge et al., 2014), and all occurred during summer when temperature generally exceeded 25°C (**Figure 2**). In summer 2020, several fresh debris flows were found in the Tianmo gully (**Figure 1B**), which can be concluded that it is highly likely that thawing can initiate mass movement activity here. To better understand the mechanics of thawing glacial tills, samples were collected from the location shown in **Figure 1C**.

MATERIALS AND METHODS

Physical Properties of Glacial Tills

Sieves and a laser particle size analyzer were used to derive particle size distributions of the till samples. Samples contained poorly graded and sorted, among 24% gravel (4.5 mm < d < 75 mm), 73% sand (0.075 mm < d < 4.5 mm) with a small amount of silt (d < 0.075 mm, nonplastic or very slightly plastic) and clay (d < 0.075 mm, plastic) (ASTM, 2017); The uniformity coefficient (C_u = 21) and the coefficient of curvature (C_c = 0.57) were calculated (**Figure 3**). Other physical properties of the samples are shown in **Table 1**. It should be noted that the maximum dry density of samples is 2.03 g/cm^3, the optimum water content is 8.03%, these values were derived from soil compaction tests which can present different soil properties.

Specimen Preparation

Soil samples were placed in an incubator at 105°C for 6 h. The shear test specimens were prepared with diameters of 61.8 mm and heights of 20 mm. Because the range and size of maximum particle diameters should remain below a 10th of specimen diameter, soil particles were redistributed following the similarity principle of dimensional analysis, samples were passed through a 2 mm standard sieve. (ASTM, 2017). Glacial till samples were prepared and spread evenly on a plastic plate, they were sprayed with de-aired water to increase their gravimetric water contents to the target values (i.e., 8, 12 and 16%, were approached the optimum water content, plastic limit and liquid limit respectively). where the mixtures were kept 1 day for moisture equalization. To obtain uniform specimens, the

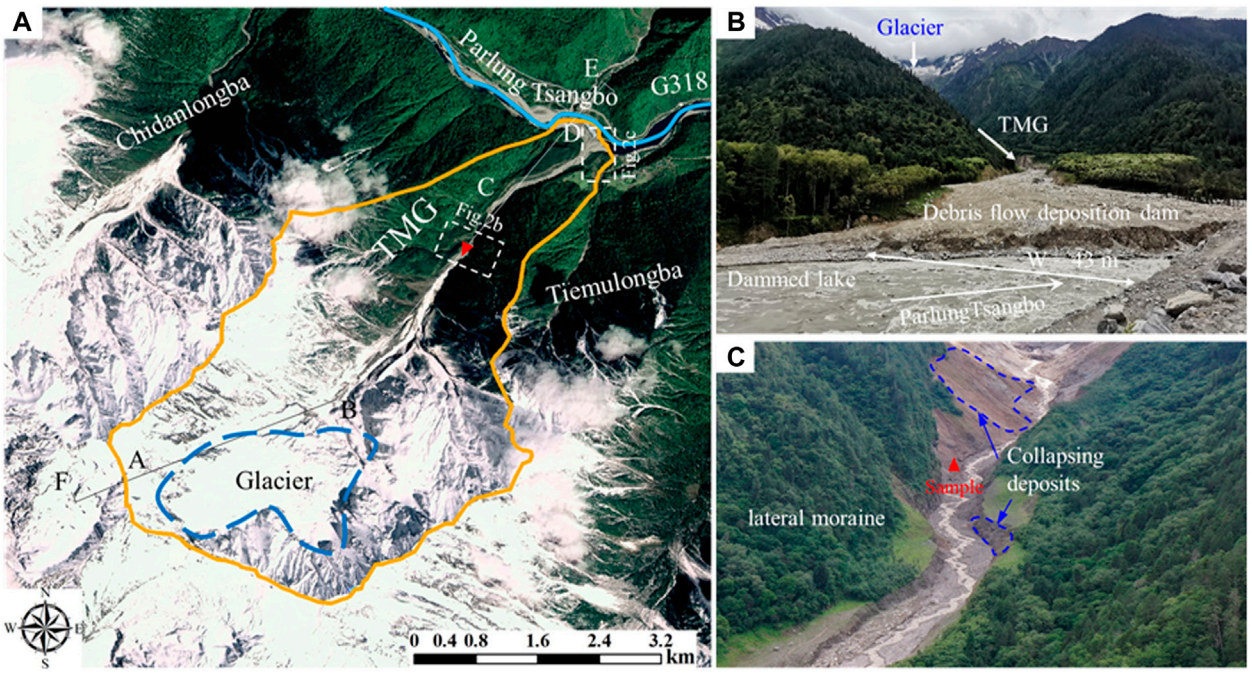

FIGURE 1 | Satellite image of the Tianmo gully **(A)**; The scene of the 2020 debris flow event in Tianmo gully **(B)**; Example of collapsed glacial tills and sample location **(C)**.

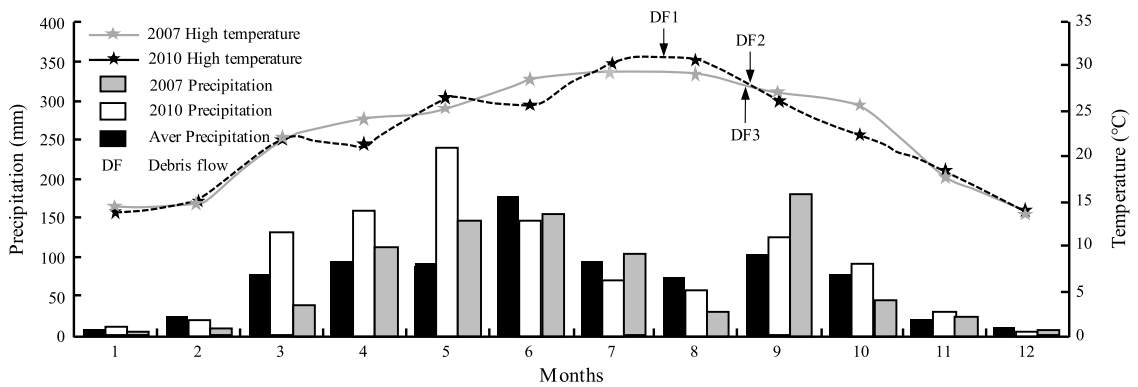

FIGURE 2 | Monthly precipitation and temperature data of Tianmo gully in 2007 and 2010. Data sourced from Ge et al. (2014).

static compaction method was used, the each of the soil specimens were compacted in four layers using a mold. The target dry density of each specimen is 1.70, 1.85 and 2.00 g/cm^3 (it's bound by the maximum dry density), more details are given in **Table 2**.

Water can freeze into solid state (ice) at standard atmospheric pressure when the temperature is at 0 ˚C. Based on the filed investigations and monitoring, the air temperature in high mountain aeras can decrease with elevation at rate of 0.54˚C per 100 m (Deng et al., 2017; Wei et al., 2017). Considering the purpose of the present study, the freezing temperature was selected at –15˚C for 24 h to ensure that the water in all samples can be froze. Based on temperature of debris flows (**Figure 2**), the temperature of thawing phase of experiment were set 25˚C. On the basis of their study of frozen soil specimens, Fu et al. (2021) reported that specimen diameters remained unchanged and all ice had completely converted to liquid water after 4 h of thawing. Therefore, complete thawing was assumed that after 4 h, and used increments of 0.25 h between 0 and 4 h to represent different phases of thawing (t = 0, 0.25, . . . , 3.75, 4 h). Specimens at t = * were not subjected to freeze–thaw action. **Table 2** shows thawing times and preparation details of 18 groups of specimens (t = *, 0, 0.25, . . . , 3.75, 4 h).

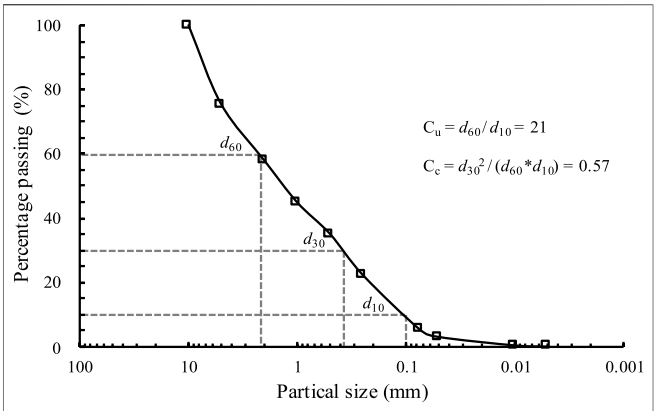

FIGURE 3 | Particle size distributions of glacial till samples.

Direct Shear Tests Plan

Direct shear tests are commonly used to measure soil shear strength. Compared with triaxial tests, direct shear tests can achieve failure in frozen samples in considerably less time (Gan et al., 1988). According to the filed investigations, glacial tills wasting processes are demonstrated to rapid loading/shearing conditions, and the potential water could not immediately move from the sediments. Therefore, the undrained test was normally selected to study the shear behavior in laboratory (Nickling and Bennett, 1984; Wang et al., 2007). To measure uniform residual strength, all shear tests were terminated when horizontal displacement reached 10 mm at a shear rate of 2.4 mm per minute (Jewell, 1989). Considering the glacial tills may fail at different shallow depths (several meters) due to freezing-thawing effects (Ferrick et al., 2005; Kos et al., 2016), four normal stresses (i.e., 50, 100, 150 and 200kPa) were selected to examine the shear behavior and then to determine the strength profile. A total of 648 specimens were tested. Details of the tests and shear strength of the specimens are shown in **Table 2**.

Parameters Characterizing Shear Behavior

Shear tests were performed on till specimens to investigate the effect of thawing time on shear behavior and variations of shear strength and deformation. Stress–strain curves provide important information for the evaluation of till shear behavior, instability, failure and deformation modes (Ling et al., 2007). The peak stress (τ_p), residual stress (τ_r), cohesion (C), and internal friction angle (φ) were measured. The initial elastic modulus (K_i) was used to characterize the stage of shear stress growth (between $\tau = 0$ and $\tau = \tau_p$), and the softening index (I_B) was used to characterize the strain softening that occurred between $\tau = \tau_p$ and $\tau = \tau_r$. Between $\tau = 0$ and $\tau = \tau_0$, the relationship between shear stress and horizontal displacement was linear and the specimen underwent approximately elastic deformation. To characterize the stage of elastic deformation, the elastic coefficient K_i was used, which is the ratio between the initial shear stress at the end of this stage (τ_0) and the corresponding horizontal displacement increment (Δx_0):

$$K_i = \frac{\tau_0}{\Delta x_0} \tag{1}$$

The difference between peak strength and residual strength ($\tau_p - \tau_r$) was used to characterize the stage of plastic deformation, and the softening coefficient I_B to characterize the softening characteristics of the shear process (Yang and Wei 2012):

$$I_B = \frac{\tau_p - \tau_r}{\tau_p} \tag{2}$$

As seen in **Eq. (2)**, if there is a peak stress (τ_p), the range of I_B is between 0 and 1, and the larger the I_B, the more pronounced the softening after the peak.

RESULTS

Shear Behavior and Thawing Time

For all specimens, horizontal displacement (Δx) was less than 3 mm at peak stress and the stage of uniform $\tau_p - \tau_r$ was reached before the end of the tests. A group of samples with same physical state (ρ_d = 2.0 g/cm^3, w = 8%) was selected, shear behavior as shown in **Figure 4**. Specimens with thawing time of t = 0 h softened and contracted considerably; shear strength was considerably lower in specimens with t = 4 h; the largest reduction in shear strength was found in specimens with t = 2 h. Peak stress to displacement ratio (τ/σ) was largest for specimens with t = 0 h (0.857), and smaller for specimens with t = 2 h (0.716), t = 4 h (0.745), and t = * (0.776). These results show that the shear behavior of glacial tills subjected to freeze–thaw action is different from the behavior of tills that have not been subjected to freeze–thaw, which is in agreement with the results of Ferrick and Gatto (2005). More interesting is that our results indicate the shear behavior of glacial tills is affected by thawing time which provides direct experimental evidence for the influence of solid ice on the shear behavior of soil samples.

There were considerable variations of K_i and I_B with thawing time; five phases can be identified from **Figure 5** (Condition of

TABLE 1 | Physical properties of glacial till samples.

Index	Specific gravity *Gs*	Maximum dry density ρ_d (g/cm^3)	Optimum water content w_{opt} (%)	Liquid limit w_l (%)	Plastic limit w_p (%)	Plastic index I_p
value	2.78	2.03	8.03	16.40	12.07	4.33

TABLE 2 | Program and result of direct shear test on glacial till specimens.

Group no	Soil sample no	ρ_d (g/cm³)	w (%)	Specimen preparation	c (kPa)	φ (°)
1	G^*_1-w_8	1.70	8	Without freezing treatment, used for References	0.13	32.14
	G^*_1-w_{12}		12		0.36	31.73
	G^*_1-w_{16}		16		0.54	33.46
	G^*_2-w_8	1.85	8		0.65	32.69
	G^*_2-w_{12}		12		0.72	34.23
	G^*_2-w_{16}		16		0.87	35.27
	G^*_3-w_8	2.00	8		1.29	36.68
	G^*_3-w_{12}		12		1.52	35.83
	G^*_3-w_{16}		16		1.22	35.93
2	G^0_1-w_8	1.70	8	Frozen at -15 °C for 12 h without melting, represents frozen state	5.02	30.09
	G^0_1-w_{12}		12		6.90	29.52
	G^0_1-w_{16}		16		8.58	30.55
	G^0_2-w_8	1.85	8		8.64	30.74
	G^0_2-w_{12}		12		10.00	32.17
	G^0_2-w_{16}		16		10.82	32.73
	G^0_3-w_8	2.00	0		9.75	34.83
	G^0_3-w_{12}		12		8.90	33.78
	G^0_3-w_{16}		16		10.70	33.57
3–18	$G^{0.25}_1$-w_8 ~ G^4_1-w_8	1.70	8	Frozen at -15 °C for 12 h, and melted at 24 °C for 0.25–4 h, represents partly frozen state	2.94–0.13	30.49–32.15
	$G^{0.25}_1$-w_{12} ~ G^4_1-w_{12}		12		4.41~0.36	30.19~31.74
	$G^{0.25}_1$-w_{16} ~ G^4_1-w_{16}		16		5.86~0.54	31.29–33.48
	$G^{0.25}_2$-w_8 ~ G^4_2-w_8	1.85	8		6.23~0.66	31.10–32.71
	$G^{0.25}_2$-w_{12} ~ G^4_2-w_{12}		12		7.79~0.72	32.68–34.29
	$G^{0.25}_2$-w_{16} ~ G^4_2-w_{16}		16		8.52~0.87	33.44–35.28
	$G^{0.25}_3$-w_8 ~ G^4_3-w_8	2.00	8		7.50~1.30	35.12~36.72
	$G^{0.25}_3$-w_{12} ~ G^4_3-w_{12}		12		6.54~1.53	34.24~35.86
	$G^{0.25}_3$-w_{16} ~ G^4_3-w_{16}		16		7.31~1.23	34.26~35.95

G^t_{pd}: glacial tills, subscript represents dry density, superscript represents melting time (refers to non-freeze-thaw samples), t: short-term thawing time; ρ_d: dry density; w: initial water content of sample preparation; c: Cohesion; φ: Internal friction angle.*

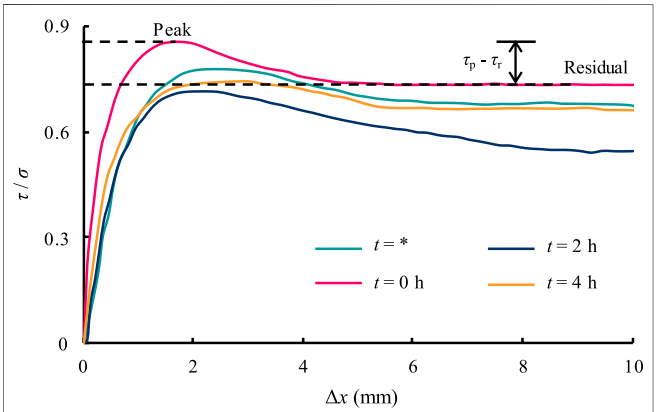

FIGURE 4 | The shear stress—displacement curve of samples under different thawing time.

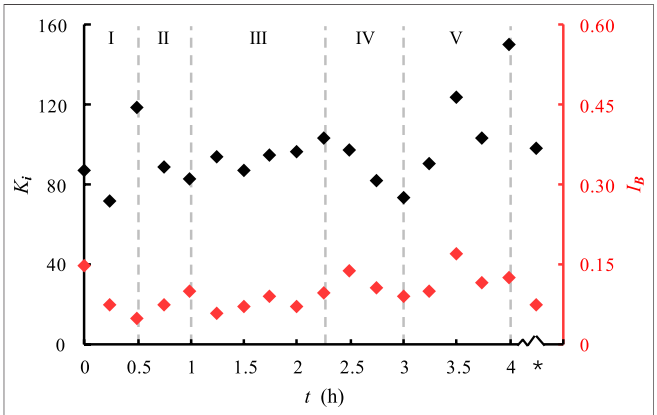

FIGURE 5 | The relationship of K_i, I_B with thawing time.

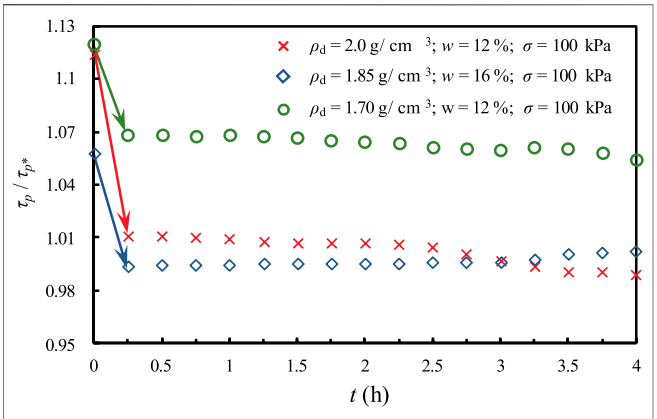

FIGURE 6 | Shear strength with short-term thawing time.

the samples: ρ_d = 1.85 g/cm^3, w = 16%, σ = 100 kPa). Using K_i as a measure of the resistance of specimens to elastic deformation, a large K_i indicates high stiffness and large variations of shear stress per unit horizontal displacement increment. In stage I, the ability of glacial tills to resist elastic deformation increases with the decrease of ice content because solid ice prevents the specimen from recovering from deformation. For stages I, III, IV and V, the relationship between I_B and t and that between K_i and t follow similar trends. Softening was minimal for specimens with t = 0.5 h, which implies the movement of ice particles into the soil skeleton during initial thawing; as a result, the structure of the specimens becomes more unstable. These findings suggest that the shear behavior of thawing samples is affected by the combined action of ice and water and varies with thawing time.

Using experimental results, the hypothesis is tested that shear behavior of specimens with t = 4 h is similar to that of specimens that have not been subjected to freeze–thaw action (t = *). One possible reason is that solid ice affects the arrangement of soil particles. Specimens that are subjected to freeze–thaw action are more compact at the early stage of loading, and are therefore more resistant to shear. However, under freeze–thaw action, solid ice forms and disappears rapidly. As a result, the arrangement of soil particles within the specimens become more random (Atkinson and Little, 1988) and specimens become less resistant to shear deformation as loading continues and shear stress increases.

Relationship Between Peak Strength and Thawing Time

The variation of the strength of thawing soil samples can be considered as a quasi-dynamic transition. As shown in **Figure 6**, the variation of τ_p/τ_{p^*} with thawing time for the different series of experiments. Peak strengths of specimens not subjected to freeze–thaw action (τ_{p^*}) were used as the reference value, and our main observations are as follows:

a) Peak shear strengths of specimens with t = 0 h were considerably higher than peak shear strengths of specimens with any other thawing time. This indicates that high ice content was associated with high shear strength.
b) Shear strengths of specimens with t = 0.25 h were considerably lower than those of specimens with t = 0 h. Specimens with t = 0.25–4 h had similar peak strengths. This indicates that thawing of solid ice at the beginning of the thawing process is the key factor that controls peak strengths; its impact on peak strength is greater than the combined impact of loading and the physical characteristics of the specimen.
c) Peak strengths decreased with increasing thawing time for some specimens with $t \geq$ 0.25 h, and increased with increasing thawing time in others. This suggests that the shear strength of thawing specimens is not controlled by a single universal factor.

To examine the effects of different stages of thawing on the attainable shear strength of glacial tills, thawing time as a quantitative test was used control to represent different stages of thawing and also of the transformation of solid ice. It is shows that the relationship between peak strength and thawing time at initial thawing stage is little or not affected independent of loading conditions and the physical characteristics of the specimens.

However, these results show that except for the initial thawing stage, shear strength at different thawing times may be controlled by dry density and water content. Water content (w) is a measure of the liquid water content of ice particles and dry density (ρ_d) is a measure of the water channels in the thawing specimen (Ladanyi and Morel, 1990). As shown in **Figure 7**, it normalized total normal stress, the relationship between shear strength and dry density and water content of unthawed (t = 0 h) and thawed state (t = 4 h) is presented. For unthawed specimens (t = 0 h), peak strength increased with increasing w for specimens with ρ_d of 2.00 g/cm^3, and decreased with increasing w for specimens with ρ_d of 1.70 and 1.85 g/cm^3. However, for all thawed specimens (t = 4 h), peak strengths decreased with increasing w. It can be found that the shear strength decreases with the increase of water content when the dry density is 2.00 g/cm^3 in both states.

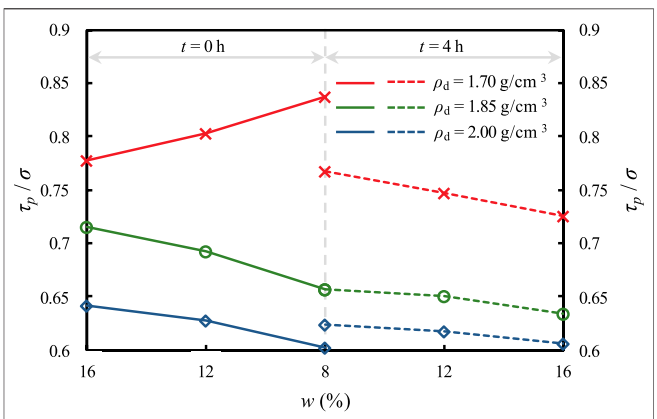

FIGURE 7 | Effect of dry density and water content on shear strength under different thawing conditions.

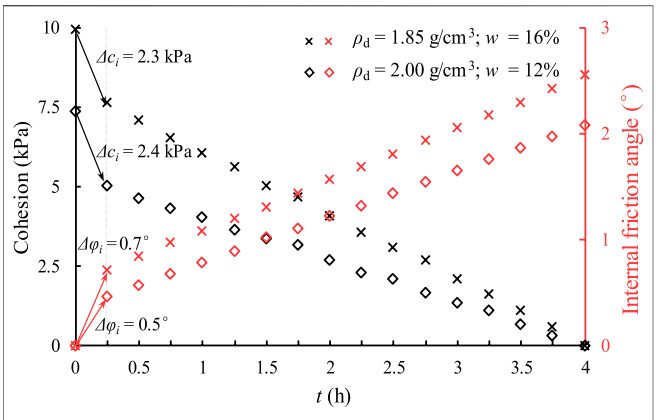

FIGURE 8 | Cohesion and Internal friction angle with thawing time.

Hence, the amount of contact between soil particles is determined by dry density and affects the bonding of solid ice. In addition, further analysis of the variation trend of ρ_d at 1.70 and 1.85 g/cm^3 in t = 0 h and t = 4 h can be obtained the shear strength of frozen soils can be increased by increasing initial water content in loose soils. It's not hard to understand there is little or no water transfer within the internal pore structure of frozen samples theoretically (Burt and Williams, 1976), which can be inferred the looser the soil sample, the greater the effect of solid ice.

Effect of Short-Term Thawing on Shear Strength

In addition to shear strength, other parameters are needed to characterize soil shear behavior (Arenson and Springman, 2005a). While experiments have established the effect of solid ice on shear strength, the effects of cohesion 3) and internal friction angle (φ) on shear strength are less clear. In thawing soils, the relationship between peak stress, cohesion, normal stress and angle of friction are as follows:

$$\tau_p = c - \sigma \tan \varphi \tag{3}$$

There are also films of unfrozen water in the soil (Chamberlain and Gow, 1979); therefore, the cohesion (c_i) and internal friction angle (φ_i) exerted by solid ice at different thawing times can be rewritten as:

$$c_{ik} = c_k - c_* \tag{4}$$

$$\varphi_{ik} = \varphi_k - \varphi_0 \tag{5}$$

where c_* is the cohesion of the soil sample itself, φ_0 refers to the internal friction of the sample before thawing (i.e., t = 0 h), and k = 1, 2, . . . , 17, 18 corresponds to t_i = 0 h, 0.25 h, . . . , 3.75 h, 4 h; c_* represents the unique condition of each frozen soil sample.

Cohesion is the shear strength without any normal stress on the shear failure surface and is the result of the combined action of gravitational attraction and repulsion between soil particles (Seo et al., 2004). Glacial tills have the characteristics of sand; they generally have no cohesion or a weak false cohesive force (Zhou et al., 2019). However, the black symbols in **Figure 8** indicate that the highest c_i was reached at 9.95 kPa and t = 0 h. Cementation ice formed by *in situ* freezing of liquid water can significantly increase the proportion of cohesive strength in the shear strength of frozen glacial till specimens (Sterpi, 2015). Moreover, for specimens with $t \geq 0.25$ h, c_i decreased linearly with increasing thawing time.

The red symbols in **Figure 9** indicate the variation of internal friction angle with thawing time. Least square linear regression shows that, for specimens with $t \geq 0.25$ h, φ_i increased linearly with thawing time; this result is consistent with the findings of Nater et al. (2015). However, liquid water reduces the friction between soil particles, and an exponential relationship between the internal friction angle and ice content ignores the effect of films of unfrozen water on the friction between soil particles.

For specimens with t = 0.25 h (gray dashed line in **Figure 8**), maximum friction was 2.58°, which was far below the value of cohesion. This suggests that the effects of frozen water and ice on cohesion are stronger at the initial phase of thawing, and that the effect of ice on soil friction and cohesion is stronger in loose soils.

These results show that the cohesion of glacial till specimens decreases considerably with increasing thawing time. They support the hypothesis that the self-perpetuating destruction of thawing soils depends on the short-term destruction of ice bonding (Arenson and Springman, 2005a). This mechanism could explain the frequent sediment recharge of gullies, although interactions between ice and soil particles can only be used as qualitative approximations of the soil mechanics of natural slopes.

DISCUSSION

Shear strength of thawing soils indicate that thawing evolves with time. Therefore, it is necessary to examine the mechanisms of phase transformation of solid ice. Unfrozen water, ice, and frozen water change phase as temperature reaches the melting point. **Figure 9** shows the four typical states of thawing soils.

In frozen soils, individual soil grains may not be in contact with one other (**Figure 9A**). The main form of ice is the ice body; it has a relatively stable structure because of the tetrahedral arrangement of molecules (Liu and Peng, 2009). The soil skeleton comprises the ice body and soil grains, which increase shear resistance (Özgan et al., 2015). Friction contributes little to shear resistance, and shear strength mainly comes from cohesion. The experimental results show that the largest amount of softening and the highest peak strength occurred in specimens with t = 0 h (**Figure 4**); this could be an explanation of the control of shear resistance and strength of frozen soils by cohesion at the particle scale.

After initial thawing, ice volume decreases; the ice body transforms into ice crystals with broken hydrogen bonds between the ice molecules; liquid water is absent (**Figure 9B**). The soil skeleton is ruptured and reduced in volume. Soil grains are in contact with ice crystals. Friction increases while cohesive bonding decreases; there are large increases in internal friction angle and large decreases in cohesion (**Figure 8**). The ice body and soil particles form an integrated whole, which has a higher resistance to deformation

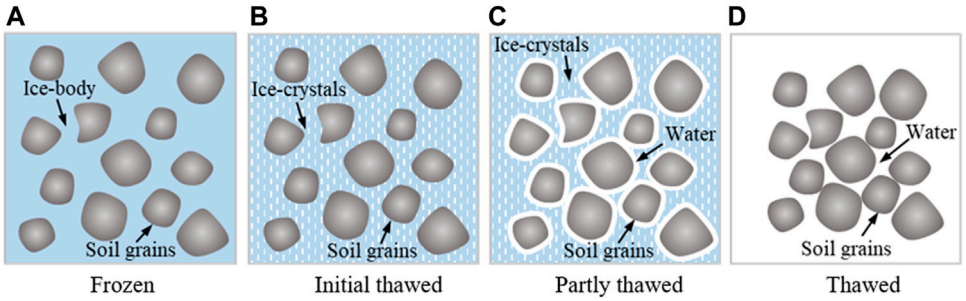

FIGURE 9 | Different states in frozen specimens during thawing. **(A)** Frozen state; **(B)** initial thawed state; **(C)** Partly thawed state; **(D)** Thawed state.

than soils comprising ice crystals and soil particles (Ewertowski and Tomczyk, 2015). During this stage, the ice body transforms into ice crystals in discrete steps, and soil structure is unstable.

In partly thawed soils, both ice crystals and unfrozen water are present in the voids between particles; soil grains are surrounded by films of unfrozen water, which are in contact with one another (**Figure 9C**) (Arenson and Springman, 2005a). Ice molecules break apart to form water substructures with reduced order. Ice bonding weakens and lubrication by liquid water increases; as a result, cohesion decreases and granular friction increases. Partly thawed soils have increased shear resistance and the corresponding horizontal displacement under a given level of stress also increases (i.e., shear behavior at t = 2 h in **Figure 4**).

In thawed soils, all pore water is in the liquid phase and ice is absent (**Figure 9D**) (Ladanyi and Morel, 1990); there is little order in the spatial distribution of water molecules, and is similar to the arrangement of any conventional unfrozen soils (Fredlund et al., 1978). However, thawed soils also differ from unfrozen soils; the transition from frozen to thawed soil changes pore structure, and allows full contact between soil grains (Nater et al., 2015). Over the long term, ice bonding completely disappears from drained thawed soils. Glacial tills are widely distributed in alpine environments. Therefore, it is likely that there is zero cohesion in drained soils under extremely high temperatures. Moreover, a larger sliding friction is needed to resist shear deformation and gives rise to a peak internal friction angle (**Figure 8**).

The thawing of frozen soils typically includes the breaking up of the ice body, thawing of ice crystals, formation of films of unfrozen water, and contact between soil grains facilitated by liquid water. This process gives rise to the shear deformation of the glacial till specimens that was observed in our experiments. The morphological changes and phase transformation of solid ice affect the mechanical behavior of thawing soils over time. The amount of solid ice decreases and the amount of liquid water increases with increasing thawing time and affect shear strength. Changes in cohesion and friction vary with thawing time.

CONCLUSION

In this study, the experiments were conducted to examin the role of thawing on the mechanical properties of glacial tills. Direct shear tests were performed on till specimens with three different dry densities and three different initial water contents after 18 thawing times. Our primary findings are as follows:

a) Shear softening decreases with increasing thawing time. The difference between peak and critical resistances decreases with increasing thawing time and reflects changes in shear behavior. Dry density can enhance shear strength. However, in soils with high density, initial water content may result in the decrease of shear strength.
b) Shear strength decreases considerably after initial thawing time. Decrease is larger in soils with higher initial water content. For loose soils, shear strength increases with increasing initial water content.
c) In accordance with the Mohr–Coulomb theory, the internal friction angle increases and cohesion decreases with increasing thawing time. This indicates that the cemented ice formed by *in situ* freezing of water can significantly improve the cohesive component of the shear strength of frozen soils.
d) Completely frozen soils are more stable than partly thawed or unfrozen soils. Partly thawed soils are less stable than frozen or unfrozen soils because they are made up of ice crystals that have low resistance to deformation. This analysis depicted changes in ice and intergranular contact modalities and mechanisms with thawing time, and provides a useful framework to understand variations in the shear behavior of glacial tills.

DATA AVAILABILITY STATEMENT

The raw data supporting the conclusion of this article will be made available by the authors, without undue reservation.

AUTHOR CONTRIBUTIONS

YF performed the tests and wrote this manuscript. YJ contributed to the conceptualization, supervision and funding acquisition. JW carried out the field investigation. ZL and XL reviewed and edited

the manuscript. All authors listed have contributed sufficiently to the project to be included as authors, and all those who are qualified to be authors are listed in the author byline.

FUNDING

This study was funded by the Chinese Academy of Sciences Grant (No. QYZDY-SSW-DQC006), by the National Nature Science Foundation of China Grants (Nos. U20A20112, 41807278). A special acknowledgement should be expressed to China-Pakistan Joint Research Center on Earth Sciences that supported the implementation of this work. YJ acknowledges support from the CAS Pioneer Hundred Talents.

ACKNOWLEDGMENTS

We thank the reviewers and editor for their helpful and constructive reviews that improved this paper.

REFERENCES

Arenson, L. U., and Springman, S. M. (2005a). Mathematical Descriptions for the Behaviour of Ice-Rich Frozen Soils at Temperatures Close to 0 °C. *Can. Geotech. J.* 42 (2), 431–442. doi:10.1139/t04-109

Arenson, L. U., and Springman, S. M. (2005b). Triaxial Constant Stress and Constant Strain Rate Tests on Ice-Rich Permafrost Samples. *Can. Geotech. J.* 42 (2), 412–430. doi:10.1139/t04-111

ASTM (2017). *Standard Practice for Classification of Soils for Engineering Purposes (Unified Soil Classification System)*. ASTM standard D2487- 17. West Conshohocken, Pennsylvania: American Society for Testing Materials.

Atkinson, J. H., and Little, J. A. (1988). Undrained Triaxial Strength and Stress-Strain Characteristics of a Glacial till Soil. *Can. Geotech. J.* 25 (3), 428–439. doi:10.1139/t88-048

Burt, T. P., and Williams, P. J. (1976). Hydraulic Conductivity in Frozen Soils. *Earth Surf. Process.* 1 (4), 349–360. doi:10.1002/esp.3290010404

Chamberlain, E., Groves, C., and Perham, R. (1972). The Mechanical Behaviour of Frozen Earth Materials under High Pressure Triaxial Test Conditions. *Géotechnique* 22 (3), 469–483. doi:10.1680/geot.1972.22.3.469

Chamberlain, E. J., and Gow, A. J. (1979). Effect of Freezing and Thawing on the Permeability and Structure of Soils. *Eng. Geology.* 13 (14), 73–92. doi:10.1016/b978-0-444-41782-4.50012-9

Cossart, E., Mercier, D., Decaulne, A., Feuillet, T., Jónsson, H. P., and Saemundsson, Þ. (2014). Impacts of post-glacial Rebound on Landslide Spatial Distribution at a Regional Scale in Northern Iceland (Skagafjörður). *Earth Surf. Process. Landforms* 39 (3), 336–350. doi:10.1002/esp.3450

Cui, P., Deng, H.-Y., Wang, C.-H., et al. (2018). *Mountain Hazards*. Beijing, China: Higher Education Press, pp189–216. (In Chinese).

Czurda, K. A., and Hohmann, M. (1997). Freezing Effect on Shear Strength of Clayey Soils. *Appl. Clay Sci.* 12 (1-2), 165–187. doi:10.1016/s0169-1317(97)00005-7

Deng, M., Chen, N., and Liu, M. (2017). Meteorological Factors Driving Glacial till Variation and the Associated Periglacial Debris Flows in Tianmo Valley, South-Eastern Tibetan Plateau. *Nat. Hazards Earth Syst. Sci.* 17 (03), 345–356. doi:10.5194/nhess-17-345-2017

Eskişar, T., Altun, S., and Kalıpcılar, İ. (2015). Assessment of Strength Development and Freeze-Thaw Performance of Cement Treated Clays at Different Water Contents. *Cold Regions Sci. Tech.* 111 (mar), 50–59. doi:10.1016/j.coldregions.2014.12.008

Ewertowski, M. W., and Tomczyk, A. M. (2015). Quantification of the Ice-Cored Moraines' Short-Term Dynamics in the High-Arctic Glaciers Ebbabreen and Ragnarbreen, Petuniabukta, Svalbard. *Geomorphology* 234 (apr.1), 211–227. doi:10.1016/j.geomorph.2015.01.023

Ferrick, M. G., and Gatto, L. W. (2005). Quantifying the Effect of a Freeze-Thaw Cycle on Soil Erosion: Laboratory Experiments. *Earth Surf. Process. Landforms* 30 (10), 1305–1326. doi:10.1002/esp.1209

Fredlund, D. G., Morgenstern, N. R., and Widger, R. A. (1978). The Shear Strength of Unsaturated Soils. *Can. Geotech. J.* 15 (3), 313–321. doi:10.1139/t78-029

Fu, Y., Liu, Z., and Jiang, Y. (2021). *Effect of Short-Term Thawing on the Mechanical Properties of Frozen Glacial Tills, EGU General Assembly, Online, 19-30 Apr 2021*. doi:10.5194/egusphere-egu21-12139

Gan, J. K. M., Fredlund, D. G., and Rahardjo, H. (1988). Determination of the Shear Strength Parameters of an Unsaturated Soil Using the Direct Shear Test. *Can. Geotech. J.* 25 (3), 500–510. doi:10.1139/t88-055

Ge, Y. G., Cui, P., Su, F. H., Zhang, J. Q., and Chen, X. Z. (2014). Case History of the Disastrous Debris Flows of Tianmo Watershed in Bomi County, Tibet, China: Some Mitigation Suggestions. *J. Mountain Sci.* 11 (05), 1253–1276. doi:10.1007/s11629-014-2579-2

Hivon, E. G., and Sego, D. C. (1995). Strength of Frozen saline Soils. *Can. Geotech. J.* 32 (2), 336–354. doi:10.1139/t95-034

Huggel, C., Clague, J. J., and Korup, O. (2012). Is Climate Change Responsible for Changing Landslide Activity in High Mountains? *Earth Surf. Process. Landforms* 37 (1), 77–91. doi:10.1002/esp.2223

Jewell, R. A. (1989). Direct Shear Tests on Sand. *Géotechnique* 39 (2), 309–322. doi:10.1680/geot.1989.39.2.309

King, G. E., Herman, F., and Guralnik, B. (2016). Northward Migration of the Eastern Himalayan Syntaxis Revealed by OSL Thermochronometry. *Science* 353 (6301), 800–804. doi:10.1126/science.aaf2637

Konrad, J.-M. (2010). Hydraulic Conductivity Changes of a Low-Plasticity till Subjected to Freeze-Thaw Cycles. *Géotechnique* 60 (09), 679–690. doi:10.1680/geot.08.P.020

Konrad, J.-M., and Morgenstern, N. R. (1980). A Mechanistic Theory of Ice Lens Formation in fine-grained Soils. *Can. Geotech. J.* 17 (04), 473–486. doi:10.1139/t80-056

Kos, A., Amann, F., Strozzi, T., Delaloye, R., Ruette, J., and Springman, S. (2016). Contemporary Glacier Retreat Triggers a Rapid Landslide Response, Great Aletsch Glacier, Switzerland. *Geophys. Res. Lett.* 43 (24), 12466–12474. doi:10.1002/2016GL071708

Ladanyi, B., and Morel, J.-F. (1990). Effect of Internal Confinement on Compression Strength of Frozen Sand. *Can. Geotech. J.* 27 (1), 8–18. doi:10.1139/t90-002

Lai, Y., Li, S., Qi, J., Gao, Z., and Chang, X. (2008). Strength Distributions of Warm Frozen clay and its Stochastic Damage Constitutive Model. *Cold Regions Sci. Tech.* 53 (2), 200–215. doi:10.1016/j.coldregions.2007.11.001

Ling, H.-I., Callisto, L., Leshchinsky, D., and Koseki, J. (2007). Soil Stress-Strain Behavior: Measurement, Modeling and Analysis. *Solid Mech. Its Appl.* 146 (5), 83–93. doi:10.1007/978-1-4020-6146-2

Liu, J.-K., and Peng, L.-Y. (2009). Experimental Study on the Unconfined Compression of a Thawing Soil. *Cold Regions Sci. Tech.* 58 (1-2), 92–96. doi:10.1016/j.coldregions.2009.03.008

Moore, P. L. (2014). Deformation of Debris-Ice Mixtures. *Rev. Geophys.* 52 (3), 435–467. doi:10.1002/2014rg000453

Nater, P., Arenson, L. U., and Springman, S. M. (2015). *Choosing Geotechnical Parameters for Slope Stability Assessments in Alpine Permafrost Soils*. Alaska, America: Ninth International Conference on Permafrost, 1260–1266.

Nickling, W. G., and Bennett, L. (1984). The Shear Strength Characteristics of Frozen Coarse Granular Debris. *J. Glaciol.* 30 (106), 348–357. doi:10.1017/S0022143000006201 10.3189/s0022143000006201

Nie, Y., Pritchard, H. D., Liu, Q., Hennig, T., Wang, W., Wang, X., et al. (2021). Glacial Change and Hydrological Implications in the Himalaya and Karakoram. *Nat. Rev. Earth Environ.* 2, 91–106. doi:10.1038/s43017-020-00124-w

Özgan, E., Serin, S., Ertürk, S., and Vural, I. (2015). Effects of Freezing and Thawing Cycles on the Engineering Properties of Soils. *Soil Mech. Found. Eng.* 52 (2), 95–99. doi:10.1007/s11204-015-9312-1

Sayles, F. H., and Carbee, D. L. (1981). Strength of Frozen silt as a Function of Ice Content and Dry Unit Weight. *Eng. Geology.* 18 (1-4), 55–66. doi:10.1016/0013-7952(81)90046-6

Schomacker, A. (2008). What Controls Dead-Ice Melting under Different Climate Conditions? A Discussion. *Earth-Science Rev.* 90 (3-4), 103–113. doi:10.1016/j.earscirev.2008.08.003

Seo, M. W., Park, I. J., and Park, J. B. (2004). Development of Displacement-Softening Model for Interface Shear Behavior between Geosynthetics. *Soils and Foundations* 44 (6), 27–38. doi:10.3208/sandf.44.6_27

Sterpi, D. (2015). Effect of Freeze-Thaw Cycles on the Hydraulic Conductivity of a Compacted Clayey silt and Influence of the Compaction Energy. *Soils and Foundations* 55 (5), 1326–1332. doi:10.1016/j.sandf.2015.09.030

Ting, J. M., Torrence Martin, R., and Ladd, C. C. (1983). Mechanisms of Strength for Frozen Sand. *J. Geotech. Engrg.* 109 (10), 1286–1302. doi:10.1061/(asce)0733-9410(1983)109:10(1286)

Vanapalli, S. K., and Han, Z. (2016). Modelling the Mechanical Properties of a Compacted Glacial till. *Indian Geotech J.* 46 (3), 261–271. doi:10.1007/s40098-016-0183-9

Viklander, P. (1998). Permeability and Volume Changes in till Due to Cyclic Freeze-Thaw. *Can. Geotechnical J.* 35 (03), 471–477. doi:10.1139/cgj-35-3-47110.1139/t98-015

Wang, H., Cui, P., Liu, D., Liu, W., Bazai, N. A., Wang, J., et al. (2019). Evolution of a Landslide-Dammed lake on the southeastern Tibetan Plateau and its Influence on River Longitudinal Profiles. *Geomorphology* 343, 15–32. doi:10.1016/j.geomorph.2019.06.023

Wang, J., Dove, J. E., and Gutierrez, M. S. (2007). Discrete-continuum Analysis of Shear Banding in the Direct Shear Test. *Géotechnique* 57 (6), 513–526. doi:10.1680/geot.2007.57.6.513

Wei, R., Zeng, Q., Davies, T., Yuan, G., Wang, K., Xue, X., et al. (2018). Geohazard cascade and Mechanism of Large Debris Flows in Tianmo Gully, SE Tibetan Plateau and Implications to hazard Monitoring. *Eng. Geology.* 233, 172–182. doi:10.1016/j.enggeo.2017.12.013

Yang, J., and Wei, L. M. (2012). Collapse of Loose Sand with the Addition of Fines: the Role of Particle Shape. *Géotechnique* 62 (12), 1111–1125. doi:10.1680/geot.11.p.062

Yao, T., Thompson, L., Yang, W., Yu, W., Gao, Y., Guo, X., et al. (2012). Different Glacier Status with Atmospheric Circulations in Tibetan Plateau and Surroundings. *Nat. Clim Change* 2 (09), 663–667. doi:10.1038/nclimate1580

Zhang, L., Ma, W., Yang, C., and Yuan, C. (20142014). Investigation of the Pore Water Pressures of Coarse-Grained sandy Soil during Open-System Step-Freezing and Thawing Tests. *Eng. Geology.* 181, 233–248. doi:10.1016/j.enggeo.2014.07.020

Zhou, G. G. D., Chen, L.-L., Mu, Q.-Y., Cui, K. F. E., and Song, D.-r. (2019). Effects of Water Content on the Shear Behavior and Critical State of Glacial till in Tianmo Gully of Tibet, China. *J. Mt. Sci.* 16 (8), 1743–1759. doi:10.1007/s11629-019-5440-9

Zimmermann, M., and Haeberli, W. (1992). Climatic change and debris flow activity in highmountain areas. *Catena supplement* 22 (1), 59–72. doi:10.1016/j.atherosclerosis.2015.04.310

Conflict of Interest: The authors declare that the research was conducted in the absence of any commercial or financial relationships that could be construed as a potential conflict of interest.

Publisher's Note: All claims expressed in this article are solely those of the authors and do not necessarily represent those of their affiliated organizations, or those of the publisher, the editors and the reviewers. Any product that may be evaluated in this article, or claim that may be made by its manufacturer, is not guaranteed or endorsed by the publisher.

frontiers in Earth Science

ORIGINAL RESEARCH
published: 22 December 2021
doi: 10.3389/feart.2021.799742

Influences of Spillway Section Morphologies on Landslide Dam Breaching

Meng Yang[1], *Qiming Zhong*[1,2]*, *Shengyao Mei*[1] *and Yibo Shan*[1]

[1]Department of Geotechnical Engineering, Nanjing Hydraulic Research Institute, Nanjing, China, [2]Key Laboratory of Reservoir Dam Safety of the Ministry of Water Resources, Nanjing, China

Spillway excavation is often adopted as a precautionary engineering measure for disaster mitigation before landslide dam breaching. Based on the landslide dam breach mechanisms, this paper focuses on developing a numerical model to comprehensively discuss the issue based on three documented landslide dam failures, such as Tangjiashan, Xiaogangjian, and Baige landslide dams. The spillway cross section morphologies were modeled with different sizes under common shape (i.e., an inverted trapezoid) and slope conditions. The influence of cross section on dam breach processes was analyzed under conditions of different depth, bottom width, slope ratio in the cross and longitudinal sections, with/without spillway. The following conclusions can be drawn: 1) excavation of a spillway can effectively reduce the peak breach flow, therefore delay the time to peak; 2) the peak breach flow dramatically decreases and the time to peak delays as the spillway depth increases; 3) the peak breach flow changes little and the time to peak occurs earlier with the increment in spillway bottom width; 4) the peak breach flow decreases and the time to peak delays with the decrease of slope ratio in cross section in the spillway; 5) the slope ratio in the longitudinal section has little influence on the breach process. Hence, if conditions permit, the spillway with large spillway depth, small bottom width, and gentle slope ratio in the cross section is the preferable section morphology for the emergency disposal of the landslide dam.

Keywords: landslide dam breaching, spillway, section type, numerical simulation, comparative analysis, risk mitigation

OPEN ACCESS

Edited by:
Dongri Song,
Institute of Mountain Hazards and Environment (CAS), China

Reviewed by:
Ming Peng,
Tongji University, China
Gang Fan,
Sichuan University, China

***Correspondence:**
Qiming Zhong
qmzhong@nhri.cn

Specialty section:
This article was submitted to Geohazards and Georisks, a section of the journal Frontiers in Earth Science

Received: *22 October 2021*
Accepted: *02 December 2021*
Published: *22 December 2021*

Citation:
Yang M, Zhong Q, Mei S and Shan Y (2021) Influences of Spillway Section Morphologies on Landslide Dam Breaching. Front. Earth Sci. 9:799742. doi: 10.3389/feart.2021.799742

INTRODUCTION

Landslide dam is formed by mass movements of rock and debris blocking the river channel due to earthquakes and intense rainfall (Costa and Schuster, 1988); **Figure 1** presents the Hongshiyan landslide dam that occurred on August 3rd, 2014 in China. The landslide dam stability is usually related to grain-size distribution of landslide debris, landslide volume, and hydrodynamic conditions (Liao et al., 2019; Shan et al., 2020; Peng et al., 2021). Dissimilar to artificial dams, landslide dams do not have a structure that enables flood discharge (Zhong et al., 2021). The water level in the dammed lake increases eventually after the landslide dam formation due to the continuous inflow from the upstream; hence, overtopping is the most common cause of failure mode for the dam (Zhong et al., 2018).

The failure of a landslide dam may pose a tremendous threat to human life and property in the downstream region; hence, risk mitigation of landslide dam failure has significant implications for socio-economic development. The risk mitigation measures for landslide dams can be categorized

FIGURE 1 | Hongshiyan landslide dam in China.

into engineering and non-engineering. Non-engineering measures include warning and evacuation of people in the risk area, whilst engineering measures consist of reducing the landslide dam height or/and the reservoir of the dammed lake to minimize downstream hazards. In general, engineering measures are usually taken immediately, if conditions permit, to prevent the water level from reaching dangerous elevation and to reduce the reservoir capacity. In the current situation, commonly used engineering measures are basically the construction of drainage tunnels through abutments, installing drainage conduits, and excavating spillways through dams (Schuster and Evans, 2011; Peng et al., 2014) (**Figure 2**). Constructing a drainage tunnel is usually expensive and time-consuming, and also the transportation of apparatuses and materials requires certain external conditions to be provided. Installing a drainage conduit is less affordable and more effortless than constructing a drainage tunnel; however, it has a relatively lower discharge capacity; nevertheless, it is often used to deal with landslide dams with a small reservoir. In contrast to other methods, excavating a spillway is a more efficient way to prevent the rising water level and reduce the storage capacity, which does not require complex external conditions and is relatively convenient to construct; hence, it has become forward as the most common engineering measure for the risk mitigation of landslide dams (Peng et al., 2014).

In the literature, there are several applicable cases regarding the excavation of spillways through landslide dams that have been utilized in risk mitigation. On April 25th, 1974, a large landslide with a total volume of 1,000–1,300 × 106 m^3 took place in Mayumarca Valley, Peru, and then a landslide dam formed with the volume of about 800 × 106 m^3; the dammed lake was about 32 km long and contained the reservoir over 670 × 106 m^3 (Berrocal et al., 1978). To minimize the potential flood damage, a spillway with 3 m depth and 250 m length was excavated (Cai et al., 2021). On April 9th, 2000, a huge rock avalanche occurred at the Yigong Village of Tibet (Shang et al., 2003), formed landslide debris transported 8–10 km with high velocity, and completely blocked the Yigong Zangpo River. The length, width, and height of the landslide dam were 2.5 km, 2.5 km, and 60–110 m, respectively. Subsequently, a spillway with 30 m depth and 30 m bottom width was excavated before dam breaching, which significantly reduced the reservoir of dammed lake. Furthermore, 37 high-risk landslide dams formed by the Wenchuan Earthquake in 2008, China, were eliminated through excavating spillways (Cui et al., 2009; Yin et al., 2009; Peng et al., 2014).

The most crucial consideration for spillway excavation is efficiently reducing the maximum storage capacity of dammed lake and the breach flow discharge to mitigate the disaster in the downstream area. The majority of the landslide dams are formed in the mountainous regions with restricted transportation and breached within a short time. As a consequence, it is vital to completely consider the rate of rising of the water level in the dammed lake, the limitations of the construction conditions, and the discharge capacity of the downstream river channel, and to optimize the design of the spillway section morphology.

The current study offers a novel numerical model developed by the authors to quantitatively compare the breach hydrograph and breach size evolution process for each spillway section morphology. It is worth mentioning that, in this study, the cross section of spillway is specified as an inverted trapezoid in the numerical modeling due to the challenge in excavating the compound spillway and other section morphologies within a restricted time frame in reality (**Figure 3**). In the following sections, a brief introduction on the breach mechanisms and numerical model developed by the authors are presented. The influences on the landslide breach process under the conditions of different depth, bottom width, slope ratio in the cross and longitudinal sections, with/without spillway were comprehensively discussed.

FIGURE 2 | Engineering measures for landslide dam risk mitigation.

BREACH MECHANISMS AND PROCESSES OF OVERTOPPING-INDUCED LANDSLIDE DAMS' BREACHING

Until recently, numerous model tests on landslide dam breaching have been conducted, such as small-scale flume model tests (Yang et al., 2015; Zhou et al., 2019; Zhu et al., 2021), large-scale field model tests (Li et al., 2021; Takayama et al., 2021; Zhang et al., 2021), centrifugal model tests (Zhao et al., 2019), and *in-situ* measurements (Liu et al., 2010; Cai et al., 2020). Although different classification techniques existed in the division of the landslide dam breach process, the outburst process as a whole can be divided into three stages: initiation, acceleration, and stabilization. Further, the phenomenon of backward erosion is founded in the initiation stage; the acceleration stage occurs after the backward erosion enters the upstream dammed lake. The stabilization stage occurs when the inflow and outflow rates are balanced. Admittedly, the large-scale landslide dam breach model tests were only performed on the dam with a height of 1 m to several meters. Hence, due to the scale effect, the model tests have the following disadvantages: 1) the material composition of landslide dam deposits is relatively uniform, and the particle size of materials is considerably smaller than the actual situation. 2) The majority of the model tests have not considered the structural characteristics of landslide dams. Notwithstanding, the landslide dam breach process is preliminarily demystified and quantitatively documented based on the model tests.

In recent years, several physical model tests have been conducted to investigate the influences of spillway on the breach process of landslide dams. With this regard, the cross section of the spillway is set based on different geometries as an inverted trapezoid, a triangle, or a compound type (the upper part is an inverted trapezoid, and the bottom of the trapezoid is connected with an inverted triangle), shown as **Figure 3**. Zhao et al. (2011) defined the discharge efficiency, in which the high efficiency means the high increase rate of breach flow discharge or the short elapsed time for the arrival of peak breach flow. Based on the comparison of different model tests, Zhao et al. (2011) stated that the descending order of the discharge efficiencies of spillways is as follows: triangle, compound type, and inverted trapezoid; therewithal, suggested the compound type in the design of spillway for the emergency treatment. However, variations in the cross section areas of the spillways caused differences in the three groups of model tests. Therefore, it is debatable whether the test results can truly reflect the breach hydrographs, even under the condition that the excavated volumes are the same. Later, Zhao et al. (2018) conducted the centrifugal model tests under the condition of the same cross section area and found that the compound section is a relatively safer morphology for the spillway considering the higher initial discharge efficiency and lower peak breach flow. Due to the different environment and equipment, the physical model tests have concluded different results, the results can only reflect the breach process of landslide dam in a certain extent. The spillway with different sections has its own advantages under different conditions, it is difficult to form a unified result based on the same understanding.

The complex material and structural characteristics of landslide dams bring difficulties to accurately reflect the grain-size distribution and layered structure in the model tests; hence, a significant gap exists between the experimental results and the

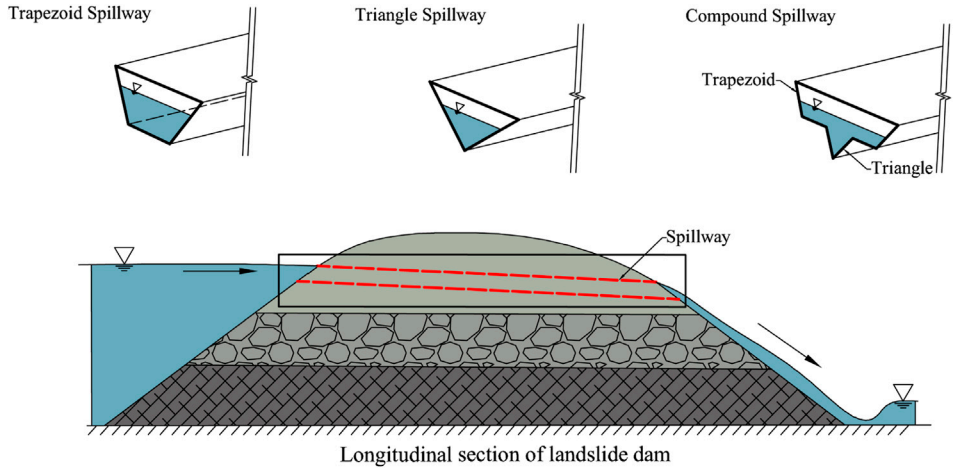

FIGURE 3 | Different cross-sections of the spillway.

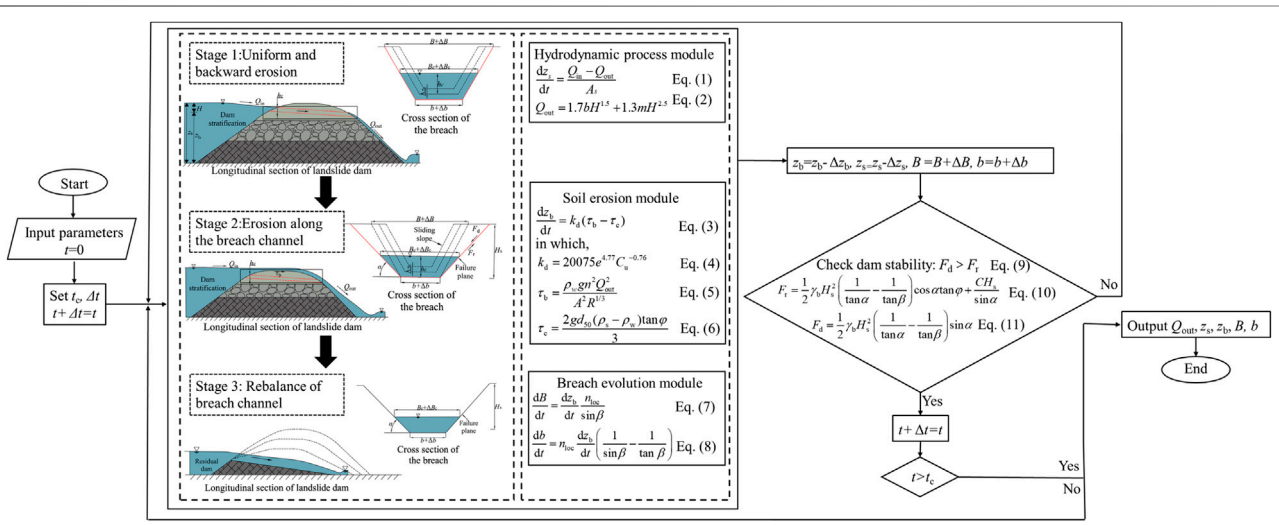

FIGURE 4 | Flow chart of the numerical model for landslide dam breaching.

real state. Numerical analysis is particularly advantageous considering the repeatability and time-saving features as simulating the discharge efficiency of the spillway with different section morphologies based on the same numerical method. Furthermore, numerical methods are widely adopted to scientifically design and quantitatively analyze the breach hydrograph and morphological evolution of landslide dams with different spillway section morphologies. You et al. (2012) proposed an optimized design method of trapezoidal cross section based on the Chezy-manning formula; however, the variation of the hydrodynamic conditions was not considered due to the enlargement of spillway cross section by the flow erosion. Based on the dam breach model DABA, Peng et al. (2014) investigated the applicability of various inverted trapezoidal spillways to different erosive landslide dams. It was concluded that with regard to the erosion resistance of landslide deposits, wide and shallow sections were suitable for low erosion, while the narrow and deep sections were suitable for high erosion. In another study, Shi et al. (2016) presented an optimal design scheme of the spillway based on the calculation of the instantaneous erosion rate of landslide dam and analysis of the influence of spillway on dam breach process, Shi et al. (2016) concluded that compared the compound cross section, the trapezoid cross section has a better risk mitigation effect. However, Chen S. S. et al. (2015) came to the opposite conclusion based the interaction between coarse and fine particles. To the best of the authors' knowledge, no scientific consensus regarding numerical modeling of landslide dam breaching has been established, different results were concluded by research scholar based different situation.

TABLE 1 | Morphological, hydrodynamic, and mechanical parameters of the three landslide dams.

Parameters	Tangjiashan	Xiaogangjian	Baige
Dam height (m)	103	72	96
Crest width (m)	300	80	270
Dam length (m)	612	300	600
Dam upstream slope ratio (V/H)	1:2.8	1:2.8	1:2.7
Dam downstream slope ratio (V/H)	1:4.2	1:1.7	1:5.5
Spillway depth (m)	13	8	13.48
Spillway bottom width (m)	8	30	3.0
Spillway slope ratio in cross section (V/H)	1:1.5	1:2.0	1:1.3
Spillway slope ratio in longitudinal section (V/H)	1:4.2	1:1.7	1:5.5
Q_{in} (m^3/s)	80	15	700
C (kPa)	30	42	3
φ (°)	35	35	38

V/H = Vertical/Horizontal.

TABLE 2 | Stratification of the three landslide dams and the physical/mechanical parameters of each layer.

Name	Layer	Thickness (m)	e	d_{50} (mm)	ρ_s (kg/m^3)	k_d ($mm^3/(N{\cdot}s)$)	τ_c (Pa)
Tangjiashan	1	20	0.87	10	1825	1770	375
	2	20	0.75	20	2,216	700	500
	3	63	0.59	60	2,408	100	1750
Xiaogangjian	1	32	0.94	60	2045	900	457
	2	40	0.70	18	1813	300	200
Baige	1	96	0.5	30	1,584	1,500	2,380

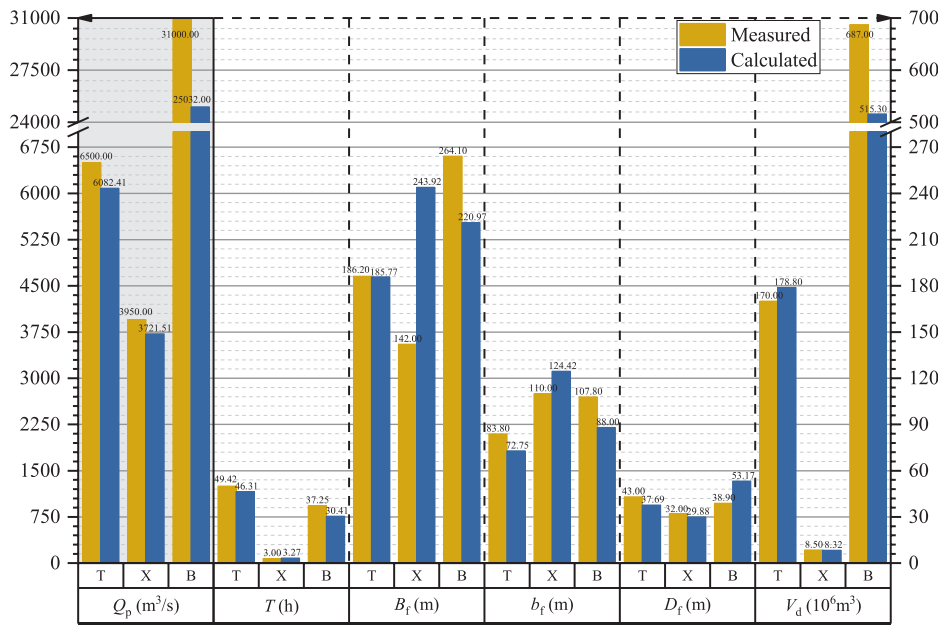

FIGURE 5 | Comparison of calculated and measured breaching parameters of the three landslide dams (T = Tangjiashan landslide dam; X = Xiaogangjian landslide dam; B = Baige landslide dam; Q_p = peak breach flow; T_p = time to peak; B_f = final breach top width; b_f = final breach bottom width; D_f = final breach depth; and V_d = released water volume. Herein, Q_p of the three dams are corresponding to the left axis, and the other indicators correspond to the right axis).

TABLE 3 | Morphological parameters of the spillways with different section types.

Landslide name	Condition	Depth (m)	Bottom width (m)	Slope ratio in cross section	Slope ratio in longitudinal section
Tangjiashan	1	13.00	8.0	1:1.5	1:4.2
	2	—	—	—	—
	3	15.00	8.0	1:1.5	1:4.2
	4	17.00	8.0	1:1.5	1:4.2
	5	13.00	4.0	1:1.5	1:4.2
	6	13.00	16.0	1:1.5	1:4.2
	7	13.00	8.0	1:2.0	1:4.2
	8	13.00	8.0	1:2.5	1:4.2
	9	13.00	8.0	1:1.5	1:3.2
	10	13.00	8.0	1:1.5	1:5.2
Xiaogangjian	1	8.00	30.0	1:2.0	1:1.7
	2	—	—	—	—
	3	9.00	30.0	1:2.0	1:1.7
	4	10.00	30.0	1:2.0	1:1.7
	5	8.00	20.0	1:2.0	1:1.7
	6	8.00	40.0	1:2.0	1:1.7
	7	8.00	30.0	1:2.5	1:1.7
	8	8.00	30.0	1:3.0	1:1.7
	9	8.00	30.0	1:2.0	1:1.5
	10	8.00	30.0	1:2.0	1:1.9
Baige	1	13.48	3.0	1:1.3	1:5.5
	2	—	—	—	—
	3	18.48	3.0	1:1.3	1:5.5
	4	23.48	3.0	1:1.3	1:5.5
	5	13.48	1.0	1:1.3	1:5.5
	6	13.48	6.0	1:1.3	1:5.5
	7	13.48	3.0	1:1.6	1:5.5
	8	13.48	3.0	1:1.9	1:5.5
	9	13.48	3.0	1:1.3	1:5.0
	10	13.48	3.0	1:1.3	1:6.0

NUMERICAL MODEL FOR OVERTOPPING-INDUCED LANDSLIDE DAM BREACHING

In the previous section, the landslide dam failure process, in detail overtopping-induced landslide dam breach process, can be generally classified into three stages according to the results of the research: 1) Uniform and backward erosion. As the upstream water level continues to rise, the overtopping flow enters into the spillway entrance, and then the spillway is gradually filled with water. Since the flow velocity is relatively small, the erosion mode is mainly characterized by uniform erosion. With the increase of water depth and velocity in the spillway, intense erosion primarily occurs at the downstream toe of the landslide dam; subsequently, backward erosion begins until it reaches the dammed lake. 2) Erosion along the breach channel. After the erosion reached the dammed lake, the overtopping water head abruptly increased, then the flow velocity and breach flow discharge continue to rise rapidly. During the elapsed time, the bottom elevation of the breach channel also decreases rapidly. The downstream slope angle gradually decreases due to the erosion by water flow; simultaneously, the breach slope is intermittently unstable, and the peak breach flow occurs in this period. 3) Rebalance of breach channel. The water level in the dammed lake begins to decline rapidly with the increase of the breach flow discharge; thus, the breach channel has gained sufficient discharge capacity, resulting in at the end of the breach process.

Based on the breach process, a numerical model that can consider the hydrodynamic conditions of the dammed lake, the morphological, structural, and material characteristics of the landslide dam was proposed by Zhong et al. (2020a). The model consisted of three parts: the hydrodynamic process module, the soil erosion module, and the breach evolution module. The flow chart of the numerical model was created using the time step iteration-based calculation method to simulate the water and soil connection during the dam failure process is shown in **Figure 4**.

The Hydrodynamic Process Module

The water level in the dammed lake is a dynamic process during landslide dam breaching. The lake area, inflow and different water level under different time should be considered to calculating the discharge flow, the breach process obey the water balance relationship.

$$\frac{\mathrm{d}zs}{\mathrm{d}t} = \frac{Q_{\mathrm{in}} - Q_{\mathrm{out}}}{As} \tag{1}$$

$$Q_{\mathrm{out}} = 1.7bH^{1.5} + 1.3mH^{2.5} \tag{2}$$

TABLE 4 | Comparison of calculated results of Tangjiashan landslide dam under different conditions.

Condition	Comparison	Peak breach flow (m^3/s)	Time to peak (h)	Final breach top width (m)	Final breach bottom width (m)	Final breach depth (m)	Released water storage ($\times10^6$ m^3)
1	Calculated	6,082.41	46.31	185.77	72.75	37.69	178.8
2	Calculated	16,291.79	17.20	240.92	88.77	41.51	279.6
	Relative change rate	167.85%	−62.86%	29.69%	22.02%	10.14%	56.38%
3	Calculated	4,480.04	60.23	175.35	65.25	36.72	160.7
	Relative change rate	−26.34%	30.06%	−5.61%	−10.31%	−2.57%	−10.12%
4	Calculated	3,106.39	83.48	163.59	57.18	35.49	141.9
	Relative change rate	−48.93%	80.26%	−11.94%	−21.40%	−5.84%	−20.64%
5	Calculated	6,152.18	59.17	182.57	68.17	38.16	180.2
	Relative change rate	1.15%	27.77%	−1.72%	−6.30%	1.25%	0.78%
6	Calculated	6,160.34	38.18	193.12	82.32	36.96	176.4
	Relative change rate	1.28%	−17.56%	3.96%	13.15%	−1.94%	−1.34%
7	Calculated	5,304.97	56.31	218.14	76.25	35.48	170.5
	Relative change rate	−12.78%	21.59%	17.42%	4.81%	−5.86%	−4.64%
8	Calculated	4,624.93	67.07	247.24	79.96	33.46	162.5
	Relative change rate	−23.96%	44.83%	33.09%	9.91%	−11.22%	−9.12%
9	Calculated	6,528.22	47.24	194.12	78.89	38.44	181.7
	Relative change rate	7.33%	2.01%	4.49%	8.44%	1.99%	1.62%
10	Calculated	5,650.15	46.62	178.29	67.74	36.87	175.6
	Relative change rate	−7.11%	0.67%	−4.03%	−6.89%	−2.18%	−1.79%

where t = time; z_s = water level in dammed lake; Q_{in} = inflow discharge; Q_{out} = breach flow discharge; A_s = surface area of dammed lake; H = water depth in breach, and $H = z_s$-z_b; m = ratio of breach slope (horizontal/vertical); and b = bottom width of breach.

The Soil Erosion Module

The bed erosion in the breach bottom is calculate by a shear stress based erosion rate formula that can simulate the soil with wide grading.

$$\frac{dz_b}{dt} = k_d(\tau_b - \tau_c) \tag{3}$$

in which,

$$k_d = 20075e^{4.77}C_u^{-0.76} \tag{4}$$

$$\tau_b = \frac{\rho_w g n^2 Q_{out}^2}{A^2 R^{1/3}} \tag{5}$$

$$\tau_c = \frac{2gd_{50}(\rho_s - \rho_w)\tan\varphi}{3} \tag{6}$$

where z_b = breach bottom elevation; k_d = erodibility coefficient of soil; τ_b = bed shear stress of water; τ_c = critical shear stress of soil; e = void ratio of soil, C_u = non-uniformity coefficient; ρ_w = density of water; ρ_s = density of soil; n = Manning's roughness coefficient; A = flow area; R = hydraulic radius; d_{50} = sediment median size; and φ = internal friction angle of soil.

The Breach Evolution Module

It is assumed that the breach side slope angles remain unchanged during the breach process until the instability of the side slopes. The increments of top and bottom widths can be calculated as following:

$$\frac{dB}{dt} = \frac{dz_b}{dt}\frac{n_{loc}}{\sin\beta} \tag{7}$$

$$\frac{db}{dt} = n_{loc}\frac{dz_b}{dt}\left(\frac{1}{\sin\beta} - \frac{1}{\tan\beta}\right) \tag{8}$$

where B = top width of breach; n_{loc} = indicator of breach location, in which, n_{loc} = 1 represents one-sided breach and n_{loc} = 2 represents two-sided breach; and β = breach side slope angle.

With the development of breach size, instability of breach side slope will occur. The slope stability is calculated by the limit equilibrium method. The slope failure surface is assumed to be a plane, the slope will be instable when the following condition are met:

$$F_d > F_r \tag{9}$$

in which,

$$F_r = \frac{1}{2}\gamma_b H_s^2\left(\frac{1}{\tan\alpha} - \frac{1}{\tan\beta}\right)\cos\alpha\tan\varphi + \frac{CH_s}{\sin\alpha} \tag{10}$$

TABLE 5 | Comparison of calculated results of Xiaogangjian landslide dam under different conditions.

Condition	Comparison	Peak breach flow (m^3/s)	Time to peak (h)	Final breach top width (m)	Final breach bottom width (m)	Final breach depth (m)	Released water storage ($\times 10^6$ m^3)
1	Calculated	3,721.51	3.27	243.92	124.42	29.88	8.32
2	Calculated	—	—	—	—	—	—
	Relative change rate	—	—	—	—	—	—
3	Calculated	3,312.15	4.43	237.67	119.3	29.59	7.88
	Relative change rate	−11.00%	35.47%	−2.56%	−4.12%	−0.97%	−5.29%
4	Calculated	2,782.14	9.63	231.23	114.11	29.28	7.44
	Relative change rate	−25.24%	194.50%	−5.20%	−8.29%	−2.01%	−10.58%
5	Calculated	3,810.31	4.47	229.63	106.78	30.71	8.44
	Relative change rate	2.39%	36.70%	−5.86%	−14.18%	2.78%	1.44%
6	Calculated	3,716.76	2.75	258.29	141.92	29.09	8.2
	Relative change rate	−0.13%	−15.90%	5.89%	14.07%	−2.64%	−1.44%
7	Calculated	3,272.61	4.1	270.02	130	28.01	8.01
	Relative change rate	−12.06%	25.38%	10.70%	4.48%	−6.26%	−3.73%
8	Calculated	2,775.38	5.12	293.74	135.44	26.36	7.71
	Relative change rate	−25.42%	56.57%	20.42%	8.86%	−11.78%	−7.33%
9	Calculated	3,740.39	3.39	247.82	128.15	29.90	8.33
	Relative change rate	0.51%	3.67%	1.60%	3.00%	0.07%	0.12%
10	Calculated	3,692.49	3.18	240.13	120.91	29.81	8.31
	Relative change rate	−0.78%	−2.75%	−1.55%	−2.82%	−0.23%	−0.12%

$$F_d = \frac{1}{2}\gamma_b H_s^2 \left(\frac{1}{\tan\alpha} - \frac{1}{\tan\beta}\right)\sin\alpha \tag{11}$$

where F_d = driving force; F_r = resistant force; γ_b = bulk specific weight of soil; H_s = breach slope height; α = breach side slope angle after instability; and C = soil cohesion.

CASE STUDIES

The Classification of Landslide Dams

The landslide dams' body is formed by the accumulation of landslide debris; its structure and constituents are strongly associated with the movement and material composition of slide mass. The rock slides, rock falls, and debris flows are the most prominent forms of slides that lead to the formation of landslide dams (Fan et al., 2020; Mei et al., 2021). 1) Rock slides are a phenomenon that results in rocks sliding and blocking the river when the driving force on a potential failure surface surpasses the resistance force. Due to the limited movement distance, the sliding rocks often do not completely disintegrate, a portion of which still retain the original structure. The internal structure of landslide dams formed due to rock slides can be divided into two or more layers that have a structure in which the particle sizes of landslide deposits increase gradually with the depth. Depth-dependent particle size variation results in the landslide dam base being composed of intact strata, while the upper sections have a fragmented fraction of rock debris and soil. 2) Rock falls, as another phenomenon that causes the landslide dam formation, occurs when the rock slope loses stability under external loads; subsequently, the upper rock and soil drop by falling, leaping, or rolling. The internal structure can be split into two layers due to the various movement directions of rocks and soils; the bottom layer is composed of highly fragmented rock debris and fine-grained soil, while the top layer is composed of large-grained rocks. 3) Debris flows can be defined as the accumulation of the loose materials on the river channel derived due to the disintegration of large rock particles under high-speed sliding action and mutual collision after an avalanche occurs at the high elevation of the rock slope. Therefore, landslide dams formed by debris flows are typically dominated by relatively loose particles and fine-grained soil rather than rock structures.

In this section, corresponding to the landslide dams of the three types, three landslide dam failure cases, such as Tangjiashan (Liu et al., 2010; Chen Z. Y. et al., 2015), Xiaogangjian (Chen et al., 2018), and Baige (Cai et al., 2020; Zhong et al., 2020b) in China with documented information on the breach process are chosen as the representatives.

Introduction of the Three Landslide Dams

Tangjiashan landslide dam was formed by Wenchuan earthquake on May 12, 2008, China. Based on the geological investigation, the landslide dam belongs to the first type (rock slide induced) of

TABLE 6 | Comparison of calculated results of Baige landslide dam under different conditions.

Condition	Comparison	Peak breach flow (m^3/s)	Time to peak (h)	Final breach top width (m)	Final breach bottom width (m)	Final breach depth (m)	Released water storage ($\times 10^6$ m^3)
1	Calculated	25,032.00	30.41	220.97	88.0	53.17	515.3
2	Calculated	80,569.91	16.28	367.76	141.43	90.53	726
	Relative change rate	221.87%	–46.46%	66.43%	60.72%	70.27%	40.89%
3	Calculated	15,743.74	47.97	196.44	70.95	50.19	397.79
	Relative change rate	–37.11%	57.74%	–11.10%	–19.38%	–5.61%	–22.80%
4	Calculated	9,151.75	52.78	170.11	53.15	46.78	278.8
	Relative change rate	–63.44%	73.56%	–23.02%	–39.60%	–12.02%	–45.90%
5	Calculated	26,254.34	35.75	221.56	86.70	53.94	518.2
	Relative change rate	4.88%	17.56%	0.27%	–1.48%	1.45%	0.56%
6	Calculated	24,069.06	25.84	221.80	90.80	52.40	512.3
	Relative change rate	–3.85%	–15.03%	0.38%	3.18%	–1.45%	–0.58%
7	Calculated	22,993.6	31.73	251.88	90.18	50.53	504.2
	Relative change rate	–8.14%	4.34%	13.99%	2.48%	–4.97%	–2.15%
8	Calculated	21,257.8	32.98	276.02	92.49	48.27	493.8
	Relative change rate	–15.08%	8.45%	24.91%	5.10%	–9.22%	–4.17%
9	Calculated	26,407.68	30.09	227.21	91.72	54.20	519.6
	Relative change rate	5.50%	-1.05%	2.82%	4.23%	1.94%	0.83%
10	Calculated	23,824.84	30.79	215.45	84.81	52.26	511.2
	Relative change rate	–4.82%	1.25%	–2.50%	–3.63%	–1.71%	–0.80%

landslide dams; further, it has three internal layers from dam crest to bottom, which are composed of fine-grained soils, layered fractured rock mass, and block rock mass, respectively. Tangjiashan landslide dam has the height of about 103 m, and width of 300 m on the crest, and a volume of 2.04×107 m^3. After the emergency response from May 26 to May 31, a spillway with the depth of 13 m and bottom width of 8 m was excavated on the right bank of the dam. The spillway began to discharge at 7:08, June 7, and the peak breach flow was 6,500 m^3/s, which occurred at 12:30, June 10.

Xiaogangjian landslide dam was also formed by Wenchuan earthquake, which belongs to the second type (rockfall induced) of landslide dams. The landslide dam has two internal layers from dam crest to bottom, the upper part is composed of large blocks, while the lower part is mainly composed of highly fragmented debris. Xiaogangjian landslide dam has the height of about 72 m, and width of 173 m on the crest, and a volume of 2×106 m^3. After the field reconnaissance, and comprehensively considered the factors of construction conditions and the available time for risk migration, a spillway with 8 m depth and 30 m bottom width was constructed on the left bank of the dam. The water began to discharge at 12:00, June 12, and the peak breach flow was 3,950 m^3/s, which occurred at 13:05, June 12.

On October 10, 2018 and November 3, 2018, two successive landslides occurred at the border of Sichuan Province and Tibet Autonomous Region, and totally blocked the Jinsha River twice at the same location. The first landslide dam breached naturally on October 12 due to the overtopping flow. In this study, the second Baige landslide dam which breached after the manual intervention is the study object. The Baige landslide dam belongs to the third type (debris flow induced) of landslide dams. The landslide dam is composed of loose debris, and there is no obvious layered structures. The total volume of Baige landslide dam was 3.7×106 m^3, with an average height of 96 m. The excavated spillway in the dam crest has the depth of 13.48 m at the entrance, and the bottom width of 3 m. The water began to discharge at 10:50, November 12, and the peak breach flow was 31000 m^3/s, which occurred at 18:00, November 13.

Calculated Results

Based on the numerical model developed by the authors, the breach processes of the three cases have been simulated. The morphological, hydrodynamic, and mechanical parameters of the three landslide dams are listed in **Table 1**. The stratification of the landslide dams, physical and mechanical parameters of each layer are shown in **Table 2**. The comparison of measured and calculated breaching parameters (i.e., peak breach flow, time to peak, final breach top width, final breach bottom width, final breach depth, and released water storage) of the three landslide dams are shown in **Figure 5**.

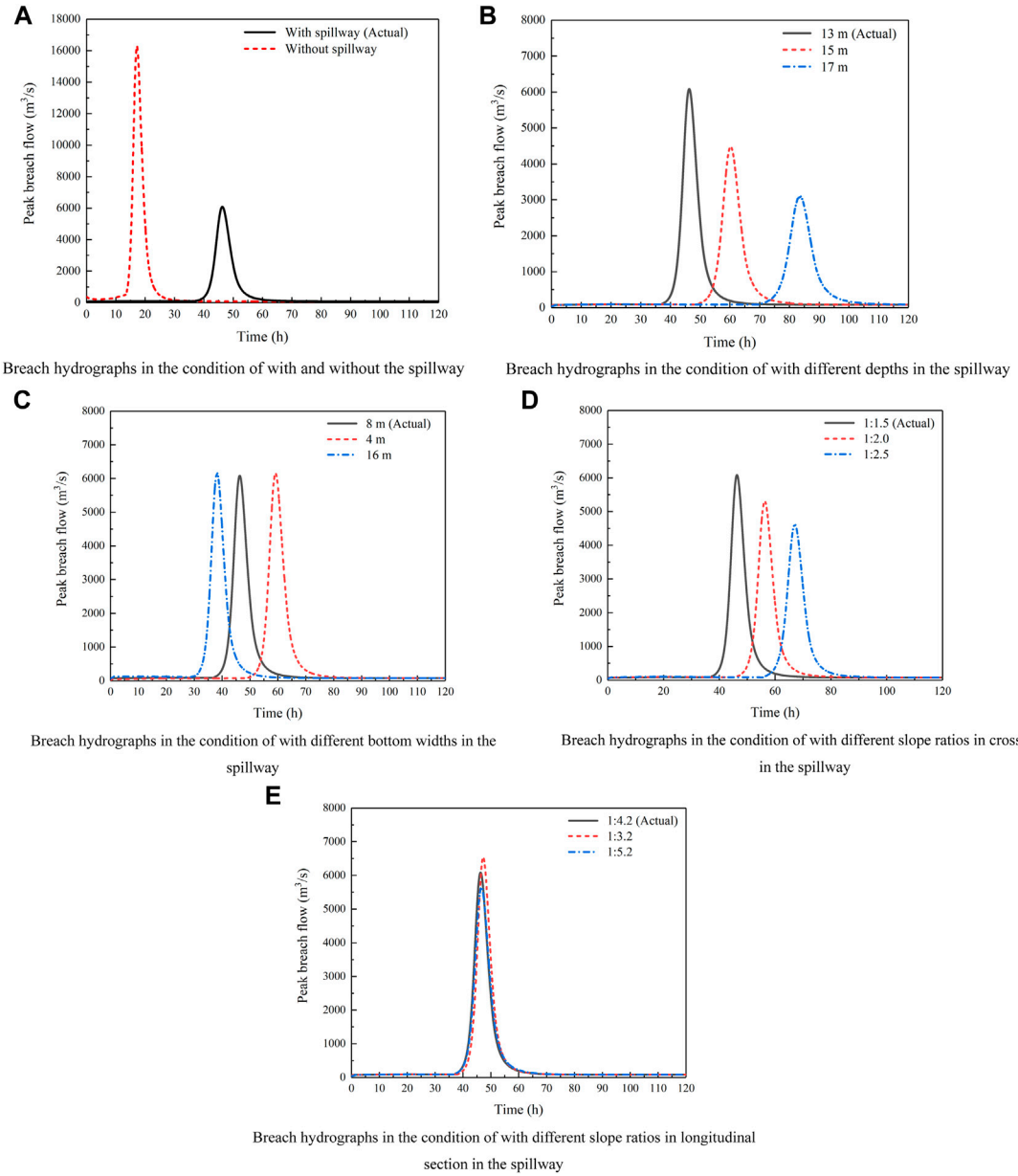

FIGURE 6 | Comparison of breach hydrographs of Tangjiashan landslide dam under different conditions. **(A)** Breach hydrographs in the condition of with and without the spillway. **(B)** Breach hydrographs in the condition of with different depths in the spillway. **(C)** Breach hydrographs in the condition of with different bottom widths in the spillway. **(D)** Breach hydrographs in the condition of with different slope ratios in cross-section in the spillway. **(E)** Breach hydrographs in the condition of with different slope ratios in longitudinal section in the spillway.

The comparison in **Figure 5** shows that, for Tangjiashan landslide dam, the relative errors of all breaching parameters of are less than ±15%; for Xiaogangjian landslide dam, except for the final breach top width has a relative error of 71.8%, the relative errors of all the other breaching parameters are less than ±15%; for Baige landslide dam, except for the final breach depth has a relative error of 36.7%, the relative errors of all the other breaching parameters are less than ±25%. As the top layer of the Xiaogangjian landslide dam is composed of large grained rocks, the spillway is excavated with the help of the explosion. Hence, the erosion characteristics of landslide dam deposits in the breach channel become complex. In general, the numerical model developed by the authors gives reasonably calculated results for landslide dam breaching. The following section utilizes the numerical model to study the influence of spillway section morphologies on landslide dam breaching.

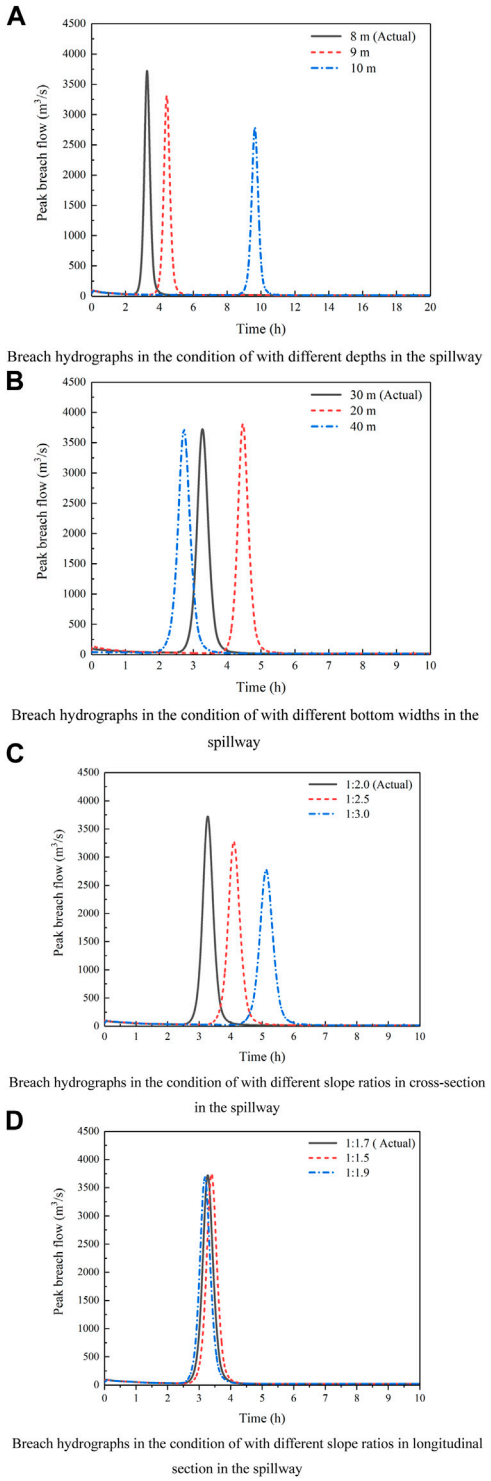

FIGURE 7 | Comparison of breach hydrographs of Xiaogangjian landslide dam under different conditions. **(A)** Breach hydrographs in the condition of with different depths in the spillway. **(B)** Breach hydrographs in the condition of with different bottom widths in the spillway. **(C)** Breach hydrographs in the condition of with different slope ratios in cross-section in the spillway. **(D)** Breach hydrographs in the condition of with different slope ratios in longitudinal section in the spillway.

COMPARISON OF BREACH PROCESSES OF LANDSLIDE DAMS WITH DIFFERENT SPILLWAY SECTION MORPHOLOGIES

An ideal efficient spillway for landslide dam drainage should provide the following requirements: 1) Excavation should be conducted at the lower position of the dam crest, and the excavated volume should be relatively small. 2) In the initial stage of landslide dam breaching, the spillway bottom can be undercut immediately, thereby rapid increment of breach flow discharge and effective reduction the water level of the dammed lake can be maintained. 3) During the accelerated stage, although the breach bottom continues to undercut, the mass failures due to the instability of the breach side slope should be less likely to happen, and the outburst flood could run forward within the downstream channel. The breach hydrograph curve should exhibit a flat shape rather than a spike. 4) After landslide dam breaching, the downcutting depth of the breach should be large enough, which could effectively reduce the storage capacity of the dammed lake.

The cross section of the spillways of the selected Tangjiashan, Xiaogangjian, and Baige landslide dams is all trapezoidal. Here, ten conditions of spillways are set to comprehensively reflect the influence due to the variations of the spillway on the breach process of landslide dams. The first condition is the actual situation on-site, which is expounded in the "Case studies" section. The second condition is set as the landslide dams without spillways. In addition, eight other conditions aim to highlight the effect of variations in depth (conditions 3 and 4), bottom width (conditions 5 and 6), slope ratio in cross section (7 and 8), and longitudinal section (conditions 9 and 10) are also set for the comparison. The morphological parameters of spillways for each condition are listed in **Table 3**.

The comparison of measured and calculated results of Tangjiashan, Xiaogangjian, and Baige landslide dams under different conditions are shown in **Tables 4–6**, respectively. The relative change rates of breaching parameters calculated in **Tables 4–6** are the errors between each corresponding condition and condition 1. Since the breach flow discharge is the key to the disaster consequence, **Figures 6–8** also presents the comparison of breach hydrographs of the three landslide dams under different conditions, respectively.

With and Without Spillways

The comparison in **Figures 6A**, **8A** shows that excavating spillway or not has a significant influence on the three landslide dams' breach processes. For Tangjiashan and Baige landslide dams, it was observed that in the absence of a spillway, peak breach flow increases sharply, the volume of released water increases significantly, and the time to peak breach flow is shortened. This situation shows that if there is no spillway, severe disasters will occur. For Xiaogangjian landslide dam, without the spillway, it would not breach because the dam structure and the upper coarse particles have a strong anti-erosion ability, and the upstream flow is small to erode the landslide deposits. However, there still has the risk of dam failure in the future if the upstream inflow increases to a certain extent to wash the large particles away.

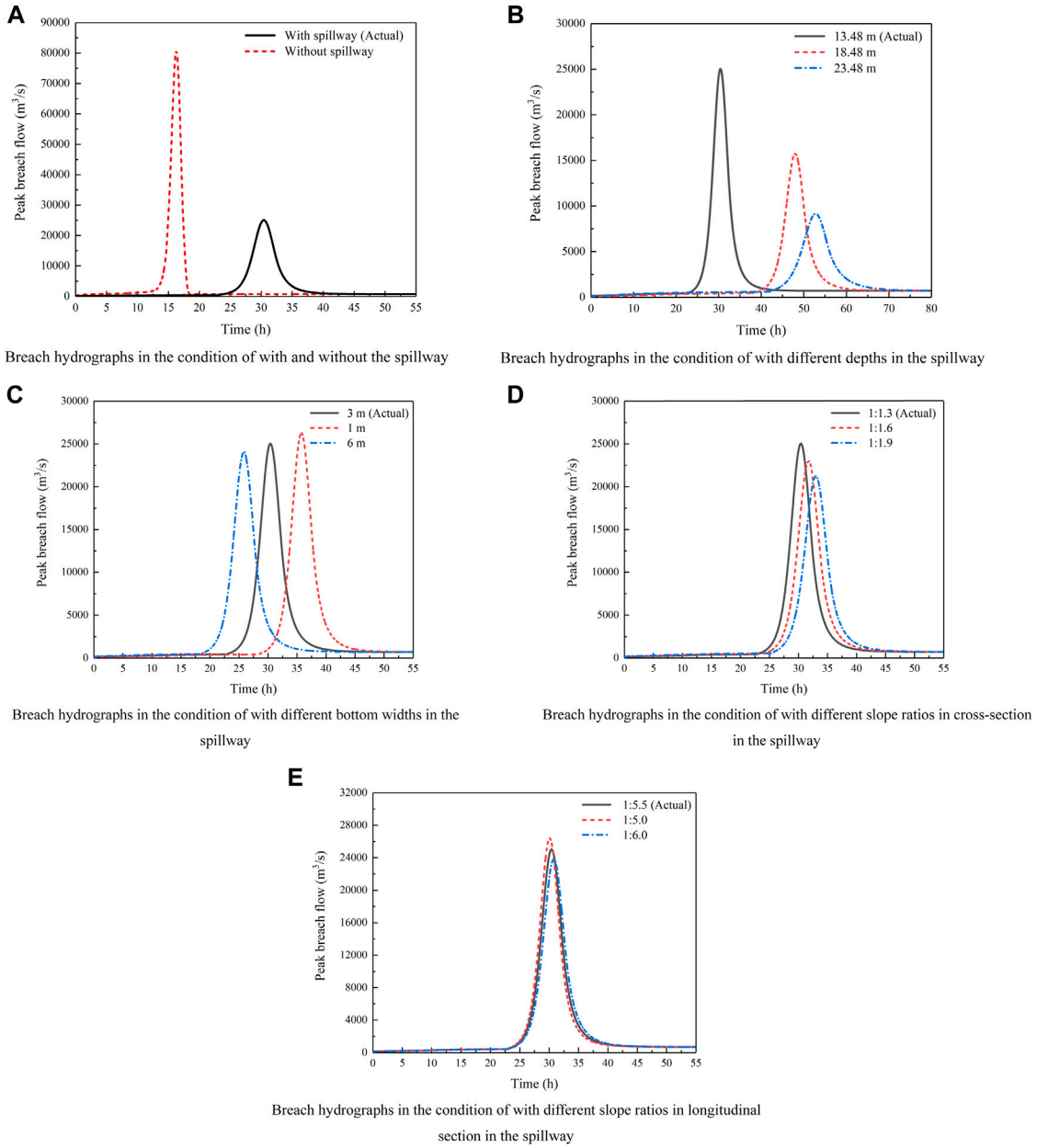

FIGURE 8 | Comparison of breach hydrographs of Baige landslide dam under different conditions. **(A)** Breach hydrographs in the condition of with and without the spillway. **(B)** Breach hydrographs in the condition of with different depths in the spillway. **(C)** Breach hydrographs in the condition of with different bottom widths in the spillway. **(D)** Breach hydrographs in the condition of with different slope ratios in cross-section in the spillway. **(E)** Breach hydrographs in the condition of with different slope ratios in longitudinal section in the spillway.

Different Spillway Depths

The comparison in **Figures 6B**, **7A**, **8B** shows that spillway depth plays an essential role in the breach processes of the three landslide dams, and the influence on the three landslide dams demonstrates a similar regularity. With the increase of spillway depth, the water storage capacity of the dammed lake reduces, and the hydrodynamic conditions gradually weaken. The most distinctive feature observed in the landslide dam breaching due to the variations of spillway depth is that the peak breach flow discharge decreases sharply, while the time to peak delays. In addition, the final breach top and bottom widths decrease with the increasing spillway depth, mainly because it lies in the attenuation of erosion ability as the peak breach flow decreases.

Different Spillway Bottom Widths

The comparison in **Figures 6C**, **7B**, **8C** also shows that variation of spillway bottom width has a major impact on the time to peak for three landslide dams. It is worth mentioning that, for Tangjiashan and Xiaogangjian landslide dams, the variation of spillway bottom width has a little impact on the peak breach flow; however, for

Baige landslide dam, as the bottom width increases, the peak breach flow reduces slightly obvious due to the relatively high soil erodibility. For the landslide dam with low erodibility, the size expansion rate of spillway is very small, as well as the released water storage in the initial stage of breach process; with the intensification of soil erosion, the evolution speed of breach size increases rapidly. Hence, for the landslide dam with low erodibility, the larger the spillway bottom width is, the earlier the time to peak occurs; while the peak breach flow changes a little. For the landslide dam with high erodibility, the increment of breach size is obvious, resulted in the large released water storage in the dammed lake in the initial stage; thus, for the landslide dam with high erodibility, the larger the spillway bottom width is, the earlier the time to peak occurs, and the smaller the peak breach flow is.

Different Spillway Slope Ratios in the Cross and Longitudinal Sections

The comparison in **Figures 6D**, **7C**, **8D** shows that variation of spillway slope ratios in the cross section, and the comparison in **Figures 6E**, **7D**, **8E** shows that variation of spillway slope ratios in the longitudinal section. The cross section area of the spillway increases with the decrease of the slope ratio in the cross section of the spillway, while the depth of water flow in the spillway decreases. This weakens the erosion ability of the breach flow and resulting in reduced peak breach flow and the delay of time to peak. It also simultaneously affects the size of the breach. When it comes to the slope ratio in the longitudinal section in the spillway, the comparison shows that this influencing factor has relatively little influence on the failure process.

Different Simulation Methods

In order to provide a method for optimal design of spillways to minimize the risks, based on Tangjiashan landslide dam case, Peng et al. (2014) quantitatively evaluate practical options for spillway design with a simplified physically-based dam breach model. According to the numerical simulation, Peng et al. (2014) concluded that, a spillway with a shallow-broad and deep-narrow cross sections are suitable for low and high erodibility landslide dams, respectively, while a spillway with a large slope ratio in longitudinal section is suitable for high erodibility landslide dams with large dam widths and gentle downstream dam slopes. In addition, lowering the spillway depth is more effective than widening the spillway width in spillway design.

Compared with the conclusions proposed by Peng et al. (2014), there are some similarities and differences between the two studies. The most important one is that two studies have confirmed that spillway depth is a dominant factors for risk mitigation. However, since the section areas of different spillways remained the same in the study of Peng et al. (2014), in addition, due to the characteristics of layered structure of landslide dams are not taken into account, the soil erodibility of Tangjiashan is identified as a high value in Peng et al. (2014), there are some differences lied in the conclusions. It is worth mentioning that, if the boundary conditions and input parameters are consistent, the calculated results and conclusions in this study are in accordance with those of Peng et al. (2014).

CONCLUSION

Considering the morphological, structural, and material characteristics of the landslide dams and the hydrodynamic conditions of dammed lakes, a numerical model was developed by the authors. Three failure cases with detailed measured data are used to discuss the effects of spillway section morphologies on landslide dam breach processes. The conclusions are drawn as follows:

1) Excavating a spillway can effectively reduce the peak breach flow, thus delay the time to peak discharge. It is worth noting that, for a landslide dam with fine particles at the bottom and large particles at the top, when the hydrodynamic conditions are weak, it may not breach without spillway, but there is still a risk of dam failure.
2) In the spillway excavation, increasing the spillway depth can effectively decrease the peak breach flow, delay the time to peak, and reduce the released water storage in the dammed lake. Therefore, where conditions are concerned, care should be taken to dig as deep a spillway as possible.
3) Spillway bottom width is also an important influencing factor for the discharge efficiency, which has a major effect on time to peak, but conversely has a minor effect on the peak breach flow for the landslide dam with low erodibility. Larger spillway bottom width corresponds to the earlier time to peak, and it is also an important way to reduce the peak breach flow for the landslide dam with large erodibility.
4) A gentle slope ratio in the cross section of the spillway can decrease the peak breach flow and delay the time to peak; thus, it is recommended to reduce the slope ratio of the spillway cross section as much as possible. Moreover, the slope ratio in the longitudinal section in the spillway has little influence on the breach process.

DATA AVAILABILITY STATEMENT

The raw data supporting the conclusions of this article will be made available by the authors, without undue reservation.

AUTHOR CONTRIBUTIONS

MY: writing-original draft, calculation, and analysis. QZ: supervision, methodology, and funding acquisition. SM: methodology and revision. YS: methodology and advice. All authors contributed to the article and approved the submitted version.

FUNDING

This work was financially supported by the National Key Research and Development Program of China (Grant No. 2018YFC1508604), the National Natural Science Foundation of China (Grant Nos. U2040221 and 51779153), and the Fundamental Research Funds for Central Public Research Institutes (Grant No. Y320005).

REFERENCES

Berrocal, J., Espinosa, A. F., and Galdos, J. (1978). Seismological and Geological Aspects of the Mantaro Landslide in Peru. *Nature* 275, 533–536. doi:10.1038/275533a0

Cai, Y., Cheng, H., Wu, S., Yang, Q., Wang, L., Luan, Y., et al. (2020). Breaches of the Baige Barrier lake: Emergency Response and Dam Breach Flood. *Sci. China Technol. Sci.* 63 (7), 1164–1176. doi:10.1007/s11431-019-1475-y

Cai, Y. J., Luan, Y. S., Peng, W. X., Li, J. Q., and Xu, Y. (2021). *Analysis on Typical Cases of Barrier lake: Cause, Disaster and Emergency Response*. Wuhan, China: Changjiang River publication. (in Chinese).

Chen, S. J., Chen, Z. Y., Tao, R., Yu, S., Xu, W. J., Zhou, X. B., et al. (2018). Emergency Response and Back Analysis of the Failures of Earthquake Triggered cascade Landslide Dams on the Mianyuan River, China. *Nat. Hazards Rev.* 19 (3), 05018005. doi:10.1061/(ASCE)NH.1527-6996.0000285

Chen, S. S., Zhao, T. L., and Zhong, Q. M. (2015). Dam-break Numerical Model for a Barrier Dam and its Application. *Hydro-Science Eng.* 3, 1–8. (in Chinese). doi:10.16198/j.cnki.1009-640X.2015.03.001

Chen, Z. Y., Ma, L. Q., Yu, S., Chen, S. J., Zhou, X. B., Sun, P., et al. (2015). Back Analysis of the Draining Process of the Tangjiashan Barrier lake. *J. Hydraulic Eng.* 141 (4), 05014011. doi:10.1061/(asce)hy.1943-7900.0000965

Costa, J. E., and Schuster, R. L. (1988). The Formation and Failure of Natural Dams. *Geol. Soc. America Bull.* 100 (7), 1054–1068. doi:10.1130/0016-7606(1988)100<1054:tfafon>2.3.co;2

Cui, P., Zhu, Y.-y., Han, Y.-s., Chen, X.-q., and Zhuang, J.-q. (2009). The 12 May Wenchuan Earthquake-Induced Landslide Lakes: Distribution and Preliminary Risk Evaluation. *Landslides* 6 (3), 209–223. doi:10.1007/s10346-009-0160-9

Fan, X., Dufresne, A., Siva Subramanian, S., Strom, A., Hermanns, R., Tacconi Stefanelli, C., et al. (2020). The Formation and Impact of Landslide Dams - State of the Art. *Earth-Science Rev.* 203, 103116. doi:10.1016/j.earscirev.2020.103116

Li, L., Yang, X., Zhou, J., Zhang, J., and Fan, G. (2021). Large-scale Field Test Study on Failure Mechanism of Non-cohesive Landslide Dam by Overtopping. *Front. Earth Sci.* 9, 660408. doi:10.3389/feart.2021.660408

Liao, H.-m., Yang, X.-g., Lu, G.-d., Tao, J., and Zhou, J.-w. (2019). Experimental Study on the River Blockage and Landslide Dam Formation Induced by Rock Slides. *Eng. Geology.* 261, 105269. doi:10.1016/j.enggeo.2019.105269

Liu, N., Chen, Z., Zhang, J., Lin, W., Chen, W., and Xu, W. (2010). Draining the Tangjiashan Barrier lake. *J. Hydraul. Eng.* 136 (11), 914–923. doi:10.1061/(asce)hy.1943-7900.0000241

Mei, S., Chen, S., Zhong, Q., and Shan, Y. (2021). Effects of Grain Size Distribution on Landslide Dam Breaching-Insights from Recent Cases in China. *Front. Earth Sci.* 9, 658578. doi:10.3389/feart.2021.658578

Peng, M., Ma, C. Y., Chen, H. X., Zhang, P., Zhang, L. M., Jiang, M. Z., et al. (2021). Experimental Study on Breaching Mechanisms of Landslide Dams Composed of Different Materials under Surge Waves. *Eng. Geology.* 291, 106242. doi:10.1016/j.enggeo.2021.106242

Peng, M., Zhang, L. M., Chang, D. S., and Shi, Z. M. (2014). Engineering Risk Mitigation Measures for the Landslide Dams Induced by the 2008 Wenchuan Earthquake. *Eng. Geology.* 180, 68–84. doi:10.1016/j.enggeo.2014.03.016

Schuster, R. L., and Evans, S. G. (2011). *Engineering Measures for the hazard Reduction of Landslide Dams*. Berlin, Germany: Springer Berlin Heidelberg. doi:10.1007/978-3-642-04764-0_2

Shan, Y., Chen, S., and Zhong, Q. (2020). Rapid Prediction of Landslide Dam Stability Using the Logistic Regression Method. *Landslides* 17 (12), 2931–2956. doi:10.1007/s10346-020-01414-6

Shang, Y., Yang, Z., Li, L., Liu, D. A., Liao, Q., and Wang, Y. (2003). A Super-large Landslide in Tibet in 2000: Background, Occurrence, Disaster, and Origin. *Geomorphology* 54, 225–243. doi:10.1016/S0169-555X(02)00358-6

Shi, Z. M., Zheng, H. C., Peng, M., and Zhang, L. M. (2016). Breaching Mechanism Analysis of Landslide Dams Considering Different Spillway Schemes - A Case Study of Tangjiashan Landslide Dam. *J. Eng. Geology.* 24 (5), 741–751. (in Chinese). doi:10.13544/j.cnki.jeg.2016.05.003

Takayama, S., Miyata, S., Fujimoto, M., and Satofuka, Y. (2021). Numerical Simulation Method for Predicting a Flood Hydrograph Due to Progressive Failure of a Landslide Dam. *Landslides* 18 (11), 3655–3670. doi:10.1007/s10346-021-01712-7

Yang, Y., Cao, S.-y., Yang, K.-j., and Li, W.-p. (2015). Experimental Study of Breach Process of Landslide Dams by Overtopping and its Initiation Mechanisms. *J. Hydrodyn* 27 (6), 872–883. doi:10.1016/S1001-6058(15)60550-9

Yin, Y., Wang, F., and Sun, P. (2009). Landslide Hazards Triggered by the 2008 Wenchuan Earthquake, Sichuan, China. *Landslides* 6 (2), 139–152. doi:10.1007/s10346-009-0148-5

You, Y., Liu, J. F., and Chen, X. Z. (2012). Design of Sluiceway Channel in a Landslide Dam Triggered by the Wenchuan Earthquake. *Disaster Adv.* 5 (4), 241–249. doi:10.2151/jmsj.2012-516

Zhang, J.-y., Fan, G., Li, H.-b., Zhou, J.-w., and Yang, X.-g. (2021). Large-scale Field Model Tests of Landslide Dam Breaching. *Eng. Geology.* 293, 106322. doi:10.1016/j.enggeo.2021.106322

Zhao, T., Chen, S., Fu, C., and Zhong, Q. (2019). Centrifugal Model Test on the Failure Mechanism of Barrier Dam Overtopping. *KSCE J. Civ Eng.* 23 (4), 1548–1559. doi:10.1007/s12205-019-0375-9

Zhao, T., Chen, S., Fu, C., and Zhong, Q. (2018). Influence of Diversion Channel Section Type on Landslide Dam Draining Effect. *Environ. Earth Sci.* 77 (2), 54–62. doi:10.1007/s12665-017-7217-1

Zhao, W. Y., Chen, X. Q., Gao, Q., and Jia, S. T. (2011). Experimental Study of Dam-Break of Earthquake Barrier lake with Different Cross Sections of Drainage Channel. *J. Sediment Res.* 4, 29–37. (in Chinese). doi:10.16239/j.cnki.0468-155x.2011.04.009

Zhong, Q., Chen, S., and Shan, Y. (2020a). Prediction of the Overtopping-Induced Breach Process of the Landslide Dam. *Eng. Geology.* 274, 105709. doi:10.1016/j.enggeo.2020.105709

Zhong, Q., Chen, S., Wang, L., and Shan, Y. (2020b). Back Analysis of Breaching Process of Baige Landslide Dam. *Landslides* 17 (7), 1681–1692. doi:10.1007/s10346-020-01398-3

Zhong, Q. M., Chen, S. S., Mei, S. A., and Cao, W. (2018). Numerical Simulation of Landslide Dam Breaching Due to Overtopping. *Landslides* 15 (6), 1183–1192. doi:10.1007/s10346-017-0935-3

Zhong, Q., Wang, L., Chen, S., Chen, Z., Shan, Y., Zhang, Q., et al. (2021). Breaches of Embankment and Landslide Dams - State of the Art Review. *Earth-Science Rev.* 216, 103597. doi:10.1016/j.earscirev.2021.103597

Zhou, G. G. D., Zhou, M., Shrestha, M. S., Song, D., Choi, C. E., Cui, K. F. E., et al. (2019). Experimental Investigation on the Longitudinal Evolution of Landslide Dam Breaching and Outburst Floods. *Geomorphology* 334, 29–43. doi:10.1016/j.geomorph.2019.02.035

Zhu, X., Liu, B., Peng, J., Zhang, Z., Zhuang, J., Huang, W., et al. (2021). Experimental Study on the Longitudinal Evolution of the Overtopping Breaching of Noncohesive Landslide Dams. *Eng. Geology.* 288, 106137. doi:10.1016/j.enggeo.2021.106137

Conflict of Interest: The authors declare that the research was conducted in the absence of any commercial or financial relationships that could be construed as a potential conflict of interest.

frontiers in Earth Science

ORIGINAL RESEARCH
published: 22 December 2021
doi: 10.3389/feart.2021.795854

Upper Bound Analysis of the Stability of 3D Slopes in the Saturated Soft Clay Subjected to Seismic Effect

Biao Zhang[1]*, *Yi Jiang*[1], *Hao Cheng*[2] and *Ze Liu*[1]

[1]Department of Civil Engineering,School of Civil Engineering, Hunan University of Science and Technology, Xiangtan, China, [2]Foshan Transportation Science and Technology Limited Company, Foshan, China

In order to study the three-dimensional stability problem of the saturated soft clay slope under earthquake loads, based on the three-dimensional rotation failure model, the seismic force was introduced into the calculation by the quasi-static method. The work rate of external loads and the internal energy dissipation rate of the saturated soft clay slope were calculated using the upper bound method of limit analysis, and the analytical solution of stability coefficient of saturated soft clay slopes was derived based on the fictitious power principle. By virtue of the exhaust algorithm, the optimal solution of stability coefficient of saturated soft clay slopes was obtained. The influence of the slope angle and the horizontal and vertical seismic forces on the stability coefficient of saturated soft clay slope was analyzed. The results show that the slope angle has a great influence on the stability coefficient, and the relative difference is up to 35.7%. Therefore, the stability coefficient of saturated soft clay slopes can be effectively increased by a proper slope setting. The horizontal and vertical seismic forces also have a significant influence on the stability of saturated soft clay slopes. The relative differences of the stability coefficient under horizontal and vertical seismic forces are as high as 41 and 14.7%, respectively. If they are ignored, the stability coefficient of saturated soft clay slopes will be seriously overestimated. It is suggested that the effects of horizontal and vertical seismic forces must be considered simultaneously in the seismic design of saturated soft clay slopes.

Keywords: saturated soft clay, slope stability, three-dimensional, failure model, upper bound theorem of limit analysis, quasi-static method

OPEN ACCESS

Edited by:
Fei Meng,
Swinburne University of Technology, Australia

Reviewed by:
Yongxin Li,
Hefei University of Technology, China
R. M. Yuan,
China Earthquake Administration, China
Sheng Zhang,
University of Warwick, United Kingdom
Fu Huang,
Changsha University of Science and Technology, China

***Correspondence:**
Biao Zhang
1020176@hnust.edu.cn

Specialty section:
This article was submitted to Geohazards and Georisks, a section of the journal Frontiers in Earth Science

Received: *15 October 2021*
Accepted: *24 November 2021*
Published: *22 December 2021*

Citation:
Zhang B, Jiang Y, Cheng H and Liu Z (2021) Upper Bound Analysis of the Stability of 3D Slopes in the Saturated Soft Clay Subjected to Seismic Effect. Front. Earth Sci. 9:795854. doi: 10.3389/feart.2021.795854

1 INTRODUCTION

Safety of the slope has always been a concern in engineering. Soil slopes are usually made of clay, sand, silt, etc. These soil slopes tend to fail under the action of earthquake and other external loads, thus causing huge loss to related projects (Leong and Rahardjo 2012; Gofar and Rahardjo 2017; VandenBerge and McGuire 2019).

Alejano et al. (2011), Selcuk et al. (2015) concluded that considering the safety of slope under the action of earthquake, the limit analysis method and the limit equilibrium method are mainly adopted. Michalowski and Park (2020) believe that the principle of limit equilibrium method is simple, but it only considers the yield condition and stress equilibrium condition of soil, and ignores the constitutive relation between soils. The limit analysis method overcomes this defect and establishes the constitutive relation of soil through the flow law (Yang and Liu 2018). Compared with the limit equilibrium method, it is stricter in theory and more accurate in calculation, so it

becomes an efficacious method to ensure the slope safety (Gischig et al., 2015; Rawat and Gupta 2016). The stability of the slope is considered by using the limit analysis method, and at present, the two-dimensional plane strain problem is gradually developed into a three-dimensional problem. In view of the complex soil slope, Jongmin et al. (2002) analyzed the slope stability and found that the method of limit analysis is better than the limit equilibrium method. Yao and Yang (2017) studied the stability of the unsaturated soil slope by introducing a uniform shear strength formula to consider the influence of intermediate principal stress. For the three-dimensional stability of the slope, Huang et al. (2002) expanded the 3D stability analysis method, making it possible to use " two-directional force and moment equilibrium" in any shape of 3D failure mechanism. This method can accurately compute the sliding direction of the failure surface and reduce the tedious work of conventional methods. Gao et al. (2015) extended the plane strain analysis of the slope strengthened by pile arrangement to the three-dimensional situation and used the limit analysis upper limit method to determine the safety coefficient. Aiming at the safety of the unsaturated three-dimensional soil slope under the condition of steady seepage, Wang et al. (2019) studied the safety of the 3D slope under the suction induction effect and permeability. Han et al. (2014) analyzed the effect of heterogeneity and anisotropy on the safety of 3D slopes.

So far, there have been many results of using the upper limit method to discuss the safety of slopes under earthquake problems. In 2009, Michalowski and Drescher (2009), Michalowski (2010) put forward a 3D rotational failure mechanism of the slope and investigated the impact of seismic forces on the slope stability and safety coefficient by the upper limit method. On the basis of the upper limit theorem of limit analysis, Nian et al. (2016) introduced the quasi-static method to research the safety of the anchored slope under the action of seismic forces. Zhang et al. (2016) studied the impact of seismic forces on the safety of the 3D slope by using the limit analysis upper bound method. Sahoo et al. (2016) studied the seismic failure mechanism of the non-reinforced soil slope and reinforced soil slope in detail using the shaking table test. To sum up, there are many research studies on the seismic problem of the slope, but few studies on the simultaneous action of horizontal and vertical seismic forces and saturated soft clay. Therefore, in this work, the effect of horizontal and vertical seismic forces on the stability of the saturated soft clay slope was studied based on the 3D rotational failure mechanism of the slope and the limit analysis upper bound method combined with the quasi-static method, so as to provide reference for the seismic design of similar projects in the future.

2 UPPER BOUND THEOREM OF LIMIT ANALYSIS

The aim of the upper bound theorem of limit analysis is to solve the limit failure load; for any hypothetical failure mode satisfying the allowable velocity field of motion, the upper limit of the ultimate load is the load obtained from the external power equal to the dissipated power of internal energy. The formula can be expressed as follows (Chen 2007; Yang and Wang 2018):

$$\int_V \sigma_{ij}\dot{\varepsilon}_{ij}^{*}\mathrm{d}V = \int_S T_i v_i^{*}\mathrm{d}S + \int_V F_i v_i^{*}\mathrm{d}V, \tag{1}$$

where $\boldsymbol{\sigma_{ij}}$ and $\boldsymbol{\dot{\varepsilon}_{ij}}$ are the stress state and the volume change rate at any point in the plastic failure zone, respectively; V and F_i are the volume and volume force of the unit in the plastic failure zone respectively; S and T_i are the surface area and surface force of the element in the plastic failure zone, respectively; and v_i^* refers to the velocity along the sliding surface.

3 3D FAILURE MECHANISM

Figure 1 shows the 3D rotational failure mechanism for saturated soft clay slopes. Rotating the failure surface around O point with angular velocity ω, it passes through A point at the top of the slope and C point at the toe of the slope, forming two logarithmic spiral curves of AC and $A'C'$, where the angle between OA and OA' and the horizontal direction is θ_A, the lengths are r_0 and r_0', respectively, the radius of C is r_h, the angle of OB is θ_B, the angle between the direction diameter and the horizontal direction of any point on arcs AC and $A'C'$ is θ, and the lengths are r and r', respectively. As shown in **Figure 1**, the plane perpendicular to the paper surface at O point intersects with the 3D rotational failure mechanism to form a circle; a rectangular coordinate system is established on the circle, with the positive direction of the Y-axis along the radial direction. Here, R is the radius of the circle and r_m is the radius of the center of the circle.

According to geometry,

$$r = r_0 \exp\left[(\theta - \theta_0)\tan\varphi\right] \tag{2}$$

$$r' = r_0' \exp\left[-(\theta - \theta_0)\tan\varphi\right] \tag{3}$$

$$r_m = \frac{r + r'}{2} = r_0 f_1 \tag{4}$$

$$R = \frac{r - r'}{2} = r_0 f_2 \tag{5}$$

$$\frac{H}{r_0} = \mathrm{e}^{(\theta_h - \theta_0)\tan\varphi} \cdot \sin(\theta_h) - \sin(\theta_0), \tag{6}$$

where f_1 and f_2 are, respectively:

$$f_1 = \frac{1}{2}\left[\mathrm{e}^{(\theta-\theta_0)\tan\varphi} + \frac{r_0'}{r_0}\mathrm{e}^{-(\theta-\theta_0)\tan\varphi}\right] \tag{7}$$

$$f_2 = \frac{1}{2}\left[\mathrm{e}^{(\theta-\theta_0)\tan\varphi} - \frac{r_0'}{r_0}\mathrm{e}^{-(\theta-\theta_0)\tan\varphi}\right]. \tag{8}$$

In order to reflect the state of saturated soft clay slope failure more truly, a block with width b is inserted into the middle of the 3D rotational failure mechanism, as shown in **Figure 2**; as $b \to +\infty$, the 3D failure mechanism degenerates to a 2D plane strain condition. The combined failure mechanism can be used to analyze the 3D stability of saturated soft clay slopes of any width; in the analysis of this study, let the maximum width of the 3D rotational failure mechanism with insert block be b_2, and the maximum width of the failure mechanism without insert block be b_1, then $b + b_1 = b_2$.

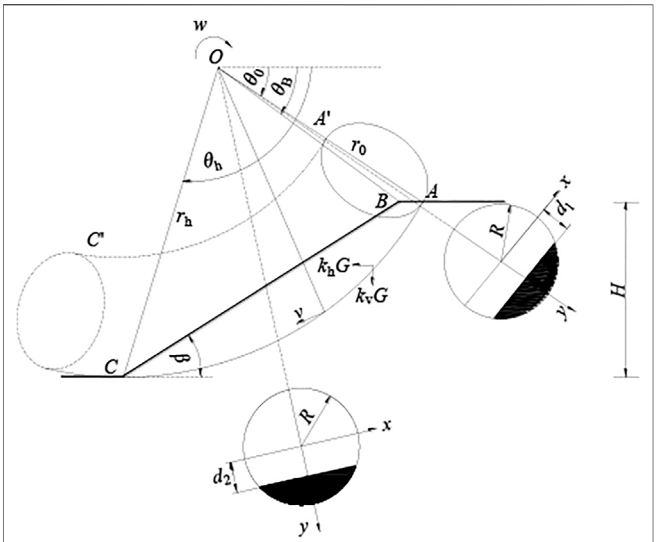

FIGURE 1 | 3D rotational failure mechanism.

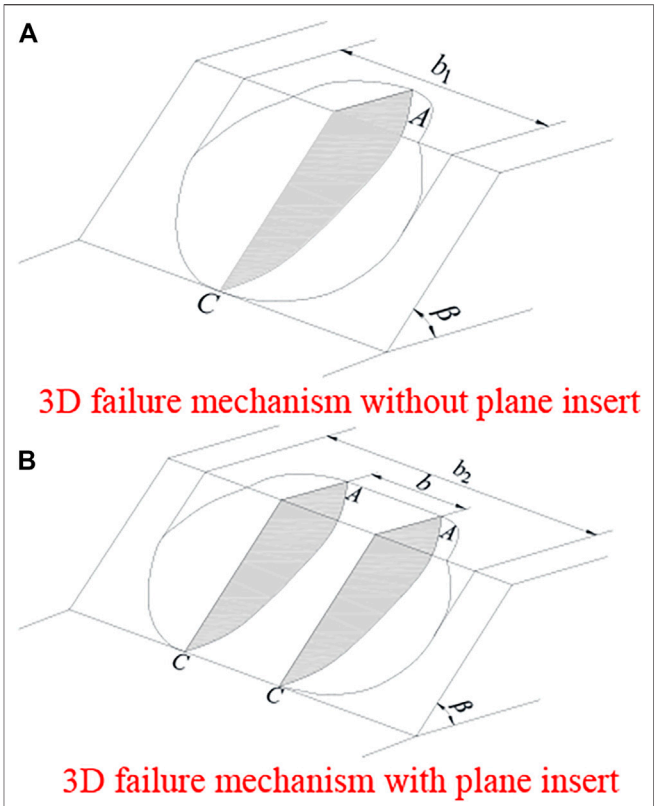

FIGURE 2 | 3D failure mechanism. **(A)** 3D failure mechanism without plane insert, **(B)** 3D failure mechanism with plane insert.

4 CALCULATION OF THE WORK RATES

In this study, the saturated soft clay slope with a single soil layer is calculated, and the following assumptions are made: 1) the soil mass satisfies the ideal elastic–plastic model and complies with the Mohr–Coulomb failure criterion and the associated flow law, and 2) for saturated soft clay, the calculation assumes that its internal friction angle value is close to 0.

4.1 The External Work Rates

In the calculation, the 3D rotational failure mechanism of the saturated soft clay slope is divided into two parts: the 3D rotational failure mechanism without the plane insert and with the plane insert, respectively; finally, the two are superimposed. The external work rates are composed of the work rates of soil weight and seismic forces.

1) The work rates of soil weight

The work rates of soil weight W_γ are divided into two parts for the calculation: the first part is the 3D rotational failure mechanism without plane insert $W_{\gamma\text{-3D}}$.

$$W_{\gamma-3D} = 2\omega\gamma \cdot \left[\int_{\theta_0}^{\theta_B} \int_0^{x_1^*} \int_{d_1}^{y^*} (r_m + y)^2 \cos\theta \mathrm{d}x\mathrm{d}y\mathrm{d}\theta + \int_{\theta_B}^{\theta_h} \int_0^{x_2^*} \int_{d_2}^{y^*} (r_m + y)^2 \cos\theta \mathrm{d}x\mathrm{d}y\mathrm{d}\theta \right] = \gamma\omega r_0^4 g_1, \tag{9}$$

where γ is the soil weight, and g_1 is the intermediate variable.

The other part is the work rate of soil weight with plane insert $W_{\gamma\text{-insert}}$.

$$W_{\gamma-\text{insert}} = 2\omega\gamma \cdot \left[\int_{\theta_0}^{\theta_B} \int_0^{\frac{b}{2}} \int_{d_1}^{R} (r_m + y)^2 \cos\theta \mathrm{d}x\mathrm{d}y\mathrm{d}\theta + \int_{\theta_B}^{\theta_h} \int_0^{\frac{b}{2}} \int_{d_2}^{R} (r_m + y)^2 \cos\theta \mathrm{d}x\mathrm{d}y\mathrm{d}\theta \right] = \gamma\omega r_0^4 g_2 \tag{10}$$

where g_2 is the intermediate variable.

In summary, the work rate of the total soil weight W_γ in the 3D rotational failure mechanism with a plane insert is as follows:

$$W_\gamma = W_{\gamma-3D} + W_{\gamma-\text{insert}}, \tag{11}$$

where

$$x_i^* = \sqrt{R^2 - d_i^2}\,(i = 1, 2) \tag{12}$$

$$y^* = \sqrt{R^2 - x^2} \tag{13}$$

$$d_1 = \frac{r_0 \sin\theta_0}{\sin\theta} - r_m = r_0 f_3 \tag{14}$$

$$d_2 = \frac{r_0 \sin(\theta_h + \beta)}{\sin(\theta + \beta)} e^{(\theta_h - \theta_0)\tan\varphi} - r_m \quad = r_0 f_4 \tag{15}$$

$$\theta_B = \arctan\frac{\sin\theta_0}{\cos\theta_0 - l} \tag{16}$$

$$l = \frac{\sin(\theta_h - \theta_0)}{\sin\theta_h} - \frac{\sin(\theta_h + \beta)}{\sin\theta_h \sin\beta}\left(\sin\theta_h e^{(\theta_h - \theta_0)\tan\varphi} - \sin\theta_0\right), \quad (17)$$

where f_3 and f_4 are dimensional functions of 1.

2) The work rates of seismic force

In this article, the pseudo-static method is used to analyze the stability of the three-dimensional slope. According to the pseudo-static method, the horizontal seismic force $F_{kh} = k_h G$ and the vertical seismic force $F_{kv} = k_v G$, where G is soil gravity and k_h is the horizontal seismic coefficient. According to the Code for Seismic Design of Buildings GB50011-2010 (China), its value generally ranges from 0 to 0.3; k_v is the vertical seismic coefficient, $k_v = \zeta k_h$, and ζ is the vertical earthquake proportional coefficient. Because the effect of vertical earthquake is less than that of horizontal earthquake, its value generally ranges from −1 to 1. When $\zeta > 0$, the vertical earthquake force is downward.

The work rate by the horizontal seismic forces in the 3D rotational failure mechanism without the plane insert W_{k_h-3D} is as follows:

$$\begin{aligned} W_{k_h-3D} &= 2k_h\omega\gamma \cdot \left[\int_{\theta_0}^{\theta_B} \int_0^{x_1^*} \int_{d_1}^{y^*} (r_m + y)^2 \sin\theta \mathrm{d}x\mathrm{d}y\mathrm{d}\theta \right. \\ &\quad \left. + \int_{\theta_B}^{\theta_h} \int_0^{x_2^*} \int_{d_2}^{y^*} (r_m + y)^2 \sin\theta \mathrm{d}x\mathrm{d}y\mathrm{d}\theta \right] \\ &= k_h\gamma\omega r_0^4 g_3, \end{aligned} \quad (18)$$

where g_3 is the intermediate variable.

Similarly, the work rate generated by the horizontal seismic forces acting on plane insert $W_{k_h-insert}$ is as follows:

$$\begin{aligned} W_{k_h-insert} &= 2k_h\omega\gamma \cdot \left[\int_{\theta_0}^{\theta_B} \int_0^{\frac{b}{2}} \int_{d_1}^{R} (r_m + y)^2 \sin\theta \mathrm{d}x\mathrm{d}y\mathrm{d}\theta \right. \\ &\quad \left. + \int_{\theta_B}^{\theta_h} \int_0^{\frac{b}{2}} \int_{d_2}^{R} (r_m + y)^2 \sin\theta \mathrm{d}x\mathrm{d}y\mathrm{d}\theta \right] \\ &= k_h\gamma\omega r_0^4 g_4, \end{aligned} \quad (19)$$

where g_4 is the intermediate variable.

In summary, the work rates generated by the total horizontal seismic forces in the 3D rotational failure mechanism without the plane insert W_{k_h} are as follows:

$$W_{k_h} = W_{k_h-3D} + W_{k_h-insert}. \quad (20)$$

Similar to the work done by the horizontal seismic forces, the work rates of vertical seismic forces are also composed of two parts: the 3D rotational failure mechanism without plane insert W_{k_v-3D} is given as follows:

$$\begin{aligned} W_{k_v-3D} &= 2\zeta k_h\omega\gamma \cdot \left[\int_{\theta_0}^{\theta_B} \int_0^{x_1^*} \int_{d_1}^{y^*} (r_m + y)^2 \cos\theta \mathrm{d}x\mathrm{d}y\mathrm{d}\theta \right. \\ &\quad \left. + \int_{\theta_B}^{\theta_h} \int_0^{x_2^*} \int_{d_2}^{y^*} (r_m + y)^2 \cos\theta \mathrm{d}x\mathrm{d}y\mathrm{d}\theta \right] \\ &= \zeta k_h\gamma\omega r_0^4 g_1, \end{aligned} \quad (21)$$

the work rate generated by the horizontal seismic forces acting on plane insert $W_{k_v-insert}$ is given as follows:

$$\begin{aligned} W_{k_v-insert} &= 2\zeta k_h\omega\gamma \cdot \left[\int_{\theta_0}^{\theta_B} \int_0^{\frac{b}{2}} \int_{d_1}^{R} (r_m + y)^2 \cos\theta \mathrm{d}x\mathrm{d}y\mathrm{d}\theta \right. \\ &\quad \left. + \int_{\theta_B}^{\theta_h} \int_0^{\frac{b}{2}} \int_{d_2}^{R} (r_m + y)^2 \cos\theta \mathrm{d}x\mathrm{d}y\mathrm{d}\theta \right] \\ &= \zeta k_h\gamma\omega r_0^4 g_2, \end{aligned} \quad (22)$$

Therefore, the total work rates of vertical seismic forces, which act on the 3D rotational failure mechanism without plane insert W_{k_v}, are as follows:

$$W_{k_v} = W_{k_v-3D} + W_{k_v-insert}, \quad (23)$$

In summary, the work rates of soil weight and seismic forces in the 3D rotational failure mechanism with plane insert, namely, the external work rates can be expressed as follows:

$$W = W_\gamma + W_{k_h} + W_{k_v}, \quad (24)$$

4.2 Internal Energy Dissipation

The internal energy dissipation rates of the 3D rotational failure mechanism without the plane insert are calculated, and the saturated soft clay slope is divided into *AB* and *BC* parts along the extension line of *OB*, the internal energy dissipation rates are $D_{AB\text{-}3D}$ and $D_{BC\text{-}3D}$, respectively:

$$\begin{aligned} D_{AB-3D} &= 2\omega cR \cdot \int_{\theta_0}^{\theta_B} \int_0^{\alpha_1^*} (r_m + R\cos\alpha)^2 \mathrm{d}\alpha\mathrm{d}\theta \\ &= \omega c r_0^3 g_5 \end{aligned} \quad (25)$$

$$\begin{aligned} D_{BC-3D} &= 2\omega cR \cdot \int_{\theta_B}^{\theta_h} \int_0^{\alpha_2^*} (r_m + R\cos\alpha)^2 \mathrm{d}\alpha\mathrm{d}\theta \\ &= \omega c r_0^3 g_6, \end{aligned} \quad (26)$$

where c is the cohesion of soil, and g_5 and g_6 are intermediate variables, respectively.

The internal energy dissipated rates acting on the plane insert D_{insert} are as follows:

$$\begin{aligned} D_{insert} &= b \int_{\theta_0}^{\theta_h} cv\cos\varphi \frac{r}{\cos\varphi} \mathrm{d}\theta \\ &= \omega c r_0^3 g_7, \end{aligned} \quad (27)$$

where v is the velocity and g_7 is the intermediate variable.

In summary, the total internal energy dissipated rates can be expressed as follows:

$$D = D_{AB-3D} + D_{BC-3D} + D_{insert}, \quad (28)$$

where

$$\alpha_1^* = \arccos(d_1/R), \quad (29)$$

$$\alpha_2^* = \arccos(d_2/R), \quad (30)$$

$$v = \omega\rho = (r_m + y)\omega, \quad (31)$$

where ρ is the direction diameter of any point and ω is the angular velocity at this point.

TABLE 1 | Comparing the results between this study and Michalowski and Drescher (2009).

B/H	Result	$\beta = 45^{\circ}$	$\beta = 60^{\circ}$	$\beta = 75^{\circ}$	$\beta = 90^{\circ}$
0.5	N_L (Michalowski and Drescher 2009)	13.541	11.484	9.987	8.753
	N_L (this study)	13.029	10.992	9.707	8.784
	Relative errors Δ_1	3.8%	4.3%	2.8%	0.4%
0.6	N_L (Michalowski and Drescher 2009)	12.326	10.493	9.126	7.969
	N_L (this study)	11.818	9.855	8.671	7.730
	Relative errors Δ_1	4.1%	6.1%	5.0%	3.0%
0.8	N_L (Michalowski and Drescher 2009)	10.786	9.241	8.036	6.977
	N_L (this study)	10.424	8.554	7.516	6.606
	Relative errors Δ_1	3.4%	7.4%	6.5%	5.3%
1	N_L (Michalowski and Drescher 2009)	9.847	8.478	7.371	6.373
	N_L (this study)	9.574	7.828	6.864	5.990
	Relative errors Δ_1	2.8%	7.7%	6.9%	6.0%
1.5	N_L (Michalowski and Drescher 2009)	8.078	7.441	6.469	5.554
	N_L (this study)	8.454	6.910	6.031	5.198
	Relative errors Δ_1	4.6%	7.1%	6.8%	6.4%
2	N_L (Michalowski and Drescher 2009)	7.630	6.897	6.008	5.136
	N_L (this study)	7.952	6.467	5.639	4.828
	Relative errors Δ_1	4.2%	6.2%	6.1%	6.0%
3	N_L (Michalowski and Drescher 2009)	6.969	6.163	5.498	4.694
	N_L (this study)	7.445	6.040	5.254	4.473
	Relative errors Δ_1	6.8%	2.0%	4.4%	4.7%
5	N_L (Michalowski and Drescher 2009)	6.522	5.758	5.115	4.334
	N_L (this study)	7.054	5.725	4.967	4.204
	Relative errors Δ_1	8.2%	0.6%	2.9%	3.0%
10	N_L (Michalowski and Drescher 2009)	6.151	5.473	4.768	4.018
	N_L (this study)	6.776	5.492	4.763	4.016
	Relative errors Δ_1	10.2%	0.3%	0.1%	0.1%

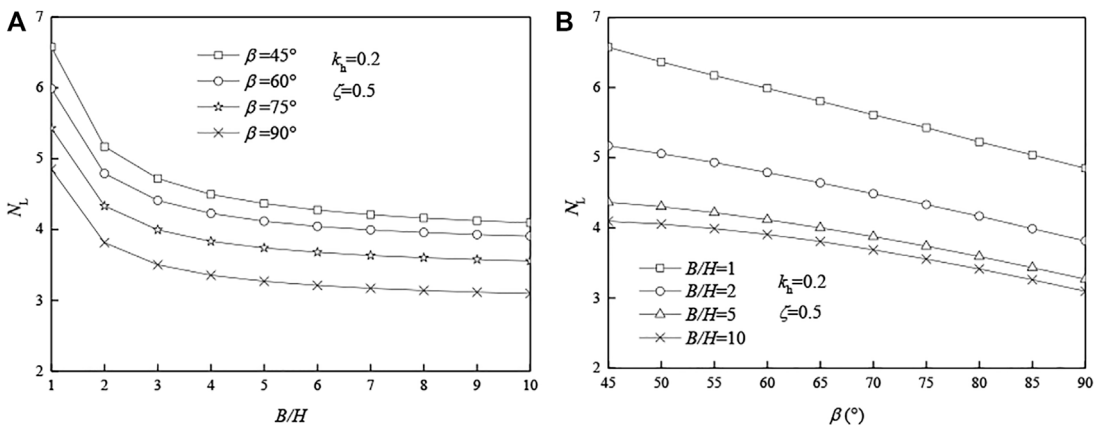

FIGURE 3 | Effects of the ratio *B/H* and slope angle β on stability factor N_L: **(A)** *B/H*; **(B)** β.

4.3 Upper Bound Solution

As the internal energy dissipation rate and external work rate are equal, the critical height of the saturated soft clay slope can be obtained as follows:

$$H_c = \frac{c\cot\varphi}{\gamma}\cdot\left[e^{(\theta_h-\theta_0)\tan\varphi}\sin\theta_h - \sin\theta_0\right] \cdot \frac{g_5+g_6+g_7}{(1+\zeta k_h)(g_1+g_2)+k_h(g_3+g_4)}, \quad (32)$$

In order to analyze the stability of the 3D saturated soft clay slope, the stability factor N_L is introduced in this article. Under the Mohr–Coulomb failure criterion, the stability factor of the saturated soft clay slope can be defined as follows:

$$N_L = \gamma H_c/c, \quad (33)$$

The stability of the slope is different with the sliding surface. Therefore, we need to take different θ_0 and θ_h to

TABLE 2 | Effects of the ratio *B/H* on stability factor N_L (k_h = 0.2, ζ = 0.5).

B/H	β = 45°		β = 60°		β = 75°		β = 90°	
	N_L	Δ_2	N_L	Δ_2	N_L	Δ_2	N_L	Δ_2
1	6.58	—	5.99	—	5.43	—	4.85	—
2	5.17	21.4%	4.79	20.0%	4.33	20.3%	3.81	21.3%
3	4.72	8.7%	4.41	7.9%	3.99	7.8%	3.50	8.2%
4	4.49	4.8%	4.23	4.1%	3.83	4.0%	3.35	4.2%
5	4.36	2.9%	4.12	2.6%	3.74	2.4%	3.27	2.5%
6	4.27	2.1%	4.04	1.7%	3.68	1.6%	3.21	1.8%
7	4.21	1.5%	3.99	1.2%	3.63	1.2%	3.17	1.3%
8	4.16	1.1%	3.96	0.9%	3.60	0.9%	3.14	1.0%
9	4.12	0.9%	3.93	0.7%	3.58	0.7%	3.11	0.7%
10	4.09	0.7%	3.91	0.6%	3.56	0.6%	3.10	0.6%

TABLE 3 | Effects of slope angle β on stability factor N_L (k_h = 0.2, ζ = 0.5).

β(°)	*B/H* = 1		*B/H* = 2		*B/H* = 5		*B/H* = 10	
	N_L	Δ_3	N_L	Δ_3	N_L	Δ_3	N_L	Δ_3
90	4.85	—	3.81	—	3.27	—	3.10	—
85	5.04	3.9%	3.99	4.7%	3.43	4.9%	3.26	5.2%
80	5.23	7.8%	4.17	9.4%	3.59	9.8%	3.41	10.0%
75	5.43	12.0%	4.33	13.6%	3.74	14.4%	3.56	14.8%
70	5.61	15.7%	4.49	17.8%	3.88	18.7%	3.69	19.0%
65	5.80	19.6%	4.64	21.8%	4.00	22.3%	3.81	22.9%
60	5.99	23.5%	4.79	25.7%	4.12	26.0%	3.91	26.1%
55	6.17	27.2%	4.93	29.4%	4.22	29.1%	3.99	28.7%
50	6.37	31.3%	5.06	32.8%	4.30	31.5%	4.05	30.6%
45	6.58	35.7%	5.17	35.7%	4.36	33.3%	4.09	31.9%

calculate different N_L according to **Eqs. 32**, **33**. The minimum N_L is the stability factor of the slope, and the corresponding θ_0 and θ_h determine the slip surface of the slope. The formula to solve the stability factor N_L is complicated, and it needs to be calculated by MATLAB software.

In addition, in the calculation, $f_3 \sim f_{10}$ and $g_1 \sim g_7$ are functions of dimension 1, and their expressions are, respectively, given as follows:

$$f_3 = \frac{\sin\theta_0}{\sin\theta} - \frac{1}{2}\left[\mathrm{e}^{(\theta-\theta_0)\tan\varphi} + \frac{r_0'}{r_0}\mathrm{e}^{-(\theta-\theta_0)\tan\varphi}\right] \tag{34}$$

$$f_4 = \frac{\sin(\theta_h+\beta)}{\sin(\theta+\beta)}e^{(\theta_h-\theta_0)\tan\varphi} - \frac{1}{2}\left[\mathrm{e}^{(\theta-\theta_0)\tan\varphi} + \frac{r_0'}{r_0}\mathrm{e}^{-(\theta-\theta_0)\tan\varphi}\right] \tag{35}$$

$$f_5 = \frac{1}{3(1+9\tan^2\varphi)}\cdot\left[(3\tan\varphi\cos\theta_h + \sin\theta_h)e^{3(\theta_h-\theta_0)\tan\varphi} - (3\tan\varphi\cos\theta_0 + \sin\theta_0)\right] \tag{36}$$

$$f_6 = \frac{1}{6}\left(2\cos\theta_0 - \frac{L}{r_0}\right)\frac{L\sin\theta_0}{r_0} \tag{37}$$

$$f_7 = \frac{H}{3r_0}\cdot\left[(\cos^2\theta_h + \sin\theta_h\cos\theta_h\cot\beta)\mathrm{e}^{2(\theta_h-\theta_0)\tan\varphi} + \frac{H}{2r_0}(\cos\theta_h\cot\beta + \sin\theta_h\cot^2\beta)\mathrm{e}^{(\theta_h-\theta_0)\tan\varphi}\right] \tag{38}$$

$$f_8 = \frac{1}{3(1+9\tan^2\varphi)}\cdot\left[(3\tan\varphi\sin\theta_h - \cos\theta_h)e^{3(\theta_h-\theta_0)\tan\varphi} - 3\tan\varphi\sin\theta_0 + \cos\theta_0\right] \tag{39}$$

$$f_9 = \frac{1}{3}\frac{L}{r_0}\sin^2\theta_0 \tag{40}$$

$$f_{10} = \frac{H}{3r_0}\cdot\left[(\cos\theta_h\sin\theta_h + \sin^2\theta_h\cot\beta)\mathrm{e}^{2(\theta_h-\theta_0)\tan\varphi} - \frac{H}{2r_0}(\cos\theta_h + \sin\theta_h\cot\beta)\mathrm{e}^{(\theta_h-\theta_0)\tan\varphi}\right] \tag{41}$$

$$\begin{aligned} g_1 &= 2\int_{\theta_0}^{\theta_B}\left[\left(\frac{f_2^2f_3}{8} - \frac{f_3^3}{4} - \frac{2f_1f_2^2}{3} - \frac{f_3f_1^2}{2} + \frac{2f_1f_2^2}{3}\right)\cdot\sqrt{f_2^2-f_3^2} + \left(\frac{f_2^4}{8} + \frac{f_2^2f_1^2}{2}\right)\cdot\arcsin\left(\frac{\sqrt{f_2^2-f_3^2}}{f_2}\right)\right]\cos\theta\mathrm{d}\theta \\ &+2\int_{\theta_B}^{\theta_h}\left[\left(\frac{f_2^2f_4}{8} - \frac{f_4^3}{4} - \frac{2f_1f_4^2}{3} - \frac{f_4f_1^2}{2} + \frac{2f_1f_2^2}{3}\right)\cdot\sqrt{f_2^2-f_4^2} + \left(\frac{f_2^4}{8} + \frac{f_2^2f_1^2}{2}\right)\cdot\arcsin\left(\frac{\sqrt{f_2^2-f_4^2}}{f_2}\right)\right]\cos\theta\mathrm{d}\theta \end{aligned} \tag{42}$$

$$g_2 = \frac{b}{H}(f_5 - f_6 - f_7)\cdot\left[\mathrm{e}^{(\theta_h-\theta_0)\tan\varphi}\sin\theta_h - \sin\theta_0\right] \tag{43}$$

$$\begin{aligned} g_3 &= 2\int_{\theta_0}^{\theta_B}\left[\left(\frac{f_2^2f_3}{8} - \frac{f_3^3}{4} - \frac{2f_1f_3^2}{3} - \frac{f_3f_1^2}{2} + \frac{2f_1f_2^2}{3}\right)\cdot\sqrt{f_2^2-f_3^2} + \left(\frac{f_2^4}{8} + \frac{f_2^2f_1^2}{2}\right)\arcsin\left(\frac{\sqrt{f_2^2-f_3^2}}{f_2}\right)\right]\sin\theta\mathrm{d}\theta \\ &+2\int_{\theta_B}^{\theta_h}\left[\left(\frac{f_2^2f_4}{8} - \frac{f_4^3}{4} - \frac{2f_1f_4^2}{3} - \frac{f_4f_1^2}{2} + \frac{2f_1f_2^2}{3}\right)\cdot\sqrt{f_2^2-f_4^2} + \left(\frac{f_2^4}{8} + \frac{f_2^2f_1^2}{2}\right)\arcsin\left(\frac{\sqrt{f_2^2-f_4^2}}{f_2}\right)\right]\sin\theta\mathrm{d}\theta \end{aligned} \tag{44}$$

$$g_4 = \frac{b}{H}(f_8 - f_9 - f_{10})\cdot\left[\mathrm{e}^{(\theta_h-\theta_0)\tan\varphi}\sin\theta_h - \sin\theta_0\right] \tag{45}$$

$$g_5 = 2\int_{\theta_0}^{\theta_B}\left[f_2\left(f_1^2 + \frac{f_2^2}{2}\right)\arccos\left(\frac{f_3}{f_2}\right) + f_2\left(2f_1 + \frac{f_3}{2}\right)\sqrt{f_2^2-f_3^2}\right]\mathrm{d}\theta \tag{46}$$

$$g_6 = 2\int_{\theta_B}^{\theta_h}\left[f_2\left(f_1^2 + \frac{f_2^2}{2}\right)\arccos\left(\frac{f_4}{f_2}\right) + f_2\left(2f_1 + \frac{f_4}{2}\right)\sqrt{f_2^2-f_4^2}\right]\mathrm{d}\theta \tag{47}$$

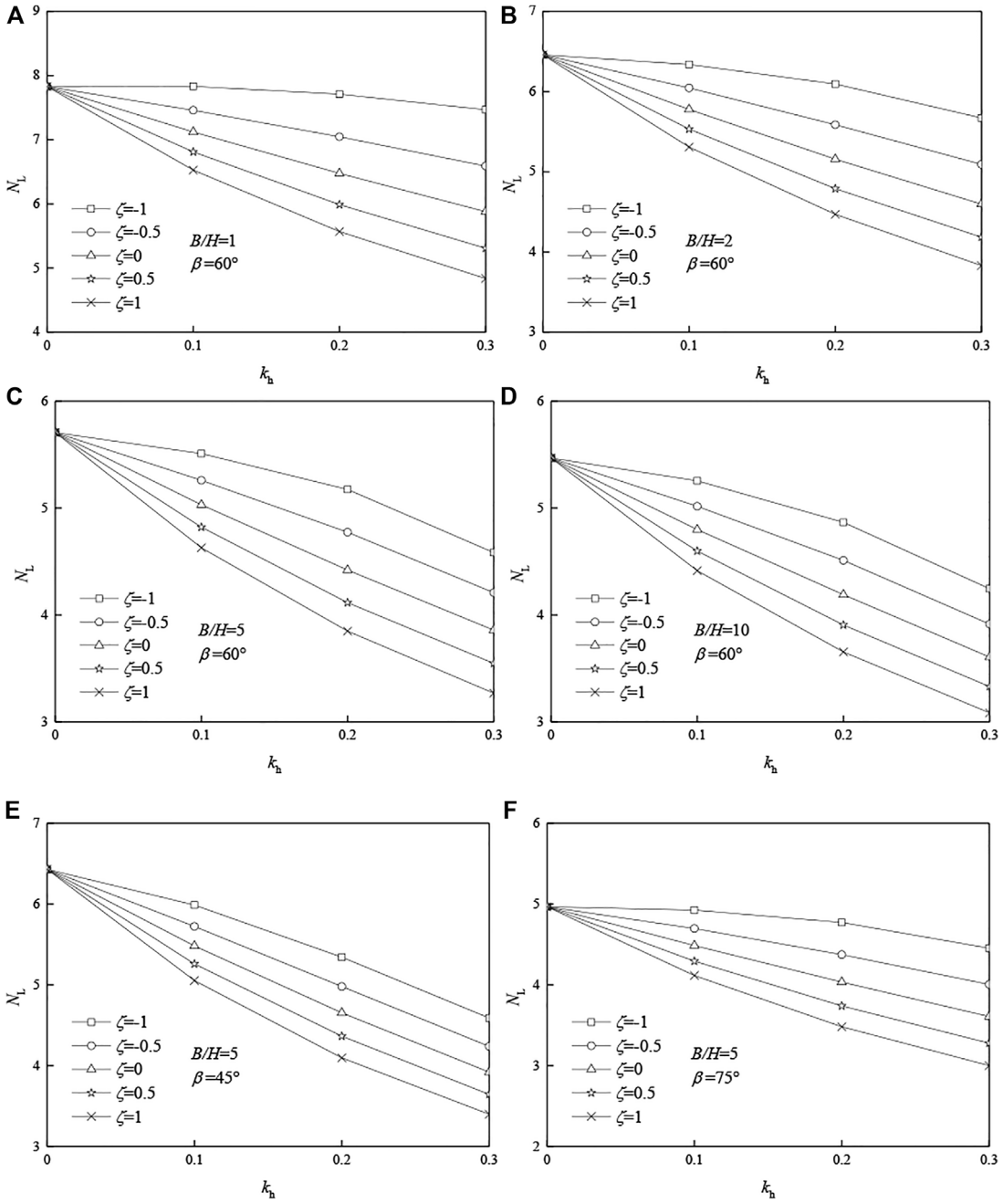

FIGURE 4 | Effects of the horizontal seismic effect coefficient k_h on stability factor N_L: **(A)** $B/H = 1$, $\beta = 60^\circ$; **(B)** $B/H = 2$, $\beta = 60^\circ$; **(C)** $B/H = 5$, $\beta = 60^\circ$; **(D)** $B/H = 10$, $\beta = 60^\circ$; **(E)** $B/H = 5$, $\beta = 45^\circ$; **(F)** $B/H = 5$, $\beta = 75^\circ$.

$$g_7 = \frac{b}{H}\left[e^{(\theta_h-\theta_0)\tan\varphi}\sin\theta_h - \sin\theta_0\right]\cdot\int_{\theta_0}^{\theta_h} e^{2(\theta-\theta_0)\tan\varphi}d\theta, \quad (48)$$

5 COMPARISON

In order to simplify the study, the research object of this article is the same as Michalowski and Drescher (2009), and the friction problem of complex clays is not considered. Without considering the seismic load ($k_h = 0$, $k_v = 0$), the stability factor N_L of the saturated soft clay slope ($\varphi = 0$) is calculated. **Table 1** shows the comparisons between the stability factors calculated in the work and the results of Michalowski and Drescher (2009). As can be seen from **Table 1**, the results of the two methods are quite similar, and the maximum error is only 10.2%. It shows that calculation in this article is effective.

TABLE 4 | Effects of the horizontal seismic effect coefficient k_h on stability factor N_L (ζ = 0).

B/H	β(°)	k_h = 0	k_h = 0.1		k_h = 0.2		k_h = 0.3	
		N_L	N_L	Δ_4 (%)	N_L	Δ_5 (%)	N_L	Δ_6 (%)
1	45	9.06	7.98	11.9	7.08	21.9	6.33	30.2
2	45	7.36	6.37	13.4	5.55	24.7	4.84	34.3
5	45	6.43	5.48	14.7	4.65	27.6	3.92	39.0
10	45	6.15	5.20	15.5	4.36	29.2	3.63	41.0
1	60	7.83	7.12	9.0	6.48	17.3	5.88	24.9
2	60	6.46	5.78	10.5	5.16	20.1	4.60	28.8
5	60	5.71	5.03	11.8	4.42	22.5	3.86	32.4
10	60	5.47	4.80	12.3	4.19	23.4	3.61	34.0
1	75	6.86	7.12	3.7	5.89	14.2	5.42	21.1
2	75	5.64	5.78	2.5	4.68	17.0	4.25	24.6
5	75	4.97	5.03	1.3	4.03	18.8	3.61	27.3
10	75	4.76	4.80	0.7	3.83	19.6	3.41	28.4
1	90	5.99	5.64	5.9	5.27	12.1	4.92	17.9
2	90	4.83	4.48	7.2	4.14	14.3	3.81	21.1
5	90	4.20	3.86	8.1	3.53	16.0	3.22	23.3
10	90	4.02	3.67	8.5	3.35	16.7	3.05	24.1

6 RESULTS ANALYSIS

6.1 Influence of Slope Width-to-Height Ratio and Slope Angle

Considering the seismic load ($k_h = 0.2$, $\zeta = 0.5$), the influence of *B/H* and β on stability factors is shown in **Figure 3**. As shown in **Figure 3A**, the slope stability factor N_L decreases with the increase in *B/H*, and the decreasing trend becomes more gentle and finally tends to level. As can be seen from **Table 2**, when $B/H \geq 8$ and β = 45°, 60°, 75°, and 90°, the relative error between stability factors is only 1%. Assume that the relative error allowed is 1%, and the conclusions are as follows:

1) When *B/H* = 1 or 2, the three-dimensional effect of the slope is very prominent, and the relative error between stability factors can reach 21.4%.
2) As *B/H* increases from 1 to 7, the stability coefficient of the slope decreases gradually, and the three-dimensional effect of the slope becomes less and less prominent.
3) When $B/H \geq 8$, the stability factor of the slope is approximate to a certain value, and the three-dimensional slope can be simplified as a two-dimensional problem.

As shown in **Figure 3B**, when β increases, the slope stability factor N_L decreases, and when B/H is larger (B/H = 10), N_L decreases more. Compared with the original slope, when the slope angle increases, the sliding surface does not change, but the soil mass of the slope increases. The internal energy dissipation rate remains unchanged, and the external work rate increases, so the slope stability factor N_L decreases. The larger the B/H is (such as B/H = 10), the more soil mass increases, and the greater the slope stability factor decreases.

As can be seen from **Table 3**, when the slope angle β decreases by 5° each time from 90° to 45°, the stability factor N_L approximately increases by 1/3. The slope angle has a significant effect on slope stability, and reasonable design of a smaller slope angle is particularly important, which greatly increases the safety of the slope and reduces the possibility of slope landslide.

In conclusion, *B/H* and β significantly affect the stability factor N_L. The ratio *B/H* represents the three-dimensional effect degree of the slope. When *B/H* is large enough ($B/H \geq 8$), the slope stability can be simplified into a two-dimensional problem.

$$\Delta_2 = \left|\frac{N_L(B/H = n+1) - N_L(B/H = n)}{N_L(B/H = n)}\right| \times 100\%$$

$$\Delta_3 = \left|\frac{N_L(\beta = n) - N_L(\beta = 90°)}{N_L(\beta = 90°)}\right| \times 100\%.$$

6.2 Influence of Horizontal Seismic Force

It can be seen from **Figure 4**, the stability factor N_L of the saturated soft clay slope decreases with the increase in k_h. As the critical height H_c decreases, both the rate of external work and the rate of internal energy dissipation decrease, but the work rate of external force decreases more. When the horizontal seismic force increases, the work rate of the three-dimensional slope increases. According to the conservation of energy, the critical height H_c of the slope decreases, so the stability factor N_L decreases.

As can be seen from **Table 4**, taking $B/H = 1$, $\beta = 45°$ as an example, without considering the effect of horizontal seismic force ($k_h = 0$), the safety factor is 9.06. When k_h increased from 0.1 to 0.3, the safety factor N_L decreased from 7.98 to 6.33. Compared with $k_h = 0$, the minimum relative error was 11.9% and the maximum was 30.2%.

Taking $B/H = 10$, $\beta = 45°$ as an example, without considering the effect of horizontal seismic force ($k_h = 0$), the safety factor is 6.15. When k_h increased from 0.1 to 0.3, the safety factor N_L decreased from 5.20 to 3.63. Compared with $k_h = 0$, the minimum relative error was 15.5% and the maximum was 41.0%.

It shows that the horizontal seismic force obviously affects the safety factors of saturated soft clay slope. Especially when *B/H* is large, the slope stability problem can be regarded as a two-dimensional problem. If the influence of the horizontal seismic force is ignored, the stability factor of the slope will be significantly overestimated.

$$\Delta_4 = \left|\frac{N_L(k_h = 0.1) - N_L(k_h = 0)}{N_L(k_h = 0)}\right| \times 100\%,$$

$$\Delta_5 = \left|\frac{N_L(k_h = 0.2) - N_L(k_h = 0)}{N_L(k_h = 0)}\right| \times 100\%,$$

$$\Delta_6 = \left|\frac{N_L(k_h = 0.3) - N_L(k_h = 0)}{N_L(k_h = 0)}\right| \times 100\%$$

6.3 Influence of Vertical Seismic Force

It can be seen from **Figure 5**, when the vertical seismic effect proportion coefficient ζ increases, the stability factor N_L of the saturated soft clay slope decreases. When $\zeta > 0$, the vertical seismic force is downward, which is not conducive to the stability of the slope. When the vertical seismic force increases, the work rate of the three-dimensional slope increases. According to the conservation of energy, the critical height H_c of the slope decreases, so the stability factor N_L decreases.

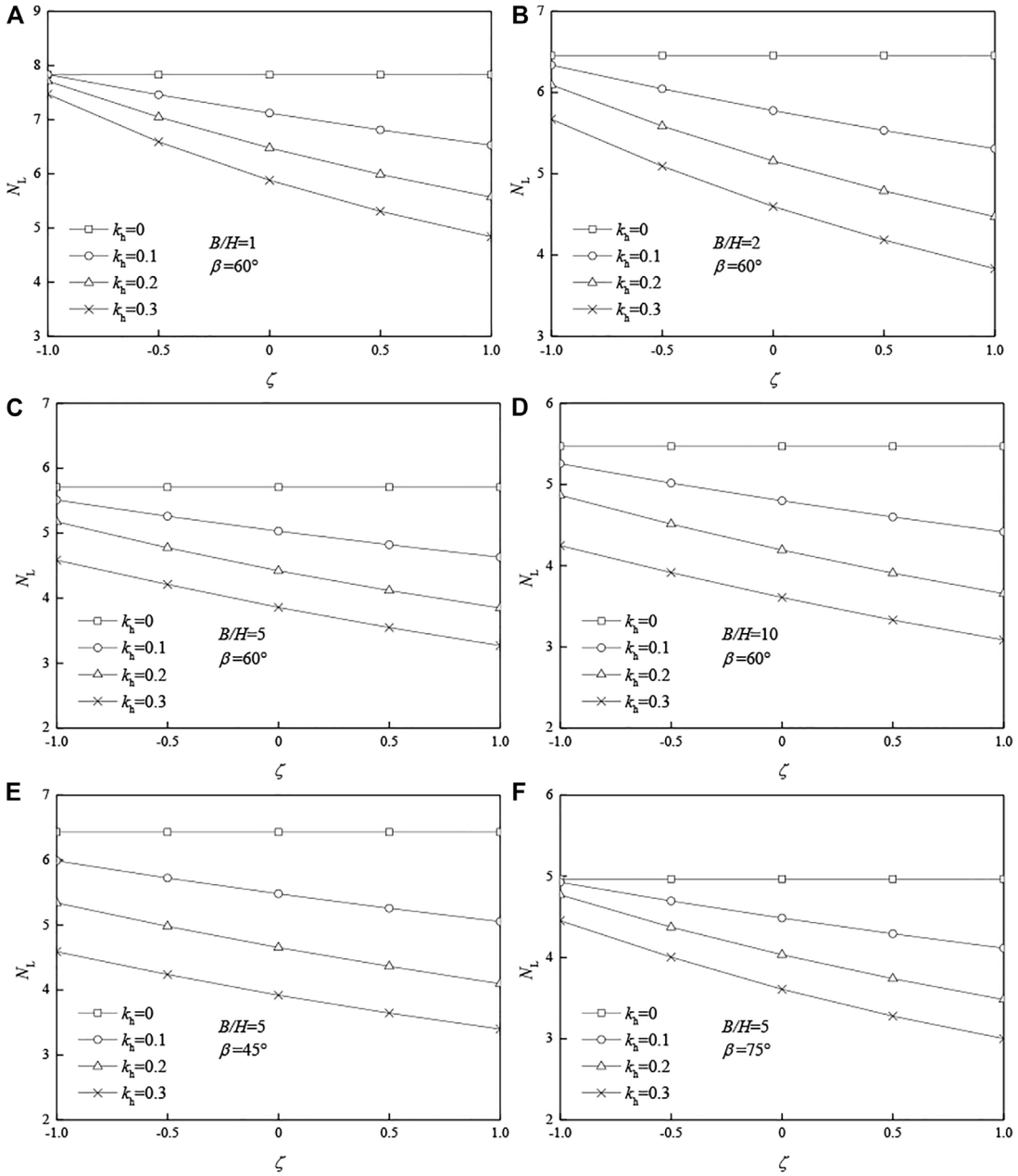

FIGURE 5 | Effects of the vertical seismic effect proportion coefficient ζ on stability factor N_L. **(A)** B/H = 1, β = 60°; **(B)** B/H = 2, β = 60°; **(C)** B/H = 5, β = 60°; **(D)** B/H = 10, β = 60°; **(E)** B/H = 5, β = 45°; **(F)** B/H = 5, β = 75°.

As can be seen from **Table 5**, taking B/H = 1, β = 45° as an example, without considering the effect of vertical seismic force (ζ = 0), the safety factor is 7.08. When ζ increased from 0.5 to 1, the safety factor N_L decreased from 6.58 to 6.14. Compared with ζ = 0, the minimum relative error was 7.1% and the maximum was 13.2%.

Taking B/H = 10, β = 45° as an example, without considering the effect of vertical seismic force (ζ = 0), the safety factor is 4.36. When ζ increased from 0.5 to 1, the safety factor N_L decreased from 4.09 to 3.86. Compared with ζ = 0, the minimum relative error was 6.1% and the maximum was 11.5%.

It shows that the vertical seismic force also has great influence on the stability of the saturated soft clay slope. If the vertical seismic force effect is ignored, the accuracy of calculation results will be directly affected.

Horizontal and vertical seismic loads have significant effects on slope stability. Therefore, in practical engineering, the influence of earthquake on slope stability needs to be considered, and the slope structure must be designed according to relevant seismic design code in order to ensure the stability of the slope.

TABLE 5 | Effects of the vertical seismic effect proportion coefficient ζ on stability factor N_L (k_h = 0.2).

B/H	β(°)	ζ = 0	ζ = −1		ζ = −0.5		ζ = 0.5		ζ = 1	
		N_L	N_L	Δ_7 (%)	N_L	Δ_8 (%)	N_L	Δ_9 (%)	N_L	Δ_{10} (%)
1	45	7.08	8.35	18.0	7.66	8.3	6.58	7.1	6.14	13.2
2	45	5.55	6.47	16.7	5.99	7.9	5.17	6.8	4.84	12.8
5	45	4.65	5.34	14.8	4.98	7.0	4.36	6.2	4.10	12.0
10	45	4.36	4.95	13.7	4.64	6.4	4.09	6.1	3.86	11.5
1	60	6.48	7.71	19.1	7.05	8.8	5.99	7.5	5.57	14.0
2	60	5.16	6.10	18.2	5.59	8.3	4.79	7.1	4.47	13.3
5	60	4.42	5.17	17.1	4.77	8.0	4.12	6.9	3.85	12.9
10	60	4.19	4.87	16.1	4.51	7.6	3.91	6.8	3.65	12.8
1	75	5.89	7.06	20.0	6.42	9.1	5.43	7.8	5.03	14.5
2	75	4.68	5.57	19.0	5.09	8.7	4.33	7.5	4.03	14.0
5	75	4.03	4.77	18.3	4.37	8.4	3.74	7.3	3.48	13.7
10	75	3.83	4.52	17.8	4.15	8.2	3.56	7.2	3.32	13.5
1	90	5.27	6.36	20.8	5.76	9.4	4.85	7.9	4.49	14.7
2	90	4.14	4.96	19.9	4.51	9.1	3.81	7.8	3.54	14.5
5	90	3.53	4.22	19.4	3.85	8.8	3.27	7.5	3.04	14.1
10	90	3.35	3.99	19.3	3.64	8.8	3.10	7.5	2.88	14.0

$$\Delta_7 = \left|\frac{N_L(\zeta=-1) - N_L(\zeta=0)}{N_L(\zeta=0)}\right| \times 100\%,$$

$$\Delta_8 = \left|\frac{N_L(\zeta=-0.5) - N_L(\zeta=0)}{N_L(\zeta=0)}\right| \times 100\%$$

$$\Delta_9 = \left|\frac{N_L(\zeta=0.5) - N_L(\zeta=0)}{N_L(\zeta=0)}\right| \times 100\%,$$

$$\Delta_{10} = \left|\frac{N_L(\zeta=1) - N_L(\zeta=0)}{N_L(\zeta=0)}\right| \times 100\%,$$

7 CONCLUSION

1) The safety factors calculated in this article are very close to the results of Michalowski and Drescher (2009). The maximum error is only 7.7%, which shows that the calculation method in this article is effective.
2) The ratio *B/H* represents the three-dimensional effect degree of the saturated soft clay slope. Considering the effect of seismic load (k_h = 0.2, ζ = 0.5), the conclusions are as follows:
   (a) When *B/H* = 1 or 2, the three-dimensional effect of the slope is very obvious.
   (b) When *B/H* increases from 1 to 7, the three-dimensional effect of the slope gradually weakens.
   (c) When the *B/H* ≥ 8, the three-dimensional slope stability problem can be simplified to a two-dimensional problem.
3) The stability factor N_L increases with the decrease in slope angle β. When the slope angle decreases from 90° to 45°, the stability coefficient N_L increases approximately 1/3. It is suggested that slope angle should be considered in the design of saturated soft clay slope.

DATA AVAILABILITY STATEMENT

The original contributions presented in the study are included in the article/Supplementary Material; further inquiries can be directed to the corresponding author.

AUTHOR CONTRIBUTIONS

The overarching research goals were developed by BZ. BZ established the models and analyzed the formal. YJ analyzed the results and wrote the initial draft of the manuscript. BZ and ZL revised and polished the manuscript. HC offered proposals and polished the manuscript. All authors listed have made a substantial, direct, and intellectual contribution to the work and approved it for publication.

FUNDING

This study was funded by the National Natural Science Foundation of China (52004088 and 52074116) and the Science Foundation of Hunan University of Science and Technology (E52076).

REFERENCES

Alejano, L. R., Ferrero, A. M., Ramírez-Oyanguren, P., and Álvarez Fernández, M. I. (2011). Comparison of Limit-Equilibrium, Numerical and Physical Models of wall Slope Stability. *Int. J. Rock Mech. Mining Sci.* 48, 16–26. doi:10.1016/j.ijrmms.2010.06.013

Alemdag, S., KayaMustafa, A. K., Karadag, M., Gurocak, Z., and Bulut, F. (2015). Utilization of the Limit Equilibrium and Finite Element Methods for the Stability Analysis of the Slope Debris: An Example of the Kalebasi District (NE Turkey). *J. Afr. Earth Sci.* 106, 134–146. doi:10.1016/j.jafrearsci.2015.03.010

Ausilio, E., Conte, E., and Dente, G. (2000). Seismic Stability Analysis of Reinforced Slopes. *Soil Dyn. Earthquake Eng.* 19, 159–172. doi:10.1016/S0267-7261(00)00005-1

Chen, W. F. (2007). *Limit Analysis and Soil Plasticity*. Florida: J. Ross Publishing.

Gao, Y.-f., Ye, M., and Zhang, F. (2015). Three-dimensional Analysis of Slopes Reinforced with Piles. *J. Cent. South. Univ.* 22, 2322–2327. doi:10.1007/s11771-015-2757-6

Gischig, V. S., Eberhardt, E., Moore, J. R., and Hungr, O. (2015). On the Seismic Response of Deep-Seated Rock Slope Instabilities - Insights from Numerical Modeling. *Eng. Geology.* 193, 1–18. doi:10.1016/j.enggeo.2015.04.003

Gofar, N., and Rahardjo, H. (2017). Saturated and Unsaturated Stability Analysis of Slope Subjected to Rainfall Infiltration. *MATEC Web Conf.* 101, 05004. doi:10.1051/matecconf/201710105004

Han, C.-y., Chen, J.-j., Xia, X.-h., and Wang, J.-h. (2014). Three-dimensional Stability Analysis of Anisotropic and Non-homogeneous Slopes Using Limit Analysis. *J. Cent. South. Univ.* 21, 1142–1147. doi:10.1007/s11771-014-2047-8

Huang, C.-C., Tsai, C.-C., and Chen, Y.-H. (2002). Generalized Method for Three-Dimensional Slope Stability Analysis. *J. Geotech. Geoenviron. Eng.* 128128, 83610–83848. doi:10.1061/(ASCE)1090-024110.1061/(asce)1090-0241(2002)128:10(836)

Jongmin, K., Rodrigo, S., and Lee, J. (2002). Stability Analysis of Complex Soil Slopes Using Limit Analysis. *J. Geotechnical Geoenvironmental Eng.* 128128, 5467–5557. doi:10.1061/(ASCE)1090-0241

Leong, E. C., and Rahardjo, H. (2012). Two and Three-Dimensional Slope Stability Reanalyses of Bukit Batok Slope. *Comput. Geotechnics* 42, 81–88. doi:10.1016/j.compgeo.2012.01.001

Li, A. J., Lyamin, A. V., and Merifield, R. S. (2009). Seismic Rock Slope Stability Charts Based on Limit Analysis Methods. *Comput. Geotechnics* 36, 135–148. doi:10.1016/j.compgeo.2008.01.004

Michalowski, R. L., and Drescher, A. (2009). Three-dimensional Stability of Slopes and Excavations. *Géotechnique* 59 (10), 839–850. doi:10.1680/geot.8.p.136

Michalowski, R. L., and Martel, T. (2011). Stability Charts for 3D Failures of Steep Slopes Subjected to Seismic Excitation. *J. Geotech. Geoenviron. Eng.* 137, 183–189. doi:10.1061/(asce)gt.1943-5606.0000412

Michalowski, R. L., and Park, D. (2020). Stability Assessment of Slopes in Rock Governed by the Hoek-Brown Strength Criterion. *Int. J. Rock Mech. Mining Sci.* 127, 1–12. doi:10.1016/j.ijrmms.2020.104217

National Standard of the People's Republic of China (2010). *Code for Seismic Design of Building (GB50011-2010)*. Beijing, China: China Architecture and Building Press.

Nian, T.-K., Jiang, J.-C., Wang, F.-W., Yang, Q., and Luan, M.-T. (2016). Seismic Stability Analysis of Slope Reinforced with a Row of Piles. *Soil Dyn. Earthquake Eng.* 84, 83–93. doi:10.1016/j.soildyn.2016.01.023

Rawat, S., and Gupta, A. K. (2016). Analysis of a Nailed Soil Slope Using Limit Equilibrium and Finite Element Methods. *Int. J. Geosynth. Ground Eng.* 2, 34. doi:10.1007/s40891-016-0076-0

Selcuk, A., Ayberk, K., and Mustafa, K (2015). Utilization of the limit equilibrium and finite element methods for the stability analysis of the slope debris: An example of the Kalebasi District (NE Turkey). *Afr. Earth Sci.*. doi:10.1016/j.jafrearsci.2015.03.010

Sahoo, S., Manna, B., and Sharma, K. G. (2016). Seismic Stability Analysis of Unreinforced and Reinforced Soil Slopes. *Geo-china. Int. Conf.*. doi:10.1061/9780784480007.009

VandenBerge, D. R., and McGuire, M. P. (2019). Practical Use of Modified Hoek-Brown Criterion for Soil Slope Stability Analysis. *Geotech Geol. Eng.* 37 (6), 5441–5455. doi:10.1007/s10706-019-00991-1

Wang, L., Hu, W., Sun, D. A., and Li, L. (2019). 3D Stability of Unsaturated Soil Slopes with Tension Cracks under Steady Infiltrations. *Int. J. Numer. Anal. Methods Geomech* 43 (6), 1184–1206. doi:10.1002/nag.2889

Yang, X. L., and Liu, Z. A. (2018). Reliability Analysis of Three-Dimensional Rock Slope. *Geomechanics Eng.* 15 (6), 1183–1191. doi:10.12989/gae.2018.15.6.1183

Yang, X. L., and Wang, H. Y. (2018). Catastrophe Analysis of Active-Passive Mechanisms for Shallow Tunnels with Settlement. *Geomechanics Eng.* 15 (1), 621–630. doi:10.12989/gae.2018.15.1.621

Yao, C., and Yang, X. (2017). Limit Analysis of Unsaturated Soil Slope Stability Considering Intermediate Principal Stress and Strength Nonlinearity. *Geotech Geol. Eng.* 35, 2053–2063. doi:10.1007/s10706-017-0226-8

Zhang, F., Gao, Y., Wu, Y., Zhang, N., and Qiu, Y. (2016). Effects of Vertical Seismic Acceleration on 3D Slope Stability. *Earthq. Eng. Eng. Vib.* 15, 487–494. doi:10.1007/s11803-016-0338-9

Conflict of Interest: Author HC is employed by Foshan Transportation Science and Technology Limited Company.

The remaining authors declare that the research was conducted in the absence of any commercial or financial relationships that could be construed as a potential conflict of interest.

frontiers in Earth Science

ORIGINAL RESEARCH
published: 05 January 2022
doi: 10.3389/feart.2021.814672

Mining Hazards to the Safety of Segment Lining for Tunnel Boring Machine Inclined Tunnels

Hui Zhuo[1], *Dan Xie*[2], *Jinglai Sun*[3,4] *and Xiaomeng Shi*[5]*

[1]China Energy Investment Corporation, Beijing, China, [2]China Civil Engineering Construction Cooperation, Beijing, China, [3]Beijing Municipal Engineering Research Institute, Beijing, China, [4]Beijing Key Laboratory for Prediction and Early Warning of Underground Engineering Construction, Beijing, China, [5]School of Civil Engineering, Beijing Jiaotong University, Beijing, China

The segment lining is a new type of support structure for mining tunnels. The disturbance of coal excavation leads to the deformation of segment lining and has great hazards to the safety of the tunnels. Based on the tunnel boring machine (TBM) inclined tunnels in Xinjie mine, the ultimate span L_0 of the rock beam on the top slab of the coal seam was calculated according to the bending (tension) damage theory. A numerical model was built to simulate the bottom area of the inclined tunnels. During the coal mining, the additional displacements and additional stresses of the segment lining were analyzed, and then the safety factors of the support structure were calculated. Finally, the width of the coal pillar to protect the inclined tunnels was determined. The results showed that the ultimate span of the rock beam on the top of the coal seam is 31.7 m, the deformation of the inclined tunnel has a fish-belly shape, and the deformation leads to the increase of maximum axial force and bending moment. For the inclined tunnels in Xinjie coalmine, a total width of 91.3 m of coal pillar must be reserved to keep the safety factor of the structure higher than 2.0 and prevent the inclined tunnels from the mining hazards.

Keywords: mining hazards, segment lining, mining excavation, numerical simulation, safety factor

OPEN ACCESS

Edited by:
Xuewei Liu,
Institute of Rock and Soil Mechanics (CAS), China

Reviewed by:
Zhizhen Zhang,
China University of Mining and Technology, China
Chunjiang Zou,
Monash University, Australia

***Correspondence:**
Xiaomeng Shi
shixm@bjtu.edu.cn

Specialty section:
This article was submitted to Geohazards and Georisks, a section of the journal Frontiers in Earth Science

Received: *14 November 2021*
Accepted: *26 November 2021*
Published: *05 January 2022*

Citation:
Zhuo H, Xie D, Sun J and Shi X (2022) Mining Hazards to the Safety of Segment Lining for Tunnel Boring Machine Inclined Tunnels. Front. Earth Sci. 9:814672. doi: 10.3389/feart.2021.814672

INTRODUCTION

The tunnel boring machine (TBM) has been widely used to build transportation and hydraulic tunnels, but its application in mining engineering is still limited (Liu et al., 2013). A TBM was first used in a coal mine in 1971 in Germany (Handewith 1983). In 1978, a 5.1-m-diameter TBM was used to excavate a 1.6-km-long decline for coal cliff collieries in the southern coalfields of New South Wales (White, 1978). In Germany, five sections of a total 13-km roadway tunnel in the Rheinland and Friedrich Heinrich collieries were excavated using a 6-m-diameter TBM between 1973 and 1980 (Boldt and Henneke, 1981). A TBM was used to excavate two drifts (762 and 933 m long) at Anglo American's Grosvenor Mine in Moranbah, Queensland, Australia, in 2013 (Donnelly et al., 2014). Xinjie coalmine, Ordos, China, has planned to construct two inclined tunnels by TBM method, which will face technical difficulties because of the lack of relevant design experience (Yang et al., 2016). In the process of coal excavation, the movement of the overlying strata and the distribution of ground stress have a severe impact on the safety of the support structures, a problem that has not been encountered in the traditional design of segment lining support. Kulatilake et al. (2013) studied the stability of a tunnel in a deep coal mine in China. Xu et al. studied the mining-induced strata movement and roof behavior in an underground coal mine. Shi et al. (2016) and Shi et al. (2017) studied the influence of coal mining on the safety of the tunnels

by using physical model test and Three-Dimension Distinct Element Code (3DEC) numerical simulation method. Qi et al. (2021) used 2D model tests and numerical simulation methods to optimize the design method of the width of the coal pillar to protect the tunnels. However, these studies mainly focus on the stress and deformation of the whole area caused by coal mining activities from the surface to the coal seam, rather than the most intense area at the bottom part of the tunnel near the coal seam, which has the largest additional stress and deformation. In this paper, the displacement and stress changes of the support structure are studied in detail for the most dangerous area, the safety factor is calculated, and the coal pillar calculation method is proposed.

PROJECT OVERVIEW

Xinjie coalmine is located in the south-central part of Ordos city, the planned area of the mine is 737.8 km^2, and the coal resource is 13,884.46 Mt. The planned TBM tunnels go down from the surface to a depth of 660 m with 6° inclined angle. With the increase of the depth, the load on the surrounding rock of the support structure increases, and the disturbance of coal excavation on the tunnels is the most serious, so the bottom area is considered to be the most dangerous area, as shown in **Figure 1**. The support structure is a segment lining with a thickness of 0.35 m and an outer radius of 3.65 m, using a staggered assembly structure. The material of the lining is C40 reinforced concrete. The tunnels cross coarse-grained sandstone, mudstone, and fine-grained sandstone up to 2-1 coal seam, and the lower part is mudstone, 2-2 coal seam, and sandy mudstone. The layer thickness and properties are shown in **Table 1**.

THEORETICAL ANALYSIS OF COAL ROOF DAMAGE

In the process of coal excavation, the coal seam roof collapse will induce overlying strata movement and stress redistribution, which leads to the additional stress and deformation of the lining structure (Liu et al., 1981; Yang et al., 2012). The coal excavation causes bending deformation of the roof strata, and both sides of the working face are coal seams to provide reaction force and bending moment to the roof structure, which can be regarded as a fixed beam structure at both ends. When the roof suspension span gradually increases, the roof will be the first to rupture above both sides of the working face, at which time the original beam structure constraints change, and the original fixed beam structure at both ends evolves into a simply supported beam structure as shown in **Figure 2** (Zhao et al., 2009).

The rock beam in **Figure 2** is subjected to the overlying ground load q_1 and the self-weight q_2. Based on the calculation method of the solid-supported beam at both ends of the beam, the bending moments at both ends (M_A) and the middle (M_o) of the fixed beam (**Figure 2A**) can be obtained as

$$M_A = \frac{(q_1 + q_2)L_0^2}{12} \tag{1}$$

$$M_O = \frac{(q_1 + q_2)L_0^2}{24} \tag{2}$$

By comparing Eq. (Boldt and Henneke, 1981). and Eq. (Donnelly et al., 2014), it can be seen that the maximum bending moment occurs at the edge of the beam structure. In addition, since the rock is a brittle material, the tensile strength that it can withstand is low, so the maximum tensile strength criterion is used as the strength criterion for the destruction of the roof.

$$\sigma_0 = \frac{M_A}{W} = [\sigma_t] \tag{3}$$

where σ_0 is the tensile stress; W is the section modulus of the rock beam; M_A is the section bending moment at the end of the rock beam; and $[\sigma_t]$ is the maximum tensile stress of the roof rock.

When $\sigma_0 > [\sigma_t]$, the rock beam will rupture and form a simply supported beam structure (**Figure 2B**), and the bending moments are

$$M_A^{'} = 0 \tag{4}$$

$$M_0^{'} = \frac{qL_0^2}{8} = \frac{(q_1 + q_2)L_0^2}{8} \tag{5}$$

Comparing the bending moments of the two types of beams, it can be found that the sum of the bending moments at both ends and the middle of the fixed beam is equal to the bending moment in the middle of the simply supported beam. So in the coal excavation process, the roof rock beam changes from the fixed beam to the simply supported beam, and the bending moment transfers from the two ends to the middle (Huang, 2002). Therefore, the mechanical process and conditions of the gradual development of the coal roof from bending to damage can be divided into two stages, as follows.

1) The working face advances forward, and when the rock beam overhanging span reaches the limit value L_0, the tensile stress σ_A at the end of the beam is

$$\sigma_A = \frac{M_A}{W} = \frac{(q_1 + q_2)L_0^2/12}{h^2/6} = \frac{q_1 + q_2}{2h^2}L_0^2 \geq [\sigma_t] \tag{6}$$

If the overlying stratum has a hard layer, when the roof rock is bent and deformed, the overlying strata are delaminated and the rock beam is subjected to self-weight only, and the tensile stress σ_A at the end of the beam is damaged, as follows:

$$\sigma_A = \frac{\gamma L_0^2}{2h} \geq [\sigma_t] \tag{7}$$

If the overlying stratum has a soft layer, it forms a combined rock beam with a hard bottom and a soft top, and the tensile stress σ_A at the end of the beam breaks is

$$\sigma_A = \frac{\left(h\gamma + \sum_{i=1}^{n} h_i\gamma_i\right)}{2h^2}L_0^2 \geq [\sigma_t] \tag{8}$$

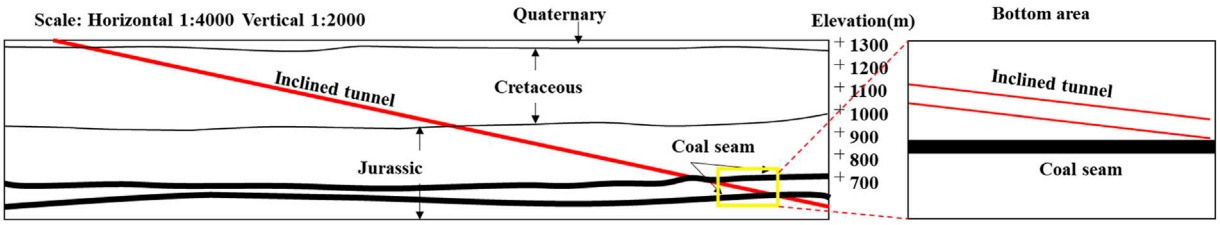

FIGURE 1 | Overview of the TBM inclined shaft in Xinjie coalmine. TBM, tunnel boring machine.

TABLE 1 | Properties of the strata in the bottom region.

No.	Type	Thickness h (m)	Density ρ (g/cm^3)	Compressive strength σ_c (MPa)	Tensile strength σ_t (MPa)	Poisson ratio μ_c	Cohesion c (MPa)	Friction angle φ (°)
1	Coarse-grained sandstone	24.0	2.18	23.6	1.28	0.17	6.15	33.14
2	Mudstone	4.0	2.36	32.31	0.93	0.20	6.35	33.51
3	Fine-grained Sandstone	10.0	2.47	33.74	1.24	0.15	8.35	34.43
4	2-1 coal seam	4.0	1.35	16.3	0.23	0.31	0.73	26.3
5	Mudstone	4.0	2.36	32.31	0.93	0.20	6.35	33.51
6	2-2 coal seam	4.0	1.35	16.3	0.23	0.31	0.73	26.3
7	Sandy mudstone	20.0	2.38	31.23	1.12	0.18	5.65	32.43

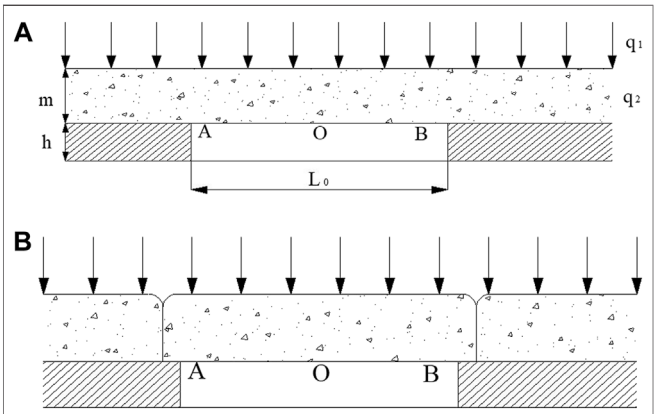

FIGURE 2 | Supporting conditions and bending moments of rock beams. **(A)** Fixed beam structure at two ends. **(B)** Simple beam structure at two ends.

where h is the thickness of the support layer of the roof and h_i is the thickness of each layer of the overlying strata.

2) After the damage occurs at the end of the beam, the constraint condition gradually transforms from a super-stationary beam to a simply supported beam, and the bending moment gradually decreases, regardless of whether the bending moment in the middle of the beam increases. When the damage occurs in the middle of the beam, the bending moment is

$$\sigma_0^{'} = \frac{\left(h\gamma + \sum_{i=1}^{n} h_i\gamma_i\right)}{2h^2} L_0^2 \geq [\sigma_t] \tag{9}$$

At this stage, the central part of the roof will be cracked, and the rock beam will fall or reach the state of "pseudo plastic rock beam" (Zhai, 2002). The ultimate span of rock beam overhang L_0 is

$$L_0 = \sqrt{\frac{2h^2[\sigma_t]}{\left(h\gamma + \sum_{i=1}^{n} h_i\gamma_i\right)}} \tag{10}$$

When bending damage occurs in a single rock formation, $\sum h_i = 0$, the ultimate span is

$$L_0 = \sqrt{\frac{2h[\sigma_t]}{\gamma}} \tag{11}$$

Based on the geological survey data of Xinjie coalmine, the overlying ground pressure of the coal seam is 14.4 MPa, and the coal roof is fine-grained sandstone with a thickness of 10 m, density of 2.47 × 103 kg/m^3, and tensile strength of 1.24 MPa. According to Eq. (Shi et al., 2017), the ultimate span of the rock beam can be obtained as L_0 = 31.7 m.

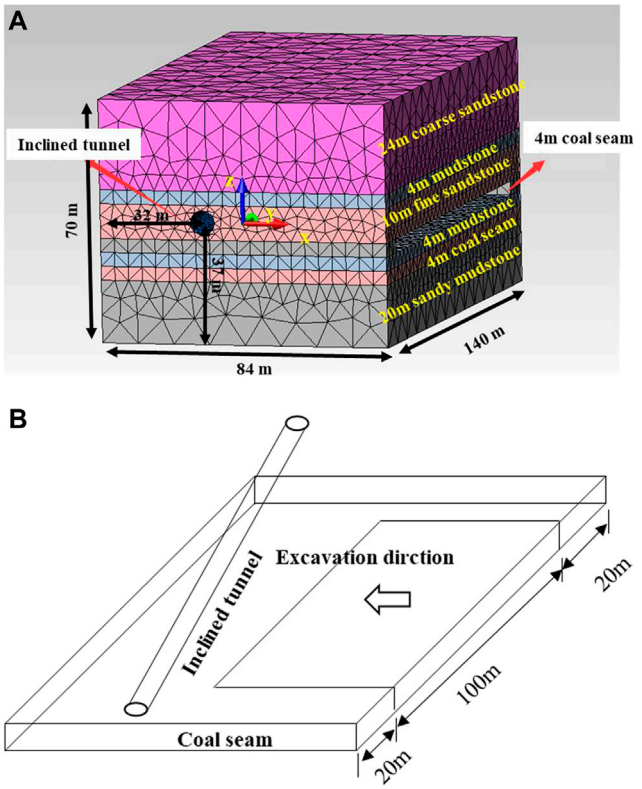

FIGURE 3 | Numerical simulation model. **(A)** MIDAS/GTS model. **(B)** Mining process diagram.

NUMERICAL SIMULATION ANALYSIS

Numerical Model Setup

In order to study the effect of coal mining on the deformation and stress of the inclined shaft, numerical simulation was carried out using the finite element numerical analysis software MIDAS/GTS. As shown in **Figure 3**, the model dimensions are 140 × 84 × 70 m, and the width of the working face of the simulated coal seam excavation is 100 m. The stratigraphic parameters are shown in **Table 1**. The material of segment lining is C40 concrete. The Mohr–Coulomb criterion is used as the yield criterion, the load of the overlying strata is simulated by applying a loading of 14.4 MPa on the top, and the displacement boundary conditions are used around and at the bottom of the model with zero displacement perpendicular to the direction of the face.

MIDAS/GTS has the operation of "replicate grid group," which is used to replicate each excavated seam at each step, set its elastic modulus to 0.01 kN/m^2, "blunt" each section of the excavated seam, and "activate" the set replica "activation," so as to simulate the bulk after a collapse. There is little influence when the coal seam is excavated far from the inclined tunnels. According to the calculated ultimate span L_0 = 31.7 m, the change rules of the lining displacement, axial force, and bending moment with the advance distance of the working face are recorded at 32, 36, 40, and 44 m respectively.

Additional Deformation of the Segment Lining

The coal excavation causes the deformation of the segment lining. Considering the position of the coal seam, the deformation mainly happens in the X direction and the Z direction. **Figure 4** shows the displacement at the top of the lining at each step in the X direction and the Z direction.

During the excavation of the coal seam, the vertical displacements of the monitoring sites gradually increase, and the rate accelerates, indicating that the strata are becoming more and more unstable. Along the axis direction, the displacement increases and then decreases, and the middle part has the largest displacement. The deformation of the tunnel has a fish-belly shape. The maximum vertical settlement was 5.59 mm when the excavation reached 44 m.

Additional Stress in the Segment Lining

After the excavation of the coal seam, the additional stresses of the lining are expressed in the numerical software mainly as two results of axial force and bending moment. **Figure 5** shows the bending moment in the X direction and the axial force in the Y direction for an excavation of 44 m. In each step, the maximum bending moment in the X direction and the axial force in the Y direction are shown in **Table 2**.

Calculation of Safety Factor

For concrete segment lining structures, the safety factor could be calculated based on the maximum compressive stress in the compressed area and the design strength of concrete material (Vogel et al., 2000). According to the provisions in the Code for the Design of Concrete Structures, the maximum compressive stress and strength criterion for concrete eccentric compressive structures can be expressed by the Eq. (Vogel and Rast, 2000).

$$\sigma_c = \gamma_0 \gamma_s \left(\frac{N}{bh_0} + \frac{6M}{bh_0^2} \right) < f_c \tag{12}$$

Converting the Eq. (Vogel and Rast, 2000), the safety factor is calculated as follows.

$$K = \frac{f_c}{\sigma_c} = \frac{bh_0^2 f_c}{\gamma_0 \gamma_s (Nh + 6M)} \tag{13}$$

where K is the safety factor of structural bearing capacity, and $K \geq 2$; f_c is the design value of concrete axial compressive strength (MPa); b is the cross-sectional width of segment lining (m), and b = 1.5 m; h_0 is the cross-sectional height of segment lining (m), and h_0 = 0.35 m; γ_0 is the important factor of structure, and γ_0 = 1.1; γ_s is the load sub-factor, and γ_s = 1.35; N is the maximum axial force value (kN) in the lining; M is the maximum bending moment value (kN m) in the lining; and the design value of axial compressive strength of C40 concrete is f_c = 19.1 MPa.

By substituting the maximum axial force and bending moment in **Table 2** into Equation (Shi et al., 2017), the change of safety coefficient of the lining structure during the coal seam excavation can be calculated as shown in **Table 3**. **Figure 6** shows the change rule of safety factor with the excavation distance. The empirical equation is as (**Eq. 14**).

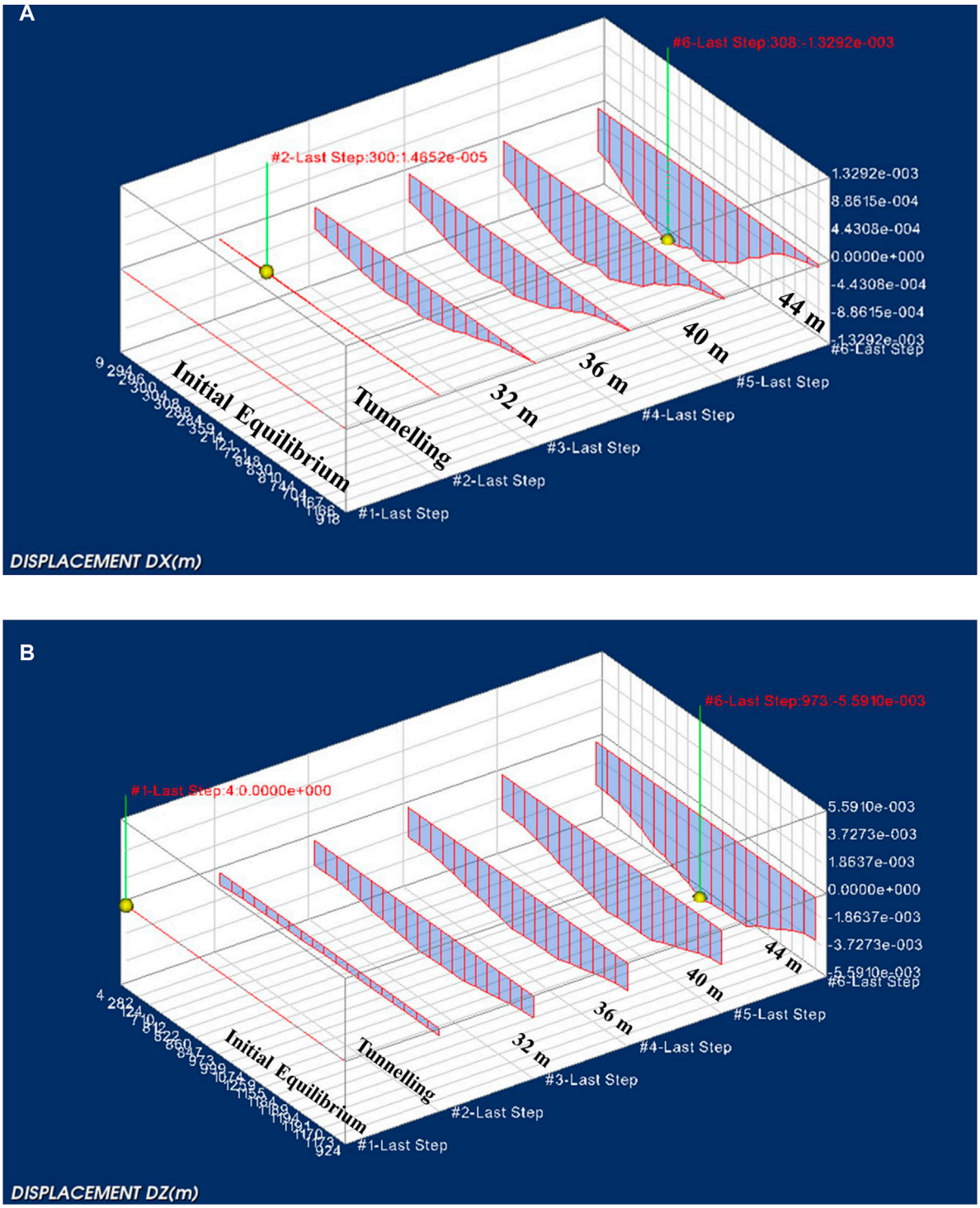

FIGURE 4 | Deformation of the segment lining caused by mining (m). **(A)** In the X direction. **(B)** In the Z direction.

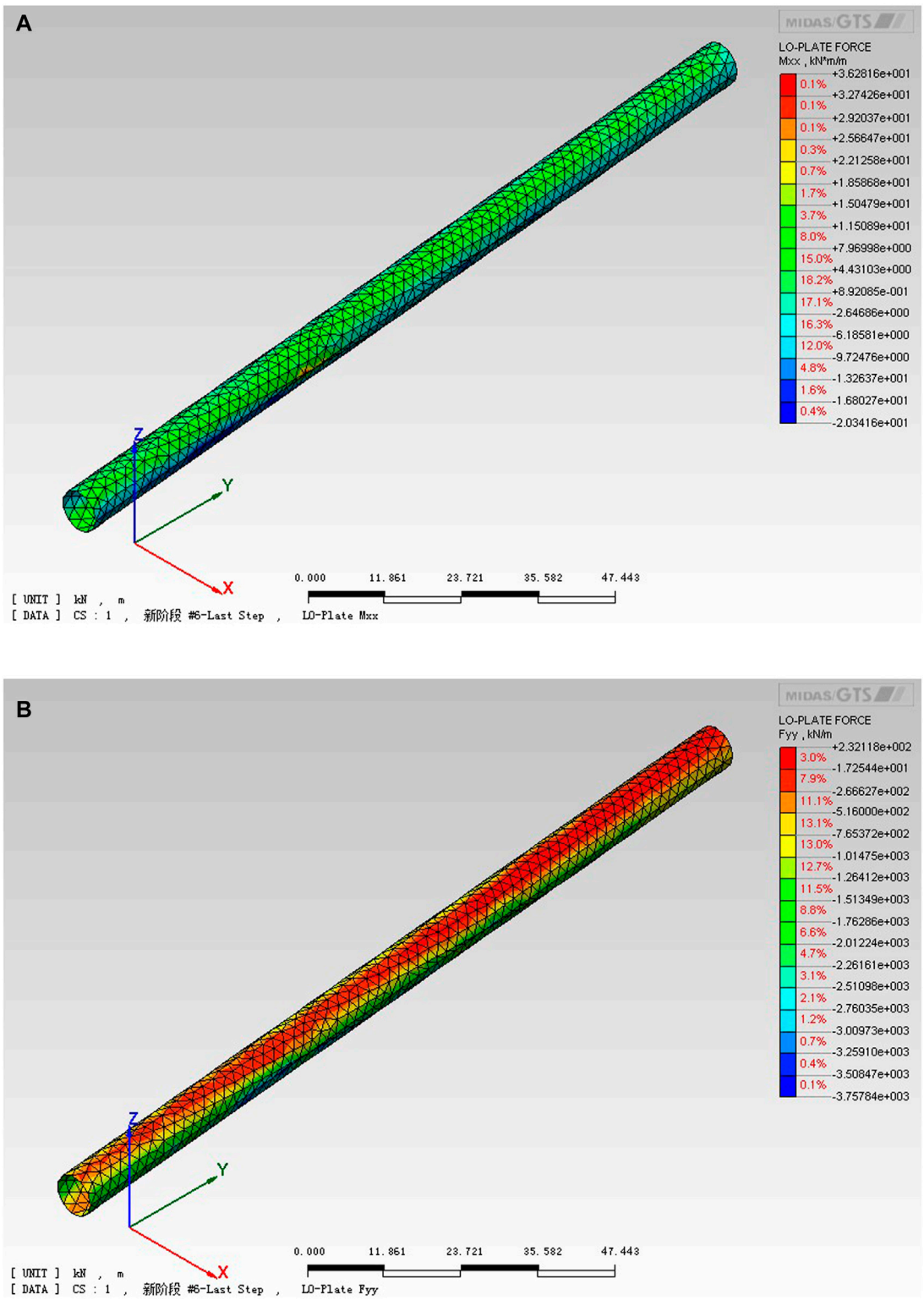

FIGURE 5 | Bending moment in the X direction and axial force in the Y direction after excavating 44 m. **(A)** Bending moment in the X direction. **(B)** Axial force in the Y direction.

TABLE 2 | Maximum axial force and bending moment.

	Excavation process				
	Initial	32 m	36 m	40 m	44 m
Axial force (kN)	1,650	2,335	2,660	3,134	3,758
Bending moment (kN m)	11.36	17.86	21.47	26.83	36.28

TABLE 3 | Safety factor of the most dangerous section.

	Excavation process				
	Initial	32 m	36 m	40 m	44 m
Safety factor	3.65	2.55	2.23	2.03	1.86

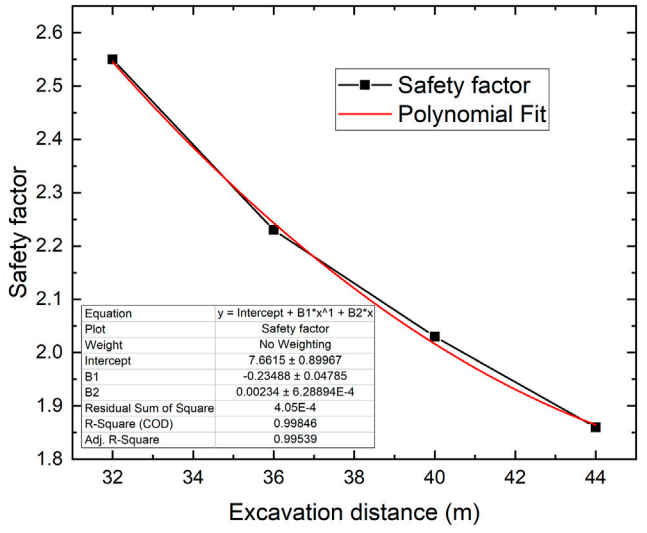

FIGURE 6 | Change rule of safety factor of the segment lining with the excavation distance.

$$y = 1.66 - 0.23x + 0.0023x^2 \tag{14}$$

where y is the safety factor and x is the excavation distance, m.

Reasonable Coal Pillar Width Theoretical Calculation

Xinjie coalmine has two inclined tunnels, and the distance between the two tunnels is 60 mm. According to the code for coal pillar design (Hu et al., 2017), the calculation of the width of the protective coal pillar is shown in **Figure 7**, and the width of the coal pillar L is

$$L = S + 60 = 2S_1 + 2a + 60 \tag{14}$$

where a is the radius of the inclined tunnel and S_1 is the width of the coal pillar protected on one side.

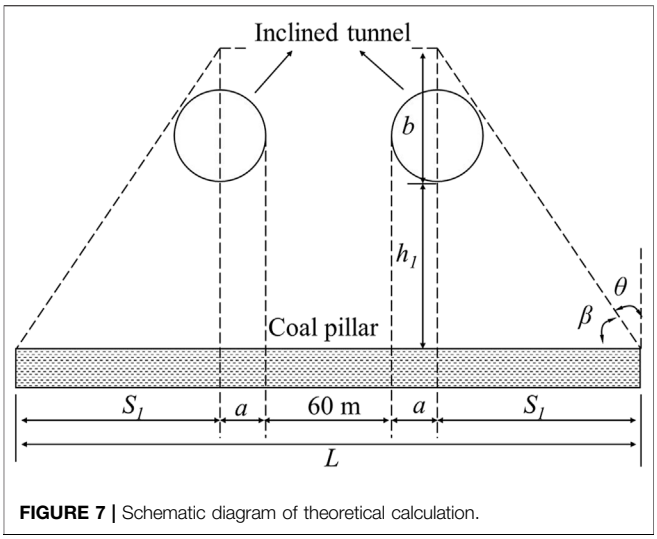

FIGURE 7 | Schematic diagram of theoretical calculation.

In **Figure 7**, β is the angle of strata movement, φ is the angle of internal friction of the rock, and $\beta = \pi/4 + \varphi/2$. According to the geometric triangulation, it could be obtained as

$$\tan\theta = \frac{S_1}{b + a + h_1} \tag{15}$$

$$\sin\theta = \frac{a}{b} \tag{16}$$

And then

$$S_1 = \frac{a}{\cos\theta} + \tan\theta(a + h_1) = \frac{a}{\cos(\pi/4 - \varphi/2)} + \tan\left(\frac{\pi}{4} - \frac{\varphi}{2}\right)(a + h_1) \tag{17}$$

where $\varphi = 34.4^\circ$ is the internal friction angle for the fine-grained sandstone; $h_1 = 14.7$ m is the maximum distance from the coal seam to the bottom of the inclined tunnel in the numerical model; $a = 3.65$ m is the outer diameter of the tunnel.

S_1 is calculated to be 13.78 m, and substitute the parameters into **Eq. 14**, and the width of the coal pillar is calculated to be 94.86 mm.

In the numerical simulation, the safety factor when the concrete reaches the ultimate compressive strength is required to be greater than 2.0, so the reasonable excavation distance is 40 m, and the corresponding S_1 is 12 mm. The width of the coal pillar for the two inclined tunnels is about 91.3 mm. The theoretical calculation results have high consistency with the numerical simulation, and the error is within a reasonable range, so it shows that the numerical simulation results are accurate and valid.

CONCLUSION

The segment lining is a new type of support structure for mine tunnels. In this paper, the behavior of the structure under the

influence of coal excavation was studied using theoretical analysis and numerical simulation. It was proposed that the coal pillar with reasonable width must be reserved to prevent the tunnels from mining hazards. The main conclusions are as follows (Liu and Zhong, 1981; Handewith, 1983; Huang, 2002; Kulatilake et al., 2013; Liu et al., 2013; Shi et al., 2016; Hu et al., 2017; Qi et al., 2021; White, 1978; Zhai, 2002; Zhao et al., 2009; Yang et al., 2012; Yang and Xia, 2016):

1) According to the theory of bending (tension) damage, the limit span of rock beam at the top of the coal seam is L_0 = 31.7 m for the coal seam in Xinjie coalmine.
2) During the excavation of the coal seam, the vertical displacement of the inclined tunnel gradually increases, and the rate accelerates with the excavation process, indicating that the excavation of the coal seam causes the stratum to be increasingly unstable. In the axial direction of the tunnel, the middle part has the largest displacement, so the deformation of the inclined tunnel has a fish-belly shape.
3) During the excavation of the coal seam, the deformation leads to the increase of the maximum axial force and bending moment of the structure. And the safety of the segment lining is gradually reduced.
4) The width of the single-side protection coal pillar of the inclined tunnel is 13.78 mm calculated according to the theory, while in the numerical simulation, the width is 12 mm when the safety factor is 2, which has a high consistency, and the error is within a reasonable range, so it shows that the numerical simulation results are accurate and effective.
5) For the inclined tunnels in Xinjie coalmine, a total width of 91.3 m of coal pillar must be reserved to keep the safety factor of the structure higher than 2 and prevent the inclined tunnels from mining hazards.

DATA AVAILABILITY STATEMENT

The raw data supporting the conclusions of this article will be made available by the authors, without undue reservation.

AUTHOR CONTRIBUTIONS

HZ formulated the problem studied in this paper and wrote the paper. DX contributed to the numerical simulation in this paper. JS contributed to the theoretical analysis in this paper. XS directed the research for this paper.

FUNDING

This work is supported by the Beijing Natural Science Foundation for Young Scientists (Grant No. 8214052), Open Fund of State Key Laboratory of Water Resource Protection and Utilization in Coal Mining (Grant No. GJNY-18-73.2), and National Science and Technology Support Program (2013BAB10B06).

REFERENCES

Boldt, H., and Henneke, J. (1981). *Tunnel Boring under Coal Mining Conditions. 1981 Rapid Excavation and Tunneling Conference*, 722–737.

Donnelly, C., Rammage, G., and Donghi, M. (2014). The Australasian Institute of Mining and Metallurgy & Mine Managers Association of Australia, In Alternative Excavation Methods in Undeground Coal Mining. 14th Coal Operators' Conference. Australia: University of Wollongong, 216–223.

Handewith, H. J. (1983). TBM Tunnels in the Western Hemisphere; an Overview Tunneling. *Technology Newsl.* 41, 1–8.

Hu, B. N., Zhang, H. X., and Shen, B. H. (2017). *Code for Coal Pillar Retention and Pressed Coal Mining in Buildings, Water Bodies, Railways and Main Shafts*. Beijing: China Coal Industry Publishing House.

Huang, Q. X. (2002). Ground Pressure Behavior and Definition of Shallow Seams. *Chin. J. Rock Mech. Eng.* 8, 1174–1177. doi:10.3321/j.issn:1000-6915.2002.08.014

Kulatilake, P. H. S. W., Wu, Q., Yu, Z., and Jiang, F. (2013). Investigation of Stability of a Tunnel in a Deep Coal Mine in China. *Int. J. Mining Sci. Technology* 23, 579–589. doi:10.1016/j.ijmst.2013.07.018

Liu, Q. S., Shi, K., and Huang, X. (2013). Feasibility of Application of TBM in Construction of Deep Coal Mine and its Key Scientific Problems. *J. Mining Saf. Eng.* 30 (5), 633–641.

Liu, T. Q., and Zhong, W. L. (1981). *Law of Surface Movement and Overburden Failure in Coal Mine and its Application*. Beijing: China Coal Industry Publishing House.

Qi, Y., Liu, B., Tannant, D., Zheng, W., Wang, Y., and Shi, X. (2021). Protective Coal Pillar Design for Segmental Lining-Supported TBM Mine Tunnels Using Physical Model Tests. *Geomech. Geophys. Geo-energ. Geo-resour.* 7, 21. doi:10.1007/s40948-021-00221-0

Shi, X.-m., Liu, B.-g., Tannant, D., and Qi, Y. (2017). Influence of Consolidation Settlement on the Stability of Inclined TBM Tunnels in a Coal Mine. *Tunnelling Underground Space Technology* 69, 64–71. doi:10.1016/j.tust.2017.06.013

Shi, X. M., Liu, B. G., Li, T., and Du, X., (2016). Stress and Deformation Analysis of Shield Incline Shafts Segment Due to Dewater Settlement of Aquifer. *Chin. J. Rock Mech. Eng.* 35 (S1), 3057–3063. doi:10.13722/j.cnki.jrme.2014.1717

Vogel, M., and Rast, H. P. (2000). AlpTransit-safety in Construction as a challenge: Health and Safety Aspects in Very Deep Tunnel Construction. *Tunnelling Underground Space Technology* 15 (4), 481–484. doi:10.1016/S0886-7798(01)00018-9

White, S. B. (1978). *The Use of a Tunnel Boring Machine on a Coal Mine Decline* in *Australian Tunnelling Conference*. 3rd edition (Sydney, NSW, 66–70.

Xu, T., Yang, T.-h., Chen, C.-f., Liu, H.-l., and Yu, Q.-l. (2015). Mining Induced Strata Movement and Roof Behavior in Underground Coal Mine. *Geomech. Geophys. Geo-energ. Geo-resour.* 1, 79–89. doi:10.1007/s40948-015-0010-2

Yang, J. Z., and Xia, G. B. (2016). *Key Technology of TBM Construction for Long Distance Inclined Shaft in Coalmine*. Beijing: China Railway Publishing House.

Yang, Y. G., Zhang, H. Y., and Gan, Q. C. (2012). Study on Surrounding Rock Deformation Mechanism and Supporting Technology along Goaf Roadway with High Ground Pressure in Deep Wells. *Coal Eng.* 6, 76–79. doi:10.3969/j.issn.1001-8972.2012.12.028

Zhai, X. X. (2002). Simulation Testing Study on Roof Strata Displacement of Top-Coal Caving Face. *Chin. J. Rock Mech. Eng.* 21 (11), 1667–1671. doi:10.3321/j.issn:1000-6915.2002.11.018

Zhao, H. J., Ma, F. S., Ding, D. M., and Zhang, Y. M., (2009). Roadway Deformation Mechanism and Failure Model under the Influence of Mining. *J. China Coal Soc.* 34 (5), 599–604. cnki:sun:mtxb.0.2009-05-005

Conflict of Interest: Author HZ is employed by China Energy Investment Corporation.

The remaining authors declare that the research was conducted in the absence of any commercial or financial relationships that could be construed as a potential conflict of interest.

Publisher's Note: All claims expressed in this article are solely those of the authors and do not necessarily represent those of their affiliated organizations, or those of the publisher, the editors, and the reviewers. Any product that may be evaluated in this article, or claim that may be made by its manufacturer, is not guaranteed or endorsed by the publisher.

frontiers in Earth Science

ORIGINAL RESEARCH
published: 14 January 2022
doi: 10.3389/feart.2021.808086

Development Trend and Stability Analysis of Creep Landslide With Obvious Slip Zone Under Rainfall-Taking Xinchang Xiashan Basalt Slope as an Example

Chunyan Bao[1,2], *Lingtao Zhan*[1,2], *Yingjie Xia*[3]*, *Yongliang Huang*[1] *and Zhenxing Zhao*[4]

[1]School of Civil Engineering, Shaoxing University, Shaoxing, China, [2]Collaborative Innovation Center for Prevention and Control of Mountain Geological Hazards of Zhejiang Province, Shaoxing, China, [3]State Key Laboratory of Coastal and Offshore Engineering, Dalian University of Technology, Dalian, China, [4]China Railway Construction Bridge Engineering Bureau Group 3rd Engineering Co., Shenyang, China

The creep slope is a dynamic development process, from stable deformation to instability failure. For the slope with sliding zone, it generally creeps along the sliding zone. If the sliding zone controlling the slope sliding does not have obvious displacement, and the slope has unexpected instability without warning, the harm and potential safety hazard are often much greater than the visible creep. Studying the development trend of this kind of landslide is of great significance to slope treatment and landslide early warning. Taking Xiashan village landslide in Huishan Town, Xinchang County, Zhejiang Province as an example, the landslide point was determined by numerical simulation in 2006. Generally, the landslide is a typical long-term slow deformation towards the free direction. Based on a new round of investigation and monitoring, this paper shows that there are signs of creeping on the surface of the landslide since 2003, and there is no creep on the deep sliding surface. The joint fissures in the landslide area are relatively developed, and rainfall infiltration will soften the soft rock and soil layer and greatly reduce its stability. This paper collects and arranges the rainfall data of the landslide area in recent 30 years, constructs the slope finite element model considering rainfall conditions through ANSYS finite element software, and carries out numerical simulation stability analysis. The results show that if cracks appear below or above the slope's sliding surface, or are artificially damaged, the sliding surface may develop into weak cracks. Then, the plastic zone of penetration is offset; In the case of heavy rain, the slope can unload itself under the action of rainfall. At this time, the slope was unstable and the landslide happened suddenly.

Keywords: xiashan village landslide, numerical simulation, rainfall, slope stability, creep

OPEN ACCESS

Edited by:
Dongri Song,
Institute of Mountain Hazards and Environment (CAS), China

Reviewed by:
Xiangyu Li,
University of Alberta, Canada
Yu Wang,
University of Science and Technology Beijing, China

***Correspondence:**
Yingjie Xia
xiayingjie@dlut.edu.cn

Specialty section:
This article was submitted to Geohazards and Georisks, a section of the journal Frontiers in Earth Science

Received: *03 November 2021*
Accepted: *24 November 2021*
Published: *14 January 2022*

Citation:
Bao C, Zhan L, Xia Y, Huang Y and Zhao Z (2022) Development Trend and Stability Analysis of Creep Landslide With Obvious Slip Zone Under Rainfall-Taking Xinchang Xiashan Basalt Slope as an Example. Front. Earth Sci. 9:808086. doi: 10.3389/feart.2021.808086

INTRODUCTION

With the development of large-scale construction projects in the fields of mining, water conservancy, transportation and construction, a large number of large-scale and complex geological conditions have been encountered, such as mine slopes, dam collapses and reservoir bank landslides, which have made a big step forward in the study of landslide stability. A variety of methods based on elastic-

plastic theory and the application of improved limit equilibrium methods emerge as times require. In particular, people try to use the finite element method to study the stability of slope, which creates conditions for the quantitative evaluation of landslide stability and makes it gradually transit to the numerical method (Kaya and Midili, 2020; Shaller et al., 2020).

Over the years, many scholars have carried out a lot of research on landslide failure mechanism and stability (Marino et al., 2020; Wasowski and Pisano, 2020; Zhang, 2020; Zhang et al., 2020; Ramesh, 2021; Zheng et al., 2021), considering the slope in water (Salmasi et al., 2020). Study the Impact of Climate Change on Landslides (Lin et al., 2020; Shan et al., 2020; Zheng et al., 2021). Under the action of seepage, the failure mechanism and stability of slope are studied. Through the investigation of the landslide site, the formation mechanism of landslides was studied. Analysis of slope by field investigation and numerical simulation of body stability under heavy rainfall; through the combination of physical simulation and numerical simulation, the failure mechanism of landslides induced by heavy rainfall after coal seam mining is analyzed (Rauter et al., 2021; Zhou et al., 2021). The deformation and failure mechanism is as follows: goaf rock → slope deformation → rainfall-induced slope overall deformation evolution → sliding surface expansion → landslide occurrence (Li et al., 2021; Yang et al., 2021).

The activities of rainfall and groundwater level are the main factors that cause landslides. Foreign scholars (Naidu et al., 2018) have proposed analyzing and establishing a correlation between rainfall and the safety factor of landslides. According to the field test data of the Xiashan landslide, it is found that there are obvious differences in the seepage amount at different survey points. Using numerical software, we can simulate a slope landslide under different rainfall conditions.

Creep slope refers to the slope whose sliding deformation of rock and soil mass has obvious creep characteristics under the action of gravity, that is, its deformation has the characteristics of slow growth and evolution with time. This kind of slope is a dynamic development process, from stable deformation to instability failure. The stress and strain of rock and soil mass constantly develop and change with the change of time, and the change process often lasts for a long time (Yu et al., 2006; Guang et al., 2008; He et al., 2016; Marin and Velásquez et al., 2020).

Alpine landslides have strong destructive power when they occur, which can change the topography of the earth's surface (alpine and deep valley systems located on land and ocean). The valley's landscape is severely affected by the downhill movement of large landslides and the destruction of forest vegetation, threatening wildlife living on the surface of the earth and rivers, lakes and oceans. Secondly, whether the building is located on or near a landslide, landslide will affect it. Residential houses built on unstable slopes may suffer partial or complete damage, because landslides can cause instability or damage to the foundation, wall, surrounding facilities, ground and underground facilities of houses. Rock falls may cause damage to travellers and pedestrians. Alpine landslides not only cause casualties and property losses within a certain range, one of the greatest possible hazards should be the impact on traffic. This worldwide impact brings inconvenience to the lives of many people. All types of landslides may cause short-term or long-term road congestion and inconvenience to commercial transportation, tourism transportation and even emergency transportation, which is a very headache.

Xinchang Huishan Town Xiashan landslide is located in the southwest of basalt platform in Xinchang County, Zhejiang Province (average altitude 375.0 m). There were several heavy rainfalls after the landslide slipped in 1989, but it did not induce accelerated sliding. The main reason is that the accumulated energy of the landslide sliding force has been released in 1989, and the landslide may have entered a new stable state after sliding in that year. The accumulated energy of the sliding force is insufficient to promote the accelerated sliding of the landslide. When enough sliding force energy is accumulated, the landslide will continue to slide. The Xiashan slope model is established by computer (Yu et al., 2006), and the stability analysis of numerical simulation shows that the landslide is still dominated by creep motion under general conditions. This kind of slope is typical creep - stop motion - in the event of sliding landslide disaster. It is of great significance to study the creep development trend of Xiashan landslide for such unstable landslide disasters.

The landslide monitoring and early warning research base was established here by the Zhejiang Provincial Special fund project of basic public strategic geological work in 2019. The Xiashan landslide is a natural landslide without modification and reinforcement. The landslide monitoring project mainly relies on relatively advanced and reliable new technologies such as landslide monitoring instruments and equipment (Zhu et al., 2008; Abraham et al., 2020; Yang et al., 2020), and relies on cloud platform transmission technology based on 3G/4G. In order to achieve the purpose of landslide monitoring and early warning and prediction, a digital monitoring and early warning and popular science education platform integrating monitoring, early warning and prediction release and popular science education training was established. In order to achieve this goal, it is considered to focus on monitoring the surface displacement, deep displacement, groundwater level and rainfall of the landslide, supplemented by video monitoring, early warning broadcasting and manual monitoring in the periphery of the landslide. Based on the landslide survey results and related data of Xiashan Village, Huishan Town, Xinchang County, Zhejiang Province in 2019, this paper describes the geological conditions, the current situation of the landslide and the analysis of the sudden occurrence of the landslide. The historical rainfall data of nearly 30 years in Xinchang County was collected and the future rainfall situation was predicted. The displacement of the Xiashan landslides has been monitored in the past year. The finite element software ANSYS was used to build the slope model considering the rainfall condition, and the stability analysis of the Xiashan landslide was carried out according to the numerical simulation results, and the prevention and control suggestions and measures were put forward.

SLOPE PROFILE

Status and Characteristics of Landslide

The landslide is located in Xiashan Village, Huishan Town, Xinchang County, which is an old landslide hazard point. The mountain terrain in the region where the landslide is located is

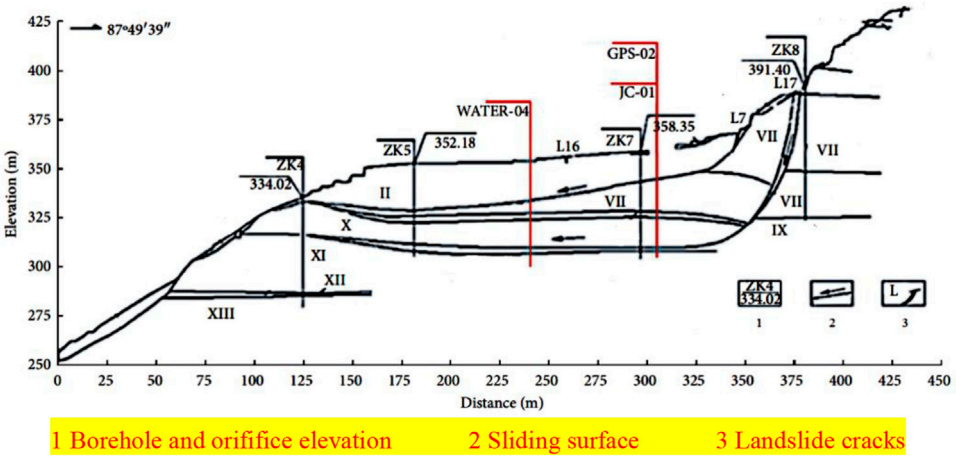

FIGURE 1 | Engineering geological map of typical section.

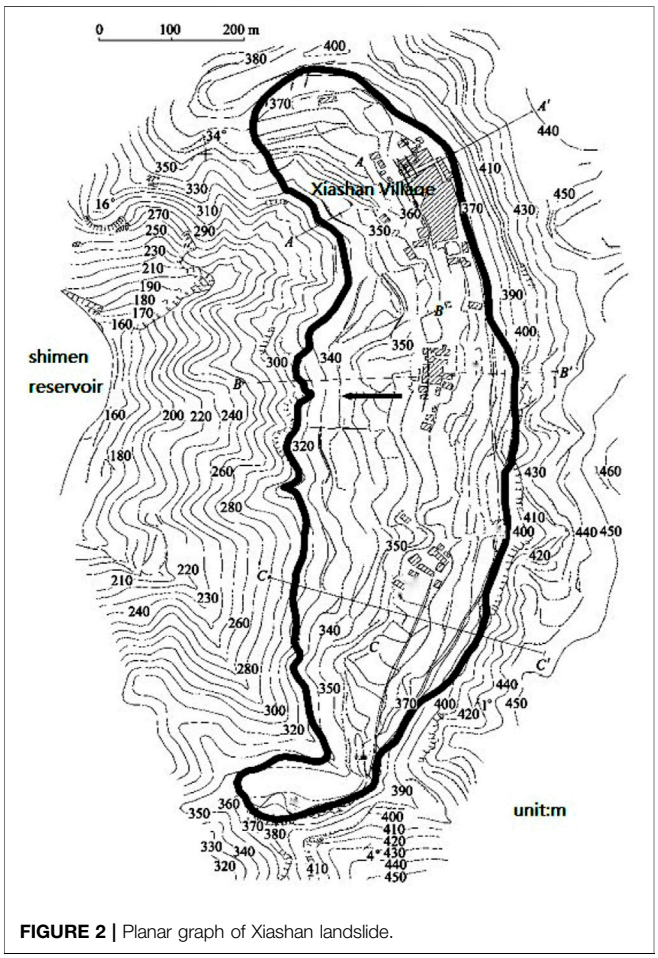

FIGURE 2 | Planar graph of Xiashan landslide.

generally high in the east and low in the west, which has the typical characteristics of a basalt platform. The mountain terrain in the upper part of the platform is relatively flat, with little fluctuation. The highest altitude of the Xiashan landslide area is 507.5m, the lowest altitude is 121m, and the relative altitude difference is 386.5 m. The natural terrain is about 15°–20°. The terrain in the middle of the platform suddenly becomes steep, and the slope gradient becomes large. The natural terrain slope is generally between 25° and 50°. The front edge of the platform is usually cut by the valley, showing a deep trench, forming a' V′ type valley landform. The bottom is the Shimen Reservoir, with a height difference of more than 200 m, and a strong landscape contrast (Wasowski and Pisano, 2020; Xie et al., 2021). The trailing edge of the landslide and the central terrain slope is relatively gentle, formerly mostly farmland, now because of village relocation, more to dry land, mainly to grow tea and fruit trees, landslide plane **Figure 2**. The engineering geological conditions of the rock and soil mass in the area vary greatly, and there are many layers, which have the characteristics of typical multiple eruption-sedimentary interbedding and residual slope loose layer thickness. Especially in the Zhutongling Formation of the Shengxian Group of the Upper Pliocene, the sedimentary-eruption cycle is complex, and the diagenesis of each sedimentary layer is extremely poor–very poor. Affected by weather and long-term immersion and infiltration of groundwater, it is mostly soil-like and sand-like. The content of local clay minerals and organic matter is high, and the thickness, nature and weathering degree of the basalt eruption zone are significantly different. Therefore, the engineering geological conditions of rock and soil in landslide areas are complex. The joint fissures in the landslide exploration area are relatively developed, and the rocks are strongly weathered and broken. On the basis of the large scale of the original vertical joint fissures in basalt, the rock mass is further opened and the opening width is large, and the rock mass is locally cut into small blocks or large blocks. The joint fissures along the slope in basalt are relatively developed, and some of them have large opening widths. The basic feature of the sliding surface is that the trailing edge is steep, and the sliding surface of the middle leading edge is flat (**Figure 1** typical profile). There are mainly two weak structural planes in the landslide. The cracks in the landslide are developed,

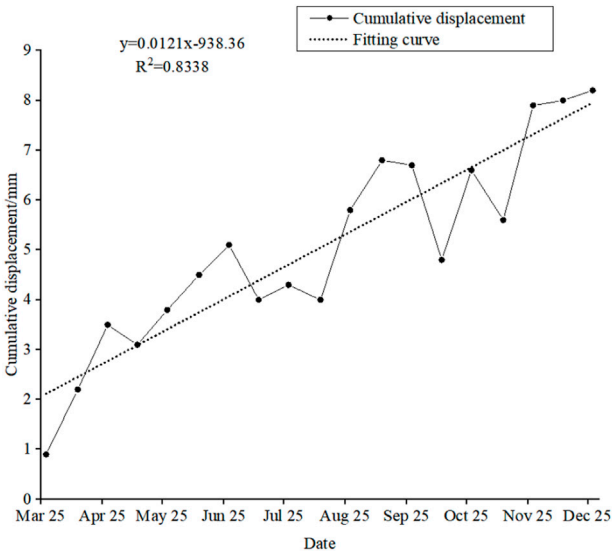

FIGURE 3 | Surface displacement of GPS-02 monitoring point in 2020.

and the landslide is cut into a net shape. There are tension cracks in the trailing edge of the landslide, and the trailing edge of the sliding surface has a large inclination.

According to the exploration operation and the original exploration-related data, the engineering geological conditions of rock and soil mass in the region have changed greatly, and there are many layers, which have the characteristics of typical multiple eruption-deposition interred and thick residual slope accumulation loose layer. Especially in the Zhutongling Formation of the Shengxian Group, the sedimentary-explosive cycle is complex, and the diagenetic range of each sedimentary layer is very poor. Affected by weather and long-term immersion and infiltration of groundwater, it is mostly soil-like and sandy. The content of local clay minerals and organic matter is high. The thickness, nature, and weathering degree of the basalt eruption zone are significantly different. Therefore, the engineering geological conditions of rock and soil in landslide areas are complex.

The Hangzhou-Shaoxing-Taizhou Expressway, a key construction project in Zhejiang Province, is now planned in the Xiashan landslide area. The Hangzhou-Shaoxing-Taizhou Expressway is scheduled to be fully implemented in 2021. Hangzhou-Shaoxing-Taizhou Expressway passes through the Xiashan landslide zone. If a sudden large-scale landslide occurs on the slope, the river channel could be blocked and the highway could be destroyed. It is very harmful to the construction and transportation facilities in mountainous areas, and affects the speed of highway construction.

Landslide Monitoring and Analysis

The weak structural plane exists in the landslide body, and through drilling exploration, the slope sliding is mainly controlled by two deep and shallow slide zones, and the deep slide zone is the main one, which plays a controlling role. As shown in **Figure 1**. The deep main sliding zone belongs to the weak interlayer, and below the contact surface of the weak interlayer are the stable and strongly weathered basalt layers. The weak strata are lithologically complex and mainly affected by the sedimentary environment, including sandy clay, clay rock and peataceous soil, etc. There are obvious abrupt changes on the top and bottom of the weak interlayer. According to the supplementary exploration holes, it can be seen that the interlayer is extruding, friction, claying, brecca crushing, and there is Soft plastic-Flow plastic-Soft plastic.

In order to study the current state and development trend of landslides, this paper summarizes the deep displacement and surface displacement of relevant monitoring points near the typical profile of landslides in recent years. **Figure 3** shows that the cumulative displacement range of GPS-02 surface displacement monitoring points from March to December 2020 is 1.94–7.7 mm, and the overall trend is increasing over time. The slope is not sliding at present, and the surface displacement is mainly caused by surface floating soil displacement under gravity and rain erosion.

Domestic researchers used the generalized Kelvin model to simulate the creep displacement of the Xiashan landslide (Yu et al., 2006). The results show that the cumulative displacement of the Xiashan landslide is 43.87 mm after 20.89 months. As shown in **Figure 4**, this paper fitted and predicted the deep displacement of the slope after about 14 years of the generalized Kelvin model and the general creep landslide. The results showed that the cumulative displacement of the former was about 60.8 mm, and with the passage of time, the annual cumulative displacement gradually decreased, and the annual cumulative displacement was only about 0.6 mm from June 2020 to June 2021. The cumulative displacement of the latter is about 162.3 mm, and the cumulative displacement from June 2020 to June 2021 is about 9.5 mm. From June 2020 to June 2021, the cumulative displacement value at 30.5 m underground of the JC-01 deep displacement monitoring point of the Xiashan landslide fluctuated between −0.6 and 0.0 mm with time. Taking into account factors such as the accuracy of monitoring instruments and the difficulty of field monitoring, the slope does not produce negative displacement. Based on the above monitoring data, it is concluded that the Xiashan slope is different from the general creep landslide. The deep sliding zone that plays a controlling role will continue to move over time at the beginning, but the displacement decreases year by year, and finally approaches zero, basically in a non-sliding state. If the landslide is affected by rainfall, the slope stability will be further reduced, and the accumulated energy is sufficient to produce rapid sliding.

In this paper, based on the research on the prediction method of potential locking landslide (Pan et al., 2014; Yin et al., 2021), the locking property of Xiashan landslide in Xinchang County, Zhejiang Province is as follows: the slope of Xiashan landslide is 15°–45°; the lithology of the strata is mostly soil and sand, and the content of local clay minerals and organic matter is high. The strata occur in the gently inclined slope and the dip angle is less than the slope angle. The front landslide is sliding and extruded, and the trailing edge has tensile cracks. The region belongs to the subtropical monsoon climate area. The overall temperature is warm and humid, and the rainfall is abundant. The seismic activity intensity is low, the magnitude is small and

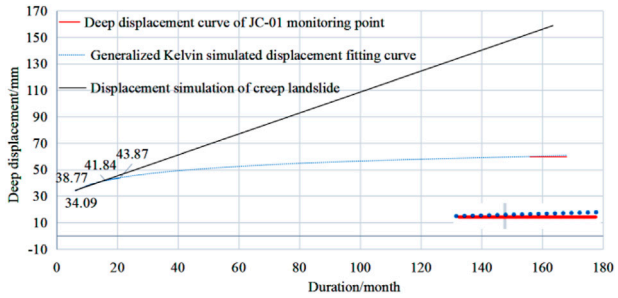

FIGURE 4 | Cumulative deep displacement duration curve of B-B section.

the frequency is low in Xinchang County. This kind of landslide is composed of multiple rocks and soil layers and distributed according to a certain layer occurrence. Under the action of static aging or dynamic vibration deformation, the stress concentration in the locking section of the potential sliding surface. When the locking section is not connected, even if the landslide produces a creeping phenomenon, it will not immediately cause overall instability and lead to landslide hazard. However, when the slope accumulates sufficient sliding force energy, it will lead to the high-speed start of the landslide. This sudden hazard is often beyond prevention. According to the formation conditions and characteristics of various landslides, it is consistent with the formation conditions of a locking landslide, and it can be preliminarily determined that this slope is a locking landslide with potential static aging deformation instability.

Theoretical Stability Calculation of Control Slip Band

When a landslide occurs failure along the existing sliding surface, landslide stability analysis is often based on limit equilibrium theory. The sliding surface can be approximately simplified as a broken line. The transfer coefficient method is used to solve the remaining sliding force and stability evaluation. According to the shape of the broken line, the landslide body is divided into several sections. The sliding force is transferred along the direction of the sliding surface. The overall remaining sliding force can be calculated and the stability of the landslide can be judged (Liu et al., 2009). According to the characteristics of bedding creep failure of the Xinchang Xiashan landslide, the bedding landslide under creep mode is taken as the research object. The terrain line and sliding zone of the landslide are simplified as broken lines (**Figure 5**). The specific calculation method of the calculation model is as **Eq. 1**–**4**. The calculation results are shown in **Table 1**.

$$K_f = \frac{\sum_{i=1}^{n-1}\left(R_i \prod_{j=i}^{n-1} \psi_j\right) + R_n}{\sum_{i=1}^{n-1}\left(T_i \prod_{j=i}^{n-1} \psi_j\right) + T_n} \quad (1)$$

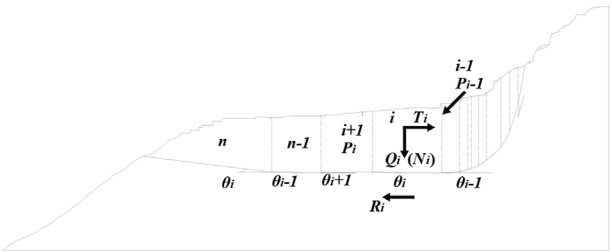

FIGURE 5 | Calculation diagram of transfer coefficient method.

CH2O:

$$R_i = (W_i((1 - r_U)\cos\alpha_i - A\sin\alpha_i) - R_{Di})\tan\varphi_i + C_i L_i$$

$$T_n = (W_i(\sin\alpha_i + A\cos\alpha_i)) + T_{Di}$$

$$\prod_{j=i}^{n-1} \psi_j = \psi_i\psi_{i+1}\psi_{i+2}\ldots\ldots\psi_{n-1}$$

$$\psi_i = \cos(\alpha_i - \alpha_{i+1}) - \sin(\alpha_i - \alpha_{i+1})\tan\varphi_{i+1}$$

CH2O: K_f—Landslide stability coefficient;

ψ_i—Coefficient of transmission;

$\Psi = \cos(\beta_{n-1} - \beta_n) - \sin(\beta_{n-1} - \beta_n)\tan\varphi_n$

R_i—Section i Calculation of Slip Resistance of Strip Block (kN/m);

Calculation of landslide stability coefficient by following formula.

$$T_n = T_{n-1}\psi + A\gamma\sin\beta_n + D_i\cos(\beta_n - \alpha_n) \quad (2)$$

$$R_n = R_{n-1}\psi + A\gamma\cos\beta_n + D_i\sin(\beta_n - \alpha_n)\tan\varphi_n + c_n l_n \quad (3)$$

$$F_s = \frac{R_n}{T_n} \quad (4)$$

CH2O: γ—Weighted average gravity;

A—Section area of sliding body, m^2; T_n and T_{n-1}—The remaining sliding force of block N and block N-1;

ψ—Coefficient of transmission;

φ_n, c_n—The standard value of friction Angle and cohesion of the sliding body in block N along the sliding surface;

l_n—Length of block N sliding body along the sliding surface;

D_i—Water penetration, $D_i = r_\omega A\sin\alpha_i = F_i\sin\alpha_i$, A is the soil area under the water level line, α_i is the inclination of water surface, β_i is the inclination angle of landslide.

According to the stability calculation in **Table 1**, the stability of the deep sliding zone is significantly lower than that of the shallow sliding zone. The landslide has two sliding zones, shallow and deep, and the deep sliding zone is the main one, which plays a controlling role. It can be seen that the landslide is a typical long-term slow deformation in the free direction by means of the gravity of the soil itself. Due to the large range of landslide distribution, and irregular character, under normal conditions, the possibility of overall speed skating is not large. The

TABLE 1 | Calculation results of landslide stability.

	Calculated work condition	Coefficient of stability
Typical section of Xiashan landslide	Shallow sliding zone	1.571
	Deep slide zone	1.142

exploration area is located in the subtropical monsoon climate zone. It is generally warm and humid, with abundant rainfall. During persistent rainfall or heavy rainfall, the local sliding speed of the leading edge will accelerate and the slope stability will be greatly reduced.

The geological environment conditions of the three natural villages in Yuanxiashan, Lishan and Tang (Yin et al., 2021), which are involved in the range of Xiashan landslide area, become more fragile under the action of human engineering activities. The free surface formed by topographic and geomorphologic conditions provides sufficient unloading space for the landslide. There are a large number of clay groups in the soft rock strata, and the mechanical properties are significantly lower than those of clay rocks and argillaceous siltstone in the upper and lower rock strata. Mudstone, clay rock, argillaceous shale, silty clay rock and argillaceous siltstone are common in soft rock strata. Most of them belong to soft rock with uniaxial compressive strength of less than 30 MPa. The weak interlayer refers to the soft rock stratum with low mechanical strength, high clay or carbon content, easy softening of rainwater, long extension and thin thickness. A mudded interlayer refers to the part of the weak interlayer and weak rock layer that has been modded. It is a shear smooth surface or soft rock surface formed by interlayer dislocation, which is ground by hard rock, and soaked and softened by groundwater, so that the material composition of rock powder changes into viscoplastic soft mud. Good joint crack connectivity, rock fragmentation, accelerated groundwater activity; strong rainfall has formed seepage channels in landslides; natural gullies have been scouring the slope during rainfall. From the perspective of the whole geological environment, the slope has the geological conditions for landslides.

The landslide has had three large slides since 1958. The frequent activities in the past 40 years are closely related to the reclamation and deforestation of human beings and the opening of irrigation channels around mountains. Human activities have accelerated soil erosion, increased the large amount of rainwater and surface irrigation, infiltrated into the aquifer in the landslide, lubricated and softened the deep rock and soil mass (landslide), and directly destroyed the stability of the natural slope. Induced by sliding in 2000, although one-time (daily) precipitation intensity is not large, the sliding force energy accumulation has reached the induced limit point, so the sliding. The deformation failure mode is the creep-cracking type, as shown in **Figure 6**. Due to the fact that the rock and soil of the landslide are broken and there are many cracks on the surface, as the rainwater on the slope invades the interior of the slope, the groundwater level is greatly improved, which aggravates the weakening of the properties of the rock and soil, and the

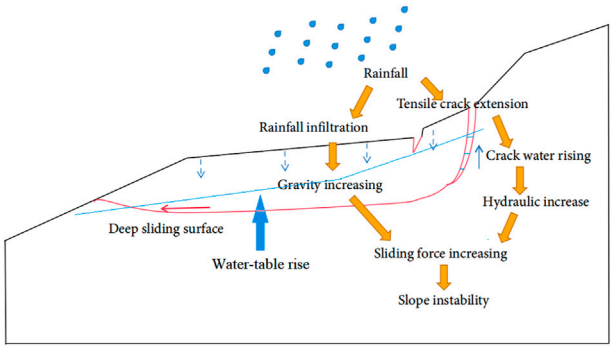

FIGURE 6 | Schematic of hydraulic driving type.

rainwater has a lag in the interior of the slope. It increases the self-weight of the slope in a short time, increases the hydrostatic pressure and hydrodynamic pressure in the slope, and the energy of the sliding force continues to increase. Rainfall reduces the shear strength of the sliding zone. Under the action of self-weight, the landslide begins to slide toward the free surface (Stark and Xu et al., 2020; Zhu et al., 2020).

As shown in **Figure 6**, In the process of continuous accumulation of groundwater on the sliding surface, the shear stress on the sliding shear surface is concentrated. After the landslide occurred in 2000, the surface cracks at the trailing edge of the landslide increased and the number of cracks increased sharply, resulting in more surface water invading the slope along the tensile cracks at the trailing edge, accelerating the creeping process, and weakening the shear strength of the shear surface, so as to promote the landslide again to the leading edge. Finally, the leading edge of the landslide was completely sheared and the landslide phenomenon occurred. Due to the long-term immersion of the sliding zone by groundwater, the sliding body showed plastic flow characteristics.

Because there is a "bowl-like" structure on the front edge of sliding, it can well resist the impact of sliding, which is the main reason why the landslide has had several strong rainfalls after sliding, but does not induce accelerated sliding. Although the' bowl' structure can prevent the slope from sliding in a short time, it also causes the accumulation of landslide sliding force energy. When the accumulation of sliding force energy has reached the induced limit point, it will slide again. When the groundwater level increases, the self-weight of water increases the energy of sliding force and accelerates the formation of landslides. On the one hand, the lubrication of water reduces the matric suction and cohesion between soil particles. On the other hand, the buoyancy generated by the increase in groundwater level supports soil particles, which makes the sliding force transmitted from the trailing edge easier to promote the slip of the soil layer.

RAINFALL HISTORY STATISTICS

The landslide has had three major slides since 1958. From the cause, the main factors are as follows: first, the frequent

TABLE 2 | Statistical table of typhoons affecting rainfall in Xinchang county from 1990 to 2021.

Name of typhoon	Start and end dates	Daily rainfall/(mm)
Abe	1990/8/31–1990/9/1	110.3
Ted	19,929/23–1992/9/24	125.8
Rananim	2004/8/13	141
Khanun	2005/9/11	153.6
Krosa	2007/10/7–2007/10/8	134.7
Fitow	2013/10/7–2013/10/8	134.9
Lekima	2019/8/10–2019/8/11	221
Mitag	2019/10/2–2019/10/3	101.5
In-fa	2021/7/24–2021/7/25	200–250

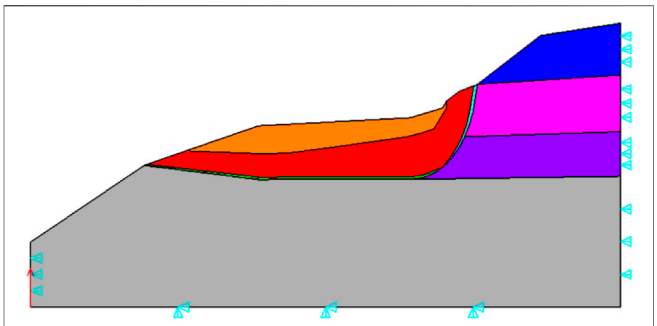

FIGURE 7 | Calculation model of Xiashan landslide in Xinchang.

activities in the past 40 years are closely related to human's reclamation and deforestation, the development of irrigation channels around mountains, and human activities accelerate soil erosion. Second, the leading edge of the landslide is mostly cliff or steep slope, and the landslide body is in the air state. However, because the rock layer in the landslide is nearly horizontal, the sliding surface of the leading edge of the landslide is not inclined, and the sliding momentum of the landslide body is not large, and stagnation often occurs after a slip. Third, under the influence of continuous rainfall or heavy rain, surface irrigation water infiltrates into the aquifer of the landslide body, lubricating and softening the deep rock and soil mass (landslide), and directly damaging the stability of the natural slope locally (Bontemps et al., 2020; Løvholt et al., 2020).

There were several heavy rainfalls after landslide sliding in 1989, but no accelerated sliding was induced. The main reason was that the accumulated energy of landslide sliding force had been released in 1989. The insufficient accumulated sliding force energy promoted the accelerated sliding of landslides. When sufficient sliding force energy was accumulated and lubrication was sufficient, the landslide continued to slide. For example, the sliding induced in 2000, although one-time (daily) rainfall intensity is not large, the energy accumulation of the sliding force has reached the induced limit point, so the sliding occurs again. It is speculated that the sliding of the Xiashan landslide is intermittent and delayed.

The front edge of the landslide is worse than the rear edge, and the aquifer in the middle and rear part of the landslide is thick. In rainy season, a natural underground water storage site is often formed with the front of the landslide as the earth-rock dam, and the middle and rear parts and the rear edges as water bodies. Strongly weathered sandy soil mixed with silty clay basalt contains more pore water, locally under the action of strong rock and soil sliding force was grinded into glue, thin layer containing water. Quaternary gravel layer, sedimentary rock sand (gravel eggs) stone layer and basalt fracture development permeability is good. Groundwater is rich, seasonal variation.

The precipitation in landslide areas mainly concentrated in the typhoon period and meiflood rainy season, and short-term or continuous heavy precipitation often occurred, which promoted the formation and induction of landslides. In this paper, the number of heavy rains (daily rainfall >100 mm) in xinchang county in recent 30 years was counted, among which 9 days were obviously affected by typhoons. As can be seen from **Table 2**, the average daily rainfall in 9 days is 149.76 mm, and the process rainfall can reach 200–500 mm (Huang et al., 2021).

Data from **Table 2** show that the frequency and intensity of rainstorms caused by typhoons have increased in recent years, which may lead to persistent rainfall and flood disasters (Huang et al., 2021). According to rainfall statistics from several stations in Shaoxing at 15: 00 p.m. on July 24, 2021, the 12-h rainfall total exceeded 200 mm. Care should be taken to prevent existing water and drainage facilities from adapting to increased rainfall each year.

LANDSLIDE STABILITY PREDICTION

The Slope Model

Through geological exploration and investigation, the two-dimensional landslide calculation model of the Xiashan landslide is established, as shown in **Figure 7**. Ansys modelling was used for numerical simulation, and the slope changes caused by continuous rainfall were analyzed in detail. Five rainfall conditions were analyzed, and compared. Working Condition 1: gravity + dry groundwater level; Working condition 2: gravity + low groundwater table; Working condition 3: gravity + normal groundwater level; Working condition 4: gravity + high groundwater table; Working condition 5: gravity + highest groundwater level.

A typical profile consistent with the main sliding direction of the Xiashan landslide is selected as an example for SRM (strength reduction method) analysis. The advantage of this method is that the dangerous sliding surface of the slope is automatically obtained by the program without assuming the shape and position of the sliding surface (Zhao et al., 2002; Gao et al., 2020). The physical and mechanical parameters of landslides adopted by the model (**Table 3**).

Stability Calculation and Analysis

Figure 8 shows the total displacement of the sliding body on the deep sliding surface of the landslide under normal circumstances. The total displacement and horizontal displacement of the sliding body are usually the largest at the trailing edge. The sliding displacement along the sliding surface decreases from the back

TABLE 3 | Mechanical parameters of rock and soil.

Structural layer	Elastic modulus *E* (MPa)	Poisson's ratio *μ*	Volumetric weight *γ* (kN/m^3)	Cohesion intercept *c* (kPa)	Angle of internal friction *φ* (°)
Sliding mass	15	0.33	19.7	37	22
Weak Interlayer	—	—	—	10	7
Strata III–IX	4,000	0.23	21	—	—
Stratum X	5,000	0.21	22	—	—

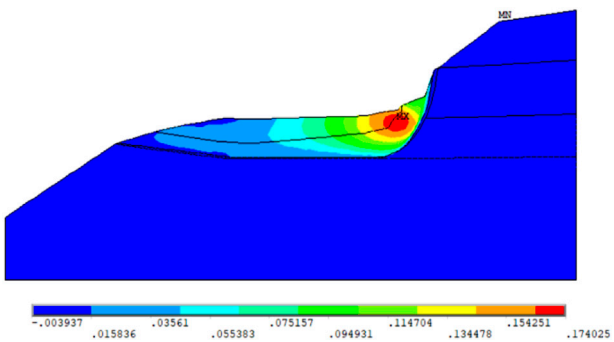

FIGURE 8 | Displacement value diagram of sliding body in deep sliding surface of Xiashan section.

edge to the front edge and decreases rapidly when the sliding surface changes from gentle to locked section. **Figure 9** shows five types of the slope under the condition of effective plastic strain figure, the figure shows the main strain inside the sliding body to focus on the rear of the deep slip band contact belt, slope is mainly controlled by two sliding surface, under the action of heavy rainfall and groundwater seepage of deep rock mass near weak structural plane prone to plastic deformation, and the trailing edge is relatively obvious in landslide, The maximum thickness of the sliding body is about 60.0 m, and the average thickness is about 34.25 m. Rainfall intensity has a great influence on the slope plastic zone. With the gradual increase of rainfall intensity, the slope plastic zone first accumulates energy at the back edge. When the energy is enough to push the locked section, the rock mass in the plastic zone is prone to drastic sliding. If cracks appear below or above the slope slip surface or are damaged artificially, the sliding surface may develop towards the failure of weak cracks, Thus, the plastic zone of the landslide is no longer through the original slip zone. The results of simulation show that, with the continuous infiltration of rain, the slope weight increases, the matrix suction and shear strength decrease, and the soil at the back edge of the slope continues to settle. Due to the continuous infiltration of rainwater from the slope surface and the continuous aggregation of pore water at the back edge of the slope, the strength of the soil at the front edge of the slope is significantly reduced, which does not provide enough skid resistance, and the overall instability of the slope will occur at last.

The calculation results of the Mohr-Coulomb hexagon circumcircle yield criterion (DP1) used in Ansys software are different from those of the traditional Mohr-Coulomb criterion. In order to make the slope safety factor obtained by the finite element strength reduction method consistent with the safety factor used in traditional engineering practice, the plane strain Mohr-Coulomb matching D-P criterion is adopted (Zheng and Zhao et al., 2005). **Eq. 5–7** are shown below.

$$c_i = \frac{c}{F_i} \tag{5}$$

$$tan\,\varphi_i = \frac{\tan\varphi}{F_i} \tag{6}$$

$$F_2 = \sqrt{\frac{\left(3\sqrt{cos^2\varphi_0 F_i^2 + sin^2\varphi_0} - sin\varphi_0\right)^2 - 12\sin^2\varphi_0}{12cos^2\varphi_0}} \tag{7}$$

Where *C* is the standard value of bond strength (kPa) of rock and soil mass on the sliding surface; *φ*-standard value of internal friction Angle of sliding belt soil (°); Fi-Strength reduction coefficient; Safety factor of F2-mol-Coulomb matching with D-P criterion.

Table 4 and **Figure 10** show that the slope safety factor decreases with the increase in rainfall intensity. When the groundwater level is normal, the rainwater infiltrates into the shallow soil, and the increase in the saturation of the shallow soil leads to the decrease of the shear strength and safety factor of the slope. The slope is mainly controlled by the shallow sliding surface. When the rainfall intensity increases, the rainwater infiltration rate increases, and the rainwater infiltrates into the deep soil. The groundwater level increases. The landslide begins to be affected by the deep sliding zone, and the dangerous sliding surface of the slope turns to the deep sliding surface. At this time, the share strength of the slope decreases significantly, and the attenuation of the slope safety factor is the largest. When the rainfall infiltration rate reaches the maximum, the soil tends to be saturated, the shear strength is close to the minimum, and the decline trend of slope safety factor is gradually flat. Therefore, the landslide is actually controlled by the deep sliding surface. When the groundwater level reaches the highest, the slope safety factor reaches the lowest, and the slope is in an unstable state.

The slope safety factor range is 1.039–1.168. When the groundwater level is high, the slope safety factor is greater than 1.05, and the slope is basically stable. When the groundwater level reaches the highest, the slope safety factor is less than 1.05, and the slope is unstable. Therefore, the landslide is

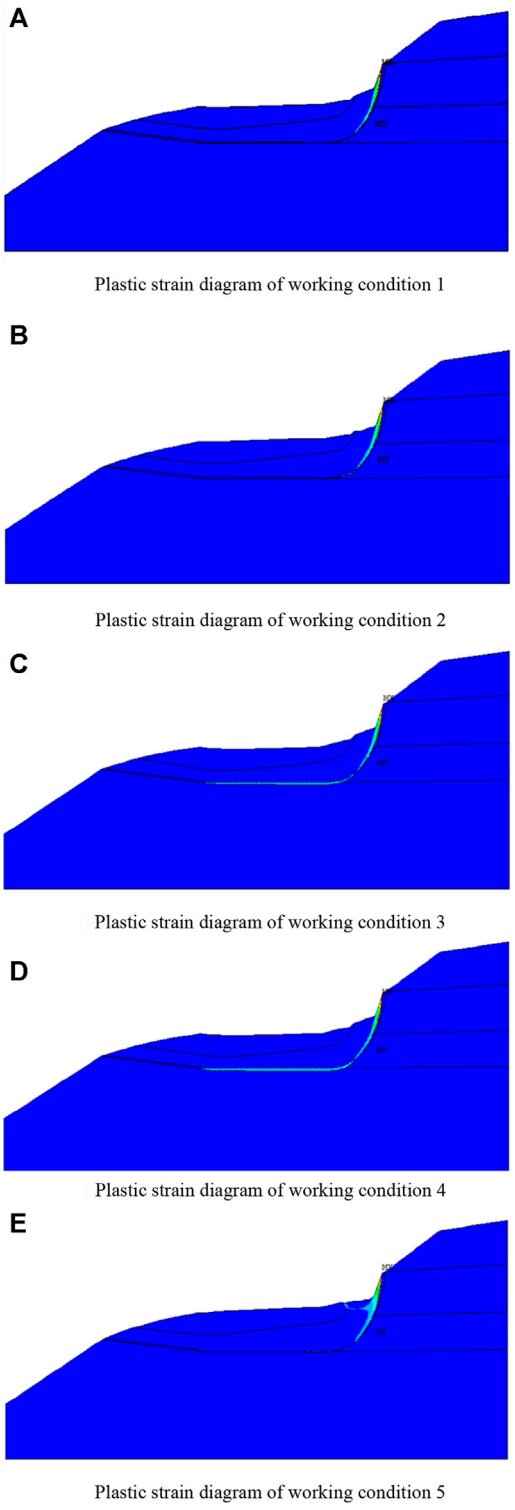

FIGURE 9 | Plastic strain diagram of working conditions 1–5.

basically stable on the whole. When encountering heavy rain, it is in an unstable state, and the creep speed of the slope will gradually increase. When the locking section accumulates sufficient sliding force energy, it may lead to the high-speed start of a landslide, which will cause harm to the buildings in the downstream area of the Xiashan slope, and even threaten the safety of people.

TABLE 4 | Slope safety coefficient in five working conditions.

	Model 1	Model 2	Model 3	Model 4	Model 5
Factor of safety	1.168	1.133	1.078	1.052	1.039

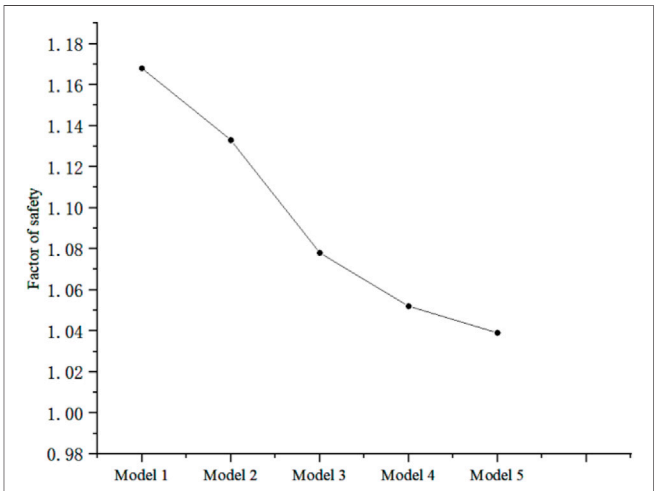

FIGURE 10 | Variation diagram of slope stability coefficient with different rainfall intensity.

SUGGESTIONS OF PREVENTION AND CURE

The treatment of such landslides should be early detection and prevention first. In order to deal with working conditions such as heavy rain that significantly affects the safety of the slope, drainage should be set up on the slope. When necessary, comprehensive treatment schemes such as slope cutting at the top of the slope, slope toe retaining, and reinforcement in the middle of the landslide are adopted. The specific recommendations are as follows:

1) In the past 10 years, the slip velocity of the landslide front was 36–77 mm/a, and the accurate sliding time and sliding range of the landslide are uncertain. Excavating large-section intercepting ditches on the stable stratum outside the slope top effectively prevents surface water from entering the landslide area. Increase the number of drainage ditches on landslide surface, increase drainage ditch section, and accelerate surface water drainage.
2) The front, rear edge and surface cracks of the slope are filled with waterproof and impermeability materials. Increase the density of underground drainage facilities such as seepage ditches, blind ditches, drainage holes and collecting wells.

3) If technical measures are taken to strengthen the slope in the later stage, the height of the slope instability can be reduced by slope cutting and load reduction. In addition, anti-slide piles, retaining walls, bolts, anchor cables and other reinforcement components can be reasonably arranged to improve the stability of slope soil.
4) Regular inspection and maintenance of slope waterproof and drainage facilities and reinforcement measures.

CONCLUSION

1) There are mainly two weak structural planes in the landslide. The fracture of landslides is developed, the development of weak structural planes is poor, and the landslides are cut into a net shape. There are tension cracks at the trailing edge of the landslide, which are not conducive to slope stability.
2) The landslide generally moves along the sliding zone, but the existence of the locking section curbs the creep displacement, and the slope will accumulate energy. When the slope is artificially damaged, resulting in the generation or intensification of cracks, the plastic zone of the landslide may develop to a weak point and no longer move along the sliding zone.
3) The field monitoring results show that the slope is basically in a static state. The numerical model calculation results show that when the groundwater level reaches the highest, the stability coefficient is less than 1.05, and the slope creep begins to intensify, and the slope is in an unstable stage.
4) In general, the follow-up landslide is basically static, and the overall slip is small. The main displacement is concentrated on the surface floating soil movement. In the case of heavy rainfall, when the energy gathered by the slope is greater than the anti-sliding force, it may lead to accelerated creeping of the slope until the landslide starts at high speed.
5) The results of the slope numerical model show that rainfall has an important influence on slope stability. Under normal conditions, the tensile stress at the top of the trailing edge of the landslide is close to its saturated tensile strength. If heavy rainfall occurs, the tensile stress at the top of the trailing edge exceeds the saturated tensile strength, which will lead to tensile cracks, and the cracks will gradually expand over time and affect the stability of the slope.
6) This kind of risk is high, with delay and intermittency. When it comes to external factors such as rainstorm and artificial activities, it will suddenly explode. It is not easy to determine immediately that landslides should be monitored and predicted for a long time, and the water treatment is mainly based on a variety of drainage measures. When necessary, the slope can be comprehensively treated.

DATA AVAILABILITY STATEMENT

The original contributions presented in the study are included in the article/Supplementary Material, further inquiries can be directed to the corresponding author.

AUTHOR CONTRIBUTIONS

All authors listed have made a substantial, direct, and intellectual contribution to the work and approved it for publication.

FUNDING

The study was funded by the National Natural Science Foundation of China (Grant Nos. 42077251 and 41807269). The work presented in this paper was also supported by Open Research Fund of State Key Laboratory of Geomechanics and Geotechnical Engineering, Institute of Rock and Soil Mechanics, Chinese Academy of Sciences (Grant No. Z020011), Fundamental Research Funds for the Central Universities (Grant No. DUT20RC (3)011), Collaborative Innovation Center for Prevention and Control of Mountain Geological Hazards of Zhejiang Province (PCMGH-2016-Z-04).

REFERENCES

Abraham, M. T., Satyam, N., Bulzinetti, M. A., Pradhan, B., Pham, B. T., and Segoni, S. (2020). Using Field-Based Monitoring to Enhance the Performance of Rainfall Thresholds for Landslide Warning. *Water* 12 (12), 3453. doi:10.3390/w12123453

Bontemps, N., Lacroix, P., Larose, E., Jara, J., and Taipe, E. (2020). Rain and Small Earthquakes Maintain a Slow-Moving Landslide in a Persistent Critical State. *Nat. Commun.* 11 (1), 780. doi:10.1038/s41467-020-14445-3

Gao, F., Li, X. J., and Chi, M. J. (2020). Analysis of Stability of Single and Double Side Soil Slopes with FEM Strength Reduction Method. *J. Eng. Geol.* 28 (3), 650–657. doi:10.13544/j.cnki.jeg.2018-080

Guang, S., Mao, Z. L.-r., Zhen-gao, L. K.-d. C., and En-kun, M. (2008). The Geological Characteristics and Stability Analysis of the Xiashan Village Landslide in Xinchang County, Zhejiang Province. *Chin. J. Geol. Hazard. Control.* 4. doi:10.3969/j.issn.1003-8035.2008.04.004

He, K. Q., Chen, W. G., and Zhang, P. (2016). Real-time Monitoring of Dynamic Stability Coefficient and Displacement Criterion of the Creep Slope. *Chin. J. Rock Mech. Eng.* 35 (7), 1377–1385. doi:10.13722/j.cnki.jrme.2015.1535

Huang, Y., Sun, Z., Bao, C., Huang, M., Li, A., and Liu, M. (2021). A Typical Basalt Platform Landslide: Mechanism and Stability Prediction of Xiashan Landslide. *Adv. Civil Eng.* 2021, 1–14. doi:10.1155/2021/6697040

Kaya, A., and Midilli, Ü. M. (2020). Slope Stability Evaluation and Monitoring of a Landslide: a Case Study from NE Turkey. *J. Mt. Sci.* 17 (11), 2624–2635. doi:10.1007/s11629-020-6306-x

Li, S.-Y., Li, D.-D., Liu, H.-D., Wang, S.-W., Geng, Z., and Peng, B. (2021). Formation and Failure Mechanism of the Landslide: a Case Study for Huaipa, Western Henan, China. *Environ. Earth Sci.* 80 (15), 1–12. doi:10.1007/s12665-021-09781-6

Lin, Q., Wang, Y., Glade, T., Zhang, J., and Zhang, Y. (2020). Assessing the Spatiotemporal Impact of Climate Change on Event Rainfall Characteristics Influencing Landslide Occurrences Based on Multiple GCM Projections in China. *Climatic Change* 162 (2), 761–779. doi:10.1007/s10584-020-02750-1

Liu, C. H., Jaksa, M. B., and Meyers, A. G. (2009). A Transfer Coefficient Method for Rock Slope Toppling. *Can. Geotech. J.* 46 (1), 1–9. doi:10.1139/t08-094

Løvholt, F., Glimsdal, S., and Harbitz, C. B. (2020). On the Landslide Tsunami Uncertainty and hazard. *Landslides* 17, 2301–2315. doi:10.1007/s10346-020-01429-z

Marin, R. J., and Velásquez, M. F. (2020). Influence of Hydraulic Properties on Physically Modelling Slope Stability and the Definition of Rainfall Thresholds for Shallow Landslides. *Geomorphology* 351, 106976. doi:10.1016/j.geomorph.2019.106976

Marino, P., Peres, D. J., Cancelliere, A., Greco, R., and Bogaard, T. A. (2020). Soil Moisture Information Can Improve Shallow Landslide Forecasting Using the Hydrometeorological Threshold Approach. *Landslides* 17 (9), 2041–2054. doi:10.1007/s10346-020-01420-8

Naidu, S., Sajinkumar, K. S., Oommen, T., Anuja, V. J., Samuel, R. A., and Muraleedharan, C. (2018). Early Warning System for Shallow Landslides Using Rainfall Threshold and Slope Stability Analysis. *Geosci. Front.* 9 (6), 1871–1882. doi:10.1016/j.gsf.2017.10.008

Pan, X. H., Xue, L., Qin, S. Q., Li, G. L., Pei, L., and Wang, M. M. (2014). Types, Formation Conditions and Pre-decision Method for Large Landslides with Potential Locked Patches. *J. Eng. Geol.* 22 (6), 1159–1167. doi:10.13544/j.cnki.jeg.2014.06.021

Ramesh, G. (2021). Slope and Landslide Stabilization: A Review. *Indian J. Struct. Eng.* 1 (2), 13–16. doi:10.35940/ijse.A1304.111221

Rauter, M., Hoße, L., Mulligan, R. P., Take, W. A., and Løvholt, F. (2021). Numerical Simulation of Impulse Wave Generation by Idealized Landslides with OpenFOAM. *Coastal Eng.* 165, 103815. doi:10.1016/j.coastaleng.2020.103815

Salmasi, F., Norouzi, R., Abraham, J., Nourani, B., and Samadi, S. (2020). Effect of Inclined clay Core on Embankment Dam Seepage and Stability through LEM and FEM. *Geotech. Geol. Eng.* 38 (6), 6571–6586. doi:10.1007/s10706-020-01455-7

Shaller, P. J., Doroudian, M., and Hart, M. W. (2020). The Eureka Valley Landslide: Evidence of a Dual Failure Mechanism for a Long-Runout Landslide. *Lithosphere* 2020 (1), 8860819. doi:10.2113/2020/8860819

Shan, W., Zhang, C., Guo, Y., Shan, M., Zeng, X., and Wang, C. (2020). "Climate Change and Surface Deformation Characteristics in Degradation Area of Permafrost in Lesser Khingan Mountain, China," in *Understanding and Reducing Landslide Disaster Risk. WLF 2020. ICL Contribution to Landslide Disaster Risk Reduction*. Editors V. Vilímek, F. Wang, A. Strom, K. Sassa, P. T. Bobrowsky, and K. Takara (Cham: Springer), 209–219. doi:10.1007/978-3-030-60319-9_24

Stark, T. D., and Xu, Z. (2020). "Oso Landslide: Failure Mechanism and Runout Analyses," in *Understanding and Reducing Landslide Disaster Risk. WLF 2020. ICL Contribution to Landslide Disaster Risk Reduction*. Editors B. Tiwari, K. Sassa, P. T. Bobrowsky, and K. Takara (Cham: Springer), 47–63. doi:10.1007/978-3-030-60706-7_3

Wasowski, J., and Pisano, L. (2020). Long-term InSAR, Borehole Inclinometer, and Rainfall Records Provide Insight into the Mechanism and Activity Patterns of an Extremely Slow Urbanized Landslide. *Landslides* 17 (2), 445–457. doi:10.1007/s10346-019-01276-7

Xie, W.-l., Guo, Q., Wu, J. Y., Li, P., Yang, H., and Zhang, M. (2021). Analysis of Loess Landslide Mechanism and Numerical Simulation Stabilization on the Loess Plateau in Central China. *Nat. Hazards* 106 (1), 805–827. doi:10.1007/s11069-020-04492-w

Yang, H., Wang, L. W., and Hao, S. W. (2020). Landslide Monitoring and its Stabilization Process Based on an *In-Situ* Tilt Monitoring System. *Eng. Mech.* 37 (S), 193–199. doi:10.6052/j.issn.1000-4750.2019.04.S035

Yang, W., Wang, F., Tie, Y., Wang, D., and Ouyang, C. (2021). Characteristics and Dynamic Process Modeling of the Rainfall-Induced Landslide on August 21, 2020 in Hanyuan County, China. *Front. Earth Sci.* 9, NA. doi:10.3389/feart.2021.720872

Yin, X., Lin, H., Chen, Y., Tang, Y., Wang, Y., Zhao, Y., et al. (2021). Stability Analysis of Slope Considering the Energy Evolution of Locked Segment. *Geotech. Geol. Eng.* 1–10. doi:10.21203/rs.3.rs-191198/v1

Yu, B. T., Sun, H. Y., Shang, Y. Q., and Li, H. Q. (2006). Characteristics and Stability Analysis of Xiashan Landslide in Zhejiang Province. *Chin. J. Rock Mech. Eng.* 25, 2875–2881. doi:10.1007/s11631-006-0407-2

Zhang, J. M. (2020). State of Art and Trends of Rock Slope Stability with Soft Interlayer. *J. Eng. Geol.* 28 (3), 626–638. doi:10.13544/j.cnki.jeg.2019-377

Zhang, Y. S., Renji, B., Sanshao, R., and Zongliang, L. (2020). An Analysis of Geo-Mechanism of the Baige Landslide in Jinsha River, Tibet. *Geol. China* 47 (6), 1637–1645. doi:10.12029/gc20200603

Zhao, S. Y., Zheng, Y. R., Shi, W. M., and Wang, J. L. (2002). Analysis on Safety Factor of Slope by Strength Reduction FEM. *Chin. J. Geotech. Eng.* 24 (3), 343–346. doi:10.3321/j.issn:1000-4548.2002.03.017

Zheng, H., Shi, Z., Shen, D., Peng, M., Hanley, K. J., Ma, C., et al. (2021). Recent Advances in Stability and Failure Mechanisms of Landslide Dams. *Front. Earth Sci.* 9, 201. doi:10.3389/feart.2021.659935

Zheng, S. Y., and Zhao, Y. R. (2005). Limit State Finite Element Method for Geotechnical Engineering Analysis and its Applications. *Chin. Civ. Eng. J.* 1. doi:10.3321/j.issn:1000-131X.2005.01.012

Zhou, J.-w., Li, H.-b., Lu, G.-d., Zhou, Y., Zhang, J.-y., and Fan, G. (2021). Initiation Mechanism and Quantitative Mass Movement Analysis of the 2019 Shuicheng Catastrophic Landslide. *Q. J. Eng. Geology. Hydrogeology* 54 (2), qjegh2020–052. doi:10.1144/qjegh2020-052

Zhu, C., He, M., Karakus, M., Cui, X., and Tao, Z. (2020). Investigating Toppling Failure Mechanism of Anti-dip Layered Slope Due to Excavation by Physical Modelling. *Rock Mech. Rock Eng.* 53 (11), 5029–5050. doi:10.1007/s00603-020-02207-y

Zhu, J. W., Zhuang, H. Z., Li, J. W., Zhang, L. Q., and Yang, Z. F. (2008). RESEARCH ON REINFORCEMENT TECHNIQUE OF SLOP WITH LARGE DIMENSIONS. *J. Eng. Geol.* 16 (3), 365–370. doi:10.3969/j.issn.1004-9665.2008.03.014

Conflict of Interest: Author ZZ was employed by the company China Railway Construction Bridge Engineering Bureau Group 3rd Engineering Co.

The remaining authors declare that the research was conducted in the absence of any commercial or financial relationships that could be construed as a potential conflict of interest.

Publisher's Note: All claims expressed in this article are solely those of the authors and do not necessarily represent those of their affiliated organizations, or those of the publisher, the editors and the reviewers. Any product that may be evaluated in this article, or claim that may be made by its manufacturer, is not guaranteed or endorsed by the publisher.

frontiers in Earth Science

ORIGINAL RESEARCH
published: 25 January 2022
doi: 10.3389/feart.2022.830371

Modelling of Critical Acceleration for Regional Seismic Landslide Hazard Assessments by Finite Element Limit Analysis

Cheng Li[1,2], *Shuhe Wei*[1], *Xingqian Xu*[3]* *and Xin Qu*[4]*

[1]School of Architectural Engineering, Kaili University, Guizhou, China, [2]Key Laboratory of Mountain Hazards and Earth Surface Process, Institute of Mountain Hazards and Environment, Chinese Academy of Sciences (CAS), Chengdu, China, [3]College of Water Conservancy, Yunnan Agricultural University, Kunming, China, [4]School of Civil and Architecture Engineering, Anyang Institute of Technology, Anyang, China

The critical acceleration model plays an important role in seismic slope stability and determines the predictive accuracy of regional seismic landslide hazard assessments. Recently, the critical acceleration model based on the limit equilibrium method has been used to evaluate the seismic stability of regional slopes. However, when the Hoek-Brown failure criterion is used to evaluate the seismic stability of slopes with angles greater than 60°, the results obtained is unconservative by limit equilibrium method. Therefore, based on the simulation of a typical slope model with finite element limit analysis, prediction equations of the critical acceleration are established. The corresponding results are compared with the prediction results from the limit equilibrium method. This comparison shows that the proposed critical acceleration model has higher predictive accuracy than the limit equilibrium method, especially when the Hoek-Brown failure criterion is used to evaluate the slopes with angles greater than 60°. The proposed model is applicable to the global scope and can be effectively applied to regional seismic landslide hazard assessments.

Keywords: critical acceleration modeling, newmark sliding block, limit equilibrium method, finite element limit analysis, regional assessment, seismic landslide

OPEN ACCESS

Edited by:
Yun Zheng,
Institute of Rock and Soil Mechanics (CAS), China

Reviewed by:
Wu Wenan,
Beijing University of Technology, China
Mikhail Rodkin,
Institute of Earthquake Prediction Theory and Mathematical Geophysics (RAS), Russia

***Correspondence:**
Xingqian Xu
xuxingqian_123@163.com
Xin Qu
xqu1987@163.com

Specialty section:
This article was submitted to Geohazards and Georisks, a section of the journal Frontiers in Earth Science

Received: *07 December 2021*
Accepted: *04 January 2022*
Published: *25 January 2022*

Citation:
Li C, Wei S, Xu X and Qu X (2022) Modelling of Critical Acceleration for Regional Seismic Landslide Hazard Assessments by Finite Element Limit Analysis. Front. Earth Sci. 10:830371. doi: 10.3389/feart.2022.830371

1 INTRODUCTION

Earthquakes have induced a large number of landslides, which buried towns and farmland and damaged infrastructure, causing substantial economic losses and casualties in the disaster area (Qi et al., 2010; Xu et al., 2015; Chen et al., 2018; Fan et al., 2018). Therefore, seismic landslides have been widely studied by geoscience experts. Relevant researchers have made beneficial exploration in the evaluation of slope stability and deformation (Yang et al., 2019a; Yang et al., 2019b; Wu et al., 2020; Yang et al., 2021), the compilation of landslide database (Xu et al., 2012; Xu et al., 2013) and landslide hazard assessment (Caccavale et al., 2017; Chen et al., 2018; Wang et al., 2018; Li and Su, 2021), which provided important theoretical scientific support for exploring the mechanisms driving seismic landslides and reducing seismic landslide disasters. Regional seismic landslide hazard assessment is one of the most important research directions, and the results from these assessments can provide a reference for reconstructing post-earthquake disaster areas and predicting future earthquake-induced landslides.

Traditionally, there are two quantitative methods to evaluate the hazards of regional seismic landslides, including statistical analysis methods and mechanical model methods based on physical slope models. The statistical analysis method mainly uses seismic landslides that have occurred, establishes a mathematical statistical model of these landslides and the related landslide influence factors, and then applies this model to the whole earthquake area. The advantages of this method are that it is based on actual landslides and that the evaluation results are objective; however, this method lacks an understanding of the mechanism of seismic landslides (Xu et al., 2012; Xu et al., 2013). In the mechanical model method, Newmark's sliding block analysis (Newmark, 1965) (referred to hereinafter as the Newmark method) is commonly used to estimate regional seismic landslide hazards (Jibson et al., 2000; Jibson, 2007; Rodríguez-Peces et al., 2011; Bozzano et al., 2013; Dreyfus et al., 2013; Rodríguez-Peces et al., 2014; Caccavale et al., 2017; Liu et al., 2017; Shinoda and Miyata 2017; Chen et al., 2018; Wang et al., 2018; Li and Su, 2021). In the Newmark method, the slope model should be assumed to be an infinite plane (i.e., an infinite slope), and the failure depth of the slope should be known in advance (usually assumed to be less than 3 m) (Jibson et al., 2000). However, according to previous studies (Wilson and Keefer 1983; Keefer 1984; Huang et al., 2011; Wartman et al., 2013; Li et al., 2021), seismic landslides are widely developed in soil and rock units, and there are many failure modes. This shows that the assumption of an infinite slope may be too simplistic in many cases, thereby underestimating the risk area of sliding. Some scholars have realized the limitations of the Newmark method in regional seismic landslide hazard assessment and put forward measures to improve the predictive accuracy of the Newmark method (Shinoda and Miyata 2017; Jin et al., 2019; Zang et al., 2020). Although the predictive accuracy of the Newmark method has been improved through some measures (e.g., modified strength parameters), the limitations of the Newmark method are still difficult to overcome (Shinoda and Miyata 2017; Jin et al., 2019; Zang et al., 2020). Therefore, it is urgent and important to develop new mechanical model methods for regional seismic landslide hazard assessments.

Some scholars have recently proposed new mechanical models and used these models to carry out regional seismic landslide hazard assessments (Saade et al., 2016; Yuqiao et al., 2019; Tsai et al., 2019). Compared with the traditional Newmark model, the mechanical models proposed by these scholars have made the following improvements. 1) The modified models are not limited to a single shallow sliding mode. 2) The failure depth of the slope does not need to be assumed. 3) The strength parameters do not need to be reduced to improve the predictive accuracy of the model. 4) Moreover, the modified models have obvious advantages in predicting the potential sliding area. Although these mechanical models provide a new perspective for regional earthquake landslide hazard assessments, they are still not sufficiently comprehensive as they have the following shortcomings. 1) For Saade et al., 2016 and Yuqiao et al., 2019, obtaining the critical acceleration of the slope with the limit equilibrium method (LEM) and the finite element method (FEM) requires many iterative calculations, which are estimated by trial and error and may therefore affect the calculation efficiency. 2) Saade et al., 2016, the safety factor and critical acceleration of the slope calculated by the Hoek-Brown (HB) criterion will be overestimated for steep slopes (Li et al., 2009; Li et al., 2019). 3) For Yuqiao et al., 2019, the mechanical model requires a slope angle <45°. 4) For Tsai et al., 2019, 12 equations and six steps are needed to evaluate the permanent displacement of landslides caused by earthquakes, which makes it difficult for engineers to quickly evaluate earthquake-induced landslide hazards.

A modified model of the critical acceleration for regional seismic landslide hazard assessments is proposed based on the work of Saade et al. (2016) to overcome the limitations of the above mechanical models. In this model, finite element limit analysis (FELA) is used to build a simplified slope model, and the material strength parameter and slope angle are taken as variables to conduct simulations of the slopes. Through two-step regression analysis, the prediction equations for the strength parameters, slope angle and critical acceleration are obtained. The predicted results of the proposed model are compared with those of the Newmark method and the LEM (Saade et al., 2016). The validity of the proposed model is verified through this comparison. In addition, the proposed model can be effectively applied to regional seismic landslide hazard assessments.

2 MODELLING OF SLOPE CRITICAL ACCELERATION MODEL

2.1 Review of the Mechanical Modelling Methods

2.1.1 LEM

Saade et al. (2016) conducted a series of numerical simulations to establish the predicted equations of linear function between the slope angle β, the unit weight γ, strength parameters and the critical acceleration (A_c). In addition, Saade et al. (2016) used the Mohr-Coulomb (MC) failure criterion and the HB failure criterion to calculate the critical acceleration when the slope angle <45° and when the slope angle ≥45°, respectively. The prediction equations of two linear functions for critical acceleration is as follows:

$$A_{c(MC)} = C1_{(MC)}\frac{c}{\gamma H} + C2_{(MC)} \tag{1}$$

$$A_{c(HB)} = C1_{(HB)} \ln \frac{\sigma_{ci}}{\gamma H} + C2_{(HB)} \tag{2}$$

Where $A_{c(\mathrm{MC})}$ is the critical acceleration for the MC failure criterion, c is the cohesion, γ is the unit weight, H is the slope height, $\mathrm{C1}_{(\mathrm{MC})}$ is the coefficient related to slope angle β and friction angle φ for the MC failure criterion, and $\mathrm{C2}_{(\mathrm{MC})}$ is the coefficient related to slope angle β for the MC failure criterion, $A_{c(\mathrm{HB})}$ is the critical acceleration for the HB failure criterion, σ_{ci} is unconfined compressive strength, and $\mathrm{C1}_{(\mathrm{HB})}$ and $\mathrm{C2}_{(\mathrm{HB})}$ are the coefficient related to slope angle β for the HB failure criterion.

2.1.2 FELA

In this study, FELA can be used to obtain the collapse load of slope (Lyamin et al., 2005; Sloan 2013; Ali et al., 2016). By

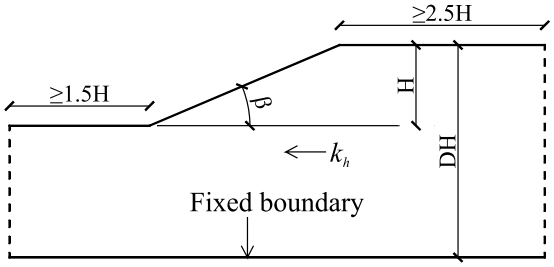

FIGURE 1 | Simple slope model.

establishing strict upper and lower bounds with a certain level of error, it is possible to accurately estimate the collapse load. For a given problem, L is the lower limit of the collapse load and U is the upper limit of the collapse load. Then, the estimate of the exact solution is simply taken as the average of the upper and lower limits:

$$M = \frac{L + U}{2} \tag{3}$$

In addition, the exact solution is denoted e. Since $L \le e \le U$, the following expressions can be derived:

$$M(1 - \varepsilon) \le e \le M(1 + \varepsilon) \tag{4}$$

$$\varepsilon = \frac{U - L}{U + L} \tag{5}$$

where ε is the relative error. Previous experience shows that when appropriate upper and lower bounds are used, the actual error of the average value is usually less than the estimated value. Hence, the average value is an excellent estimate of the exact solution. Therefore, we calculate the upper—and lower-limit solutions of the critical acceleration in this paper. The average bound solution of the critical acceleration is obtained according to the upper- and lower-limit solutions of the critical acceleration. The critical accelerations mentioned hereinafter are all average bound solutions. Detailed information about the technologies and solution algorithms used in FELA can be found in the literature (Sloan 1988; Sloan 1989; Lyamin and Sloan 2002a; Lyamin and Sloan 2002b; Lyamin et al., 2005; Sloan 2013; Krabbenhoft and Lyamin, 2015; Li et al., 2019).

3 PARAMETRIC STUDY

3.1 Calculation Settings and Input Parameters

At present, the design using pseudostatic analysis is usually based on the horizontal seismic coefficient (k_h). The critical acceleration mentioned hereafter corresponds to the critical horizontal seismic coefficient (k_c) multiplied by the gravitational acceleration. FELA can directly solve the ultimate load of a slope subjected to an earthquake (such as the critical horizontal acceleration) without requiring iterative calculations, thereby significantly reducing the computational effort (Sloan 2013; Utili and Abd 2016).

TABLE 1 | Calculation parameters of the MC failure criterion.

c (kPa)	φ (deg)	β (deg)
15	20, 25, 30, 35, 40, 45	15, 20, 25, 30, 35, 40, 45
20	20, 25, 30, 35, 40, 45	15, 20, 25, 30, 35, 40, 45
25	20, 25, 30, 35, 40, 45	15, 20, 25, 30, 35, 40, 45
30	20, 25, 30, 35, 40, 45	15, 20, 25, 30, 35, 40, 45
35	20, 25, 30, 35, 40, 45	15, 20, 25, 30, 35, 40, 45
40	20, 25, 30, 35, 40, 45	15, 20, 25, 30, 35, 40, 45
45	20, 25, 30, 35, 40, 45	15, 20, 25, 30, 35, 40, 45

TABLE 2 | Calculation parameters of the HB failure criterion.*GSI* is geological strength index and m_i is rock-type constant.

GSI	m_i	σ_{ci} (MPa)	β (deg)
20	5, 10, 15, 20, 25	1, 2, 5, 10, 20, 25, 30	45, 50, 60, 70, 80
30	5, 10, 15, 20, 25	1, 2, 5, 10, 20, 25, 30	45, 50, 60, 70, 80
40	5, 10, 15, 20, 25	1, 2, 5, 10, 20, 25, 30	45, 50, 60, 70, 80
50	5, 10, 15, 20, 25	1, 2, 5, 10, 20, 25, 30	45, 50, 60, 70, 80

A typical slope model (slope height H is 30 m; unit weight γ is 22 kN/m^3) is applied for parametric study (**Figure 1**). To obtain the minimum critical acceleration for the MC failure criterion, DH is set as 100 m when the slope height is 30 m (Loukidis et al., 2003; Saade et al., 2016). Besides, to eliminate the influence of the lateral boundary on the sliding surface of the slope, the lateral boundary is set away from the slope surface. The bottom boundary of the slope model is fixed. The numerical model uses the adaptive mesh generation method, in which the number of adaptive iterations is 3, the initial number of elements is 2,000, and the maximum number of elements is 4,000. The control variable of adaptive meshing is shear dissipation. The mesh refinement factor is 0.25, and the mesh coarsening factor is 1.50.

Based on Saade et al., 2016, we also use the MC failure criterion and HB failure criterion to calculate the critical acceleration of the slope when the slope is less than 45° and when the slope is greater than or equal to 45°, respectively. **Table 1** and **Table 2** show the slope angle and strength parameters for the two failure criteria. For each combination described in **Table 1** and **Table 2**, two slope models (including the upper-limit solution and lower-limit solution) are established. While keeping the gravity load constant, the horizontal load multiplier is maximized (lower-bound simulation) and minimized (upper-bound simulation), and the critical horizontal acceleration is calculated. The results of finite element discretization of the upper- and lower-limit solutions of the MC failure criterion and HB failure criterion are shown in **Figure 2**.

3.2 Regression Equations

3.2.1MC Failure Criterion

Based on the Saade et al., 2016, we use the same linear function, as shown in **Eq 1**. **Figure 3A** shows the relationship between the

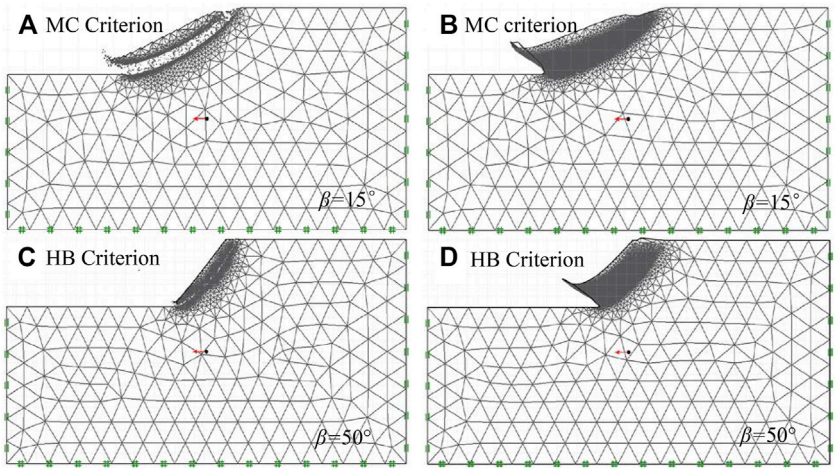

FIGURE 2 | Examples of finite element discretization: **(A–C)** lower-bound simulations and **(B–D)** upper-bound simulations.

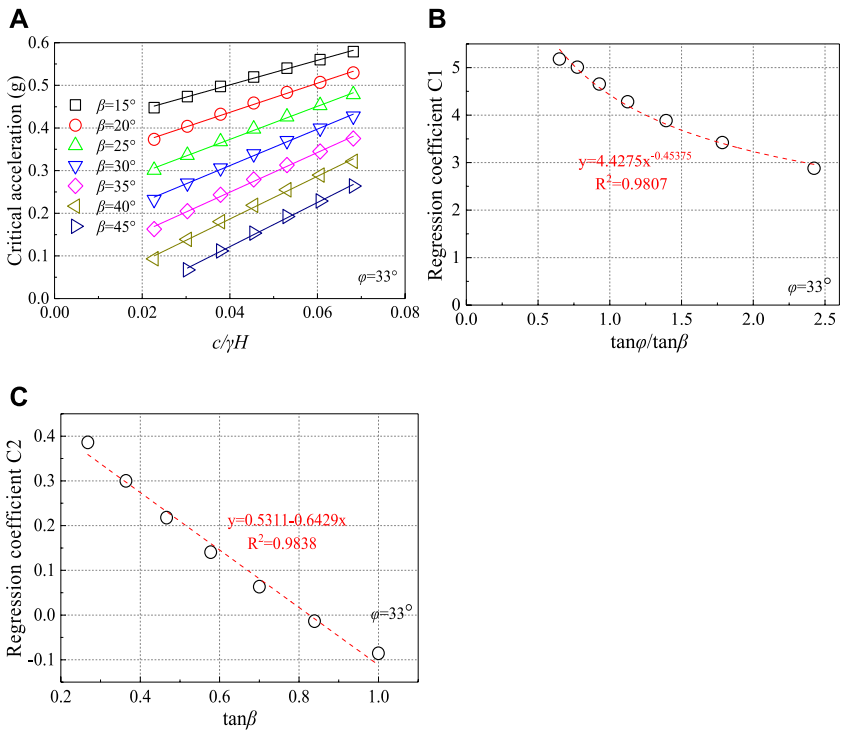

FIGURE 3 | Example of **(A)** A_c versus $c/\gamma H$ and **(B)** coefficient $C1_{(MC)}$ and **(C)** coefficient $C2_{(MC)}$ when friction angle is 33°.

critical acceleration and non-dimensional term ($c/\gamma H$) when the friction angle is 33°. For each friction angle between 25° and 45°, similar curves are generated (with increments of 5°). According to different functions of slope angle β, the $C1_{(MC)}$ and $C2_{(MC)}$ are obtained respectively, as shown in **Figures 3B,C**. In addition, the optimal fit equations of the $C1_{(MC)}$ and $C2_{(MC)}$ for other friction angles are considered in this study, as shown in **Table 3**. The $C1_{(MC)}$ and $C2_{(MC)}$ of any other friction angle can be calculated by interpolation method. The fit index (R2 adjusted) is greater than 0.99 for any condition. **Figure 4** shows the predicted and calculated results of critical acceleration using LEM, Newmark method and FELA when the friction angle is 30°, cohesion is 20 kPa and $15° \leq \beta < 45°$. From **Figure 4**, the results of the Newmark method seriously overestimate the critical acceleration: $A_{cNewmark} = 1.6707A_{c(MC)}$-0.0179 (Saade et al., 2016). However, the results when using FELA are in good

TABLE 3 | Equations of $C1_{(MC)}$ and $C2_{(MC)}$ (slope angle $\beta < 45^{\circ}$).

No	φ (deg)	Coefficient $C1_{(MC)}$	Coefficient $C2_{(MC)}$	R2 adjusted
1	20	$3.0849\left(\frac{\tan\delta}{\tan\beta}\right)^{-0.5204}$	−0.6341tanβ+0.2894	0.9962
2	25	$3.6360\left(\frac{\tan\delta}{\tan\beta}\right)^{-0.4902}$	−0.61001tanβ+0.3676	0.9961
3	30	$4.1629\left(\frac{\tan\delta}{\tan\beta}\right)^{-0.4858}$	−0.6369tanβ+0.4717	0.9962
4	35	$4.6314\left(\frac{\tan\delta}{\tan\beta}\right)^{-0.4499}$	−0.6576tanβ+0.5756	0.9960
5	40	$5.0169\left(\frac{\tan\delta}{\tan\beta}\right)^{-0.3981}$	-0.6804tanβ+0.6838	0.9958
6	45	$5.3335\left(\frac{\tan\delta}{\tan\beta}\right)^{-0.3432}$	−0.7171tanβ+0.8034	0.9959

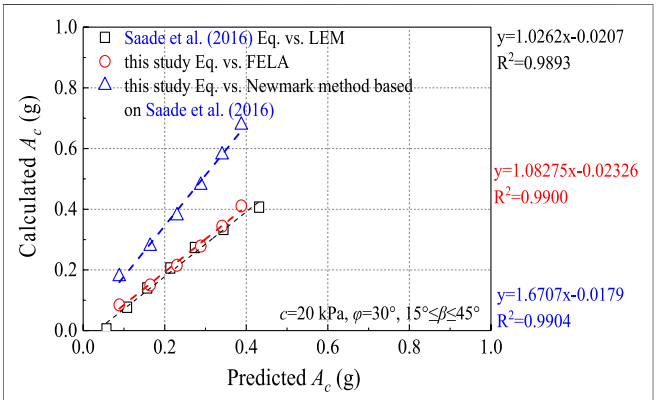

FIGURE 4 | Comparison between the A_c values predicted and calculated with the LEM, Newmark method, and FELA for c = 20 kPa, $\varphi = 30^{\circ}$ and $15^{\circ} \leq \beta < 45^{\circ}$.

agreement with the critical acceleration: $A_{cFELA} = 1.0827A_{c(MC)}$-0.0233. This is very consistent with the results reported by Saade et al. (2016) using the LEM: $A_{cLEM} = 1.0262A_{c(MC)}$-0.0207.

3.2.2 HB Failure Criterion

Based on Saade et al., 2016, we also use the same linear function, as shown in **Eq 2**. **Figure 5A** shows the relationship between the critical acceleration and non-dimensional term ($\sigma_{ci}/\gamma H$) when the *GSI* is 20 and m_i is 25. For each *GSI* (20, 30, 40, 50) and m_i (5, 10, 15, 20, 25), similar curves are generated. According to different functions of slope angle β, the $C1_{(HB)}$ and $C2_{(HB)}$ are obtained respectively, as shown in **Figures 5B,C**. In addition, the optimal fit equations of the $C1_{(HB)}$ and $C2_{(HB)}$ for other *GSI*-m_i conditions are considered in this study, as shown in **Table 4**. The $C1_{(HB)}$ and $C2_{(HB)}$ of any other conditions can be calculated by interpolation method. The fit index (R2 adjusted) is greater than 0.92 for any conditions. **Figure 6** shows the predicted and calculated results of critical acceleration using the LEM, the Newmark method and FELA when the *GSI* is 20, m_i is 25, σ_{ci} is 5 MPa and $45^{\circ} \leq \beta \leq 80^{\circ}$. As shown in **Figure 6**, the results of the Newmark method substantially overestimate the critical acceleration: $A_{cNewmark} = 1.8819A_{c(HB)}$+0.0006 (Saade et al., 2016). However, the results when using FELA are in good agreement with the critical acceleration: $A_{cFELA} = 1.02454A_{c(HB)}$−0.00134. This is very consistent with the results reported by Saade et al. (2016) using the LEM: $A_{cLEM} = 1.0218A_{c(HB)}$+0.0006.

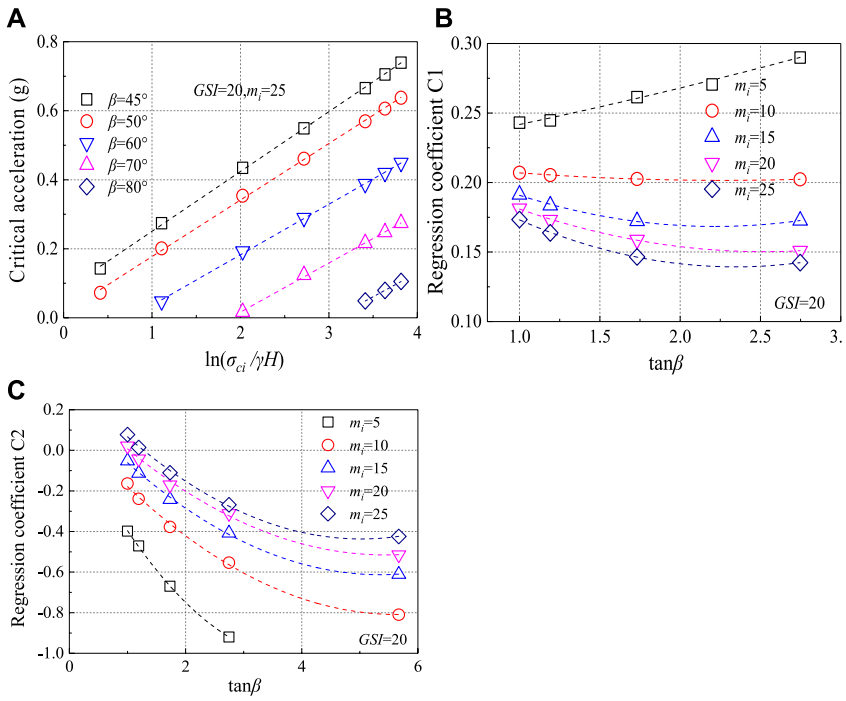

FIGURE 5 | Example of **(A)** A_c versus ln ($\sigma_{ci}/\gamma H$), **(B)** coefficient C1 and **(C)** coefficient C2 for *GSI* = 20 and m_i = 25.

TABLE 4 | Equations of $C1_{(HB)}$ and $C2_{(HB)}$ (slope angle $\beta \geq 45^{\circ}$).

No	*GSI*	m_i	Coefficient $C1_{(HB)}$	Coefficient $C2_{(HB)}$	R2 adjusted
1	20	5	$0.0019\tan\beta^2+0.0206\tan\beta+0.2193$	$0.0711\tan\beta^2-0.5665\tan\beta+0.0994$	0.9968
2		10	$0.0034\tan\beta^2-0.0153\tan\beta+0.2189$	$0.0292\tan\beta^2-0.3299\tan\beta+0.1218$	0.9989
3		15	$0.0152\tan\beta^2-0.0672\tan\beta+0.2428$	$0.029\tan\beta^2-0.3109\tan\beta+0.2205$	0.9994
4		20	$0.0132\tan\beta^2-0.0668\tan\beta+0.2344$	$0.0265\tan\beta^2-0.2882\tan\beta+0.2687$	0.9995
5		25	$0.0187\tan\beta^2-0.0876\tan\beta+0.2421$	$0.0311\tan\beta^2-0.3122\tan\beta+0.3479$	0.9991
6	30	5	$-0.0028\tan\beta^2+0.0319\tan\beta+0.2546$	$0.0404\tan\beta^2-0.4198\tan\beta+0.0434$	0.9904
7		10	$0.0012\tan\beta^2-0.0046\tan\beta+0.2381$	$0.0318\tan\beta^2-0.3431\tan\beta+0.2204$	0.9951
8		15	$0.0026\tan\beta^2-0.0208\tan\beta+0.2279$	$0.0324\tan\beta^2-0.3311\tan\beta+0.3287$	0.9975
9		20	$0.0037\tan\beta^2-0.0309\tan\beta+0.2221$	$0.0313\tan\beta^2-0.3190\tan\beta+0.3890$	0.9986
10		25	$0.0044\tan\beta^2-0.0371\tan\beta+0.2157$	$0.0313\tan\beta^2-0.3170\tan\beta+0.4432$	0.9990
11	40	5	$-0.0054\tan\beta^2+0.5033\tan\beta+0.2939$	$0.0423\tan\beta^2-0.4197\tan\beta+0.0763$	0.9911
12		10	$-0.0023\tan\beta^2+0.0197\tan\beta+0.2511$	$0.0396\tan\beta^2-0.3953\tan\beta+0.3409$	0.9968
13		15	$0.0020\tan\beta^2-0.01893\tan\beta+0.2569$	$0.0382\tan\beta^2-0.3704\tan\beta+0.4304$	0.9903
14		20	$0.0042\tan\beta^2-0.0354\tan\beta+0.2522$	$0.0309\tan\beta^2-0.3182\tan\beta+0.4515$	0.9928
15		25	$0.0053\tan\beta^2-0.0442\tan\beta+0.2449$	$0.0310\tan\beta^2-0.3167\tan\beta+0.5043$	0.9944
16	50	5	$-0.0094\tan\beta^2+0.0844\tan\beta+0.3310$	$0.0634\tan\beta^2-0.5801\tan\beta+0.3359$	0.9664
17		10	$0.0070\tan\beta^2-0.576\tan\beta+0.4263$	$0.0294\tan\beta^2-0.3236\tan\beta+0.3073$	0.9746
18		15	$0.0051\tan\beta^2-0.0440\tan\beta+0.3651$	$0.0303\tan\beta^2-0.3211\tan\beta+0.4169$	0.9781
19		20	$0.0028\tan\beta^2-0.0281\tan\beta+0.2914$	$0.0304\tan\beta^2-0.3205\tan\beta+0.4961$	0.9259
20		25	$0.0097\tan\beta^2-0.0757\tan\beta+0.3199$	$0.0264\tan\beta^2-0.2907\tan\beta+0.5202$	0.9849

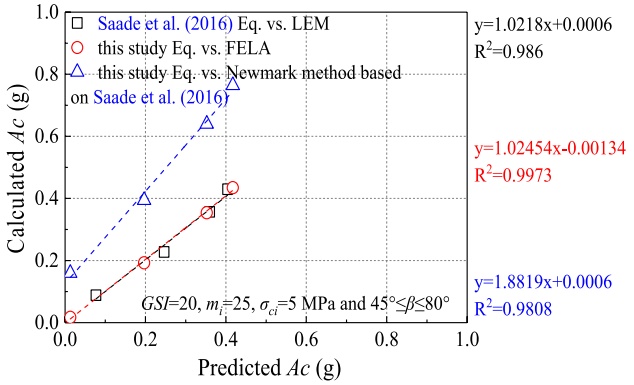

FIGURE 6 | Comparison between the A_c values predicted and calculated with the LEM, Newmark method, and FELA for *GSI* = 20, m_i = 25, σ_{ci} = 5 MPa and $45^{\circ} \leq \beta \leq 80^{\circ}$.

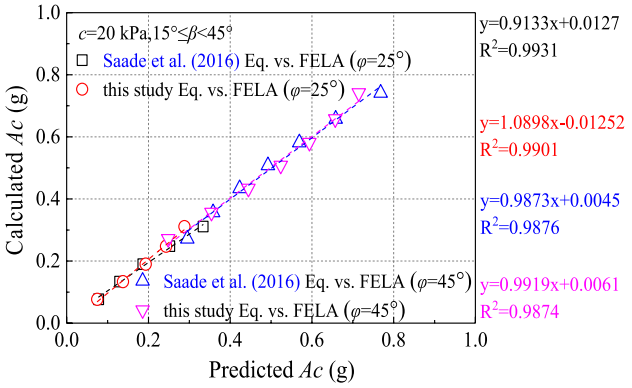

FIGURE 7 | Comparison between the A_c values predicted and calculated with FELA for c = 20 kPa, $\varphi = 25^{\circ}$ and 45° and $15^{\circ} \leq \beta < 45^{\circ}$ when using the MC failure criterion.

3.3 Comparison of the LEM and FELA Results

From **Section 3.2**, specific strength parameters are selected to compare the critical acceleration values predicted by the LEM and FELA. This shows that the two methods have good consistency. However, to extend the predicted regression equation to additional conditions, the results of other strength parameters and geometric parameters need to be further tested to assess their validity, especially when used the HB failure criterion. Notably, since the FELA results are closer to the real solution than the LEM results, the calculated critical accelerations adopt the results from the FELA simulation (Li et al., 2009; Sloan 2013; Li et al., 2019) as the *Y*-axis in **Figure 7** and **Figure 8**. **Figure 7** compares the results of predicted A_c and FELA simulation for c = 20kPa, and $\varphi = 25^{\circ}$ and $\varphi = 45^{\circ}$ at variable β when use MC failure criterion. This shows that the regression equations from the LEM and FELA are in good agreement under different strength parameters. This is consistent with the conclusion of Loukidis et al. (2003).

Figure 8 compares the *Ac* values predicted and calculated with FELA for m_i = 25, σ_{ci} = 5 and 25 MPa, $45^{\circ} \leq \beta \leq 80^{\circ}$ and *GSI* = 20, 30, 40 and 50 when using the HB failure criterion. **Figure 8** shows that the $A_{c(HB)}$ values predicted and calculated with FELA are very consistent under any combination of parameters (the relationship is almost one to one). However, the $A_{c(HB)}$ values predicted with the LEM and FELA are not consistent, and the difference between these values increases gradually as the strength parameter and slope angle increase. Taking **Figures 8A,D** as an example, when *GSI* = 20, m_i = 25, and σ_{ci} = 5 MPa, the regression equation from Saade et al. (2016) is y = 1.2594x-0.1004, whereas when *GSI* = 50,

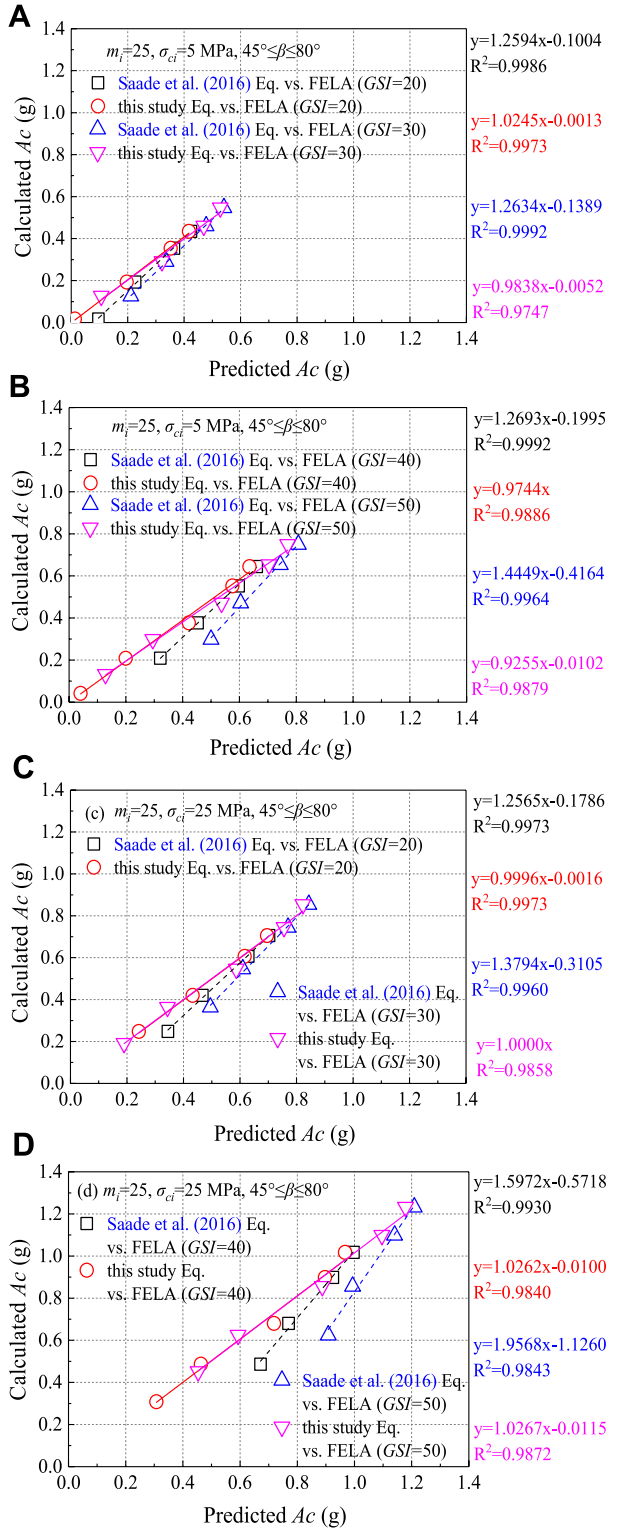

FIGURE 8 | Comparison between the A_c values predicted and calculated with FELA for m_i = 25, σ_{ci} = 5 and 25 MPa, 45°≤β ≤ 80° and *GSI* = 20, 30, 40 and 50 when using the HB failure criterion. **(A)** *GSI* = 20 and 30 and σ_{ci} = 5 MPa; **(B)** *GSI* = 40 and 50 and σ_{ci} = 5 MPa; **(C)** *GSI* = 20 and 30 and σ_{ci} = 25 MPa; and **(D)** *GSI* = 40 and 50 and σ_{ci} = 25 MPa.

m_i = 25, and σ_{ci} = 25 MPa, the regression equation from Saade et al. (2016) is y = 1.9568x-1.1260. When the slope angle β is 70°, the predicted critical acceleration obtained by the LEM regression equation is 29.76–86.58% higher than that obtained by the FELA regression equation. In addition, the FELA regression equation can accurately estimate the critical acceleration of slopes with 60°<β ≤ 80°, which is difficult to determine with the regression equation from Saade et al. (2016).

4 EXAMPLES

From Sections 3.2 and 3.3, we compare the A_c values predicted and calculated with FELA when H is 30 m and γ is 22 kN/m^3. To further test the influence of the slope height and unit weight on the regression equation, **Table 5** and **Table 6** compares the A_c values predicted and calculated with FELA for different slope heights (H is 10 and 50 m) and unit weights (γ is 18 kN/m^3 and 28 kN/m^3). From **Table 5** and **Table 6**, at a certain slope height and unit weight, the larger the slope angle is, the larger the error in the critical acceleration predicted by the LEM. The critical acceleration predicted and calculated by FELA are in good agreement.

Case

Case 1. is a 10-m-tall slope with β = 45° composed of rock with *GSI* is 40, m_i is 25, γ is 22 kN/m^3, σ_{ci} is 10 MPa.

1) The process for predicted critical acceleration of LEM from the regression coefficient (Saade et al., 2016) and **Eq 2** is as follows:

$$\begin{aligned} &\text{Predicted } A_{cLEM(HB)} = C1_{(HB)} \ln \frac{\sigma_{ci}}{\gamma H} + C2_{(HB)} \\ &= (0.020\tan 45^2 - 0.070\tan 45 + 0.258)\ln \frac{10000}{22\times 10} + (0.048\tan 45^2 - 0.387\tan 45 + 0.578) \\ &= 1.034 \end{aligned}$$

2) The process for predicted critical acceleration of FELA from the 15th regression coefficient in **Table 4** in combination with **Eq 2** is as follows:

$$\begin{aligned} &\text{Predicted } A_{cFELA(HB)} = C1_{(HB)} \ln \frac{\sigma_{ci}}{\gamma H} + C2_{(HB)} \\ &= (0.005\tan 45^2 - 0.044\tan 45 + 0.245)\ln \frac{10000}{22\times 10} + (0.031\tan 45^2 - 0.317\tan 45 + 0.504) \\ &= 1.005 \end{aligned}$$

5 DISCUSSION

In the existing mechanical model framework of earthquake-induced permanent displacements, there are four crucial factors that determine the final predicted results for a fixed study area: the digital elevation model resolution, the material strength parameter, the empirical sliding displacement model and the critical acceleration model. The digital elevation model, material strength parameter and empirical sliding displacement model are subjective factors determined by

TABLE 5 | Comparison between the results of predicted A_c and FELA simulation for different slope heights and slope angles (Note: *GSI* is 40, m_i is 25, γ is 22 kN/m^3, σ_{ci} is 10 MPa).

Case	β (°)	H (m)	Predicted A_c-LEM (g)	Predicted A_c-FELA (g)	Calculated A_c-FELA (g)	LEM error (%)	FELA error (%)
1	45	10	1.034	1.005	1.071	3.455	6.162
2	50	—	0.961	0.933	0.949	–1.264	1.686
3	60	—	0.806	0.752	0.724	–11.326	–3.867
4	70	—	0.711	0.493	0.494	–43.927	0.202
5	80	—	—	0.338	0.366	—	7.650
6	45	50	0.699	0.673	0.681	–2.643	1.175
7	50	—	0.634	0.612	0.586	–8.191	–4.437
8	60	—	0.488	0.455	0.407	–19.902	–11.794
9	70	—	0.361	0.229	0.235	–53.617	2.553
10	80		—	0.071	0.070	—	–1.429

TABLE 6 | Comparison between the results of predicted A_c and FELA simulation for different unit weights and slope angles (Note:*GSI* is 40, m_i is 25, H is 30 m, σ_{ci} is 10 MPa).

Case	β (°)	γ (kN/m^3)	Predicted A_c-LEM (g)	Predicted A_c-FELA (g)	Calculated A_c-FELA (g)	LEM error (%)	FELA error (%)
11	45	18	0.847	0.820	0.831	–1.925	1.324
12	50	—	0.779	0.754	0.727	–7.153	–3.714
13	60	—	0.629	0.587	0.532	–18.233	–10.338
14	70	—	0.516	0.346	0.353	–46.176	1.983
15	80	—	—	0.189	0.183	—	–3.279
16	45	28	0.755	0.729	0.735	–2.721	0.816
17	50	—	0.689	0.666	0.637	–8.163	–4.553
18	60	—	0.542	0.505	0.453	–19.647	–11.479
19	70	—	0.420	0.273	0.280	–50.000	2.500
20	80	—	—	0.115	0.113	—	–1.770

engineers. Every engineer may obtain different values for the material strength parameter in the same region, and there are also differences in the empirical sliding displacement models in each region. However, the critical acceleration model is an objective and unified factor that can serve global applications and plays an important role in the framework of earthquake-induced permanent displacements. In addition, critical acceleration can not only be used as a criterion to evaluate the susceptibility of seismic landslides (Chen et al., 2014), but also be used to evaluate the hazard of seismic landslides by comparing with known peak ground acceleration (Chen et al., 2018). Therefore, it is of great significance to establish a reliable critical acceleration model for regional seismic landslide hazard assessments.

In previous studies, due to the inherent limitations of the traditional Newmark method and its modified versions, the calculated critical accelerations are substantially different from the numerical simulations. Compared with the Newmark method, the critical acceleration models from Saade et al. (2016), Yuqiao et al., 2019, Tsai et al. (2019) and this study offer obviously higher predictive accuracy, providing strong support for regional seismic landslide hazard assessments. In addition, in the regional scale analysis, the vertical acceleration, slope direction, groundwater conditions, water content, material degradation and rock slope disturbance coefficient may affect the critical acceleration model, which were not discussed in this study. Therefore, the development of a more comprehensive critical acceleration model should be the direction of future research. However, our model can directly estimate strength parameters from a good engineering geological description while still providing an accurate quantitative index, which can quickly measure the behaviour of a seismic slope at a regional scale.

On the other hand, Li et al. (2008) found that the difference of safety factor from limit analyses and LEM is less than 4% for steep slopes when used the HB failure criterion. However, Li et al. (2008) reported this conclusion when the safety factor of the slope is near 1. Saade et al. (2016) did not seem to notice this phenomenon. In addition, for lower *GSI* values ($GSI \leq 50$), the stability numbers of slope (the stability number is equal to $\sigma_{ci}/\gamma HF$, wherein F is the safety factor of slope) obtained using the LEM are 18–30% lower than the average bound solutions obtained with FELA (Li et al., 2009). Moreover, the $\sigma_{ci}/\gamma HF$ from the LEM are close to the results of FELA when $\beta \leq 60^{\circ}$. However, the difference of the $\sigma_{ci}/\gamma HF$ between FELA and the LEM tends to be substantial when $\beta \geq 75^{\circ}$ (Li et al., 2019). Therefore, according to the research of Li et al. (2009, 2019), we revised the model from Saade et al. (2016).

6 CONCLUSION

Our model improves the limitations of previous mechanical models for regional seismic landslide hazard assessments. Herein, FELA is used to calculate the average bound solution of the critical acceleration of the simplified slope model. The proposed model of critical acceleration is not limited to failures of shallow sliding slopes nor does it require the failure depth to be assumed in advance. The MC failure criterion and the HB failure criterion are used to simulate the seismic behaviour of soil and rock slopes. The prediction equations for the critical horizontal acceleration, material strength and slope gradient are established. The corresponding results are compared with the prediction results from the Newmark sliding analysis and the LEM. The results show that the predictive accuracy of FELA and the LEM is significantly higher than that of the Newmark sliding analysis. When the MC failure criterion is used, the prediction results from the FELA and LEM regression equations are consistent. However, the prediction results from the FELA and LEM regression equations are significantly different, especially when the slope gradient is greater than 60° and uses HB failure criterion. In general, the predictive accuracy of our model is higher than that of the LEM. Therefore, the proposed model can be effectively applied to regional seismic landslide hazard assessments.

DATA AVAILABILITY STATEMENT

The original contributions presented in the study are included in the article/supplementary material further inquiries can be directed to the corresponding authors.

AUTHOR CONTRIBUTIONS

CL: Conceptualization, Investigation, Writing—original draft, Writing—review and editing. SW: Formal analysis, Investigation, Writing—review and editing, XX: Methodology, Resources, Writing—review and editing, Supervision, XQ: Formal analysis, Investigation, Writing—review and editing, Project administration, Funding acquisition.

FUNDING

This study has been financially supported by National Natural Science Foundation of China (Grant No. 41867040), Qiandongnan Science and Technology plan project: Study on the consistency of Hoek Brown parameter and equivalent Mohr Coulomb parameter in slope stability calculation, Qiandongnan Science and technology plan project ((2019) No.107), National Natural Science Foundation of China (Grant No.42107195) and National Natural Science Foundation of China (Grant No. 52069007).

REFERENCES

Ali, A., Lyamin, A. V., Huang, J., Li, J. H., Cassidy, M. J., and Sloan, S. W. (2016). Probabilistic Stability Assessment Using Adaptive Limit Analysis and Random fields. *Acta Geotech.* 12, 937–948. doi:10.1007/s11440-016-0505-1

Bozzano, F., Esposito, C., Martini, G., Martino, S., Prestininzi, A., Rinaldis, D., et al. (2013). Earthquake-reactivated Landslide Scenarios in Southern Italy Based on Spectral-Matching Input Analysis. *Bull. Earthquake Eng.* 11 (6), 1927–1948. doi:10.1007/s10518-013-9477-9

Caccavale, M., Matano, F., and Sacchi, M. (2017). An Integrated Approach to Earthquake-Induced Landslide hazard Zoning Based on Probabilistic Seismic Scenario for Phlegrean Islands (Ischia, Procida and Vivara), Italy. *Geomorphology* 295, 235–259. doi:10.1016/j.geomorph.2017.07.010

Chen, X.-L., Liu, C.-G., Yu, L., and Lin, C.-X. (2014). Critical Acceleration as a Criterion in Seismic Landslide Susceptibility Assessment. *Geomorphology* 217 (15), 15–22. doi:10.1016/j.geomorph.2014.04.011

Chen, X., Liu, C., and Wang, M. (2018). A Method for Quick Assessment of Earthquake-Triggered Landslide Hazards: a Case Study of the Mw6.1 2014 Ludian, China Earthquake. *Bull. Eng. Geol. Environ.* 78 (4), 2449–2458. doi:10.1007/s10064-018-1313-7

Dreyfus, D., Rathje, E. M., and Jibson, R. W. (2013). The Influence of Different Simplified Sliding-Block Models and Input Parameters on Regional Predictions of Seismic Landslides Triggered by the Northridge Earthquake. *Eng. Geology.* 163, 41–54. doi:10.1016/j.enggeo.2013.05.015

Fan, X., Scaringi, G., Xu, Q., Zhan, W., Dai, L., Li, Y., et al. (2018). Coseismic Landslides Triggered by the 8th August 2017 Ms 7.0 Jiuzhaigou Earthquake (Sichuan, China): Factors Controlling Their Spatial Distribution and Implications for the Seismogenic Blind Fault Identification. *Landslides* 15 (5), 967–983. doi:10.1007/s10346-018-0960-x

Huang, R., Xu, Q., and Huo, J. (2011). Mechanism and Geo-Mechanics Models of Landslides Triggered by 5.12 Wenchuan Earthquake. *J. Mt. Sci.* 8 (2), 200–210. doi:10.1007/s11629-011-2104-9

Jibson, R. W., Harp, E. L., and Michael, J. A. (2000). A Method for Producing Digital Probabilistic Seismic Landslide hazard Maps. *Eng. Geol.* 58 (3), 271–289. doi:10.1016/s0013-7952(00)00039-9

Jibson, R. W. (2007). Regression Models for Estimating Coseismic Landslide Displacement. *Eng. Geol.* 91 (2), 209–218. doi:10.1016/j.enggeo.2007.01.013

Jin, K. P., Yao, L. K., Cheng, Q. G., Xing, A. G., and Xing, A. G. (2019). Seismic Landslides hazard Zoning Based on the Modified Newmark Model: a Case Study from the Lushan Earthquake, China. *Nat. Hazards* 99 (1), 493–509. doi:10.1007/s11069-019-03754-6

Keefer, D. K. (1984). Landslides Caused by Earthquakes. *Geol. Soc. America Bull.* 95 (4), 406–421. doi:10.1130/0016-7606(1984)95<406:lcbe>2.0.co;2

Krabbenhoft, K., and Lyamin, A. V. (2015). Strength Reduction Finite-Element Limit Analysis. *Géotechnique Lett.* 5 (4), 250–253. doi:10.1680/jgele.15.00110

Li, A.-J., Qian, Z., Jiang, J.-C., and Lyamin, A. (2019). Seismic Slope Stability Evaluation Considering Rock Mass Disturbance Varying in the Slope. *KSCE. J. Civ. Eng.* 23 (3), 1043–1054. doi:10.1007/s12205-019-0963-8

Li, A. J., Lyamin, A. V., and Merifield, R. S. (2009). Seismic Rock Slope Stability Charts Based on Limit Analysis Methods. *Comput. Geotech.* 36 (1–2), 135–148. doi:10.1016/j.compgeo.2008.01.004

Li, A. J., Merifield, R. S., and Lyamin, A. V. (2008). Stability Charts for Rock Slopes Based on the Hoek-Brown Failure Criterion. *Int. J. Rock Mech. Mining Sci.* 45 (5), 689–700. doi:10.1016/j.ijrmms.2007.08.010

Li, C., and Su, L. (2021). Influence of Critical Acceleration Model on Assessments of Potential Earthquake-Induced Landslide Hazards in Shimian County, Sichuan Province, China. *Landslides* 18, 1659–1674. doi:10.1007/s10346-020-01578-1

Li, C., Su, L., Liao, H., Zhang, C., and Xiao, S. (2021). Modeling of Rapid Evaluation for Seismic Stability of Soil Slope by Finite Element Limit Analysis. *Comput. Geotechnics* 133 (9), 104074. doi:10.1016/j.compgeo.2021.104074

Liu, J., Shi, J., Wang, T., and Wu, S. (2017). Seismic Landslide hazard Assessment in the Tianshui Area, China, Based on Scenario Earthquakes. *Bull. Eng. Geol. Environ.* 77 (3), 1263–1272. doi:10.1007/s10064-016-0998-8

Loukidis, D., Bandini, P., and Salgado, R. (2003). Stability of Seismically Loaded Slopes Using Limit Analysis. *Géotechnique* 53 (5), 463–479. doi:10.1680/geot.53.5.463.37509

Lyamin, A. V., Sloan, S. W., Krabbenhøft, K., and Hjiaj, M. (2005). Lower Bound Limit Analysis with Adaptive Remeshing. *Int. J. Numer. Meth. Engng* 63 (14), 1961–1974. doi:10.1002/nme.1352

Lyamin, A. V., and Sloan, S. W. (2002a). Lower Bound Limit Analysis Using Non-linear Programming. *Int. J. Numer. Meth. Engng.* 55, 573–611. doi:10.1002/nme.511

Lyamin, A. V., and Sloan, S. W. (2002b). Upper Bound Limit Analysis Using Linear Finite Elements and Non-linear Programming. *Int. J. Numer. Anal. Meth. Geomech.* 26, 181–216. doi:10.1002/nag.198

Newmark, N. M. (1965). Effects of Earthquakes on Dams and Embankments. *Géotechnique* 15, 139–160. doi:10.1680/geot.1965.15.2.139

Qi, S. W., Xu, Q., Lan, H. X., Zhang, B., and Liu, J. Y. (2010). Spatial Distribution Analysis of Landslides Triggered by 2008.5.12 Wenchuan Earthquake, China. *Eng. Geol.* 116 (1-2), 95–108. doi:10.1016/j.enggeo.2010.07.011

Rodríguez-Peces, M. J., García-Mayordomo, J., Azañòn, J. M., and Jabaloy, A. (2014). GIS Application for Regional Assessment of Seismically Induced Slope Failures in the Sierra Nevada Range, South Spain, along the Padul Fault. *Environ. Earth. Sci.* 72 (7), 2423–2435. doi:10.1007/s12665-014-3151-7

Rodríguez-Peces, M. J., Pérez García, J. L., García-Mayordomo, J., Azañòn, J. M., sua-Arévalo, J. M., and Delgado-García, J. (2011). Applicability of Newmark Method at Re-gional, Sub-regional and Site Scales: Seismically Induced Bullas and La Paca Rock-Slidecases (Murcia, SE Spain). *Nat. Hazards* 59, 1109–1124. doi:10.1007/s11069-011-9820-x

Saade, A., Abou-Jaoude, G., and Wartman, J. (2016). Regional-scale Co-seismic Landslide Assessment Using Limit Equilibrium Analysis. *Eng. Geology.* 204, 53–64. doi:10.1016/j.enggeo.2016.02.004

Shinoda, M., and Miyata, Y. (2017). Regional Landslide Susceptibility Following the Mid NIIGATA Prefecture Earthquake in 2004 with NEWMARK'S Sliding Block Analysis. *Landslides* 14 (6), 1887–1899. doi:10.1007/s10346-017-0833-8

Sloan, S. W. (2013). Geotechnical Stability Analysis. *Géotechnique* 63 (7), 531–571. doi:10.1680/geot.12.rl.001

Sloan, S. W. (1988). Lower Bound Limit Analysis Using Finite Elements and Linear Programming. *Int. J. Numer. Anal. Methods Geomech.* 12 (1), 61–77. doi:10.1002/nag.1610120105

Sloan, S. W. (1989). Upper Bound Limit Analysis Using Finite Elements and Linear Programming. *Int. J. Numer. Anal. Methods Geomech.* 13 (3), 263–282. doi:10.1002/nag.1610130304

Tsai, H.-Y., Tsai, C.-C., and Chang, W.-C. (2019). Slope Unit-Based Approach for Assessing Regional Seismic Landslide Displacement for Deep and Shallow Failure. *Eng. Geology.* 248, 124–139. doi:10.1016/j.enggeo.2018.11.015

Utili, S., and Abd, A. H. (2016). On the Stability of Fissured Slopes Subject to Seismic Action. *Int. J. Numer. Anal. Meth. Geomech.* 40 (5), 785–806. doi:10.1002/nag.2498

Wang, T., Wu, S. R., Shi, J. S., Xin, P., and Wu, L. Z. (2018). Assessment of the Effects of Historical strong Earthquakes on Large-Scale Landslide Groupings in the Wei River Midstream. *Eng. Geology.* 235, 11–19. doi:10.1016/j.enggeo.2018.01.020

Wartman, J., Dunham, L., Tiwari, B., and Pradel, D. (2013). Landslides in Eastern Honshu Induced by the 2011 Tohoku Earthquake. *Bull. Seismological Soc. America* 103 (2B), 1503–1521. doi:10.1785/0120120128

Wilson, R. C., and Keefer, D. K. (1983). Dynamic Analysis of a Slope Failure from the 6 August 1979 Coyote Lake, California, Earthquake. *Bull. Seismol. Soc. Am.* 73 (3), 863–877. doi:10.1785/bssa0730030863

Wu, W., Yang, Y., and Zheng, H. (2020). Hydro-mechanical Simulation of the Saturated and Semi-saturated Porous Soil-Rock Mixtures Using the Numerical Manifold Method. *Comput. Methods Appl. Mech. Eng.* 370 (3), 113238. doi:10.1016/j.cma.2020.113238

Xu, C., Dai, F., Xu, X., and Lee, Y. H. (2012). GIS-based Support Vector Machine Modeling of Earthquake-Triggered Landslide Susceptibility in the Jianjiang River Watershed, China. *Geomorphology* 145-146 (2), 70–80. doi:10.1016/j.geomorph.2011.12.040

Xu, C., Xu, X., Dai, F., Wu, Z., He, H., Shi, F., et al. (2013). Application of an Incomplete Landslide Inventory, Logistic Regression Model and its Validation for Landslide Susceptibility Mapping Related to the May 12, 2008 Wenchuan Earthquake of China. *Nat. Hazards.* 68 (2), 883–900. doi:10.1007/s11069-013-0661-7

Xu, C., Xu, X., and Shyu, J. B. H. (2015). Database and Spatial Distribution of Landslides Triggered by the Lushan, China Mw 6.6 Earthquake of 20 April 2013. *Geomorphology* 248, 77–92. doi:10.1016/j.geomorph.2015.07.002

Yang, Y., Sun, G., Zheng, H., and Qi, Y. (2019b). Investigation of the Sequential Excavation of a Soil-Rock-Mixture Slope Using the Numerical Manifold Method. *Eng. Geology.* 256, 93–109. doi:10.1016/j.enggeo.2019.05.005

Yang, Y., Sun, G., Zheng, H., and Yan, C. (2019a). An Improved Numerical Manifold Method with Multiple Layers of Mathematical Cover Systems for the Stability Analysis of Soil-Rock-Mixture Slopes. *Eng. Geol.* 264, 105373. doi:10.1016/j.enggeo.2019.105373

Yang, Y., Wu, W., and Zheng, H. (2021). An Uzawa-type Augmented Lagrangian Numerical Manifold Method for Frictional Discontinuities in Rock Masses. *Int. J. Rock Mech. Mining Sci.* 148, 104970. doi:10.1016/j.ijrmms.2021.104970

Yuqiao, Q, Hua, T, Qin, D, Xiaotao, Y, and Dongying, W (2019). Regional Seismic Slope Assessment Improvements Considering Slope Aspect and Vertical Ground Motion. *Eng. Geology*. 259, 105148. doi:10.1016/j.enggeo.2019.105148

Zang, M., Qi, S., Zou, Y., Sheng, Z., and Zamora, B. S. (2020). An Improved Method of Newmark Analysis for Mapping Hazards of Coseismic Landslides. *Nat. Hazards Earth Syst. Sci.* 20 (3), 713–726. doi:10.5194/nhess-20-713-2020

Conflict of Interest: The authors declare that the research was conducted in the absence of any commercial or financial relationships that could be construed as a potential conflict of interest.

Publisher's Note: All claims expressed in this article are solely those of the authors and do not necessarily represent those of their affiliated organizations, or those of the publisher, the editors and the reviewers. Any product that may be evaluated in this article, or claim that may be made by its manufacturer, is not guaranteed or endorsed by the publisher.

frontiers in Earth Science

ORIGINAL RESEARCH
published: 08 March 2022
doi: 10.3389/feart.2022.858542

Deep-Seated Deformation Mechanisms of Excavated Slope and Control Methods: A Case Study

Yongjin Wu[1,2], *Qing Zhang*[1]*, *Xiuli Ding*[2], *Hui Wang*[3], *Shuling Huang*[2] *and Xiansong Yin*[3]

[1]*Department of Engineering Mechanics, College of Mechanics and Materials, Hohai University, Nanjing, China,* [2]*Key Laboratory of Geotechnical Mechanics and Engineering of Ministry of Water Resources, Changjiang River Scientific Research Institute, Wuhan, China,* [3]*Changjiang Institute of Survey, Planning, Design and Research, Wuhan, China*

OPEN ACCESS

Edited by:
Yongtao Yang,
Institute of Rock and Soil Mechanics (CAS), China

Reviewed by:
Dongdong Xu,
Changjiang River Scientific Research Institute (CRSRI), China
Xiaodong Fu,
Institute of Rock and Soil Mechanics (CAS), China
Wu Wenan,
Beijing University of Technology, China

***Correspondence:**
Qing Zhang
lxzhangqing@hhu.edu.cn

Specialty section:
This article was submitted to Geohazards and Georisks, a section of the journal Frontiers in Earth Science

Received: *20 January 2022*
Accepted: *21 February 2022*
Published: *08 March 2022*

Citation:
Wu Y, Zhang Q, Ding X, Wang H, Huang S and Yin X (2022) Deep-Seated Deformation Mechanisms of Excavated Slope and Control Methods: A Case Study. Front. Earth Sci. 10:858542. doi: 10.3389/feart.2022.858542

High slope stability control is a crucial technical issue in water conservancy and hydropower project construction. This issue is relevant throughout the entire engineering-related survey, design, construction, and operation process. This paper reports a recent case in which significant deep-seated deformation occurred during slope excavation. Several unfavorable structural surfaces were revealed throughout the slope's undercutting process, particularly fault fz39, which ran diagonally through the entire slope from top to bottom. On the slope surface, damage such as cracking, bulging, and local slippage appeared. The measured value of multipoint displacement meters increased in a stepwise pattern with each blast, and the maximum measured value exceeded 100 mm. The studied slope's whole excavation and reinforcement process is described in detail. We analyzed the deformation mechanism of the excavation slope by combining the geological conditions, real-time safety monitoring findings, and site deformation characteristics. The slope reinforcement scheme was optimized based on the preceding analyses. We used a three-dimensional numerical calculation program to simulate the slope excavation and unloading process to reproduce the current mechanical state of the slope, evaluate the reinforcement measures, and provide a useful reference for decision making. The analysis shows that the deformation behavior of the studied slope is closely related to fault fz39 and fracture L920, and presents a typical wedge failure mode. The deep-seated deformation of the excavation slope occurs at the junction of the wedge and bedrock, which is mainly affected by unfavorable geological structure surfaces, excavation unloading, and blasting vibration. The reinforcement scheme of unloading at the top of the slope and large-tonnage cables are established. The numerical analysis results showed that the design of the slope reinforcement measures was appropriate and ensured slope stability. The work described in this paper deepens our understanding of the occurrence of large deep-seated deformation on the structural-controlled slope under the action of excavation and improves the design philosophy.

Keywords: rock slope, fault, deep-seated deformation, blasting, movement monitoring, support design

INTRODUCTION

High rock slopes are the main geological environment found in large-scale hydraulic projects, such as the Three Gorges Project, the Southwest Large Hydropower Group, and the Hanjiang-to-Weihe River Valley Water Diversion Project. Most of these projects are located in high mountain valley areas with steep valley slopes, high *in situ* stress in the riverbed, complex geological structures, and frequent geological disasters, including landslides. The excavation scale of engineered slopes is large and requires multiple blasting excavations over a certain period. The unloading mechanism of slope excavation is complex, which may aggravate or trigger new landslide disasters. For example, the resurrection of ancient landslides occurred in Tianshengqiao II Hydropower Station because of blasting excavation of the plant slope (Xia and Lu, 1986); 106,000 m^3 of landslides occurred during the excavation of the left bank slope of Manwan Hydropower Station (Liu, 1990); buckling failure of the Dabengliugou Stockyard Slope of Jinping I Hydropower Station occurred because of excavation (Dong et al., 2013); toppling failure of antidip layered rock high slope occurred at the left bank intake of Longtan Hydropower Station (Zhou, 2015); the wedge-shaped rock block failure during the excavation of the Tongjiashan reach of the Qinhuai East River in Nanjing (Qin et al., 2022); and a landslide occurred on the left bank of Vajont Reservoir, Italy, triggered by water storage (Mantovani and Vita-Finzi, 2003).

Landslide control is the key to the construction and safe operation of projects. Several scholars have analyzed the key factors leading to landslides (Ersmann, 1979; Petley and Allison, 1997; Huang, 2008; De Blasio, 2011). Rock mass structure is one of the most important conditions for landslide formation. Huang (2007) summarized and analyzed large-scale landslides in China since the beginning of the 20th century. Qiao (2002) summarized 14 main structural types of landslides. In slope excavation research, qualitative and quantitative studies have been conducted on rock stress and rock structure changes, unloading mechanical properties, crack growth and properties evaluation of the rock materials, intrinsic models and yield criteria, slope evolution, and disaster-causing mechanisms during engineering unloading (Ha, 1997; Sheng et al., 2000; Wyllie and Mah, 2004; Zhou et al., 2004; Lu et al., 2013; Ersöz and Topal, 2018; Yang et al., 2019; Zheng et al., 2019; Yang et al., 2020b; Yang et al., 2021c). In slope-blasting excavation research, Lu et al. (2008) studied the transient characteristics of excavation unloading. Onederra et al. (2013) simulated fully coupled explosive blast-induced hazards, and Hu et al. (2018) conducted a numerical experimental study on blasting damage control. The main objective of landslide control is to reduce the sliding force or increase landslide resistance (Segalini and Giani, 2004; Petley et al., 2005; Wei et al., 2006). Regarding landslide control, Zhang et al. (2002) and Dai (2002) carried out theoretical and experimental studies on the interaction between landslides and antislip piles. Ge and Liu (1988), Li (2010), and Zhu et al. (2021) carried out theoretical studies on the interaction mechanism between prestressed anchor cables and landslides, and Gu et al. (2000) and Zhu et al. (2017) carried out relevant studies by experiments. In terms of slope stability analysis, the limit equilibrium method and numerical analysis methods have been further developed (Giani, 1992; Donald and Chen, 1997; Dawson et al., 1999; Chen et al., 2001; Zheng and Zhao, 2004; Zheng, 2007; Zhu and Qian, 2007; Yang et al., 2020a; Yang et al., 2021a; Yang et al., 2021b).

Overall, research on the excavation and unloading process of high rock slope is still based on qualitative and semiquantitative studies, which focus mainly on slope stability analysis, scheme optimization, and control effects. The disaster-causing mechanism, phased control of the evolution process, and control methods based on real-time monitoring information, however, still require further research. This paper introduces a case study of the rock slope at Huangjinxia Water Control Project. In the process of slope excavation, unfavorable structural surfaces such as fz39 and L920 were revealed. Deformation phenomena, such as cracking and bulging, appeared on the excavated face, and tension cracks occurred at the rear edge of the origin slope. In addition, the monitoring data showed that the deformation was mostly located in the deep part of the slope and jumped in a stepwise growth after each blast. As of June 2019, the maximum measured deformation value had exceeded 100 mm. The entire excavation and reinforcement process of the studied slope are detailed in this paper. On the basis of real-time safety monitoring, we categorized the deformation process into three stages, and each stage included the processes of "excavation–deformation and damage–verification–reinforcement–deformation convergence." These stages provide insight into issues related to rock slope stability. Finally, we simulated the excavation process of the slope by numerical analysis to reproduce its current mechanical state and evaluate subsequent reinforcement design. This successful case study involving large, deep-seated deformation control of an excavated slope improves design philosophy and provides valuable references for the design and construction of similar projects.

AN OUTLINE OF THE STUDIED SLOPE

Project Overview

The Hanjiang-to-Weihe River Valley Water Diversion Project, also known as the South-North Water Transfer Project in Shaanxi Province, is the first water transfer project to have crossed the Yellow River Basin, the Yangtze River basins, and the Qinling Mountains (**Figure 1**). The project diverts water from the Hanjiang River into the Weihe River. The major projects include the Huangjinxia Water Control Project, Sanhekou Water Control Project, and Qingling Water Tunnel. The Huangjinxia Water Control Project is one of the main water sources for the whole project, which is located in the upper reaches of the Hanjiang River. The major structures consist of water-retaining, water release, pumping station, power station, and navigation structures. The water-retaining building is a concrete gravity dam with a crest elevation of 455 m and a maximum dam height of 63 m. The pumping station and power station are located on the left bank of the river. The

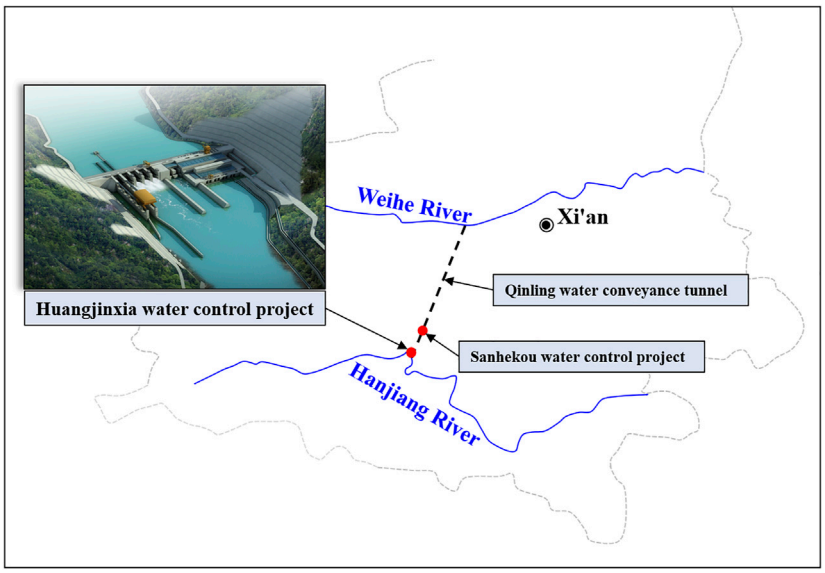

FIGURE 1 | Schematic diagram of the project.

riverbed pumping station and the hydropower station behind the dam are placed forward and backward along the flow direction, respectively.

Design of the Study Slope

The object of study was the slope of the pump station and power station inlet of the Huangjinxia Water Control Project (**Figure 2A**). The slope is located along the left bank, from 16.8 to 162.9 m upstream of the dam axis. According to the Design Code for Engineering Slopes in Water Resources and Hydropower Projects (The Water Conservancy Standards Compilation Group of the People's Republic of China, 2007a), the slope grade is Grade 1. In the preliminary design stage, no controlling structural surfaces, such as fz39 and L920, were found on the slope. The basic principle of slope design is to ensure the stability of strongly weathered rock mass. The design scheme of the slow follows (**Figure 2B**):

1. The maximum height of the excavation slope was 133.4 m. The top elevation was approximately 540 m, and the lowest elevation was 406.6 m. The middle of the excavated slope was Highway 1 with an elevation of 455 m. The slope above Highway 1 was 85 m in height, which was excavated in five levels, and the design excavation slope ratio was 1:0.4–1:0.7. The slope below Highway 1 was 48.4 m in height, which was excavated in three levels, and the designed excavation slope ratio was 1:0.3–1:0.7.

2. The support measures included system anchors, mat reinforcement, and shotcrete. In addition, two rows of cables with a length of 25 m and a prestress of 1,000 kN were arranged on the slopes with an elevation of 519–502 m and an elevation of 502–485 m.

3. The drainage measures included drainage holes with a length of 4 m, and two rows were arranged on each stage slope.

Geological Conditions

Lithology

The studied slope was located at a protrusion between two small gullies, revealing a three-sided empty shape. The natural slope was 290–313° in direction and 37–45° in slope angle. The strata were mainly Early Proterozoic Qingbaikou diorite invaded by felsic dykes and monzonitic granite dykes. The strongly weathered rock masses were mainly distributed above 485 m in elevation and generally had a fractured structure. The rock fractures were extremely developed, and the cores were mostly fragmented.

Geological Structure

The results of statistical analysis showed that four main groups of structural surfaces had developed on the studied slope. The distribution of representative structural surfaces is shown in **Figures 3A,B**.

1. Strike direction NNW group: These structural surfaces were inclined to the upstream riverbed side, which were most developed at the slope. Their orientation was on average 255°–270°∠60°–270°; the intersection angle with the slope was on average 55°–70°. The developmental spacing was generally 0.5–2.0 m, with representative ones being long fractures L919 and L920.

2. Strike direction NEE group: Their orientation was on average 160°–180°∠ 60°–80°; the intersection angle with the slope was on average 20°–30°. These structural surfaces were nearly parallel to the slope direction and

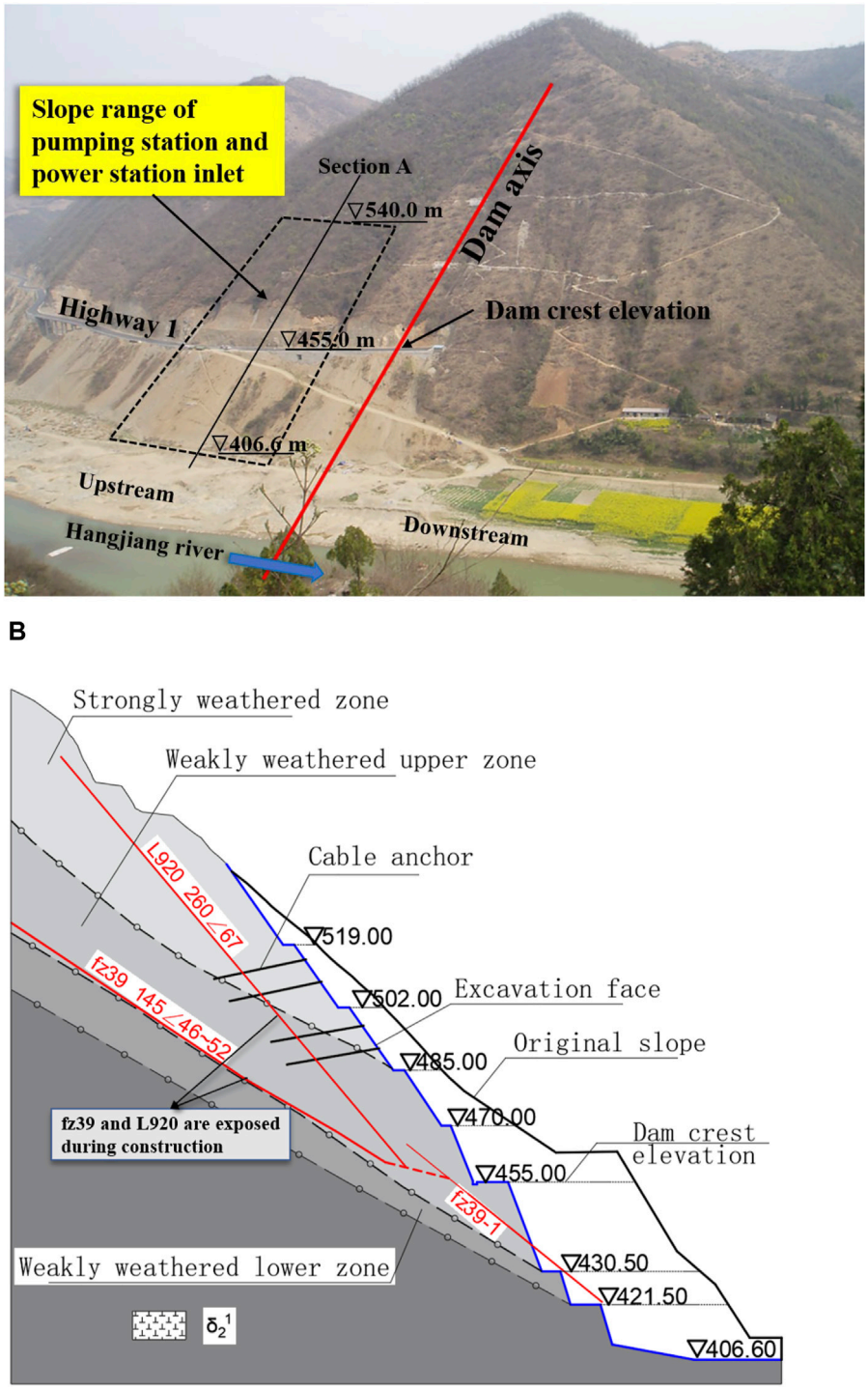

FIGURE 2 | Basic situation of the study slope: **(A)** covering range; **(B)** original design.

inclined to the downstream riverbed side, and representative ones were small faults fz46 and fz54.

3. Strike direction NE group: Their orientation was on average 120°–150°∠35°–55°. The number of structural surfaces in this group was small, but they generally were developed on a larger scale, such as fault fz39.
4. Strike direction NWW group: Their orientation was on average 10°–30°∠45°–75°. These structural surfaces were

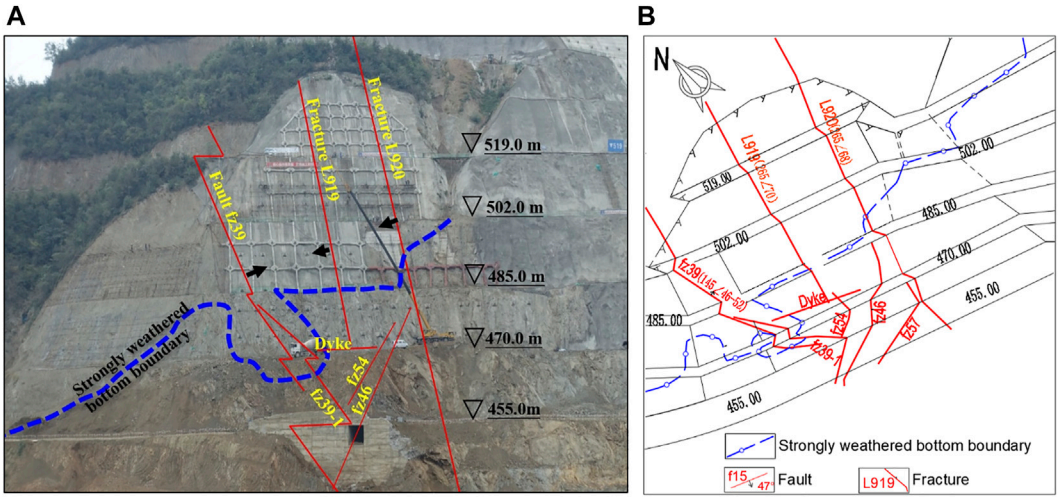

FIGURE 3 | Distribution of main structural surfaces: **(A)** photograph; **(B)** geological sketch.

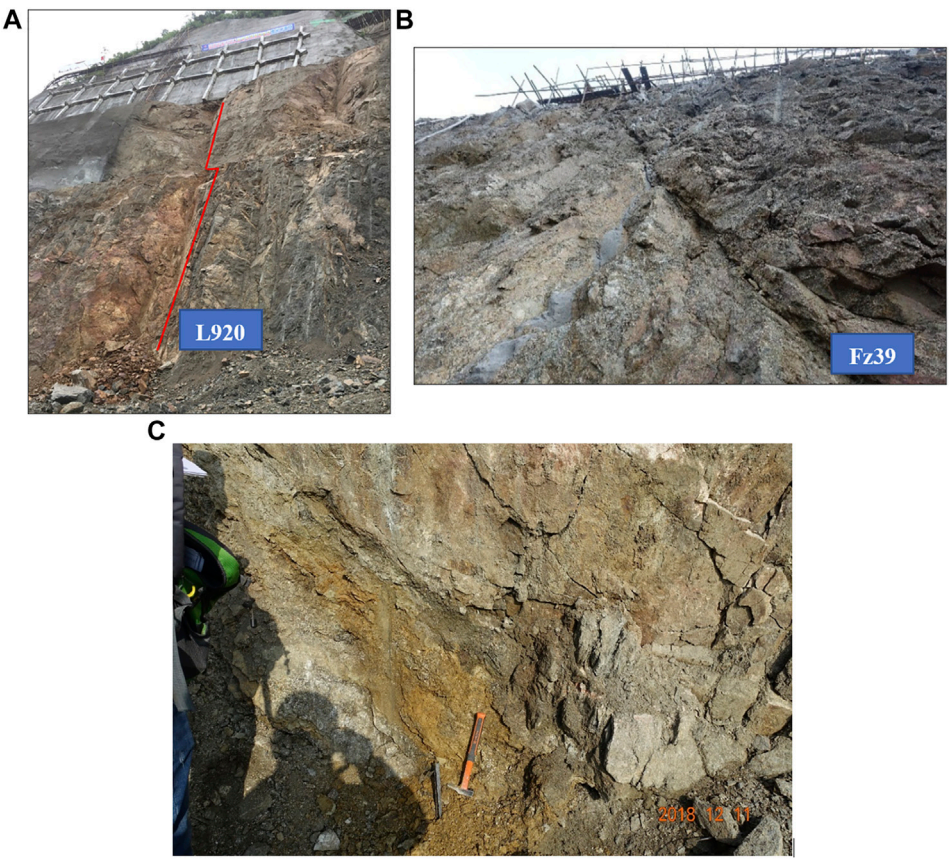

FIGURE 4 | Photographs of main structural surfaces: **(A)** fracture L920; **(B)** fault fz39; **(C)** mud of fault fz39.

nearly parallel to the slope direction and inclined toward the inside of the slope. Mainly monzonitic granite dykes were dominant.

Characteristics of Main Structural Surfaces

Fracture L920 developed at an elevation of 502 to 455 m. The orientation was on average 265°–270°∠55°–67°. The fracture

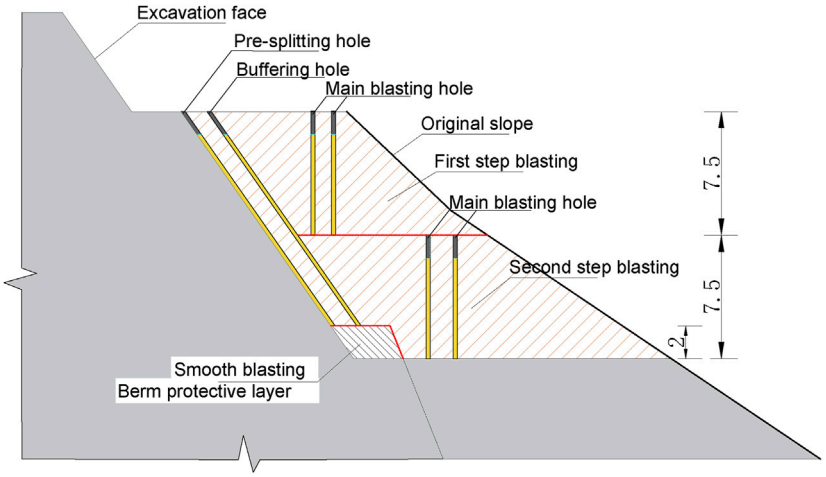

FIGURE 5 | Blasting excavation method.

planes were generally planar and infilled with debris and locally attached with mud films. Below an elevation of 485 m, the developmental spacing was generally 0.2–0.5 m (**Figure 4A**).

Fault fz39 was the largest fault revealed by slope excavation (**Figure 4B**), which ran through the whole slope from top to bottom. Its extension length was more than 150 m, and its width was approximately 0.1–0.3 m. The orientation was on average 145°∠46°–52° (the branch fault fz39-1 below the elevation of 470 m: 136°–144°∠43°–47°). The intersection angle with the slope was on average 51°–55°. The fault inclined toward the downstream riverbed side, which was an extroverted structural surface with a medium dip angle. According to the direction of scratch and step, fault fz39 was a positive translation fault. The fault was mainly cataclastic rock, and mud attached to the fault surface or local mud phenomenon was a severe problem (**Figure 4C**). The mud thickness was generally 1–3 cm and could reach 10 cm locally. Overall, the physical and mechanical properties of fault fz39 were very poor.

Hydrogeology

The groundwater type of the slope was mainly bedrock fracture water. The excavation faces were dry. Through drainage holes, boreholes, and anchor holes, we found that the groundwater was located below an elevation of 470 m and was buried at a shallow level inside the slope. The horizontal depth of the water table was 15–25 m—thus, the lower the elevation, the shallower the depth of burial.

BEHAVIOR OF THE SLOPE ROCK MASSES

Construction Process of the Slope

The slope was excavated mainly by presplitting blasting (**Figure 5**). The presplitting hole and buffering hole were designed as inclined holes according to the excavation face, and the main blasting hole was designed as a vertical hole with a depth of 7.5 m. For each stage of the slope, the presplitting holes were formed once, and the main blasting holes were formed by blasting in two steps.

The excavation of the slope started in November 2015. By May 2016, the excavation of the slope above an elevation of 485 m was finished. The construction of the slope was suspended until April 2018, and construction resumed on April 9, 2018. Then, until May 9, 2018, the slope at an elevation range of 485–470 m was excavated in place. From July 2018 to March 2019, the excavation of the slope at an elevation range of 470–455 m was finished, during which time six blasts were carried out. As of June 2019, the slope above Highway 1 (elevation 455 m) had been excavated completely, and a total of five sets of multipoint displacement meters (M18-22ZPR) and nine sets of anchor dynamometers (D01ZBP, D10–17ZPR) had been installed.

Deformation and Failure Process of the Slope

The main deformation process of the excavation slope was categorized into three stages (**Figure 6A**), and each stage included to the process of "excavation–deformation and damage–verification–reinforcement–deformation convergence." Curves of the maximum deformation vs. time of multipoint displacement meters are shown in **Figure 6B**. The arrangement of the monitoring instruments, as well as the time and range of each blast, are shown in **Figure 6C**.

Stage 1

After excavation of the slope in the elevation range of 485–470 m, we found cracks on the inner side of the road at an elevation of 502 m, and three horizontal cracks appeared on the excavated face above an elevation of 519 m. On July 8, 2018, after the first presplitting blasting of the slope at the elevation range of 470–455 m, the shotcrete on the downstream side of the slope in the elevation range of 519–502 m showed a bulging phenomenon. In addition,

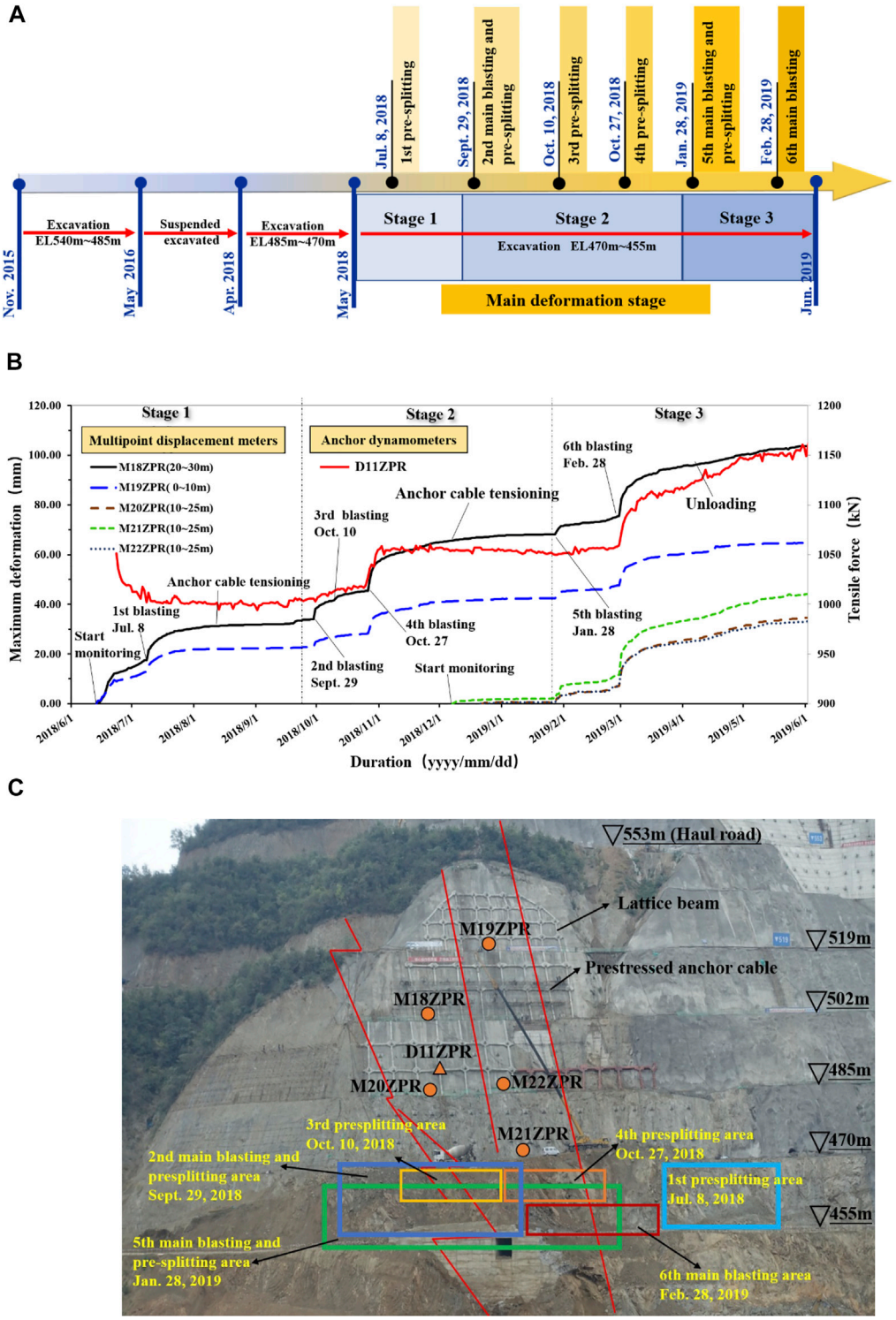

FIGURE 6 | Deformation process of the excavation slope: **(A)** three stages; **(B)** deformation curves; **(C)** range of each blasting.

cracks also appeared in the anchor pier and lattice beam (**Figure 7A**).

Multipoint displacement meters M18ZPR and M19ZPR were installed on June 13, 2018. After installation, the measured value continued to increase. The deep deformation measured by M18ZPR and M19ZPR mainly occurred in intervals of 20–30 m and 0–10 m, respectively. After the first blasting on 8 July 2018, all meters showed a step-

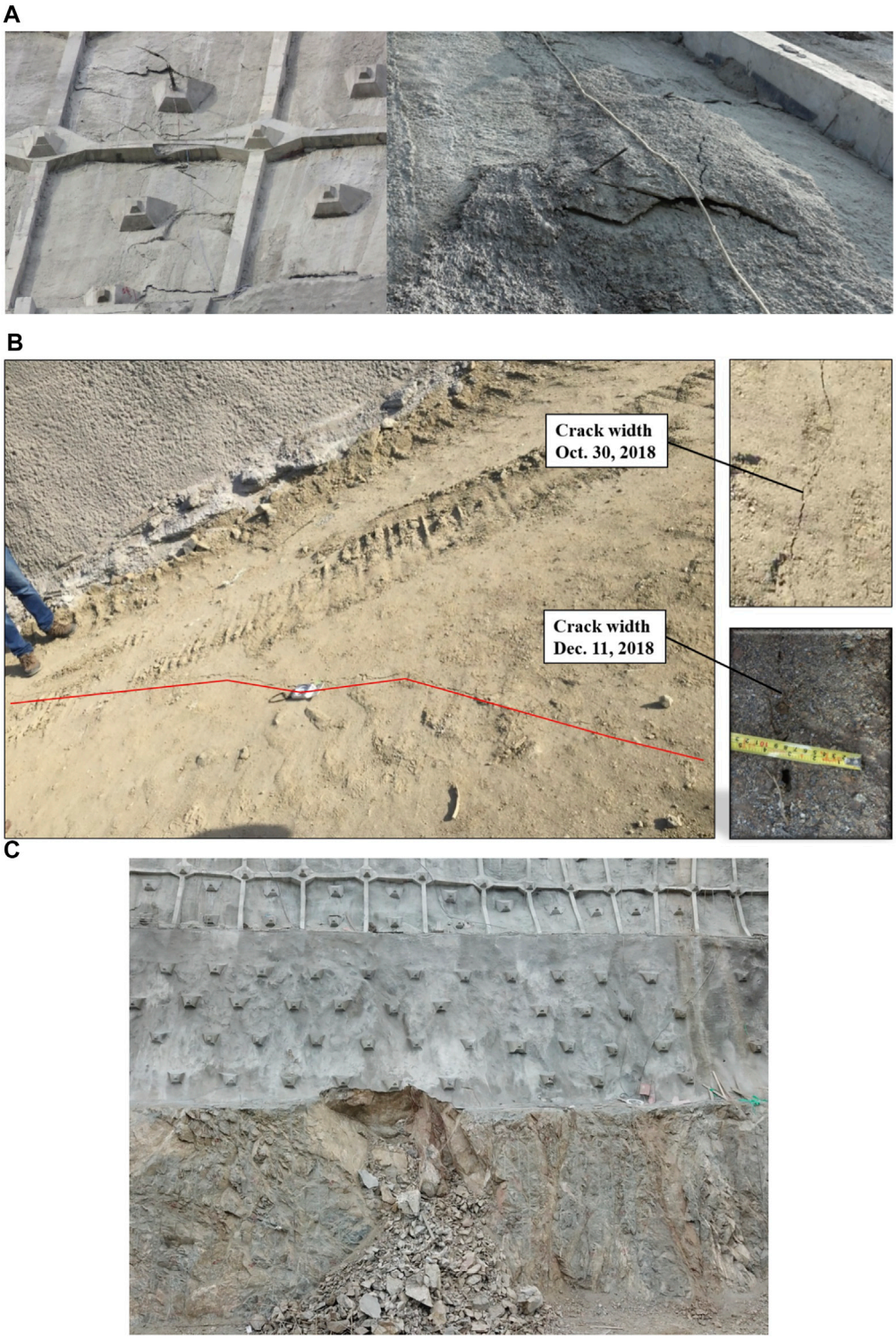

FIGURE 7 | Failure behaviors of the excavation slope: **(A)** stage 1; **(B)** stage 2; **(C)** stage 3.

like jump in growth. Then, the excavation was suspended, and additional support measures were considered to reinforce the slope. The reinforcing support measures featured the use of long prestressing cables that ran through the structural surfaces fz39 and L920. The prestressing cable tension was either 1,000 or 1,500 kN, and the length was between 35 m and 60 m. With the installation of additional cable support measures, the curves of deformation vs. time gradually

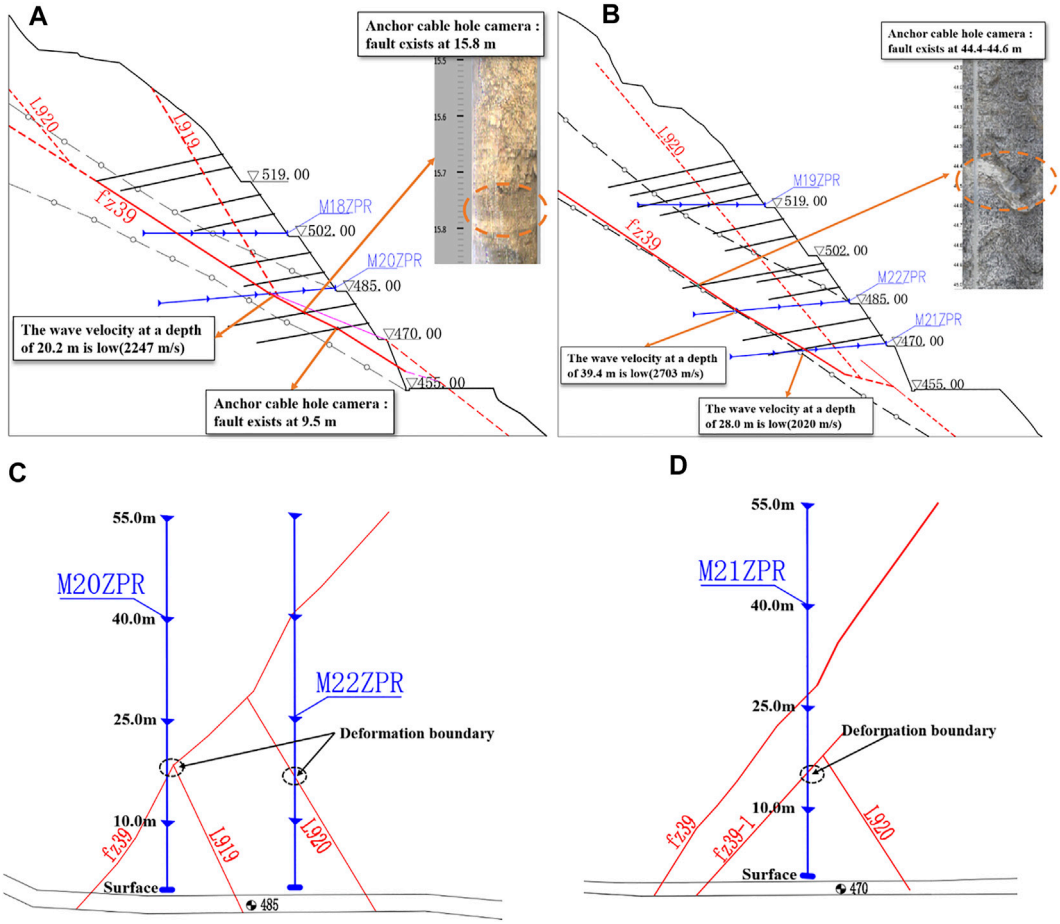

FIGURE 8 | The positional connection between multipoint displacement meters, cables, and structural surfaces in typical sections: **(A)** upstream longitudinal profile; **(B)** downstream longitudinal profile; **(C)** elevation 485 m flat section; **(D)** elevation 470 m flat section.

converged. By the end of September 2018, the deformation obtained by the multipoint displacement meters M18ZPR (20–30 m) and M19ZPR (0–10 m) reached 26.2 and 14.6 mm, respectively.

Stage 2

On September 29, October 10, and October 27, 2018, the slope was excavated by blasting three times in the elevation range of 470–455 m. The measured values of M18ZPR and M19ZPR in each blasting also showed a step-like jump in growth with a large value. Obvious cracking occurred at the excavation face and along the rear edge of the slope (elevation 553 m), and the cracks tended to grow (**Figure 7B**).

Thereafter, the excavation was suspended again. Priority was given to the construction of prestressed cables. By the end of December 2018, the additional support measures (designed in the first stage) above 470 m were completed. The curves of deformation vs. time gradually converged again. By the end of January 2019, the deformation of the multipoint displacement meters M18ZPR (20–30 m) and M19ZPR (0–10 m) reached 51.9 and 30.83 mm, respectively. In addition, three sets of multipoint displacement meters M20ZPR, M21ZPR, and M22ZPR were installed in December 2018. By the end of January 2019, the measured values increased slightly, with a maximum of 1.86 mm.

Stage 3

From January 28 to February 28, 2019, the remaining part of the slope with an elevation range of 470–455 m was excavated by blasting. After blasting, one anchor pier cover at an elevation of 472 m appeared to be fractured, the transverse crack width of the slope with an elevation of 471 m increased significantly, and the shotcrete on the slope above an elevation 471 m showed a bulging phenomenon. On March 8, 2019, after rainfall, local collapse failure occurred along the slope below an elevation of 472 m and above fault fz39, with a volume of approximately 40 m^3 (**Figure 7C**).

After the sixth blasting, the measured values of five sets of multipoint displacement meters increased greatly. As of June 2019, the measured values of M18ZPR, M20ZPR, M19ZPR, M22ZPR, and M21ZPR increased by 23.46, 29.36, 15.04, 21.90, and 34.85 mm, respectively.

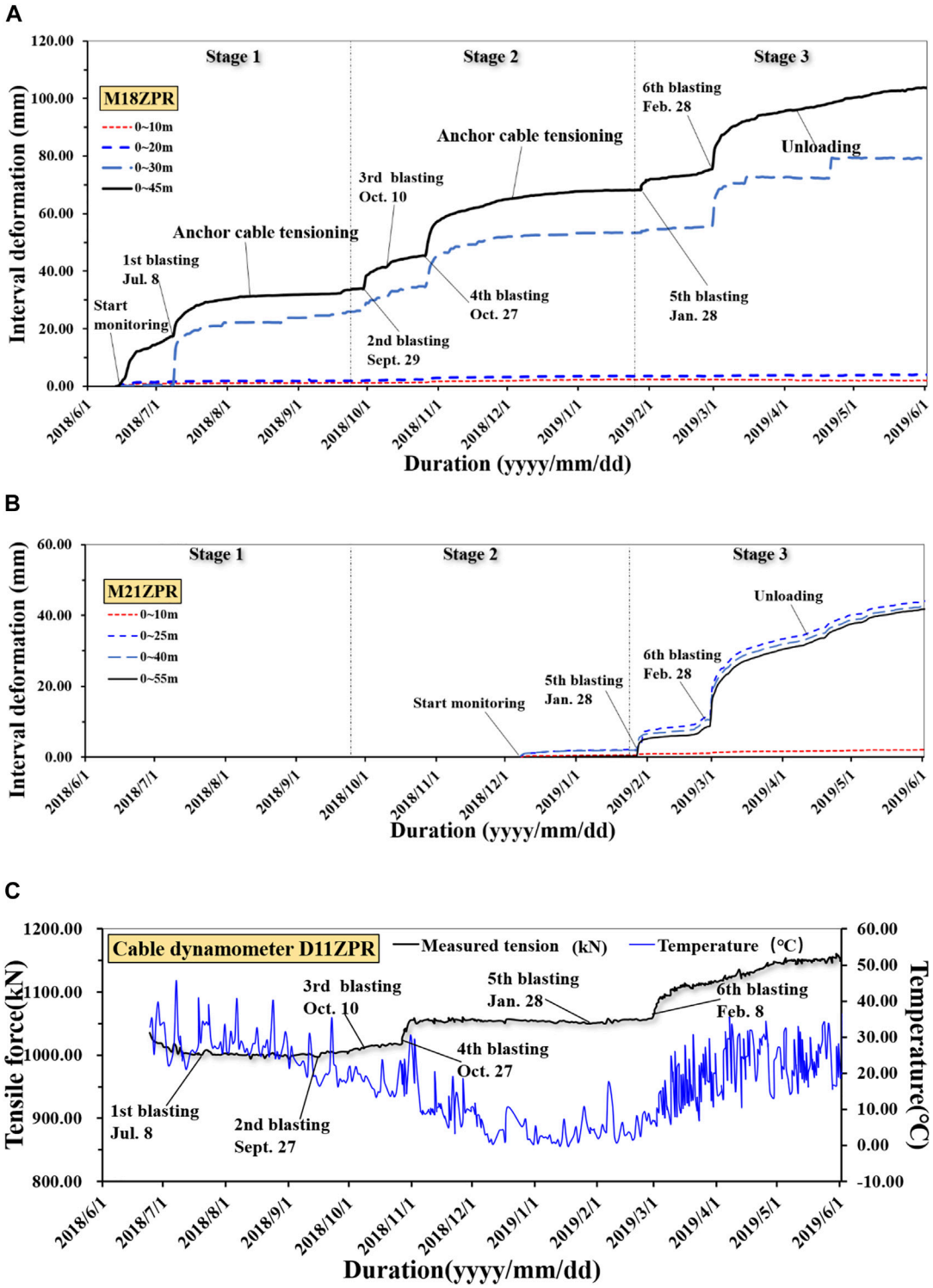

FIGURE 9 | The curves of deformation vs. time and cable tension vs. time: **(A)** M18ZPR; **(B)** M21ZPR; **(C)** D11ZPR.

Monitoring Data Analysis

Five sets of multipoint displacement meters constituted two monitoring sections perpendicular to the excavation face. The multipoint displacement meters M18ZPR and M20ZPR were located on the upstream side, and M19ZPR, M22ZPR, and M21ZPR were located on the downstream side. **Figures 8A–D** shows the positional connection between the multipoint displacement meters, cables, and structural surfaces in typical

sections. **Figures 9A–C** shows the curves of deformation vs. time and cable tension vs. time.

Relationship Between Deformation Depth and Structural Surface

The deep-seated deformation measured by the multipoint displacement meters occurred mainly in the hole-depth ranges of 20–30 m (M18ZPR), 0–10 m (M19ZPR), 10–25 m (M20ZPR), 10–25 m (M21ZPR), and 10–25 m (M22ZPR). These results were consistent with the inferred location of structural surfaces fz39 and L920 in the slope. This finding indicated that the deformation failure of the slope was controlled mainly by the structural surfaces fz39 and L920 and mainly occurred in the area within the intersection of structural surfaces fz39 and L920. The failure showed obvious block deformation behaviors, and the deformation of the structural surface accounted for a high proportion of the total deformation.

Curves of Deformation vs. Time

The measured values of the multipoint displacement meters all showed step-like jump growth, and the jumping times were all related to the nearby blasting times. As of June 2019, the measured values were 104.84 mm (M18ZPR), 64.92 mm (M19ZPR), 36.57 mm (M20ZPR), 46.42 mm (M21ZPR), and 35.20 mm (M22ZPR). Although the overall deformation of the slope has not yet converged, the deformation rate has been decreasing gradually. Because M20ZPR, M21ZPR, and M22ZPR detected only the deformation caused by the partial excavation of the slope at the elevation range of 470–455 m, the total deformation was smaller than that measured by M18ZPR and M19ZPR, but the recent increments varied significantly.

Temporal and Spatial Characteristics of Deformation

The time-dependent deformation characteristics of the slope were not obvious. The deformation mainly occurred at the blasting time of each stratified excavation and gradually stabilized after the excavation stops. This meant that the deformation was affected mainly by unfavorable geological structural surfaces, excavation unloading, and blasting vibrations. Furthermore, the stress-rebalancing adjustment time after excavation and blasting disturbance was increased.

According to spatial deformation characteristics, the deformation of the multipoint displacement meter crossing fault fz39 in the upstream was large, whereas that of crossing fracture L920 was slightly smaller and showed non-coordinated deformation along the upstream and downstream sides. After the blasting on 28 February 2019, the deformation increment showed that the deformation in the lower part was larger than that in the middle and upper parts.

Curves of Cable Tension vs. Time

The cable tension continued to change with the deformation of the slope. Since late October 2018, affected by blasting, the cable tension began to grow simultaneously along with the deformation. In particular, since the blasting on 28 February 2019, the cable tension growth significantly accelerated, and the measured jumping growth time and change law were consistent with the deformation. As of June 2019, the measured value of D11ZPR in the lower part of the slope reached 114.3% of the cable locked value 1,000 kN.

INFLUENCING FACTORS OF DEEP-SEATED DEFORMATION

Internal Factors

A large number of rock engineering accidents have shown that unstable rock masses often suffer a slip, tensile fracture, or distorted deformation along a suitable structural surface or the combined boundary of multiple structural surfaces, resulting in the instability of the rock slope. According to an analysis of the geological conditions and deformation characteristics, the deformation behavior of the slope was closely related to fault fz39 and fracture L920. Fault fz39 was inclined toward the downstream riverbed side, which was an extroverted structural surface with a medium dip angle. Fault fz39 ran through the entire slope from top to bottom, and the physical and mechanical properties were very poor. Combining fault fz39 with fracture L920 could form a double-sided sliding block, KT21 (**Figure 10A**). The orientation of the intersection line was on average 190°∠38°, which was inclined toward the outside of the slope. The dip angle of the intersection line was less than the slope angle, and block KT21 was a potentially unstable block. The top elevation of block KT21 was approximately 570 m, the revealed elevation of the intersection line was approximately 420 m, and the total volume was approximately $7.9 \times 104\ m^3$ (**Figures 10B,C**). The block KT21 is a typical double-sided sliding wedge (**Figure 10D**).

Extrinsic Factors

Excavation and Unloading

The slope was excavated and unloaded from top to bottom on a large scale. The excavated volume at each grade of slope gradually increased, and the grade of the excavation slope became steeper. The rock masses were affected by unloading disturbance, and the *in situ* stress field was constantly changing, which made the slope structure and its intermechanical relationship changed adversely. In particular, in the process of excavating the slope at an elevation range of 485–455 m, fault fz39 was gradually revealed on the excavation face. Fault fz39 was inclined toward the outside and cut along the foot of the excavation slope. As a result, the supporting effect of the "locking section" at the foot of the slope was weakened, and the bearing capacity decreased significantly.

Blasting Vibration

The blasting load acted directly on the slope as an external force, which reduced the shear resistance of the rock mass structure. The repeated vibration of blasting reduced the mechanical strength of the structural surface (Wang and Qian, 1995; Liu, 2007). By analyzing the curves of deformation vs. time, blasting vibration was undoubtedly an important external inducement to aggravate slope deformation. The deformation occurred mainly after each

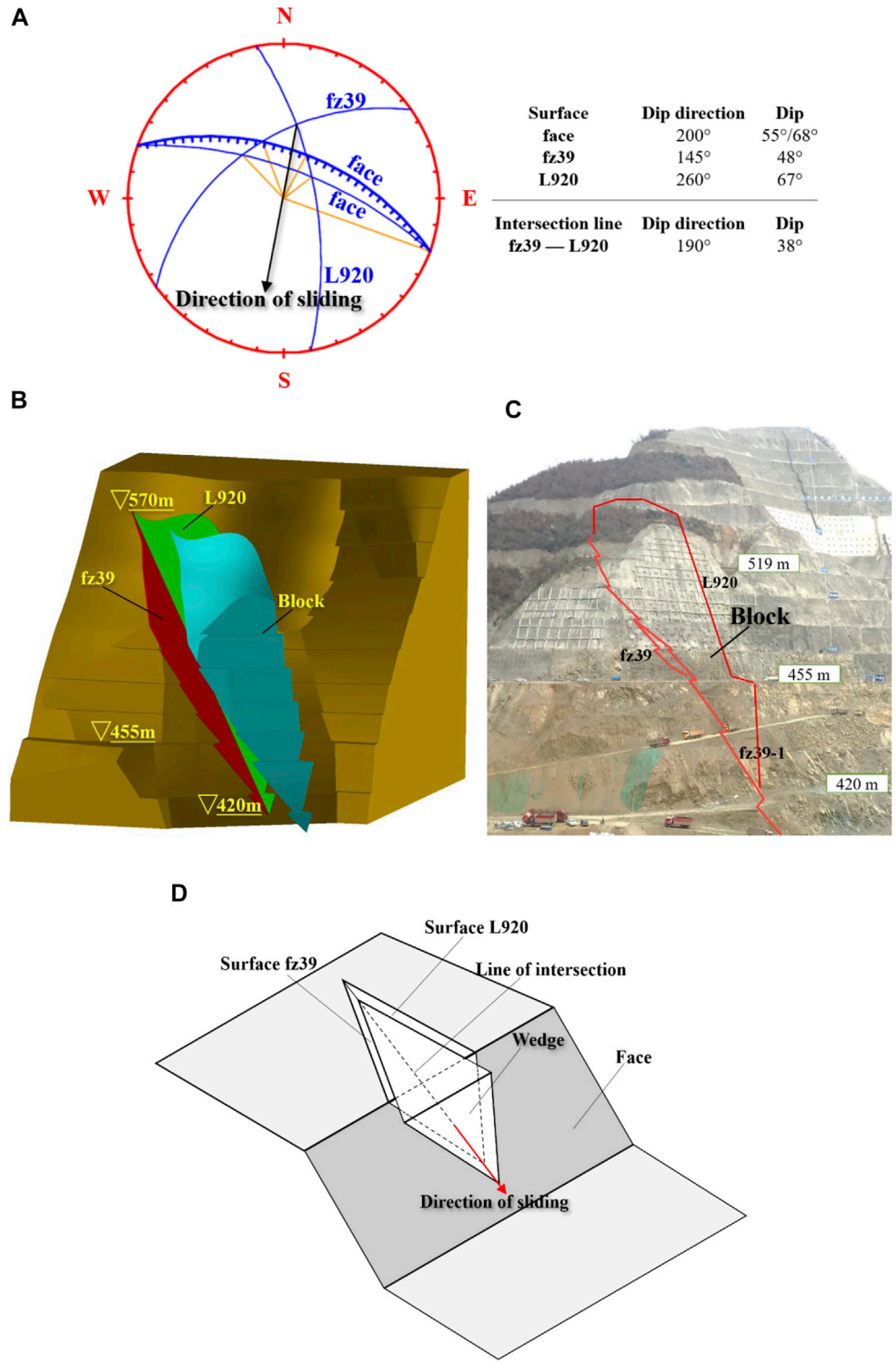

Surface	Dip direction	Dip
face	200°	55°/68°
fz39	145°	48°
L920	260°	67°
Intersection line	**Dip direction**	**Dip**
fz39 — L920	190°	38°

FIGURE 10 | Block KT21: **(A)** stereographic projection; **(B)** block shape; **(C)** block location; **(D)** wedge failure mode.

blasting time. The increments of multipoint displacement meters measured values ranged from 1.0 to 16.00 mm within 7 days after each blasting, which then gradually stabilized after excavation stopped. After the sixth blasting at the end of February 2019, the deformation rate was large in the first 3 days, and the maximum deformation rate of the orifice reached 5.74 mm/d (M18ZPR), 3.10 mm/d (M19ZPR), 4.87 mm/d (M20ZPR), 6.45 mm/d (M21ZPR), and 5.13 mm/d

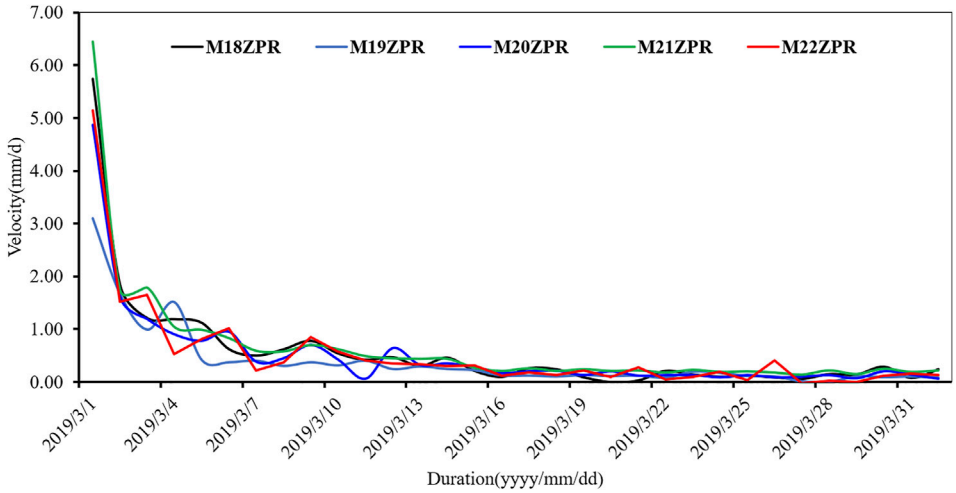

FIGURE 11 | Deformation rate after the sixth blasting.

(M22ZPR) (**Figure 11**). Then, the deformation rate gradually decreased. Certain fluctuations, however, did not fully converge, which indicated that the stress rebalancing adjustment time was long after blasting disturbances during slope excavation.

Rain

Rainfall also had a certain influence on deformation, according to monitoring data analysis, and the observed values of multipoint displacement meters rose slightly after rainfall. Fault fz39 had a certain water-blocking effect. Groundwater activity was strong in the poorly weathered rock mass above fault fz39 and below 470 m elevations. Groundwater had a shallow burial depth, with a horizontal depth of less than 30 m, which was the major enhanced drainage region.

Deformation Mechanism

The slope presented a typical wedge failure mode. Fault fz39 was the upstream slip surface A of the wedge, with poor properties and a relatively slow dip, which was the main controlling structural surface of the wedge. Fracture L920 and the same group of fractures were the downstream slip surface B of the wedge, which was a release surface of the wedge. The sliding direction was downward sliding along the intersection line of fz39 and L920. The deep-seated deformation of the excavation slope occurred at the junction of the wedge and bedrock, which was affected mainly by unfavorable geological structure surfaces, excavation unloading, and blasting vibration. With the excavation of the slope, fault fz39 was gradually revealed on the excavation face, and the supporting effect of the "locking section" at the foot of the slope was weakened. These factors contributed to a decrease in the overall bearing capacity of the slope. For the blasting near the area, because of the action of stress waves, the rock mass would deform under the instantaneous impact of the blasting power and collapsed locally, which generally was a local failure. For the blasting far area, such as the area near fault fz39, the stress wave evolved into a seismic wave. The original structural surfaces were dislocated or expanded by seismic inertia force, which reduced the shear performance of the rock mass structure. This kind of damage affected a wide spatial range and penetrated deep into the interior of the rock mass. As a result, when the seismic inertia force caused by the seismic wave reached a certain intensity, it may have contributed to dynamic instability.

REINFORCEMENT DESIGN AND NUMERICAL ANALYSIS OF THE SLOPE STABILITY

Reinforcement Support Measures

We established the reinforcement design scheme of unloading at the top of the slope and large-tonnage cables based on geological circumstances, deformation characteristics, site construction, and general project needs.

Unloading Measures

The unloading area had the lowest elevation of 519 m and the highest elevation of 637 m. Seven floors were dug in the unloading area. The overall slope ratio was one to one. The entire volume of the unloading area was around 107,400 m^3, with block KT21's capacity reduced by roughly 29,000 m^3.

Prestressed Cable Measures

On the slope with an elevation range of 502–470 m, 195 cables with tensile forces of 1,000–1,500 kN have been installed. Additionally, concrete slabs and three rows of wires (T = 2,700 kN) were placed on the slope between 485 and 470 m, concrete slabs and four rows of cables (T = 2,700 kN) were placed between 470 and 455 m, and concrete slabs and four

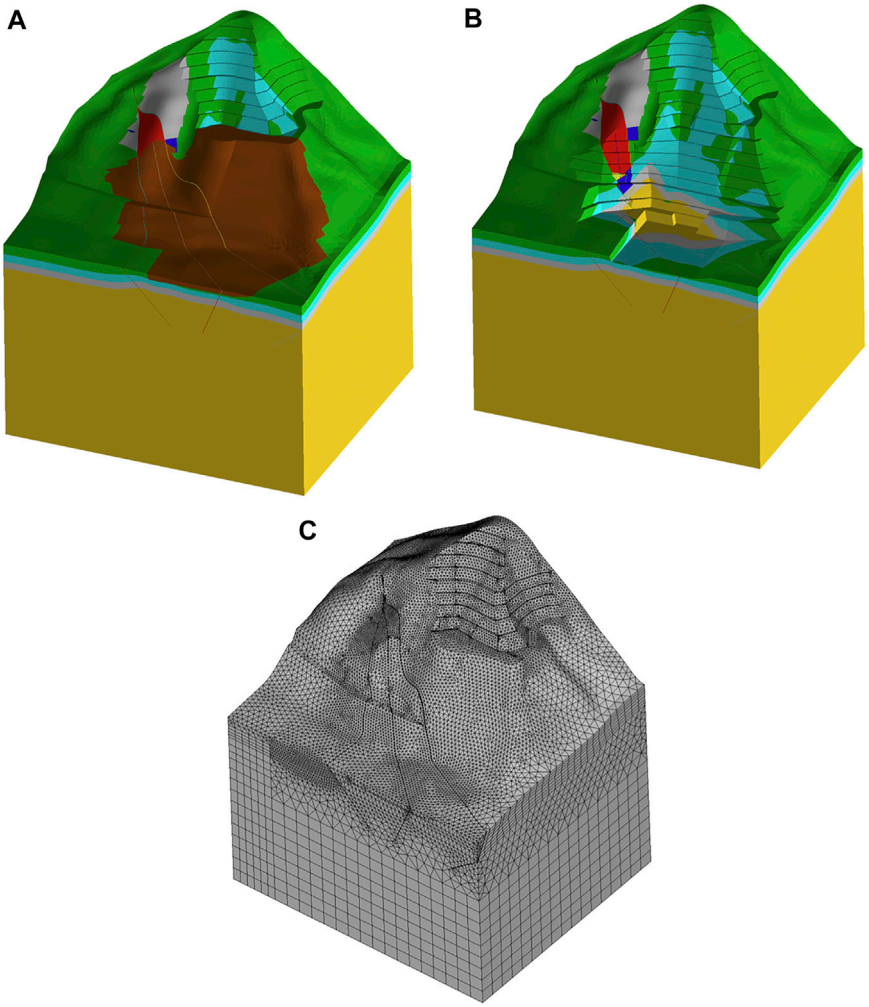

FIGURE 12 | Analysis model: **(A)** origin slope; **(B)** excavation slope; **(C)** mesh grid.

rows of cables (T = 2,700 kN) were placed between 455 and 429 m.

Drainage Measures

At altitudes of 455 m and 519 m, two draining adits were constructed, and 35 m deep drainage holes were installed at the top of the adit to lower groundwater levels.

Numerical Analysis of Slope Stability

The use of a numerical method to analyze the stability of rock slopes has wide applicability. This method not only can simulate the complex mechanical and structural characteristics of a rock mass but also can analyze various boundary value problems and construction processes as well as predict and forecast the project. We adopted the commercial software FLAC^{3D} for numerical calculations. First, we established a 3D numerical analysis model of the studied slope and simulated the current excavation state by combining forward and backward analysis. Second, we simulated the subsequent excavation and reinforcement process of the slope. Finally, we used the strength reduction method to calculate the stability safety factor of the slope under various working conditions during the construction period and operation period.

Numerical Analysis Models

The numerical analysis model of the slope is shown in **Figures 12A–C**; its dimensions were 600 × 500 × 700 m (X × Y × Z). The *X*-direction of the model was parallel to the water flow direction, and its positive direction pointed downstream. The *Y*-direction was consistent with the dam axis, and its positive direction pointed from the river valley to inside the mountain. The *Z*-direction was vertical, and its positive direction pointed upward. The mesh model was composed of 106,000 nodes and 585,600 elements.

The lithology of the slope stratigraphy was mainly diorite. Based on weathering characteristics of the rock mass, the model was divided into four zones from top to bottom: a strongly weathered zone, weakly weathered upper zone, weakly weathered lower zone and micro-neoliths. The geological

TABLE 1 | Mechanical parameters of slope rock mass and structural surfaces.

	Unit weight (kN/m^3)	Deformation modulus (GPa)	Poisson's ratio	Friction coefficient	Cohesion (MPa)
Strong weathering	26.50	0.50	0.32	0.45	0.15
Weakly weathered upper	28.20	4.50	0.27	0.85	0.80
Weakly weathered lower	28.40	6.50	0.26	1.00	0.90
Fresh rock mass	28.50	18.00	0.25	1.20	1.10
Fault fz39				0.25	0.02
Fracture L920				0.40	0.07

structure mainly considered six structural surfaces: faults fz39, fz46, and fz54, fractures L919 and L920, and dykes. In the model, the excavation area, unloading area, and cable measures were considered in the simulation of the excavation process of the slope.

The prestressed anchor cables were simulated using the structural element "cable" in flac3d, which considers the cable's axial tensile-compression properties, the contact properties of the cable-rock interface, and the magnitude of the prestress value.

Mechanical Parameters

The thickness of the strongly weathered zone on the slope was relatively large, generally 15–30 m. The rock mass was broken and mainly of a granular structure. Affected by blasting excavation, the strongly weathered rock mass was disturbed, and the strength of the rock mass decreased. According to the results of rock laboratory tests, *in situ* tests, and the development of structural surfaces, combined with the characteristics of the rock mass of the excavated slope, we proposed the main mechanical indexes (**Table 1**).

We concluded that structural surfaces fz39, L920, and their combined block were the controlling factors of slope stability, and the decrease of shear strength of the structural surfaces caused by blasting excavation was an important reason for deep-seated deformation. Therefore, the shear strength parameter of structural surfaces is a dynamic parameter, which is a key variable for slope stability analysis. According to macroscopic geological characterizations, fault fz39 is a weak structural surface of "mud with rock debris type," and fracture L920 is a structural surface of "rock block and rock debris with mud type." On this basis, we used the uniform design method for inversion and evaluation. The inversion analysis had two goals: 1) the incremental deformation values measured by the multipoint displacement meters; and 2) the current slope should be close to the critical state, and the safety factor of slope stability should be between 1.05 and 1.00. According to the inversion results, the cohesion of fault fz39 was 20 kPa, and the friction coefficient was 0.25; the cohesion of fracture L920 was 70 kPa, and the friction coefficient was 0.40.

Blast Vibration Load

Because of the large number of elements in the numerical model, the quasi-static method was utilized in this research to analyze the blasting vibration effect of slope equivalently. Define $\boldsymbol{a_i}$ as the corresponding static acceleration of blast vibration, the blasting vibration force of element $\boldsymbol{i}$ is $\boldsymbol{F_i} = \boldsymbol{m_i a_i}$, which is decomposed into the nodes of the element. Ultimately, the blasting vibration forces are applied to the numerical model as equivalent nodal forces. Taking into account the decreasing characteristics of the peak acceleration of blast vibration with distance from the blast source (Zheng et al., 2014), $\boldsymbol{a_i}$ can express as a function of position

$$\boldsymbol{a_i} = \boldsymbol{\beta_0 k}\left[\frac{\boldsymbol{Q}^{\frac{1}{3}}}{\sqrt{(\boldsymbol{x_i}-\boldsymbol{x_0})^2+(\boldsymbol{y_i}-\boldsymbol{y_0})^2+(\boldsymbol{z_i}-\boldsymbol{z_0})^2}}\right]^{\boldsymbol{\alpha}}\cdot\left(\frac{\boldsymbol{Q}^{\frac{1}{3}}}{|\boldsymbol{z_i}-\boldsymbol{z_0}|}\right)^{\boldsymbol{\beta}} \tag{1}$$

Where, (x_i, y_i, z_i) are the centroid coordinates of element $\boldsymbol{i}$, (x_0, y_0, z_0) are the coordinates of the blast source, and $\boldsymbol{Q}$ is the amount of detonating charge (kg), and $\boldsymbol{k}$ is a constant related to geological conditions, blasting parameters, and $\boldsymbol{\alpha}, \boldsymbol{\beta}$ are the decay index related to geological conditions, blasting parameters.

Numerical Analysis Results

We simulated the "excavation-support" process in which the slope was excavated at an elevation of 455 m using the structural surface mechanics parameters obtained from the inversion. The results better reflected the actual deformation behavior of the excavation slope. The areas with significant deformation were concentrated mainly in the range of block KT21, composed of structural surfaces fz39 and L920 (**Figure 13A**), and the deformation vectors were mainly downward along the slope (**Figure 13B**). When excavating the slope in the elevation range of 470–455 m, the deformation changed abruptly, with a growing range of 60.0–160.0 mm.

The distributions of the incremental shear strain on the excavation slope are shown in **Figures 14A–C**. When the slope was excavated above an elevation of 485 m, the shear strain concentration zones were distributed mainly in the structural surfaces fz39 and L920 in the middle of the slope, and there were no obvious deformation signs at this stage. When the slope was excavated at an elevation of 485–470 m, the shear strain concentration zones appeared on the excavation face, and deep shear strain concentration zones developed along the structural surfaces. At this stage, cracks appeared on the excavation face, and the deep parts of the slope began to deform. When the slope was excavated at an elevation range of 470–455 m, a shear strain concentration zone appeared at the front edge of the excavation slope, and the deep shear strain concentration zone had been penetrated, corresponding to local slippage at the front edge of the slope and a sudden change of the deep deformation.

On the basis of the current state of the excavation slope, we used the latest reinforcement support measures to simulate the

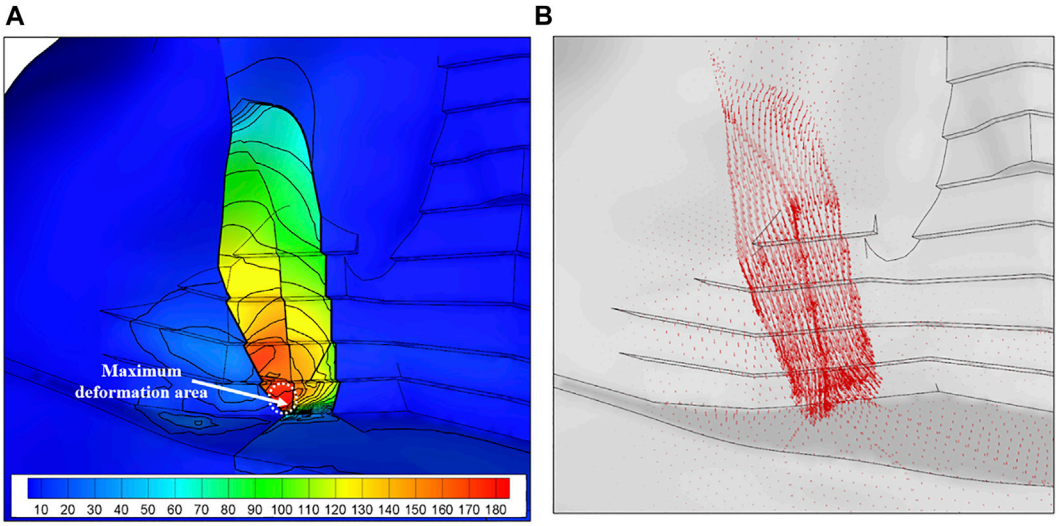

FIGURE 13 | Distribution of incremental displacement when excavating to elevation 455 m: **(A)** displacement; **(B)** displacement vector.

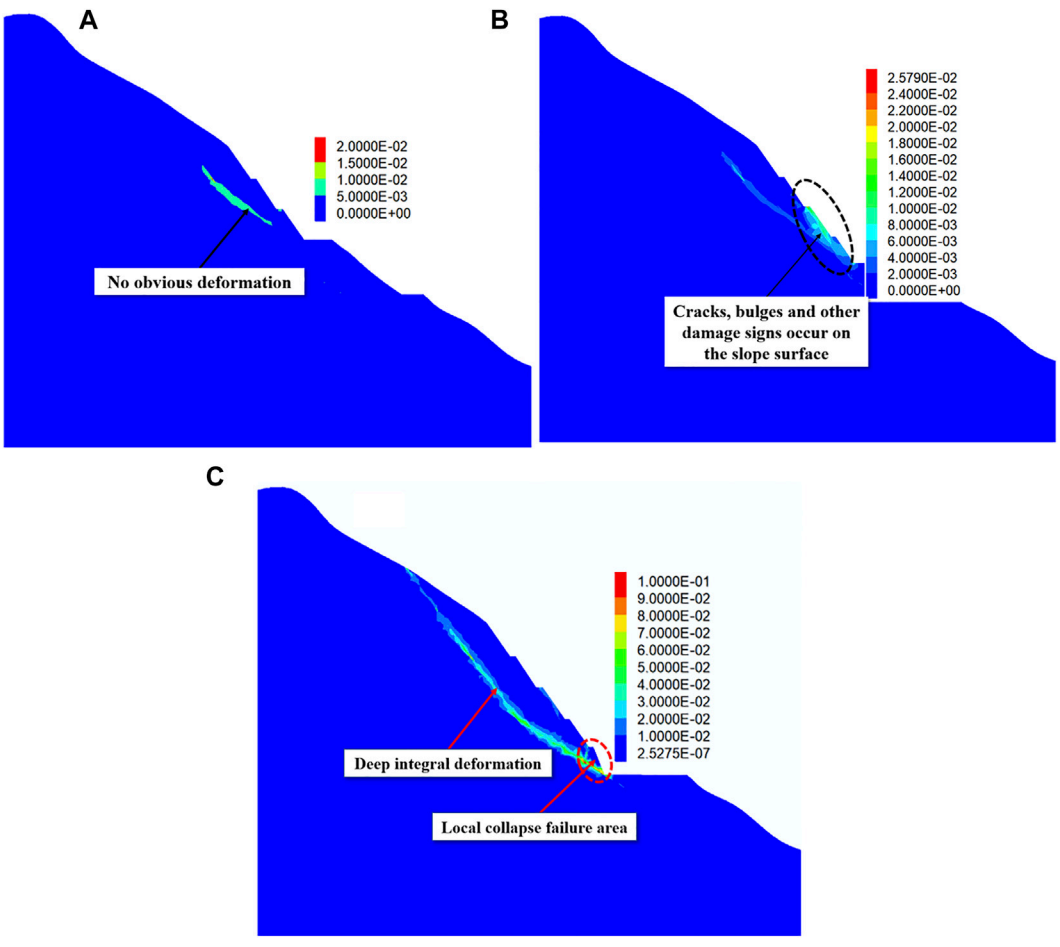

FIGURE 14 | Evolution law of shear strain zone: **(A)** elevation 485 m; **(B)** elevation 470 m; **(C)** elevation 455 m.

construction process of "unloading-support-excavation-support" for the subsequent slope. The results showed that the excavation of the slope below an elevation of 455 m had a limited influence on the reinforced upper slope. The incremental deformation of the excavation slope at an elevation range of 470–455 m was less than 10.0 mm, and the incremental deformation of the excavation slope above an elevation of 470 m was generally less than 5.0 mm. For the excavation of the slope below an elevation of 455 m, the maximum incremental deformation within block KT21 was approximately 50.0 mm, and the remaining parts generally were less than 20 mm.

The essence of sliding failure of the slope is an unstable failure caused by insufficient shear strength of the rock mass or structural surfaces. We used the strength reduction method to calculate the failure mode and stability safety factor of the slope. The results showed that 1) the failure mode is the sliding of the combined block of structural surfaces fz39 and L920 along the direction of the intersection line. 2) In the current state, the safety factor increased from 1.04 to 1.80 after the implementation of reinforcement measures, and the safety of the slope was significantly improved. 3) The safety factor when all excavation was completed was 1.74. 4) The safety factors during project's operation were between 1.50 and 1.70. In general, the efficacy of the reinforcing design measures was favorable, and the stability of the excavation slope was guaranteed.

DISCUSSIONS

We identified five consistent correspondences in the mechanical response of the slope rock mass. Deformation depth corresponded to the buried depth of structural surfaces. The significant deformation region corresponded to the cracking failure on the slope surface. The region with the most deformation was also the area with the most cable force. The stepwise growth of slope deformation was consistent with nearby blasting. The obvious increase in deformation was consistent with a significant rainfall. This relationship of the excavation slope occurred mostly within the range of structural surfaces fz39 and L920, demonstrating the existence of the block. Block KT21 was the key to controlling the stability of the whole slope.

Fault fz39 was the controlling structural surface for slope stability. Identifying the extension and development of fault fz39 in the slope was essential for further understanding the damage range, stability analysis, and reinforcement design. During the construction period, in-hole video recording and acoustic testing were conducted on the boreholes, multipoint displacement meter holes, and cable holes. We determined the distribution characteristics of fault fz39 according to the presence of acoustic anomalies, collapse phenomena, or developed structural surfaces in the test holes. The length and arrangement scheme of cables initially were determined based on the distribution of the structural surfaces. Then, to ensure the slope's stability, the tension and quantity of cables were calculated based on the numerical analysis results.

The impact of excavation blast is frequently disregarded from slope stability analysis during the slope design stage. For this project, however, the influence of blasting on the slope was no longer local but instead had extended to the deep part of the slope. The deformation increased stepwise with the blasting excavation of the slope near the fault. It also increased significantly compared with that without blasting, particularly through the structural surfaces fz39 and L920. Rock excavation and blasting is a complex process, and present understanding of the blasting and crushing mechanisms of rock is limited. Controlling blasting vibration to ensure the safety of the slope is a challenge that must be addressed for this type of structural surface-controlled slope.

CONCLUSION

In this paper, we presented a case study of large deep-seated deformation during slope excavation. The study focused on the geological conditions, the deformation and failure characteristics during the slope excavation process, and the attempts made to enhance slope stability. The following insights and conclusions can be noted:

1. Based on real-time monitoring information, the main deformation of the excavation slope was divided into three stages, and each stage corresponded to the process of "excavation–deformation–analysis and demonstration–reinforcement design–deformation convergence." The main deformation range and depth coincided with the position of the structural surfaces fz39 and L920.
2. The block formed by fault fz39 and fracture L920 was a typical wedge failure mode, which had primary control over the stability of the slope. With the excavation of the slope, fault fz39 gradually was revealed on the excavation face, and the supporting effect of the "locking section" at the foot of the slope was weakened. The repeated vibration of blasting reduced the mechanical strength of the structural surfaces and the overall shear performance of the rock mass structure.
3. The principle of reinforcement is to reasonably increase the density, length, and tension of cables in combination with the buried depth and distribution of structural surfaces. Combined with the shape of block KT21, which is "wide at the top and narrow at the bottom, top-heavy" the sliding force of the block was reduced by unloading at the top of the excavation slope. The excavation must be stopped before the adjustment of slope foot reinforcements. In the process of excavation, it is necessary to reduce the charge of single holes, strictly control the blasting intensity, and dynamically adjust by sections and sequences.
4. At present, the slope has experienced several obvious deformation growth processes. The incremental deformation was used to invert the mechanical parameters of the structural surface. The numerical analysis results obtained were in good agreement with the monitoring data. The efficacy of the reinforcing design measures was favorable, and the stability of the excavation slope was guaranteed.

With the implementation of unloading on the natural slope and cable tensioning, the deformation rate of the measured values tended to converge, no new cracks appeared on the slope surface, and the existing failure parts, such as bulging and cracks, did not significantly develop.

DATA AVAILABILITY STATEMENT

The original contributions presented in the study are included in the article/Supplementary Material, further inquiries can be directed to the corresponding author.

AUTHOR CONTRIBUTIONS

All authors listed have made a substantial, direct, and intellectual contribution to the work and approved it for publication.

FUNDING

The research was funded by the National Key Research and Development Project of China (Grant No. 2017YFC1501305) and the National Natural Science Foundation of China (Grant No. 41807249).

REFERENCES

Chen, Z. Y., Mi, H. L., and Wang, X. G. (2001). A Three-Dimensional Limit Equilibrium Method for Slope Stability Analysis. *Chin. J. Geotechnical Eng.* 36 (07), 1579–1587. doi:10.3321/j.issn:1000-4548.2001.05.001

Dai, Z. H. (2002). Study on Distribution Laws of Landslide-Thrust and Resistance of Sliding Mass Acting on Antislide Piles. *Chin. J. Rock Mech. Eng.* 4, 517–521. doi:10.3321/j.issn:1000-6915.2002.04.013

Dawson, E. M., Roth, W. H., and Drescher, A. (1999). Slope Stability Analysis by Strength Reduction. *Géotechnique* 49 (6), 835–840. doi:10.1680/geot.1999.49.6.835

De Blasio, F. V. (2011). *Introduction to the Physics of Landslides: Lecture Notes on the Dynamics of Mass Wasting*. Berlin: Springer Science & Business Media.

Donald, I. B., and Chen, Z. (1997). Slope Stability Analysis by the Upper Bound Approach: Fundamentals and Methods. *Can. Geotech. J.* 34 (6), 853–862. doi:10.1139/t97-061

Dong, Z. H., Ding, X. L., Li, Q. J., Yu, S. X., and Lu, B. (2013). Numerical Simulation of High Slope Stability of in Construction Period at Dabenliugou Quarry in Construction Period. *Yangtze River* 14, 13–17. doi:10.16232/j.cnki.1001-4179.2013.14.008

Ersmann, T. H. (1979). Mechanisms of Large Landslides. *Rock Mech.* 12, 15–46. doi:10.1007/BF01241087

Ersöz, T., and Topal, T. (2018). Assessment of Rock Slope Stability with the Effects of Weathering and Excavation by Comparing Deterministic Methods and Slope Stability Probability Classification (SSPC). *Environ. Earth Sci.* 77 (14), 1–18. doi:10.1007/s12665-018-7728-4

Ge, X. R., and Liu, J. W. (1988). Study on the Shear Resistance Behaviour of Bolted Rock Joints. *Chin. J. Geotechnical Eng.* 10 (1), 8–19. doi:10.3321/j.issn:1000-4548.1988.01.002

Giani, G. P. (1992). *Rock Slope Stability Analysis*. Boca Raton: CRC Press.

Gu, J. C., Shen, J., Chen, A. M., and Ming, Z. P. (2000). Damage Tests of Pre-Stressed Anchor Bars in Corrosion Environment. *Chin. J. Rock Mech. Eng.* S1, 917–921. doi:10.3321/j.issn:1000-6915.2000.z1.021

Ha, Q. L. (1997). Rock Slope Engineering and Unloading Nonlinear Rock Mass Mechanics. *Chin. J. Rock Mech. Eng.* 4, 386–391. doi:10.3321/j.issn:1000-6915.2008.11.006

Hu, Y., Lu, W., Wu, X., Liu, M., and Li, P. (2018). Numerical and Experimental Investigation of Blasting Damage Control of a High Rock Slope in a Deep valley. *Eng. Geology.* 237, 12–20. doi:10.1016/j.enggeo.2018.01.003

Huang, R. Q. (2007). Large-Scale Landslides and Their Sliding Mechanisms in China since the 20th Century. *Chin. J. Rock Mech. Eng.* 3, 433–454. doi:10.3321/j.issn:1000-6915.2007.03.001

Huang, R. Q. (2008). Geodynamical Process and Stability Control of High Rock Slope Development. *Chin. J. Rock Mech. Eng.* 8, 1525–1544. doi:10.3321/j.issn:1000-6915.2008.08.002

Li, S. C. (2010). *Failure Mechanism and Engineering Application of Anchored Intermittent Jointed Rock Mass*. Beijing: Science Press.

Liu, J. J. (1990). Collapse Process and Cause Analysis of Left Bank Slope of Manwan Hydropower Station. *Yunnan Water Power* 2, 31–37.

Liu, M. S. (2007). The Excavation Blasting Technique of Particularly High and Steep Slope and the Influence on its Stability. Ph.D. Hefei: University of science and technology of China.

Lu, W. B., Zhou, C. B., Chen, M., Jin, L., and Yan, P. (2008). Research on Transient Characteristics of Excavation Unloading. *Chin. J. Rock Mech. Eng.* 11, 2184–2192. doi:10.3321/j.issn:1000-6915.2008.11.003

Lu, W.-B., Hu, Y.-G., Yang, J.-H., Chen, M., and Yan, P. (2013). Spatial Distribution of Excavation Induced Damage Zone of High Rock Slope. *Int. J. Rock Mech. Mining Sci.* 64, 181–191. doi:10.1016/j.ijrmms.2013.08.030

Mantovani, F., and Vita-Finzi, C. (2003). Neotectonics of the Vajont Dam Site. *Geomorphology* 54 (1-2), 33–37. doi:10.1016/S0169-555X(03)00053-9

Onederra, I. A., Furtney, J. K., Sellers, E., and Iverson, S. (2013). Modelling Blast Induced Damage from a Fully Coupled Explosive Charge. *Int. J. Rock Mech. Mining Sci.* 58, 73–84. doi:10.1016/j.ijrmms.2012.10.004

Petley, D. N., and Allison, R. J. (1997). The Mechanics of Deep-Seated Landslides. *Earth Surf. Process. Landf* 22, 747–758. doi:10.1002/(SICI)1096-9837(199708)22:83.3.CO;2-R

Petley, D. N., Mantovani, F., Bulmer, M. H., and Zannoni, A. (2005). The Use of Surface Monitoring Data for the Interpretation of Landslide Movement Patterns. *Geomorphology* 66 (1-4), 133–147. doi:10.1016/j.geomorph.2004.09.011

Qiao, J. P. (2002). Structure and Shape of Landslide. *Chin. J. Rock Mech. Eng.* 9, 1355–1358. doi:10.3321/j.issn:1000-6915.2002.09.015

Qin, B. M., Tang, B., Zhang, L. P., and Xu, B. T. (2022). Influence of Slope Excavation on Stability of Wedge-Shaped Rock Block. *Jiangsu Water Resour.* 1, 5–9. doi:10.16310/j.cnki.jssl.2022.01.004

Segalini, A., and Giani, G. P. (2004). Numerical Model for the Analysis of the Evolution Mechanisms of the Grossgufer Rock Slide. *Rock Mech. Rock Eng.* 37 (2), 151–168. doi:10.1007/s00603-003-0016-x

Sheng, Q., Ding, X. L., Feng, X. T., and Zhang, Z. Q. (2000). Displacement Back Analysis for the High Slope of the Three Gorges Project Considering the Effect of Excavation Unloading. *Chin. J. Rock Mech. Eng.* 19 (z1, 987–993. doi:10.3321/j.issn:1000-6915.2000.z1.036

Wang, M. Y., and Qian, Q. H. (1995). Attenuation Law of Explosive Wave Propagation in Cracks. *Chin. J. Geotechnical Eng.* 2, 42–46. doi:10.1007/BF02943584

Wei, Z. A., Li, S. H., Wang, J. G., and Wan, L. (2006). A Dynamic Comprehensive Method for Landslide. *control. Eng. geol.* 84 (1-2), 1–11. doi:10.1016/j.enggeo.2005.09.019

Wyllie, D. C., and Mah, C. (2004). *Rock Slope Engineering*. Boca Raton: CRC Press.

Xia, Q. F., and Lu, J. Y. (1986). Analysis of the Causes of Landslides at the Tianshengqiao II Hydropower Station Site. *Bull. Soil Water Consery.* 4, 35–40. doi:10.13961/j.cnki.stbctb.1986.04.009

Yang, Y., Sun, G., Zheng, H., and Qi, Y. (2019). Investigation of the Sequential Excavation of a Soil-Rock-Mixture Slope Using the Numerical Manifold Method. *Eng. Geology.* 256, 93–109. doi:10.1016/j.enggeo.2019.05.005

Yang, Y., Sun, G., Zheng, H., and Yan, C. (2020a). An Improved Numerical Manifold Method with Multiple Layers of Mathematical Cover Systems for the Stability Analysis of Soil-Rock-Mixture Slopes. *Eng. Geology.* 264, 105373. doi:10.1016/j.enggeo.2019.105373

Yang, Y., Xu, D., Liu, F., and Zheng, H. (2020b). Modeling the Entire Progressive Failure Process of Rock Slopes Using a Strength-Based Criterion. *Comput. Geotechnics* 126, 103726. doi:10.1016/j.compgeo.2020.103726

Yang, Y., Wu, W., and Zheng, H. (2021a). Stability Analysis of Slopes Using the Vector Sum Numerical Manifold Method. *Bull. Eng. Geol. Environ.* 80 (1), 345–352. doi:10.1007/s10064-020-01903-x

Yang, Y., Wu, W., and Zheng, H. (2021b). An Uzawa-Type Augmented Lagrangian Numerical Manifold Method for Frictional Discontinuities in Rock Masses. *Int. J. Rock Mech. Mining Sci.* 148, 104970. doi:10.1016/j.ijrmms.2021.104970

Yang, Y., Xia, Y., Zheng, H., and Liu, Z. (2021c). Investigation of Rock Slope Stability Using a 3D Nonlinear Strength-Reduction Numerical Manifold Method. *Eng. Geology.* 292, 106285. doi:10.1016/j.enggeo.2021.106285

Zhang, Y. L., Feng, X. T., Fan, J. H., and Fang, X. R. (2002). Study on the Interaction between Landslide and Passive Piles. *Chin. J. Rock Mech. Eng.* 6, 839–842. doi:10.3321/j.issn:1000-6915.2002.06.015

Zheng, Y. R., and Zhao, S. Y. (2004). Application of Strength Reduction Fem in Soil and Rock Slope. *Chin. J. Rock Mech. Eng.* 19, 3381–3388. doi:10.3321/j.issn:1000-4548.2001.05.001

Zheng, Y., Chen, C. X., Zhu, X. X., Pan, Z. Y., Ou, Z., Zhou, Y. C., et al. (2014). Node Quasi-Static Stability Analysis of Rock Slope under Excavation Blasting Based on UDEC. *Chin. J. Rock Mech. Eng.* 33 (s2), 3932–3940. doi:10.13722/j.cnki.jrme.2014.s2.068

Zheng, H., Yang, Y., and Shi, G. (2019). Reformulation of Dynamic Crack Propagation Using the Numerical Manifold Method. *Eng. Anal. Boundary Elem.* 105, 279–295. doi:10.1016/j.enganabound.2019.04.023

Zheng, H. (2007). A Rigorous Three-Dimensional Limit Equilibrium Method. *Chin. J. Rock Mech. Eng.* 8, 1529–1537. doi:10.3321/j.issn:1000-6915.2007.08.002

Zhou, H. M., Sheng, Q., Li, W. S., and Xiao, G. Q. (2004). Excavation-Disturbed Zone and Weaken Degree of Mechanical Properties for Rockmass of TGP Shiplock Slope. *Chin. J. Rock Mech. Eng.* 7, 1078–1081. doi:10.3321/j.issn:1000-6915.2004.07.004

Zhou, Y. (2015). Stability Improvement of Left Bank Slope of Toppling and Creeping Rock Mass of Longtan Hydropower Station. *Hongshui River* 1, 16–21. doi:10.3969/j.issn.1001-408X.2015.01.005

Zhu, D. Y., and Qian, Q. H. (2007). Rigorous and Quasi-Rigorous Limit Equilibrium Solutions of 3D Slope Stability and Application to Engineering. *Chin. J. Rock Mech. Eng.* 8, 1513–1528. doi:10.3321/j.issn:1000-6915.2007.08.001

Zhu, J. B., Li, C., Liu, Z. J., Wang, B., Jiang, Y. Z., Liu, X. H., et al. (2017). Damage Tests of Pre-Stressed Anchor Bars in Corrosion Environment. *Chin. J. Rock Mech. Eng.* 36 (07), 1579–1587. doi:10.13722/j.cnki.jrme.2016.1097

Zhu, C., He, M., Karakus, M., Zhang, X., and Tao, Z. (2021). Numerical Simulations of the Failure Process of Anaclinal Slope Physical Model and Control Mechanism of Negative Poisson's Ratio cable. *Bull. Eng. Geol. Environ.* 80 (4), 3365–3380. doi:10.1007/s10064-021-02148-y

Conflict of Interest: The authors declare that the research was conducted in the absence of any commercial or financial relationships that could be construed as a potential conflict of interest.

The reviewer DX declared a shared affiliation with several of the authors XD, SH to the handling editor at time of review

Publisher's Note: All claims expressed in this article are solely those of the authors and do not necessarily represent those of their affiliated organizations, or those of the publisher, the editors and the reviewers. Any product that may be evaluated in this article, or claim that may be made by its manufacturer, is not guaranteed or endorsed by the publisher.

frontiers in Earth Science

ORIGINAL RESEARCH
published: 15 March 2022
doi: 10.3389/feart.2022.865697

Shear Strength Characteristics of Clay-Gravel Layer and Its Slope Failure Law and Mechanism

Zhangjun Dai[1], Kang Huang[1,2], Lingfa Jiang[1], Jian Li[1], Fei Yu[1] and Shanxiong Chen[1]*

[1]State Key Laboratory of Geomechanics and Geotechnical Engineering, Institute of Rock and Soil Mechanics, Chinese Academy of Sciences, Wuhan, China, [2]University of Chinese Academy of Sciences, Beijing, China

The Anqing Formation clay-gravel layer is widely distributed in the Anqing area of the upper reaches of the Wanjiang River. It is a typical soil-rock mixture composed of gravel and clay. The poor engineering properties of the clay-gravel layer are the main factors for the failure of the slope. On the basis of regional geological survey, the clay-gravel threshold, clay mineral composition and cementation characteristics of clay-gravel layer were studied. The *in-situ* horizontal push-shear tests under different gravel content, water environment and overlying load were designed and carried out, and its shear failure mode and strength were analyzed. The study found that the shear zone was in the shape of a broken line and was controlled by the particle size and distribution of the gravel. The shear strength of the clay-gravel layer is relatively high in the natural state due to the structure of the gravel and the friction and cementation force between the clay and the gravel. Water had the greatest influence on the shear strength of the clay-gravel layer, and the overlying load affected its shear strength within a certain range. The indoor rainfall erosion model test of the clay-gravel slope was carried out, and the failure and instability modes and mechanisms of the slope with different gravel contents were studied. When the gravel content was 30%, the failure of the slope surface was the development of gullies. The erosion damage process was similar to the soil slope. When the gravel content was 50%, affected by the distribution of gravel, the slope failure was manifested as the development of erosion pits, followed by local slumps, and finally the overall sliding in layers. When the gravel content was 70%, the clay particles on the slope were quickly washed away by the water flow, and the gravel skeleton of the slope formed a temporary relatively stable structure. After being disturbed, the gravel layer collapsed as a whole.

Keywords: clay-gravel layer, shear zone, shear strength, slope erosion, failure mechanism

OPEN ACCESS

Edited by:
Tingting Liu,
Wuhan University of Technology, China

Reviewed by:
XM Li,
Zhongyuan University of Technology, China
Li Wei,
China University of Geosciences Wuhan, China

****Correspondence:***
Zhangjun Dai
zjdai@whrsm.ac.cn

Specialty section:
This article was submitted to Geohazards and Georisks, a section of the journal Frontiers in Earth Science

Received: *30 January 2022*
Accepted: *22 February 2022*
Published: *15 March 2022*

Citation:
Dai Z, Huang K, Jiang L, Li J, Yu F and Chen S (2022) Shear Strength Characteristics of Clay-Gravel Layer and Its Slope Failure Law and Mechanism. Front. Earth Sci. 10:865697. doi: 10.3389/feart.2022.865697

INTRODUCTION

The unique diagenetic environment in the upper reaches of the Wanjiang River, coupled with the special topographical features and tectonic environment, determine the unique engineering attributes of the strata in this area. The Anqing Formation clay-gravel layer is widely distributed in the Anqing section along the upper reaches of the Wanjiang River. It is a set of Neogene to Early Pleistocene clay and gravel alluvial strata. It is composed of gravel as aggregate and clay as filler, which is a special river alluvial soil-rock mixture. Soil-rock mixture is a heterogeneous, discontinuous, complex and irregular geological body (You and Tang, 2002; Hu et al., 2020).

The engineering geological characteristics and mechanical properties of soil-rock mixtures of different regions, origins and types are quite different (Jin et al., 2017; Xia et al., 2017). The poor engineering properties of the Anqing Formation clay-gravel layer are the main factors that cause the instability and failure of engineering structures, and determine the instability deformation mechanism and failure mode of the slope to a large extent.

Many researchers have carried out a series of experimental and numerical simulation studies around the soil-rock mixture. Tang et al. (2018) used a large-scale single-shear tester to study the effect of rock content on the shear characteristics of soil-rock mixtures. Tao et al. (2019) studied the mechanical properties of soil-rock mixture under different rock content, water content and rock integrity through large-scale triaxial shear tests, and used Duncan-Zhang model to invert the parameters of the triaxial test. Chen et al. (2020) used the particle discrete element method to establish a mesoscopic model of particle flow in a soil-rock mixed slope, and discussed the influence of the mesoscopic structure on the development of the slip surface and the stability of the slope. However, the environment and stress conditions of the samples in the above studies are very different from those in the field, and it is difficult to reflect a more realistic deformation mechanism, strength characteristics and failure mode. Wang et al. (2016) studied the horizontal push-shear test of soil-rock mixed-fill foundation under different water environments, and concluded that saturated water immersion has a great influence on the shear surface, shear strength and push-shear deformation process. Xu and Hu (2008) carried out cyclic loading and unloading tests using a large-scale field horizontal shear tester, and achieved some meaningful results in deepening the study of soil-rock mixture and the deformation and failure mechanism of soil-rock mixture slopes. These studies have made some important progress in the strength characteristics and failure modes of soil-rock mixtures by carrying out *in-situ* tests, but the designed single-factor tests are difficult to fully reflect the engineering properties of soil-rock mixtures under the influence of complex on-site environments, and the engineering properties of soil-rock mixtures of different origins and types are significantly different. In the Anqing Formation clay-gravel layer, the gravel content is high, the gravel surface is smooth, the roundness is high, and the super-sized gravel content is small, which is relatively uniform on the whole. The matrix of the clay-gravel layer is mostly clay, and there is a certain bonding force between the clay and the gravel. In the natural state, the stratum can maintain a certain strength and has a high stability, but when it is disturbed or the environmental conditions change, the bonding ability is significantly reduced., and the engineering stability will also be greatly affected (Nie et al., 2012; Qian et al., 2017).

Under rainfall conditions, the Anqing Formation clay-gravel layer slope undergoes various degrees of erosion damage, which in turn leads to slope instability and landslides. At present, researchers have carried out many studies on geotechnical erosion, including the influence of rainfall intensity and slope on slope rill development and rill characteristics (De Vente and Poesen, 2005; Govers et al., 2007), the complexity of rill network development (Bryan and Rockwell, 1998; Mancilla et al., 2005), as well as representative indicators of rill development, such as rill head extension time, average head erosion rate, etc. (Shen et al., 2019). In addition, the slope velocity is an important parameter reflecting the erosion process of slope rill under rainfall conditions (Zhao et al., 2018), which plays an important role in studying the dynamic mechanism of slope rill erosion (An et al., 2012). Song (2013) conducted an indoor simulated scour test on a loess slope in western Liaoning, and discussed the changes of slope displacement and moisture content during the failure process of the slope based on finite element and particle flow methods. Ren (2017) carried out scouring failure tests on the disperse soil slope in Jilin with different initial moisture content, salt content, compaction degree and slope, and found that the process of scouring and erosion damage of the disperse soil slope was divided into three stages. These research results lay the foundation for the study of the failure mechanism of the Anqing Formation clay-gravel layer slope.

In this paper, the poor engineering geological characteristics of the Anqing Formation clay-gravel layer were studied, and the *in-situ* horizontal shear tests of the clay-gravel layer under the combined action of different gravel content, water environment and overlying load were designed and carried out, and its shear failure mode and strength were analyzed. The effects of various factors, especially water and load, on the strength properties of the clay-gravel layer were explored. The indoor rainfall erosion model test of the clay-gravel slope was carried out, and the failure and instability modes and mechanisms of the slope with different gravel contents were studied. The research can provide a theoretical basis for the protection and treatment of clay-gravel layer slopes.

MATERIALS

Distribution Area and Geological Characteristics

The Anqing Formation clay-gravel layers from Neogene to Quaternary Early Pleistocene are mainly distributed along the Anqing area of the Yangtze River, and are mostly located on the highest terraces (mostly on the upper part of the base terraces), that is, the fourth-order terrace, and some are exposed in the third-order or the second-order terrace. The stratum is of river alluvial type, mainly including Anqing gravel layer and Wangjiang gravel layer. It is yellow and grayish-yellow, with a layer thickness of 10–20 m, and the main lithology is sand and gravel layer sandwiched with clay. The gravel diameter is 2–7 cm, the gravel content is 55–75%, the roundness is mainly sub-circular, and the sorting performance is average. The gravel composition is mainly quartz gravel, followed by quartz sandstone gravel, siliceous gravel, jade flint and limestone. The *in-situ* test and sampling site is located in Wangjiang County, west of the urban area of Anqing City, which is a diverse natural ecological environment and hilly area in the Yangtze River Basin. The distribution area and typical section of the clay-gravel layer are shown in **Figure 1**. The natural density of the clay-gravel layer is 1.87–2.11 g/cm^3, the permeability coefficient is 5×10^{-5}–2×10^{-4} cm/s, the natural moisture content of the clay

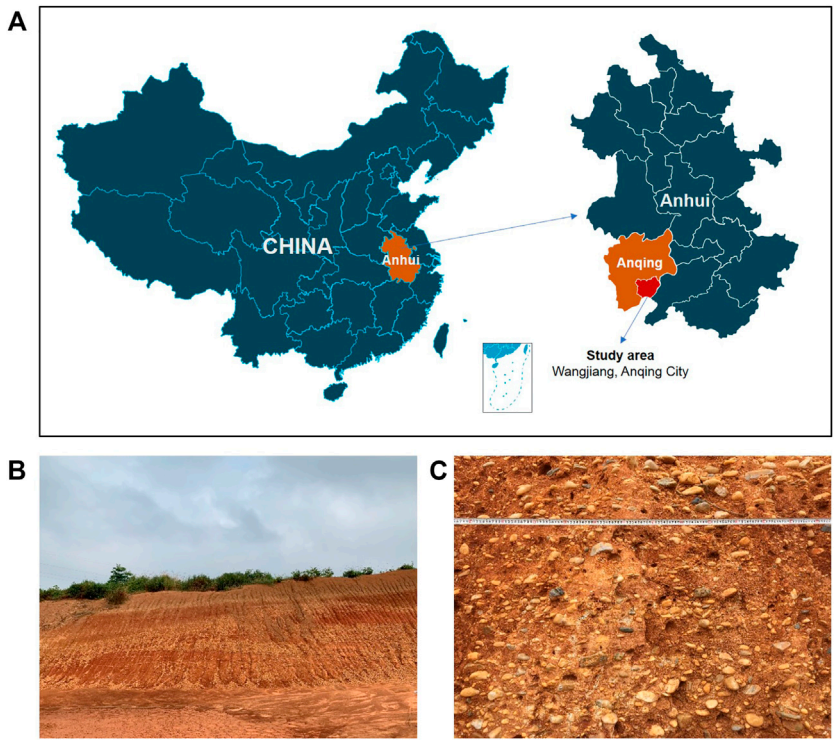

FIGURE 1 | Distribution area and typical profile of Anqing Formation clay-gravel layer **(A)** distribution area **(B)** slope **(C)** typical profile.

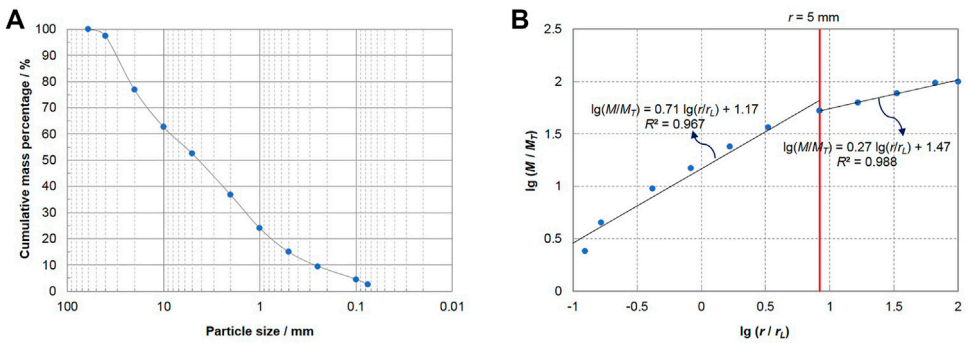

FIGURE 2 | Clay-gravel particle size fractal and clay-gravel threshold **(A)** particle size distribution curve **(B)** clay-gravel threshold.

is 12.59%, the plastic limit is 24.3%, and the liquid limit is 47.4%.

Clay-Gravel Threshold

The clay-gravel layer is composed of gravel and clay with different particle sizes. When carrying out model tests and field tests related to the content of gravel, the clay-gravel threshold should be determined first, that is, a characteristic particle size should be determined, larger than which is gravel, and smaller is clay. Medley (2001) believed that in different research scales, the particle size distribution of soil-rock mixture satisfies self-similarity, and proposed a conceptual model of soil-rock threshold and rock content. The clay-gravel threshold is obtained by fractal geometry. The fractal structure equation of particle mass distribution is as follows (Mandelbrot 1977; Wang and Li, 2015).

$$\frac{M(d<r)}{M_T} = \left(\frac{r}{r_L}\right)^{3-D} \tag{1}$$

Here, r represents the particle size; d represents the radius of the particle; D represents the fractal dimension; M_T represent the total mass; r_L represent the maximum particle size; $M(d<r)$ refers to the total mass with the particle size $d<r$, respectively.

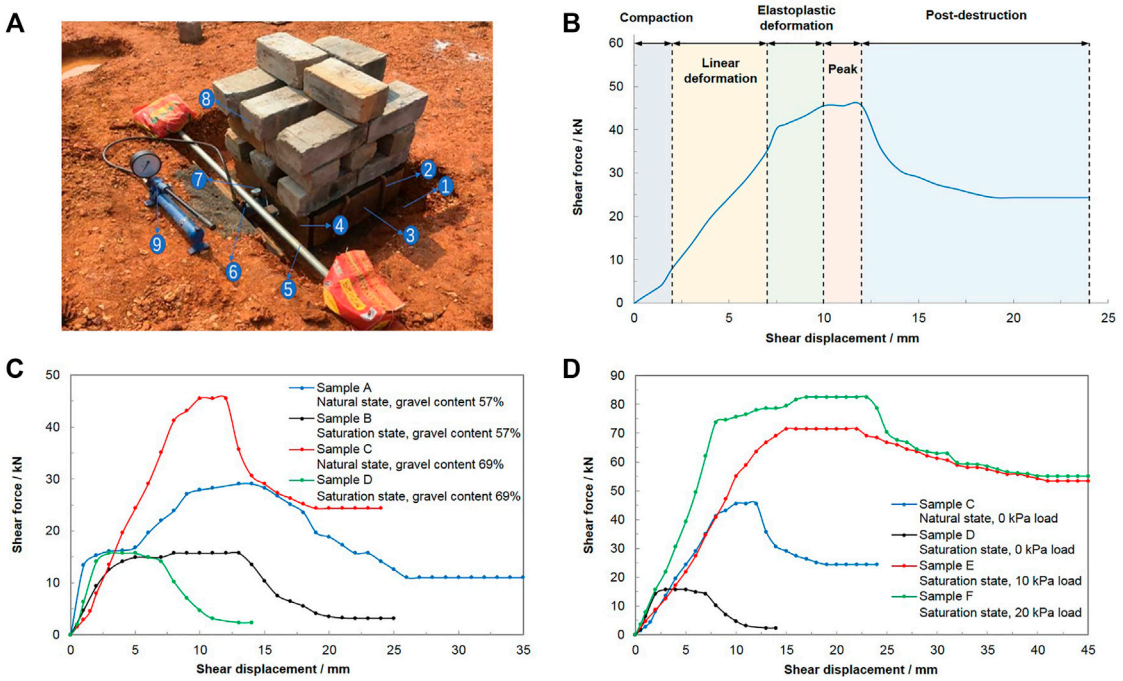

FIGURE 3 | *In-situ* horizontal push-shear test **(A)** test device (1-Test pit, 2-Steel drill, 3-Limit steel plate, 4-Thrust steel plate, 5-Reference beam, 6-Horizontal loading jack, 7-Dial indicator, 8-Load, 9-Pressure pump) **(B)** stages of a typical curve **(C)** the curves under different gravel contents and water environments **(D)** the curves under different water environments and overlying loads.

The fractal dimension of the average gradation obtained by the particle test was calculated. **Figure 2** shows the particle size distribution curve and the double logarithmic coordinate curve of the cumulative mass percentage and particle size. It can be seen that for the clay-gravel layer, the fitted particle size distribution curve is not a single linear at this research scale, but a piecewise linear relationship. Taking the particle size $r = 5$ mm as the dividing point, there is a strict scale-free interval on the left and right sides, the corresponding fractal dimensions are $D_1 = 2.3$ and $D_2 = 2.7$, respectively. It shows that the particle size distribution of the clay-gravel layer has a bifractal structure, that is, the clay-gravel threshold is $r = 5$ mm.

Composition of Clay Minerals

The clay and gravel in the clay-gravel layer were physically separated, and the separated clay was prepared into oriented sheets for XRD experiments. The illite/montmorillonite (I/S) mixed-layer ratio of the samples was tested using EG flakes treated with ethylene glycol (Zhu 1995). The test results show that the main clay minerals in the clay-gravel layer are kaolinite, illite and I/S mixed-layer. The average content of clay minerals in the clay of the clay-gravel layer is 29%, of which illite accounts for 3.99%, kaolinite accounts for 13.86%, I/S mixed-layer accounts for 11.16%, and the I/S mixed-layer ratio is 55.06%.

Clay and Gravel Cementation

Common cements formed by precipitation during freshwater diagenesis are divided into vadose zone fabrics and subcurrent zone fabrics. In the osmotic layer, due to the local contact of the particles with water, suspended microdroplet cements are generally formed on the underside of the particles; while in the subsurface layer, due to complete saturation, the distribution of the cements is relatively uniform (Qian et al., 2017).

For the cement in the clay-gravel layer, the white crystals on the interface between gravel and clay are the evaporation barriers formed by the concentration of chemical elements in the soil (Jones et al., 1984). The fissures between clay and gravel form dominant seepage channels. As the groundwater seeps down the pores, the salts are gradually concentrated and deposited on the surface of the gravel. This type of cementation is soil-rock interface cementation, and its cementing force is mainly affected by rainfall, permeability and continuous exposure time of the slope. Cementation increases the strength of the clay-gravel layer to a certain extent.

STRENGTH CHARACTERISTICS OF ANQING FORMATION CLAY-GRAVEL LAYER

In-Situ Horizontal Push-Shear Test

In order to study the effects of different gravel content, water environment and overburden load on the mechanical properties of the clay-gravel layer, the following six sets of *in-situ* horizontal push-shear tests were designed and carried out (**Figure 3**). The

TABLE 1 | *In-situ* horizontal push-shear test of clay-gravel layer.

Number	Influencing factors		
	Gravel content (%)	Water environment	Overlying load (kPa)
A	57	Natural	0
B		Saturation	0
C	69	Natural	0
D		Saturation	0
E		Saturation	10
F		Saturation	20

water environment mainly included normal state and saturated state. Tests with no overburden load under normal and saturated conditions were carried out in the site with low gravel content, and the gravel content was 57%. In the site with high gravel content, the gravel content was 69%, tests with no overburden load under normal and saturated conditions, and tests with overburden loads of 10 and 20 kPa under saturated conditions were carried out respectively (**Table 1**). The field test device is shown in **Figure 3A**. During the test, the horizontal force was applied through the jack. When the pressure gauge showed the maximum reading and fell back to a stable low value, the maximum reading of the pressure gauge at this time was the initial loading horizontal force P_1. Then, released the jack valve and continued to apply the horizontal force to the sample in the same way until the pressure gauge showed the maximum reading again, then the peak shear force at this time was the reloading horizontal force P_2. The test could be stopped when P_1 and P_2 were obtained.

Shear Force-Shear Displacement Curve

The typical shear force-shear displacement curve of the clay-gravel layer under different water environments and external loads is shown in **Figure 3B**. The curve is basically divided into five stages. 1) Compaction. With the increase of the shear force, the shear displacement increases rapidly, but the increment of the shear displacement is small. This is due to the closure of fissures in the specimen. 2) Linear deformation. The curve is approximately a straight line, and the deformation of the specimen increases linearly with the increase of the shear force. 3) Elastoplastic deformation. The curve shows a nonlinear relationship. With the increase of shear force, fissures appear in the specimen, and the fissures gradually expand. When the fissures encounter gravel during the expansion, local stress concentration occurs, and the strength of the clay-gravel layer is temporarily improved. 4) Peak. The shear force fluctuates in a small range, while the increase in the shear displacement is relatively large. The stress concentration effect formed by inter-gravel occlusion and extrusion and the stress release effect formed by inter-gravel dislocation and sliding are dynamically adjusted to achieve a relatively balanced state. 5) Post-destruction. With the increase of shear displacement, the shear force gradually decreases and tends to be stable, reaching the residual shear force.

Figure 3C shows the shear force-shear displacement curves of the clay-gravel layer under different gravel contents and different water environments. When the gravel content is 57%, the peak shear force in the natural state is only 29.05 kN, and the peak shear force in the saturated state is 45.9% lower than that in the natural state. When the gravel content is 69%, the peak shear force in the natural state is 45.53 kN, and the peak shear force in the saturated state is 65.5% lower than that in the natural state. With the increase of gravel content, the gravel skeleton effect in the clay-gravel layer is more obvious, the elastic modulus and strength are also larger, and the shear force peak value in natural state is larger. In the saturated state, due to water infiltration, lubrication and chemical interaction with cement, water fills the pores, the pore water pressure increases, the effective stress decreases, and the skeleton of the gravel is destroyed, resulting in structural damage. At the same time, the carbonate and aluminosilicate in the cement are slightly soluble in water, resulting in partial loss of the bonding force between the gravel and the clay. Therefore, the peak shear force in the saturated state is significantly lower than that in the natural state. Due to structural and cementitious failures, the peak shear force at saturation is less affected by the gravel content.

Figure 3D shows the shear force-shear displacement curves of the clay-gravel layer under different water environments and overlying loads. The peak shear force of sample C is 65.5% lower than that of sample D, the peak shear force of sample E is 56.9% higher than that of sample D, and the peak shear force of sample F is 81.0% higher than that of sample D. Meanwhile, the residual shear force values of samples E, F are close. As the overlying load increases, the peak shear force at saturation increases significantly, but the increase decreases gradually. Due to the overlying load, the sample is in a state of three-way compression, and its shear resistance is significantly improved. In the saturated state, the residual shear force when the overlying load is 10 and 20 kPa is approximately equal, indicating that only within a certain overlying load range, the residual shear force increases with the increase of the overlying load. The shear peak phase of the clay-gravel layer in the saturated state is longer than that in the normal state.

Shear Zone

The clay-gravel layer undergoes shear failure, and the shear zone (**Figure 4A**) is significantly different from the arc-shaped shear zone of the homogeneous soil. **Figures 4B,C** shows the comparison of shear zone morphology between homogeneous soil and clay-gravel layer. The shear zone of the clay-gravel layer is an irregular zigzag shape. The gravel on the sliding surface

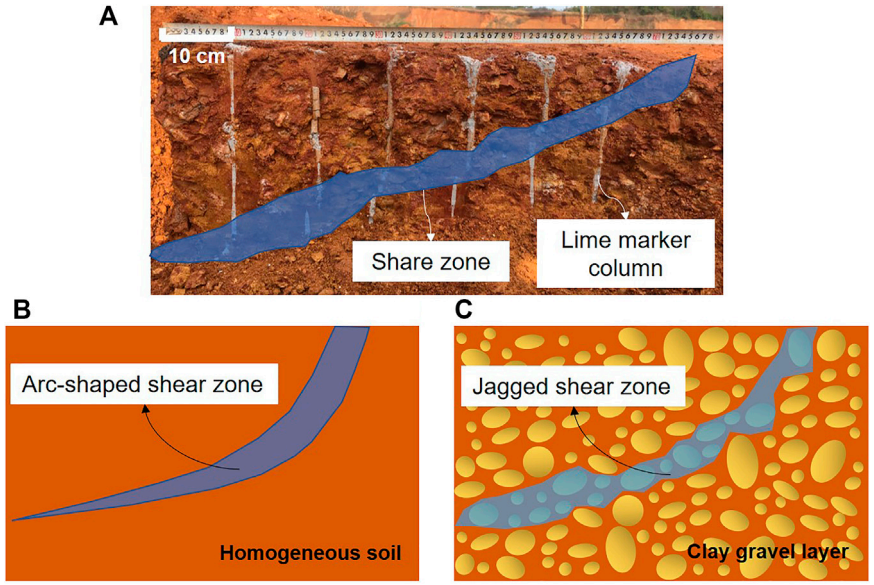

FIGURE 4 | Shear zone **(A)** excavation profile of typical shear zone **(B)** homogeneous soil **(C)** clay-gravel layer.

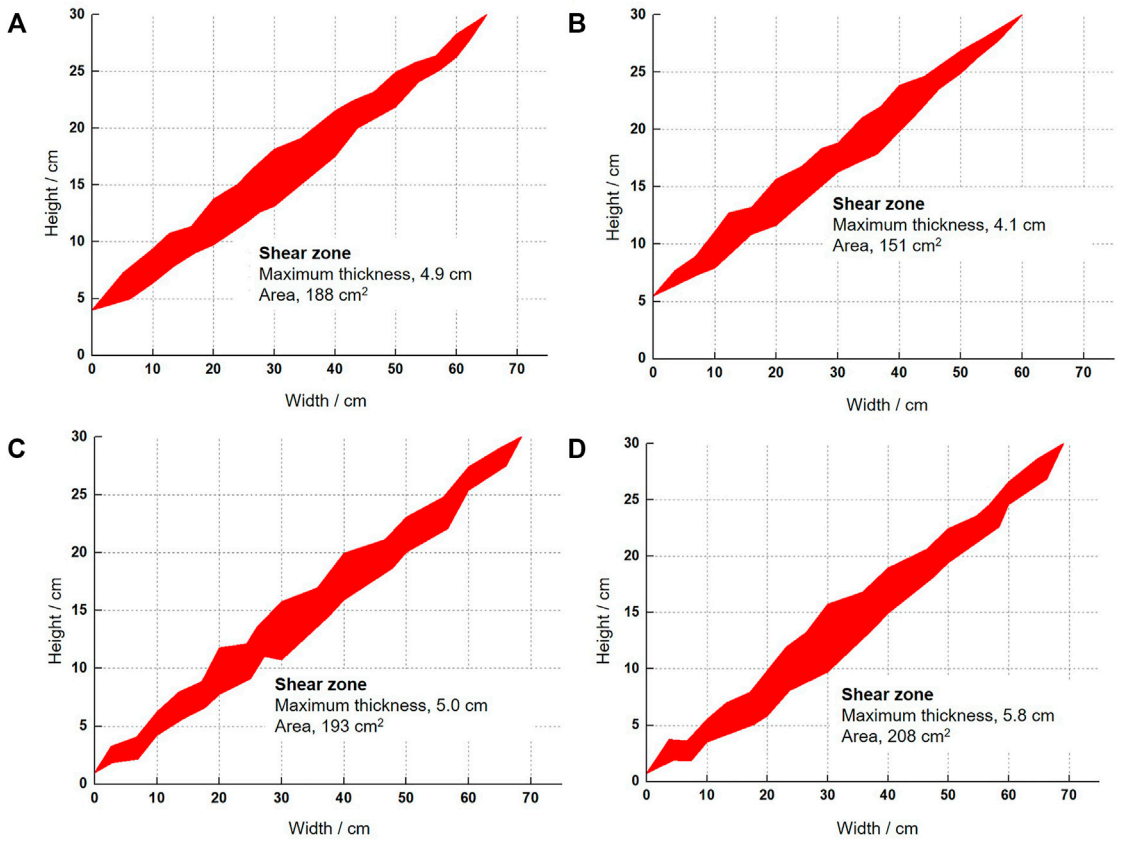

FIGURE 5 | Two-dimensional shape of shear zone in clay gravel layer **(A)** Sample C **(B)** Sample D **(C)** Sample E **(D)** Sample F.

basically does not undergo shear failure, and the shear zone extends along the clay matrix. When encountering gravel, it expands along the edge of the gravel, that is, the clay-gravel interface, and passes around the gravel. Because the clay-gravel layer is not a continuous and isotropic medium, the elastic modulus and shear strength of gravel are much larger than those of clay, and there are primary fissures at the interface between the two. When sheared, stress concentration occurs at the interface, the fissures further expand, and further expand to the weak point to form a sliding surface.

Figure 5 shows the actual 2D shape of the shear zone of the clay-gravel layer. According to the morphology of the shear zones of the samples C and D, the maximum thickness and area of the shear zones in the normal state are larger than those in the saturated state. Because the area of the shear zone is proportional to the energy consumed in its formation. In the normal state, the elastic modulus and strength of the clay-gravel layer are larger than those in the saturated state, so the former absorbs more energy than the latter in the shearing process of the same size sample.

The shear zone generally develops along the weak surface in the clay-gravel layer. Compared with the gravel and clay, the interface between the gravel and the clay has lower strength and is a potential weak surface. During shearing, stress concentration occurs at the interface between gravel and clay, which then breaks and gradually penetrates to develop into a shear plane. Theoretically, the depth of the initial shear plane should be the height of the sample, but the test results show that due to the uneven spatial distribution of gravel, there may be a concentrated gravel layer at the bottom of the sample, which makes it difficult for the shear plane to start forming here. Therefore, the depth of the initial shear plane is related to the spatial distribution of the gravel. Compared with sample C, sample D is saturated, water seeps into the fissures, the pore water pressure in the soil increases, and the initial fissures expand further. Due to the lubrication of water, the occlusal force between the clay-gravel layers is reduced, thereby reducing its overall strength, resulting in more local potential slip zones in the interior of sample D. The initial shear plane depth of the shear zone of sample D is shallow, the width is small, and the sliding body range is small.

Through the comparison of samples D, E, and F, it is found that with the increase of the overlying load of the sample, the initial depth of the shear zone deepens, and the overall width also increases. The maximum thickness and area of the shear zone increases with the overburden load. Since the vertical displacement of the surface is constrained with the increase of the overlying load, the shear zone is not easy to develop to the original spaced surface and cut out, so the width of the shear zone becomes larger. Likewise, the sample is under three-way compression, and the shear zone extends deeper. Affected by the increase of the overlying load, the extent of the shear zone increases, and its formation consumes more energy.

Shear Strength

Considering different water environments and overlying loads, a study was carried out on the calculation method of the shear strength of the clay-gravel layer (Xu et al., 2006; Xu et al., 2007), and it was concluded that

$$c = \frac{P_1 - P_2}{B\sum_{i=1}^{n} L_i} \tag{2}$$

$$\tan\varphi = \frac{\frac{P_1}{G}\sum_{i=1}^{n} g_i \cos\alpha_i - \sum_{i=1}^{n} g_i \sin\alpha_i - cB\sum_{i=1}^{n} L_i}{\frac{P_1}{G}\sum_{i=1}^{n} g_i \sin\alpha_i + \sum_{i=1}^{n} g_i \cos\alpha_i} \tag{3}$$

$$g_i = BL_i h_i \gamma \tag{4}$$

When the sample is in a saturated state, the influence of water pressure should be considered in the calculation. Add the water pressure term to **Equation 3**

$$\tan\varphi = \frac{\frac{P_1}{G}\sum_{i=1}^{n} g_i \cos\alpha_i - \sum_{i=1}^{n} g_i \sin\alpha_i - cB\sum_{i=1}^{n} L_i}{\frac{P_1}{G}\sum_{i=1}^{n} g_i \sin\alpha_i + \sum_{i=1}^{n} g_i \cos\alpha_i - \sum_{i=1}^{n} W_i} \tag{5}$$

$$W_i = BL_i h_i \gamma_w \tag{6}$$

When the sample is in a saturated state and under the action of the overlying load, the influence of the water pressure and the overlying load should be considered in the calculation. Add the water pressure term and the overlying load term to **Equation 3**

$$\tan\varphi = \frac{\frac{P_1}{G+F}\sum_{i=1}^{n} (g_i + F_i)\cos\alpha_i - \sum_{i=1}^{n} (g_i + F_i)\sin\alpha_i - cB\sum_{i=1}^{n} L_i}{\frac{P_1}{G+F}\sum_{i=1}^{n} (g_i + F_i)\sin\alpha_i + \sum_{i=1}^{n} (g_i + F_i)\cos\alpha_i - \sum_{i=1}^{n} W_i} \tag{7}$$

Here, P_1 represents the initial loading horizontal force (kN), P_2 represents the reloading horizontal force (kN), B represents the width of the sample (m), L_i represents the line length of the ith block on the slip surface (m), G represents the gravity of the sliding body (kN), α_i represents the angle between the slip surface at the ith block and the horizontal plane (°), g_i represents the gravity of the ith block (kN), h_i represents the centerline height of the ith block (m), γ represents the natural weight of the sample (kN/m^3), W_i represents the water pressure at the sliding surface of the ith block (kN), γ_m represents the water weight (kN/m^3), F_i represents the overlying load applied to the ith block.

The shear strength results of the clay-gravel layer are shown in **Table 2**.

In the natural state, the strength of the clay-gravel layer is relatively large, which is due to the gradual compaction during the long-term deposition process and fewer primary fissures. In addition, there is a certain cementation effect between clay and gravel, and its shear failure needs to overcome a larger cementation force than the general soil-rock mixture. At the same time, the gravel content is relatively high, and the spatial distribution has a certain sequence, resulting in a relatively significant skeleton effect. After the clay is filled, a relatively dense structure is formed. With the increase of the gravel content, the skeleton effect of the gravel is more obvious. A denser structure is formed, and its strength is improved within a certain range (Li et al., 2007).

TABLE 2 | *In-situ* test results and shear strength indicators of clay-gravel layer.

Number	P_1 (kN)	P_2 (kN)	G (kN)	$\sum(g_i + F_i)\cos\alpha_i$ (kN)	$\sum(g_i + F_i)\sin\alpha_i$ (kN)	$\sum L_i$ (m)	$\sum W_i$ (kN)	c (kPa)	φ (°)
A	29.06	11.00	1.4	1.29	0.55	0.65	0	34.7	32.8
B	15.69	4.69	1.15	1.05	0.48	0.64	0.62	19.1	21.4
C	45.53	24.34	1.48	1.39	0.53	0.70	0	38.1	49.8
D	14.91	3.14	1.24	1.14	0.47	0.69	0.59	22.7	14.2
E	71.44	51.81	7.33	6.76	2.82	0.75	3.14	32.8	54.3
F	82.43	58.88	12.98	11.97	4.98	0.75	5.56	39.1	51.8

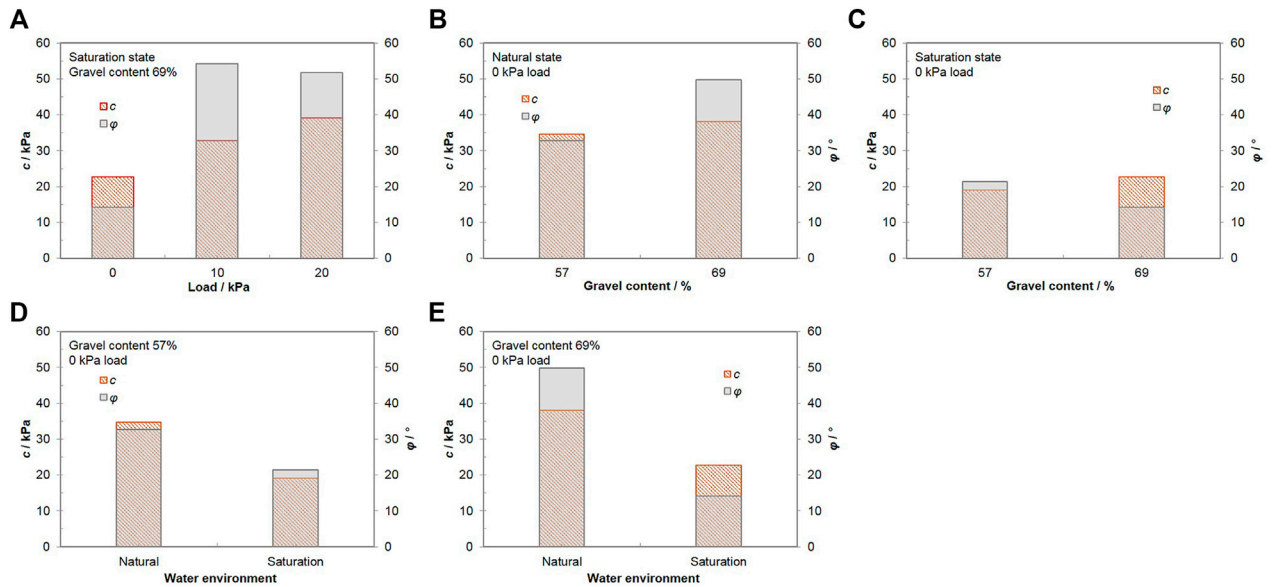

FIGURE 6 | The relationship between shear strength and influencing factors **(A)** relationship with load **(B)** relationship with gravel content in natural state **(C)** relationship with gravel content in saturation state **(D)** relationship with water environment at low gravel content **(E)** relationship with water environment at high gravel content.

The shear strength of the clay-gravel layer decreases significantly in the saturated state. The main reasons are, 1) When saturated, the initial micro-cracks of the clay-gravel layer are filled with free water, and the pore water pressure increases, resulting in further expansion of the micro-cracks. 2) Due to the lubrication of water, particles of different particle sizes rub against each other, and the occlusal effect becomes weak. 3) Natural rainwater is often weakly acidic, and the cement will be slightly soluble in water, and the cementing force will be reduced.

Figure 6 shows the relationship between shear strength and influencing factors. It can be seen that with the application of the overlying load, c and φ increase significantly, but the increasing range gradually decreases and tends to be stable. c and φ of samples C and F are almost equal. The overlying load has the effect of compaction, which not only improves the compactness of the clay-gravel layer, but also makes the occlusion between the clay and the gravel more closely, and the normal stress on the interface between the clay and the gravel increases, which improves the shear strength. In addition, in the process of shear failure, it is necessary to overcome the gravitational work and restraint of the overlying load, so the horizontal shear force is larger than that without the overlying load, which leads to an increase in the shear strength under the overlying load condition. Compared with the two-dimensional compression state of the sample without the overlying load, the sample with the overlying load is in the three-dimensional compression state, and it is more difficult for shear failure to occur under the three-dimensional compression condition. Therefore, water has a great influence on the clay-gravel layer. When it is saturated, the strength drops sharply, and the load and strength are only positively correlated within a certain range. Beyond this range, the strength of the clay-gravel layer increases with the increase of the load is not obvious.

EVOLUTION LAW AND MECHANISM OF SLOPE EROSION DAMAGE

In order to study the evolution law of erosion damage of clay-gravel layer slopes, laboratory model tests of artificial rainfall

FIGURE 7 | Artificial rainfall-slope erosion model test device.

erosion of slopes with different gravel contents were carried out. The gravel content in the test is 30, 50, and 70%, respectively. Before filling, a suitable sieve was selected to screen the clay-gravel layer to separate the clay and gravel according to the clay-gravel threshold. Then, according to the gravel content set in the test, after weighing and artificially proportioning, a certain quality of clay and gravel were mixed well. Finally, the mixed clay-gravel layer was filled into the model box. The test device is shown in **Figure 7**. Model test device includes the rainfall system, slope system, water pressure control system, camera system and scour collection system. In the test, the width of the slope was 1.0 m, the length was 1.5 m, the slope ratio was 1:1.5, and the rainfall intensity is 140 mm/h.

Evolution Law of Erosion Damage of Slope (Gravel Content 30%)

For the slope with a gravel content of 30%, the failure of the slope surface was the development of gullies (**Figure 8**). The erosion damage process was similar to the general soil slope, which was divided into three stages, 1) Sputter and sheet erosion, 2) Rill erosion, 3) Gully cutting and collapse damage.

1) Sputter and sheet erosion

In the early stage of rainfall, only very shallow groove marks appeared on the slope. Due to the low initial moisture content of the slope, the pores between soil particles were filled with air. The soil particles on the surface of the slope were relatively loose, and the kinetic energy of raindrops made the soil particles disperse, crack and splash. As the rainfall progressed, the moisture content of the topsoil increased rapidly, the pores between the particles

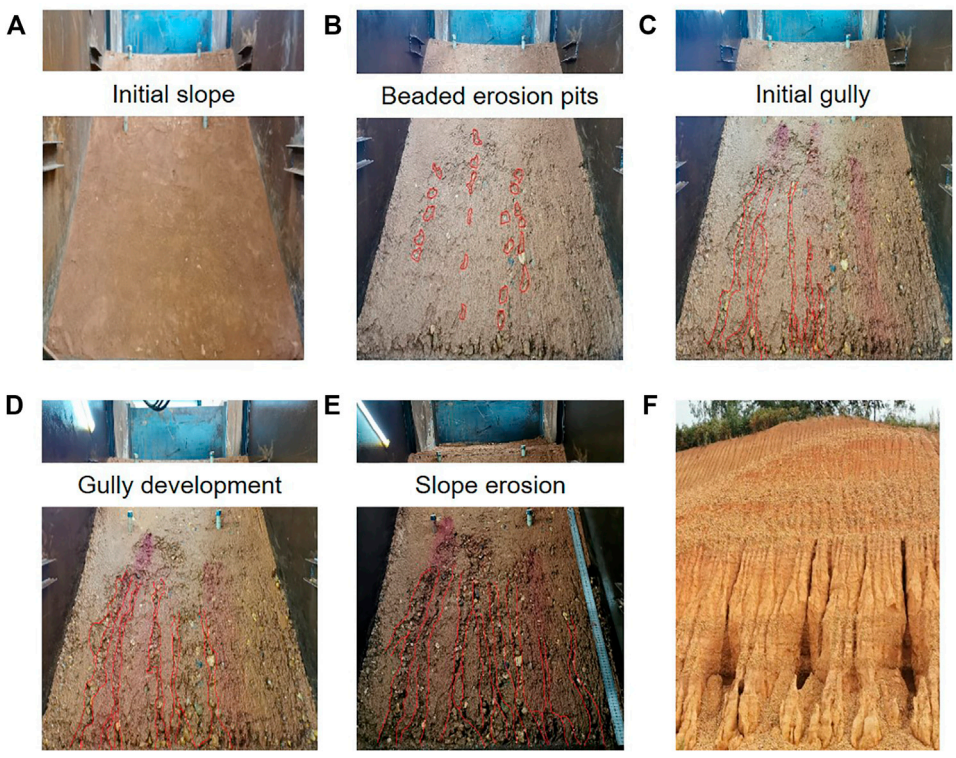

FIGURE 8 | Evolution law of erosion damage of the test slope (gravel content 30%). **(A)** Initial slope **(B)** erosion pits **(C)** gully **(D)** gully development **(E)** slope erosion **(F)** actual slope failure.

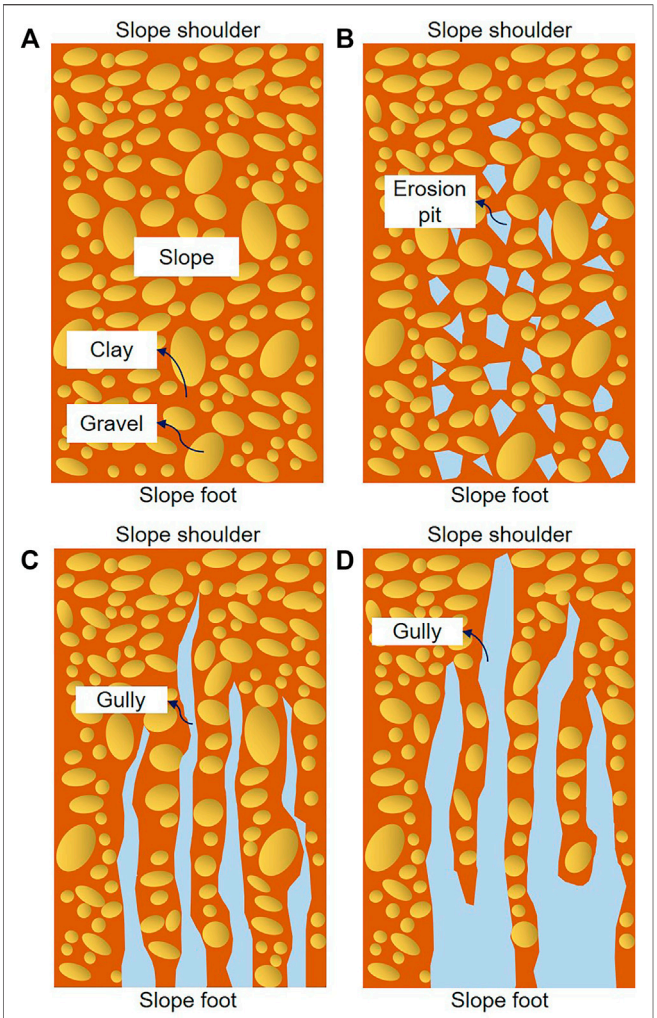

FIGURE 9 | Simplified diagram of slope erosion failure evolution law (gravel content 30%). **(A)** Initial slope **(B)** erosion pits **(C)** gully **(D)** gully development.

were filled with water, the cohesion decreased, and the impact force of the raindrops fell, the surface layer of the slope appeared honeycomb-like, and this stage was called sputter erosion. After sputter erosion, the soil structure on the surface was destroyed and the pores were blocked. Since the rainfall intensity was much greater than the infiltration intensity, runoff was formed on the slope. Smaller particles in the slope surface were suspended and taken away. This process was called sheet erosion, and rills appeared on the slope surface.

2) Rill erosion

As the rainfall continued, the erosion and scour capacity of the runoff was further enhanced. If the erosion resistance of the soil particles on the slope was less than the scour force of the runoff, the downward shear force of the runoff would wash away the soil particles, forming bead-shaped erosion pits on the slope (**Figure 8B**). The density of the erosion pits from the top of the slope to the bottom of the slope increased sequentially. Due to the infiltration of rainwater, the strength of the slope decreased, and the erosion pit gradually deepened and widened, forming trace erosion, extending to the foot of the slope to form the head of the rill (**Figure 8C**). The impact of the runoff was not strong enough for the gravel to slide off. So, gravel blocked runoff, redirected it, and complicated rill erosion. Part of the gravel was embedded on the inner wall of the rill, which absorbed the energy of the runoff, and the soil particles around the gravel were more easily washed away by the runoff. The gravel fell into the rill, and erosion pits were formed on the walls of the rill, and the width of the rill was expanded (**Figure 8D**). The obstruction of gravel caused the diversion or branching of the rill, which made the shape of the rill more complex and the network of rill denser (**Figure 8E**).

3) Gully cutting and collapse damage

Next, the erosion method was transformed from rill erosion to cut ditch erosion, and the slope surface was transformed from planar erosion to linear erosion. The runoff collected at the lower part of the slope, which had a strong erosive force, and cut down both sides of the rill violently, causing local instability at the toe of the slope. Soil particles were washed away by water and gravel built up. **Figure 8F** shows the landslide with less gravel content, which was consistent with the test results.

Figure 9 shows the evolution process of slope scour failure. During the runoff flowing through the slope, the down-shear force of the runoff was greater than the erosion resistance of the soil on the slope. The local soil on the slope was washed away in an unstable state, and erosion pits were formed there, and the erosion pits were beaded on the slope (**Figure 9B**). The erosion pits developed towards the top of the slope, forming trace erosion, and extending to the bottom of the slope to form rill head. With the progress of rainfall, the erosion pits were gradually connected to form rills (**Figure 9C**). The rills developed continuously, and the rills merged with each other to form a network of gullies. The width and depth of the gullies at the bottom of the slope were larger than those at the top (**Figure 9D**). Rainwater further scoured and infiltrated deep into the slope, and the stability of the slope was affected.

Evolution Law of Erosion Damage of Slope (Gravel Content 50%)

For the slope with a gravel content of 50%, due to the skeleton effect of gravel, there was a difference in the failure form of slope surface and soil slope, and the slope surface damage was mainly erosion pit-shallow slump (**Figure 10**). The whole process was divided into the following three stages, 1) Sputter and sheet erosion, 2) Erosion pit erosion, 3) Layer-by-layer slump.

1) Sputter and sheet erosion

This stage was similar to that of the 30% gravel content. Due to the increase of gravel content, the clay content of the slope decreased, and the degree of the erosion of the slope was relatively small.

2) Erosion pit erosion

FIGURE 10 | Evolution law of erosion damage of the test slope (gravel content 50%). **(A)** Initial slope **(B)** erosion pits **(C)** erosion pit development **(D)** slope local damage **(E)** slope extensive damage **(F)** actual slope failure.

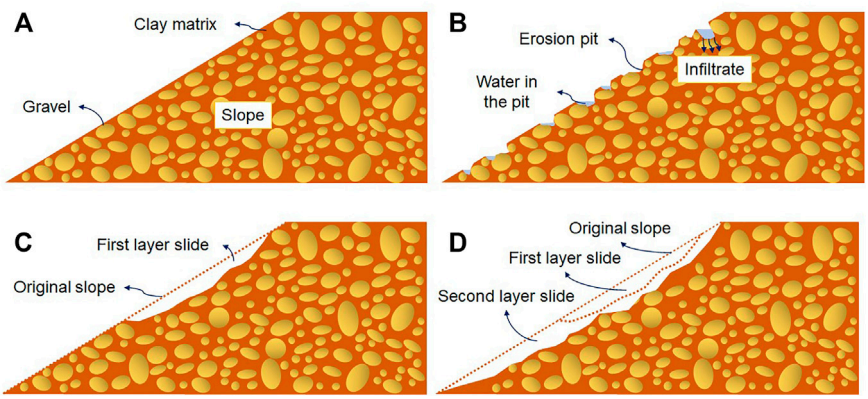

FIGURE 11 | Simplified diagram of slope erosion failure evolution law (gravel content 50%). **(A)** Initial slope **(B)** erosion pits **(C)** slope local damage **(D)** slope extensive damage.

Runoff washed away the clay particles on the slope, creating erosion pits on the slope. With the increase of the gravel content, a certain skeleton effect was formed between the gravels, and the runoff was not easy to wash away the gravel, and the gravel hindered trace erosion. The gravel beneath the erosion pit also prevented the erosion pit from forming a rill head. The presence of gravel prevented the development of erosion pits, and slope erosion did not form rills. The erosion pit developed laterally under the action of runoff. When the soil particles around the gravel were washed away, the gravel lose its supporting force and fallen into the erosion pit under the action of gravity, and the erosion pit developed gradually (**Figure 10B**). The appearance of the erosion pit enhanced the infiltration of the slope and softened the soil around the erosion pit. Under the action of runoff, the erosion pit expanded and deepened (**Figure 10D**).

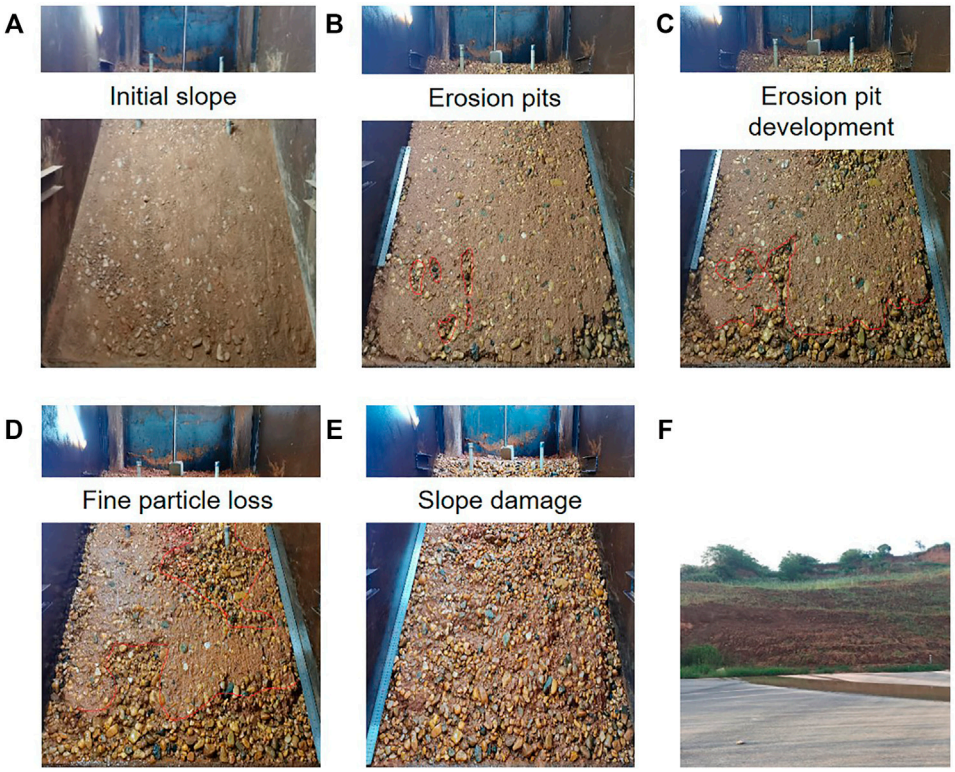

FIGURE 12 | Evolution law of erosion damage of the test slope (gravel content 70%). **(A)** Initial slope **(B)** erosion pits **(C)** erosion pit development **(D)** fine particle loss **(E)** slope damage **(F)** actual slope failure.

3) Layer-by-layer slump

As the rainfall progressed, more erosion pits formed on the slope, and their locations were randomly distributed. When the erosion pits developed to a certain depth, the depth of the erosion pits would not increase temporarily, but expanded to the surrounding area. At this time, the erosion pits on the slope were connected with each other, forming a local layered slump, and the slope was unstable and damaged in the shallow layer, and then gradually developed to the deep layer. **Figure 10F** shows the failure of the slope in this form on site.

Figure 11 shows the evolution process of scour failure on the slope. Since the clay was more easily washed away than the gravel on the slope, erosion pits were formed between the gravel on the slope (**Figure 11B**). A small area of stagnant water was in the erosion pit, which provided conditions for the infiltration of rainwater, so that the fine-grained soil around the erosion pit was softened, the strength was reduced, and local damage occurred, so that the adjacent erosion pits were gradually connected under the condition that the interval soil was gradually destroyed. As a result, shallow slump failure was gradually formed (**Figure 11C**). Then, erosion pit failure continued to appear on the slip surface of the first layer, and then the slump failure process of the first layer was repeated to appear the second layer slump failure (**Figure 11D**). During the rainfall process, the slope surface was damaged by layer-by-layer slump, resulting in the erosion damage of the clay-gravel layer slope.

For the slope with a gravel content of 70%, the clay particles on the slope were quickly washed away by the water flow, and the gravel skeleton of the slope formed a temporary relatively stable structure (**Figure 12**). After being disturbed, the gravel layer collapsed as a whole.

The sputter and sheet erosion of the clay-gravel layer slope under the rainfall were similar to the above-mentioned two slope erosion processes and mechanisms (**Figures 12A,B**). When erosion pits were formed on the slope, the runoff velocity on the slope was large, and the runoff quickly washed away the clay around the gravel. However, due to the high content of gravel, the gravels contacted each other and occluded each other to form a skeleton structure, and the slope remained transiently stable. At the same time, due to the skeleton effect between the gravels (**Figure 12C**), the erosion pit would not develop to the depth to cause the collapse of the pit wall, but expanded to the surrounding, continued to wash away the clay between the gravels (**Figure 12D**), and gradually formed a gravel slope composed of macroporous gravels (**Figure 12E**). At this time, the slope ratio had a great influence on the stability of the slope. When the slope ratio was large, the sliding force on the gravel was greater than the anti-sliding force, which would

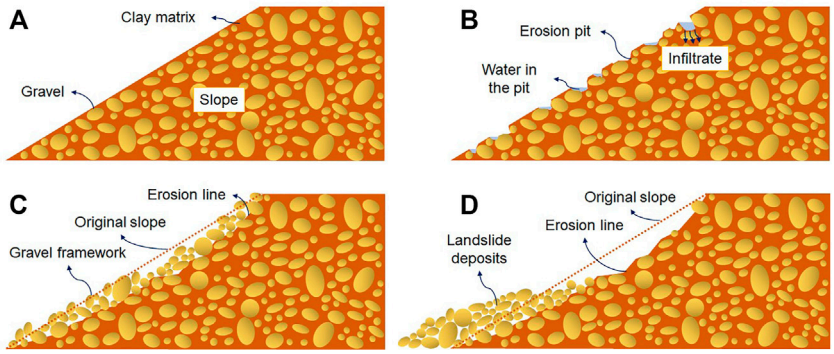

FIGURE 13 | Simplified diagram of slope erosion failure evolution law (gravel content 70%). **(A)** Initial slope **(B)** erosion pits **(C)** fine particle loss **(D)** slope damage.

cause the gravel to slide down, thereby causing the instability of the slope. In addition, since the cohesion between gravels was basically lost, when disturbed, even if the slope ratio was relatively small, the slope would suffer from extensive sliding failure (**Figure 12F**).

Figure 13 is the evolution process of slope erosion failure. In the early stage of rainfall, since the soil was more easily washed away than the gravel on the slope, erosion pits would be formed between the gravel on the slope (**Figure 13B**). However, due to the high gravel content, the contact and occlusion between the gravels formed a skeleton effect, and the slope remained transiently stable (**Figure 13C**). Moisture continued to erode deeper into the slope, softening the deep soil and washing away more clay. When disturbed or the environmental conditions changed, the gravel collapsed on a large scale and the slope was unstable (**Figure 13D**).

CONCLUSION

For the Anqing Formation clay-gravel layer, which is a special soil-rock mixture composed of gravel and clay, regional geological investigations, basic physical property tests, *in-situ* horizontal push-shear tests, and indoor large-scale slope rainfall erosion tests were carried out. The poor engineering geological properties of the clay-gravel layer and its influence on the slope deformation law and the failure mechanism of instability were studied.

The cementation of the clay-gravel layer was divided into clay-gravel interface salt cementation and clay matrix mineral cementation. The clay mineral content was 29%, including 3.99% illite, 13.86% kaolinite, and 11.16% I/S mixed layer. In the natural state, the strength of the clay-gravel layer was relatively high. When it encountered water, the cementation effect was easily lost, and the strength decreased rapidly.

The shear force-shear displacement curve was divided into five stages: compaction, linear deformation, elastoplastic deformation, peak and post-destruction. The larger the amount of gravel, the larger the peak shear force of the clay-gravel layer in the natural state. The peak shear force in the saturated state was significantly lower than that in the natural state. As the overlying load increased, the peak shear force increased. The shear zone was in the shape of a broken line. The shear zone extended along the clay matrix, and when encountering gravel, it bypassed the gravel and extended along the edge of the gravel, that was, the clay-gravel interface. At saturation, the shear strength of the clay-gravel layer decreased significantly. With the application of the overlying load, the shear strength increased within a certain range, but the increase of the strength with the increase of the load was not obvious. The effect of water than load on the strength characteristics of the clay-gravel layer was more significant.

Under rainfall conditions, the gravel content had an important influence on the erosion pattern and instability mechanism of the clay-gravel slope. When the gravel content was 30%, the failure of the slope surface was the development of gullies. The erosion damage process was similar to the soil slope. When the gravel content was 50%, affected by the distribution of gravel, the slope failure was manifested as the development of erosion pits, followed by local slumps, and finally the overall sliding in layers. When the gravel content was 70%, the clay particles on the slope were quickly washed away by the water flow, and the gravel skeleton of the slope formed a temporary relatively stable structure. After being disturbed, the gravel layer collapsed as a whole.

DATA AVAILABILITY STATEMENT

The original contributions presented in the study are included in the article/Supplementary Material, further inquiries can be directed to the corresponding author.

AUTHOR CONTRIBUTIONS

ZD: Writing–review & editing, Supervision, Validation, Funding acquisition. KH: Methodology, Writing–original draft. LJ: Data curation. JL: Investigation, Validation. FY: Methodology, Investigation. SC: Project administration, Supervision.

FUNDING

The work reported in this paper was financially supported by the National Natural Science Foundation of China (No. 42172308).

ACKNOWLEDGMENTS

We would like to acknowledge the reviewers and the editors for their comments and suggestions.

REFERENCES

An, J., Zheng, F., Lu, J., and Li, G. (2012). Investigating the Role of Raindrop Impact on Hydrodynamic Mechanism of Soil Erosion under Simulated Rainfall Conditions. *Soil Sci.* 177 (8), 517–526. doi:10.1097/ss.0b013e3182639de1

Bryan, R. B., and Rockwell, D. L. (1998). Water Table Control on Rill Initiation and Implications for Erosional Response. *Geomorphology* 23 (2-4), 151–169. doi:10.1016/s0169-555x(97)00110-4

Chen, X., Shi, C., and Yang, J. X. (2020). Study on the Influence of Meso-Characteristics of Mixed Earth and Rock Slope on the Formation of Sliding Surface. *J. Eng. Geology.* 28 (4), 813. doi:10.13544/j.cnki.jeg.2019-332

De Vente, J., and Poesen, J. (2005). Predicting Soil Erosion and Sediment Yield at the basin Scale, Scale Issues and Semi-quantitative Models. *Earth-Science Rev.* 71 (1-2), 95–125. doi:10.1016/j.earscirev.2005.02.002

Govers, G., Gimenez, R., and Van, O. K. (2007). Rill Erosion, Exploring the Relationship between Experiments, Modelling and Field Observations. *Earth-Science Rev.* 84 (3-4), 87–102. doi:10.1016/j.earscirev.2007.06.001

Hu, R. L., Li, X., and Wang, Y. (2020). Engineering Geomechanical Properties and Structural Effects of Soil-Rock Mixtures. *J. Eng. Geology.* 28 (2), 255. doi:10.13544/j.cnki.jeg.2020-077

Jin, L., Zeng, Y. W., and Zhang, S. (2017). Large-scale Triaxial Test on the Influence of Mass Stone Content and Shape on the Mechanical Properties of Cemented Soil-Rock Mixture. *Rock Soil Mech.* 38 (1), 141–149.

Jones, B., Lockart, E. B., and Squair, C. (1984). Phreatic and Vadose Cements in the Tertiary Bluff Formation of Grand Cayman Island, British West Indies. *Bull. Can. Pet. Geology.* 32, 382.

Li, X., Liao, Q. L., and He, J. M. (2007). *In-situ* Experimental Study of Mechanical Properties of Soil-Rock Mixtures. *J. rock Mech. Eng.* 26 (12), 2377. doi:10.3321/j.issn:1000-6915.2007.12.001

Mancilla, G. A., Chen, S., and McCool, D. K. (2005). Rill Density Prediction and Flow Velocity Distributions on Agricultural Areas in the Pacific Northwest. *Soil Tillage Res.* 84 (1), 54–66. doi:10.1016/j.still.2004.10.002

Mandelbrot, B. B. (1977). *The Fractal Geometry of Nature*. New Work: W, New York: The Freeman.

Medley, E. (2001). Evaluating Safety of Concrete Gravity Dam on Weak Rock: Scott Dam-Discussion. *J. Geotech. Geoenviron* 127 (10), 901–902. doi:10.1061/(ASCE)1090-0241(2001)127:10(901)

Nie, Z. H., Li, K., and Xia, J. (2012). Research on Coarse-Grained Soil Collapsibility in Gobi Region. *Amr* 446-449, 1450–1453. doi:10.4028/www.scientific.net/amr.446-449.1450

Qian, Z. Z., Sheng, M. Q., and Tian, K. P. (2017). Cementation Mechanism and Micromechanical Model of Gobi Gravel Soil. *Rock Soil Mech.* 38 (S2), 138–144.

Ren, J. K. (2017). *Research on Scour Mechanism of Dispersed Soil in Zhenlai Area of Jilin Province*. Changchun: Jilin, Jilin University. M.Sc.

Shen, H.-o., Zheng, F.-l., Wang, L., and Wen, L.-l. (2019). Effects of Rainfall Intensity and Topography on Rill Development and Rill Characteristics on Loessial Hillslopes in China. *J. Mt. Sci.* 16 (10), 2299–2307. doi:10.1007/s11629-019-5444-5

Song, P. R. (2013). *Characteristics and Numerical Simulation of Erosion Failure of Loess Slope*. Changchun: Jilin University. Ph.D.

Tang, J. Y., Xu, D. S., and Liu, H. B. (2018). Effect of Rock Content on Shear Characteristics of Soil-Rock Mixture. *Rock Soil Mech.* 39 (1), 93. doi:10.16285/j.rsm.2017.1527

Tao, Q. D., He, Z. Y., and Jia, Y. (2019). Strength Characteristics and Influencing Factors of Earth-Rock Mixture Based on Triaxial Test. *Sci. Technol. Eng.* 19 (26), 310. doi:10.3969/j.issn.1671-1815.2019.26.049

Wang, J. Y., Cao, W. G., Zhai, Y. C., Zhang, G. C., and Zhang, Y. J. (2016). Research on Horizontal Shear Test of Soil and Stone Mixed Fill Foundation under Different Water Environment. *J. Cent. south Univ. (natural Sci. edition)* 47 (2), 615. doi:10.11817/j.issn.1672-7207.2016.02.035

Wang, Y., and Li, X. (2015). Study of Mesoscopic Fractal Feature and Mechanical Properties for Rock and Soil Aggregates Samples. *J. Rock Mech. Eng.* 34 (S1), 3397. doi:10.13722/j.cnki.jrme.2013.1527

Xia, J. G., Hu, R. L., Qi, S. W., Gao, W., and Sui, H. Y. (2017). Large Scale Triaxial Shear Test of Soil-Rock Mixture with Super Diameter Particles. *J. rock Mech. Eng.* 36 (8), 2031. doi:10.13722/j.cnki.jrme.2016.1638

Xu, W.-J., Hu, R.-L., and Tan, R.-J. (2007). Some Geomechanical Properties of Soil-Rock Mixtures in the Hutiao Gorge Area, China. *Géotechnique* 57 (3), 255–264. doi:10.1680/geot.2007.57.3.255

Xu, W. J., and Hu, R. L. (2008). Field Experimental Study on Mechanical Properties of Soil-Rock Mixture under Cyclic Load. *J. Eng. Geology.* 16 (1), 63. doi:10.3969/j.issn.1004-9665.2008.01.013

Xu, W. J., Hu, R. L., and Zeng, R. Y. (2006). Research on Horizontal Push-Shear *In-Situ* Test of Subwater Soil-Rock Mixture. *Chin. J. Geotechnical Eng.* 28 (7), 815. doi:10.3321/j.issn:1000-4548.2006.07.002

You, X. H., and Tang, J. S. (2002). Field Horizontal Shear Test of Soil-Rock Mixture. *J. rock Mech. Eng.* 21 (10), 1537. doi:10.3321/j.issn:1000-6915.2002.10.021

Zhao, L., Hou, R., Wu, F., and Keesstra, S. (2018). Effect of Soil Surface Roughness on Infiltration Water, Ponding and Runoff on Tilled Soils under Rainfall Simulation Experiments. *Soil Tillage Res.* 179, 47–53. doi:10.1016/j.still.2018.01.009

Zhu, G. (1995). Determination of Very Low Metamorphic Grade of Clastic Sedimentary Rocks by Illite Crystallinity. *Pet. Exploration Dev.* 22 (1), 33

Conflict of Interest: The authors declare that the research was conducted in the absence of any commercial or financial relationships that could be construed as a potential conflict of interest.

Publisher's Note: All claims expressed in this article are solely those of the authors and do not necessarily represent those of their affiliated organizations, or those of the publisher, the editors and the reviewers. Any product that may be evaluated in this article, or claim that may be made by its manufacturer, is not guaranteed or endorsed by the publisher.

frontiers in Earth Science

ORIGINAL RESEARCH
published: 28 March 2022
doi: 10.3389/feart.2022.849438

Numerical Modeling of an Umbrella-Shaped Bolt and Its Anchorage Characteristics in Rock Engineering

Yong Xiong[1], *Hang Chen*[1], *Yonghui Cheng*[1]*, *Shenggang Hu*[1], *Zhaofeng Wang*[2,3] and *Yaohui Gao*[4]

[1]Key Laboratory of Geotechnical Mechanics and Engineering of Ministry of Water Resources, Changjiang River Scientific Reseatch Institute, Wuhan, China, [2]Institute of Rock and Soil Mechanics, Chinese Academy of Sciences, Wuhan, China, [3]State Key Laboratory of Geomechanics and Geotechnical Engineering, University of Chinese Academy of Sciences, Beijing, China, [4]Hydropower Engineering Institute, Power China Huadong Engineering Corporation Limited, Hangzhou, China

The umbrella-shaped bolt (U-bolt) is a novel type of mechanical bolt used for rock reinforcement. It is made of a smooth steel bar, hinges, rigid rods, and sliding blocks. During installation and operation, the tension of the bolt is converted into the extrusion force on the rock mass deep in slope, so that the higher compressive strength of the rock mass is used to obtain the greater friction force and anchoring force. In this article, the structural and mechanical analysis results of the U-bolt is provided, and the relation between penetration and point normal stress is discussed. Based on these analyses, a simulation method for the U-bolt is proposed. The bolt elements are identified at first, then the penetration on the rock mass is calculated, and the tensile strength of bolt elements is increased to a reasonable value. Meanwhile, the method is applied to deep-buried rock reinforcement and a rock slope, and simulation results reveal that the U-bolt can alleviate the fracturing degree and reduce the depth and displacement of the excavation damaged zone (EDZ), and decrease the landslide distance.

Keywords: umbrella-shaped bolt, structural analysis, simulation method, excavation damaged zone, rock supporting

OPEN ACCESS

Edited by:
Yun Zheng,
Institute of Rock and Soil Mechanics (CAS), China

Reviewed by:
Xianjie Hao,
China University of Mining and Technology, China
Rui Rui,
Wuhan University of Technology, China

***Correspondence:**
Yonghui Cheng
chengyh@mail.crsri.cn

Specialty section:
This article was submitted to Geohazards and Georisks, a section of the journal Frontiers in Earth Science

Received: *06 January 2022*
Accepted: *18 February 2022*
Published: *28 March 2022*

Citation:
Xiong Y, Chen H, Cheng Y, Hu S, Wang Z and Gao Y (2022) Numerical Modeling of an Umbrella-Shaped Bolt and Its Anchorage Characteristics in Rock Engineering. Front. Earth Sci. 10:849438. doi: 10.3389/feart.2022.849438

1 INTRODUCTION

The sustainability of underground caves (such as tunnels and caves) is mainly determined by three factors: rock quality, *in situ* stress, and the size or geometry of the cave (Li, 2012). The stress of shallow rock engineering is usually low, and the main stability problem is that the rock falls under gravity (Bizjak and Petkovšek, 2004). In the case of deep-buried hard rock engineering, the rock mass is usually hard and brittle, and the tensile failure should be the main mechanism (Su et al., 2017). In general, the loosened rock blocks or fractured rock mass can be stabilized by installing internal support devices like rock bolts (Cai et al., 2004). Therefore, the bearing capacity of the bolt is a crucial parameter in rock engineering (Chen, 2014).

Meanwhile, a rock slope is also a common kind of rock engineering. Its failure mechanisms and stability have been continuously investigated by researchers in ways of numerical methods, limit equilibrium methods (Aydan and Kawamoto, 1992; Zheng et al., 2018), and other new methods (Zheng et al., 2021). Swelling prestressed bolts and its use in the mechanized excavation of large-section tunnels (Liu et al., 2018), and also prestressed hollow grouting anchor rock burst

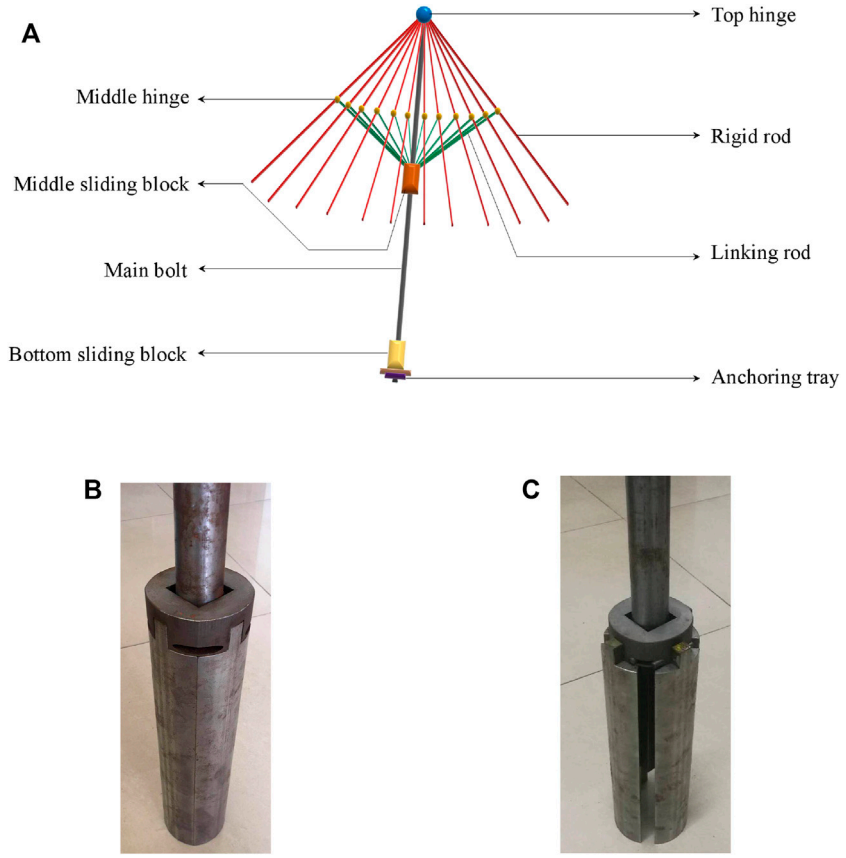

FIGURE 1 | Umbrella-shaped bolt, in which **(A)** the sketch figure, **(B)** bolt image in packing state, and **(C)** bolt image in opening state.

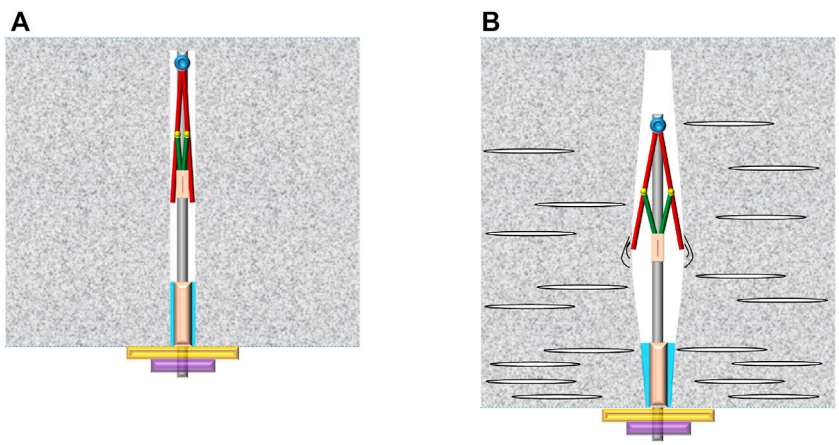

FIGURE 2 | Installation and operation of the U-bolt, in which **(A)** installation and **(B)** operation.

prevention tunnel design (Wang and He, 2011). To strengthen the stability of rock slopes, using rock bolts is a common measure, such as grouting bolt, mechanical shell-expanding bolt, and other new types of bolts. These rock bolts mentioned before have solved engineering problems faced in the process of tunnel construction.

Numerous studies have been carried out on rock bolts, and various types of bolts with high load capacity and high

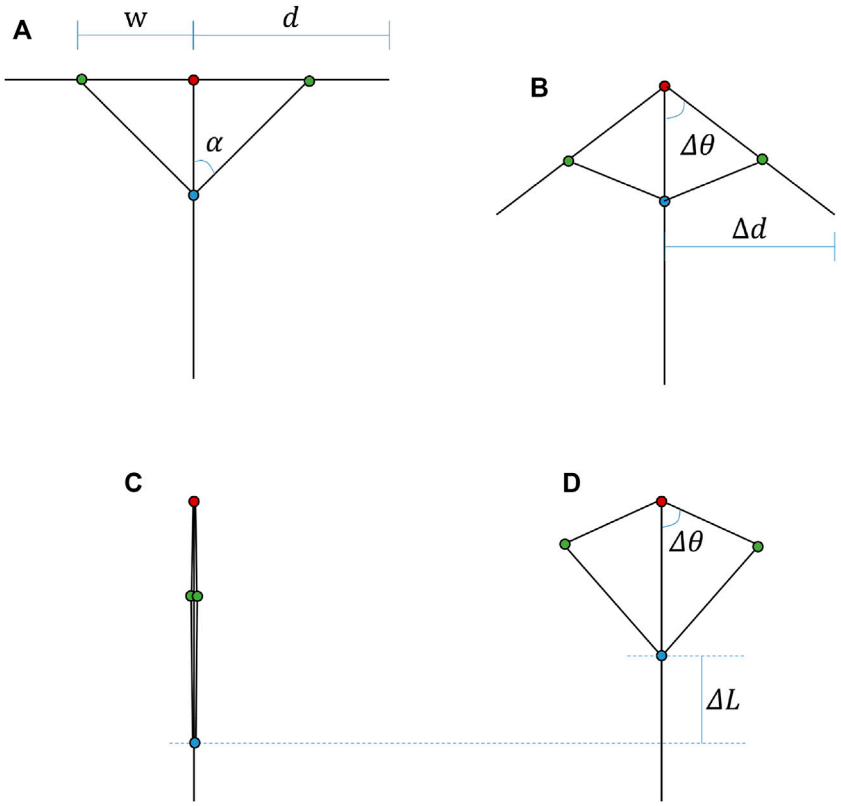

FIGURE 3 | Geometry structure of the U-bolt, where **(A)** the structure when U-bolt is totally expanding, **(B)** the structure when U-bolt is working, **(C)** the structure when U-bolt is installing, and **(D)** geometry shape of main bolt, rigid rod, and linking rod.

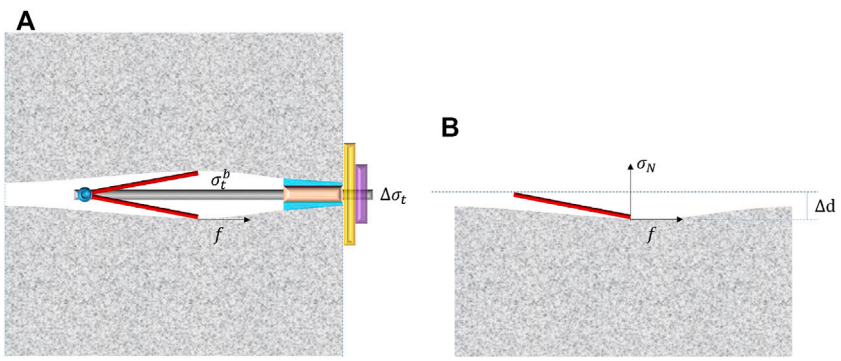

FIGURE 4 | Force analysis of the U-bolt, where **(A)** all forces and **(B)** the force on the internal surface of bore hole.

deformation capacity have been successfully developed and applied, such as cone bolts, Garford bolts, and D-bolts. The cone bolt is the first energy-absorbing-type bolts, and its rejuvenated anchor consists of a smooth steel rod with a flat, running flame forged at the distal end (Li et al., 2014), which can withstand significant deformation of the rock mass by allowing the rejuvenated anchor to move in the grouting materials such as the mortar and the resin. The Garford bolt developed in Australia consists of smooth reinforcement, unique technical anchor, and steel hull at the distal end of the anchor (Varden et al., 2008; Li et al., 2014), in which the inner diameter of the anchor is smaller than that of the bar inside the sleeve. After the rock is deformed, the bolt starts extruding from the inner hole of the bolt, absorbing the enormous energy generated by the expansion of the rock. The D-bolt developed in Norway consists of a smooth steel rod and several bolts used in the deep construction to prevent the tunnel from collapsing because of the rock

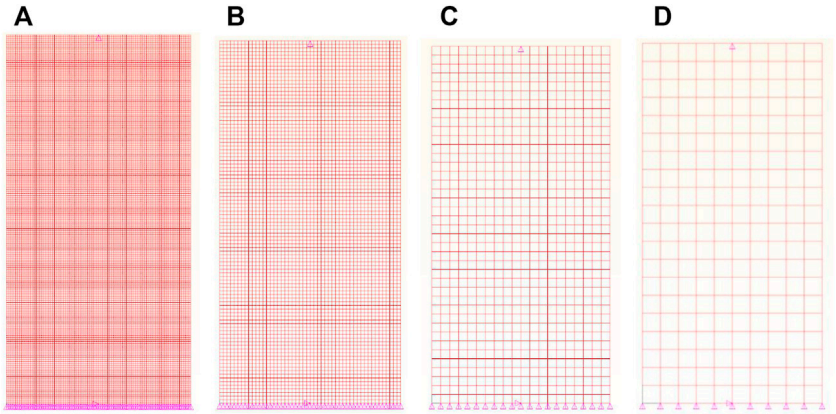

FIGURE 5 | Four grids to study the relation between penetration and point normal stress, in which the element size is set as **(A)** 0.5 mm, **(B)** 1 mm, **(C)** 2.5 mm, and **(D)** 5 mm.

TABLE 1 | Mechanical parameter settings of simulating point loading tests.

No.	Elastic modulus (GPa)	Poisson's ratio	No.	Elastic modulus (GPa)	Poisson's ratio	No.	Elastic modulus (GPa)	Poisson's ratio	No.	Elastic modulus (GPa)	Poisson's ratio
1	1	0.05	13	2	0.2	25	3	0.35	37	5	0.05
2	1	0.1	14	2	0.25	26	3	0.4	38	5	0.1
3	1	0.15	15	2	0.3	27	3	0.45	39	5	0.15
4	1	0.2	16	2	0.35	28	4	0.05	40	5	0.2
5	1	0.25	17	2	0.4	29	4	0.1	41	5	0.25
6	1	0.3	18	2	0.45	30	4	0.15	42	5	0.3
7	1	0.35	19	3	0.05	31	4	0.2	43	5	0.35
8	1	0.4	20	3	0.1	32	4	0.25	44	5	0.4
9	1	0.45	21	3	0.15	33	4	0.3	45	5	0.45
10	2	0.05	22	3	0.2	34	4	0.35			
11	2	0.1	23	3	0.25	35	4	0.4			
12	2	0.15	24	3	0.3	36	4	0.45			

burst. The D-bolt can achieve both high loading capacity and deformability by the elongation of the steel bar between anchors (Li, 2010; Li et al., 2014). These energy-absorbing bolts are considered as important support materials for rock breaking and for the crushing of soil treasures in underground construction. Generally speaking, these energy-absorbing rock bolts are considered as important support materials for rock fracturing and fragmentation.

In this study, a novel umbrella-shaped bolt (U-bolt) was proposed. It is mainly composed of hinges and rigid rods and uses the compression and friction to obtain the anchoring force. The new bolt is introduced in **Section 2**, concentrating on the structural and mechanical analyses of U-bolts, and the relation between penetration and point normal stress was discussed. The numerical model establishment method for U-bolts was described in **Section 3**. This method was then applied to the U-bolt simulation of the rock tunnel excavation and rock slope in **Section 4**, and the performance of U-bolts was compared between no supporting and U-bolt-supporting cases.

TABLE 2 | Fitting coefficients and R square of the relation between the normal stiffness K against the elastic modulus E and Poisson's ratio v.

Element size (mm)	a	b	R Square (%)
0.5	382.2	0.3797	99.99
1	209.4	0.3773	99.98
2.5	95.89	0.3697	99.99
5	53.85	0.3685	99.99

2 STRUCTURAL ANALYSIS

2.1 Basic Description of Umbrella-Shaped Bolt

As shown in **Figure 1A**, the umbrella-shaped bolt consists of the top hinge, the rigid rod, the linking rod, the anchoring tray, the bottom sliding block, the main bolt, the middle sliding block, and the middle hinge. Many rigid rods are connected to the main bolt through the top hinge, and they are also connected with the corresponding linking rods with the middle hinge. The linking rod can move with the middle sliding block along the main bolt.

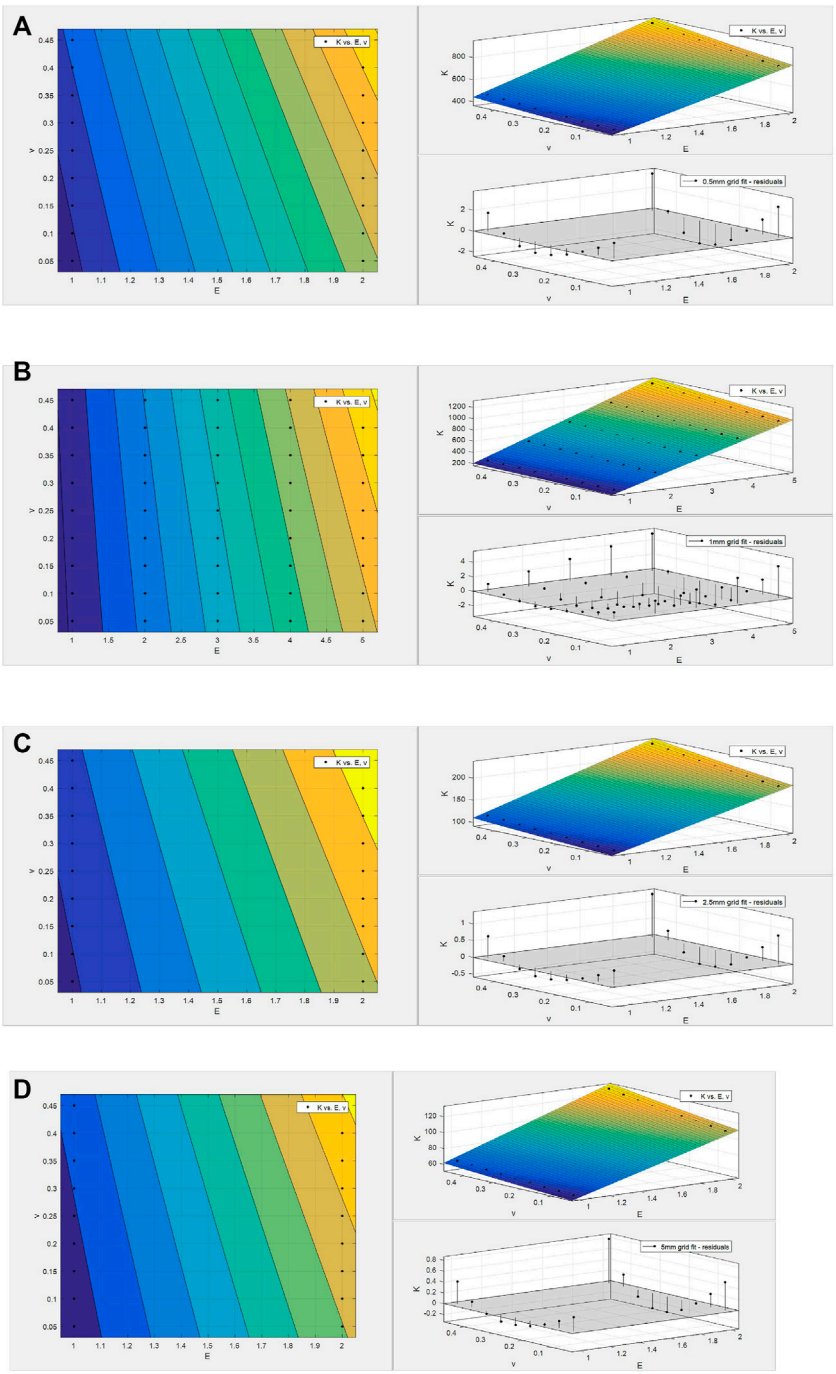

FIGURE 6 | Fitting results of stiffness K against the elastic modulus E and Poisson's ratio v, in which the element size is **(A)** 0.5 mm, **(B)** 1 mm, **(C)** 2.5 mm, and **(D)** 5 mm.

In addition, there is also a bottom sliding block adhering to the anchoring tray. The bolt in the packing state (**Figure 1B**) and opening state (**Figure 1C**) is also illustrated.

During installation (as illustrated in **Figure 2A**), a bore hole with a reasonable dimension is drilled at first and the U-bolt is then inserted into the hole of the rock mass. Both the rigid rods and linking rods shrink together, which are close to the main bolt in this process. The bottom sliding block is adhered to the rock mass with glue, and the anchoring tray is fixed on the surface of the internal tunnel free face.

When the rock mass initiates dilation with many excavation-induced fractures (as shown in **Figure 2B**), the whole section begins to expand (Wang et al., 2020). The main bolt then starts to extend, and the rigid rods initiate expanding. They squeeze the internal face

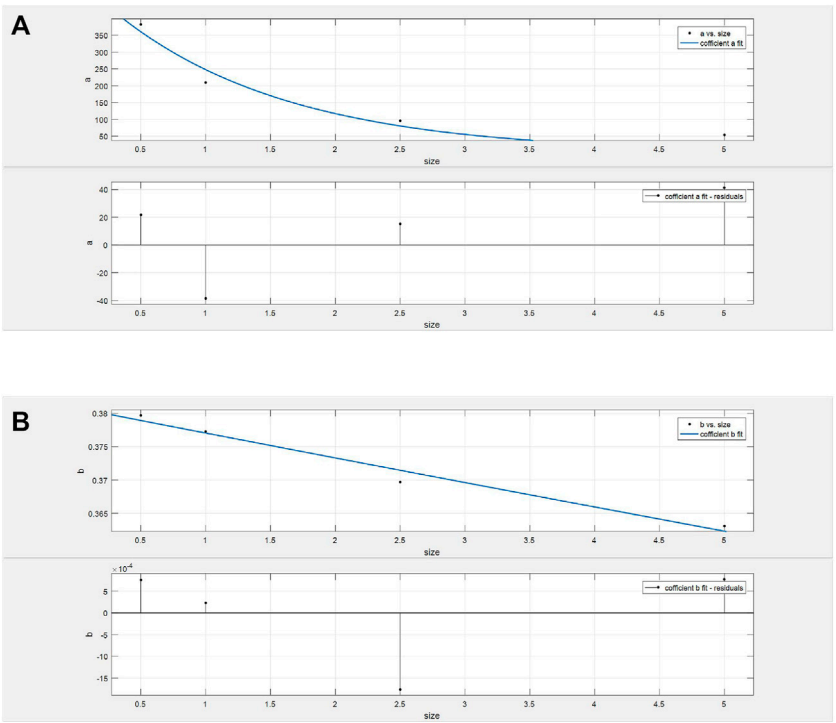

FIGURE 7 | Fitting results of coefficients against element sizes, where **(A)** coefficient *a* and **(B)** coefficient *b*.

of the bore hole, and friction emerges between the internal face and the rigid rod. This friction and the tensile strength inhibit the dilation of the rock mass. Generally speaking, the tension of the bolt is converted into the extrusion force on the rock mass, and the higher the compressive strength of the rock mass is, the greater the friction force and anchoring force the bolt can obtain.

2.2 Force Analysis

The mechanical analysis is studied in this section. As shown in **Figure 3A**, when the U-bolt is totally expanding, we define the distance between the top and middle hinges as width w, and the distance between the top hinge and the end of the rigid rod as distance d. The angle between the main bolt and the linking rod is α, and the length of the linking rod can be calculated as follows:

$$l = \frac{w}{sin\alpha}. \tag{1}$$

As illustrated in **Figure 3B**, when the U-bolt is working, the opening angle is defined as Δθ, and the expanding length can be acquired as follows:

$$\Delta d = d \cdot sin\Delta\theta. \tag{2}$$

In **Figure 3C**, we can find that the initial position distance between the top hinge and middle sliding block can be obtained as follows:

$$D = l + w. \tag{3}$$

The law of cosines (Lee, 1997) will be satisfied (as shown in **Figure 3D**), and the relation between the opening angle Δθ and the extension length ΔL is shown as follows:

$$\cos\Delta\theta = \frac{(D-\Delta L)^2 + d^2 - l^2}{2d(D-\Delta L)}. \tag{4}$$

Combining **Eqs 1**–**4**, we get

$$\Delta d = d \cdot \sqrt{1 - \frac{(D-\Delta L)^2 + d^2 - l^2}{2d(D-\Delta L)}}. \tag{5}$$

In the reasonable range of ΔL, the expanding length Δd monotonically increases with the extension length ΔL.

When the U-bolt is working (**Figure 4A**), the additional tensile stress is provided with two parts, including the tensile strength σ_t^b of the main bolt and the friction f between the bore hole inner face and the rigid rod, which indicates that

$$\Delta\sigma_t = \sigma_t^b + f. \tag{6}$$

As illustrated in **Figure 4B**, the friction can be calculated according to the Coulomb criterion (Renard, 2006), which means that

$$f = \mu\sigma_N, \tag{7}$$

where μ is the friction coefficient and σ_N is the normal stress.

The expanding length Δd in **Figures 3B**, **4B** is also known as the penetration; therefore, the normal force σ_N can be defined by a linear relation (1) as follows:

$$\sigma_N = K\Delta d, \tag{8}$$

where K is the contact stiffness, and relation between penetration and the point normal stress will be discussed in the next section.

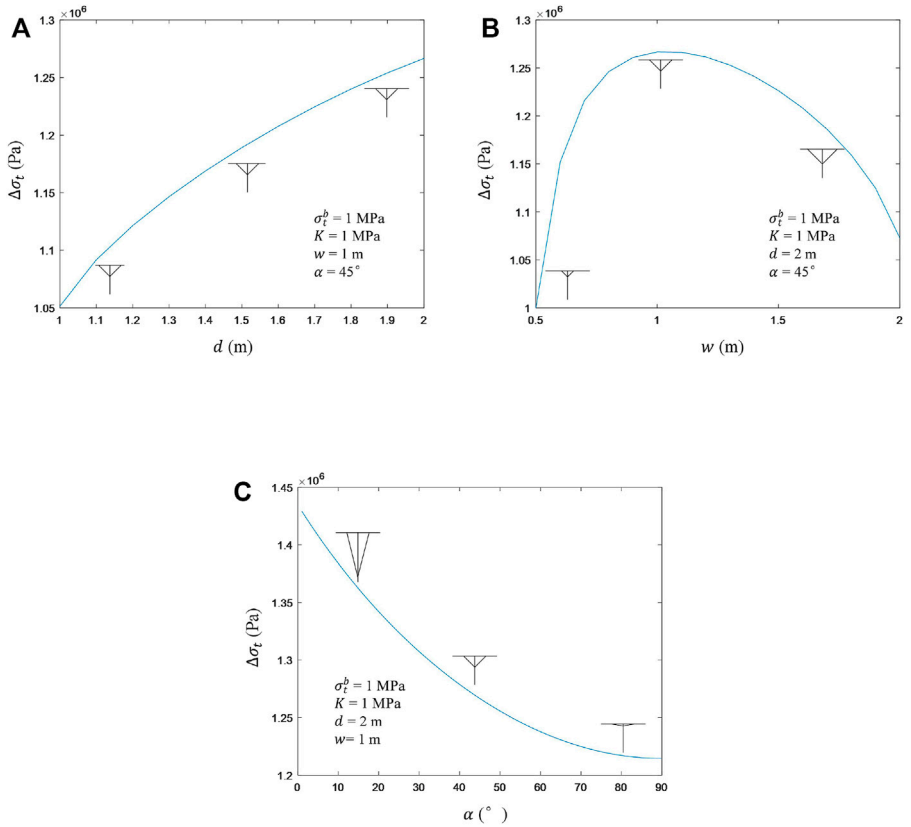

FIGURE 8 | Sensibility analysis of the structural parameters d, w, and α. **(A), (B)**, and **(C)** are the influences of d, w, and α to the enhanced tensile strength, respectively.

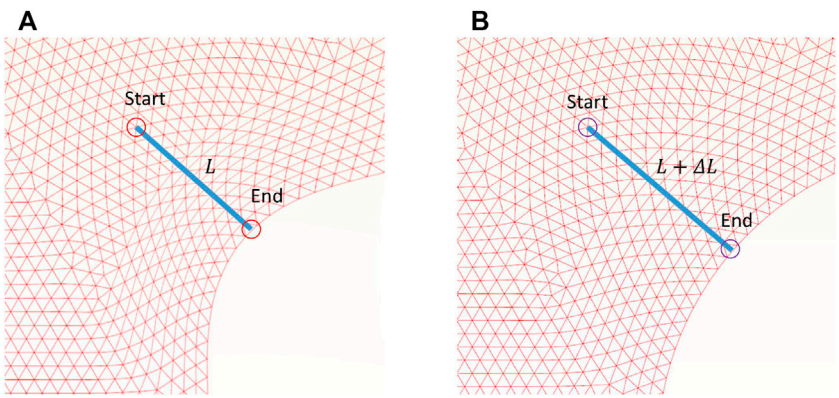

FIGURE 9 | Calculation of the penetration, in which **(A)** the moment when U-bolt installs, and **(B)** the moment when U-bolt is working.

2.3 Relation Between Penetration and Point Normal Stress

As pointed out in **Eq. 8**, in order to study the relation between the penetration and the point normal stress, it is better to establish the relation between the stiffness and the penetration in **Eq. 8**. Here, a numerical approach is provided, and the analysis zone is considered as an elastic body.

As illustrated in **Figure 5**, four simulation grids are set, including 0.5 mm (**Figure 5A**), 1 mm (**Figure 5B**), 2.5 mm (**Figure 5C**), and 5 mm (**Figure 5D**). The size of all these four grids is 0.5 mm × 0.1 mm, and the aspect ratios are all 2 to eliminate the influence of the aspect ratio effect. The bottom edge of these simulation specimens is fixed at the vertical direction, and the middle of the bottom edge is also fixed at the horizontal

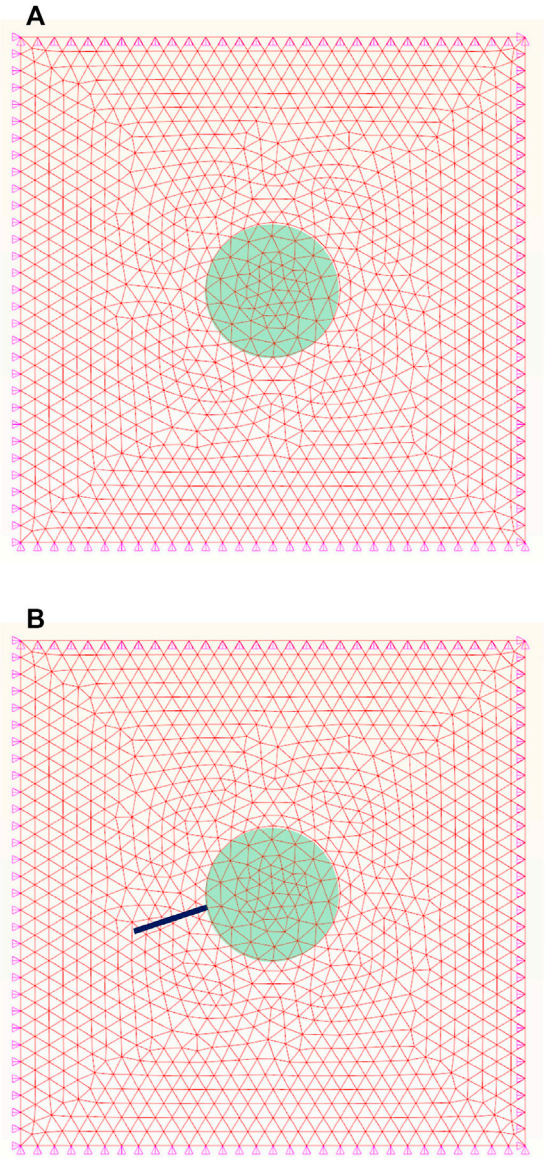

FIGURE 10 | Simulation setup, where **(A)** no support and **(B)** support with U-bolt.

direction. Only the middle of the top edge is vertical displacement loading representing the point loading.

At least 18 simulation tests were conducted for each grid, and the mechanical properties are listed in **Table 1**. It should be noted that 45 tests were conducted for 0.05 mm element size, and 18 tests (Nos. 1~18 in **Table 1**) were conducted for other element sizes.

A fitting function between the normal stiffness K_n against the elastic modulus E and Poisson's ratio v is established as follows:

$$K_n = \frac{aE}{1 - bv}, \tag{9}$$

where a and b are the fitting coefficients. The fitting coefficients and R square are provided in **Table 2**. As the simulation is conduction for the elastic body, the R squares for all the element sizes are close to 1, and the fitting function (**Figures 6A–D**) performs well.

The element size effect is also considered, an exponent function is proposed, and the following relation is obtained:

$$a = 524.3e^{-0.7489s}, \tag{10.1}$$

$$b = 0.3808e^{-0.0099s}, \tag{10.2}$$

where s is the element size. The fitting results are illustrated in **Figures 7A,B**. The R square for the coefficient a is 93.96%, and that for b is 97.46%, and they all have relatively good fitting performances.

Combing all these equations, the enhanced tensile strength provided by the U-bolt can be calculated as follows:

$$\Delta\sigma_t = \sigma_t^b + \mu\frac{524.3e^{-0.7489s}E}{1 - 0.3808e^{-0.0099s}v}d \cdot \sqrt{1 - \frac{\left(w + \frac{w}{\sin\alpha} - \Delta L\right)^2 + d^2 - \left(\frac{w}{\sin\alpha}\right)^2}{2d\left(w + \frac{w}{\sin\alpha} - \Delta L\right)}}. \tag{11}$$

In **Eq. 11**, there are only 8 parameters that need to be determined, of which E, v, and μ are the mechanical properties of the rock mass, which is known before simulation. σ_t^b is the tensile strength of the main bolt; d, w, and α are the structural parameters of the U-bolt, and they determine the reinforcement ability of the U-bolt. Only s and ΔL are the variables which need to be determined during the simulation. For the structural parameters d, w, and α, the sensibility analysis has been conducted, as illustrated in **Figure 5**, in order to study the influence of them. The results indicate that the enhanced tensile strength increases with the increase in d and decreases with the increase in α. With the increase in w, the enhanced tensile strength increases at first and then decreases.

3 NUMERICAL IMPLEMENTATION

3.1 Basic Framework

The numerical implementation of the U-bolt follows a simple framework, which is finding the element where bolts go through (they are defined as the bolt elements), then calculating the enhanced tensile strength based on the extension length ΔL, and finally adding the enhanced tensile strength to the current strength of the bolt elements. These processes will be introduced in detail in the next sections.

TABLE 3 | Crustal stress of the simulated tunnel.

σ_x (MPa)	σ_y (MPa)	τ_{xy} (MPa)
10	30	5

TABLE 4 | Mechanical properties of the simulated tunnel.

	Origin rock mass	Fractured rock mass	Failed rock mass (residual)
Elastic modulus (GPa)	10	10	10
Poisson's ratio	0.3	0.3	0.3
Cohesion strength (MPa)	10	1	1
Friction angle (°)	20	20	40
Tensile strength (MPa)	5	1	1
Critical plastic strain (‰)	0	2	4

TABLE 5 | U-bolt parameters.

Tensile strength (MPa)	d (m)	w (m)	α (°)
10	2	1	45

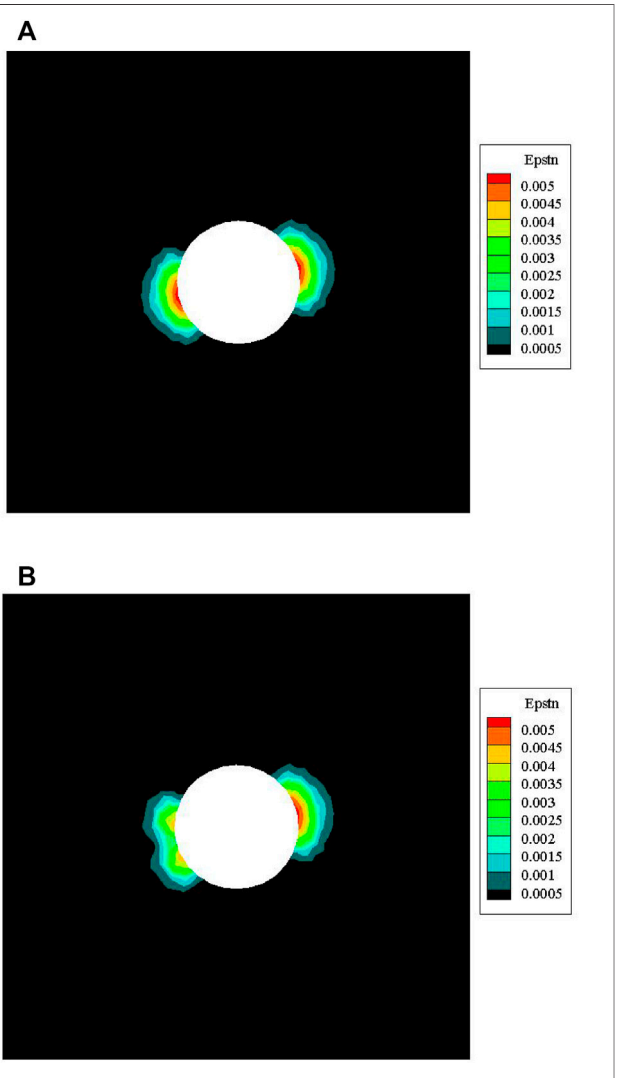

FIGURE 11 | Simulated equivalent plastic strain results, in which **(A)** no support and **(B)** support with U-bolt.

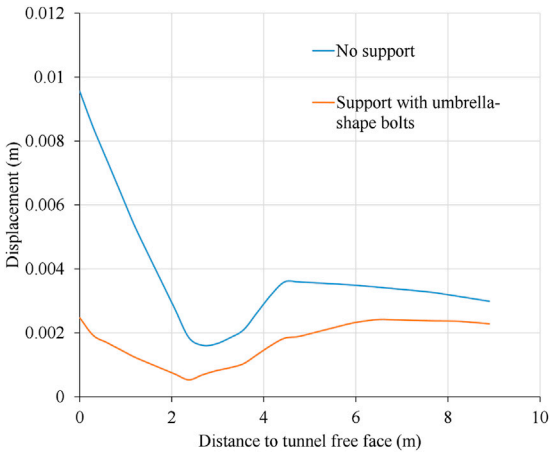

FIGURE 12 | Comparison of the displacement evolution results along the bolt direction for no support and support with U-bolt cases. In addition, the result is the displacement plotted against the distance to tunnel-free face.

3.2 Identification of Bolt Elements

The bolt elements are identified at the beginning of the simulation. There are three cases that emerge during the identification of bolt elements, as shown in **Figure 8**, including case A where the bolt does not go through any node of the bolt element, case B where the bolt goes through 1 node of the bolt element, and case C where the bolt goes through 2 nodes of the bolt element.

For cases A and B, it is easy to point out the bolt element through elements where the bolt cut across. For case C, it may be a little different, in which the 2 elements with opposite positions where the bolt goes through are all treated as the bolt elements.

3.3 Calculation of the Penetration

Figure 9 shows two moments of the U-bolt operation in the simulation. For **Figure 9A**, when the bolt is installed, the initial length of the U-bolt will be calculated using the following equation:

$$L = \left|\left[\left(x^{start} + u_x^{start}\right) - \left(x^{end} + u_x^{end}\right)\right]cos\beta + \left[\left(y^{start} + u_y^{start}\right) - \left(y^{end} + u_y^{end}\right)\right]sin\beta\right|, \tag{12}$$

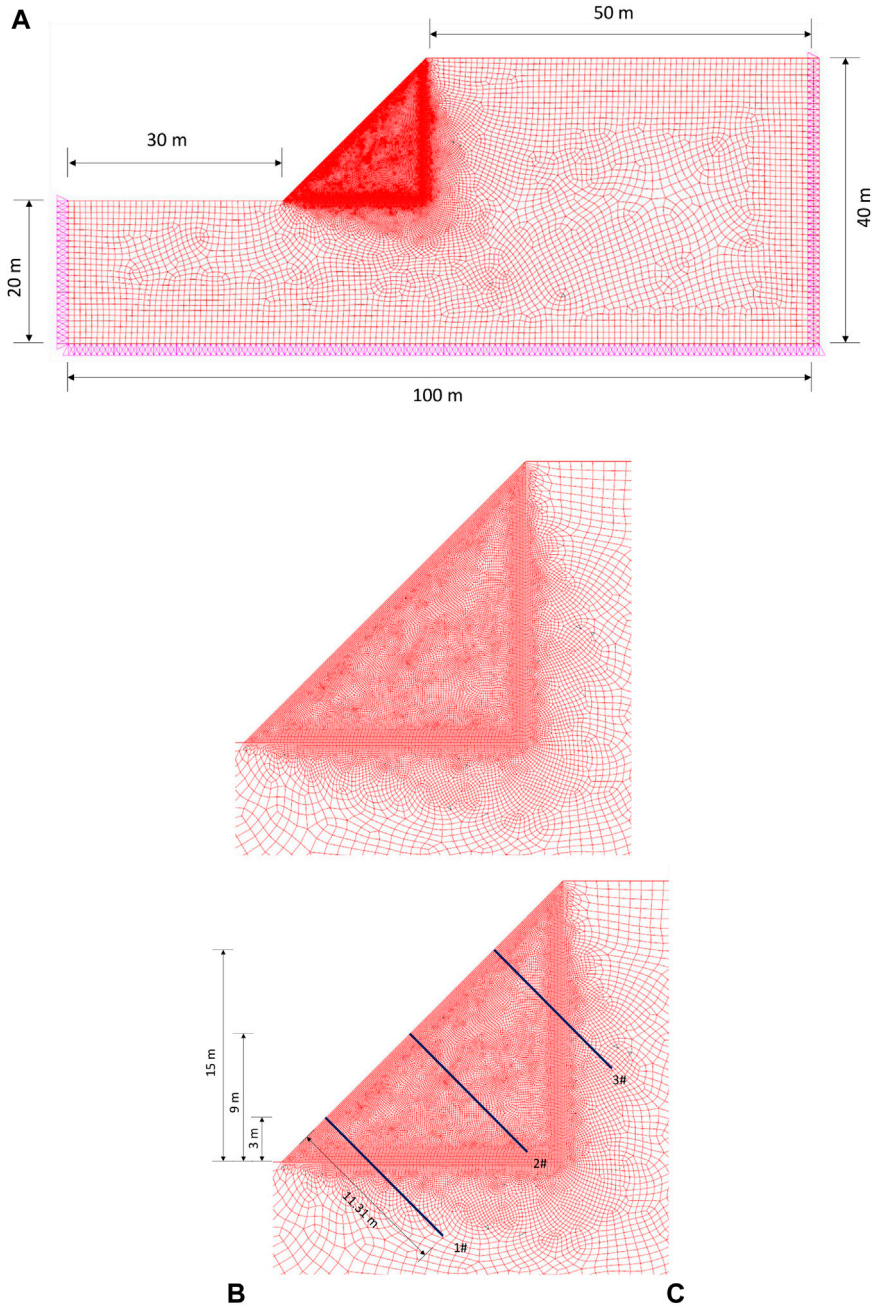

FIGURE 13 | Simulation setup of the rock slope, where **(A)** the simulation mesh and boundary set, **(B)** no support model, and **(C)** support model with U-bolt.

where x^{start}, y^{start}, x^{end}, and y^{end} are the horizontal and vertical positions of the two ends of the U-bolt, and u_x^{start}, u_y^{start}, u_x^{end}, and u_y^{end} are the horizontal and vertical displacements of the two ends of the U-bolt. β is the installation angle which is the angle between the U-bolt and the horizontal line, and it can be obtained as follows:

$$\beta = \operatorname{atan}\left(\frac{\left(y^{start} + u_y^{start}\right) - \left(y^{end} + u_y^{end}\right)}{\left(x^{start} + u_x^{start}\right) - \left(x^{end} + u_x^{end}\right)}\right). \tag{13}$$

Using **Eqs 12**, **13**, the current length of the U-bolt $L + \Delta L$ can also be calculated, and the extension length ΔL can be acquired easily. It should be pointed out that ΔL is calculated in each iteration and updated all the time.

3.4 Tensile Strength Reinforcement of Bolt Elements

Once the extension length ΔL is acquired in each simulating iteration, the enhanced tensile strength is calculated using **Eq. 11**.

TABLE 6 | Mechanical properties of the simulated slope.

	Origin rock mass	Fractured rock mass	Failed rock mass (residual)
Density (kg/m^3)	2.5	2.5	2.5
Elastic modulus (GPa)	10	10	10
Poisson's ratio	0.3	0.3	0.3
Cohesion strength (MPa)	0.15	0.01	0.01
Friction angle (°)	20	20	40
Tensile strength (MPa)	5	1	1
Critical plastic strain (‰)	0	2	4

Then, it is added to the current tensile strength and cohesion of the bolt elements. This process occurs all the time for all the U-bolt elements, which indicates that the tensile strength and cohesion of the U-bolt element vary with the calculation.

4 APPLICATION IN ROCK ENGINEERING

4.1 Case 1: Rock Tunnel Excavation

4.1.1 Simulation Preparation

Figure 10 provides the simulation setup of the rock tunnel excavation. **Figure 10A** is the no supporting case, and **Figure 10B** is the case with U-bolt supporting. The size is set to be 60 m × 60 m. Vertical displacements on the top and bottom edges are fixed to zero, and horizontal displacements on the left and right edges are also fixed to zero. The element numbers of these two grids are about 3,000. The tunnel is set up in the middle of the grid, and the radius of the tunnel is 8 m. For the U-bolt-supporting cases (**Figure 10B**), a U-bolt is installed at the bottom left point after excavation, and the length of the U-bolt is about 8 m.

The crustal stress information is shown in **Table 3**, the rock mass properties are listed in **Table 4**, and the U-bolt parameters are provided in **Table 5**. The cohesion-weakening and friction-strengthening (CWFS) model is chosen as the constitutive model (Hajiabdolmajid et al., 2002; Feng et al., 2021). It should be noted that the U-bolt length and corresponding strength are set to be long and strong in order to make results more evident.

4.1.2 Performance of Umbrella-Shaped Bolts

The equivalent plastic strain (Hajiabdolmajid and Kaiser, 2003; Faleskog and Barsoum, 2013) can be applied to reflect the failure degree and the depth of excavation damaged zone. **Figure 11** shows the simulated equivalent plastic strain results of two cases. For the no support case (**Figure 11A**), the bottom left part seems to be symmetrical to the top right part, and the equivalent plastic strain for the most seriously damaged area is about 0.005.

For the U-bolt support case (**Figure 11B**), the equivalent plastic strain result is not symmetrical for the bottom left part and the top right part. Regarding the bottom left part, the shape of EDZ sank to the tunnel-free face and the depth of EDZ became smaller. Meanwhile, the equivalent plastic strain for the most seriously damaged area in the bottom left part is about 0.004.

Figure 12 compares the displacement evolution results along the bolt direction for no support and support with U-bolt cases. The tangential displacement along the bolt direction for the U-bolt supporting case is significantly inhibited. It changes from about 1 cm for the no support case to about 2 mm for the U-bolt-supporting cases, reducing about 80%. Moreover, the displacement along the bolt direction becomes gentler than that in the fluctuant circumstance of the no support case, indicating the U-bolt makes the rock mass deform globally and entirely.

4.2 Case 2: Rock Slope

4.2.1 Simulating Preparation

Figure 13 illustrates the simulation setup of the rock slope. As shown in **Figure 13A**, the size is set to be 100 m × 40 m, and vertical displacements on the bottom edges are fixed to zero, and horizontal displacements on the left and right edges are also constrained to zero. Meanwhile, **Figure 13B** is the no supporting case, and **Figure 10C** is the U-bolt supporting-case. For the U-bolt-supporting case (**Figure 10C**), the length of each U-bolt is 11.31 m, and they are installed at the slope body, which are perpendicular to the slope surface.

Three kinds of U-bolts are set, including 1# (3 m vertical distance from the slope feet), 2# (9 m vertical distance from the slope feet), and 3# (15 m vertical distance from the slope feet). In addition, four simulation cases are conducted: no support case, support case with 1# U-bolt, support case with 1# and 2# U-bolts, and support case with 1#, 2#, and 3# U-bolts. The rock mass properties are given in **Table 6**, and the U-bolt parameters are provided in **Table 5**. Furthermore, the CWFS model is used.

4.2.2 Performance of Umbrella-Shaped Bolts

The maximum principal stress contours for all four cases are shown in **Figure 14**. The tensile stresses on elements with U-bolts are definite for all supporting cases (**Figures 14B–D**) comparing the no support one (**Figure 14A**). It indicates that the U-bolt can provide a tensile anchorage force constraining the landslide distance. Another finding of the tensile anchorage stress is illustrated in **Figure 15**. With the increase in the U-bolt extension, the tensile stresses of element with U-bolt increase, which matches with the basic design of U-bolts in **Section 2.1** and operation description **Figure 2**.

The displacement contours of four simulation cases are shown in **Figure 16**. For the no support case in **Figure 16A**, the maximum displacement is larger than 0.07 m, and the sliding volume (here, it is considered as an area whose displacement is greater than 0.03 m in the dashed area in **Figure 16**) is large. For the support case with 1# U-bolt in **Figure 16B**, the maximum displacement is about 0.06 m. For the support case with 1# and 2#

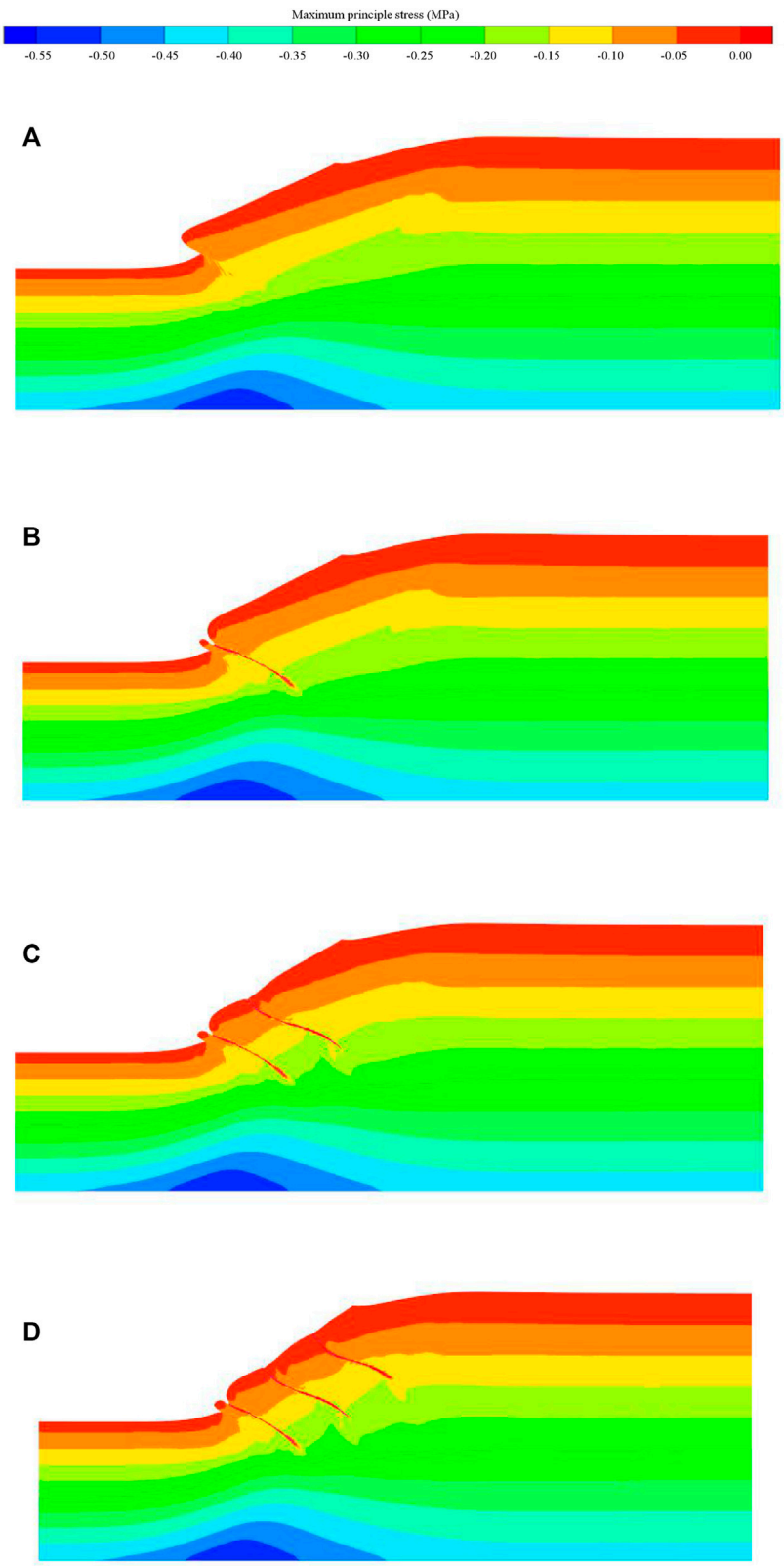

FIGURE 14 | Maximum principle stress contours, in which **(A)** no support, **(B)** support with 1# U-bolt, **(C)** support with 1# and 2# U-bolts, and **(D)** support with 1#, 2#, and 3# U-bolts.

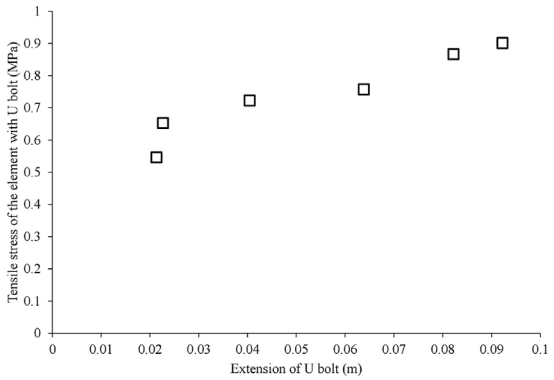

FIGURE 15 | Tensile stresses of elements with U-bolts plotted against the extension of U-bolts.

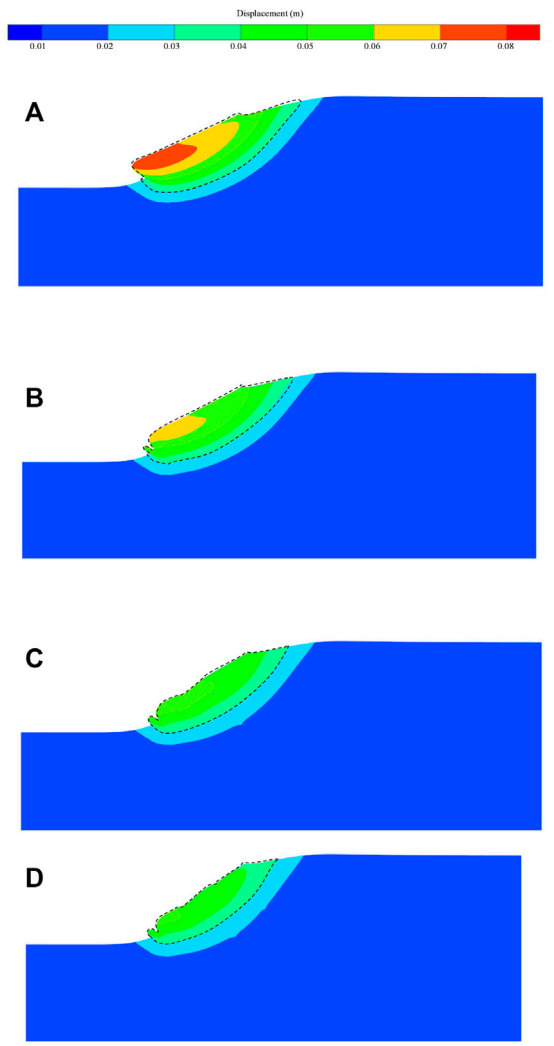

FIGURE 16 | Displacement contours, in which **(A)** no support, **(B)** support with 1# U-bolt, **(C)** support with 1# and 2# U-bolts, and **(D)** support with 1#, 2#, and 3# U-bolts.

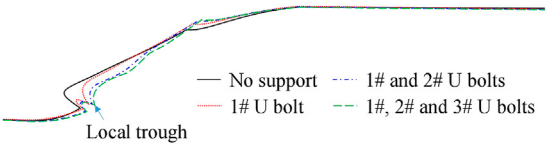

FIGURE 17 | Slope boundary comparisons of different simulations.

U-bolts (**Figure 16C**) and support case with 1#, 2#, and 3# U-bolts (**Figure 16D**), the maximum displacement is about 0.05 m. Results indicate that the U-bolts can decrease the maximum displacement and sliding volume efficiently.

Moreover, the slope boundary comparisons of different simulation cases are illustrated in **Figure 17**. It can be observed that the local constraining effect is evident, especially for 1# U-bolt near the slope feet, as local troughs emerge for the slope boundary. For the green dashed line (support case with 1#, 2#, and 3# U-bolts), the global constraining effect is prominent since the existence of 1#, 2#, and 3# U-bolts. Generally, due to the existence of the U-bolt, the decrease in the landslide distance is evident, and the global anchoring effect becomes better and better with the increase in the U-bolt number.

5 CONCLUSIONS AND DISCUSSIONS

A novel type of rock bolt, that is, the U-bolt was proposed in this study. The basic information was introduced at first, and the mechanical analysis was conducted to study the U-bolt reinforcement mechanism. In order to verify the real performance of the U-bolt, a numerical model has been established and then it was applied to the rock tunnel excavation simulation. Results reveal the rationality of the initial design goal of the U-bolt. Some important conclusions can be drawn as follows:

1) This friction and the tensile strength of the U-bolt will inhibit the dilation of the rock mass. The operating mechanism is that the tension of the bolt is converted into the extrusion force on the rock mass, which makes the U-bolt different from other rock bolts. Meanwhile, based on the characteristics of the U-bolt, the bolt can continuously compress the rock mass, and the higher compressive strength of the rock mass is used to obtain the greater friction force and anchoring force.
2) A mechanical model of U-bolt was proposed, and it concentrated on the enhanced tensile strength calculation method on the basis of structural analysis and the relation between penetration and point normal stress.
3) The proposed U-bolt mechanical model has been implemented through the identification of bolt elements, the calculation of the penetration, and the tensile strength reinforcement of bolt elements. The rock tunnel excavation simulations reveal that the U-bolt can reduce the tangential displacement along the bolt and EDZ depth, and alleviate the failure degree. Moreover, the U-bolt can also decrease the landslide distance by providing adequate anchorage force and stress with the extension.

DATA AVAILABILITY STATEMENT

The original contributions presented in the study are included in the article/supplementary material, further inquiries can be directed to the corresponding author.

AUTHOR CONTRIBUTIONS

YX: conceptualization and methodology; HC: data curation and writing—original draft preparation; YC: writing—review and editing, and project administration; SH: supervision; ZW: software and visualization; and YG: formal analysis.

FUNDING

The authors sincerely acknowledge the financial support from the National key R&D projects of China (grant No. 2017YFC1501303) and the Fundamental Research Funds for Central Public Welfare Research Institutes (grant No. CKSF2021460/YT).

ACKNOWLEDGMENTS

The authors express their gratitude to the State Key Laboratory of Geomechanics and Geotechnical Engineering, Institute of Rock and Soil Mechanics, Chinese Academy of Sciences.

REFERENCES

Aydan, Ö., and Kawamoto, T. (1992). The Stability of Slopes and Underground Openings against Flexural Toppling and Their Stabilisation. *Rock Mech. Rock Engng* 25 (3), 143–165. doi:10.1007/bf01019709

Bizjak, K. F., and Petkovšek, B. (2004). Displacement Analysis of Tunnel Support in Soft Rock Around a Shallow Highway Tunnel at Golovec. *Eng. Geology.* 75 (1), 89–106. doi:10.1016/j.enggeo.2004.05.003

Cai, Y., Esaki, T., and Jiang, Y. (2004). A Rock Bolt and Rock Mass Interaction Model. *Int. J. Rock Mech. Mining Sci.* 41 (7), 1055–1067. doi:10.1016/j.ijrmms.2004.04.005

Chen, Y. (2014). Experimental Study and Stress Analysis of Rock Bolt anchorage Performance. *J. Rock Mech. Geotechnical Eng.* 6 (5), 428–437. doi:10.1016/j.jrmge.2014.06.002

Faleskog, J., and Barsoum, I. (2013). Tension–torsion Fracture Experiments—Part I: Experiments and a Procedure to Evaluate the Equivalent Plastic Strain. *Int. J. Sol. Structures* 50 (25-26), 4241–4257. doi:10.1016/j.ijsolstr.2013.08.029

Feng, X. T., Wang, Z., Zhou, Y., Yang, C., Pan, P. Z., and Kong, R. (2021). Modelling Three-Dimensional Stress-dependent Failure of Hard Rocks. *Acta Geotechnica* 16 (6), 1647–1677. doi:10.1007/s11440-020-01110-8

Hajiabdolmajid, V., and Kaiser, P. (2003). Brittleness of Rock and Stability Assessment in Hard Rock Tunneling. *Tunnelling Underground Space Technol.* 18 (1), 35–48. doi:10.1016/s0886-7798(02)00100-1

Hajiabdolmajid, V., Kaiser, P. K., and Martin, C. D. (2002). Modelling Brittle Failure of Rock. *Int. J. Rock Mech. Mining Sci.* 39 (6), 731–741. doi:10.1016/s1365-1609(02)00051-5

Lee, J. R. (1997). The Law of Cosines in a Tetrahedron. *Pure Appl. Maths.* 4 (1), 1–6.

Li, C. C. (2010). A New Energy-Absorbing Bolt for Rock Support in High Stress Rock Masses. *Int. J. Rock Mech. Mining Sci.* 47 (3), 396–404. doi:10.1016/j.ijrmms.2010.01.005

Li, C. C. (2012). Performance of D-Bolts under Static Loading. *Rock Mech. Rock Eng.* 45 (2), 183–192. doi:10.1007/s00603-011-0198-6

Li, C. C., Stjern, G., and Myrvang, A. (2014). A Review on the Performance of Conventional and Energy-Absorbing Rockbolts. *J. Rock Mech. Geotechnical Eng.* 6 (4), 315–327. doi:10.1016/j.jrmge.2013.12.008

Liu, J., Wang, J., and Xu, T. (2018). Research of Swelling Prestressed Bolts Using inMechanized Excavation of Large Section Tunnel. *Tunnel Construction* 38 (z2), 324–329. doi:10.3973/j.issn.2096-4498.2018.S2.044

Renard, Y. (2006). A Uniqueness Criterion for the Signorini Problem with Coulomb Friction. *SIAM J. Math. Anal.* 38 (2), 452–467. doi:10.1137/050635936

Su, G., Feng, X., Wang, J., Jiang, J., and Hu, L. (2017). Experimental Study of Remotely Triggered Rockburst Induced by a Tunnel Axial Dynamic Disturbance under True-Triaxial Conditions. *Rock Mech. Rock Eng.* 50 (8), 2207–2226. doi:10.1007/s00603-017-1218-y

Varden, R., Lachenicht, R., Player, J., Thompson, A., and Villaescusa, E. (2008). "Development and Implementation of the Garford Dynamic Bolt at the Kanowna Belle Mine," in Proceedings of the 10th Underground operators Confenrence 19, Launceston, TAS, April 14–16, 2008 95–102.

Wang, B., and He, C. (2011). Application of Prestressed Hollow Grouting Anchor Rod in Rockburst Prevention Design of CangLing Tunnel. *Highway* (10), 206–210.

Wang, Z., Feng, X.-T., Yang, C., Zhou, Y., Xu, H., Han, Q., et al. (2020). Experimental Investigation on Fracturing Process of marble under Biaxial Compression. *J. Rock Mech. Geotechnical Eng.* 12 (5), 943–959. doi:10.1016/j.jrmge.2020.05.002

Zheng, Y., Chen, C., Liu, T., and Ren, Z. (2021). A New Method of Assessing the Stability of Anti-dip Bedding Rock Slopes Subjected to Earthquake. *Bull. Eng. Geol. Environ.* 80, 3693–3710. doi:10.1007/s10064-021-02188-4

Zheng, Y., Chen, C., Liu, T., Zhang, H., Xia, K., and Liu, F. (2018). Study on the Mechanisms of Flexural Toppling Failure in Anti-inclined Rock Slopes Using Numerical and Limit Equilibrium Models. *Eng. Geology.* 237, 116–128. doi:10.1016/j.enggeo.2018.02.006

Conflict of Interest: Author YG was employed by company PowerChina Huadong Engineering Corporation Limited.

The remaining authors declare that the research was conducted in the absence of any commercial or financial relationships that could be construed as a potential conflict of interest.

Publisher's Note: All claims expressed in this article are solely those of the authors and do not necessarily represent those of their affiliated organizations, or those of the publisher, the editors, and the reviewers. Any product that may be evaluated in this article, or claim that may be made by its manufacturer, is not guaranteed or endorsed by the publisher.

frontiers | Frontiers in Earth Science

ORIGINAL RESEARCH
published: 06 April 2022
doi: 10.3389/feart.2022.849046

Influence of Swelling on Shear Strength of Expansive Soil and Slope Stability

Tian Lan[1], *Rui Zhang*[2]*, *Biyu Yang*[3] *and Xiong Meng*[3]

[1]School of Traffic and Transportation Engineering, Changsha University of Science and Technology, Changsha, China, [2]National Engineering Laboratory of Highway Maintenance Technology, Changsha University of Science and Technology, Changsha, China, [3]Zhaotong Zhaoyang Ring Highway Investment and Development Corporation Ltd., Zhaotong, China

Rainfall is the main factor leading to the landslide of expansive soil slope. To deeply understand the instability mechanism of expansive soil slope under rainfall conditions, it is necessary to clarify the strength attenuation mechanism of expansive soil caused by water absorption and swelling. Therefore, the improved constant volume direct shear test was used in this study to compare with the conventional test, focusing on the variation of effective shear strength parameters with dry density (volume). The micromechanism of expansive soil strength attenuation is further studied, and the influence of expansive soil on slope stability is analyzed by numerical calculation. The results show that the improved direct shear apparatus and method can keep the volume of expansive soil specimens unchanged before and after shear and obtain the real effective shear strength parameter of soil. Under the same conditions, the shear strength parameter of the improved direct shear test is lower than that of the conventional direct shear test. The rapid thickening of the lamellar structure of montmorillonite in expansive soil will lead to the fragmentation and dispersion of clay particles, which is one of the fundamental reasons for the strength difference between expansive soil and ordinary clay. In slope stability analysis, the effect of swelling on the shear strength of slope cannot be ignored and should be considered in engineering design.

Keywords: expansive soil, dry density, improved direct shear test, slope stability, shear strength

OPEN ACCESS

Edited by:
Yun Zheng,
Institute of Rock and Soil Mechanics (CAS), China

Reviewed by:
Shunchao Qi,
Sichuan University, China
Mohammadhossein Sadeghiamirshahidi,
Montana Technological University, United States

***Correspondence:**
Rui Zhang
zr@csust.edu.cn

Specialty section:
This article was submitted to Geohazards and Georisks, a section of the journal Frontiers in Earth Science

Received: *05 January 2022*
Accepted: *10 March 2022*
Published: *06 April 2022*

Citation:
Lan T, Zhang R, Yang B and Meng X (2022) Influence of Swelling on Shear Strength of Expansive Soil and Slope Stability. Front. Earth Sci. 10:849046. doi: 10.3389/feart.2022.849046

INTRODUCTION

Under the influence of hygrothermal environment and geological conditions, landslide disasters occur frequently in expansive soil areas (Hou et al., 2013; Dai et al., 2021; Liang et al., 2021). Rainfall infiltration is an important inducement factor of slope collapse (Qi and Vanapalli, 2018; Qi et al., 2019). Some slopes will slide in the rainy season when the slope ratio is 1:3 or even 1:5 (Xiao et al., 2018; Zhai and Cai, 2018; Abeykoon and Trofimovs, 2021). Therefore, only by deeply understanding the state change of expansive soil caused by humidification and clarifying the strength attenuation mechanism of expansive soil, target economic and reasonable engineering measures can be taken.

Studies have shown that the shear strength variation of expansive soil is mainly affected by the stress state, matric suction, dry–wet cycle, crack, and moisture content (Li et al., 2013; Al Haj and Standing, 2015; Zhang et al., 2016; Dong et al., 2018a; Huang et al., 2018). The strength envelope of expansive soil has non-linear characteristics, and there is a certain gap between the parameters obtained by linear fitting and the real shear strength parameter (Lade, 2010; He

et al., 2017). In the low-stress range (0–50 kPa), the cohesion is only a few kPa, but the internal friction angle is as high as 30°–40°. In the high-stress range (greater than 50 kPa), the cohesion obtained by fitting is more than 20 kPa, and the internal friction angle is about 20°, in the stress range of conventional strength tests, the cohesion and internal friction angles obtained by fitting are not low (Xiao et al., 2017). Many slope failures still occur when strength parameters are obtained by the conventional direct shear test and can be kept stable by calculation (Zhang et al., 2020a). Therefore, the actual shear strength parameter value of expansive soil is lower than that measured by conventional tests. The variation of matric suction can express the strength variation of general clay from unsaturated to saturated. However, for expansive soil, the saturated strength of specimens under different initial suction states varies greatly, so the unsaturated strength model cannot be effectively used for calculation and analysis. The dry–wet cycles and cracks mainly affect the soil structure (Burton et al., 2015; Julina and Thyagaraj, 2018; Huang et al., 2021), but the number of dry–wet cycles and the development of cracks are highly subjective, and they are difficult to apply quantitatively in slope stability analysis. The change of moisture content leads to the change of matric suction of soil, and it can affect the state of water retention in soil (Kayadelen et al., 2007; Çokça and Tilgen, 2010). The essential difference between expansive soil and general clay soil is that it is rich in swelling minerals such as montmorillonite and exhibits remarkable expansibility after humidification (Zhang et al., 2020b). For non-expansive soil, the change of soil moisture content only affects the volume of pore gas and pore water, while the volume of the soil skeleton remains constant. However, with the increase of soil skeleton volume, the dry density of expansive soil decreases, and the influence of humidifying swelling on the effective stress shear strength parameter cannot be ignored (Mašín and Khalili, 2016).

The expansive clay mineral particles expand with the increase of moisture content and compress with the increase of overburden, thus changing the microstructure and average particle size of soil (Katti and Shanmugasundaram, 2001). To reflect the effect of pore ratio on the shear strength of clay and its parameter, scholars proposed true strength theory and true strength parameter based on experiments. It was suggested that saturated clay should be obtained with different effective stresses but the same pore ratio by loading and unloading and then sheared to obtain the true strength parameter (Hvorslev, 1961). At present, the shear strength parameter of expansive soil is obtained by a triaxial and a direct shear apparatus (Ye et al., 2010; Dong et al., 2018b), but there are no specific measures and methods to ensure that the specimen volume (dry density) remains unchanged before and after shear. The reason is that, in the conventional test, the specimen will be saturated with water after applying different confining pressure or overburden loads, and the specimen will have different degrees of swelling or compression, which leads to the change of the dry density of the specimen before shear. This makes it difficult to obtain the real shear strength parameter of expansive soil under specific dry density conditions at present and also leads to the landslide failure of many expansive soil slopes that can be kept stable by design calculation.

This study aims to investigate the effect of swelling deformation on the effective shear strength parameter of expansive soil and reveal the attenuation mechanism of expansive soil strength caused by water absorption and swelling. Based on the true strength theory, direct shear tests of expansive soil at constant dry density under different initial saturation conditions were carried out by using the improved direct shear test apparatus, and the effective cohesion and effective internal friction angle of expansive soil at this dry density state were measured. Then, several groups of improved direct shear tests under different dry densities were carried out, and the results were compared with those of conventional direct shear tests, to obtain the variation rule of effective shear strength parameter with the decrease of dry density. A scanning electron microscope (SEM) and particle analyzer were used to obtain the changes of the microstructure of the specimens before and after shear and to reveal the attenuation mechanism of the saturated strength of expansive soil. Through numerical analysis, the influence of swelling on slope stability is studied, and the results can provide a reference for the instability mechanism analysis and support structure design of expansive soil slopes.

SELECTED SOIL SAMPLE

The soil sample used in the laboratory study is a brown–yellow expansive soil taken from the cutting slope of Anxiao Road, Zhijiang, Hubei Province, China. It was obtained from three different test pits at a depth of 0.5, 1.5, and 2.5 m below the ground surface and transferred to the laboratory for full geotechnical characterization. The natural moisture content of the samples is 20.8%. The block samples were protected from loss of moisture using a plastic membrane and sealed metal box. The sampling process is shown in **Figure 1**.

Laboratory tests shall be carried out immediately after the soil samples are brought back. The particle-size distribution shows that the soil has 52.1% silt and 47.9% clay, and the liquid limit and plastic limit are 54.3 and 29.9%, respectively. Hence, this soil can be described as clay with intermediate plasticity. The predominant clay minerals in the soil, as determined by X-ray diffractometry, are smectite (18.6%). The values of one-dimensional free swelling are approximately 11% for the natural and compacted specimens, respectively. **Table 1** shows the index properties of the soil.

IMPROVED DIRECT SHEAR APPARATUS AND METHOD FOR EXPANSIVE SOILS

Improved Direct Shear Apparatus

To keep the volume of expansive soil unchanged before and after shearing, an improved direct shear apparatus is used to test the

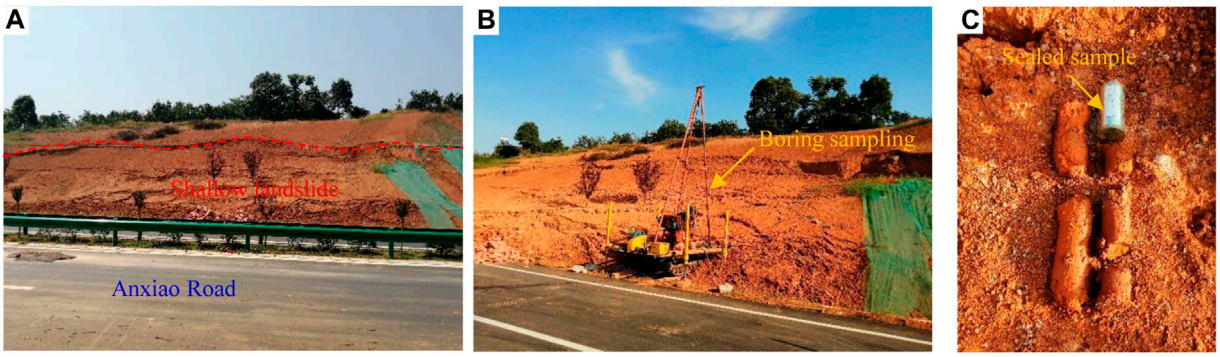

FIGURE 1 | Scene investigation and sampling. **(A)** Anxiao Road cutting landslide. **(B)** Field sampling. **(C)** Sealed sample storage.

TABLE 1 | Physical properties of tested soil.

Physical properties	Value	Physical properties	Value
Sand (%)	0	Soil specific gravity	2.75
Silt (%)	52.1	Montmorillonite content, MC (%)	18.6
Clay (%)	47.9	Specific surface area, SSA ($m^2 \cdot g^{-1}$)	215.8
Liquid limit, w_l (%)	54.3	Free swelling ratio, f_s (%)	40.7
Plastic limit, w_p (%)	29.9	Standard absorption moisture content, w_s (%)	5.0
Plasticity index, *PI* (%)	24.4	Optimum moisture content, w_{opt} (%)	17.9
Unified soil classification system	CH	Maximum dry unit weight, γ_{dmax} (kN/m^3)	17.2

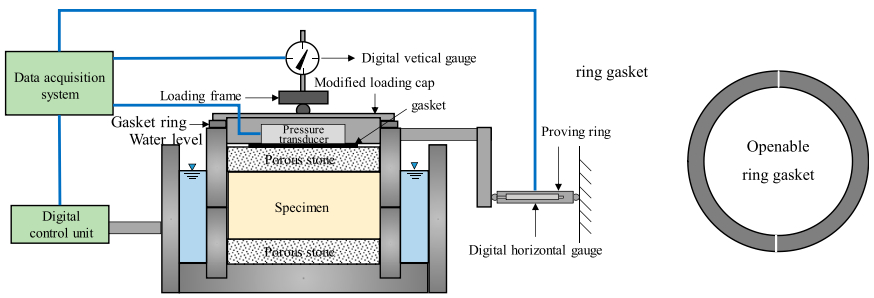

FIGURE 2 | Profile of the improved direct shear test apparatus.

shear strength of expansive soil. Compared with the conventional direct shear apparatus, the major improvements include increasing the top diameter of the loading plate so that it is at least 5 mm larger than the inner diameter of the shear box, adding a ring gasket with a limit function between the loading plate and the shear box, and adding grooves at the bottom of the loading plate and placing pressure sensors. The pressure sensor is used to measure the vertical swelling pressure of expansive soil specimens in the process of saturation. After the above improvement, the ring gasket can control the loading plate to only slightly contact the porous stone at the top of the specimen before the specimen is soaked, and the load applied is all borne before the specimen swells, to ensure that the volume of the expansive soil specimen is not compressed before the specimen is soaked. After the specimen is immersed in water, the loading plate with a pressure sensor can read the vertical swelling pressure of the specimen from the initial moisture content to the process of saturation. Before shearing, as long as the initial load is slightly greater than the maximum vertical swelling pressure under the initial moisture content of the specimen, the specimen volume can be guaranteed to remain unchanged during shearing. The section of the improved direct shear apparatus is shown in **Figure 2**.

Improved Direct Shear Test Method

Swelling of expansive soil is a process of dry density reduction. If expansive soil swells before and after shearing, the dry density of the actual shear specimen will be less than the set dry density, which cannot effectively represent the strength parameter of a specific dry density. Considering that compared with the triaxial apparatus, the

TABLE 2 | Summary of testing program conditions.

Test type	Test ID	Initial dry density ρ_{d0} (g/cm^3)	Degree of saturation S_{r0} (%)	Water content w_0 (%)	Vertical stress p_v (kPa)
Improved direct shear	MD1	1.40	90, 75, 60, 45	16.20	Vertical swelling pressure at constant volume
	MD2	1.45	90, 75, 60, 45	15.87	
	MD3	1.50	90, 75, 60, 45	15.63	
	MD4	1.55	90, 75, 60, 45	15.22	
	MD5	1.60	90, 75, 60, 45	14.82	
Conventional direct shear	CD1	1.40	49.91	17.9	12.5, 25, 37.5, 50, 100, 150, 200, 250
	CD2	1.50	57.23	17.9	
	CD3	1.60	66.96	17.9	

direct shear apparatus is easier to realize the saturated condition and control the dry density of the sample before shear, and the conventional direct shear apparatus is used for the test. However, by changing the loading mode of the conventional direct shear test and using the suction unloading mode, the dry density of specimens before shear remains unchanged, and the specimens are guaranteed to be subjected to different effective stresses. The swelling test with load was carried out before the direct shear test to obtain the relationship between dry density and swelling deformation of the compacted specimen after soaking in water in the initial wet dense state. The lower limit of dry density control for subsequent improved direct shear test specimens was determined by referring to the dry density after no-charge swelling. The steps of the improved direct shear test are as follows:

1) The specimens were prepared using the static compaction method. At a predetermined dry density and saturation (45–90%), four soil specimens with the same dry density and different initial moisture content were prepared at a time.
2) The specimens were put into the direct shear box and soaked (suction unloading), using the balance compression method to control the overburden and keep the height (dry density) of the specimen in the soaking process unchanged.
3) When the overburden load did not change, the slow shear test was carried out to obtain the critical strength and peak strength by a shear displacement of 7 mm under the overburden load. The moisture content of the specimen after shearing was determined, and the saturation was calculated.
4) Repeat steps 2) and 3) for other specimens to obtain the peak strength and ultimate strength corresponding to different overburden loads and then obtain the peak and ultimate effective shear strength parameters by fitting.
5) Direct shear tests with different initial dry densities were carried out according to steps 1) to 4), and then the peak effective shear strength parameter and ultimate effective shear strength parameter were obtained with the decrease of dry density (regarded as the swelling process).

TESTING PROGRAM

The test scheme for this laboratory study is presented in **Table 2**. Both improved direct shear tests and conventional direct shear tests were carried out on expansive soil slope in Zhijiang City, Hubei Province.

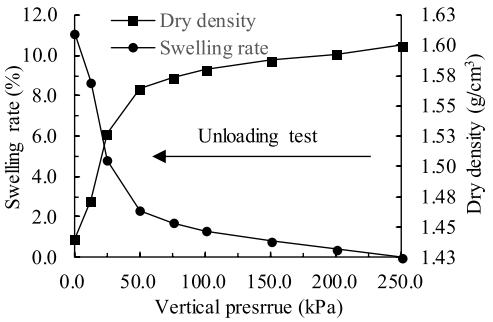

FIGURE 3 | Relationship between the swelling rate and dry density under different loads.

The Improved Direct Shear Test Program

Five groups of specimens with different dry densities were selected within the range of the initial dry density of 1.6 g/cm^3 and the minimum dry density of 1.44 g/cm^3 after saturated swelling. The moisture content of the specimen was determined according to the saturation of expansive soil of 45 ~ 90%, as shown in **Table 2**. One-dimensional unloading swelling tests were carried out on the specimens with different initial dry densities under different initial saturation conditions to determine the vertical swelling pressure generated when the test reached saturation. The variation of swelling deformation and dry density with vertical pressure is shown in **Figure 3**. Then, the swelling pressure value was taken as the vertical load value in the direct shear process to conduct the direct shear test. The effective internal friction angle and cohesion of expansive soil at constant dry density were obtained.

There is a one-to-one relationship between the swelling rate and dry density, so the decrease of dry density can indicate swelling of expansive soil. The dry density of expansive soil samples decreased from 1.60 g/cm^3 to 1.43 g/cm^3, and the swelling rate increased by 11%. Considering that the actual swelling of expansive soil slope includes not only vertical swelling but also lateral swelling, the lower limit of dry density is set as 1.40 g/cm^3 in the test.

TABLE 3 | Values of state parameters for improved direct shear tests.

Test ID	Specimen No.	Initial condition		After soaking			After shearing
		w_i (%)	S_{ri} (%)	p_v (kPa)	τ_p (kPa)	τ_c (kPa)	w_f (%)
MD1 (1.40 g/cm^3)	MD1-1	30.42	90.00	49.80	13.00	10.90	34.30
	MD1-2	25.91	75.00	68.10	17.30	14.60	34.40
	MD1-3	22.33	60.00	94.70	23.10	20.40	34.30
	MD1-4	16.20	45.00	121.10	29.90	24.90	34.20
MD2 (1.45 g/cm^3)	MD2-1	29.38	90.00	54.20	16.20	14.00	32.10
	MD2-2	25.26	75.00	75.60	21.80	18.20	32.50
	MD2-3	21.47	60.00	103.20	27.20	24.00	34.30
	MD2-4	15.87	45.00	137.50	38.10	34.10	33.40
MD3 (1.50 g/cm^3)	MD3-1	26.25	90.00	71.30	24.60	21.10	32.70
	MD3-2	24.47	75.00	84.30	28.10	24.60	32.50
	MD3-3	20.21	60.00	115.80	37.50	31.50	32.40
	MD3-4	15.63	45.00	158.90	50.60	44.70	32.10
MD4 (1.55 g/cm^3)	MD4-1	26.63	90.00	71.60	25.70	23.30	29.00
	MD4-2	24.10	75.00	148.80	50.00	46.30	28.60
	MD4-3	18.85	60.00	190.20	64.80	58.90	28.60
	MD4-4	15.22	45.00	212.60	69.50	63.90	28.60
MD5 (1.60 g/cm^3)	MD5-1	23.90	90.00	153.60	55.30	53.10	27.40
	MD5-2	22.45	75.00	178.90	66.10	63.70	27.40
	MD5-3	17.31	60.00	215.50	76.00	73.10	27.40
	MD5-4	14.82	45.00	242.10	88.20	82.10	27.40

Note: w_i, initial moisture content; w_f, final moisture content; S_{ri}, initial degree of saturation; τ_p, peak strength; τ_c, critical strength; p_v, vertical pressure.

Conventional Direct Shear Test Program

Combined with the direct shear test method under low-stress conditions, the load classification was added based on the conventional direct shear test. Conventional tests in this paper adopted eight different vertical loads of 12.5, 25, 37.5, 50, 100, 150, 200, and 250 kPa. The conventional direct shear tests with different densities of 1.4 g/cm^3, 1.5 g/cm^3, and 1.6 g/cm^3 were carried out under the same moisture content.

EXPERIMENTAL RESULTS AND ANALYSIS

Improved Direct Shear Test Results

As shown in **Table 2**, the improved direct shear test was divided into five groups (MD1–MD5) according to different dry densities, and each group was equipped with four specimens with different moisture content according to 45, 60, 75, and 90% saturation. For the improved direct shear test, the water content of saturated samples under different dry densities is different, and the water content given in **Table 2** is saturated water content. For the conventional direct shear test, the water content refers to the initial water content of the specimens. However, the overburden load is uniformly set according to the maximum swelling pressure obtained by the one-dimensional loaded swelling test, which is set here as 250 kPa. The values of state parameters of the improved direct shear test are shown in **Table 3**.

As shown in **Table 3**, the vertical stress, peak strength, and critical strength of specimens with different dry densities increase with the decrease of initial saturation. This is because the specimen with lower saturation has lower corresponding moisture content. In the process of saturation, the soil will absorb more water, thus releasing greater swelling force. Under the vertical load on the top of the specimen, the vertical deformation is constrained, and the swelling force will act on the soil skeleton in the form of vertical stress. A larger swelling force corresponds to a larger effective stress, thus obtaining a higher strength value. The small difference of moisture content after saturation indicates that the pore ratio of specimens with different initial saturations is the same after saturation, which avoids the influence of pore ratio change on soil structure and strength.

Conventional Direct Shear Test Results

Conventional direct shear tests were carried out on three specimens with different dry densities. To compare with the improved direct shear specimen under constant volume conditions, the maximum vertical load was set at 250 kPa. As the expansive soil slope usually has the characteristics of the shallow slide, the shear test under low-stress conditions is added according to the practice of Xiao et al. (2017), and the test results are shown in **Table 4**.

As shown in **Table 4**, after saturation, the dry density of the same specimen changes with different vertical pressure. The specimen with a dry density of 1.4 g/cm^3 swells greatly under low-stress conditions, and the maximum vertical swelling rate is 3.21%. The moisture content (saturation) of the specimen decreases with the increase of the dry density of the specimen, indicating that the compaction expansive soil under the loading condition is not the only saturated state but also affected by the vertical pressure. Under the same dry density after consolidation, the dry density of the specimen after swelling increases with the increase of vertical effective stress, which is caused by the swelling of expansive soil.

TABLE 4 | Values of state parameters for conventional direct shear tests.

Specimen No.	Initial condition		After soaking					After shearing
	w_i (%)	S_{ri} (%)	p_v (kPa)	τ_p (kPa)	τ_r (kPa)	ε_h (%)	ρ_s (g/cm^3)	w_f (%)
CD1 (1.40 g/cm^3)	17.90	49.91	12.50	2.76	2.76	3.21	1.36	37.52
		49.91	25.00	5.87	5.28	2.28	1.37	37.31
		49.91	37.50	12.39	11.87	1.92	1.37	37.13
		49.91	50.00	20.39	20.39	1.47	1.38	36.70
		49.91	100.00	26.80	23.40	0.56	1.39	36.21
		49.91	150.00	39.80	36.20	(–0.11)	1.40	36.08
		49.91	200.00	52.80	49.30	(–0.20)	1.40	35.69
		49.91	250.00	67.30	61.26	(–0.26)	1.40	35.24
CD2 (1.50 g/cm^3)	17.90	57.23	12.50	4.23	4.08	4.21	1.44	36.13
		57.23	25.00	8.21	7.96	2.15	1.44	35.94
		57.23	37.50	14.87	13.27	1.78	1.46	35.66
		57.23	50.00	23.12	22.19	1.52	1.47	35.28
		57.23	100.00	34.66	30.40	0.01	1.49	35.02
		57.23	150.00	52.37	49.20	0.00	1.50	34.71
		57.23	200.00	62.16	58.31	(–0.01)	1.50	34.47
		57.23	250.00	75.39	70.33	(–0.02)	1.50	34.05
CD3 (1.60 g/cm^3)	17.90	66.96	12.50	6.07	4.89	6.05	1.51	35.31
		66.96	25.00	12.44	9.44	3.50	1.55	35.12
		66.96	37.50	18.10	12.27	2.41	1.56	34.78
		66.96	50.00	24.56	19.10	1.72	1.57	34.46
		66.96	100.00	43.94	34.63	1.15	1.58	34.10
		66.96	150.00	62.00	51.10	0.03	1.60	33.84
		66.96	200.00	70.22	67.90	0.00	1.60	33.53
		66.96	250.00	81.00	84.10	(–0.01)	1.60	33.21

Note: ρ_s, dry density after swelling; ε_h, swelling ratio.

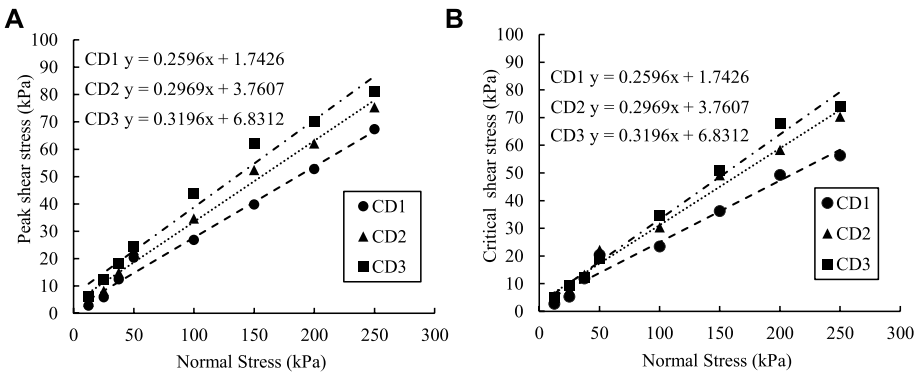

FIGURE 4 | Conventional direct shear test results of expansive soil. **(A)** Variation of peak shear strength with normal stress. **(B)** Variation of critical shear strength with normal stress.

Effects of Dry Density on Shear Strength for Expansive Soil

As shown in **Figure 4**, the variation of shear strength with normal pressure of three kinds of dry density specimens in the conventional direct shear test shows that the peak strength and critical strength of Zhijiang expansive soil increase with the increase of dry density. Under low-stress conditions, the measured values are mostly below the fitting line. The main reason is that the expansive soil has swelling properties. The smaller the overburden pressure is, the larger the volume swelling of the specimen with the same initial dry density is.

Figure 4 shows a comparison of shear strength and its parameter between the different dry density specimens. **Figure 4** is constructed by plotting the peak values of shear strength from **Table 4** against the corresponding dry density. As discussed previously, the peak value increases with an increase in the applied normal stress for different dry

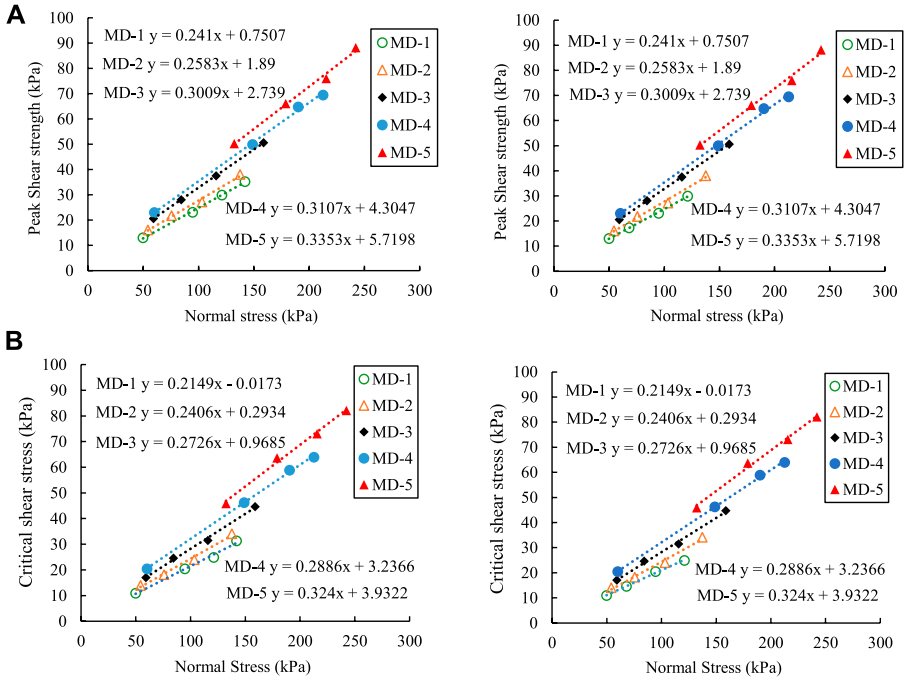

FIGURE 5 | Improved direct shear test results of expansive soil. **(A)** Variation of peak shear strength with normal stress. **(B)** Variation of critical shear strength with normal stress.

density compacted specimens. For a given density, the peak shear strength of the higher dry density specimens is always greater than that of the lower dry density specimens.

The test values and fitting lines of the improved direct shear test of five expansive soil samples with different dry densities are shown in **Figure 5**. By comparing **Figures 5A,B**, it is seen that the values of peak strength and ultimate strength of expansive soil with different dry densities have a little difference under test-stress conditions. This is because the value of saturated shear strength can be determined by two shear strength parameters, cohesion and internal friction angle, regardless of peak strength or ultimate strength. Under the condition of low stress, the true cohesion between saturated soil particles without cementation is very small, and the contribution of vertical stress to strength is also low, resulting in a little difference in strength values. The internal friction angle of expansive soil with high dry density is larger, which is more significantly affected by vertical stress. With the increase of vertical stress, the strength difference increases. The comparison between **Figures 4**, **5** shows that, under the same stress state, the strength difference obtained by the conventional direct shear test is larger than that obtained by the improved direct shear test. This is because the improved direct shear test keeps the volume constant during the whole direct shear process, and the dry density does not change during the shear process. However, the strength of conventional direct shear specimens is lower under low stress and higher under high stress due to volume change.

There was a good linear correlation between the peak shear strength and the ultimate shear strength obtained by the improved direct shear test method and the vertical loading. This method not only ensures the consistency of the dry density of specimens under different vertical loadings but also ensures the consistency of the structure of specimens before shearing as far as possible. Therefore, the obtained shear strength parameters can represent the true cohesive and frictional properties of expansive soil under the condition of dry density.

As shown in **Figure 6**, when the initial dry density is 1.6 g/cm^3, the effective cohesive of expansive soil is only about 4 kPa, and the effective friction angle is 18.1°. The friction strength mainly comes from the interaction between particles on the contact surface. The peak shear strength and residual shear strength decrease with the decrease of dry density. The effective internal friction angle of saturated compacted expansive soil is only 12.1° and the cohesion is close to 0 when the dry density is 1.4 g/cm^3. Under the condition of low stress, the shear strength parameter of expansive soil measured by the improved direct shear test is 8 ~ 36% higher than that measured by the conventional direct shear test. Some scholars classify this situation as the weakening of bond strength caused by the increase of expansive soil volume and the thickening of the granular water film. The clay particles dispersed gradually, and the adsorption weakened. The test results show that the true shear strength of expansive soil is very low.

The influence of different dry densities on expansion deformation of expansive soil was referred (Zhang et al., 2020b). To establish the relationship between dry density and

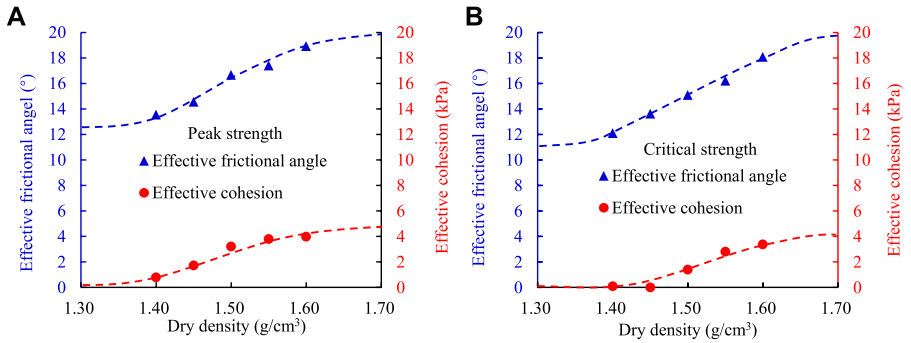

FIGURE 6 | Variation of the effective shear strength parameter with dry density. **(A)** Variation of the peak shear strength parameter with dry density. **(B)** Variation of the critical shear strength parameter with dry density.

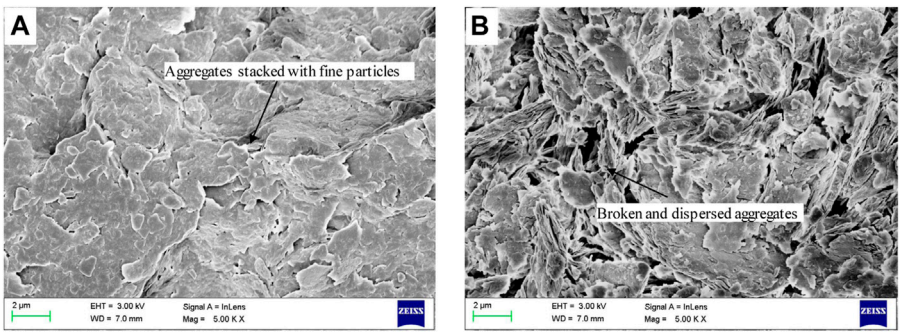

FIGURE 7 | Microstructure changes during swelling (5,000 times larger): **(A)** before swelling, ρ_d = 1.6 g/cm^3; **(B)** after swelling, ρ_d = 1.45 g/cm^3.

saturated shear strength parameters, the following equations are used to fit them:

$$c' = \frac{a_1}{1 + b_1 e^{-k_1 \rho_d}}, \quad (1)$$

$$\varphi' = \frac{a_2}{1 + b_2 e^{-k_2 \rho_d}}, \quad (2)$$

where c' is the effective cohesion, ρ_d is the dry density, φ' is the effective internal friction angle, e is the void ratio, and a_1, b_1, k_1, a_2, b_2, k_2 are the fitting parameters.

The fitting results are as follows: $a_1 = 4.86$, $b_1 = 5.34$, $k_1 = 18.37$, $a_2 = 18.86$, $b_2 = 8.73$, $k_2 = 13.37$, and the correlation coefficients are, respectively, 0.974 and 0.990.

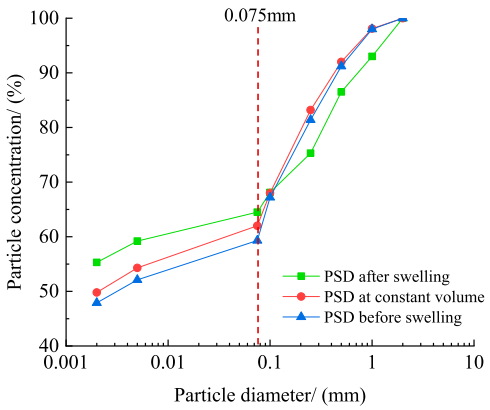

FIGURE 8 | Particle size distribution (PSD) curve before and after swelling.

Influence of Microstructure Change on Shear Strength Parameter

For expansive soils, swelling not only changes the macroscopic volume but also changes the microstructure (Lin and Cerato, 2014). To understand the actual effect of humidification and swelling on the microstructure of the specimen, the saturated specimen before and after swelling was analyzed by an SEM. Three expansive soil specimens with the same initial saturation were prepared at the dry densities of 1.4 g/cm^3, 1.5 g/cm^3, and 1.6 g/cm^3, respectively, and saturated by the improved direct shear method. As the SEM scanning process needs to be carried out in a dry environment, a vacuum freeze-drying method is needed to dry the specimen. After saturation, specimens with different dry densities were taken out of the ring knife and cut into small soil blocks of 1.0 × 1.0 × 1.0 cm. Then, the specimens were quickly put into liquid nitrogen and

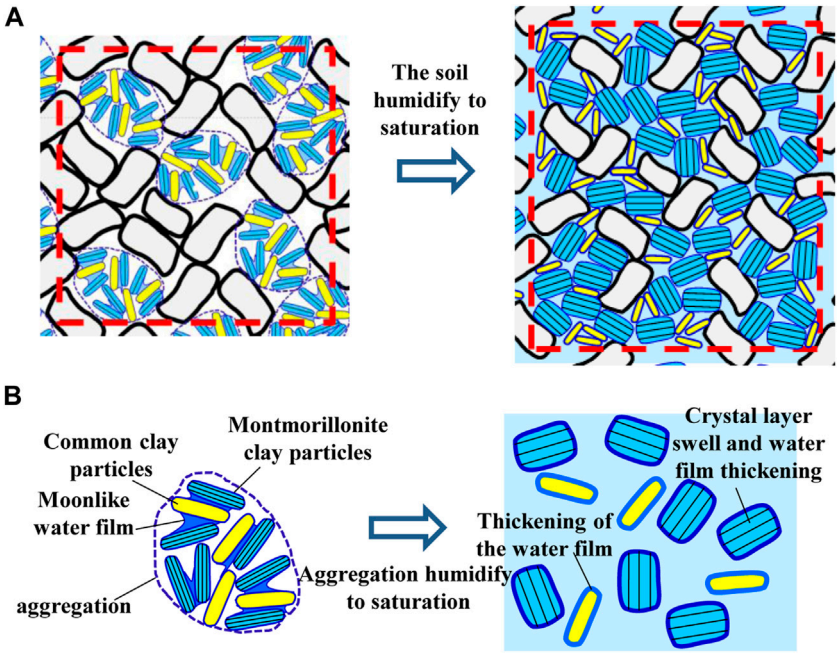

FIGURE 9 | Humidification of clay aggregates in expansive soils.

frozen for 15 min, so that the liquid in the specimens became amorphous ice without swelling. Finally, at −50°C, the amorphous ice in the soil specimen was sublimated by a vacuum freeze dryer for more than 8 h, to maintain the structure of the soil skeleton and saturated soil particles.

It can be seen from **Figure 7** that, with the decrease of dry density, the original particles of expansive soil become more broken and become smaller flaky structures stacked upon each other. At the same time, the fragmented lamellar structure leads to the relative sliding of the lamellar in the humidification process, and the reduction of interlamellar friction makes the lamellar dislocation relatively easy which is also the factor leading to the reduction of the internal friction angle of the soil on the macro level. This is consistent with the relationship between shear strength and dry density found in macroscopic tests.

To verify the particle fragmentation of the specimen after swelling, a particle analyzer was used to measure the particle content of the specimen with 1.6 g/cm^3 dry density before and after swelling, and the cumulative curve of particle distribution was obtained, as shown in **Figure 8**. After swelling, the particle size below 0.1 mm increased significantly, and the smaller the particle size, the greater the change of cumulative content. The particles in the range of 0.1~2 mm are reduced correspondingly, which also proves from the side that the large particles of soil will be broken and dispersed after swelling and the large particles will be replaced by more small particles. However, under constant volume conditions, the swelling is limited, the particle size changes little, and the swelling potential energy is mainly released in the form of swelling force, and the influence of microstructure on soil strength is relatively small.

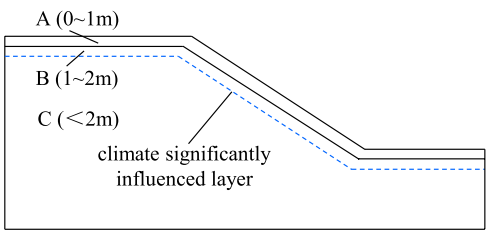

FIGURE 10 | Expansive soil slope zoning.

As shown in **Figure 9A**, when unsaturated expansive soil is humidified, the crystal layer of montmorillonite mineral grains expands significantly due to water absorption, which results in a change in the volume of the soil skeleton. **Figure 9B** shows montmorillonite clay particles will expand significantly from the inside after absorbing water, leading to the gradual dispersion of aggregates and local fragmentation. The contact morphology of particles is affected, which results in partial contact between silt particles and silt particles into silt particles and clay particles. The change of contact surface shape will change the friction force between each other, and the effective internal friction angle will decrease. However, the general shear strength theory of saturated–unsaturated soil does not consider the swelling effect of soil particles in the soil, and the contact surface of soil particles does not change in the process of humidification, so the effective internal friction angle and cohesion remain unchanged.

TABLE 5 | Comparison of dry density before and after swelling.

Sampling location (m)	Natural dry density (g/cm^3)	Dry density after swelling (g/cm^3)
A (0.5)	1.56	1.47
B (1.5)	1.60	1.56
C (3)	1.60	1.60

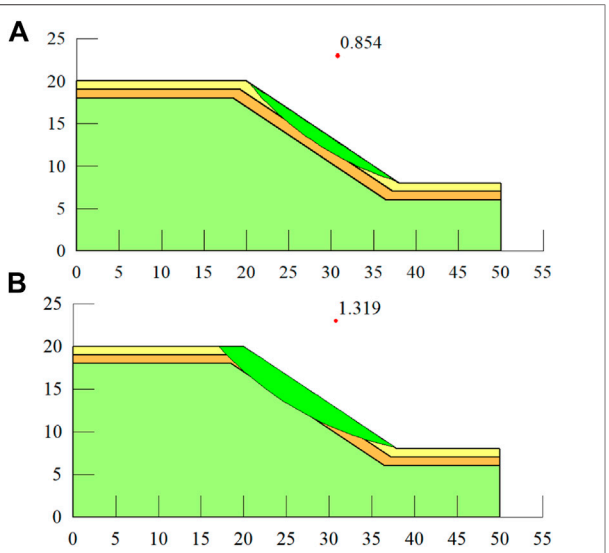

FIGURE 11 | Safety factors and the potential sliding surface of the cutting slope. **(A)** Before swelling. **(B)** After swelling.

ENGINEERING APPLICATION

Numerical simulation is an important means for slope collapse analysis and prediction (Zheng et al., 2019). In order to have a deeper understanding of the long-term stability of expansive soil slope affected by swelling, taking the Zhijiang typical expansive soil cutting slope as the research object, the influence of swelling (decrease of dry density) on slope stability is analyzed. The height of the expansive soil slope is 12 m, and the slope ratio is 1:1.5. Under the long-term atmospheric humid and hot environment, cracks are continuously connected and developed in a large number within 2 m of the slope. The local stagnant water zone is easily formed after rainfall, which makes the soil in the region reach the saturation state. According to the field test data, the average dry density of soil within 1 m depth is 1.56 g/cm^3, and the average dry density of soil below 1 m depth is 1.60 g/cm^3. Therefore, the expansive soil slope can be roughly divided into three areas, as shown in **Figure 10**. The average dry density of layer A soil is 1.56 g/cm^3 which is in the range of significant influence of the atmospheric dry–wet cycle, and the soil can reach saturation after rainfall. The average dry density of layer B is 1.60 g/cm^3, but it is within the range of significant influence of the atmospheric dry–wet cycle. Layer C is not affected by the atmospheric environment, and its average dry density (1.60 g/cm^3) generally does not change during rainfall. For Zhijiang expansive soil with an initial dry density of 1.56 g/cm^3 and 1.6 g/cm^3 and initial moisture content of 17.9%, the loaded swelling test was carried out, respectively, and the maximum saturated swelling was 6.16 and 2.56% under the condition of overburden load of 10 kPa (the overlying soil layer is about 0.5 m) and 30 kPa (the overlying soil layer is about 1.5 m). Then, the dry density of expansive soil could be obtained. The test results are shown in **Table 5**.

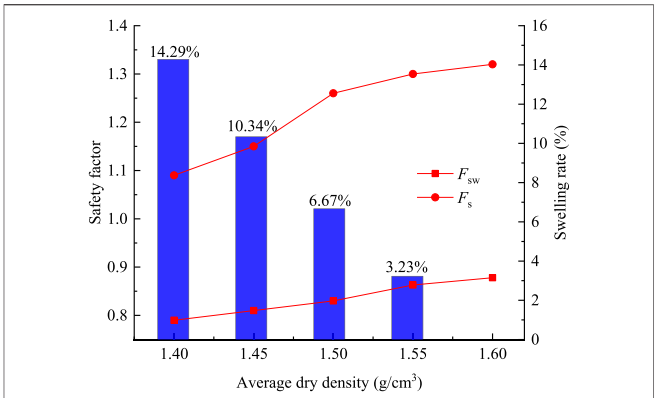

FIGURE 12 | Slope safety factors obtained by different test methods.

Since the moisture content of shallow soil is close to saturation after rain, it can be assumed that layer A soil of expansive soil slope can be completely saturated under continuous rainfall conditions. According to **Table 5**, the dry density of soil in this region decreases from 1.56 g/cm^3 to 1.47 g/cm^3 under saturation, decreasing by 5.77%. The dry density of layer B soil decreased from 1.60 g/cm^3 to 1.56 g/cm^3, reduced by 2.50%. In layer C, the dry density remains constant due to the little change in humidity. It can be seen from the above that the decrease of dry density caused by swelling will directly affect the effective shear strength parameter of soil. The dry density values after attenuation of soil in layers A and B are substituted into **Eqs 1**, **2** for calculation, to obtain the real effective cohesion and effective internal friction angle after swelling. Then, the shear strength parameter is used to calculate the slope stability, and the safety factor of expansive soil slope under the condition of strength attenuation is obtained.

Under the influence of atmospheric wetting and drying cycle, soil in the region will swell after rainfall. Calculating the slope stability after the rain, not only should the intensity of the attenuation caused by the loss of matric suction be considered but also the effect of swelling on effective shear strength parameters should be considered. As shown in **Figure 11**, when calculating the slope safety factor, the other parameters are set in the same way, and only the influence of shallow soil swelling on shear strength is considered. The safety factor of slope considering swelling is much smaller than that calculated by the conventional method. To understand the stability state of an expansive soil slope in a larger density range after rain, the F_s, F_{sw} parameters of shear strength before and after swelling obtained by different test methods were used for stability analysis under the

condition that other working conditions remained unchanged. The calculation results are shown in **Figure 12**.

As shown in **Figure 12**, the safety factor (F_{sw}) of slope considering the swelling effect is 28–33% lower than that (F_s) without swelling effect. The higher the dry density of expansive soil is, the greater the saturated swelling deformation is, and the slope safety factor decreases more obviously under the influence of swelling. Therefore, in the treatment of expansive soil slope, special attention should be paid to the prevention and drainage measures of high dry density expansive soil slope; at the same time, attention should also be paid to not keep the moisture content of backfill expansive soil too low and to avoid excessive attenuation of strength caused by soil swelling, and the influence of swelling on slope stability cannot be ignored.

CONCLUSIONS

1) The linear correlation between peak and critical strength and overlying load obtained by the improved direct shear test method is excellent. This method ensures the consistency of the dry density of the specimens before shearing and the consistency of the structure of the specimens before shearing. Therefore, the obtained shear strength parameters can represent the real cohesive and frictional properties of the expansive soil under the dry density condition.
2) Under the condition of low stress, the shear strength of expansive soil measured by the improved direct shear test is 8 ~ 36% higher than that measured by the conventional direct shear test. With the decrease of dry density, the peak and ultimate shear strength parameters decrease. Under different densities, the fitting formula related to dry density can be used to characterize the shear strength parameters.
3) The decrease of cohesion is due to the increase of interparticle spacing and the decrease of intermolecular forces. The decrease of internal friction angle is because the large particles of soil are broken into fine particles due to swelling. The contact between large particles and large particles is replaced by the contact between large particles and small particles, and the friction decreases gradually.
4) When analyzing the stability of expansive soil slope under rainfall conditions, it is suggested to determine the dry density state of the shallow soil after the swelling of the slope and then calculate the effective shear strength parameter under the dry density state. Under the condition of the maximum dry density of 1.40 g/cm^3 ~ 1.60 g/cm^3, the safety factor calculated by using the improved direct shear test data is 28–33% lower than that obtained by the conventional direct shear test. The influence of dry density change caused by swelling on the shear strength of expansive soil cannot be ignored.

DATA AVAILABILITY STATEMENT

The original contributions presented in the study are included in the article/supplementary material, and further inquiries can be directed to the corresponding author.

AUTHOR CONTRIBUTIONS

All authors listed have made a substantial, direct, and intellectual contribution to the work and approved it for publication.

FUNDING

This work was supported by the National Natural Science Foundation of China (Grant No. 51978085) and the Highway Industry Standard Compilation Project of Ministry of Transportation, China (Grant No. JTG-201507).

REFERENCES

Abeykoon, T., and Trofimovs, J. (2021). Shear Strength of Unsaturated Expansive Soils from Queensland Natural Slopes. *Geomate* 20 (20), 53–60. doi:10.21660/2021.82.Gx353

Al Haj, K. M. A., and Standing, J. R. (2015). Mechanical Properties of Two Expansive clay Soils from Sudan. *Géotechnique* 65 (4), 258–273. doi:10.1680/geot.14.p.139

Burton, G. J., Pineda, J. A., Sheng, D., and Airey, D. (2015). Microstructural Changes of an Undisturbed, Reconstituted and Compacted High Plasticity clay Subjected to Wetting and Drying. *Eng. Geology*. 193, 363–373. doi:10.1016/j.enggeo.2015.05.010

Çokça, E., and Tilgen, H. P. (2010). Shear Strength-Suction Relationship of Compacted Ankara clay. *Appl. Clay Sci.* 49 (4), 400–404. doi:10.1016/j.clay.2009.08.028

Dai, Z., Zhang, C., Wang, L., Fu, Y., and Zhang, Y. (2021). Interpreting the Influence of Rainfall and Reservoir Water Level on a Large-Scale Expansive Soil Landslide in the Danjiangkou Reservoir Region, China. *Eng. Geology*. 288, 106110. doi:10.1016/j.enggeo.2021.106110

Dong, J.-g., Lv, H.-b., and Wu, W. (2018a). Development and Application of an Instrument for Simulating Wetting-Drying Cycles of Expansive Soils under Loads. *J. Mt. Sci.* 15 (11), 2552–2560. doi:10.1007/s11629-018-4934-1

Dong, J.-g., Xu, G.-y., Lv, H.-b., and Yang, J.-y. (2018b). Prediction of Expansive Soil Strength Based on Micro-scale Properties. *Geotech Geol. Eng.* 37, 869–882. doi:10.1007/s10706-018-0657-x

He, P., Li, S.-c., Xiao, J., Zhang, Q.-q., Xu, F., and Zhang, J. (2017). Shallow Sliding Failure Prediction Model of Expansive Soil Slope Based on Gaussian Process Theory and its Engineering Application. *KSCE J. Civ Eng.* 22 (5), 1709–1719. doi:10.1007/s12205-017-1934-6

Hou, T.-s., Xu, G.-l., Shen, Y.-j., Wu, Z.-z., Zhang, N.-n., and Wang, R. (2013). Formation Mechanism and Stability Analysis of the Houba Expansive Soil Landslide. *Eng. Geology*. 161, 34–43. doi:10.1016/j.enggeo.2013.04.010

Huang, Z., Wei, B., Zhang, L., Chen, W., and Peng, Z. (2018). Surface Crack Development Rules and Shear Strength of Compacted Expansive Soil Due to Dry-Wet Cycles. *Geotech Geol. Eng.* 37, 2647–2657. doi:10.1007/s10706-018-00784-y

Huang, Z., Zhang, H., Liu, B., Wei, B., and Wang, H. (2021). Using CT to Test the Damage Characteristics of the Internal Structure of Expansive Soil Induced by Dry-Wet Cycles. *AIP Adv.* 11 (7), 075305. doi:10.1063/5.0057450

Hvorslev, M. J. (1961). *Physical Components of the Shear Strength of Saturated Clays*. Fort Collins, United States: American Society of Civil Engineering.

Julina, M., and Thyagaraj, T. (2018). Determination of Volumetric Shrinkage of an Expansive Soil Using Digital Camera Images. *Int. J. Geotechnical Eng.* 15, 1–9. doi:10.1080/19386362.2018.1460961

Katti, D. R., and Shanmugasundaram, V. (2001). Influence of Swelling on the Microstructure of Expansive Clays. *Can. Geotech. J.* 38 (1), 175–182. doi:10.1139/t00-079

Kayadelen, C., Tekinsoy, M. A., and Taşkıran, T. (2007). Influence of Matric Suction on Shear Strength Behavior of a Residual Clayey Soil. *Environ. Geol.* 53 (4), 891–901. doi:10.1007/s00254-007-0701-2

Lade, P. V. (2010). The Mechanics of Surficial Failure in Soil Slopes. *Eng. Geology.* 114 (1-2), 57–64. doi:10.1016/j.enggeo.2010.04.003

Li, Z., Tang, C., Hu, R., and Zhou, Y. (2013). Research on Model Fitting and Strength Characteristics of Critical State for Expansive Soil. *J. Civil Eng. Management* 19 (1), 9–15. doi:10.3846/13923730.2012.734857

Liang, C., Wu, Z., Liu, X., Xiong, Z., and Li, T. (2021). Analysis of Shallow Landslide Mechanism of Expansive Soil Slope under Rainfall: a Case Study. *Arab J. Geosci.* 14 (7). doi:10.1007/s12517-021-06829-6

Lin, B., and Cerato, A. B. (2014). Applications of SEM and ESEM in Microstructural Investigation of Shale-Weathered Expansive Soils along Swelling-Shrinkage Cycles. *Eng. Geology.* 177, 66–74. doi:10.1016/j.enggeo.2014.05.006

Mašín, D., and Khalili, N. (2016). Swelling Phenomena and Effective Stress in Compacted Expansive Clays. *Can. Geotech. J.* 53 (1), 134–147. doi:10.1139/cgj-2014-0479

Qi, S., and Vanapalli, S. K. (2018). Simulating Hydraulic and Mechanical Responses of Unsaturated Expansive Soil Slope to Rainfall: Case Study. *Int. J. Geomech.* 18 (6), 1–17. 05018002. doi:10.1061/(asce)gm.1943-5622.0001106

Qi, S., Vanapalli, S., Yang, X., Zhou, J., and Lu, G. (2019). Stability Analysis of an Unsaturated Expansive Soil Slope Subjected to Rainfall Infiltration. *Int. J. Geomech.* 1. doi:10.12989/gae.2019.19.1.001

Xiao, J., Yang, H.-p., Zhang, J.-h., and Tang, X.-y. (2018). Surficial Failure of Expansive Soil Cutting Slope and its Flexible Support Treatment Technology. *Adv. Civil Eng.* 2018, 1–13. doi:10.1155/2018/1609608

Xiao, J., Yang, H., Zhang, J., and Tang, X. (2017). Properties of Drained Shear Strength of Expansive Soil Considering Low Stresses and its Influencing Factors. *Int. J. Civil Eng.* 16. doi:10.1007/s40999-017-0268-6

Ye, W., Zhang, Y., Chen, B., Zhou, X., and Xie, Q. (2010). Shear Strength of an Unsaturated Weakly Expansive Soil. *J. Rock Mech. Geotechnical Eng.* 2 (2), 155–161. doi:10.3724/sp.j.1235.2010.00155

Zhai, J.-y., and Cai, X.-y. (2018). Strength Characteristics and Slope Stability of Expansive Soil from Pingdingshan, China. *Adv. Mater. Sci. Eng.* 2018, 1–7. doi:10.1155/2018/3293619

Zhang, J., Niu, G., Li, X., and Sun, D. a. (2019). Hydro-mechanical Behavior of Expansive Soils with Different Dry Densities over a Wide Suction Range. *Acta Geotech.* 15, 265–278. doi:10.1007/s11440-019-00874-y

Zhang, J., Sun, D. a., Zhou, A., and Jiang, T. (2016). Hydromechanical Behaviour of Expansive Soils with Different Suctions and Suction Histories. *Can. Geotech. J.* 53 (1), 1–13. doi:10.1139/cgj-2014-0366

Zhang, R., Liu, Z., Zheng, J., and Zhang, J. (2020a). Experimental Evaluation of Lateral Swelling Pressure of Expansive Soil Fill behind a Retaining Wall. *J. Mater. Civ. Eng.* 32 (2), 04019360. doi:10.1061/(asce)mt.1943-5533.0003032

Zhang, R., Long, M.-x., Lan, T., Zheng, J.-l., and Geoff, C. (2020b). Stability Analysis Method of Geogrid Reinforced Expansive Soil Slopes and its Engineering Application. *J. Cent. South. Univ.* 27 (7), 1965–1980. doi:10.1007/s11771-020-4423-x

Zheng, Y., Chen, C., Liu, T., Xia, K., Sun, C., and Chen, L. (2019). Analysis of a Retrogressive Landslide with Double Sliding Surfaces: a Case Study. *Environ. Earth Sci.* 79 (1). doi:10.1007/s12665-019-8741-y

Conflict of Interest: Author BY and XM were employed by Zhaotong Zhaoyang Ring Highway Investment and Development Corporation Ltd.

The remaining authors declare that the research was conducted in the absence of any commercial or financial relationships that could be construed as a potential conflict of interest.

frontiers | Frontiers in Earth Science

ORIGINAL RESEARCH
published: 13 April 2022
doi: 10.3389/feart.2022.878782

Experimental Study on the Accumulation Characteristics and Mechanism of Landslide Debris Dam

Xiangping Xie, Xiaojun Wang, Shenzhou Zhao, Zhongli Li, Xuyang Qin and Shu Xu*

Department of Civil and Architectural Engineering, Anyang Institute of Technology, Anyang, China

According to physical model tests, we analyzed the accumulation characteristics of landslide dams formed under three different slope characteristics, namely, uniform slope, parallel slope, and intersecting slope and investigated the accumulation mechanisms of the debris dams. The relationship between slope types and accumulation characteristics was also explored using the tracer particle analysis method. The damming process and accumulation mechanism of the landslide dam were changed with slope conditions, which lead to the difference in the accumulation characteristics of the dam, especially in transverse cross-sectional shape and grain size distribution. The transverse cross-sectional shape of the landslide dams formed by different slope conditions can be divided into three categories: the flat pattern, unidirectional pattern, and undulating pattern. The characteristics of the slope body are closely related to those of the landslide dam with respect to debris distribution. The debris distributions in the longitudinal and transverse directions of the slope body are consistent with those in the longitudinal and sliding regions of the dam. A general inverse grading characteristic of debris gains occurs in the vertical direction of landslide dams. For the uniform and parallel slopes, obvious inverse grading distribution is induced by overall-starting initiation of the slope body and strong vertical infiltration of the fine sands during the movement. However, inverse grading distribution is generated by the effects of pushing–climbing and lateral infiltration that existed among particles caused by a layered-starting mode for the intersecting slope body. This study provides a basis for the prediction of landslide dam formation and backtracks the initial structure of the slope.

Keywords: landslide dam, slope characteristic, accumulation characteristic, sorting mechanism, dynamic process

OPEN ACCESS

Edited by:
Dongri Song,
Institute of Mountain Hazards and Environment (CAS), China

Reviewed by:
Qiming Zhong,
Nanjing Hydraulic Research Institute, China
Hongchao Zheng,
Tongji University, China
Shaojie Zhang,
Institute of Mountain Hazards and Environment (CAS), China

****Correspondence:***
Xiangping Xie
xxp_imde@163.com

Specialty section:
This article was submitted to Geohazards and Georisks, a section of the journal Frontiers in Earth Science

Received: *18 February 2022*
Accepted: *21 March 2022*
Published: *13 April 2022*

Citation:
Xie X, Wang X, Zhao S, Li Z, Qin X and Xu S (2022) Experimental Study on the Accumulation Characteristics and Mechanism of Landslide Debris Dam. Front. Earth Sci. 10:878782. doi: 10.3389/feart.2022.878782

INTRODUCTION

According to statistical data worldwide, landslide and debris flow are the main reasons for the formation of barrier dams (Costa and Schuster, 1988; Shi et al., 2014; Nian et al., 2018; Zheng et al., 2021). They can block both large rivers and little channels. Earthquakes often induce a large number of landslides that form large-scale river-blocking dams, such as Tangjiashan landslide dam, Yangjiagou landslide dam induced by the 2008 Wenchuan earthquake, and Hongshiyan landslide dam triggered by the 2014 Ludian earthquake (Hu et al., 2009; Fan et al., 2012; Zhou J.-w. et al., 2013; Zhang et al., 2015; Shi et al., 2017). Such river-blocking dams have poor stability and often fail in a short time after their formation, which poses great threat to the lives and properties of the surrounding areas and downstream people. The Tangjiashan dam collapsed 29 days after its

formation, forcing 200,000 people downstream to evacuate (Shi et al., 2015). The Baige dam on the Jinsha River collapsed within 3 days, affecting more than 500 km downstream, forcing 25,000 people to evacuate (Fan et al., 2019). Meanwhile, as reported by Fan et al. (2012), the 2008 Wenchuan earthquake triggered approximately 60,000 co-seismic landslides, where only 800 or so blocked the rivers, and numerous more might form small and medium-sized dams in mountain valleys. These relatively small dams may also bring negative disastrous effects. As Zhou et al., 2013b pointed out, under certain inflow conditions, the dam in the channel will have a cascading collapse effect, resulting in collapsed debris flow or enlarging the discharge of debris flow, such as the 2010 Tangfanggou debris flow in Pingwu County and July 2013 Qipangou debris flow in Sichuan Province of China (Liu et al., 2010; Qin et al., 2016). Therefore, it is of great significance to analyze and evaluate the stability of landslide dams for the identification and mitigation of the landslide-debris flow disasters.

There are many factors that affect the stability of landslide dams. Among them, material distribution characteristics and geometric parameters of the dam body are the main internal factors which affect the permeability and mechanical properties of the dam body, thus determining the stability and failure mode of the dam (Costa and Schuster 1988; Casagli et al., 2003; Dunning, et al., 2005; Dunning, 2006; Shan et al., 2020; Zheng et al., 2022). The accumulation characteristics of landslide dams were mainly studied by means of survey statistics, laboratory model tests, and numerical simulations. Casagli et al. (2003) analyzed 42 landslide dams and found that the grain size gradation of the dam body appeared in double peaks. The median particle size d_{50} could not be used as a representative value of particle gradation. Chang et al. (2011) found that the parameters such as particle gradation, porosity, and plasticity index and other parameters of the dam material varied significantly with depth. Lei et al. (2016) studied the sliding and accumulation movement process of a cohesive soil slope along the inclined plane under unconfined conditions through model tests and found that factors such as volume of the slope, particle size, slope height, and slope angle of the start area have influences on the accumulation range and shape of the landslide debris dam. Peng et al. (2019) used the image recognition system PCAS to analyze the particle size distribution characteristics of the surface material of the landslide debris deposits in the Pusa Village collapse. Zhao et al. (2019) studied the effects of channel section shape, landslide velocity, and channel bed slope on the horizontal and vertical geometry of the dam based on the DEM. (Zhou et al., 2019a; Zhou et al., 2019b) studied the influence of the angle of the starting section, the angle and roughness of the sliding section on the morphology, and debris distribution of the deposits through model experiments and numerical simulations.

The aforementioned studies show that the debris distribution of landslide dams is complicated and the morphological features are also affected by many factors. However, most of the studies took the slope as homogenous and did not consider the influence of the structural characteristics of the slope body itself on the landslide damming process and accumulation characteristics. In addition, in natural conditions, it is difficult to directly know the internal structure and material composition of the dam in time because the formation of landslide dams is often sudden and difficult to reach (Wang et al., 2015). If the characteristics of the unstable slope in the source area can be linked with the accumulation characteristics of the landslide dam, we can quickly identify the characteristics of the dam by slope characteristics, which will provide a basis for rapid stability assessment and decision-making. Therefore, this study focused on the propagation and accumulation process of the landslide under different slope characteristics through physical model tests. The relationship between slope characteristics and accumulation characteristics of the dam was analyzed.

METHOD AND MATERIAL

Scaling

Model tests must consider scaling issues. According to the typical landslides in China since the 20th century reported by many researchers (Huang, 2007; Huang et al., 2008; Li et al., 2010), the ranges of typical landslide parameters are listed in **Table 1**. The length scale is selected as $\lambda_L = L_p/L_m = 500$, and the volume scale can be calculated as $\lambda_V = {\lambda_L}^3 = 1.25 \times 10^8$. For gravity-driven motion of landslides and debris flows, dynamic scaling involves a characteristic time scale $(L/g)^{1/2}$ (Iverson, 2015), where g is the magnitude of gravitational acceleration and L is the characteristic length of the moving mass. Then, the time scale for this study can be calculated as $\lambda_T = {\lambda_L}^{1/2} = 22.4$.

The comparison of model and prototype parameters is listed in **Table 1**.

Experiment Apparatus

A rotatable start-up landslide device was especially designed, as displayed in **Figures 1A–C**. The device was divided into three parts: starting section, sliding section, and accumulating section. The starting section simulated the sliding source area, which consisted of the rear wall, two side walls, and a rotatable bottom plate. The inclination of the rear wall was 50°, and the side walls were vertical with a height of 100 cm. The rotatable plate was 71 cm long and 67 cm wide. The inclination of the rotatable plate was set to 50° when it connected with the sliding section. The sliding section was a rectangle channel. It comprised two glass side walls and a steel bottom. The length of the channel was 230 cm, and the inclination was 30°. The accumulating section was designed as a narrow channel to form the landslide debris dam. The dimension of the channel was 400 cm (length)×26.5 cm (width)×30 cm (height). A transparent glass plate was installed on the side away from the sliding section. Three cameras were installed to record the process of initiation, propagation, and accumulation of the landslide. A 3D laser scanner was used to scan the geometry of the entire damming body.

Material and Test Conditions

This study mainly considered variables of the slope body features including types of material, slope accuracy, and layer sequence. The slope comprises three different kinds of debris, that is, coarse

TABLE 1 | Prototype and model parameters for the experiments (length scale $\lambda_L = L_p/L_m$ = 500).

Items	Parameters	Prototype	Model	Specific value for the tests
Slope body	1) Vertical height(m)	200–900	0.4–1.8	0.15–0.2
	2) Slope angle (°)	10–40	10–40	34.9–45.6
Sliding bed	1) The length of the sliding bed(m)	200–2,450	0.4–4.9	3.0
	2) The width of the sliding bed (m)	100–1,500	0.2–3.0	0.67–0.77
	3) Source area inclination (°)	22–75	22–75	50
	4) Sliding area inclination (°)	18–45	18–45	30
Sliding body	1) Vertical distance (m)	190–1,500	1.0–10	1.72
	2) Horizontal distance (m)	400–1900	0.8–3.8	2.41
	3) The volume (m^3)	(0.9–742)×10^7	0.072–59.4	0.012–0.325
Time	Duration(s)	<300	<13.4	<5

Note: Considering the safety and operability of the device, the height of the slope and the volume of the sliding body have been appropriately reduced. Since the prototype data were all derived from well-documented super-large landslides, there are more relatively small-scale landslides in nature, so it is reasonable to reduce them appropriately.

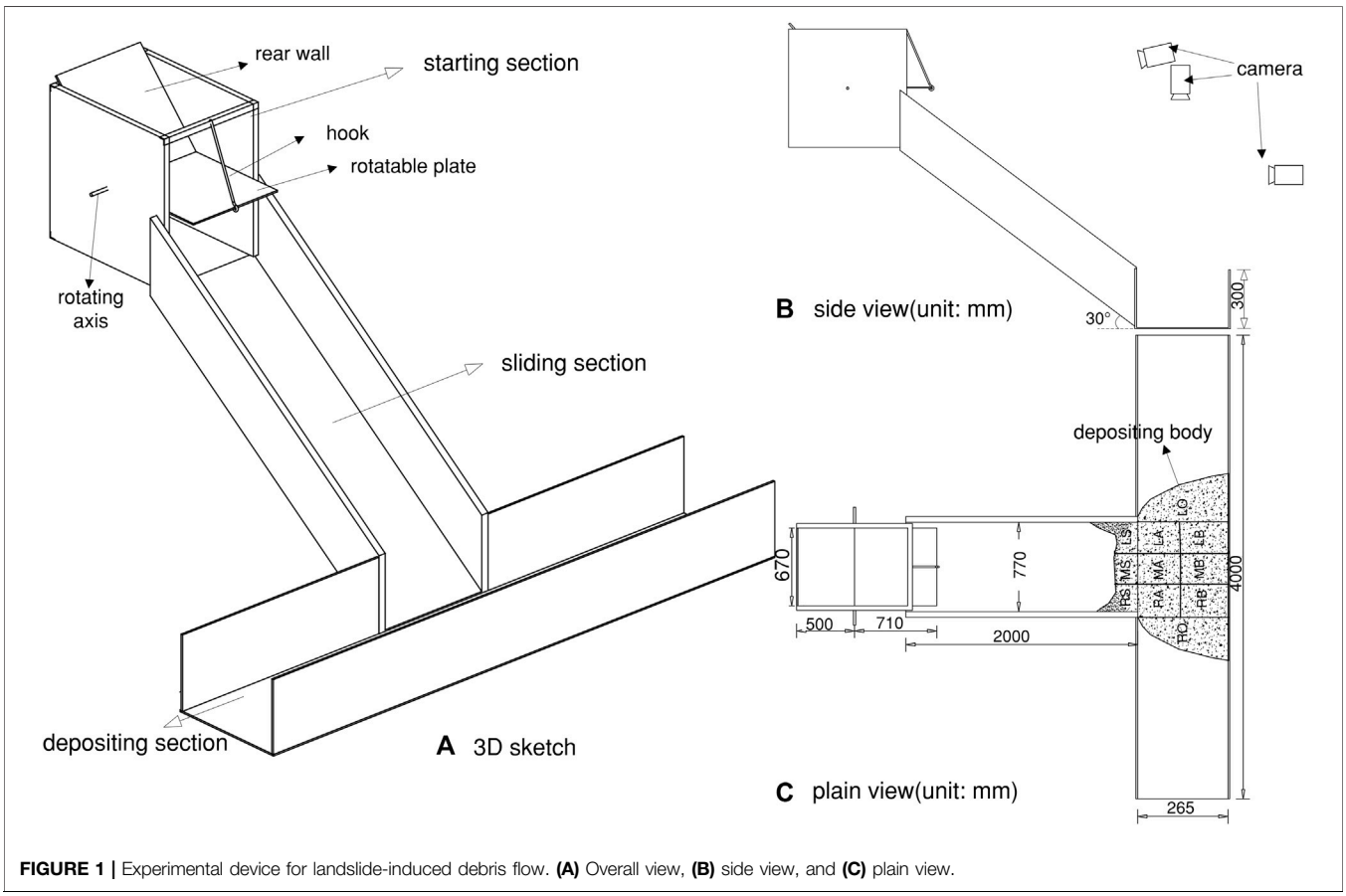

FIGURE 1 | Experimental device for landslide-induced debris flow. **(A)** Overall view, **(B)** side view, and **(C)** plain view.

gravel, medium gravel, and fine sand, as shown in **Figure 2**. The physical parameters of the material are shown in **Table 2**. In addition, all the coarse gravels were equally divided into three parts and colored red, green, and blue lacquer. They were used as tracers after the lacquer was completely dry.

The slope occurrence included uniform slope and layered slope. The uniform slope was made of the mixture of the three kinds of debris, as sketched in **Figure 3A**. The layered slope can be further divided into two types according to the relationship between the stratum surface and sliding surface. One was a parallel slope, which is referred to the stratum surface parallel to the sliding surface (**Figure 3B**). The other was an intersecting slope representing that the stratum surface was intersecting with the sliding surface (**Figure 3C**). As **Figure 3** showed, different strata were coded by Arabic numerals 1, 2, and 3. Different stratum sequences could be obtained by changing the types of materials at different layers. All the test conditions by combining these variables are listed in **Table 3**.

TABLE 2 | Physical and mechanical parameters of the material used in the tests.

Types of material	Diameter (mm)	Bulk density (kg/m^3)	Water content (%)	Total mass (kg)	Bulk volume (×10^{-3}m^3)	Friction angle (°)
C[a]	20–40	1,690	1.2	20	11.8	36.8
M[b]	5–10	1,562	1.3	20	12.8	33.1
F[c]	<0.5	1,405	1.5	20	14.2	30.9

Note:
[a]*C, coarse gravel.*
[b]*M, medium gravel.*
[c]*F, fine sand.*

FIGURE 2 | Material samples for the model tests.

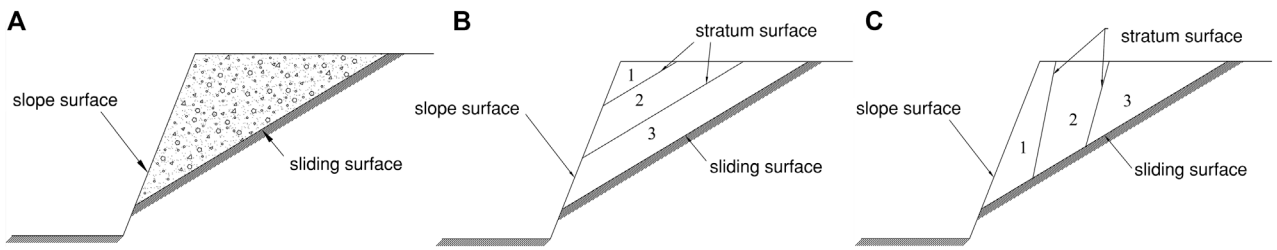

FIGURE 3 | Schematic of the slope structure **(A)** uniform slope; **(B)** parallel slope, that is, stratum surface paralleling with the sliding surface; **(C)** intersecting slope, that is, stratum surface intersecting with the sliding surface. The numbers 1, 2, and 3 are stratum sequence codes.

Test Procedure and Measurements

1) The entire test device is cleaned up, and the rotatable plate is fixed in the horizontal position.
2) The slope body model is constructed; In order to stimulate the layered slope body, we placed the slope body in the horizontal position first and then released the rotatable plate to form a slope body in an inclined state. It is easy to construct a uniform slope body by just putting the fully mixed debris on the horizontal plate and then rotating the plate to form an inclined uniform slope. However, it is a bit more complete to make the layered slope model. Different debris are stacked horizontally from the bottom to top and laterally from the rear wall to the free surface to form a parallel slope and intersecting slope, respectively, as shown in **Figures 4A1,A2**. The tracers were carefully placed as shown in **Figures 4B1,B2**. The initial slope body was basically kept complete during the rotating process because of the inertia and was not really started until the plate rotated to the designed position. The slope angle for the horizontal state slope is the particle repose angle and is approximately equal to the sum of the plate inclination and repose angle when in the inclined state.
3) The accumulation width and depth of different materials in the landslide dam is recorded, and the geometric characteristics of the entire deposition are scanned with a 3D laser scanner.
4) Areas of the deposition and sampling, sieving, and weighing the materials are divided in each corresponding area. The plain view of the subareas of the dam is shown in **Figure 1C**. Along the longitudinal direction (along the valley), it was divided into the main accumulation body corresponding to the width of the sliding section and the expansion on both

TABLE 3 | Test conditions.

Slope feature code	Slope occurrence	Stratum sequence			Tracer particle distribution
		Coarse gravel (C)	Medium gravel (M)	Fine sand (F)	
M-CMF	Uniform mixed	-	-	-	-
P-CMF	Parallel	1	2	3	Longitudinal[a]
P-FMC		3	2	1	Longitudinal
P-MCF		2	1	3	Longitudinal
P-CFM		1	3	2	Transverse[b]
P-MFC		3	1	2	Transverse
P-FCM		2	3	1	Transverse
I-CMF	Intersecting	1	2	3	Longitudinal
I-FMC		3	2	1	Longitudinal
I-MCF		2	1	3	Longitudinal
I-CFM		1	3	2	Vertical[c]
I-MFC		3	1	2	Vertical
I-FCM		2	3	1	Vertical

[a]*Longitudinal distribution of the tracer particles in the slope body means the tracers were displayed along the valley direction, as shown in* ***Figure 4B1,I*** *and* ***Figure 4B2,III****.*
[b]*Transverse distribution in parallel slope means the tracers distributed from the rear wall to free surface* ***Figure 4B1,II****.*
[c]*Vertical distribution in the intersecting slope indicated that the tracers distributed from the top to the sliding surface of the slope* ***Figure 4B2,IV****.*

sides. The main accumulation body was further equally divided into left (L), middle (M), and right (R) sub-areas, and the expansion included left outer (LO) and right outer (RO) sub-areas. In the sliding direction, we only sub-divided the main accumulation body into the slope toe area (S), near slope area (A), and far away slope area (B). In the vertical direction, the main accumulation body was equally divided into the upper layer (U) and the lower layer (D) according to its thickness.

RESULTS AND DISCUSSION

Accumulation Characteristics of Landslide Debris Dam

Morphology of the Landslide Dam

It is obvious from **Figures 5A,B** that the damming bodies formed under different slope conditions were basically similar in plain view and longitudinal section. Most of the material accumulated in the main channel, which was fan

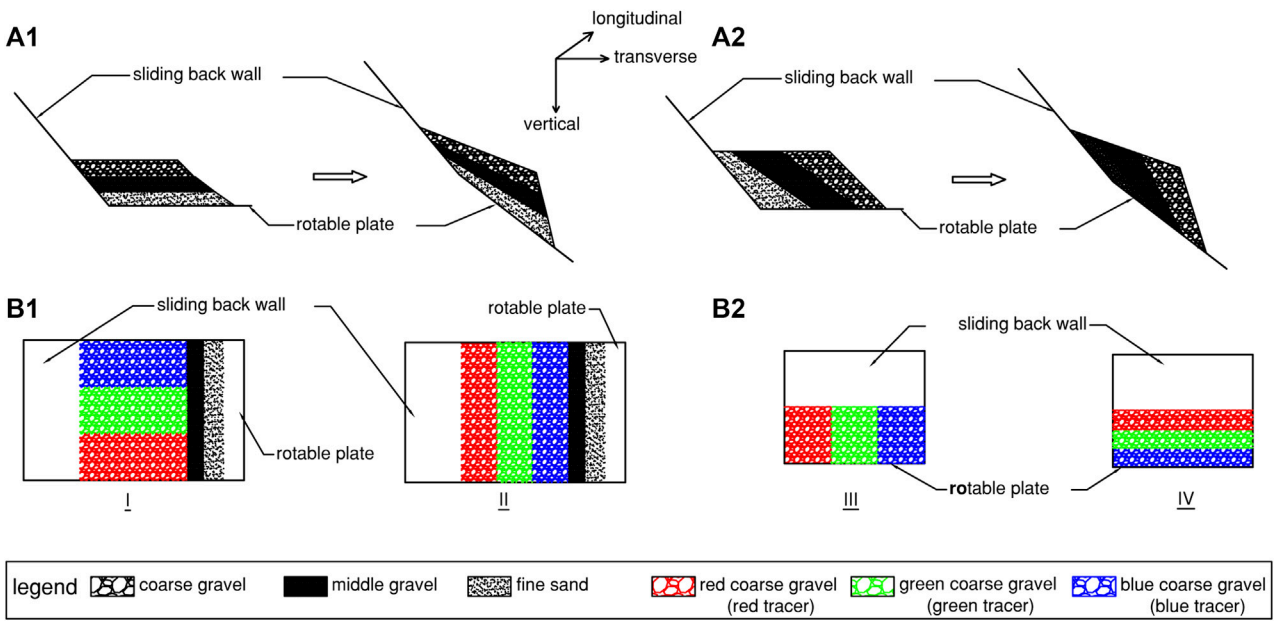

FIGURE 4 | Schematic diagram of slope-making and the distribution of tracer particles; **(A1)** the method of making a parallel slope, taking the P-CMF as an example; **(A2)** the method of making an intersecting slope, taking the I-CMF as an example **(A)**; **(B1)** the plain view of the tracer particle distribution in the parallel slope, in which I displays longitudinal distribution and II transverse distribution; **(B2)** the front view of the tracer particle distribution in the intersecting slope, in which III displays longitudinal distribution and IV vertical distribution.

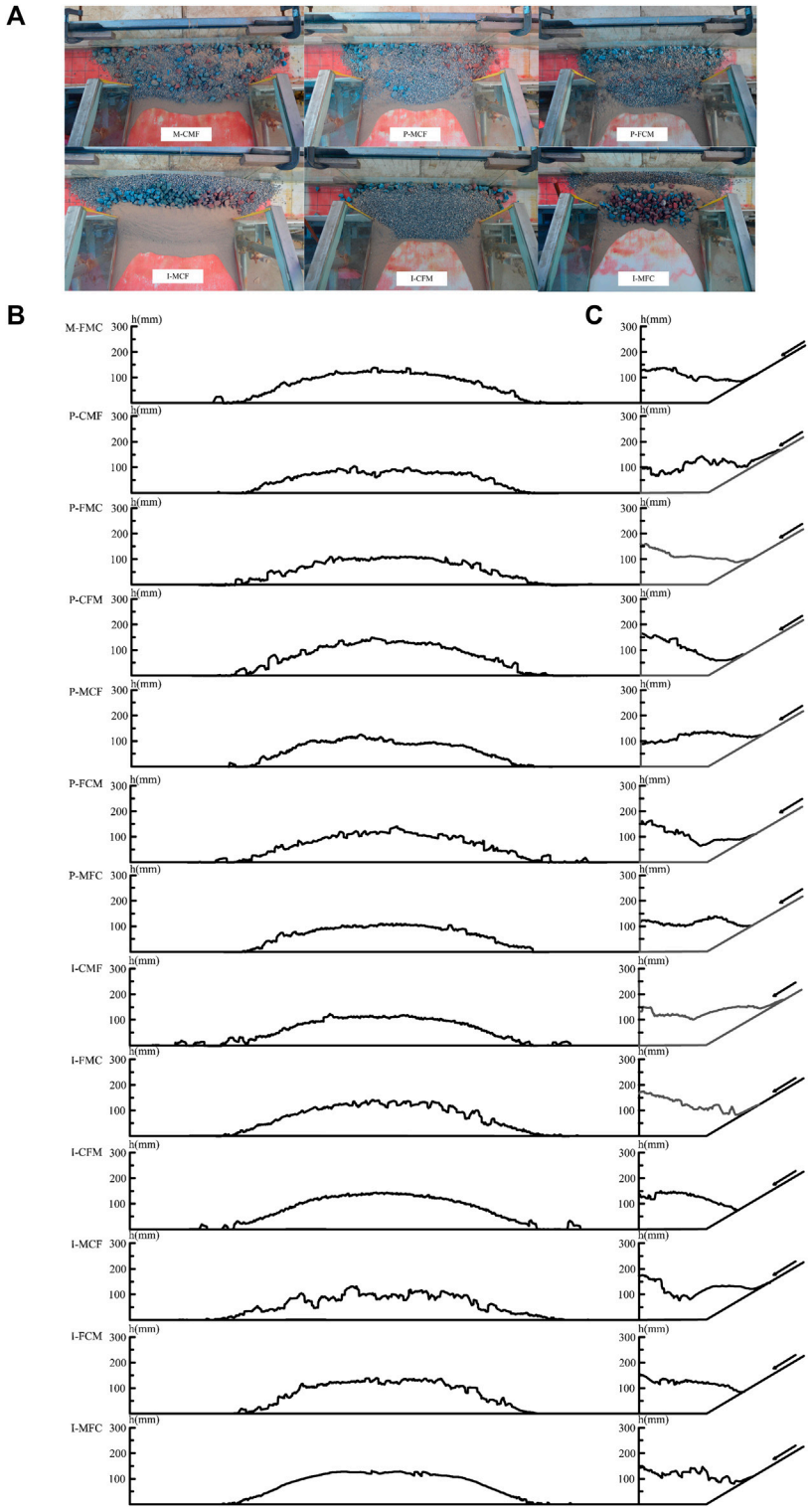

FIGURE 5 | Profiles of the landslide debris dams under different slope conditions. **(A)** Plain view; **(B)** longitudinal section; **(C)** cross section.

plain–shaped; a small amount of the material deposited on the bottom of the slope, which was saddle-shaped, and the saddle shape formed by the oblique slope was the most obvious. The longitudinal cross-section of the dams was of symmetrical parabolic shape, and the inclination angle on both sides was about 13°–16°.

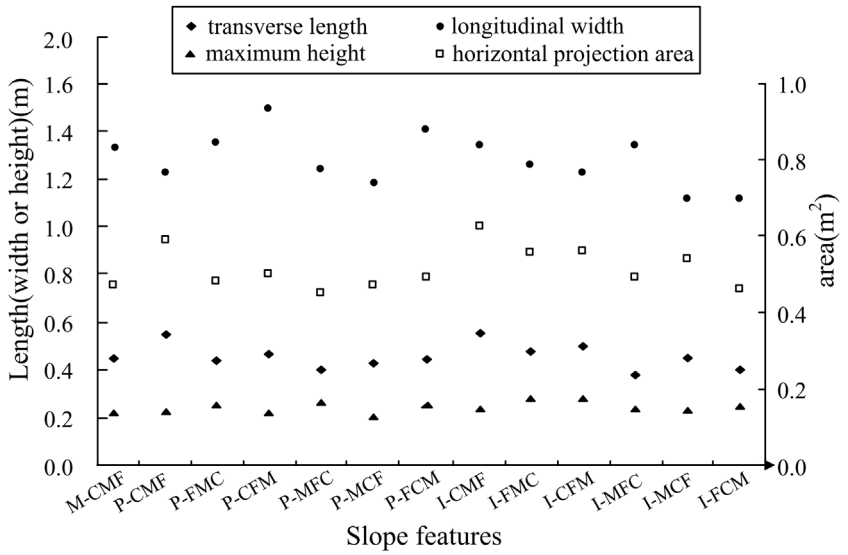

FIGURE 6 | Morphological parameters of the landslide debris dam under different conditions.

However, **Figure 5C** showed that the cross-section shapes of the dams formed by different slopes were quite different. Under the condition of uniform slope, the shape of the cross section was relatively flat, with the front part slightly higher than the rear part. However, it varied dramatically under the conditions of layered slopes. In general, the morphology of the cross section can be divided into three types: 1) the flat pattern, as the typical examples of P-MCF and P-MFC. The overall profile of the cross section was relatively flat without obvious undulations, and the average inclination angle from the front edge to the tail of the accumulation was less than 10°; 2) unidirectional inclined pattern, such as the condition of P-CFM and I-FMC. The inclination direction was mostly toward the sliding bank, and the inclination angle from the front edge to the tail of the accumulation was about 10–20°; 3) undulating pattern: it showed that the profile of the entire cross section presented large fluctuations. Specifically, it could be further divided into two-segment type (e.g., P-FCM, P-FMC, I-FCM, and I-MCF) and multi-segment type (e.g., P-CMF and I-CMF).

Figure 6 showed the morphological parameters such as longitudinal bottom width (W_{bd}), transverse length (L_d), maximum height (h_{max}), and horizontal projected area (A_d) of the landslide dam under different conditions. The geometric parameters of the dam were also different with the difference of the stratum sequence in parallel slopes and intersecting slopes. The longitudinal width of the dams formed by the parallel slope was generally larger than that of the intersecting slope. The distribution of the transverse length and horizontal projected area was basically the same; the maximum height did not change much, but there was a difference in its position according to **Figure 5C**. Among these parameters, the longitudinal width altered the most, indicating that it was affected most by the stratum sequence.

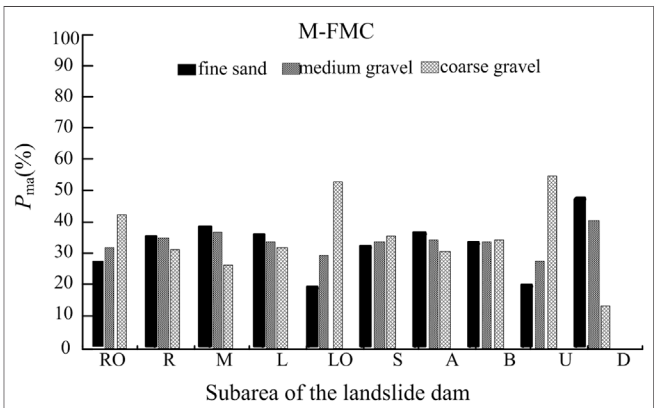

FIGURE 7 | Distribution characteristics of material composition in the dam formed by the uniform slope.

Material Distribution of Landslide Dam

We can intuitively observe from **Figure 5A** that there were obvious differences in the material distribution of the dams formed by different slopes. The sieving data are used to calculate the percentage of different materials in each area to the total substance in the area (P_{ma}) for further analysis. **Figure 7** showed that along the longitudinal direction in the dam formed by the uniform slope, the content of coarse gravel was relatively the largest in the outer expansion area, and the content of each material in the main deposit areas was pretty much the same; in the sliding direction, the three kinds of material in each area distributed more evenly, with P_{ma} more than 30%; in the vertical direction, the largest content in the upper layer was fine sand, followed by medium gravel, and coarse gravel consequently and vice versa in the layer below.

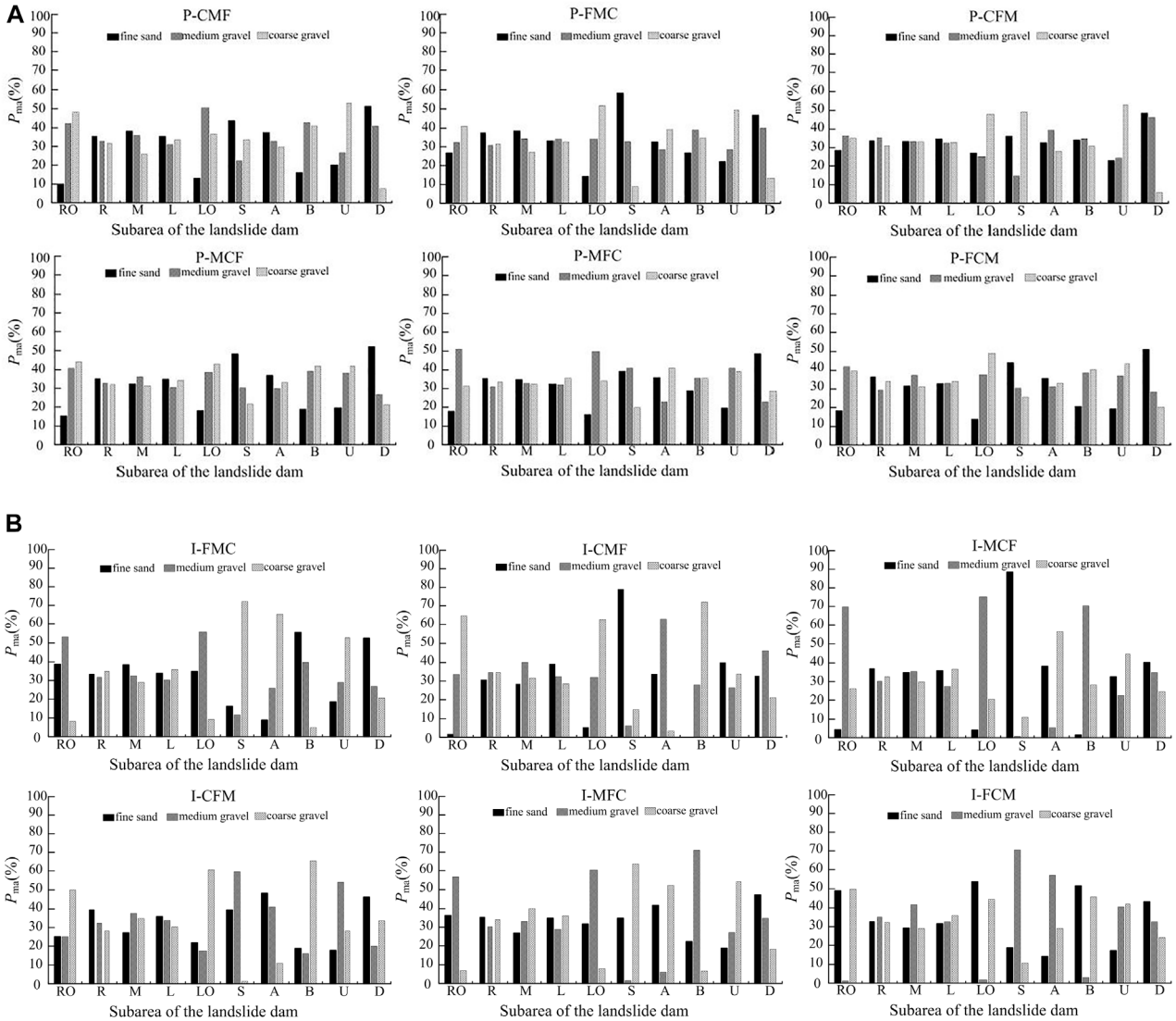

FIGURE 8 | Distribution characteristics of material composition in the dam formed by the parallel slope and intersecting slope. **(A)** Parallel slope. **(B)** Intersecting slope.

This phenomenon was called the inverse grading according to Heim (1932).

Figure 8A demonstrates that the material distribution characteristics of the dam formed by parallel slopes were basically similar to those of the uniform slope in the longitudinal and vertical directions. In the sliding direction, the feature of fine particles prevailing in the area of *S* and coarse particles in the area of *B* could be observed, which indicated a regularity that coarse particles move much farther than fine particles.

Figure 8B shows that the material distributions of the dam formed under various conditions of the intersecting slope were quite different compared with those of the uniform slope and the parallel slope. In the longitudinal direction, the substances located in the 1st[s] layer of the slope were most abundant in the outward expansion areas (LO and RO), and the distribution of the substances in the main accumulation areas (L, M, and R) was relatively uniform. In the sliding direction, the most abundant material in the S, A, and B areas always came from the 3rd, 2nd, and 1st layers in the slope body respectively, which indicated that the material distribution of the dam was consistent with the material distribution of the slope body. In the vertical direction, the contents of medium and coarse gravel in the upper layer were greater than those of fine sand under some working conditions (I-FMC, I-MFC, I-MCF, and I-FCM), which basically met the inverse grain distribution characteristics. But, for the condition of I-CMF, the contents of fine sand were greater than those of coarse gravel in both the upper layer and lower layer. This could be explained by the sorting mechanism in the process of movement and accumulation.

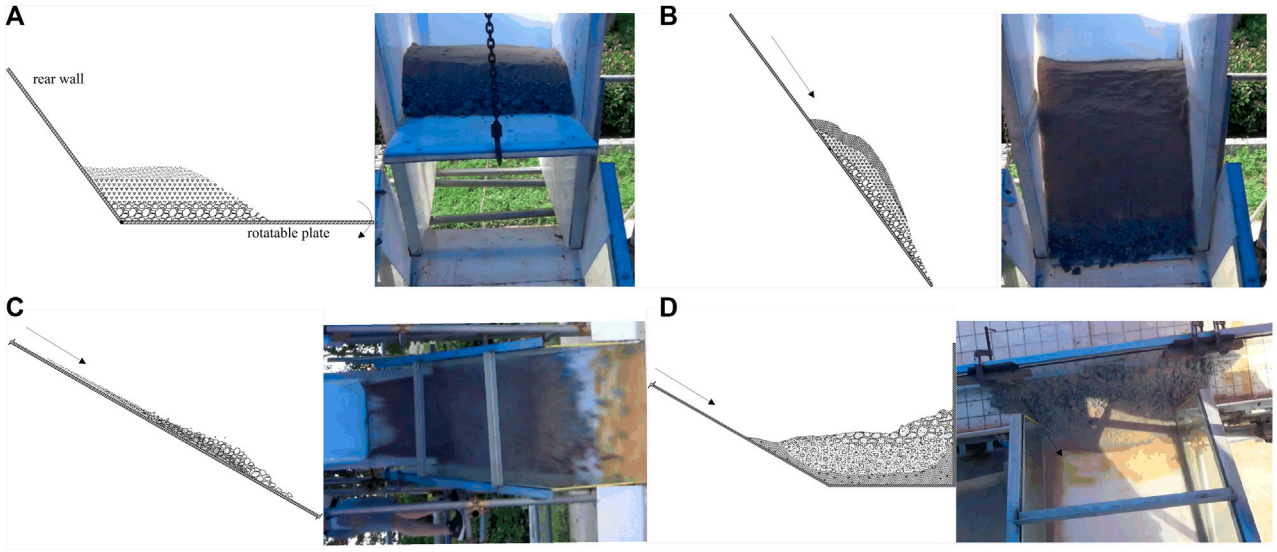

FIGURE 9 | Damming process of a landslide under parallel slope conditions (e.g. P-FMC). **(A)** Initial state of the slope body; **(B)** starting stage; **(C)** sliding stage; and **(D)** depositing stage.

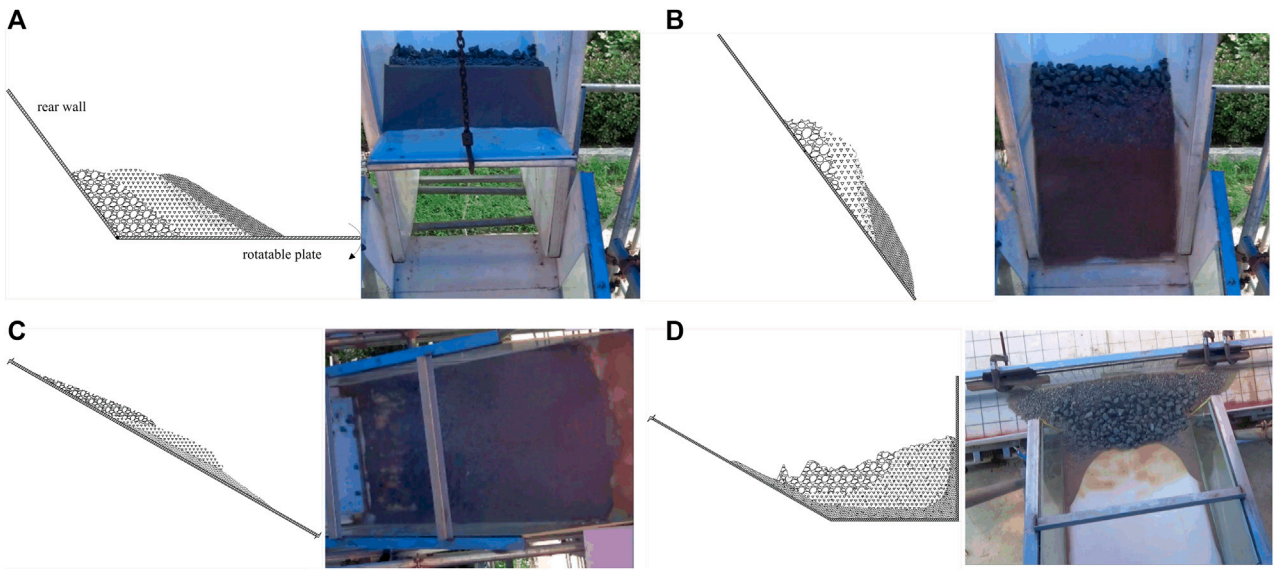

FIGURE 10 | Damming process of a landslide under intersecting slope conditions (e.g. I-FMC). **(A)** Initial state of the slope body; **(B)** starting stage; **(C)** sliding stage; **(D)** depositing stage.

Accumulation Mechanisms of Landslide-Debris Dams

Dynamic Process of Landslide-Debris Dams

The characteristics of the propagation and accumulation under different slope conditions were different. In general, it could be divided into three stages:

(1) The rotating–starting stage: It refers to the process where the rotatable plate rotated from a horizontal state to the designed angle and caused the material to start, with an average time of 0.36–0.4 s. This stage could be sub-divided into a rotating process and starting process based on the motion state of the slope body. The rotating stage refers to the process of rotating, which lasted 0.24 s. In the rotating process, the overall shape of the slope body was kept complete, and no obvious sliding appeared. The debris started to slide due the vibration of the rotatable plate contacting with the sliding bed and gravity. Two typical starting modes of the slope body

FIGURE 11 | Average velocity and accumulation stage duration of a landslide under different slope conditions.

were observed in different slope conditions. Visible overall depression and deformation can be observed in the uniform and parallel slope body, as shown in **Figures 9A,B**, which demonstrated an overall initiation mode of the slope body. However, a layered initiation mode was observed in the intersecting slopes. The debris at the 1st stratum declined apparently with no obvious movement in the 2nd and 3rd strata (**Figures 10A,B**).

(2) The sliding stage: It refers to the stage where the faucet of the sliding body moves in the sliding section. For uniform slopes and parallel slopes, the faucet of the sliding body mainly comprised coarse particles, with a mixture of the three kinds of debris in the middle and fine sand in the tail, as shown in **Figure 9C**. However, the faucet of the sliding body only comprised the debris in the 1st stratum for the intersecting slope conditions, and the 2nd and 3rd strata started and moved successively (**Figure 10C**). The average velocity of the sliding stage varied from 3.0 m/s to 4.4 m/s under different slope conditions, as shown in **Figure 11**. The tongue-like cross section of the sliding body indicated that the middle moved faster than both sides.

(3) The depositing stage: This stage starts from the accumulation of the sliding body faucet until all the debris accumulated, which could be sub-divided into the main channel accumulation stage and slope accumulation stage. The faucet of the sliding body moved to the accumulation area and stopped when it encountered the valley bank. The debris that arrived subsequently quickly rose and spread to both sides, forming a fan-shaped accumulation body; a small amount of the materials accumulated at the foot of the slope, and the fine sand near the side wall of the sliding bed continued to slide down, eventually forming a saddle-shaped tail, as shown in **Figures 9D**, **10D**.

Vertical Infiltration Under Parallel Slope

Figure 11 showed that the average velocity of the sliding stage and the duration of the accumulation stage varied greatly under different slope conditions. The largest velocity appeared in the condition of I-CMF, followed by P-CMF and M-FMC, which indicated that the coarser the faucet of the sliding body, the faster the moving speed, and the larger average velocity of the sliding stage. As is elaborated previously, the faucet of the sliding body for I-CMF only comprised coarse gravel, while the other two counterparts consisted of a mixture of different debris. The mixture of the parallel slope was formed by the vertical infiltration effect, which means that fine debris at the upper layer penetrated to the lower layer when making a parallel slope model and during movement, thus causing a certain mixture at the 3rd layer.

Further analysis of the sliding velocity of different parallel slope conditions implies that even the debris at the 3rd layer was the same particle; the sliding velocity was different when the fine sand is at a different layer. The velocity was generally smaller when the content of fine sand at the 2nd layer was greater than that at the 1st layer, such as P-MFC < P-FMC and P-CFM < P-FCM. This further verified the vertical infiltration effect of fine particles to the coarse particles during the damming process. The closer the fine sand was to the 3rd layer, the more it penetrated down to the 3rd layer, and the greater effect the slowing on the movement speed. Vertical infiltration not only affected the sliding velocity but also caused inverse grading in material distribution of the dam.

Pushing–Climbing Effect and laterial Infiltration Under Intersecting Slope

Figure 11 also showed that the shortest and longest duration of the accumulation stage was I-FMC and I-CMF, respectively, which all belonged to the inclined slope. The fine and coarse particles moved and accumulated successively under the condition of I-FMC. The coarse gravels with the largest velocity at the end exerted a pushing effect to the medium gravels in front, and the medium gravels in turn pushed the fine sand. The progressive pushing effect between different debris accelerated the entire sliding and accumulating process.

In addition, due to the larger velocity of the coarse particles, the coarse particles climbed up and accumulated on the top of the fine particles, resulting in a large overlapping area of the dam in the vertical direction (see **Figures 10D**, **12A**). This is the main reason why the dams formed by some intersecting slopes presented the inverse grading distribution regularity.

In addition to this, the pushing effect can also make the dam more compact. **Figure 6** displayed that the transverse length of the dam body with the pushing effect in the damming process was generally low, such as I-CFM, I-MFC, and I-FCM. Among the aforementioned conditions, the transverse length under the

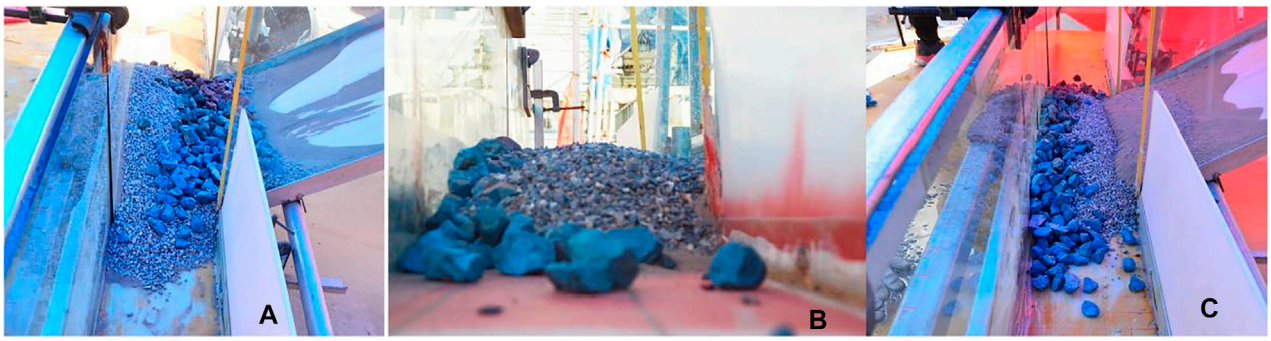

FIGURE 12 | Landslide debris deposits under intersecting slope with different sequences. **(A)** I-FMC with an obvious pushing–climbing effect; **(B)** I-CFM with strong horizontal infiltration; **(C)** I-CMF without obvious an pushing–climbing effect.

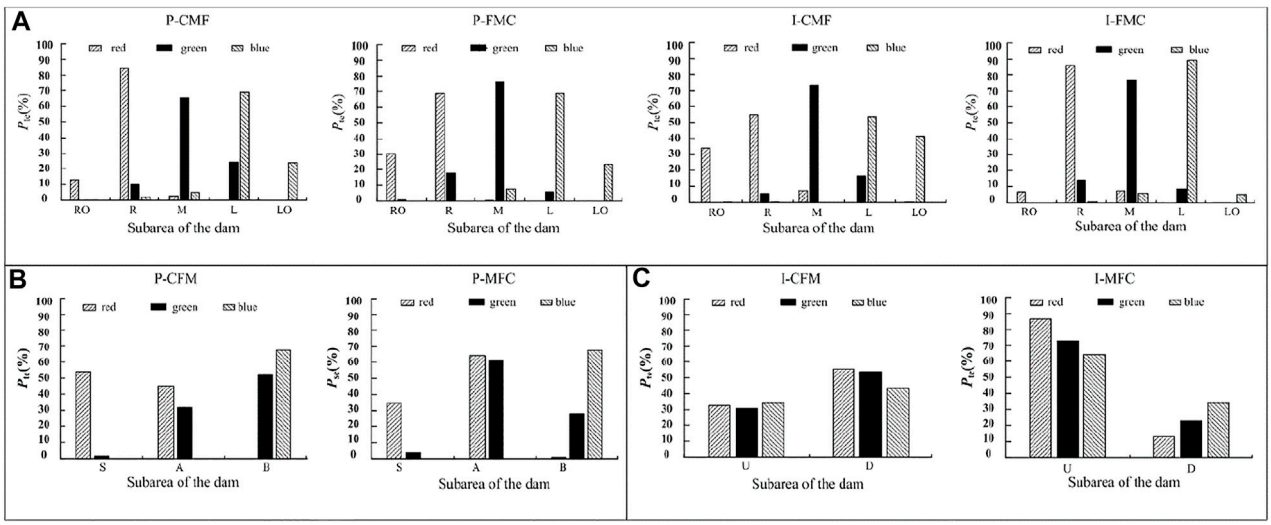

FIGURE 13 | Distribution of tracer particles in different areas of landslide dams under different distributions in the slope body. **(A)** Tracer particle distributed along the longitudinal direction in the slope; **(B)** tracer particle distributed along the transverse direction in the parallel slope; **(C)** tracer particle distributed along the vertical direction in intersecting slope. The parameter P_{ts} represented the mass percentage of different tracer particles in each area of the dam to the total amount of each kind of tracer particles.

condition of I-CFM was the lowest, which indicated another mechanism—lateral infiltration. The fine sand penetrated much into the voids of the coarse gravel in front due to the pushing effect exerted by the medium gravel behind. As a result, little fine sand could be observed in the dam from the side view as shown in **Figure 12B**. As for I-MFC, the lateral permeability of the fine sand reduced significantly because the porosity of the medium gravel was apparently lower than that of the coarse gravel so that the transverse length was relatively larger than that of the I-CFM.

On the contrary, the coarse particles and fine particles started moving successively under the condition of I-CMF (see **Figure 12C**). The coarse particles moved ahead and faster than the fine particles. Neither the pushing effect nor the lateral infiltration effect was obvious during the damming process, resulting in the longest duration of the accumulation and the longest distance of the transverse length of the dam. As different debris stacked mainly side by side in the sliding direction, the content of the upper and lower layers of each kind of debris was not much different. Due to the different repose angles of the materials, there was obvious fluctuation at the junction of different materials, which was manifested as obvious multisegment undulations in the transverse cross section (**Figure 5C**).

DISCUSSION

Accumulation Characteristics of Landslide Dam

The cross-section morphology of landslide dams has an important influence on the mechanism of dam breach. The lowest point of the cross section determines the location of the initial breach and the erosion pattern (Zhao et al., 2019).

Numerous studies have reported that the cross-sectional shape of a landslide dam is affected by the topographic and morphological conditions such as the starting section angle, inclination of the sliding section, distance and roughness of the sliding bed, shape of the depositing channel, and volume of the sliding body (Okura et al., 2003; Di Luzio et al., 2004; Wang, et al., 2012; Zhao et al., 2017; Crosta et al., 2017; Zhao et al., 2019; Zhou et al., 2019a; Zhou et al., 2019b). However, under the same topography, morphology, and volume conditions in this experiment, the cross-sectional shapes of the dams are also quite different due to different slope structure. The cross-sectional morphology that appears in this experiment includes almost all morphologies mentioned in the studies of Zhao et al. (2019) and Zhou et al., (2019a), which demonstrate that the geometrical morphology of landslide dams is not only affected by the topography but also by the geological conditions of the slope body.

The material distribution characteristics of landslide dams affect the permeability and mechanical properties of the dam. Previous studies have concluded some rules for the material distribution characteristics of landslide deposits. It is generally believed that there is an inverse grading along the vertical direction in landslide debris dams (Savage and Lun, 1988; Zhou and Ng, 2010; Zhang and Yin, 2013; Gray, 2018). Many researchers proposed different hypotheses to explain the mechanism, such as the dispersive pressure proposed by Bagnold (1956) that made the coarse particles move to the debris flow surface. The kinematic sieving during the movement also contributed to the sorting (Zheng et al., 2019). This study basically yielded the same results of inverse grading distribution, but with different sorting mechanisms under different slope conditions. For the uniform and parallel slopes, obvious inverse grading distribution is induced by overall initiation of the slope body and strong vertical infiltration of the fine sands during the movement. However, inverse grading distribution is generated by the effects of pushing–climbing, and lateral infiltration existed among particles.

Relationship Between Material Distribution Characteristics of the Landslide Dam and Slope Body

By analyzing the distribution of tracer particles, we could easily obtain a conclusion that the debris distributed longitudinally in the slope is mainly accumulated in the corresponding longitudinal area of the dam, as shown in **Figure 6** of P-MCF and I-MCF. **Figure 13A** further demonstrated that about 70–80% of the tracer particles slide to the corresponding areas of the dam and 10–30% to the adjacent areas on both sides. There was no cross-regional distribution phenomenon, that is, no green tracer particles from the middle of the slope were found in the outer expansion areas of the dam, and no blue tracer particles from the left side of the slope appeared in the right side of the dam and vice versa. **Figure 13B** indicated that the tracer particles distributed transversely in the slope body accumulated in the corresponding area of the dam along the sliding direction, which was also illustrated by **Figure 5A**P-FCM. However, different tracer particles distributed vertically in the intersecting slope appeared randomly in the vertical direction of the dam, and it was even affected by the layer sequence of the tracer particles in the slope. For I-CFM, the mass percentages of different tracer particles in the lower part of the dam were all greater than those in the upper part. About 60% of the red tracer located in the upper part of the slope body accumulated in the lower part of the damming body (**Figure 13C** I-CFM), while more tracer particles located in the upper part of dam when the tracer particles were at the 3rd layer, as shown in **Figure 5A** I-MFC and **Figure 13C** I-MFC. This phenomenon indicated that there was a vertical exchange of the same particles in the process of damming, which was consistent with the study by Umbanhowar et al. (1998).

Although we elaborated the accumulation characteristics of the landslide dam formed by different slope conditions and discussed the relationship between the accumulation characteristic of the landslide dam and the slope body and analyzed the sorting mechanism, further research is still needed on the mechanism from the perspective of mechanics.

CONCLUSION

Through the model tests, we investigated the damming process of the landslide debris dam under different slope characteristics and analyzed the morphological characteristics and composition distribution characteristics of the dams. The main conclusions are listed as follows:

1) The morphological characteristics of the landslide debris dam are regulated by the slope structure, especially for the transverse cross-sectional shape. Three typical cross-sectional shapes are obtained: flat, unidirectional inclined, and undulating shapes. The cross section of the dam formed by the uniform slope is flat. The dams formed by the parallel slopes mostly present flat or unidirectional inclined cross-sectional shape, while undulating shapes occur for the intersecting slopes.
2) The debris distribution of the landslide dams is also affected by the slope body features. The debris grains are relatively uniformly distributed in the longitudinal and sliding directions of the dams formed by the uniform slope, but an obvious inverse distribution appears in the vertical distribution. The debris distributions of the dams formed by the parallel slopes are similar in the longitudinal and vertical direction but show a bimodal structure where fine gravel is close to the slope and coarse gravels are far away from the slopes. The debris distributions of the dams formed by the intersecting slopes depend on the stratum sequence.
3) The debris distribution of the landslide dam is closely related to the debris structure of the slope body. Debris distributed in the longitudinal and transverse directions of the slope body is located in the longitudinal and sliding regions of the dam body. However, debris along the vertical direction of the slope body is weakly correlated with the debris in the vertical direction of the dam due to a vertical exchange effect.
4) The damming process and sorting mechanisms are affected by slope structure. The debris grains are well mixed for the uniform and parallel slopes during the movement process. The inverse distribution of the dam in the vertical direction

is caused by the vertical infiltration effect of fine particles during the movement process. The original stratum sequence is maintained for the intersecting slope with layered debris during the movement and accumulation process. Due to the successive initiation of fine and coarse gravels, the effects of pushing–climbing and lateral infiltration among the particles are generated, leading to a larger sliding velocity and shorter accumulation duration. Thus, an inverse distribution in the vertical direction of the dams occurs.

DATA AVAILABILITY STATEMENT

The original contributions presented in the study are included in the article/Supplementary Material, further inquiries can be directed to the corresponding author.

AUTHOR CONTRIBUTIONS

XX and XW contributed to the conception and design of the study. SZ, ZL, XW, XQ and SX carried out all the experiments, XX, SZ and ZL organized the database. XX performed the statistical analysis and wrote the first draft of the manuscript. All authors contributed to manuscript revision and read and approved the submitted version.

FUNDING

This work is supported by the National Natural Science Foundation of China (Grant No. 41907258) and Doctoral Research Start-up Fund of Anyang Institute of Technology (BSJ2019011).

REFERENCES

Bagnold, R. A. (1956). The Flow of Cohesionless Grains in Fluids. *Phil. Trans. R. Soc. Lond. Ser. A, Math. Phys. Sci.* 249 (964), 235.

Casagli, N., Ermini, L., and Rosati, G. (2003). Determining Grain Size Distribution of the Material Composing Landslide Dams in the Northern Apennines: Sampling and Processing Methods[J]. *Eng. Geology*. 69 (1/2), 83–97. doi:10.1016/s0013-7952(02)00249-1

Chang, D. S., Zhang, L. M., Xu, Y., and Huang, R. Q. (2011). Field Testing of Erodibility of Two Landslide Dams Triggered by the 12 May Wenchuan Earthquake. *Landslides* 8 (3), 321–332. doi:10.1007/s10346-011-0256-x

Costa, J. E., and Schuster, R. L. (1988). The Formation and Failure of Natural Dams. *Geol. Soc. America Bull.* 100 (7), 1054–1068. doi:10.1130/0016-7606(1988)100<1054:tfafon>2.3.co;2

Crosta, G. B, De Blasio, F. V, De Caro, M, Volpi, G, Imposimato, S, and Roddeman, D. (2017). Modes of propagation and deposition of granular flows onto an erodible substrate: Experimental, Analytical, and Numerical Study. *Landslides* 14, 47–68. doi:10.1007/s10346-016-0697-3

Di Luzio, E., Bianchi-Fasani, G., Esposito, C., Saroli, M., Cavinato, G. P., and Scarascia-Mugnozza, G. (2004). Massive rock-slope failure in the Central Apennines (Italy): the case of the Campo di Giove rock avalanche. *Bull. Eng. Geol. Environ.* 63 (1), 1–12. doi:10.1007/s10064-003-0212-7

Dunning, S. A., Petley, D. N., Rosser, N. J., and Strom, A. L. (2005). *The Morphology and Sedimentology of Valley Confined Rock-Avalanche Deposits and Their Effect on Potential Dam Hazard Landslide Risk Management*. London: Taylor and Francis Group, 691–701.

Dunning, S. A. (2006). The Grain Size Distribution of Rock-Avalanche Deposits in valley Confined Settings. *Ital. J. Eng. Geol. Environ.* 1, 117–121. doi:10.4408/IJEGE.2006-01.s-15

Fan, X., van Westen, C. J., Xu, Q., Gorum, T., and Dai, F. (2012). Analysis of Landslide Dams Induced by the 2008 Wenchuan Earthquake. *J. Asian Earth Sci.* 57, 25–37. doi:10.1016/j.jseaes.2012.06.002

Fan, X., Xu, Q., Alonso-Rodriguez, A., Subramanian, S. S., Li, W., Zheng, G., et al. (2019). Successive Landsliding and Damming of the Jinsha River in Eastern Tibet, China: Prime Investigation, Early Warning, and Emergency Response. *Landslides* 16 (5), 1003–1020. doi:10.1007/s10346-019-01159-x

Gray, J. M. N. T. (2018). Particle Segregation in Dense Granular Flows. *Annu. Rev. Fluid Mech.* 50, 407–433. doi:10.1146/annurev-fluid-122316-045201

Heim, A. (1932). *Landslides and Human Live*. Vancouver, B C: Bitech Publishers, 93–94.

Hu, X. W., Huang, R. Q., Shi, Y. B., Lu, X. P., and Wang, X. R. (2009). Analysis of Blocking River Mechanism of Tangjiashan Landslide and Dam-Breaking Mode of its Barrier Dam. *Chin. J. Rock Mech. Eng.* 28 (1), 181–189. doi:10.3321/j.issn:1000-6915.2009.01.024

Huang, R. Q. (2007). Large-scale Landslides and Their Sliding Mechanisms in China since the 20th century. *Chin. J. Rock Mech. Eng.* 26 (3), 433–454. doi:10.3321/j.issn:1000-6915.2007.03.001

Huang, R. Q., Pei, X. J., and Li, T. B. (2008). Basic Characteristics and Formation Mechanism of the Largest Scale Landslide at Daguangbao Occurred during the Wenchuan Earthquake. *J. Eng. Geology*. 16 (6), 730–741. doi:10.3969/j.issn.1004-9665.2008.06.002

Iverson, R. M. (2015). Scaling and Design of Landslide and Debris-Flow Experiments. *Geomorphology* 244 (sep.1), 9–20. doi:10.1016/j.geomorph.2015.02.033

Lei, X. S., Xie, W., Lu, K. L., Zhu, D. Y., and Chen, J. X. (2016). Model Tests of Sliding and Accumulation Characteristics of Cohesionless Soil. *Chin. J. Geotechnical Eng.* 38 (2), 226–236. doi:10.11779/CJGE201602005

Li, S. D., Li, X., Zhang, J., and Wang, Y. (2010). Study of Geological Origin Mechanism of Tangjiashan Landslide and Entire Stability of Landslide Dam. *Chin. J. Rock Mech. Eng.* 29 (S1), 2908–2915.

Liu, J. F., You, Y., and Chen, X. C. (2010). The Characteristics and Countermeasures of Dam-Breaking Debris Flow after Wenchuan Earthquake—A Case Study of the Tangfang Gully in Pingwu county,Sichuan Province. *J. Sichuan Univ. (Engineering Sci. Edition)* 42 (5), 68–75. doi:10.15961/j.jsuese.2010.05.007

Nian, T. k., Wu, H., Chen, G. Q., Zheng, D., and Li, D. (2018). Research Progress on Stability Evaluation Method and Disaster Chain Effect of Landslide Dam. *Chin. J. Rock Mech. Eng.* 37 (8), 1796–1812. doi:10.13722/j.cnki.jrme.2017.1655

Okura, Y., Kitahara, H., Kawanami, A., and Kurokawa, U. (2003). Topography and Volume Effects on Travel Distance of Surface Failure. *Eng. Geology*. 67, 243–254. doi:10.1016/s0013-7952(02)00183-7

Peng, S. Q., Xu, Q., Li, H. J., and Zheng, G. (2019). Grain Size Distribution Analysis of Landslide Deposits with Reliable Image Identification. *J. Eng. Geology*. 27 (6), 1290. doi:10.13544/j.cnki.jeg.2018-305

Qin, H. K., Zhang, H. Q., and Zhang, B. (2016). Formation Conditions of the Qipangou Multi Stage Dam-Breaking Debris Flow in Wenchuan Area after the Earthquake. *J. Eng. Geology*. 24 (s), 100–107. doi:10.13544/j.cnki.jeg.2016.s1.015

Savage, S. B., and Lun, C. K. K. (1988). Particle Size Segregation in Inclined Chute Flow of Dry Cohesionless Granular Solids. *J. Fluid Mech.* 189, 311–335. doi:10.1017/s002211208800103x

Shan, Y. B., Chen, S. S., and Zhong, Q. M. (2020). A Rapid Evaluation Method of Landslide Dam Stability[J]. *Chin. J. Rock Mech. Eng.* 39 (9), 1847–1859. doi:10.13722/j.cnki.jrme.2019.1240

Shi, Z. M., Guan, S. G., Peng, M., Zhang, L. M., Zhu, Y., and Cai, Q. P. (2015). Cascading Breaching of the Tangjiashan Landslide Dam and Two Smaller Downstream Landslide Dams. *Eng. Geology*. 193, 445–458. doi:10.1016/j.enggeo.2015.05.021

Shi, Z. M., Ma, X. L., Peng, M., and Zhang, L. (2014). Statistical Analysis and Efficient Dam Burst Modelling of Landslide Dams Based on a Large-Scale

Database. *J. Rock Mech. Eng.* 33 (9), 1780–1790. doi:10.13722/j.cnki.jrme.2014.09.007

Shi, Z. M., Xiong, X., Peng, M., Zhang, L. M., Xiong, Y. F., Chen, H. X., et al. (2017). Risk Assessment and Mitigation for the Hongshiyan Landslide Dam Triggered by the 2014 Ludian Earthquake in Yunnan, China. *Landslides* 14 (1), 269–285. doi:10.1007/s10346-016-0699-1

Umbanhowar, P. B., Melo, F., and Swinney, H. L. (1998). Periodic,aperiodic,and Transient Patterns in Vibrated Granular Layers. *Physica A:Statistical Mech. its Appl.* 249 (1–4), 1–9. doi:10.1016/s0378-4371(97)00425-1

Wang, G. Q., Wang, Y. Q., Liu, L., and Wang, D. (2015). Reviewed on Barrier Dam and Simulation on Dam Breach. *Yellow River* 37 (09), 1–7. doi:10.3969/j.issn.1000-1379.2015.09.001

Wang, Y. F., Chen, Q. G., and Zhu, Q. (2012). Inverse Grading Analysis of deposit from Rock Avalanches Triggered by Wenchuan Earthquake. *Chin. J. Rock Mech. Eng.* 31 (6), 1089. doi:10.3969/j.issn.1000-6915.2012.06.002

Zhang, M., and Yin, Y. (2013). Dynamics, Mobility-Controlling Factors and Transport Mechanisms of Rapid Long-Runout Rock Avalanches in China. *Eng. Geology.* 167, 37–58. doi:10.1016/j.enggeo.2013.10.010

Zhang, S., Xie, X., Wei, F., Chernomorets, S., Petrakov, D., Pavlova, I., et al. (2015). A Seismically Triggered Landslide Dam in Honshiyan, Yunnan, China: from Emergency Management to Hydropower Potential. *Landslides* 12 (6), 1147–1157. doi:10.1007/s10346-015-0639-5

Zhao, G.-W., Jiang, Y.-J., Qiao, J.-P., Yang, Z.-J., and Ding, P.-P. (2019). Numerical and Experimental Study on the Formation Mode of a Landslide Dam and its Influence on Dam Breaching. *Bull. Eng. Geol. Environ.* 78, 2519–2533. doi:10.1007/s10064-018-1255-0

Zhao, T., Dai, F., and Xu, N.-w. (2017). Coupled DEM-CFD Investigation on the Formation of Landslide Dams in Narrow Rivers. *Landslides* 14, 189–201. doi:10.1007/s10346-015-0675-1

Zheng, G., Xu, Q., and Peng, S. Q. (2019). Mechanism Analysis of the Accumulation Characteristics of Rock Avalanche. *J. Eng. Geology.* 27 (4), 842–852. doi:10.13544/j.cnki.jeg.2018-241

Zheng, H., Shi, Z., Peng, M., Guan, S., Hanley, K. J., and Feng, S. (2022). Amplification Effect of Cascading Breach Discharge of Landslide Dams. *Landslides* 19, 573–587. doi:10.1007/s10346-021-01816-0

Zheng, H., Shi, Z., Yu, S., Fan, X., Hanley, K. J., and Feng, S. (2021). Erosion Mechanisms of Debris Flow on the Sediment Bed. *Water Resour. Res.* 57 (12), 1–19. doi:10.1029/2021WR030707

Zhou, G. G. D., Cui, P., Chen, H. Y., Zhu, X. H., Tang, J. B., and Sun, Q. C. (2013b). Experimental Study on Cascading Landslide Dam Failures by Upstream Flows. *Landslides* 10 (5), 633–643. doi:10.1007/s10346-012-0352-6

Zhou, G. G. D., and Ng, C. W. W. (2010). Numerical Investigation of Reverse Segregation in Debris Flows by DEM. *Granular Matter* 12 (5), 507–516. doi:10.1007/s10035-010-0209-4

Zhou, J.-w., Cui, P., and Fang, H. (2013a). Dynamic Process Analysis for the Formation of Yangjiagou Landslide-Dammed lake Triggered by the Wenchuan Earthquake, China. *Landslides* 10 (3), 331–342. doi:10.1007/s10346-013-0387-3

Zhou, Y., Shi, Z., Zhang, Q., Jang, B., and Wu, C. (2019b). Damming Process and Characteristics of Landslide-Debris Avalanches. *Soil Dyn. Earthquake Eng.* 121, 252–261. doi:10.1016/j.soildyn.2019.03.014

Zhou, Y., Shi, Z., Zhang, Q., Liu, W., Peng, M., and Wu, C. (2019a). 3D DEM investigation on the morphology and structure of landslide dams formed by dry granular flows. *Engineering Geology* 258 (14), 105151. doi:10.1016/j.enggeo.2019.105151

Conflict of Interest: The authors declare that the research was conducted in the absence of any commercial or financial relationships that could be construed as a potential conflict of interest.

Publisher's Note: All claims expressed in this article are solely those of the authors and do not necessarily represent those of their affiliated organizations, or those of the publisher, the editors, and the reviewers. Any product that may be evaluated in this article, or claim that may be made by its manufacturer, is not guaranteed or endorsed by the publisher.

frontiers | Frontiers in Earth Science

ORIGINAL RESEARCH
published: 14 April 2022
doi: 10.3389/feart.2022.865348

Effect of Freeze-Thaw Cycles on Mechanical Properties of an Embankment Clay: Laboratory Tests and Model Evaluations

Anshun Zhang[1], *Junhui Zhang*[1]*, *Junhui Peng*[1], *Chao Huang*[1] *and Chao Zhou*[2]

[1]School of Traffic & Transportation Engineering, Changsha University of Science & Technology, Changsha, China, [2]Department of Civil and Environmental Engineering, Hong Kong Polytechnic University, Hung Hom, Hong Kong SAR, China

Freeze-thaw (FT) cycling is a crucial issue in seasonal frozen regions and it will influence the mechanical properties of soils, which must be strictly considered for embankment engineering. This study conducted a series of unconsolidated and undrained triaxial tests under various closed-system FT cycles to investigate the mechanical properties of a typical embankment clay from China. Results indicated that the stress-strain curves changed from strain hardening or stabilization to softening during FT cycles. The elastic modulus was obviously weakened by FT cycles and declined sharply after the first FT action. The failure strength gradually reduced with the accumulation of FT cycles and eventually tended to be stable when the FT cycles reached 10, and the attenuation range was approximately 6–22% compared with the condition before FT cycles. Moreover, a phenomenological model on the failure strength was established by results of the tested clay in this study and validated to be robust through multiple sets of different clays data from other published literatures. Based on that, combined with the Mohr stress circle equation and envelope theory, an innovative method for rapidly obtaining the shear strength was proposed. The ensuing discoveries were that the cohesion was damaged in the course of the first few FT cycles and then kept basically constant after 10 cycles, while the internal friction angle was not sensitive to FT cycles. The normalized empirical formula was deduced and can simultaneously apply to the strain hardening, stabilization, and softening curves given the effect of FT cycles.

Keywords: embankment clay, mechanical properties, freeze-thaw cycles, static triaxial tests, strain softening curve

OPEN ACCESS

Edited by:
Yun Zheng,
Institute of Rock and Soil Mechanics (CAS), China

Reviewed by:
Cui Xinzhuang,
Shandong University, China
Jing Wang,
Jilin Jianzhu University, China

***Correspondence:**
Junhui Zhang
zjhseu@csust.edu.cn

Specialty section:
This article was submitted to Geohazards and Georisks, a section of the journal Frontiers in Earth Science

Received: *29 January 2022*
Accepted: *11 March 2022*
Published: *14 April 2022*

Citation:
Zhang A, Zhang J, Peng J, Huang C and Zhou C (2022) Effect of Freeze-Thaw Cycles on Mechanical Properties of an Embankment Clay: Laboratory Tests and Model Evaluations. Front. Earth Sci. 10:865348. doi: 10.3389/feart.2022.865348

INTRODUCTION

In geotechnical and road areas, the mechanical properties of embankment soils have been paid sustained attention of related researchers and engineers. Moreover, given the stability and durability during the operation period, a complex and changeable climate environment is a foreseeable latent threat to the service performance of embankment soils. According to the available statistical data, the distribution area of seasonal frozen regions widely accounts for approximately 53.5 and 23% of China's and the world's total land area (Zhou et al., 2018). In such areas, every year the embankments are subjected to short-term or even continuous high-frequency freeze-thaw (FT) cycles (Hao et al.,

2022). The violent weathering attributed to FT cycles attenuates mechanical properties of soils to varying degrees, as many failures of subsistent embankments are due to this phenomenon, e.g., uneven frost heave (Miao et al., 2020), thaw subsidence (Wang et al., 2015), slope destabilization (Gowthaman et al., 2020), and retaining wall collapse (Rui et al., 2016). Thus, it is of great academic and pragmatic significance to explore the mechanical properties of embankment soils considering repeated FT cycles.

For embankment soils suffering from FT cycles, the investigations focused on mechanical properties can be acquired in previous documents. At present, it has been generally agreed that the mechanism of soil damage owing to FT cycles is as follows: 1) on the macroscopic scale, the cryogenic suction induced unfrozen water to migrate toward the frozen area and produce ice lenses; these ice lenses thawed at the positive temperature and formed cracks in the compacted soils (Zhang et al., 2014; Aldaood et al., 2016); and 2) on the microscopic scale, the growth of pore ice makes the particles be uplifted, which is the primary reason that changes soil internal structure and thus deteriorates soil properties (Nguyen et al., 2019; Liu et al., 2020). In terms of specific properties, such as the stress-strain curve transformation as well as the failure strength, shear strength, and elastic modulus, they fluctuate with the FT cycles. By the direct shear apparatus, He et al. (2020) studied the shear behavior occurs on frozen soils-concrete interface. The results indicated the relationship between shear stress and horizontal strain generally presents a strain softening type. In particular, three characteristic stages can be observed on the curve: pre-peak, post-peak, and residual can be observed on the curve. Also, for the test environment at −5°C, the peak cohesion declines with the increase of FT cycles, while the law of peak friction angle is the opposite. In the same vein, Wang et al. (2020) discovered that the internal friction angle of soft soils was not sensitive to FT cycles. Meanwhile, the first FT action weakened the cohesion weakly, then the attenuation continued to accumulate, and the 10th FT cycle was the threshold for it to achieve stability. In parallel, the mechanical properties of soils are usually revealed via the unconfined (uniaxial) compression test. As pure expansive soils suffer the entire FT cycle, Lu et al. (2020) claimed that the stress-strain curves did not change in type. At the same time, when the cycles exceed 9, the curves basically overlap, and this rule was also obtained between the failure strengths. When Ding et al. (2018) chose improved clay as the object; they showed that under the intricate impacts of FT cycles, polypropylene fibers, and cement, the stress-strain curves exhibited two forms, namely, strain softening and strain stabilization. They also reported that the failure strengths of the clay treated by various methods were reduced by 42–69% after 10 FT cycles, and then the fluctuation was negligible. In addition, Wang et al. (2017) measured the elastic modulus of fine-grained soils using a lever pressure gauge. Within the conclusions, they suggested taking the value after 6 FT cycles for designing the pavement structure in seasonal frozen areas and proposed 0.5–0.6 as the range of FT reduction coefficients. To reflect the actual engineering states more comprehensively, the researchers added considerations about the confining pressure in the test conditions. Zhou et al. (2019) carried out the orthogonal consolidated and undrained tests to underline the effect degrees on multiple factors for statics mechanical characteristics of the soil-rock mixtures. Their results highlighted that the cohesion and internal friction angle continued to decrease during the consecutive FT processes. Moreover, under the higher confining pressure, the attenuation of the failure strengths caused by FT cycles is relatively slight. Wei et al. (2019) uncovered a similar phenomenon with a series of unconsolidated and undrained (UU) tests, and three load response types, strain softening, strain stabilization, and strain hardening, all appeared in the experimental results. However, in an earlier work by Liu et al. (2016), they conducted UU tests on the silty sand at confining pressures of 100, 200, and 300 kPa, where it was noticed that the internal friction angle did not seem to reduce regularly with FT cycles and only two stress-strain relationships of strain hardening and stabilization occurred. More importantly, the authors established a normalized equation based on the Konder hyperbolic model and it can well describe the stress-strain relationship for their selected soils given the effect of FT cycles as well as confining pressures. This breakthrough was believed to be significant for predicting the stress-strain curve of other soils such as the plain or lime-treated loess in Xining, Qinghai province, China (Zhang et al., 2019).

In conclusion, these published literatures served insightful and valuable understandings on the mechanical properties of embankment soils suffering FT cycles. Nonetheless, due to the disparate soil types and test methods, the findings, especially the stress-strain relationships and shear strength indexes affected by FT cycles, are not generally unified, which limits the guidance for embankment construction. Also, existing research has concentrated on the influence factors and variation rules for mechanical properties of soils, but the corresponding evaluation models have rarely been discussed. Furthermore, the constitutive equation originating from the Konder model was applicable to hardening or stabilization soils, while the prediction for strain softening curves remains poorly understood.

To address the aforementioned imperfections, in this paper, a typical embankment clay was investigated through a series of UU tests under different FT cycles. From the experimental results, the evolution and phenomenological models for the mechanical properties of the tested clay were elucidated. In particular, in conjunction with the published data and the envelope theory, a creative method for rapidly predicting the shear strength indexes of embankment clay was highlighted. Not only that, the comprehensive normalized constitutive relationship considering the effect of FT cycles was presented and can predict the stress-strain curves with different types, especially the strain softening. These main findings can provide novel contributions to engineering construction in seasonal frozen regions.

LABORATORY EXPERIMENTS

Properties of Materials

This study selected typical clay from China as the tested soil. According to the Chinese Specification of JTG 3430-2020, Test Methods of Soils for Highway Engineering, the main basic physical properties of the tested soils were listed in **Table 1**. On the basis of

TABLE 1 | Main basic physical properties of the tested soils.

Liquid limit (%)	Plastic limit (%)	Plastic index	Maximum dry density	Optimum moisture content (%)	0.075-mm passing percentage (%)
48.2	21.4	26.8	1.86 g/cm^3	14.1	93.1

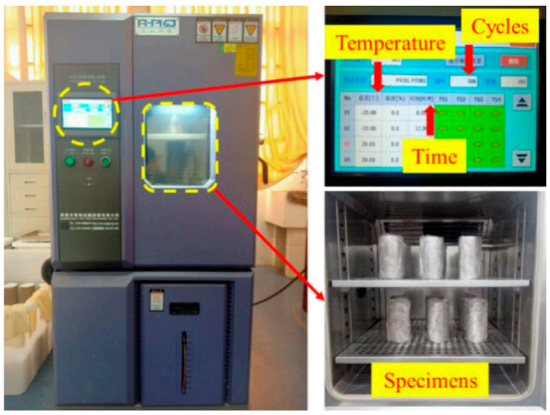

FIGURE 1 | Processing of specimens subjected to FT cycles.

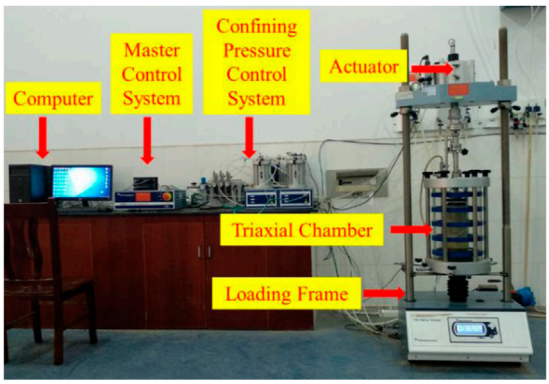

FIGURE 2 | The triaxial loading apparatus of this study.

these parameters, the soils were determined as low liquid limit clay (CL) in accordance with the Unified Soil Classification System.

Specimen Preparation

Limited by the difficulty of achieving undisturbed soils, and in order to ensure consistent humidity and density levels between specimens, the soils were remolded and tested in the laboratory. Firstly, the soils were crushed and collected after filtering by the 2-mm sieve, then dried at 105°C for 12 h. Subsequently, the dry soils were mixed with distilled water at the optimum moisture content and then stored in a sealed plastic bag for 24 h so that the moisture was uniform. The principle of this specimen preparation method is to simulate the actual humidity inside most embankments (Lin et al., 2017; Bozbey et al., 2018). At the same time, the dry density of the specimens was maintained at 1.73 g/cm^3. Afterwards, the wet soil with the calculated mass was compacted by five layers into a cylinder that was 68 mm in diameter and 140 mm in height. The rationale behind this was that ASTM D2850 states the height-to-diameter ratio should be greater than 2. Finally, the specimens were wrapped to avoid water evaporation and waited for the next tasks.

Freeze-Thaw Cycles

The closed-system FT cycle experiments were applied in this study. This method is suitable for depicting the condition that there are no obvious differences in the *in-situ* moisture content all year round. Meanwhile, given the low permeability of clay, the rate of frost penetration is significantly faster than moisture transportation, so that there is no adequate time to achieve persistent replenishment of moisture to the frozen front during the freezing process (Güllü and Khudir, 2014). Thus, it is reasonable to adopt the closed FT type here.

As shown in **Figure 1**, the entire FT cycle tests were performed in the automatic refrigerator (the range was from −60 to 150°C) with internal temperature sensors (the precision was ±0.5°C). The prepared specimens were encased in preservative film to prevent moisture exchange. The specimens were first frozen at −20°C for 12 h, and following this period, they were thawed at 20°C for 12 h. The two processes were integrated into one FT cycle, and so on. In earlier pertinent reports, it can be found that these temperatures and durations were approved by some scholars (Orakoglu and Liu, 2017; Nguyen et al., 2019; Gowthaman et al., 2020; He et al., 2020; Lu et al., 2020). The numbers of FT cycles in this study were designed as 0, 1, 3, 6, 10, and 15.

Unconsolidated and Undrained Triaxial Tests

DYNATRIAX-100/14 (**Figure 2**), a triaxial test apparatus, was employed to investigate the mechanical properties of clay in this study. Its axial load limit was 100 kN, the confining pressure could be adjusted from 0 to 1000 kPa, and the maximum axial distance of the actuator was 100 mm. The external transducer with the highest frequency of 1000 Hz collected real-time displacement and load data for the computer.

When the specimens had been subjected to the preset FT cycles, they were transferred to the triaxial chamber for UU tests. The axial loading rate was 0.8% per min and the values of confining pressures were set at 50, 100, 150, 200, 300, and 400 kPa, respectively. Once the axial strain of the specimens reached 20%, the test ended.

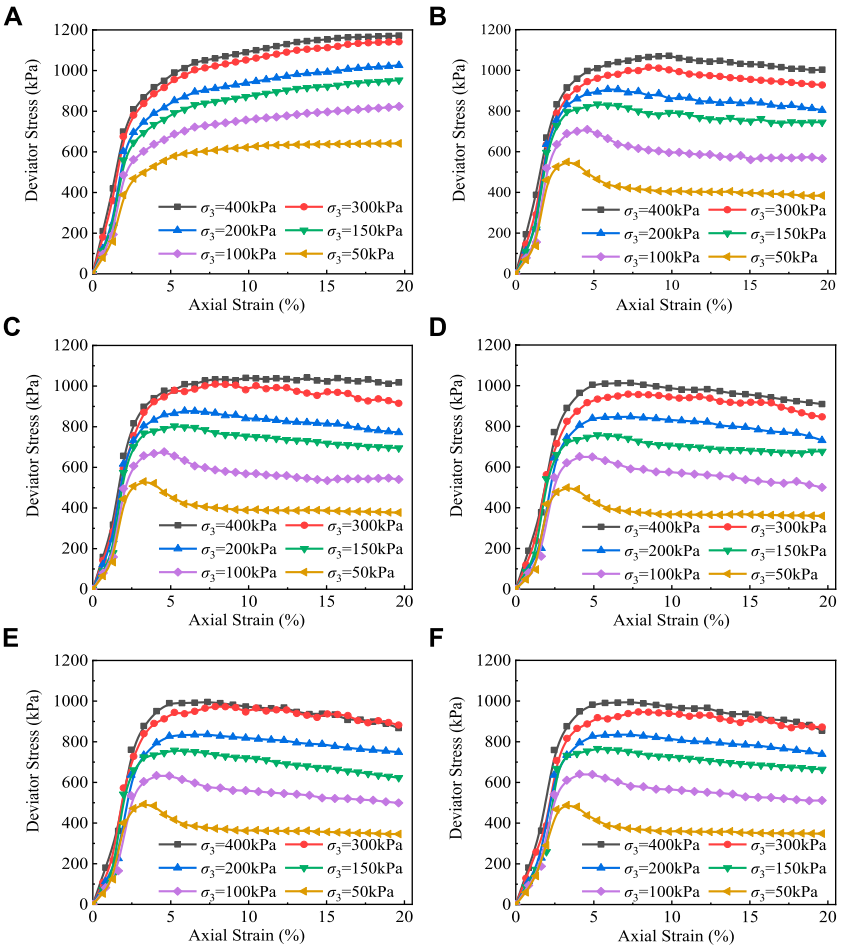

FIGURE 3 | Stress-strain curves of the tested clay suffering from various FT cycles. **(A)** 0 FT cycle. **(B)** 1 FT cycle. **(C)** 3 FT cycles. **(D)** 6 FT cycles. **(E)** 10 FT cycles. **(F)** 15 FT cycles.

EXPERIMENTAL RESULTS AND DISCUSSIONS

The stress-strain response, elastic modulus, failure strength, and shear strength are attractive indicators for the mechanical properties of soils in engineering (Zhou et al., 2015; Wei et al., 2019; Xiao et al., 2019). This section set out to present the test curves and excavated their implied information to research characteristics of the other three parameters. At the same time, a practical and innovative method for rapidly predicting the cohesion and internal friction angle of soils under FT cycles was established.

Stress-Strain Response Affected by Freeze-Thaw Cycles

Figure 3 displays the stress-strain curves of the tested soils with various FT cycles and confining pressures (σ_3). For strain softening soils, with the development of axial strain, the deviator stress first reaches its peak point and then declines gradually. While soils exhibit strain hardening characteristics, the deviator stress increases along the axial. As for strain stabilization curves, the deviator stress rise to a stable value with the accumulation of axial strain, and then continues to stabilize. Accordingly, three types of stress-strain responses can be observed in the experimental results. Moreover, at the identical confining pressures, it can be found that the more FT cycles, the smaller the peak value of softening curves, and after the 10th FT cycle, this change is not considerable.

Figure 3 also shows that, with the given FT cycles, the rise in confining pressures causes greater deviator stress when the soils achieve the same axial strain. This indicates that the constraint effect contributed by confining pressures strengthens the soils to better resist axial loads. In addition, the behaviors of strain hardening or stabilization occurred in the absence of FT cycles while the softening appeared with FT cycles. In other words, FT cycles can transform the types of stress-strain curves of the soils in this study. This phenomenon is consistent with the findings reported by Roustaei et al. (2015) and Orakoglu and Liu (2017), but different from Xian et al. (2019). One possible explanation is that the different clays with their own diverse properties were selected in this research, resulting in differences in the numbers of FT cycles and confining pressures

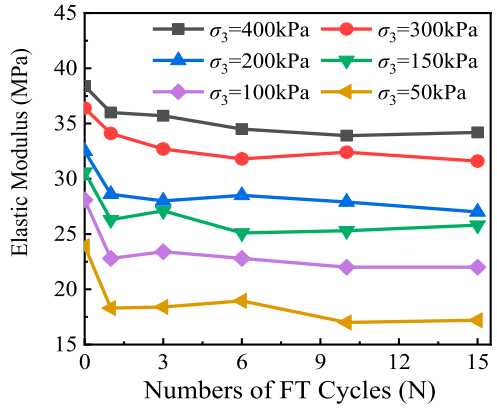

FIGURE 4 | Elastic modulus under various confining pressures and FT cycles.

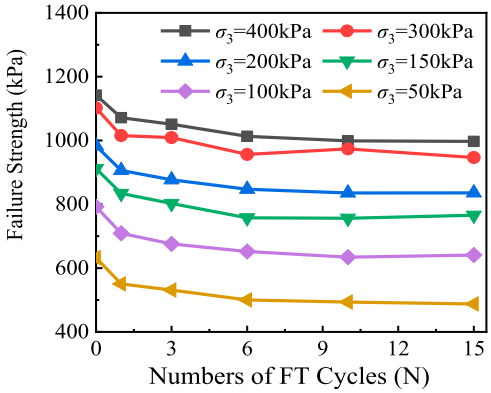

FIGURE 5 | Failure strength under various confining pressures and FT cycles.

corresponding to the critical conditions when the stress-strain curves transition.

Elastic Modulus Changes Affected by Freeze-Thaw Cycles

Elastic modulus is a key indicator for describing the stiffness and anti-deformation ability of soils. For instance, in a recent study, Ling et al. (2020) discovered that railway coarse-grained materials that had undergone 10 FT cycles lost 68, 57, and 50% of their elastic modulus at confining pressures of 30, 60, and 90 kPa, respectively. For simplicity, the stress-strain curves were considered to be linear within the 2.0% axial strain, and the slope of this point was defined as the elastic modulus value (Wei et al., 2019; Liu et al., 2021), which can be determined in **Eq. 1**:

$$E = (\sigma_{2.0\%} - \sigma_0)/(\varepsilon_{2.0\%} - \varepsilon_0) \quad (1)$$

where E denotes the elastic modulus; $\sigma_{2.0\%}$ is the deviator stress when the axial strain reaches 2.0% ($\varepsilon_{2.0\%}$); and σ_0 and ε_0 are the initial stress and strain, respectively.

Figure 4 reveals the relationship between the elastic modulus and confining pressures with different FT cycles. Taking the state of 6 FT cycles as an instance, when the confining pressure ranged from 50 kPa to 100, 150, 200, 300, and 400 kPa, the elastic modulus increased by 20, 33, 51, 67, and 85%, respectively. This analysis result means that the confining pressure has a considerable positive effect on the elastic modulus of the studied clay. On the other hand, it can be observed that the accumulated FT cycles declined the elastic modulus. Furthermore, the value decayed sharply during the first FT cycle and stabilized after a certain number of cycles, in agreement with most research on clay in the past decade (Roustaei et al., 2015; Wang et al., 2007; Xian et al., 2019). Based on the foregoing analysis, to better understand the elastic modulus of the studied clay, this study suggested a novel empirical model through the multiple regression modeling of all 36 data points in **Figure 4**, especially adopting the modificatory logarithmic form to embody the effect of FT cycles, as shown in **Eq. 2**. The result is satisfactory in reference to the recommended criteria for evaluating the determination coefficient (R^2) in geotechnical engineering (Zhang et al., 2020b; Zhang et al., 2021; Yao et al., 2022), namely, a fair fit is defined as $0.4 \le R^2 \le 0.69$, a good fit is $R^2 = 0.7–0.89$ and an excellent fit is $R^2 \ge 0.9$.

$$E = 1.83\,[Ln(e+N)]^{-0.15}\,(\sigma_3 + 99.52)^{0.49}\,(R^2 = 0.95) \quad (2)$$

where N is the number of FT cycles.

Failure Strength Affected by Freeze-Thaw Cycles

This study ascertained the failure strength of clay in accordance with the instructions of ASTM D2166: for strain softening clay, the deviator stress corresponding to the peak of the stress-strain curve is the failure strength; and if strain hardening or stabilization occurs, the deviator stress at 15% of the axial strain is taken as the failure strength. The results of the failure strength due to various confining pressures and FT cycles are presented in **Figure 5**. It can be seen that the addition of confining pressures continuously improved the failure strength. Also, the failure strength weakened throughout the FT cycles and then basically tended to be stable after 10 FT cycles with an approximate attenuation rate of 6–22% compared to the state before FT cycles. This law may be produced as follows: the water in pores freezes into ice at a negative temperature, and the volume of ice is roughly 9% larger than liquid water (Zhou and Wei, 2020). The growth of ice crystals uplifted the soil particles, but when ice crystals thaw at positive temperatures, the lifted particles cannot be completely restored (Zhou et al., 2018). Thus, a complete process comprising freezing and thawing resulted in the expansion of pores between particles and the attenuation of failure strength. Furthermore, with increasing FT cycles, the contribution of ice crystals to the lifting of particles decreased gradually until the pores between the particles were expanded by repeated FT cycles were large enough to endure the volume

TABLE 2 | Regression coefficients in **Eq. 3** of different clays.

No	References	Class	k_1	k_2	k_3	R^2	Correlation
A	This study	CL	5.23	−0.16	0.51	0.95	Excellent
B	Liu et al. (2019)	CL	1.67	−0.18	0.74	0.99	Excellent
C	Zhang et al. (2019)	CLY	1.47	−0.09	1.34	0.98	Excellent
D	Wei et al. (2019)	ML–CL	1.13	−0.27	1.37	0.99	Excellent
E	Orakoglu and Liu (2017)	CL	7.09	−0.61	0.52	0.78	Good
F	Xian et al. (2019)	CL	2.75	−0.59	0.77	0.97	Excellent
G	Roustaei et al. (2015)	CL	6.51	−0.57	1.18	0.82	Good

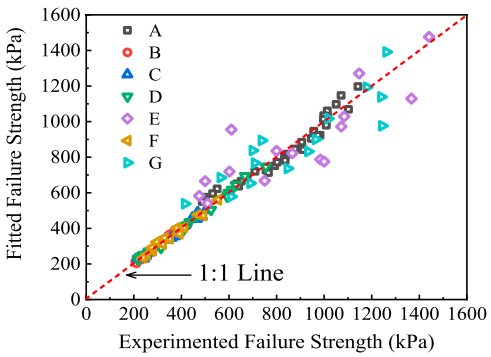

FIGURE 6 | Comparison between the fitted and experimented failure strength.

growth due to the phase transitions in water, the failure strength was no longer attenuated. Given the above discussions, a new model can be conceived as **Eq. 3**.

$$(\sigma_1 - \sigma_3)_{\lim} = k_1 P_a [Ln(e + N)]^{k_2} \left(\frac{\sigma_3}{p_a} + 1\right)^{k_3} \quad (3)$$

where $(\sigma_1 - \sigma_3)_{\lim}$ is the failure strength, σ_1 is the major principal stress; P_a = 101.3 kPa, which is the atmospheric pressure; k_1, k_2, and k_3 are regression coefficients.

In the stability analysis of embankments, the failure strength of soils must be strictly considered (Zhao et al., 2020). Obviously, it is necessary and meaningful to verify the robustness and accuracy of **Eq. 3**. As for regression coefficients, k_1 is the adjustment coefficient, that is, proportional to the failure strength, which can be ascertained to be a positive number because the failure strength cannot be negative. k_2 as an exponent must be a negative number given that with the increase in the number of FT cycles, the failure strength decreases. In order to reflect the influence of confining pressures, k_3 is a positive number as well as an exponent, since the higher the confining pressure, the larger the failure strength. This study adopted all 36 data points in **Figure 5** and, in conjunction with previous data from other researchers, fitted **Eq. 3** accordingly. The specific regression coefficients are summarized in **Table 2**, and the intuitionistic fitting effect is presented in **Figure 6**. The results demonstrated that the signs of regression coefficients in each group were consistent with the discussions, and the accuracies were mainly excellent. Simultaneously, the values of the fitted and experimented failure strength were close. The verification analysis concludes that the model established as **Eq. 3** is suitable for different clays, although it was proposed only on the basis of test results from the low liquid limit clay in this study.

TABLE 3 | Performance-related basic parameters of different soils.

No	k_1	k_2	k_3	$P_{0.075}$ (%)	w_p (%)	w_L (%)	*RH* (%)	*RC* (%)
A	5.23	−0.16	0.51	93.1	25.5	48.3	100	93
B	1.67	−0.18	0.74	69.1	17.2	25.2	102.3	93
C	1.47	−0.09	1.34	25.2	14	24.8	100	100
D	1.13	−0.27	1.37	65.1	15.8	21.3	160.7	91.2
E	7.09	−0.61	0.52	56.5	12.1	30	100	95
F	2.75	−0.59	0.77	99.3	23.5	38.4	100	95.2
G	6.51	−0.57	1.18	95.3	20	36	100	100

Shear Strength Affected by Freeze-Thaw Cycles and Its Rapid Prediction

The shear strength of soils, specifically cohesion and internal friction angle, are the most popular parameters in embankment engineering, as they are the basic inputs necessary for calculating the slope safety factor. Currently, the common practice is to plot the Mohr semicircles and envelopes based on the failure strength determined by triaxial tests to obtain the shear strength (Zhou et al., 2019). Nonetheless, triaxial instruments are still far from universal due to their high cost. Furthermore, triaxial tests require experienced personnel to operate procedures and analyze test data, which is a complex and time-consuming process. Contrary to this, trying to propose a method for rapidly predicting the shear strength through performance-related soil basic parameters is advisable due to the measurements of these parameters being faster, more simple, reliable, and accurate.

In the above scenario, the weight percent of soils passing through 0.075-mm sieve ($P_{0.075}$), the plastic limit (w_p) and the liquid limit (w_L) were selected as physical parameters; relative humidity (*RH*, the ratio of actual moisture content to optimal moisture content) and relative compaction (*RC*, the ratio of actual dry density to maximum dry density) were taken as status parameters, because they had a considerable effect on the mechanical properties of soils (Nazzal and Mohammad, 2010). Corresponding to the various soils in **Table 2**, these detailed parameters were summarized in **Table 3**. Subsequently, an excellent multiple regression relationship between these basic parameters and the model regression coefficients (k_1, k_2

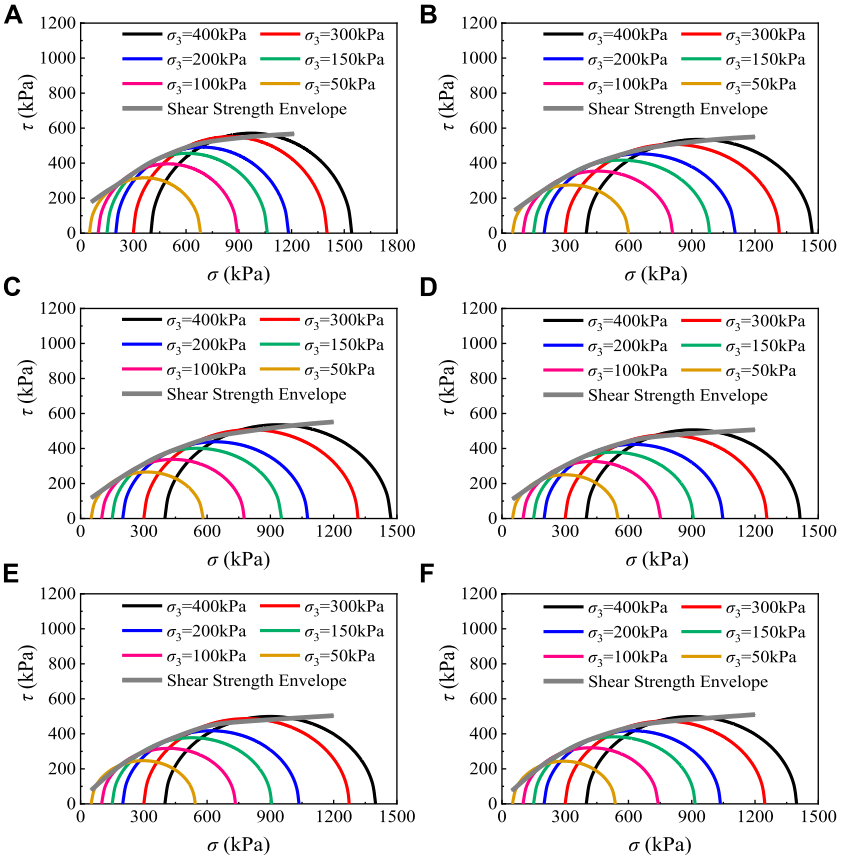

FIGURE 7 | Mohr semicircles and calculated envelopes in this study. **(A)** 0 FT cycle. **(B)** 1 FT cycle. **(C)** 3 FT cycles. **(D)** 6 FT cycles. **(E)** 10 FT cycles. **(F)** 15 FT cycles.

and k_3) of **Eq. 3** was developed utilizing the JMP statistical analysis software, as presented in **Eq. 4**.

$$\begin{cases} k_1 = -12.44 + 0.08P_{0.075} - 0.94\boldsymbol{w}_p + 0.41\boldsymbol{w}_L + 0.01RH + 0.14RC\,(R^2 = 0.97) \\ k_2 = 1.46 - 0.01P_{0.075} + 0.07\boldsymbol{w}_p - 0.01\boldsymbol{w}_L - 0.002RH - 0.02RC\,(R^2 = 0.92) \\ k_3 = -9.57 - 0.003P_{0.075} + 0.05\boldsymbol{w}_p - 0.02\boldsymbol{w}_L + 0.01RH + 0.09RC\,(R^2 = 0.95) \end{cases} \tag{4}$$

For the particular moment when the soils reach the failure state, the failure strength expressed by **Eq. 3** can also be rewritten into **Eq. 5**:

$$g(\sigma_1, \sigma_3) = \sigma_1 - \sigma_3 - k_1 P_a [Ln(e + N)]^{k_2} \left(\frac{\sigma_3}{p_a} + 1\right)^{k_3} = 0 \tag{5}$$

where $g(\sigma_1, \sigma_3)$ is the function of σ_1 and σ_3 at the failure moment with FT cycles.

Most failures in geotechnical engineering can be attributed to shear action, and thus it is meaningful to describe the failure state by the normal stress and shear stress. This study adopted the widely used Mohr stress circle to reflect this relationship, as shown in **Eq. 6**:

$$f(\sigma_1, \sigma_3) = \left(\sigma - \frac{\sigma_1 + \sigma_3}{2}\right)^2 + \tau^2 - \left(\frac{\sigma_1 - \sigma_3}{2}\right)^2 = 0 \tag{6}$$

where $f(\sigma_1, \sigma_3)$ is the function of σ_1 and σ_3 related to σ and τ, σ is the normal stress, and τ is the shear stress.

On the basis of the envelope theory, the $g(\sigma_1, \sigma_3)$ and $f(\sigma_1, \sigma_3)$ have the formulation in **Eq. 7** (Yang et al., 2013):

$$\frac{\partial f}{\partial \sigma_1}\frac{\partial g}{\partial \sigma_3} - \frac{\partial f}{\partial \sigma_3}\frac{\partial g}{\partial \sigma_1} = 0 \tag{7}$$

Substituting **Eq. 5**, **Eq. 6** into **Eq. 7**, the normal stress and shear stress on the shear plane can be derived as given in **Eq. 8**:

$$\begin{cases} \sigma = \dfrac{\sigma_1 + \sigma_3 \left\{1 + k_1 k_3 [Ln(e+N)]^{k_2} \left(\frac{\sigma_3}{P_a} + 1\right)^{(k_3 - 1)}\right\}}{2 + k_1 k_3 [Ln(e+N)]^{k_2} \left(\frac{\sigma_3}{P_a} + 1\right)^{(k_3 - 1)}} \\ \tau = \sqrt{\left(\frac{\sigma_1 - \sigma_3}{2}\right)^2 - \left\{\frac{\sigma_1 + \sigma_3 + k_1 k_3 \sigma_3 [Ln(e+N)]^{k_2} \left(\frac{\sigma_3}{P_a} + 1\right)^{(k_3 - 1)}}{2 + k_1 k_3 [Ln(e+N)]^{k_2} \left(\frac{\sigma_3}{P_a} + 1\right)^{(k_3 - 1)}} - \frac{\sigma_1 + \sigma_3}{2}\right\}^2} \end{cases} \tag{8}$$

The rationality of **Eq. 8** is logical, and the reasons are analyzed as follows. The regression model of failure strength established in this study, as shown in **Eq. 3**, has been verified to be reliable by multiple groups of clay data. Meanwhile, the Mohr stress circle and envelope theory have been proven to be successful in existing documents. Therefore, the normal stress and shear stress obtained by them together should be accurate. In order to have confidence in **Eq. 8**,

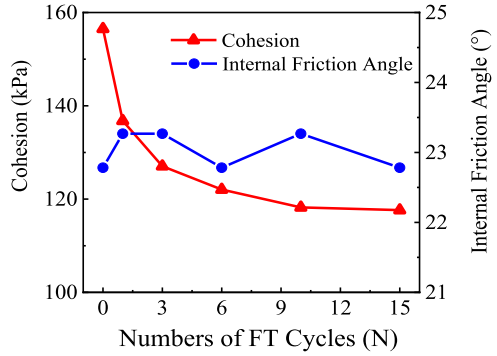

FIGURE 8 | Cohesion and internal friction angle of tested clay with FT cycles.

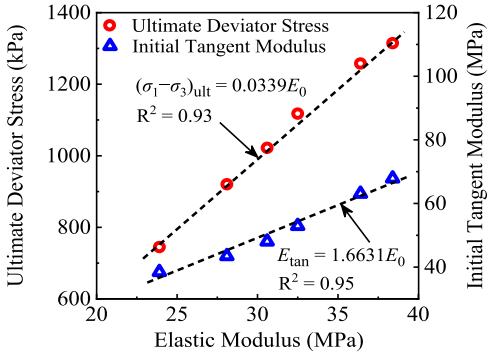

FIGURE 9 | Relationship between E_0 and E_{tan} as well as $(\sigma_1-\sigma_3)_{ult}$.

TABLE 4 | Results of the Konder model for the studied clay before FT cycles.

σ_3 (kPa)	a (10^{-5})	b (10^{-3})	R^2	E_{tan} (MPa)	$(\sigma_1-\sigma_3)_{ult}$ (kPa)
50	2.59	1.36	0.96	38.46	733.83
100	2.31	1.09	0.97	43.45	920.41
150	2.08	0.98	0.96	48.04	1022.26
200	1.89	0.87	0.96	52.95	1135.79
300	1.59	0.78	0.98	63.07	1277.89
400	1.47	0.76	0.97	67.87	1314.81

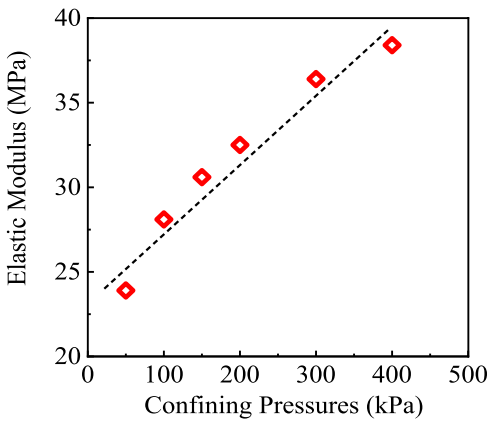

FIGURE 10 | Relationship between E_0 and σ_3.

the measured failure strength data of this study were used to draw the Mohr semicircles, and the set numbers of FT cycles (N), confining pressures (σ_3), fitted k_1, k_2 and k_3 in **Table 2**, and **Eq 5** and **Eq. 8** of this study were adopted to calculate the envelope, as shown in **Figure 7**. It can be observed that the calculated envelopes were basically anastomotic with the Mohr semicircles, which indicates that the **Eq. 8** obtained in this section can well describe the nonlinear relationship between the shear strength of clay and the numbers of FT cycles and confining pressures.

To sum up, the critical steps in the rapid prediction method for the shear strength of clay considering FT cycles were summarized and organized as follows:

1) Through a few simple laboratory basic physical tests to determine the values of $P_{0.075}$, w_p, w_L, RH and RC, and then substitute them into **Eq. 4** to calculate k_1, k_2 and k_3;
2) Investigate the climate conditions of the engineering site to determine the number of FT cycles (N), and select several confining pressure levels (σ_3, 1 m is equivalent to 20 kPa) in combination with the embankment filling height. Then, substitute k_1, k_2, k_3, N and σ_3 into **Eq. 5** to calculate the corresponding σ_1 at the failure state;
3) Substitute each group k_1, k_2, k_3, σ_1, σ_3 and N into **Eq. 8** to calculate the corresponding σ and τ, and then use the Mohr-Coulomb linear equation to fit them to obtain the shear strength indicators under various FT cycles.

Following the above steps, the results of the cohesion and internal friction angle were summarized in **Figure 8**. It can be observed that the cohesion of the tested clay decayed throughout a whole FT cycles, and the rate of attenuation gradually decreased until it became flat. This phenomenon has also been found in previous studies (Orakoglu and Liu, 2017; Wei et al., 2019). **Figure 8** also showed that the internal friction angle of the tested clay was not sensitive to the numbers of FT cycle, that is, it fluctuated repeatedly around 23°, which was consistent with the studies from Liu et al. (2016), Orakoglu and Liu (2017) and Zhang et al. (2019), but unlike the findings from Zhou et al. (2019) and Xian et al. (2019). The difference was likely due to the effect of FT cycles do not cause particles rearrangement in the tested clay such as interlocking or slipping. Not long ago, a measurement on the micro-structure of pavement recycled materials seemed to indicate that the X-ray Micro-Computed Tomography technology might be an effective means of exploring this difference (Afshar et al., 2018), however it is beyond the scope of this study.

It is noteworthy that the method proposed in this work for rapidly predicting the shear strength of embankment clay under FT cycles is generally applicable. Concretely, when this method is applied to other clay, it is only necessary to carry out several simple basic physical tests and follow the above steps 1)–3) to achieve the purpose. For situations where the triaxial tests are

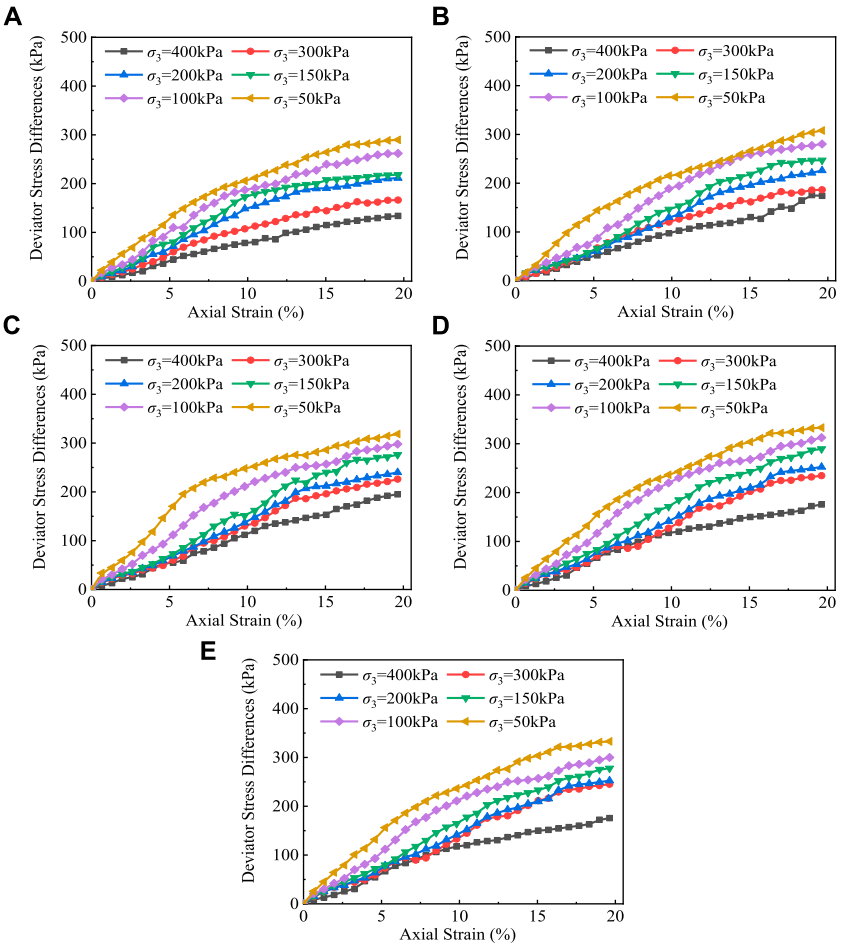

FIGURE 11 | Deviator stress differences of the tested clay with various FT cycles. **(A)** 1 FT cycle. **(B)** 3 FT cycles. **(C)** 6 FT cycles. **(D)** 10 FT cycles. **(E)** 15 FT cycles

limited or the shear strength of clay is urgently needed, this method has satisfactory engineering practicability.

EMPIRICAL CONSTITUTIVE EQUATION FOR FREEZE-THAW CLAY

Stress-strain curves are the source and foundation for investigating the mechanical properties of soils. In addition to the experimental studies, the constitutive equations also help to grasp the stress-strain relationship well (Zhang et al., 2020a). This part selected reasonable normalized factors, starting from the situation before FT cycles, and derived the empirical constitutive equation of the studied clay considering FT cycles.

Stress-Strain Relationships Before Freeze-Thaw Cycles

The studied clay before FT cycles in **Figure 3A** exhibited obvious strain hardening or stabilization behavior. Here the Konder hyperbolic model as shown in **Eq 9a**, **Eq. 9b** was adopted to describe the stress-strain relationship, and the results were listed in **Table 4**. Although this model showed high accuracy, it could not easily reflect the influence of confining pressures. In other words, for different confining pressure levels, corresponding model coefficients need to be fitted separately, which increases the difficulty and complexity of operation.

$$(\sigma_1 - \sigma_3) = \frac{\varepsilon_1}{a + b\varepsilon_1} \tag{9a}$$

$$\frac{\varepsilon_1}{\sigma_1 - \sigma_3} = a + b\varepsilon_1 \tag{9b}$$

where ε_1 represents the axial strain; $1/a$ is the initial tangent modulus $E_{\tan}$; and $1/b$ is the ultimate deviator stress $(\sigma_1{-}\sigma_3)_{\text{ult}}$.

Casey and Germaine (2013) reported that the stress-strain relationship of soils under different conditions can be expressed by a normalized function. Based on this idea, multiply both sides of **Eq. 9b** by a normalized factor of N to obtain **Eq. 10**:

$$\frac{\varepsilon_1 N}{\sigma_1 - \sigma_3} = aN + bN\varepsilon_1 = \frac{N}{E_{\tan}} + \frac{N}{(\sigma_1 - \sigma_3)_{\text{ult}}}\varepsilon_1 \tag{10}$$

TABLE 5 | Results of the Konder model for the deviator stress differences.

FT cycles	σ_3 (kPa)	c (10^{-4})	d (10^{-3})	R^2	ΔE_{tan} (MPa)	$[\Delta(\sigma_1-\sigma_3)]_{ult}$ (kPa)
1	50	1.87	2.53	0.99	5.35	395.60
	100	2.16	2.82	0.99	4.62	354.25
	150	2.49	3.54	0.97	4.02	282.22
	200	3.12	3.88	0.98	3.21	257.77
	300	3.89	4.61	0.99	2.57	216.74
	400	6.23	5.45	0.98	1.60	183.40
3	50	1.64	2.33	0.99	6.11	428.59
	100	1.96	2.50	0.97	5.10	400.37
	150	2.33	3.09	0.98	4.29	323.35
	200	2.81	3.43	0.99	3.56	291.32
	300	3.02	4.09	0.99	3.31	244.80
	400	4.30	4.84	0.99	2.33	206.67
6	50	1.57	2.19	0.98	6.39	456.45
	100	1.73	2.30	0.99	5.79	435.05
	150	1.96	2.86	0.98	5.09	350.11
	200	2.59	3.39	0.98	3.86	294.87
	300	2.78	3.78	0.98	3.60	264.48
	400	3.51	4.31	0.99	2.85	232.03
10	50	1.45	2.01	0.99	6.91	497.91
	100	1.60	2.17	0.99	6.24	460.43
	150	1.77	2.72	0.99	5.65	367.77
	200	2.11	3.21	0.99	4.74	311.90
	300	2.48	3.56	0.99	4.04	280.78
	400	3.00	3.96	0.98	3.34	252.49
15	50	1.45	1.93	0.99	6.91	517.36
	100	1.60	2.03	0.99	6.24	491.56
	150	1.77	2.61	0.99	5.65	383.23
	200	2.13	3.13	0.98	4.69	319.11
	300	2.53	3.58	0.99	3.96	279.31
	400	3.00	3.80	0.99	3.34	263.10

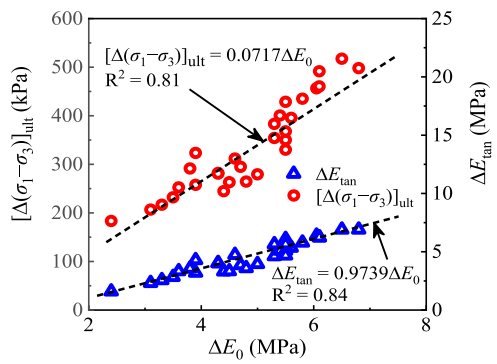

FIGURE 12 | Relationship between ΔE_0 and ΔE_{tan} as well as $[\Delta(\sigma_1-\sigma_3)]_{ult}$.

To implement the normalized function, the N should satisfy a linear relationship with the E_{tan} and $(\sigma_1-\sigma_3)_{ult}$, respectively. Through a series of attempts on the mechanical indicators obtained in **Section 3**, it was found that the elastic modulus before FT cycles (E_0) met this normalized condition, as shown in **Figure 9**.

E_0 was selected as the normalized factor N, based on **Eq. 10**, and **Eq. 11** can be deduced:

$$\frac{\varepsilon_1 E_0}{\sigma_1-\sigma_3} = \frac{E_0}{1.6631E_0} + \frac{E_0}{0.0339E_0}\varepsilon_1 = 0.601 + 29.496\varepsilon_1 \quad (11)$$

In addition, the E_0 also had a relationship with confining pressures as shown in **Figure 10** can be depicted by **Eq. 12**:

$$E_0 = 39.941\sigma_3 + 23662\,(R^2 = 0.95) \quad (12)$$

Substituting **Eq. 12** into **Eq. 11**, the stress-strain relationship of the studied clay before FT cycles can be expressed as **Eq. 13**:

$$(\sigma_1-\sigma_3)_0 = \frac{(39.941\sigma_3 + 23662)\varepsilon_1}{0.601 + 29.496\varepsilon_1} \quad (13)$$

Stress-Strain Relationships Considering Freeze-Thaw Cycles

The studied clay under FT cycles in **Figure 3B** to **Figure 4F** demonstrated strain softening behavior, and thus the Konder model cannot be adopted to describe their stress-strain relationship directly. For this reason, this study introduced a new variable, namely, the deviator stress differences caused by FT cycles, and defined it in **Eq. 14**. The results of deviator stress differences with various FT cycles are plotted in **Figure 11**.

$$\Delta(\sigma_1-\sigma_3) = (\sigma_1-\sigma_3)_0 - (\sigma_1-\sigma_3)_i \quad (14)$$

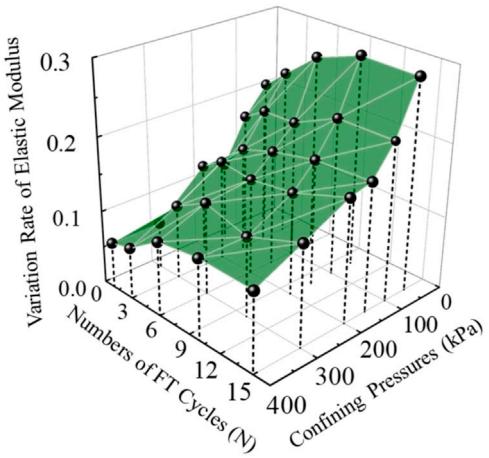

FIGURE 13 | Results of *V* with various *N* as well as σ_3.

where $\Delta(\sigma_1 - \sigma_3)$ is the deviator stress difference; $(\sigma_1 - \sigma_3)_0$ and $(\sigma_1 - \sigma_3)_i$ are respectively the deviator stress corresponding to the same axial strain before FT cycles and after the *i*-th FT cycles.

From **Figure 11**, the strain hardening behavior was found. Hence, the Konder model was applied to them, as expressed in **Eq. 15**, and the results are exhibited in **Table 5**.

$$\frac{\varepsilon_1}{\Delta(\sigma_1 - \sigma_3)} = c + d\varepsilon_1 \tag{15}$$

where $1/c$ denotes the initial tangent modulus $\Delta E_{\tan}$ corresponding to the $\Delta(\sigma_1 - \sigma_3)$; and $1/d$ is th**15**e ultimate deviator stress differences $[\Delta(\sigma_1 - \sigma_3)]_{ult}$.

Following the processing method in Section 4.1, in order to obtain a normalized relationship between the deviator stress differences and axial strain, the normalized factor here needs to have a good linear relationship with both the $\Delta E_{\tan}$ and the $[\Delta(\sigma_1 - \sigma_3)]_{ult}$. It can be discovered that the differences in elastic modulus compared with those before FT cycles (ΔE_0) adapted to this condition, as illustrated in **Figure 12**.

ΔE_0 was chosen as the normalized factor, and **Eq. 16** can be given:

$$\frac{\varepsilon_1 \Delta E_0}{\Delta(\sigma_1 - \sigma_3)} = \frac{\Delta E_0}{0.9739 \Delta E_0} + \frac{\Delta E_0}{0.0717 E_0}\varepsilon_1 = 1.027 + 13.947\varepsilon_1 \tag{16}$$

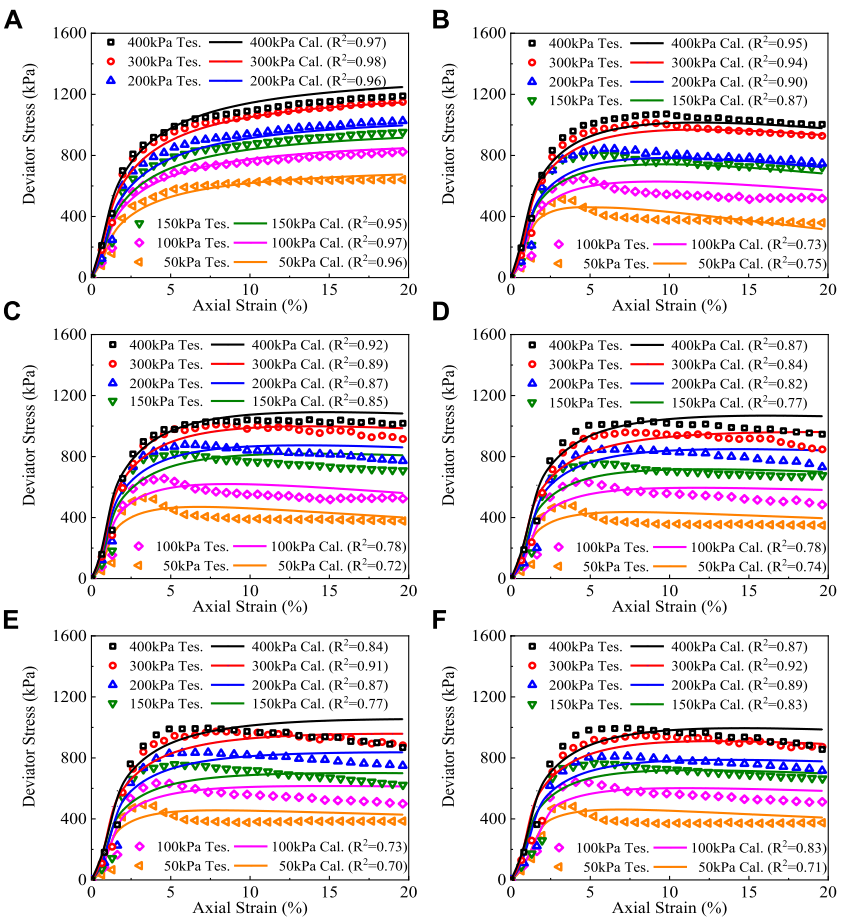

FIGURE 14 | Tested and calculated stress-strain results of tested clay. **(A)** 0 FT cycle. **(B)** 1 FT cycle. **(C)** 3 FT cycles. **(D)** 6 FT cycles. **(E)** 10 FT cycles. **(F)** 15 FT cycles.

To eliminate the intermediate variable ΔE_0, this study was aided by the variation rate (V) of elastic modulus corresponding to various confining pressures and numbers of FT cycles, as stipulated in **Eq. 17**. The results were presented in **Figure 13** can be formulated in **Eq. 18**.

$$V = \frac{\Delta E_0}{E_0} \tag{17}$$

$$V = 1.38\sigma_3^{-0.49}N^{0.15}\left(\mathrm{R}^2 = 0.94\right) \tag{18}$$

Combining **Eqs 12–14**, **16–18**, the normalized empirical constitutive equation for the tested clay considering FT cycles can be obtained as:

$$(\sigma_1 - \sigma_3)_i = \frac{(39.941\sigma_3 + 23662)\varepsilon_1}{0.601 + 29.496\varepsilon_1} - \frac{1.38\sigma_3^{-0.49}N^{0.15}(39.941\sigma_3 + 23662)\varepsilon_1}{1.027 + 13.947\varepsilon_1} \tag{19}$$

For the special case $N = 0$, the **Eq. 19** is completely transformed to **Eq. 13**, and thus **Eq. 19** is also applicable to the condition before FT cycles. Then **Eq. 19** was selected to calculate the stress-strain curves with the corresponding confining pressures and numbers of FT cycles. The tested and calculated results are shown in **Figure 14**, demonstrating that the normalized **Eq. 19** can preliminarily describe the stress-strain relationship of the tested clay affected by FT cycles, including strain hardening, stabilization, and softening forms.

CONCLUSION

This study aimed at gaining a better understanding of the mechanical properties of embankment clay subjected to FT cycles. For this purpose, a series of UU tests on a typical clay sample from China were conducted under various confining pressures as well as FT cycles. On the basis of the test results, several key findings were synthesized here:

1) With the accumulation of FT cycles, the stress-strain curves transformed from strain hardening (or stabilization) to strain softening. Meanwhile, under the same number of FT cycles, the greater the confining pressure, the higher the stress-strain curve. After 10 FT cycles, the curves with corresponding confining pressures have no obvious difference.
2) The elastic modulus was significantly affected by FT cycles and decreased sharply after the first FT action. The reduction of confining pressures also weakened the elastic modulus. From this, a phenomenological regression model was established by the modificatory logarithmic form to reflect the effect of FT cycles.
3) The failure strength was damaged by about 6–22% compared with that before the FT cycles, and the change can be ignored when the number of FT cycles exceeds 10. At the same time, the increase in confining pressure enhanced the failure strength. Similarly, a regression model for the failure strength was built and proved to be reliable by experimental results from other researchers.
4) In conjunction with the existing experimental data and the envelope theory, a method for rapidly predicting the shear strength through performance-related basic parameters was proposed. Besides, during the process of FT cycles, the cohesion gradually decreased but eventually became stable and the internal friction angle fluctuated slightly.
5) According to the Konder model, the elastic modulus before FT cycles was selected as the normalized factor to derive the empirical stress-strain formula without FT cycles. Then, by means of the elastic modulus differences, the relationship between the deviator stress differences and axial strain was normalized. Based on this, the empirical constitutive equation was deduced, which can concurrently describe the strain hardening, stabilization, and softening behaviors considering the effect of FT cycles.

DATA AVAILABILITY STATEMENT

The original contributions presented in the study are included in the article/Supplementary Material, further inquiries can be directed to the corresponding author.

AUTHOR CONTRIBUTIONS

All the authors listed have made a substantial, direct, and intellectual contribution to the work and approved it for publication.

FUNDING

The National Science Fund for Distinguished Young Scholars (52025085), the National Key Research and Development Program (2021YFB2600900), the National Natural Science Foundation of China (51927814, 51878078), the Key Research and Development Program of Hunan Province (2022SK 2083), the Science and Technology Innovation Program of Hunan Province (2020RC4048), the Project of Scientific Research of Hunan Provincial Department of Education (21C0187), and the Graduate Research Innovation Project of Hunan Province (CX20210748).

REFERENCES

Afshar, T., Disfani, M. M., Narsilio, G. A., and Arulrajah, A. (2018). Post-breakage Changes in Particle Properties Using Synchrotron Tomography. *Powder Technol.* 325, 530–544. doi:10.1016/j.powtec.2017.11.039

Aldaood, A., Bouasker, M., and Al-Mukhtar, M. (2016). Effect of Water during Freeze-Thaw Cycles on the Performance and Durability of Lime-Treated Gypseous Soil. *Cold Regions Sci. Technol.* 123, 155–163. doi:10.1016/j.coldregions.2015.12.008

Bozbey, I., Kelesoglu, M. K., Demir, B., Komut, M., Comez, S., Ozturk, T., et al. (2018). Effects of Soil Pulverization Level on Resilient Modulus and Freeze and

Thaw Resistance of a Lime Stabilized clay. *Cold Regions Sci. Technol.* 151, 323–334. doi:10.1016/j.coldregions.2018.03.023

Casey, B., and Germaine, J. T. (2013). Stress Dependence of Shear Strength in Fine-Grained Soils and Correlations with Liquid Limit. *J. Geotech. Geoenviron. Eng.* 139, 1709–1717. doi:10.1061/(ASCE)GT.1943-5606.0000896

Ding, M., Zhang, F., Ling, X., and Lin, B. (2018). Effects of Freeze-Thaw Cycles on Mechanical Properties of Polypropylene Fiber and Cement Stabilized clay. *Cold Regions Sci. Technol.* 154, 155–165. doi:10.1016/j.coldregions.2018.07.004

Gowthaman, S., Nakashima, K., and Kawasaki, S. (2020). Freeze-thaw Durability and Shear Responses of Cemented Slope Soil Treated by Microbial Induced Carbonate Precipitation. *Soils and Foundations* 60, 840–855. doi:10.1016/j.sandf.2020.05.012

Güllü, H., and Khudir, A. (2014). Effect of Freeze–Thaw Cycles on Unconfined Compressive Strength of fine-grained Soil Treated with Jute Fiber, Steel Fiber and Lime. *Cold Reg. Sci. Tech.* 106 (107), 55–65. doi:10.1016/j.coldregions.2014.06.008

Hao, J., Cui, X., Qi, H., Zheng, Y., and Bao, Z. (2022). Dynamic Behavior of Thawed Saturated saline silt Subjected to Freeze-Thaw Cycles. *Cold Regions Sci. Technol.* 194, 103464. doi:10.1016/j.coldregions.2021.103464

He, P., Mu, Y., Yang, Z., Ma, W., Dong, J., and Huang, Y. (2020). Freeze-thaw Cycling Impact on the Shear Behavior of Frozen Soil-concrete Interface. *Cold Regions Sci. Technol.* 173, 103024. doi:10.1016/j.coldregions.2020.103024

Lin, B., Zhang, F., Feng, D., Tang, K., and Feng, X. (2017). Accumulative Plastic Strain of Thawed Saturated clay under Long-Term Cyclic Loading. *Eng. Geology*. 231, 230–237. doi:10.1016/j.enggeo.2017.09.028

Ling, X., Tian, S., Tang, L., and Li, S. (2020). A Damage-Softening and Dilatancy Prediction Model of Coarse-Grained Materials Considering Freeze-Thaw Effects. *Transportation Geotechnics* 22, 100307. doi:10.1016/j.trgeo.2019.100307

Liu, H.-b., Sun, S., Wei, H.-b., and Li, W.-j. (2021). Effect of Freeze-Thaw Cycles on Static Properties of Cement Stabilised Subgrade Silty Soil. *Int. J. Pavement Eng.*, 1–13. doi:10.1080/10298436.2021.1919306

Liu, J., Chang, D., and Yu, Q. (2016). Influence of Freeze-Thaw Cycles on Mechanical Properties of a Silty Sand. *Eng. Geology*. 210, 23–32. doi:10.1016/j.enggeo.2016.05.019

Liu, J., Zha, F., Xu, L., Kang, B., Yang, C., Feng, Q., et al. (2020). Strength and Microstructure Characteristics of Cement-Soda Residue Solidified/stabilized Zinc Contaminated Soil Subjected to Freezing-Thawing Cycles. *Cold Regions Sci. Technol.* 172, 102992. doi:10.1016/j.coldregions.2020

Liu, X.-q., Liu, J.-k., Tian, Y.-h., Chang, D., and Hu, T.-f. (2019). Influence of the Freeze-Thaw Effect on the Duncan-Chang Model Parameter for Lean clay. *Transportation Geotechnics* 21, 100273. doi:10.1016/j.trgeo.2019.100273

Lu, Y., Liu, S., Zhang, Y., Li, Z., and Xu, L. (2020). Freeze-thaw Performance of a Cement-Treated Expansive Soil. *Cold Regions Sci. Technol.* 170, 102926. doi:10.1016/j.coldregions.2019.102926

Miao, Q., Niu, F., Lin, Z., Luo, J., and Liu, M. (2020). Comparing Frost Heave Characteristics in Cut and Embankment Sections along a High-Speed Railway in Seasonally Frozen Ground of Northeast China. *Cold Regions Sci. Technol.* 170, 102921. doi:10.1016/j.coldregions.2019.102921

Nazzal, M. D., and Mohammad, L. N. (2010). Estimation of Resilient Modulus of Subgrade Soils for Design of Pavement Structures. *J. Mater. Civ. Eng.* 22, 726–734. doi:10.1061/(asce)mt.1943-5533.0000073

Nguyen, T. T. H., Cui, Y.-J., Ferber, V., Herrier, G., Ozturk, T., Plier, F., et al. (2019). Effect of Freeze-Thaw Cycles on Mechanical Strength of Lime-Treated fine-grained Soils. *Transportation Geotechnics* 21, 100281. doi:10.1016/j.trgeo.2019.100281

Orakoglu, M. E., and Liu, J. (2017). Effect of Freeze-Thaw Cycles on Triaxial Strength Properties of Fiber-Reinforced Clayey Soil. *KSCE J. Civ. Eng.* 21, 2128–2140. doi:10.1007/s12205-017-0960-8

Roustaei, M., Eslami, A., and Ghazavi, M. (2015). Effects of Freeze-Thaw Cycles on a Fiber Reinforced fine Grained Soil in Relation to Geotechnical Parameters. *Cold Regions Sci. Technol.* 120, 127–137. doi:10.1016/j.coldregions.2015.09.011

Rui, D., Deng, H., Nakamura, D., Yamashita, S., Suzuki, T., and Zhao, H. (2016). Full-scale Model Test on Prevention of Frost Heave of L-type Retaining wall. *Cold Regions Sci. Technol.* 132, 89–104. doi:10.1016/j.coldregions.2016.07.010

Wang, D.-y., Ma, W., Niu, Y.-h., Chang, X.-x., and Wen, Z. (2007). Effects of Cyclic Freezing and Thawing on Mechanical Properties of Qinghai-Tibet clay. *Cold Regions Sci. Technol.* 48, 34–43. doi:10.1016/j.coldregions.2006.09.008

Wang, L., Zuo, X., Zheng, F., Wilson, G. V., Zhang, X. J., Wang, Y., et al. (2020). The Effects of Freeze-Thaw Cycles at Different Initial Soil Water Contents on Soil Erodibility in Chinese Mollisol Region. *Catena* 193, 104615. doi:10.1016/j.catena.2020.104615

Wang, T.-l., Liu, Y.-j., Yan, H., and Xu, L. (2015). An Experimental Study on the Mechanical Properties of Silty Soils under Repeated Freeze-Thaw Cycles. *Cold Regions Sci. Technol.* 112, 51–65. doi:10.1016/j.coldregions.2015.01.004

Wang, W., Qin, Y., Lei, M., and Zhi, X. (2017). Effect of Repeated Freeze-Thaw Cycles on the Resilient Modulus for fine-grained Subgrade Soils with Low Plasticity index. *Road Mater. Pavement Des.* 19, 898–911. doi:10.1080/14680629.2017.1283352

Wei, C., Apel, D. B., and Zhang, Y. (2019). Shear Behavior of Ultrafine Magnetite Tailings Subjected to Freeze-Thaw Cycles. *Int. J. Mining Sci. Technol.* 29, 609–616. doi:10.1016/j.ijmst.2019.06.007

Xian, S., Lu, Z., Yao, H., Fang, R., and She, J. (20192019). Comparative Study on Mechanical Properties of Compacted Clay under Freeze-Thaw Cycles with Closed and Open Systems. *Adv. Mater. Sci. Eng.* 2019, 1–13. doi:10.1155/2019/9206372

Xiao, Y., Long, L., Matthew Evans, T., Zhou, H., Liu, H., and Stuedlein, A. W. (2019). Effect of Particle Shape on Stress-Dilatancy Responses of Medium-Dense Sands. *J. Geotech. Geoenviron. Eng.* 145, 04018105. doi:10.1061/(ASCE)GT.1943-5606.0001994

Yang, Y., Gao, F., and Lai, Y. (2013). Modified Hoek?Brown Criterion for Nonlinear Strength of Frozen Soil. *Cold Regions Sci. Technol.* 86, 98–103. doi:10.1016/j.coldregions.2012.10.01010.1016/j.coldregions.2012.10.010

Yao, Y., Li, J., Ni, J., Liang, C., and Zhang, A. (2022). Effects of Gravel Content and Shape on Shear Behaviour of Soil-Rock Mixture: Experiment and DEM Modelling. *Comput. Geotechnics* 141, 104476. doi:10.1016/j.compgeo.2021.104476

Zhang, J., Fan, H., Zhang, S., Liu, J., and Peng, J. (2020a). Back-Calculation of Elastic Modulus of High Liquid Limit Clay Subgrades Based on Viscoelastic Theory and Multipopulation Genetic Algorithm. *Int. J. Geomech.* 20, 04020194. doi:10.1061/(ASCE)GM.1943-5622.0001841

Zhang, J., Peng, J., Zhang, A., and Li, J. (2020b). Prediction of Permanent Deformation for Subgrade Soils under Traffic Loading in Southern China. *Int. J. Pavement Eng.* 23, 673–682. doi:10.1080/10298436.2020.1765244

Zhang, J., Zhang, A., Huang, C., Yu, H., and Zhou, C. (2021). Characterising the Resilient Behaviour of Pavement Subgrade with Construction and Demolition Waste under Freeze-Thaw Cycles. *J. Clean. Prod.* 300, 126702. doi:10.1016/j.jclepro.2021.126702

Zhang, L., Ma, W., Yang, C., and Yuan, C. (2014). Investigation of the Pore Water Pressures of Coarse-Grained sandy Soil during Open-System Step-Freezing and Thawing Tests. *Eng. Geology*. 181, 233–248. doi:10.1016/j.enggeo.2014.07.020

Zhang, W., Guo, A., and Lin, C. (2019). Effects of Cyclic Freeze and Thaw on Engineering Properties of Compacted Loess and Lime-Stabilized Loess. *J. Mater. Civ. Eng.* 31, 04019205. doi:10.1061/(ASCE)MT.1943-5533.0002858

Zhao, Y., Ling, X., Gong, W., Li, P., Li, G., and Wang, L. (2020). Mechanical Properties of Fiber-Reinforced Soil under Triaxial Compression and Parameter Determination Based on the Duncan-Chang Model. *Appl. Sci.* 10, 9043. doi:10.3390/app10249043

Zhou, C., Xu, J., and Ng, C. W. W. (2015). Effects of Temperature and Suction on Secant Shear Modulus of Unsaturated Soil. *Géotechnique Lett.* 5, 123–128. doi:10.1680/jgele.14.0009610.1680/jgele.14.00096

Zhou, J., and Wei, C. (2020). Ice Lens Induced Interfacial Hydraulic Resistance in Frost Heave. *Cold Regions Sci. Technol.* 171, 102964. doi:10.1016/j.coldregions.2019.102964

Zhou, Z., Li, F., Yang, H., Gao, W., and Miao, L. (2019). Orthogonal Experimental Study of Soil-Rock Mixtures under the Freeze-Thaw Cycle Environment. *Int. J. Pavement Eng.* 22, 1376–1388. doi:10.1080/10298436.2019.1686634

Zhou, Z., Ma, W., Zhang, S., Mu, Y., and Li, G. (2018). Effect of Freeze-Thaw Cycles in Mechanical Behaviors of Frozen Loess. *Cold Regions Sci. Technol.* 146, 9–18. doi:10.1016/j.coldregions.2017.11.011

Conflict of Interest: The authors declare that the research was conducted in the absence of any commercial or financial relationships that could be construed as a potential conflict of interest.

Publisher's Note: All claims expressed in this article are solely those of the authors and do not necessarily represent those of their affiliated organizations, or those of the publisher, the editors, and the reviewers. Any product that may be evaluated in this article, or any claim that may be made by its manufacturer, is not guaranteed or endorsed by the publisher.

frontiers | Frontiers in Earth Science

ORIGINAL RESEARCH
published: 29 April 2022
doi: 10.3389/feart.2022.865017

Determining the Critical Slip Surface of Slope by Vector Sum Method Based on Strength Reduction Definition

Mingwei Guo[1,2]*, *Jiahang Li*[1,2] *and Xuechao Dong*[1,2]

[1]State Key Laboratory of Geomechanics and Geotechnical Engineering, Institute of Rock and Soil Mechanics, Chinese Academy of Sciences, Wuhan, China, [2]University of Chinese Academy of Sciences, Beijing, China

Slope-stability assessment involves the location of the critical slip surface and the corresponding factor of safety (FOS). Considering force-vector characteristics, the vector sum method was further studied based on the strength reduction definition of the FOS and stress field of slope, and the FOS can be calculated directly by the force limit equilibrium equation on the global sliding direction of the slope. For the sliding direction, it is rigidly proved to be determined only by the sliding shear stress along the slip surface based on the principle of minimum potential energy. Then, two examples with fixed slip surfaces were analyzed and the results were compared with the rigorous Morgenstern–Price method. Finally, two examples from the literature are investigated for searching the critical slip surface using the proposed method and a real-coded genetic algorithm. The calculated results revealed the rationality of the proposed method for both fixed slip surfaces and critical slip surfaces from the literatures in slope stability assessment. This proposed method provides a new path to assess the slope stability, which is worth to be further studied in practical engineering.

Keywords: slope stability, vector sum method, genetic algorithm, critical slip surface, safety factor

OPEN ACCESS

Edited by:
Fei Meng,
Swinburne University of Technology, Australia

Reviewed by:
Ashok Kumar Gupta,
Jaypee University of Information Technology, India
Yunfeng Ge,
China University of Geosciences, China

***Correspondence:**
Mingwei Guo
mwguo@whrsm.ac.cn

Specialty section:
This article was submitted to Geohazards and Georisks, a section of the journal Frontiers in Earth Science

Received: *29 January 2022*
Accepted: *31 March 2022*
Published: *29 April 2022*

Citation:
Guo M, Li J and Dong X (2022) Determining the Critical Slip Surface of Slope by Vector Sum Method Based on Strength Reduction Definition. Front. Earth Sci. 10:865017. doi: 10.3389/feart.2022.865017

1 INTRODUCTION

The slope problem generally involves how to define the factor of safety for a specific slip surface and locate the critical slip surface associated with the minimum factor of safety (FOS). Presently, there are mainly two types of definitions of FOS for a specific slip surface. One is the strength reduction definition based on the concept of limit equilibrium, in which the FOS is the factor by which the shear strength of soil would have to be divided to bring the slope to the state of limit equilibrium (Duncan, 1996; Zheng et al., 2006; Cheng et al., 2007), and the other is the overloading definition, in which the FOS is calculated based on the normal and shear stresses along the slip surface (Zou et al., 1995; Kim and Lee, 1997). Several methods based on both the aforementioned definitions are widely used in practical engineering such as the limit equilibrium method (LEM) (Huang and Tsai, 2000; Chen, 2003; Hamdhan and Schweiger, 2013), the finite element method (FEM) (Shen and Karakus, 2014), and limit analysis method (LAM). Compared with the overloading definition of FOS, the strength reduction definition of FOS is more popular in slope stability assessment, such as the strength reduction technique by the finite element method and limit equilibrium method.

Based on the inherent vector characteristics, the vector sum method was first put forward in 2008 (Ge, 2008) and the FOS was defined as the ratio of the total resisting force to total driving force in the global sliding direction. In the past few years, this method has been developed from the stress field of the slope, the determination of the global sliding direction, and the definition of FOS. For the stress field to assess the

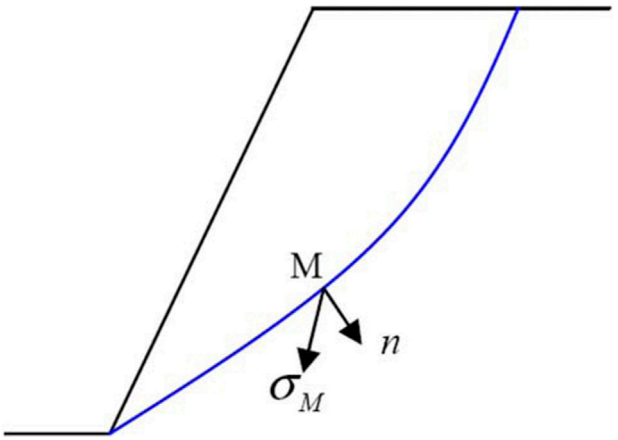

FIGURE 1 | Sketch of a simple slope.

slope stability with the vector sum method, the finite element method, the independent cover-based manifold method (Liu et al., 2017), the discontinuous deformation analysis (Fu et al., 2017), and the numerical manifold method were used. For the global sliding direction, the resisting shear stress along the slip surface was utilized based on the knowledge of the sliding failure mechanism in practical engineering (Ge, 2008), and recently, it was theoretically deduced based on the principle of minimum potential energy (Guo et al., 2019).

In this study, the vector sum method was further studied based on the strength reduction definition of FOS in slope stability assessment. For the global sliding direction, it is theoretically proved to be determined only by the sliding shear stress along the slip surface based on the principle of minimum potential energy. For the slope stability assessment with the proposed method, this study emphasizes the critical slip surface using the proposed method, and two examples studied in previous works were further analyzed by searching the critical slip surfaces. The calculating results demonstrate the rationality of the proposed method in slope stability assessment.

2 VECTOR SUM METHOD

Compared with the finite element strength reduction technique and the limit equilibrium method, the vector characteristics of force were considered in the proposed method, which is the highlight of the vector sum method. Because of the vector characteristics of force, there are two key issues in the vector sum method, the global sliding direction, and the expression of the safety factor. Therefore, how to rationally define the global sliding direction and the expression of the FOS determined the rationality and scientificity of the vector sum method.

Right now, the global sliding direction can be rigorously determined by the total sliding shear stress along the slip surface using the principle of minimum potential energy. On the basis of the strength reduction definition of the safety factor widely used in practical engineering, the vector sum method was further studied as explained in the following sections.

2.1 Global Sliding Direction

The moment the potential energy of a slope changes to a relative minimum, it will have a stationary value, which offers the mathematical method to obtain the global sliding direction of the slope. Therefore, the global sliding direction of the slope can be theoretically determined by the principle of minimum potential energy.

For a 2D simple slope (**Figure 1**), the force balance equation can be expressed as **Eq. 1**, here, **b** is just the unit weight of the simple slope and σ_M is the plane stress at the point M on the slip surface.

$$\int_V \mathbf{b} dv = \int_L \boldsymbol{\sigma}_M dL \tag{1}$$

When the slope is about to slide, it can only slide along the potential slip surface because of the restriction of bedrock. Assuming the global sliding direction is **d,** the displacement of the slope can be expressed as **Eq. 2**.

$$\mathbf{d}_s = \mathbf{d} - \mathbf{d}_n = \mathbf{d} - \mathbf{d}_n \mathrm{n} \tag{2}$$

Therefore, when the displacement of the slope is $\mathbf{d}_s$, the change of potential energy can be given by:

$$\Pi = \Pi_0 + \int_S \boldsymbol{\sigma}_M \cdot \mathbf{d}_s dS \tag{3}$$

Then, the first-order variation can be written as

$$\frac{\partial \boldsymbol{\Pi}}{\partial \mathbf{d}} = 0 \tag{4}$$

Eq. 4 can also be considered as:

$$\frac{\partial}{\partial \theta} \int_S \boldsymbol{\sigma}_M \cdot \mathbf{d}_s dS = 0 \tag{5}$$

where θ is the sliding angle defined anticlockwise from the axis X to the global sliding direction.

Finally, the global sliding angle θ can be deduced and simplified as **Eq. 6** (Guo et al., 2019).

$$\tan\theta = \frac{\int_l n_x n_y \sigma_{Mx} + \left(n_y^2 - 1\right)\sigma_{My} dl}{\int_l n_x n_y \sigma_{My} + \left(n_x^2 - 1\right)\sigma_{Mx} dl} \tag{6}$$

where σ_{Mx} and σ_{My} are the components of σ_M on the axes X and Y, respectively. n_x and n_y are the components of the unit direction n on the axes X and Y, respectively. From **Eq. 1**, it can be concluded that the global sliding direction can be theoretically determined by the stress state and the shape of the slope.

2.2 The Safety Factor Based on Strength Reduction Technique

Because of the strength decrease of the soil, the potential sliding body can gradually fail from the normal stress state, as shown in **Figure 2**.

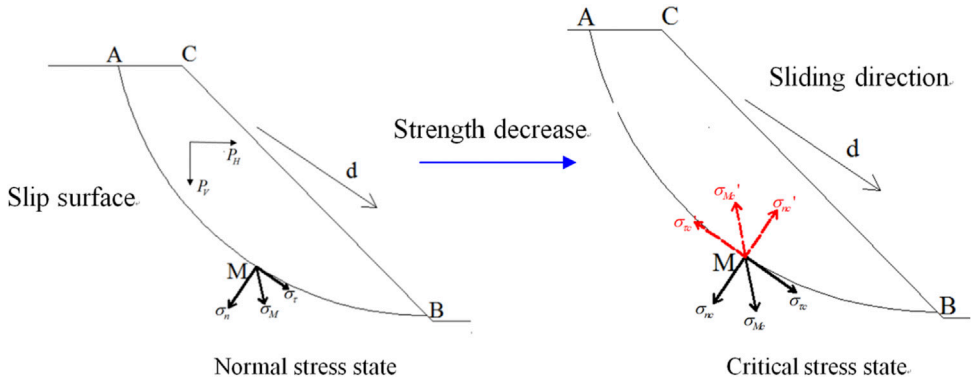

FIGURE 2 | Sketch of the stress state from normal to critical state.

At the critical stress state, the total resisting and driving forces should be equal along the global sliding direction, and the force equilibrium equation can be established by **Eq. 7**.

$$\int_l \left(\sigma'_{\tau c} + \sigma'_{nc}\right) \bullet (-\boldsymbol{d}) \boldsymbol{d}_l = \int_l (\sigma_{\tau c} + \sigma_{nc}) \bullet (\boldsymbol{d}) \boldsymbol{d}_l \tag{7}$$

where σ_{nc} and $\sigma_{\tau c}$ are the driving normal and shear stresses, respectively, at the critical state at any point on the slip surface, and correspondingly, $\sigma' nc$ and $\sigma' \tau c$ are the resisting normal and shear stresses, respectively.

For the resisting stress on the slip surface, the Mohr–Coulomb yield criterion was utilized to determine the shear strength of the soil, which can be expressed as **Eq. 8**

$$\left\|\sigma'_{\tau c}\right\| = \frac{\boldsymbol{\tau}_{\max}}{\mathbf{F}} = \frac{\mathbf{c} + \left\|\sigma'_{nc}\right\| \tan \varphi}{\mathbf{F}} \tag{8}$$

where c and φ are the cohesion and the friction angle of slope material, respectively, and $\boldsymbol{F}$ is the safety factor.

Furthermore, the loads applied on the slope remain unchanged during the evolution process from the normal to the critical state, then, the assumption was made that the normal stress remains constant during the evolution process from the normal to the critical state of the slope.

Hence, the resisting forces along the slip surface along the sliding direction can be simplified as **Eq. 9**.

$$\int_l \left(\sigma'_{\tau c} + \sigma'_{nc}\right) \bullet (-\mathbf{d}) \mathbf{d}_l = \int_l \left(\frac{\tau_{\max} \mathbf{a}}{\mathbf{F}} - \sigma_{nc}\right) \bullet (-\mathbf{d}) \mathbf{d}_l \tag{9}$$

where $\boldsymbol{a}$ stands for the unit direction of resisting shear stress at point M along a slip surface.

At the normal state of the slope, the macroscopic forces applied on the sliding body and micro forces along the slip surface should be equal to **Eq. 10**.

$$\int_{AB} (\sigma_\tau + \sigma_n) d_l = \mathrm{P}_H + \mathrm{P}_V \tag{10}$$

where P_H and P_V are the horizontal force and vertical force, respectively, applied on the potential sliding body belonging to macroscopic forces. σ_n and σ_τ are the normal and shear stresses, respectively, at any point on the potential slip surface belonging to micro forces.

Because of being considered invariable during the evolution process from the normal state to the critical state of the slope for macroscopic forces, the driving force remains constant for the potential sliding body, which can be expressed as **Eq. 11**.

$$\int_{AB} (\sigma_\tau + \sigma_n) \bullet (d) d_l = \int_{AB} (\sigma_{\tau c} + \sigma_{nc}) \bullet (d) d_l \tag{11}$$

Connecting **Eqs 7–11**, the force equilibrium equation can be simplified as

$$\int_{AB} \left(\frac{\tau_{\max} \boldsymbol{a}}{\boldsymbol{F}} - \sigma_n\right) \bullet (-\boldsymbol{d}) \boldsymbol{d}_l = \int_{AB} (\sigma_\tau + \sigma_n) \bullet (\boldsymbol{d}) \boldsymbol{d}_l \tag{12}$$

That is,

$$\int_{AB} \left(\frac{\tau_{\max} \boldsymbol{a}}{\boldsymbol{F}}\right) \bullet (-\boldsymbol{d}) \boldsymbol{d}_l + \int_{AB} (\sigma_n \bullet \boldsymbol{d}) \boldsymbol{d}_l = \int_{AB} (\sigma_\tau \bullet (\boldsymbol{d})) \boldsymbol{d}_l + \int_{AB} (\sigma_n \bullet (\boldsymbol{d})) \boldsymbol{d}_l \tag{13}$$

Further simplification can be made as **Eq. 14**:

$$\int_{AB} \left(\frac{\tau_{\max} \boldsymbol{a}}{\boldsymbol{F}}\right) \bullet (-\boldsymbol{d}) \boldsymbol{d}_l = \int_{AB} (\sigma_\tau \bullet (\boldsymbol{d})) \boldsymbol{d}_l \tag{14}$$

As an invariable along the slip surface, the safety factor can be finally expressed as:

$$\boldsymbol{F}_f = \frac{\int_l (\tau_{max} \boldsymbol{a}) \bullet (-\boldsymbol{d}) \boldsymbol{d}_l}{\int_l (\boldsymbol{\sigma}_\tau \bullet \boldsymbol{d}) \boldsymbol{d}_l} \tag{15}$$

Eq. 15 demonstrates that the resisting and driving shear stresses have an effect on the $\mathrm{F_S}$ when the force equilibrium of a slope is considered along the sliding direction. Moreover, the safety factor (**Eq. 15**) can be directly obtained by integrals along the slip surface rather than iterative calculation, which is required in the LEM and SRM in computing the $\mathrm{F_S}$.

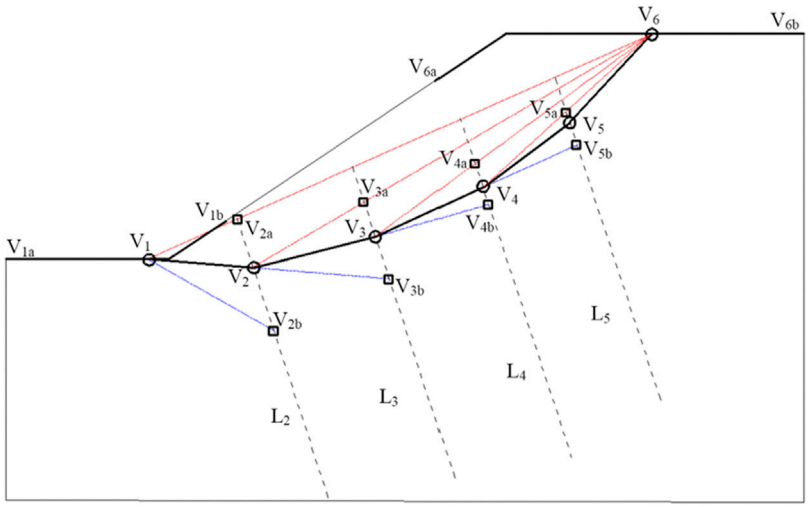

FIGURE 3 | Generating process of a feasible slip surface of the initial population.

3 A REAL-CODED GENETIC ALGORITHM

3.1 Structure of the Real-Coded Genetic Algorithm

At first, the initial population should be generated based on the geometrically feasible requirements of the individual, then, the corresponding fitness of each individual is also computed. After crossover, mutation, and selection operation to this population based on modifications to previous studies on the genetic algorithm, the next generation can be obtained as follows:

1) The parents are selected to be crossed to generate the offspring as the candidate of the next generation.
2) Meanwhile, the mutation is also operated on the same parents and the generated offspring can still be considered as the candidate for the next generation.
3) The offspring generated previously by the crossover and mutation operation are combined with the parents as the total candidates of the next generation.
4) Using the selection operation, the total candidates are selected to constitute the next generation including a specified number of individuals.

The aforementioned routine process is repeated until the requirement of convergence or a given number of generations is met. A real-coded GA for specific slope stability problems is explained in the following sections in detail.

3.2 Geometrically Feasible Individuals of Slip Surface

According to previous studies on encoding the slip surface using polygons with N nodes denoted as V_i (i = 1 … … N), the kinematically feasible, upward-concave, trail slip surface is also taken into account, which can be completely defined by the coordinates of its nodes from the bottom to top. First, the extreme nodes (i = 1 or i = N) are randomly generated lying within specific intervals on the slope boundary. Then, similarly, the interior nodes must lie within an allowable search domain restricted by specific requirements of the feasible and upward-concave slip surface.

Figure 3 shows a feasible slip surface with N = 6 nodes from bottom to top, and the top to bottom generation has a similar process with obvious changes of nodes, which is not presented in detail in this study. As shown in **Figure 3**, the feasible slip surface with six nodes can be generated by fulfilling the following geometrical and kinematical compatibility constraints.

1) The extreme nodes V_1 and V_6 randomly located within their allowable intervals using a uniform probability distribution on the slope boundary have to be constrained by their corresponding lower and upper intervals, (V_{1a} V_{1b}) and (V_{6a} V_{6b}) (**Figure 3**).
2) For the interior nodes, the parallel and equidistant auxiliary lines perpendicular to V_1V_N (L_i in **Figure 3**) are used to produce feasible intervals for these interior nodes. Take the node V_3 for example, a feasible interval can be defined by the lower (V_{3a}) from the intersection of L_3 with the V_1V_6 segment and upper extreme (V_{3b}) from the intersection of L_3 and the line V_1V_2. In terms of V_4 and V_5, the aforementioned procedure can be repeated to produce their feasible intervals on the corresponding lines L_4 and L_5. For the interior node V_2, the soil mechanics can be used to estimate the slope toe angle to determine the upper extreme V_{2b} except the lower extreme V_{2a} from the intersection of L_2 with the V_1V_6 segment (Rafael and Rafael, 2015).
3) Once the feasible intervals are defined, the nodes can be randomly located within the intervals using a uniform probability distribution.

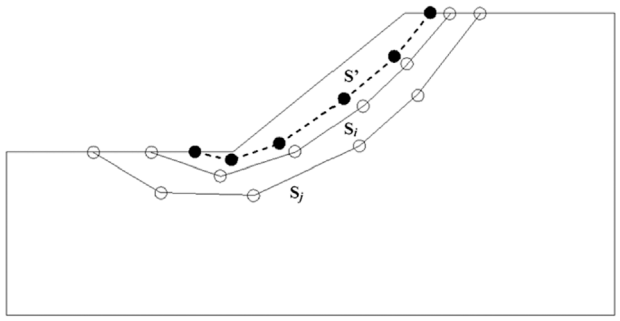

FIGURE 4 | Sketch of the heuristic crossover operator.

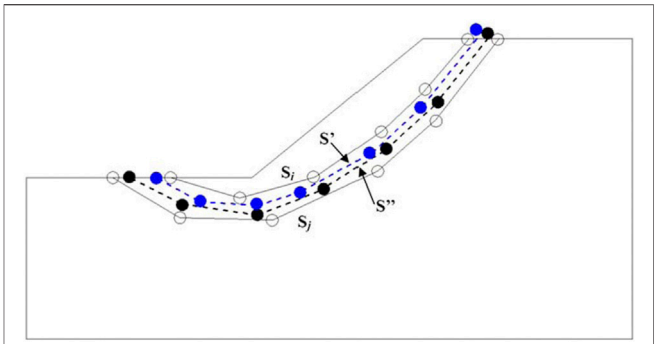

FIGURE 5 | Sketch of the arithmetic crossover operator.

A feasible slip surface within the slope can be generated through the procedure mentioned previously, then, the initial population with certain individuals can be produced by repeating this procedure.

3.3 Selection Schemes

For the fitness of an individual of the population, the factor of safety (F_S) can be naturally defined as the fitness of this individual. The critical slip surface of the slope we are trying to search corresponds to the global minimum F_S within the slope, that is to say, the lower the FS of a slip surface is, the better it will be as the search target. The F_S can be computed by the vector sum method in **Section 3**, therefore, the fitness of each individual can be determined as the basis of the selection schemes.

According to the fitness ranking (i.e., the individual can be ranked with a fitness from low to high), the selecting probability of an individual is computed by **Eq. 16**

$$P_k = cq(1-q)^{k-1} \tag{16}$$

where P_k means the selecting probability of the individual with the kth fitness ranking, c is a parameter meeting all P_k must add up to one, and q is a user-defined parameter between zero and one.

3.4 Crossover Operators

Based on previous studies on GA operators to work with the slip surface, the heuristic and arithmetic crossover operators are used in this study.

Before this crossover operator is performed, two parents must be selected with a specified probability (r_{crs}). Given two feasible slip surfaces, S_i and S_j, with factors of safety F_S (S_i) $\leq$ F_S (S_j), a new polygonal slip surface can be produced as the offspring using the heuristic crossover operator (**Figure 4**), which is denoted as S' computed on the basis of **Eq. 17**.

$$S' = S_i + \xi(S_i - S_j) \tag{17}$$

where ξ is a random number between 0 and 1. The new offspring S′ has to be tested whether it is valid or not. Under some conditions, the new offspring cannot meet the requirement of geometrical constraints described in **Section 3.2**. If it is valid, the slip surface S′ can be considered as the candidate of the next generation, or else, it will be rejected and a new trial offspring is generated till a user-defined number of trials come to the end.

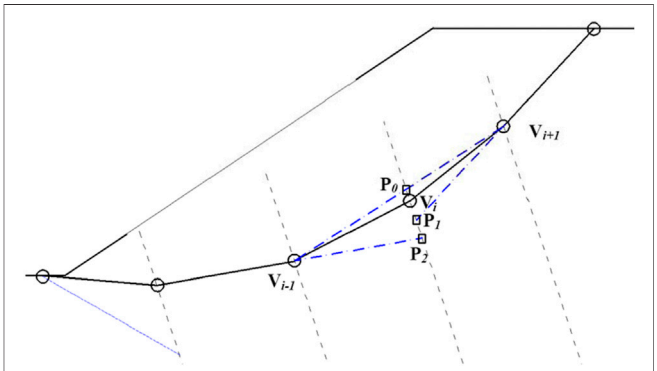

FIGURE 6 | Sketch of uniform and non-uniform mutations of interior nodes.

Figure 5 shows the description of the arithmetic crossover operator, and two auxiliary polygonals, S′ and S″, can be produced by the given two parents, S_i and S_j, as the offspring (**Eqs 18**, **19**).

$$S' = \xi S_i + (1-\xi)S_j \tag{18}$$

$$S'' = \xi S_i + (1-\xi)S_j \tag{19}$$

Similarly, the offsprings S′ and S″ also need to be individually tested through geometrical constraints described in **Section 4.2**, and if they are valid, they will be taken as the candidateS of the next generation. If no valid offspring is produced after a user-defined number of trails, the arithmetic operation of the parents, S′ and S″, returns no offspring.

3.5 Mutation Operators

Based on the custom mutation operators, four types are mainly used in this study, that is, uniform mutation, non-uniform mutation of single nodes, total non-uniform mutation, and extreme vertices mutation.

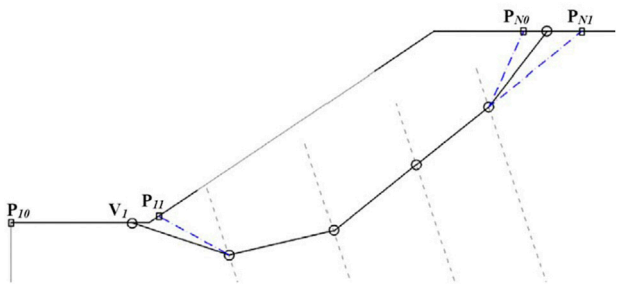

FIGURE 7 | Sketch of uniform and non-uniform mutations of extreme nodes.

3.5.1 Uniform and Non-Uniform Mutation of a Single Node

For uniform and non-uniform mutations of a single node, there is a little difference between the interior node and extreme node. **Figure 6** shows the mutation procedure on an interior node V_i randomly selected from all interior nodes of the slip surface. For the interior node, the feasible interval [P_0, P1, or P2] can be computed based on geometrical constraints. As the minimum value, P_0 can be determined by the intersection between L_i and the $V_{i+1}V_{i-1}$ segment. P_1 can be obtained by the extension of the $V_{i+1}V_{i+2}$ segment if i < N-1, similarly, P_2 can also be obtained by the extension of the $V_{i-2}V_{i-1}$ segment if i >2, then, for P_1 and P_2, the closer one to V_i can be considered as the maximum value of the feasible interval. If i = 2 or i = N-1, only the P_1 or P_2 can be obtained, respectively. In addition, P_0, P_1, or P_2 should be tested whether it is inside the slope, or else, it could be substituted by the intersection of L_i with its boundary.

For the extreme node, the feasible interval can be similarly obtained with a slight difference for interior nodes. Take the V_n for example, the feasible interval [P_{N0} or P_{N1}] can be obtained as follows (**Figure 7**): P_{N0} is computed at the intersection between the slope boundary and a line traced from V_{n-1} with a user-defined angle considering Rankine's limit state (Li et al., 2010; Rafael and Rafael, 2015), whereas P_{N1} results as the intersection between the extension of the $V_{n-1}V_{n-2}$ segment and the slope boundary. If P_{N0} or P_{N1} lies outside the allowable extreme interval, it should be moved to the nearest interval extreme. The other extreme node V1 has a similar procedure and will not be discussed here.

Using the feasible interval for all the nodes, the mutation can be operated. For uniform mutation of a single node, the mutated node V_i can be computed as $V_i^{'} = V_i + (P_j - V_i)\xi$, where j indicates the direction of mutation (j = 0 or 1) and for non-uniform mutation, V_i will be computed as $V_i^{'} = V_i + (P_j - V_i)f(g)$, where $f(g) = \xi(1 - g/N_{gen})^{\delta}$, with $1 \le g \le N_{gen}$ being the generation number, and δ is a predefined parameter determining the degree of non-uniformity of the mutation.

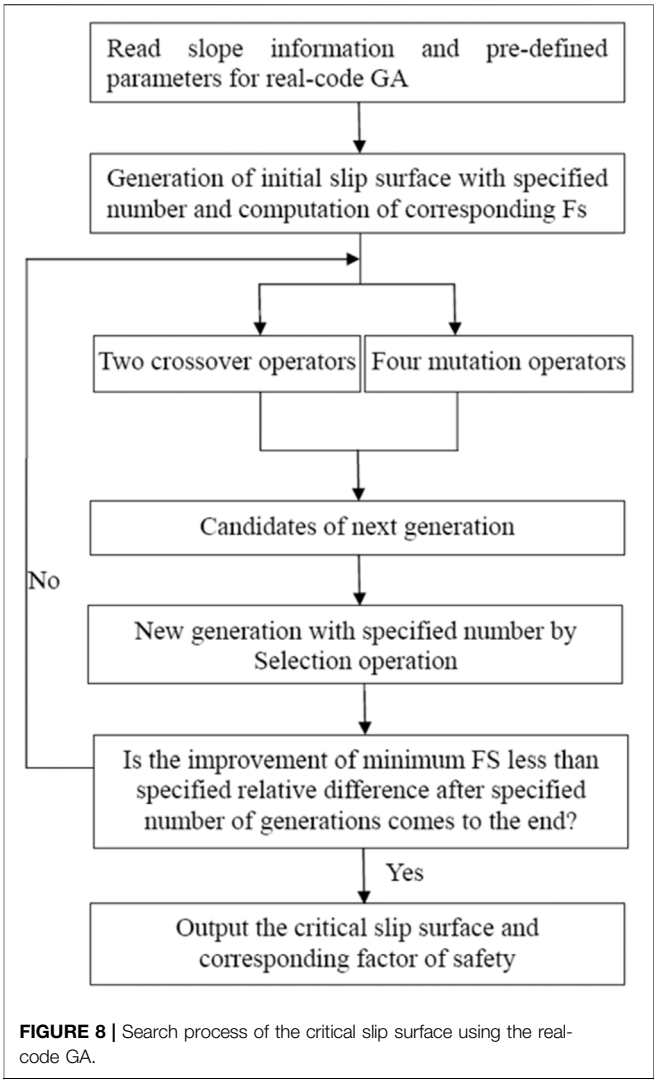

FIGURE 8 | Search process of the critical slip surface using the real-code GA.

3.5.2 Total Non-Uniform Mutation and Extreme Vertices Mutation

The non-uniform mutation operator (**Section 3.5.1**) is applied to all nodes of a slip surface randomly selected from the population.

For extreme vertices mutation, the extreme nodes are mutated and the procedure is as follows: first, a valid individual (slip surface) is selected from the population, and the extreme nodes are mutated based on the procedure mentioned previously (**Section 3.5.1**). Then, the interior nodes will be newly generated using the new positions of both extreme nodes and the generation procedure in **Section 3.2**. Finally, a new slip surface will be produced as the candidate for the offspring.

TABLE 1 | Parameters of the material.

c/kPa	*ϕ*/(°)	*γ*/kN·m^{-3}	*E*/kPa	*μ*
3.0	19.6	20.0	1.0e^4	0.25

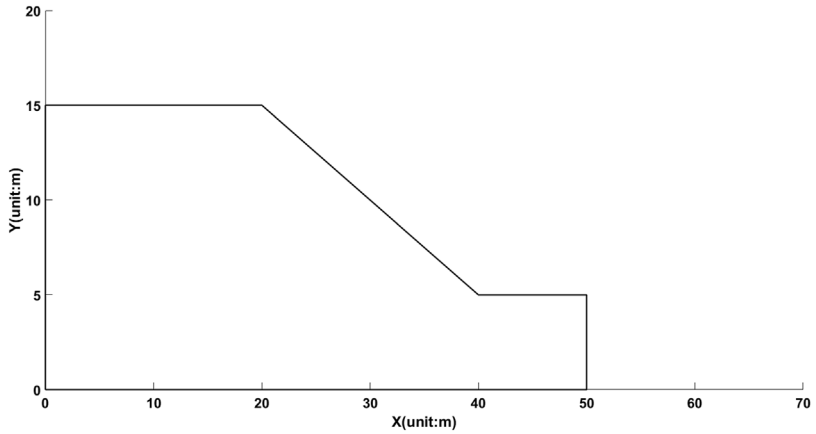

FIGURE 9 | Geometry of the slope.

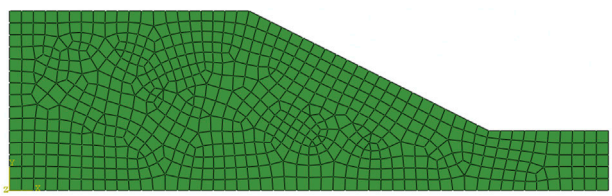

FIGURE 10 | Calculating model of the finite element analysis.

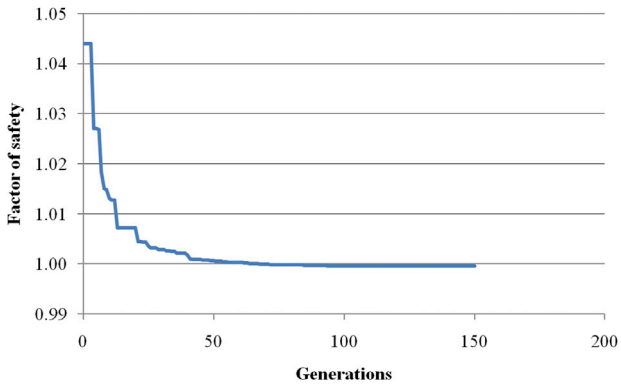

FIGURE 11 | Evolution of Fs with the number of generations for example 1.

In addition, a user-defined number of trails for each mutation operator is defined, and just like the crossover operation, if no valid offspring is produced after a user-defined number of trails, it will return no offspring.

3.6 Search Process

According to the description in **Section 3**, the search process of the real-coded GA to locate the critical slip surface is shown in **Figure 8**.

4 APPLICATION

To verify the reliability of the proposed approach, two examples are investigated from the literature and the results are compared with those in the literature. According to the theory of the vector sum method in **Section 2**, the finite element technique is used to obtain the stress field of the slope composed of elasto-plastic materials. The ideal elasto-plastic constitutive model, Mohr–Coulomb yield criterion, and non-associated flow rule are used in the elasto-plastic finite element analysis. As we know, the Gaussian integration points are used to integrate the stiffness matrix in the finite element analysis, and the discontinuous stresses with low accuracy at the boundary of elements are computed by the direct calculation of the stress integral. This study adopts the global stress smoothing technique to overcome the low accuracy deficiency. The stress at any position within an element can be calculated by

$$\sigma = \sum_{i=1}^{n} N_i \sigma_i \tag{20}$$

where n is the number of nodes of the element, N_i is the shape function about a nodal point i, and σ_i is the corresponding nodal stress.

For the real-coded GA, many parameters, that is, the number of vertices N_{vts} defining the slip surface, the number of slip surfaces M_{slip}, probability of the crossover operator r_{crs}, probability of the mutation operator r_{mut}, minimum number of generations M_{term} before termination of search is allowed, and specified relative difference ε_{term} for the terminating search approach need to be previously defined before searching the critical slip surface. Based on the studies reported in the literature, these parameters are determined as follows: $N_{vts} = 6$, $M_{slip} = 50$, $r_{crs} = 0.85$, $r_{mut} = 0.15$, $M_{term} = 150$, and $\varepsilon_{term} = 0.00005$. In addition, for the purpose of efficient reproduction and killing by selection (**Eq. 16**), $q = 0.01$ is used for the first 2/3 out of the M_{term} generations, and $q = 0.1$ for the remaining.

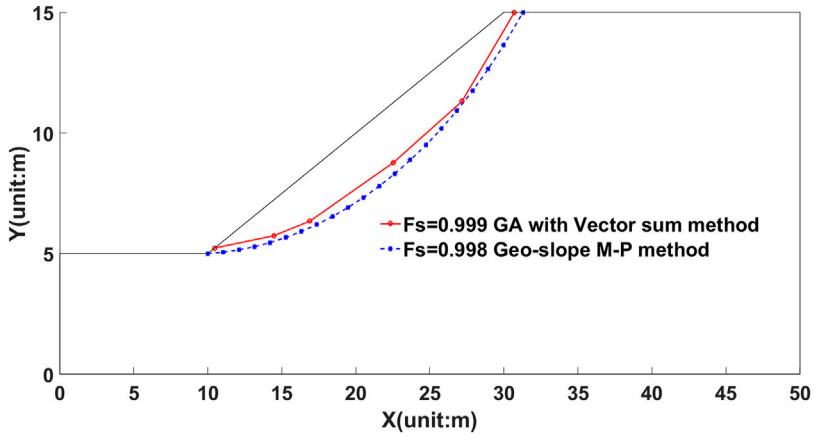

FIGURE 12 | Locations of critical slip surfaces and corresponding Fs for example 1.

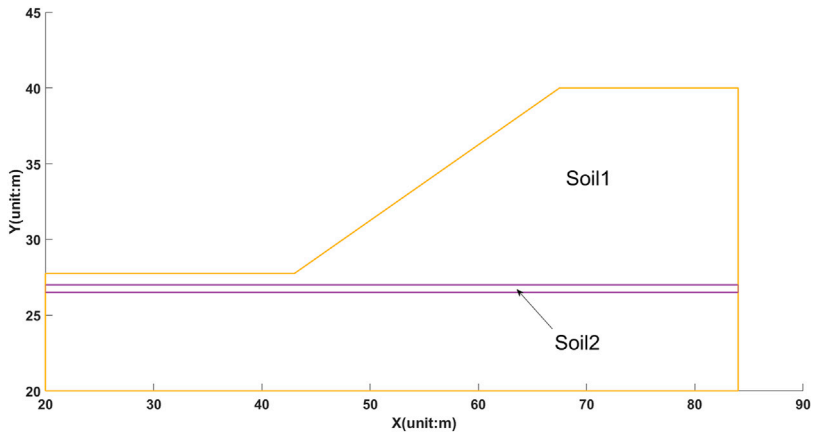

FIGURE 13 | Profile of the slope for example 2.

TABLE 2 | Parameters of the material for example.2.

Material	*c*/kPa	ϕ/°	γ/kN·m^{-3}	*E*/kPa	μ
Soil 1	28.5	20.0	18.84	6.04	0.25
Soil 2	0.0	10.0	18.84	2.03	0.25

4.1 Example 1

This example analyzes a homogenous benchmark slope organized by ACADS (Chen, 2003), and the standard F_S of the slope is 1.0, that is, the slope is a critical slope.

These material properties of the homogenous slope are shown in **Table 1**. For computing conditions, the elastic model is adopted because this example is a critical slope, for which the standard F_S is 1.00. For boundary conditions, the bottom is fixed and the lateral boundaries are normally restricted. The size of the slope is shown in **Figure 9** and the calculating model of the finite element analysis is shown in **Figure 10**, and the total element number is 636.

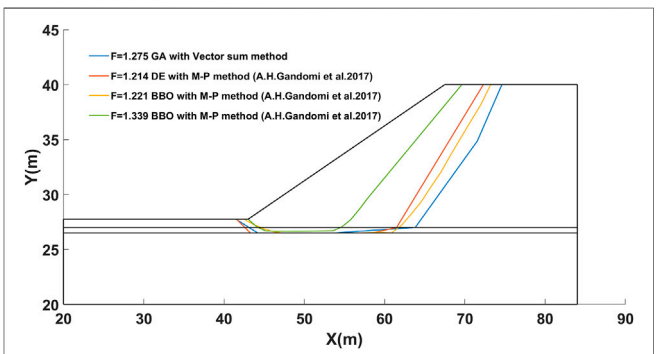

FIGURE 14 | Locations of critical slip surfaces and corresponding Fs for example 2.

The critical slip surface of this example can be searched using the real-code GA in **Section 3** and the vector sum method in **Section 2**. **Figure 11** shows the evolution with the number of

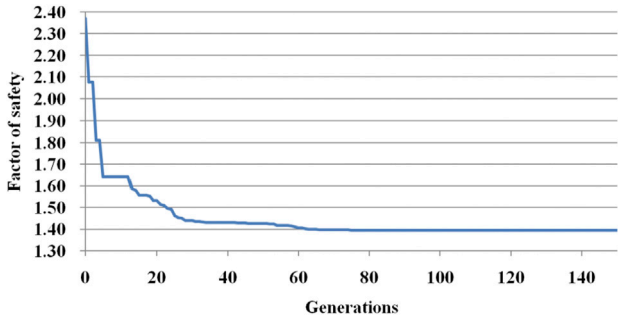

FIGURE 15 | Evolution of Fs with the number of generations for example 2.

generations using the real-code GA, of the minimum Fs with the vector sum method, which demonstrates the search process of the GA. **Figure 12** shows the geometry and locations of the critical slip surfaces using the proposed approach and rigorous Morgenstern–Price method for comparison. From **Figure 11** and **Figure 12**, it can be seen that either the location of the critical slip surface or corresponding minimum F_S is in good agreement with the results obtained with the rigorous Morgenstern–Price method by the commercial software Geo-slope. Moreover, for this example, the minimum Fs by the proposed method or M–P method is almost equal to 1.0, which revealed that the vector sum method can reliably assess this example using this real-code GA.

4.2 Example 2

This example is also initially organized by ACADS [Chen, 2003; Giam and Donald, 1989;], and used to test the ability of the proposed procedure for a non-circle slip surface. This slope includes a weak layer located between two strong layers, which is shown is **Figure 13**. **Table 2** presents the properties of two types of soil layers. The factor of safety published by ACADS was equal to 1.26 for the specified slip surface, and for the critical slip surface, the FOS was organized to be 1.24. For boundary conditions, it is similar to that in example 1, that is, the bottom is fixed and the lateral boundaries are normally restricted.

Moreover, this case was also studied with different optimization algorithms (Gandomi et al., 2017). **Figure 14** shows the locations of critical slip surfaces and the corresponding F_S by different optimization approaches, in which BBO means biogeography-based optimization and DE stands for differential evolution algorithm. From this figure, the exits of the critical slip surfaces with different approachs are almost located near the slope toe, and the entrances are located in a little different place on the top boundary of the slope. For the minimum F_S, F_S = 1.275, 1.214, 1.221, and 1.339, is obtained by GA with the vector sum method, DE with the M–P method, BBO with the M–P method, and GA with the M–P method, respectively. Except for F_S = 1.339, the rest are consistent with the standard answer 1.24 organized by ACADS for this example. **Figure 15** demonstrates the evolution process with the generations of the minimum F_S, in which the global minimum FS can be obtained through almost 60 generations in the proposed GA (**Figure 15**).

5 DISCUSSIONS

1) Just like the conclusions of high efficiency to locate the critical slip surface for the real-coded GA reported in the literature (Sun et al., 2008; Sabhahit and Rao, 2011; Richard and Sitar, 2012; Rafael and Rafael, 2015), the real-coded GA presented in this study actually exhibits an excellent ability to find the critical slip surface for these complex slopes. From comparing the results of two examples with those reported in the literature, the vector sum method proposed in this study is verified to be reliable to assess slope-stability problems. Over traditional methods, that is, the limit equilibrium method and strength reduction technique, the vector sum method emphasizes the direction of the force and the global sliding direction of the slope, which brings new insights into the way we assess the slope problem. More importantly, this proposed method can not only provide the global sliding direction of the slope determined by rigorous theory but also directly compute the safety factor by force equilibrium of the sliding body on the basis of the stress state of the slope, which is also helpful to evaluate the slope stability under dynamic loads or some other complex loads. At present, the vector sum method still has a long distance to go for approval by researchers and engineers, but it explores a new approach to treat slope problems from other perspectives over traditional approaches.
2) Merely from the viewpoint of the formula to calculate the safety factor, the computing formula by force equilibrium (**Eq. 15**) of the proposed method is just the vector expression of the formula recognized as an important supplement for the theory of slope-stability analysis over the traditional LEM and SRM. The slope-stability problem is essentially a nondeterministic polynomial-time complete problem, and one approach cannot completely replace the other because of the approximation feature of all approaches to slope-stability problems (Tang et al., 2015). To be honest, for 2D slope-stability problems, it is not difficult to accurately evaluate the stability of the slope using either commercial software Geo-slope with the LEM or other with the SRM. However, in 3D complex problems, it is not easy to reasonably assess the slope problem, especial for dynamic slope problems. The proposed approach in this study also has high efficiency for 3D slope-stability problems with complex conditions as long as the stress state of the slope can be rationally obtained by numerical simulation.

6 CONCLUSION

1) Based on the popular strength reduction definition in the slope stability analysis, the vector sum method was further

studied and the safety factor was deduced on the basis of the force equilibrium equation along the global sliding direction.
2) The proposed approach was proved to be reliable in assessing the slope stability by comparing the locations of critical slip surfaces and corresponding F_S of examples with those obtained using the M–P method and other optimization algorithms in the literature.
3) For the real-coded GA, though only six vertices are considered in this study for finding the critical slip surface, it still exhibits high efficiency on locating the critical slip surface for two examples.

DATA AVAILABILITY STATEMENT

The original contributions presented in the study are included in the article/Supplementary Material; further inquiries can be directed to the corresponding author.

AUTHOR CONTRIBUTIONS

MG contributed to conception and design of the study. JL organized the database. XD performed the statistical analysis. MG wrote the first draft of the manuscript.

FUNDING

This study was funded by the National Science Foundation of China under Grant No. 51674239.

ACKNOWLEDGMENTS

The authors gratefully acknowledge the financial support of the National Science Foundation of China under Grant No. 51674239.

REFERENCES

Chen, Z. Y. (2003). *Earth Slope Stability Analyses—Theory, Method and Programs*. Beijing: China Water Power Press.

Cheng, Y. M., Lansivaara, T., and Wei, W. B. (2007). Two-dimensional Slope Stability Analysis by Limit Equilibrium and Strength Reduction Methods. *Comput. Geotechnics* 34, 137–150. doi:10.1016/j.compgeo.2006.10.011

Duncan, J. M. (1996). State of the Art: Limit Equilibrium and Finite-Element Analysis of Slopes. *J. Geotechnical Eng.* 122 (7), 577–596. doi:10.1061/(asce)0733-9410(1996)122:7(577)

Fu, X., Sheng, Q., Zhang, Y., Chen, J., Zhang, S., and Zhang, Z. (2017). Computation of the Safety Factor for Slope Stability Using Discontinuous Deformation Analysis and the Vector Sum Method. *Comput. geotechnics* 92, 68–76. doi:10.1016/j.compgeo.2017.07.026

Gandomi, A. H., Kashani, A. R., Mousavi, M., and Jalalvandi, M. (2017). Slope Stability Analysis Using Evolutionary Optimization Techniques. *Int. J. Numer. Anal. Methods geomechanics* 41, 151–264. doi:10.1002/nag.2554

Ge, X. R. (2008). Deformation Control Law of Rock Fatigue Failure,real-Time X-ray CT Scan of Geotechnical Testing, and New Method of Stability Analysis of Slopes and Dam Foundations. *Chin. J. Geotechnical Eng.* 30 (1), 1–20.

Giam, P. S. K., and Donald, I. B. (1989). Example Problems for Testing Soil Slope Stability Programs. *Civil Eng. Res.* 8, 1989.

Guo, M. W., Li, C. G., Wang, S. L., Yin, S. D., Liu, S. J., and Ge, X. R. (2019). Vector-Sum Method for 2D Slope Stability Analysis Considering Vector Characteristics of Force. *Int. J. geomechanics* 19 (6), 1436. doi:10.1061/(ASCE)GM.1943-5622.0001436

Hamdhan, I. N., and Schweiger, H. F. (2013). Finite Element Method-Based Analysis of an Unsaturated Soil Slope Subjected to Rainfall Infiltration. *Int. J. Geomech.* 13 (5), 653–658. doi:10.1061/(asce)gm.1943-5622.0000239

Huang, C.-C., and Tsai, C.-C. (2000). New Method for 3D and Asymmetrical Slope Stability Analysis. *J. Geotech. Geoenviron. Eng.* 126 (10), 917–927. doi:10.1061/(asce)1090-0241(2000)126:10(917)

Kim, J. Y., and Lee, S. R. (1997). An Improved Search Strategy for the Critical Slip Surface Using Finite Element Stress fields. *Comput. Geotechnics* 21 (4), 295–313. doi:10.1016/s0266-352x(97)00027-x

Li, Y.-C., ChenZhan Tony, Y.-M. L. T., Zhan, T. L. T., Ling, D.-S., and Cleall, P. J. (2010). An Efficient Approach for Locating the Critical Slip Surface in Slope Stability Analyses Using a Real-Coded Genetic Algorithm. *Can. Geotech. J.* 47 (7), 806–820. doi:10.1139/t09-124

Liu, G., Zhuang, X., and Cui, Z. (2017). Three-dimensional Slope Stability Analysis Using Independent Cover Based Numerical Manifold and Vector Method. *Eng. Geology.* 225, 83–95. doi:10.1016/j.enggeo.2017.02.022

Rafael, J. P., and Rafael, J. (2015). A Genetic Algorithm for Slope Stability Analyses with Concave Slip Surfaces Using Custom Operators. *Eng. Optimization* 47 (4), 453–472. doi:10.1080/0305215X.2014.895339

Richard, O. C., and Sitar, N. (2012). *bSLOPE A General Limit Equilibrium Slope Stability Analysis Code for iOSGeotechnicalEngineering Report No. UCB/GT/12-01 2012*. Berkeley, CA: Department of Civil and Environmental Engineering, University ofCalifornia.

Sabhahit, N., and Rao, A. (2011). Genetic Algorithms in Stability Analysis of Non-homogeneous Slopes. *Int. J. Geotechnical Eng.* 5 (1), 33–44. doi:10.3328/ijge.2011.05.01.33-44

Shen, J., and Karakus, M. (2014). Three-dimensional Numerical Analysis for Rock Slope Stability Using Shear Strength Reduction Method. *Can. Geotech. J.* 51, 164–172. doi:10.1139/cgj-2013-0191

Sun, J., Li, J., and Liu, Q. (2008). Search for Critical Slip Surface in Slope Stability Analysis by Spline-Based GA Method. *J. Geotech. Geoenviron. Eng.* 134 (2), 252–256. doi:10.1061/(asce)1090-0241(2008)134:2(252)

Tang, H., Liu, X., Xiong, C., Wang, Z., and Ez Eldin, M. A. M. (2015). Proof of Nondeterministic Polynomial-Time Complete Problem for Soil Slope-Stability Evaluation. *Int. J. Geomechanics* 16 (5), 595. doi:10.1061/%28ASCE%29GM.1943-5622.0000595

Zheng, H., Tham, L. G., and Liu, D. (2006). On Two Definitions of the Factor of Safety Commonly Used in the Finite Element Slope Stability Analysis. *Comput. Geotechnics* 33, 188–195. doi:10.1016/j.compgeo.2006.03.007

Zou, J.-Z., Williams, D. J., and Xiong, W.-L. (1995). Search for Critical Slip Surfaces Based on Finite Element Method. *Can. Geotech. J.* 32 (2), 233–246. doi:10.1139/t95-026

Conflict of Interest: The authors declare that the research was conducted in the absence of any commercial or financial relationships that could be construed as a potential conflict of interest.

Publisher's Note: All claims expressed in this article are solely those of the authors and do not necessarily represent those of their affiliated organizations, or those of the publisher, the editors, and the reviewers. Any product that may be evaluated in this article, or claim that may be made by its manufacturer, is not guaranteed or endorsed by the publisher.

frontiers | Frontiers in Earth Science

ORIGINAL RESEARCH
published: 02 May 2022
doi: 10.3389/feart.2022.884453

Mechanical Characteristics of Heishan Bentonite for Hazardous Waste Contamination Prevention

Jian-Hua Xu[1,2], *Kai Li*[3]*, *Ke-Ming Sun*[3] *and Shu-Cui Zhang*[3]

[1]POWERCHINA Huadong Engineering Corporation Limited, Hangzhou, China, [2]Zhejiang Huadong Engineering Consulting Corporation Limited, Hangzhou, China, [3]Department of Science, Qingdao University of Technology, Qingdao, China

A series of laboratory-based water infiltration tests at room temperature have been conducted to investigate the mechanical characteristics of Heishan bentonite as a potential backfill material. The experiments were performed with an oedometer testing apparatus which facilitates the mechanical loading, the water infiltration, and the deformation measurement. The results show that both swelling pressure-initial dry density and swelling strain-moisture content have an exponential relationship. Moreover, swelling strain dramatically decreases when the applied stress exceeds a reference stress of 100 kpa. Finally, permeability tests were carried on Heishan bentonite specimen and the studied material reaches an impermeable state when the moisture content is larger than 40%. The presented properties certificate that Heishan bentonite can be employed as a backfill material in engineering practice.

Keywords: soil mechanics, heishan bentonite, mechanical behavior, hazardous waste contamination prevention, analytical modeling

OPEN ACCESS

Edited by:
Yun Zheng,
Institute of Rock and Soil Mechanics (CAS), China

Reviewed by:
Zhongzheng Wang,
Queensland University of Technology, Australia
Di Wu,
Liaoning Technical University, China

***Correspondence:**
Kai Li
kai.li@live.com

Specialty section:
This article was submitted to Geohazards and Georisks, a section of the journal Frontiers in Earth Science

Received: *26 February 2022*
Accepted: *04 April 2022*
Published: *02 May 2022*

Citation:
Xu J-H, Li K, Sun K-M and Zhang S-C (2022) Mechanical Characteristics of Heishan Bentonite for Hazardous Waste Contamination Prevention. Front. Earth Sci. 10:884453. doi: 10.3389/feart.2022.884453

INTRODUCTION

Bentonite has been widely considered as backfill materials in the underground storage of high-level nuclear waste in many countries, because of its low hydraulic conductivity and high swelling capacity (Kanno and Wakamatsu, 1992; Chapman 2006; Chen et al., 2014). In many repository concepts, the backfill material is pre-compacted to a relatively dense state and it is installed in the vicinity of waste canisters (Martin et al., 2006; Romero et al., 2011; Jobmann et al., 2017). The initially unsaturated bentonite can absorb the surrounding fluids to retard the radioactive liquid waste from being transported to the underground water system, and the high swelling capacity imposes sufficient swelling pressure to the adjacent restraints. Therefore, it is critically important to evaluate the swelling behavior of compacted bentonite for the long-term stability of the underground high-level nuclear waste disposal repositories.

In this regard, numerous studies have been carried out to investigate the swelling properties for different types of bentonites (Lloret et al., 2003; Cui et al., 2011; Tang et al., 2011; Wang et al., 2012; Sun et al., 2013; Cui and Si 2014; Ye et al., 2014; Zhang et al., 2021). For example, Komine and Ogata (2003), Komine and Ogata (2004) performed a series of laboratory swelling tests and introduced new equations to quantify the swelling behavior of bentonite for the bentonite/sand mixture. Tanaka and Nakamura investigated the impacts of seawater and temperature on the swelling response of bentonite (Tanaka and Nakamura, 2005). In recent years, many works have been performed on the swelling properties of bentonite using salty water. These researches show that the compacted bentonite is an ideal backfill material in the deep disposal, especially Calcigel in Germany and Kunigel in Japan.

TABLE 1 | Geotechnical properties of bentonite tested.

Property	Value
Specific gravity	2.5
Plastic limit (%)	48.83
Liquid limit (%)	960
PH	8.5
Total specific surface area (m^2/g)	584
Free swelling ratio (%)	528.7
Montmorillonite content (%)	81.6
Cristobalite content (%)	17.4

In China, Gaomiaozi bentonite has been accepted as backfill materials in the deep disposal of high-level radioactive waste. This bentonite is extracted from an open deposit in Gaomiaozi, Inner Mongolia autonomous region, northern China. Regarding Gaomiaozi bentonite, many researches have been conducted using oedometer tests and mockup tests. Xie et al. (2006) performed constant volume tests to study the swelling behavior and the influential factors on swelling behavior. Zhang et al. (2016) studied the swelling characteristics and compared two types of GMZ bentonites. Zhao et al. (2017) investigated the mechanical behavior on wetting-drying cycles and proposed a model based on the concept of the critical swelling-shrinkage state. Recently, Sun et al. (2020) have focused on the swelling characteristics with alkaline chemical conditions to simulate the long-term environment of Chinese repository. Great effort and progress have been made in studying the swelling behavior of different types of bentonites to better understand their mechanical behavior and optimize their engineering applications for nuclear waste disposal.

Engineering uses and industrial demands of bentonites give continued impetus to the study of these materials and a variety of bentonites should be investigated to improve the comprehension of their mechanical properties to better serve the practical engineering. On the basis of geological survey, Heishan bentonite turns out to be the most attractive competitor as a backfill material, because of its large reserves and prominent properties. In the present work, a series of oedomenter tests on Heishan bentonite have been performed for the first time to investigate the swelling behavior as a possible backfill material.

MATERIAL

The studied bentonite in this work is mined from Heishan County in Liaoning province, 600 km northeast from Beijing, China. The Heishan bentonite is a gray powder and its main composition is montmorillonite approximately 81.6%. As a calcium-based bentonite, it has a plastic limit 48.83%, liquid limit of 960% and specific gravity of 2.5. **Table 1** summarizes the basic physical properties of the studied material. Prior to preparing the bentonite samples, the studied material is processed through 74 μm sieve, oven-dried for 24 h and stored in a large airtight container for future use in laboratory testing. The bentonites are molded into specimens of 10 mm height and 61.8 mm in diameter under different statically compacted loads and these samples have dry densities of 0.983, 1.081, 1.177, and 1.278 g/cm^3, respectively. A series of tests have been performed on these initial states to investigate the swelling behavior of Heishan bentonite.

METHODS

The oedometer testing apparatus is used in this research and it is illustrated in **Figure 1**. As the main part of the testing device, the oedometer cell consists of three parts, i.e., the mechanical part to apply the vertical loadings (No.5 in **Figure 1**), the infiltration part to allow water moving during wetting paths (No. 1, No. 4, and No. 9) and the monitoring part to measure the vertical deformation during tests (No. 6). In the process of testing, the cutting ring (No. 3) containing the bentonite sample (No. 8) is working with other parts of the oedometer testing apparatus (No. 7) and a series of one-dimensional tests (No. 2) are carried out under various vertical stresses. During the hydration of bentonite samples, the vertical deformation is recorded by the dial gauge for every 2 h. Once the difference of two successive values is small enough (0.01 mm), the current step is completed and water to be added in water carrier continues the following step. **Figure 2** is a summary of varied experimental paths to investigate the hydromechanical behavior of Heishan bentonite.

In this study, the amount of adding water provided by the Standard for geotechnical testing method (GB/T50123-2019) is adopted,

$$\Delta m_w = 0.01 \cdot \rho_d V \cdot \Delta w \tag{1}$$

where, Δm_w is the amount of adding water (g), ρ_d is the initial dry density (g/cm^3), V is the volume of the cutting ring (cm^3) and Δw is the difference between the target moisture content and the initial moisture content of dry soil specimen.

The moisture content of soil specimen is employed to represent hydraulic property and it is defined by,

$$\theta = m_w / m_s \times 100\% \tag{2}$$

where, θ is the moisture content, m_w is the mass of water and m_s is the mass of dry soil.

Swelling Pressure-Dry Density Plot

Swelling pressure is defined as the pressure required to compress the expansive clays back to its original configuration when the specimen is completely soaked. As a backfill material, the swelling pressure is of particular interest because it basically controls sealing properties. The constant-volume swelling pressure experiments have been performed to measure the swelling pressure. In these tests, the impact of initial dry density has been taken into account on the swelling pressure of the studied material.

Figure 3 is aimed at relating the swelling characteristics with the initial dry density of Heishan bentonite. To study the influence of absorbed water on the swelling behavior, the

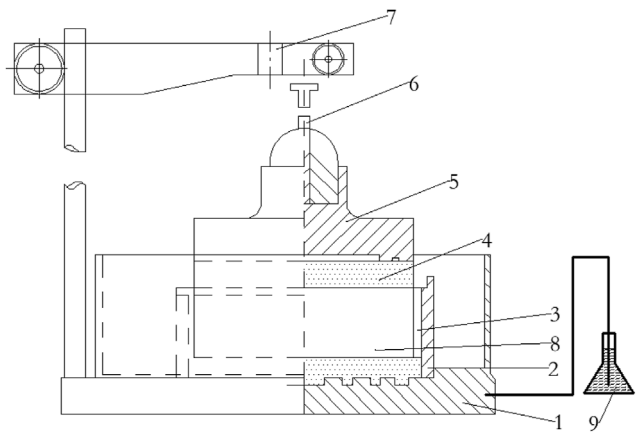

FIGURE 1 | Schematic view of one-dimensional oedometer device.

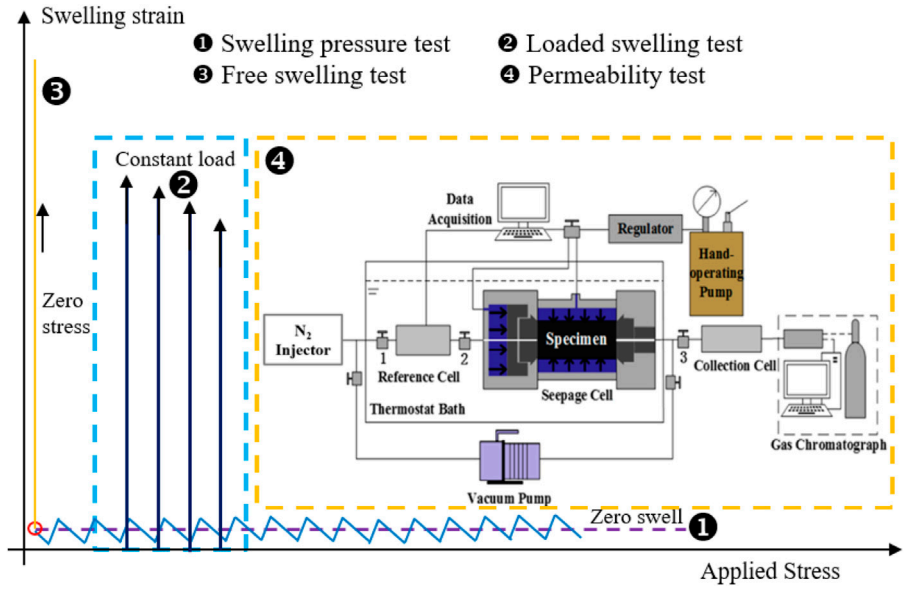

FIGURE 2 | Stress path of various experimental methods.

relationship between the swelling pressure and the water absorption is presented in **Figure 3**. Based on the plotted relationship between different dry density and swelling pressure, the swelling pressure increases exponentially as the initial dry density increases and the amount of absorbed water also amplifies the swelling pressure. Apart from attributing material swelling to the mineral phases, the pore water is exclusively attached to the swelling behavior of studied bentonite. Therefore, the initial dry density and the water absorption are key factors to affect the swelling behavior of Heishan bentonite.

As a result, the swelling pressure at different dry densities for Heishan bentonite can be calculated by the following empirical formula,

$$P_e = a \cdot \exp(b \cdot \rho_d) \tag{3}$$

where, P_e is the swelling pressure (kPa), ρ_d is initial dry density (g/cm^3), a and b are model constants presented in **Figure 3**.

Swelling Strain-Elapsed Time Plot

To determine the swelling characteristics of Heishan bentonite under the condition of different loadings, swelling strain is employed in this work and it is defined as follows:

$$\varepsilon_{exp} = \frac{Z_1 - Z_2}{h_0} \times 100\% \tag{4}$$

where ε_{exp} is the swelling strain, Z_1 is the deformation of the specimen at the current loading stage, Z_2 is the deformation at the

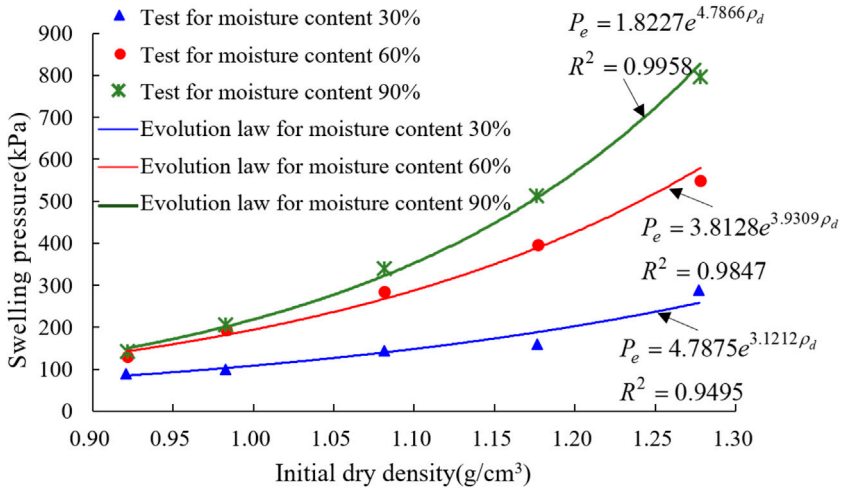

FIGURE 3 | Relationship between swelling pressure and initial dry density for different moisture contents.

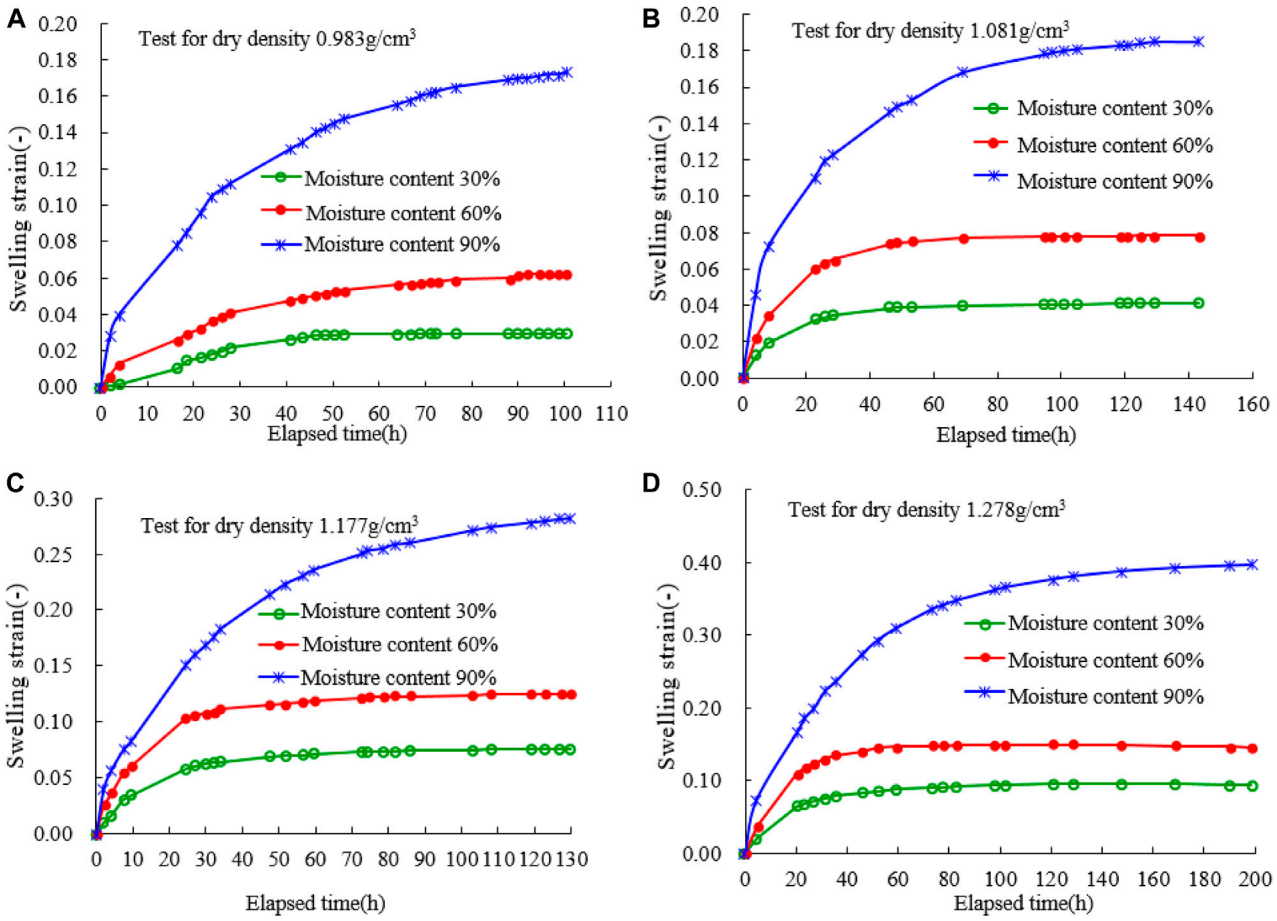

FIGURE 4 | Variation of swelling behavior with initial dry density at the constant applied stress of 50 kPa.

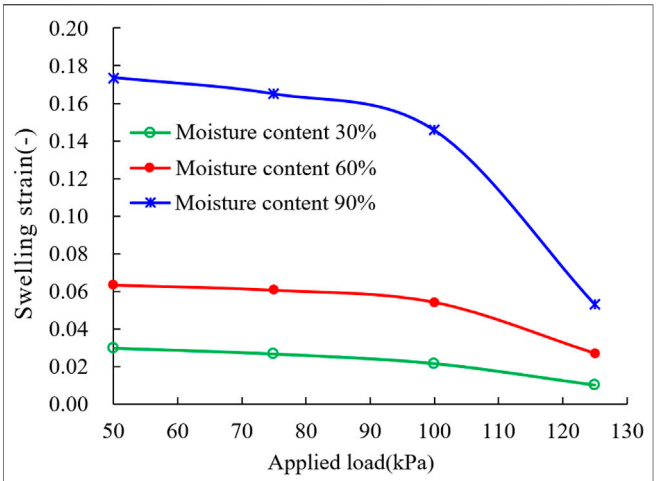

FIGURE 5 | Variation of swelling behavior with vertical stress at the constant initial dry density of 0.983 g/cm^3.

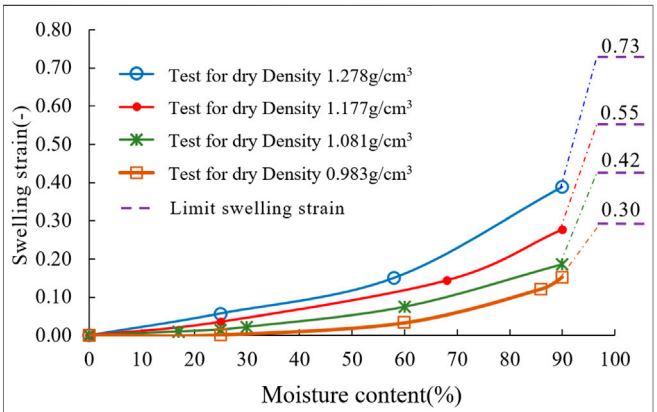

FIGURE 6 | Variation of swelling behavior with moisture content at the constant applied stress of 50 kPa.

beginning of the current loading stage, and h_0 is the initial height of the specimen.

Constant applied stress and varied initial dry density. The mobilization of swelling strain with passage of time is illustrated in **Figure 4** for the studied material. Taking test results at the constant applied stress of 50 kPa for instance, the curves demonstrate a distinct change in both the shapes of curves and the mobilized swelling strain for different moisture contents. For various initial dry densities (0.983, 1.081, 1.177, and 1.278 g/cm^3), the increase of swelling strain is rapid at the earlier stage of tests and the curve of swelling strain tends progressively flatter with the elapsed time.

Constant dry density and varied vertical stress. To study the impact of applied stress on the swelling behavior of Heishan bentonite, typical tests of swelling behavior with different vertical stresses are carried out. **Figure 5** plots the curves of swelling strain with the elapsed time under different vertical stresses of 50, 75, 100, and 125 kPa. For the initial dry density of 0.983 g/cm^3, it is obvious that the swelling strain decreases with the increase of vertical stress. When the vertical stress in inferior to a reference stress p_c, swelling strain varies relatively small. However, the swelling strain has a dramatic reduction as the vertical stress exceeds p_c value and it indicates the bentonite expansion occurs in micro-structural level leading to a dense state of the studied sample.

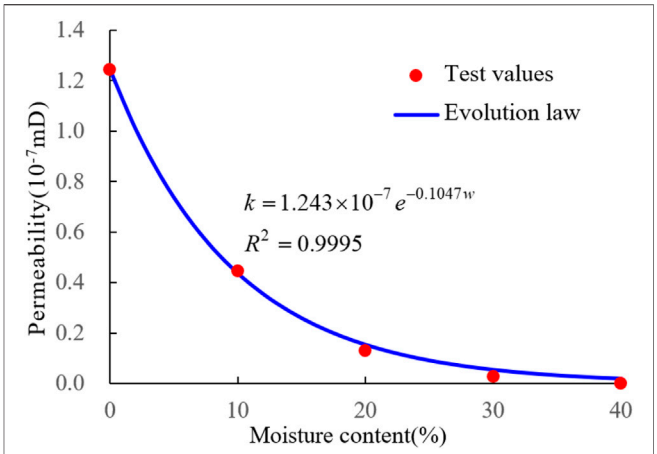

FIGURE 7 | Relationship between permeability and moisture content.

Swelling Strain-Moisture Content Plot

The amount of adding water is calculated according to **Eq. 1** and the wetting path under a constant vertical stress of 50kpa is performed on the studied material. **Figure 6** experimentally demonstrates the relationship between the moisture content and the swelling behavior of Heishan bentonite. In this plot, the swelling strains of several moisture contents have been tested and the swelling strain exponentially increases with the moisture content. To investigate the maximum swelling strain of each initial dry density, the soil specimen is wetted until it cannot absorb water and the limit swelling strain is portrayed in **Figure 6**. For different initial dry densities in this work, the limit swelling strain of Heishan bentonite varies from 0.3 to 0.73.

Permeability-Moisture Content Plot

As a potential backfill material, low permeability is required to evaluate the sealing efficiency of the bentonite barrier. To study this property, the experimental testing system based on Darcy's law is developed and it mainly consists of a N_2 injector, a reference cell, a seepage cell, and a collection cell as shown in **Figure 2**. The soil specimen is firstly vacuumed and the confining pressure is imposed on the specimen. N_2 is injected into the reference cell under pressure and the seepage test starts when the pressure in reference cell is stable. The collection cell is employed to measure the flow rate of injected gas and the permeability is defined by

$$k = \frac{2 \cdot \mu \cdot p_2 \cdot L \cdot Q}{(p_1^2 - p_2^2) \cdot A} \tag{5}$$

where, p_1 and p_2 are the upstream and downstream pressure, A is the cross-sectional area, μ is the viscosity of N_2, L is the length of the specimen and Q is the flow rate.

Figure 7 describes the relationship between soil permeability and moisture content and an empirical expression is proposed to simulate the fore-mentioned relationship,

$$k = k_0 \cdot \exp(-\lambda \cdot \theta) \quad (6)$$

where, k_0 is the permeability of soil specimen at the dry state (mD), θ is the moisture content and λ is a constant.

In **Figure 7** we can find that the soil permeability is exponential reduction with the moisture content increasing. When the moisture content reaches 40%, the permeability of bentonite barrier is so dense that no gas can be collected in collection cell. This suggests that Heishan bentonite has a relatively low permeability under an enough pressure and a proper moisture content.

CONCLUSION

A series of swelling pressure tests, loaded swelling tests, free swelling tests and permeability tests have been conducted on Heishan bentonites and the experimental results allow the following conclusion to be drawn.

1) swelling pressure-initial dry density relationship.

The swelling pressure of the studied material exponentially increases with the initial dry densities rising, and this value is greatly influenced by the amount of absorbed water during wetting. The proposed empirical formula is able to estimate the swelling pressure because of the small fitting tolerance.

2) Swelling strain-elapsed time relationship.

Under the condition of constant applied stress and varied initial dry density, swelling strain increases rapidly at the earlier stage of tests and then it tends progressively flatter with the elapsed time. The higher moisture content, the larger is the swelling strain. In case of constant initial dry density and varied vertical stress, swelling strain reduces significantly when the vertical stress exceeds the reference stress and it can be explained that the bentonite expansion occurs in micro-structural level under a relatively large vertical stress.

3) Swelling strain-moisture content relationship.

The swelling strain increases with the moisture content mounting and its relationship abides by an exponential law. The limit swelling strain is investigated when the soil sample cannot absorb more water and this value varies from 0.3 to 0.73 for different initial dry densities.

4) Permeability-moisture content relationship.

The bentonite permeability is exponential reduction with the increase of moisture content and the soil specimen becomes impermeable when the moisture content is larger than 40%. This suggests that Heishan bentonite has a relatively low permeability and Heishan bentonite can be employed as a backfill material in the future.

DATA AVAILABILITY STATEMENT

The original contributions presented in the study are included in the article/Supplementary Material, further inquiries can be directed to the corresponding author.

AUTHOR CONTRIBUTIONS

J-HX contributed to conception and design of the study. KL wrote the whole draft of the manuscript and carried out statistical analysis. K-MS and S-CZ performed the experimental tests. All authors contributed to the submitted manuscript.

ACKNOWLEDGMENTS

The authors would like to acknowledge National Natural Science Foundation of China and Shandong Province for funding this work through research grant 51808306 and ZR2021ME099.

REFERENCES

Chapman, N. A. (2006). Geological Disposal of Radioactive Wastes-Concept, Status and Trends. *J. Iberian Geology.* 32 (1), 7–14.

Chen, Y.-G., Cui, Y.-J., Tang, A. M., Wang, Q., and Ye, W.-M. (2014). A Preliminary Study on Hydraulic Resistance of Bentonite/host-Rock Seal Interface. *Géotechnique* 64 (12), 997–1002. doi:10.1680/geot.13.p.209

Cui, S.-L., and Si, D.-D. (2014). Experimental Research of Swelling Behaviors with Initial Water Content and Matric Suction of Bentonite-Sand Mixtures. *Geosystem Eng.* 17 (6), 317–324. doi:10.1080/12269328.2014.994788

Cui, Y.-J., Tang, A.-M., Qian, L.-X., Ye, W.-M., and Chen, B. (2011). Thermal-mechanical Behavior of Compacted GMZ Bentonite. *Soils and Foundations* 51 (6), 1065–1074. doi:10.3208/sandf.51.1065

Jobmann, M., Flügge, J., Gazul, R., Hammer, J., Herold, P., Krone, J., et al. (2017). *Investigation on Long-Term Safety Aspects of a Radioactive Waste Repository in a Diagenetic Clay Formation*. (Technical report, GRS BGR DBE TEC).

Kanno, T., and Wakamatsu, H. (1992). Water Uptake and Swelling Properties of Unsaturated Bentonite Buffer Materials. *Can. Geotech. J.* 29, 1102–1107. doi:10.1139/t92-127

Komine, H., and Ogata, N. (2003). New Equations for Swelling Characteristics of Bentonite-Based Buffer Materials. *Can. Geotech. J.* 40, 460–475. doi:10.1139/t02-115

Komine, H., and Ogata, N. (2004). Predicting Swelling Characteristics of Bentonites. *J. Geotech. Geoenviron. Eng.* 130 (8), 818–829. doi:10.1061/(asce)1090-0241(2004)130:8(818)

Lloret, A., Villar, M. V., Sánchez, M., Gens, A., Pintado, X., and Alonso, E. E. (2003). Mechanical Behaviour of Heavily Compacted Bentonite under High Suction Changes. *Géotechnique* 53 (1), 27–40. doi:10.1680/geot.2003.53.1.27

Martin, P. L., Barcala, J. M., and Huertas, F. (2006). Large-scale and Long-Term Coupled Thermo-Hydro-Mechanic Experiments with Bentonite: The Febex Mock-Up Test. *J. Iberian Geology.* 32 (2), 259–282. doi:10.5209/JIGE.33935

Romero, E., Della Vecchia, G., and Jommi, C. (2011). An Insight into the Water Retention Properties of Compacted Clayey Soils. *Géotechnique* 61 (4), 313–328. doi:10.1680/geot.2011.61.4.313

Sun, D. a., Zhang, J., Zhang, J., and Zhang, L. (2013). Swelling Characteristics of GMZ Bentonite and its Mixtures with Sand. *Appl. Clay Sci.* 83-84 (10), 224–230. doi:10.1016/j.clay.2013.08.042

Sun, Z., Chen, Y., Ye, W. M., Cui, Y. J., and Wang, Q. (2020). Swelling Deformation of Gaomiaozi Bentonite under Alkaline Chemical Conditions in a Repository. *Eng. Geology.* 279, 105891. doi:10.1016/j.enggeo.2020.105891

Tanaka, Y., and Nakamura, K. (2005). Effect of Seawater and High-Temperature History on Swelling Characteristics of Bentonite. *Doboku Gakkai Ronbunshu* 2005 (806), 93–111. doi:10.2208/jscej.2005.806_93

Tang, C. S., Tang, A. M., Cui, Y. J., Delage, P., Schroeder, C., and Shi, B. (2011). A Study of the Hydro-Mechanical Behaviour of Compacted Crushed Argillite. *Eng. Geology.* 118, 93–103. doi:10.1016/j.enggeo.2011.01.004

Wang, Q., Tang, A. M., Cui, Y.-J., Delage, P., and Gatmiri, B. (2012). Experimental Study on the Swelling Behaviour of Bentonite/claystone Mixture. *Eng. Geology.* 124, 59–66. doi:10.1016/j.enggeo.2011.10.003

Xie, Y., Chen, Z. H., and Li, G. (2006). Test Research on Three-Dimensional Swelling Pressure of Nanyang Expansive Soil (23). *J. Logist Eng. Univ.* 22 (1), 11–14. (in Chinese).

Ye, W. M., Zhang, F., Chen, B., Chen, Y. G., Wang, Q., and Cui, Y. J. (2014). Effects of Salt Solutions on the Hydro-Mechanical Behavior of Compacted GMZ01 Bentonite. *Environ. Earth Sci.* 72, 2621–2630. doi:10.1007/s12665-014-3169-x

Zhang, L., Sun, D. A., and Liu, Y. M. (2016). Comparison between Swelling Properties of Two GMZ Bentonites. *Rock Soil Mech.* 37 (12), 3447–3454. doi:10.16285/j.rsm.2016.12.013

Zhang, S.-C., Li, K., Sun, K.-M., and Wang, S. (2021). Impact of Initial Moisture Content on the Shrinkage-Swelling Behavior of Heishan Bentonite. *KSCE J. Civ Eng.* 26 (2), 550–555. doi:10.1007/s12205-021-0060-7

Zhao, N. F., Ye, W. M., Chen, Y. G., Chen, B., and Cui, Y. J. (2017). Investigation on Swelling-Shrinkage of Unsaturated Compacted Gmz Bentonite on Wetting-Drying Cycles. *Bull. Eng. Geology. Environ.* 78, 1–11. doi:10.1007/s10064-017-1095-3

Conflict of Interest: Author J-HX is employed by POWERCHINA Huadong Engineering Corporation Limited and Zhejiang Huadong Engineering Consulting Corporation Limited.

The remaining authors declare that the research was conducted in the absence of any commercial or financial relationships that could be construed as a potential conflict of interest.

frontiers | Frontiers in Earth Science

ORIGINAL RESEARCH
published: 31 May 2022
doi: 10.3389/feart.2022.918386

Landslide Susceptibility Prediction Based on Frequency Ratio Method and C5.0 Decision Tree Model

Mingqiang Sheng[1], *Jianqi Zhou*[1], *Xiaogang Chen*[1], *Yuxin Teng*[1], *Anyu Hong*[1]* and *Gengzhe Liu*[2]

[1]School of Cival Engineering and Architecture, Nanchang University, Nanchang, China, [2]University of Pennsylvania School of Design, Philadelphia, PA, United States

This paper aims to propose an efficient landslide susceptibility prediction (LSP) model based on the frequency ratio method and C5.0 Decision Tree (C5.0 DT) model. Taking Ruijin City as the study area, local landslide inventory and 12 environmental factors are collected. Then the nonlinear correlations between landslide inventory and environmental factors are established by frequency ratio (FR) method. Thirdly, the FR values of these environmental factors are taken as the input variables of the C5.0 DT/SVM models; landslide samples and non-landslide samples are set as the output variables with values of 1 and 0, respectively. The mathematical relationship between input variables and output variables is established by C5.0 DT/SVM models. Finally, the performance of LSP of both models is evaluated by the Area Under Receiver Operation Characteristic Curve (AUC). Results show that: 1) The landslide susceptibility mapping (LSM) of the C5.0 DT and the SVM models are similar on the whole, high and very high susceptibility levels are mainly distributed in the north and in the edge of the study area. 2) The AUC values of C5.0 DT and SVM are 0.886 and 0.819, respectively. Both models have good LSP accuracy, however, the overall LSP accuracy of the C5.0 DT model is better than that of SVM. 3) It is significant and reliable to carry out LSP based on frequency ratio method and C5.0 DT model.

Keywords: landslide susceptibility prediction, C5.0 decision tree, support vector machine, frequency ratio, LSP accuracy

OPEN ACCESS

Edited by:
Yongtao Yang,
Institute of Rock and Soil Mechanics (CAS), China

Reviewed by:
Ting Xiao,
Beijing Institute of Technology, China
Yankun Wang,
Yangtze University, China

***Correspondence:**
Anyu Hong
honganyu@ncu.edu.cn

Specialty section:
This article was submitted to Geohazards and Georisks, a section of the journal Frontiers in Earth Science

Received: *12 April 2022*
Accepted: *09 May 2022*
Published: *31 May 2022*

Citation:
Sheng M, Zhou J, Chen X, Teng Y, Hong A and Liu G (2022) Landslide Susceptibility Prediction Based on Frequency Ratio Method and C5.0 Decision Tree Model. Front. Earth Sci. 10:918386. doi: 10.3389/feart.2022.918386

1 INTRODUCTION

China's geological environment is fragile and geological disasters occur frequently. Especially in the southwest and south area of China, landslides are densely distributed, causing serious casualties and heavy economic losses (Fu et al., 2017; Zheng et al., 2019b; Yang et al., 2020a). Therefore, landslide susceptibility prediction (LSP) is very important, which can provide a scientific and effective basis for the prevention and control of landslide geological hazards, road planning, and the formulation of appropriate risk mitigation strategies in the southwestern and southern areas of China (Akgun et al., 2012; Bai et al., 2015; Jiang et al., 2017; Lin et al., 2021; Huang et al., 2022a).

The study of LSP is to estimate the spatial probability of landslide occurrence in a certain area so as to effectively provide early warning to high landslide-prone area and reduce the occurrence of related safety accidents (Bui et al., 2020). LSP models are generally classified into deterministic, heuristic and machine learning models (Huang et al., 2017b; Huang et al., 2020b). At present, there are many LSP methods, including Remote Sensing (RS) research on surface deformation area to predict the occurrence of landslides (Chang et al., 2020; Dai et al., 2021; Zhu et al., 2022), and to establish a LSP

model coupled with multiple connection methods. Among them, the connection method of landslide inventory and environmental factors, and the determination of LSP models play an important role in the LSP modelling (Huang et al., 2020a). The LSP modelling mainly includes three processes: one is landslide inventory and division of prediction units; the second is the core process including selecting appropriate basic environmental factors and establishing models, and the final step is the LSP results testing (Dou et al., 2019).

At present, the LSP models coupled with various connection methods mainly include analytic hierarchy process (AHP) model (Ma et al., 2021), information value (IV) model (Zhao B. et al., 2021), mathematical statistics (Kouhartsiouk and Perdikou 2021) and machine learning models, where the machine learning models applied to LSP usually refer to C5.0 Decision Tree (C5.0 DT) (Mao et al., 2017), logistic regression (Shahabi et al., 2015), artificial neural network (Huang et al., 2019), extreme learning machine (Huang et al., 2017a), support vector machine (SVM) (Marjanović et al., 2011), gray correlation degree (Yu et al., 2021), random forest (Sun et al., 2020), clustering algorithm (Guo Z. et al., 2021), semi-supervised multilayer perceptron model (Huang et al., 2020b), etc. In general, the machine learning models are considered to have higher LSP performance than those of the heuristic models and conventional statistical models, due to their efficient nonlinear prediction abilities of machine learning models (Xiao et al., 2021; Wang et al., 2022). The most suitable model for LSP is inconclusive. Among many models, C5.0 DT and SVM models have widely-recognized nonlinear prediction performance (Chang et al., 2020; Li W. et al., 2021; Su et al., 2021). Both models have achieved ideal LSP results.

For the above-mentioned machine learning such as C5.0 DT and SVM, it is necessary to connect the landslide susceptibility index and environmental factors. There is a complex nonlinear correlation between environmental factors (Zhu et al., 2022). According to many studies (Chang et al., 2020; Huang et al., 2021a; Li W. et al., 2021; Guo Z. et al., 2021), the accuracy of the LSP model without considering the nonlinear connection is slightly lower than that of the coupled model considering the connection. The connection methods include the weight of evidence (Wu R. et al., 2020), IV model (Zhao B. et al., 2021) and the frequency ratio (FR) method (Nanda et al., 2020). FR method is used to characterize the spatial relationship between landslide distribution and condition factors. Machine learning model based on FR method is commonly used in LSP(Li et al., 2020; Huang et al., 2021b; Zhu et al., 2022). Therefore, this study intends to use the FR method to establish the nonlinear relationship between landslides and environmental factors. For the LSP modelling by the FR-C5.0 DT/SVM models, firstly, the FR values of the environmental factors are set as the input variables of the C5.0 DT and SVM models, then the C5.0 DT and SVM models for LSP are further established through training and testing the input-output variables.

In this study, Ruijin City in China is taken as the research area. A total of 12 basic environmental factors are obtained by remote sensing and ArcGIS 10.3 software. The C5.0 DT/SVM models are then used for LSP in Ruijin City. Then, the area under receiver operating characteristic curve (AUC) is used to assess the accuracy of LSP results of the C5.0 DT/SVM models (Panchal and Shrivastava 2021).

2 LANDSLIDE SUSCEPTIBILITY PREDICTION MODELLING

2.1 Research Framework

In this study, the FR method is used to connect the C5.0 DT/SVM models with the environmental factors of landslide inventory to perform the LSP and analyze their results. The main contents (**Figure 1**) include:

1) Based on the landslide inventory Information and geological environment, a total of 12 basic environmental factors are acquired (Jiang et al., 2018b; Xiao et al., 2021).
2) The nonlinear correlation between each environmental factors and the relative density of landslides is established by FR method, and the importance of various environmental factors are quantified (Huang et al., 2022b).
3) The FR values of these environmental factors are taken as the input variables of the C5.0 DT/SVM models, the output variables are landslide and non-landslide (marked as 1 and 0, respectively). The mathematical relationship between input variables and output variables is established (Liu et al., 2021).
4) The input-output variables are randomly divided by 70 and 30% as training dataset and test dataset, respectively. Training dataset is used for model training and building, test dataset is used to evaluate the generalization capability of the final model (Sun et al., 2020).
5) The performance of LSP of the two models is evaluated based on various indicators such as ROC (Xiao et al., 2020).

2.2 Frequency Ratio Method

The FR method can reflect the response relationship between landslides and basic environmental factors, and characterize the relative influence degree of each attribute interval of environmental factors on the occurrence of landslides (Zhang Y.-x. et al., 2020). If FR values are greater than 1, it indicates that the corresponding environmental factors are conducive to promoting the occurrence of landslides. If FR values are close to 1, it indicates that the relationship between the environmental factors and the occurrence of landslides in the corresponding interval is weak. If FR values are less than 1, it indicates that landslides are not likely to occur in this attribute interval. Based on the FR method and the natural break method, the environmental factors are divided into eight attribute interval levels, and the discrete lithology factors are classified according to the actual state as the interval classification basis. The formula for calculating the FR values of each environmental factor is:

$$FR = \frac{A_i/A}{B_i/B} \tag{1}$$

where A_i is the number of landslide grids in the interval for each type of environmental factor, A is the total number of landslide

grids in the area, B_i is the total number of grids for each type of environmental factor in the corresponding interval, and B is the total number of grids in the study area, and FR represents the FR values of environmental factors.

2.3 C5.0 Decision Tree Model

The decision tree (DT) model is a concise prediction model, and it is also a very powerful and comprehensive machine learning algorithm (Gkioulekas and Papageorgiou 2021). It has been widely used in practical applications such as radar signal identification and classification, medical diagnosis, etc. The DT model is used to analyze and establish the most suitable label value of each pixel eigenvalue node, and then classify the data set according to the label value. The size of the data set has no influence on the size of the DT model, and a large number of data can be used to centrally construct decision trees. This study intends to use the C5.0 algorithm to construct a classification model, which is to conduct classification and regularization of a large number of data sets and then convey knowledge. Compared with other algorithms, it is more suitable for processing large data sets.

When the model is engaged in classification, each classifier is assigned a leaf and it is assigned to the class with the largest number. After the regression tree processing in the algorithm, the missing data is pruned and the classification tree reclassifies the data to generate the optimal binary tree. Then, the optimal segmentation value of the node is selected by citing the Gini coefficient of the economics category. The formula is:

$$\omega(X) = \frac{Gini(X)}{\sum_1^n a_i} \tag{2}$$

where n is the number of branches, and a_i is the number of leaves when the branch is i.

2.4 Support Vector Machine Model

The SVM model increases the dimension of the independent variable on the basis of the kernel function. And it finds the optimal hyperplane with the largest category distance, then the support vector is used on the hyperplane to construct the model (Huang et al., 2020c). The input variables are linearly separable by transforming the nonlinear data into an n-dimensional hyperplane space based on a kernel function. Based on a set of linearly separable data, including 12 basic environmental factors and their corresponding output quantities $(x_i, y_i), i = 1, 2, 3 \ldots, n$, the corresponding output categories are $y_i = \{0, 1\}$. Then the landslide inventory is distinguished by the maximum gap of the n-dimensional hyperplane space. Its formula is:

$$y_i = \frac{1}{2}\|\lambda\|^2 \tag{3}$$

For linear inseparable data, the slack variable ξ_i is used to control the classification error, the constraint condition for correct classification is $y_i(\lambda x_i + b) \geq 1 - \xi_i$, and the wrong classification is $y_i(\lambda x_i + b) \geq 1 - \xi_i$, the distance formula of the hyperplane is

$$L = \frac{1}{2}\|\lambda\|^2 - \frac{1}{sn}\sum_{i=1}^{n}\delta_i \tag{4}$$

where $||\lambda||^2$ is the norm of the normal hyperplane, and L is the Lagrange multiplier. In addition, the Radial basis kernel function is used as kernel function of SVM model.

2.5 Accuracy Evaluation of Landslide Susceptibility

The ROC curve is widely used in the overall accuracy evaluation of binary classification in the LSP modelling due to its satisfactory performance (Vakhshoori and Zare 2018). ROC curve is threshold independent curve. Its main advantage is that it is independent of the number and spacing of thresholds used for calculation (Fawcett 2006). Assuming n classes of the landslide susceptibility indexes, n+1 thresholds can be defined, where the first threshold value (i = 1) is lower than the minimum susceptibility index observed in the most stable category, and the last threshold value (i = n+1) is higher than the maximum susceptibility index in the most sensitive category. Each threshold forms a confusion matrix in which four types of pixels are defined: true positive (TP), false positive (FP), true negative (TN), and false negative (FN) pixels. According to the number of pixels in each threshold, two statistics can be calculated, namely TPR (true positive rate) and FPR (false positive rate), as shown as:

$$TPR = \frac{TP}{TP + FN} \tag{5}$$

$$FPR = \frac{FP}{TN + FP} \tag{6}$$

TPR and FPR are plotted on the Y-axis and X-axis of the ROC curve, respectively. Then the AUC is calculated as:

$$AUC = \sum_{i=2}^{n+1}\frac{1}{2}\sqrt{(x_i - x_{i+1})^2} \bullet (y_i + y_{i+1}) \tag{7}$$

The success rate of the model can be displayed through the participation of AUC values in the training data set, meanwhile, the prediction rate of the test data set can be displayed (Vakhshoori and Zare 2018).

3 ANALYSIS OF STUDY AREA AND BASIC ENVIRONMENTAL FACTORS

3.1 Introduction to the Study Area and Landslide Inventory

Ruijin is a city under the jurisdiction of Jiangxi Province (**Figure 2**). It is located on the west side of the southern end of the Wuyi Mountains. Ruijin City has a humid subtropical monsoon climate with concentrated rainfall in summer. Ruijin City is dominated by low mountains and hills, with an area of 1,967.85 km^2, which is 80.35% of the whole area. The main landform types include dissolved karst area, eroded moderate and low mountainous area, eroded and denuded hilly area, and river valley accumulation terraces. The rock in the study area is

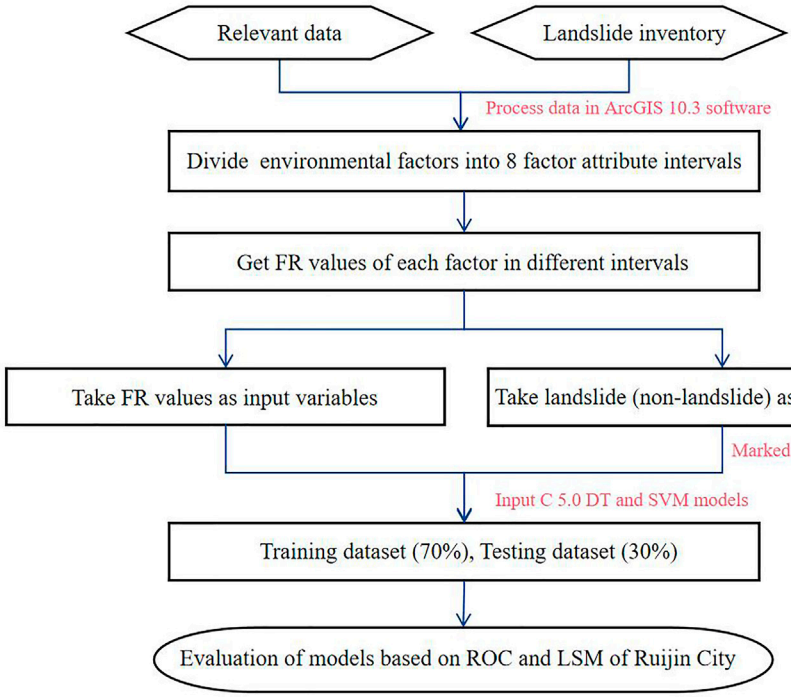

FIGURE 1 | The flow chart of research framework.

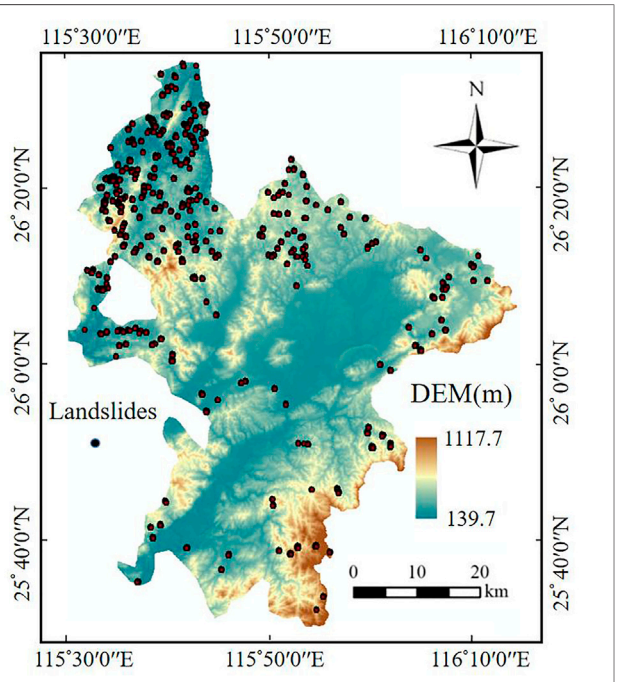

FIGURE 2 | The DEM and landslide catalog in Ruijin City.

severely weathered, fault folds are developed, the territory is mountainous and rainy, and landslides are densely distributed, causing serious casualties and economic losses (Jiang and Huang 2016; Huang et al., 2020c).

According to the statistics of Disasters Prevention Departments, the cumulative number of landslides reached 370 by the end of 2014. The distribution area of these landslides and potential landslides are converted into 5515 landslide unit grids based on ArcGIS 10.3 software (Zhao Z. et al., 2021). Landslides mainly occur in the north and west of the study area, while landslides in the south and the central plain are sparse. The occurrence of landslides is characterized by the dense gullies and is concentrated in moderate terrain relief.

3.2 Landslide Data Sources

The relevant basic data sources in the study area are: 1) historical landslide inventory map of Ruijin City and relevant data recorded in the field. 2) The Digital Elevation Model data (DEM) is freely downloaded by the Earth Observation Center of the Chinese Academy of Sciences. Then, the DEM is processed through ArcGIS 10.3 software to obtain topographic factors such as slope, aspect, plane curvature, profile curvature, and terrain relief. 3) The lithology factor in the study area is obtained from China Hydrogeological map with 1:100,000 scale. 4) The Landsat-8 remote sensing images are freely downloaded by the Earth Observation Center of the Chinese Academy of Sciences. They are used to obtain surface coverage factors such as NDVI, NDBI, and MNDWI.

In addition, since the overall terrain relief in Ruijin City is moderate, and the territory is mostly hills, the 30 m resolution grid can well reflect the distribution of hills and plains (Ismail et al., 2016). Therefore, the landslide inventory selects a grid with 30 m resolution as the LSP unit. Since the data of the 366 landslides are not

TABLE 1 | FR values of each environmental factors.

Environmental factors	Variable value	Type	Grids in the study area	Proportion of grid in the whole area (%)	Grids in landslide	Proportion of grid in landslide (%)	FR values
Elevation (m)	139.7–239.4	Continuous	730520	26.59	1963	35.60	1.34
	239.4–308.4		647040	23.52	1561	28.31	1.20
	308.4–373.6		558255	20.30	978	17.73	0.87
	373.6–446.5		369909	13.45	579	10.50	0.78
	446.5–534.7		231806	8.43	256	4.64	0.55
	534.7–642.1		121420	4.41	103	1.87	0.42
	642.1–780.2		66007	2.40	44	0.80	0.33
	780.2–1117.8		25734	0.94	31	0.56	0.60
Aspect (°)	−1	Continuous	499	0.02	0	0	0.00
	0–22.5 337.5–360		324819	11.81	669	12.13	1.03
	22.5–67.5		297924	10.83	578	10.48	0.97
	67.5–112.5		354479	12.89	945	17.14	1.33
	112.5–157.5		359791	13.08	806	14.61	1.12
	157.5–202.5		332830	12.10	708	12.84	1.06
	202.5–247.5		332144	12.07	631	11.44	0.95
	247.5–292.5		378011	13.74	660	11.97	0.87
	292.5–337.5		370194	13.46	518	9.39	0.70
Slope (°)	0–3.6	Continuous	569215	20.69	64	1.16	0.06
	3.6–7.0		489765	17.81	551	9.99	0.56
	7.0–10.6		532423	19.36	1435	26.02	1.34
	10.6–14.0		439314	15.97	1413	25.62	1.60
	14.0–17.6		338236	12.30	1071	19.42	1.58
	17.6–21.6		221050	8.04	621	11.26	1.40
	21.6–26.8		121804	4.43	292	5.29	1.20
	26.8–51.2		38884	1.41	68	1.23	0.87
Plane curvature	0–10.2	Continuous	448120	16.29	1530	27.74	1.70
	10.2–18.8		523668	19.04	1438	26.07	1.37
	18.8–27.8		429736	15.62	989	17.93	1.15
	27.8–37.7		347077	12.62	639	11.59	0.92
	37.7–48.2		272740	9.92	363	6.58	0.66
	48.2–59.1		223773	8.14	137	2.48	0.31
	59.1–70.6		204976	7.45	126	2.28	0.31
	70.6–81.5		300601	10.93	293	5.31	0.49
Profile curvature	0–1.5	Continuous	671143	24.40	873	15.83	0.65
	1.5–3.2		695512	25.29	1623	29.43	1.16
	3.2–4.8		534956	19.45	1231	22.32	1.15
	4.8–6.6		378810	13.77	843	15.29	1.11
	6.6–8.7		243825	8.86	507	9.19	1.04
	8.7–11.0		137931	5.01	272	4.93	0.98
	11.0–14.4		68397	2.49	137	2.48	1.00
	14.4–30.5		20117	0.73	29	0.53	0.72
Lithology	*Pt2*	Discrete	28700	1.04	70	1.27	1.22
	Z、*Pt3*		692349	25.17	1579	28.63	1.14
	ϵ		335994	12.21	371	6.73	0.55
	O		10175	0.37	19	0.34	0.93
	S		66549	2.42	324	5.87	2.43
	C		262308	9.54	143	2.59	0.27
	P		67776	2.440	126	2.28	0.93
	T		389314	14.15	982	17.81	1.26
	J、*K*		556796	20.24	452	8.20	0.40
	Q		318940	11.59	1367	24.79	2.14
Terrain wetness index	2.4–5.0	Continuous	908630	33.03	2400	43.52	1.32
	5.0–6.5		963107	35.01	2081	37.73	1.08
	6.5–8.4		525704	19.11	785	14.23	0.74
	8.4–10.8		223510	8.13	175	3.17	0.39
	10.8–14.2		97941	3.56	59	1.07	0.30
	14.2–22.8		31281	1.14	15	0.27	0.24
	22.8–32.7		449	0.02	0	0	0.00
	32.7–41.4		69	0	0	0	0.00
Gully density (km/km^2)	0–0.2	Continuous	356258	12.95	343	6.22	0.48
	0.2–0.4		429400	15.61	750	13.60	0.87
	0.4–0.6		469701	17.08	847	15.36	0.90

(Continued on following page)

TABLE 1 | (*Continued*) FR values of each environmental factors.

Environmental factors	Variable value	Type	Grids in the study area	Proportion of grid in the whole area (%)	Grids in landslide	Proportion of grid in landslide (%)	FR values
	0.6–0.8		471136	17.13	790	14.32	0.84
	0.8–1.0		413179	15.02	1193	21.63	1.44
	1.0–1.2		338047	12.29	916	16.61	1.35
	1.2–1.5		200346	7.28	615	11.15	1.53
	1.5–2.6		72624	2.64	61	1.11	0.42
Terrain relief	0–29.6	Continuous	454732	16.53	161	2.92	0.18
	29.6–54.1		456555	16.60	1478	26.80	1.61
	54.1–76.0		564745	20.53	1562	28.32	1.38
	76.0–97.9		483338	17.57	994	18.02	1.03
	97.9–122.4		379836	13.81	634	11.50	0.83
	122.4–150.8		239799	8.72	503	9.12	1.05
	150.8–186.8		128344	4.67	175	3.17	0.68
	186.8–328.7		43342	1.58	8	0.15	0.09
NDVI	0.40–0.60	Continuous	17412	0.63	18	0.33	0.52
	0.60–0.68		55627	2.02	23	0.42	0.21
	0.68–0.73		109216	3.97	172	3.12	0.79
	0.73–0.77		233155	8.48	531	9.63	1.14
	0.77–0.80		498261	18.11	1138	20.63	1.14
	0.80–0.83		711401	25.86	1537	27.87	1.08
	0.83–0.86		724179	26.33	1455	26.38	1.00
	0.86–1		401440	14.59	641	11.62	0.80
NDBI	0.03–0.13	Continuous	512160	18.62	752	13.64	0.73
	0.13–0.16		766433	27.86	1499	27.18	0.98
	0.16–0.19		641254	23.31	1607	29.14	1.25
	0.19–0.22		338433	12.30	834	15.12	1.23
	0.22–0.26		217537	7.91	451	8.18	1.03
	0.26–0.31		149173	5.42	259	4.70	0.87
	0.31–0.35		85133	3.10	97	1.76	0.57
	0.35–1		40568	1.47	16	0.29	0.20
MNDWI	0–0.13	Continuous	132113	4.80	206	3.74	0.78
	0.13–0.27		256111	9.31	415	7.52	0.81
	0.27–0.39		375374	13.65	750	13.60	1.00
	0.39–0.50		449343	16.34	1009	18.30	1.12
	0.50–0.62		464964	16.90	1077	19.53	1.16
	0.62–0.74		435803	15.84	858	15.56	0.98
	0.74–0.86		363305	13.21	744	13.49	1.02
	0.86–1		273678	9.95	456	8.27	0.83

enough used as the input variables of the model (Huang et al., 2022c). Therefore, the "surface to raster" tool in ArcGIS 10.3 is further used to convert the 366 landslide areas into 5,515 landslide units. At the same time, the whole study area is divided into 2,750,691 units.

Finally, the grid units of the whole study area are classified into data layers representing environmental factors: 1) topographic and landform factors, including elevation, slope, aspect, plane curvature, profile curvature, terrain relief and gully density; 2) hydrology environmental factors, including terrain wetness index and MNDWI; 3) land cover factors, including NDVI and NDBI; 4) basic geotechnical factors, such as lithology.

3.3 Basic Environmental Factors and Frequency Ratio Analysis

The interaction of various environmental factors leads to landslide occurrence (Wang et al., 2014; Huang et al., 2016; Zheng et al., 2020). By studying the evolution characterization of the landslide plane in Ruijin City, 12 representative environmental factors, such as elevation, slope, terrain relief, NDVI, NDBI, are selected as the input variables of the C5.0 DT and SVM models. According to the natural break method, each environmental factor is divided into eight attribute interval levels, and the discrete lithology factor is classified according to the actual state. Thus, the FR values of the attribute intervals divided by FR method for each environmental factor are obtained, as shown in **Table 1**.

3.3.1 Topographic Factors

As shown in **Table 1** and **Figure 3A**, when the elevation is between 139.7 and 308.4 m, the FR values are greater than 1, which indicates that the area is favorable for landslides occurrence. On the contrary, when the elevation is between 308.4 and 1117.8 m, the FR values are less than 1 or close to 1. This shows that the relationship between the attribute intervals of this environmental factor and the occurrence of landslides is weak. The areas with elevations between 308.5 and 1117.8 m are not contributed to landslide occurrence.

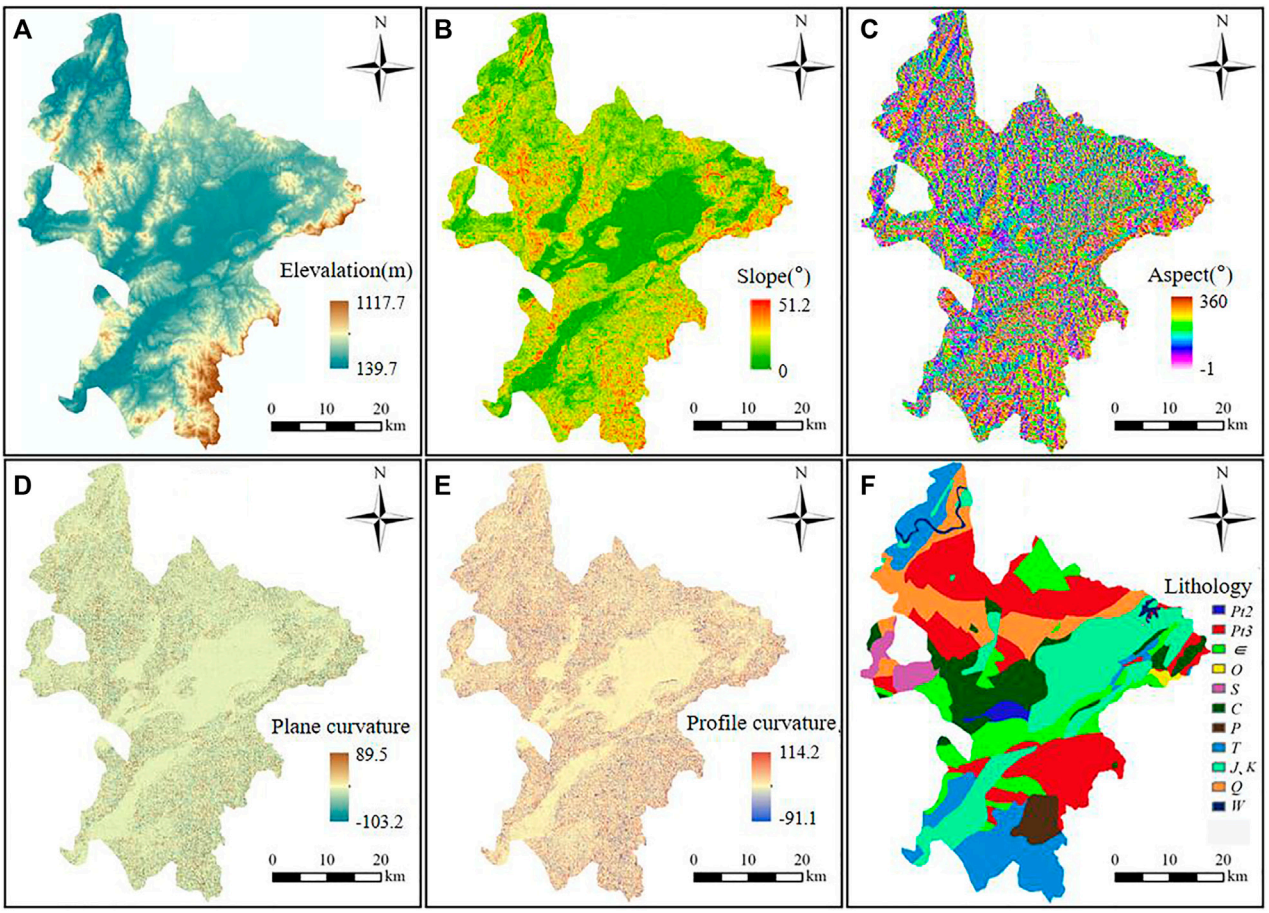

FIGURE 3 | Environmental Factors: **(A)** Elevation, **(B)** Slope, **(C)** Aspect, **(D)** Plan curvature, **(E)** Profile curvature, **(F)** Lithology.

Both aspect and slope are also extracted from DEM data. Slope can effectively reflect the physical relationship between landslides and basic topographic elements (Huang et al., 2021a). As shown in **Table 1**, when the aspect is smaller than 202.5° or the slope is higher than 7.0°, landslides occurrence is more likely to happen. The plane curvature can reflect all the ridge lines and valley lines on the surface in the horizontal direction, and the profile curvature can describe the slope in the vertical direction, both of which are generally considered as important factors affecting landslides (Hong et al., 2019). As shown in **Table 1**, when the plane curvature is smaller than 27.8° and the profile curvature is in the range of 1.5°–8.7°, landslides are more likely to occur in this area.

Characteristic parameters such as gully density and terrain relief are also extracted from DEM, as shown in **Figures 4B,C**. The gully density expresses the degree of ground cutting and fragmentation, and local landforms play an important role in determining the susceptibility of landslides (Conforti and Ietto 2019). As shown in **Table 1**, when the gully density is between 0.8 and 1.6, it is more likely for landslides occurrence. Terrain relief is also one of the important factors that trigger landslides. It describes the undulation of the terrain surface (Qiu et al., 2017), which is prone to landslides at 29.6–150.8.

3.3.2 Basic Geological Factors

Some studies have pointed out that lithology also plays an important role in affecting the occurrence of landslides (Conforti and Ietto 2019; Zhou et al., 2022). The evolution degree of cracks in soil layers of different lithology groups is quite different, and cracks have a great influence on the progressive failure process of soil landslides (Zheng et al., 2019a; Yang et al., 2020b; Jiang et al., 2020). This study adopts the latest geotechnical evaluation method, and analyzes the Mesoproterozoic Erathem (*Pt2*), Neoproterozoic Erathem (*Pt3*), Cambrian (∈), Ordovician (*O*), Silurian (*S*), Carboniferous (*C*), Permian (*P*), Triassic (*T*), Jurassic and Cretaceous (*J*、*K*), Quaternary (*Q*) and Waters (*W*) to improve the accuracy of LSP. As shown in **Table 1**, FR values are greater than 1 in the *Pt2*, *Pt3*, *S*, *T*, and *Q* lithology. Therefore, *Pt2*, *Pt3*, *S*, *T*, and *Q* lithology are prone to landslides.

3.3.3 Hydrological Environment and Land Cover Factors

The hydrological environment and the surface cover factors affect the shear strength of the soil. The decrease of the shear strength of the soil slope is also an important reason for the occurrence of

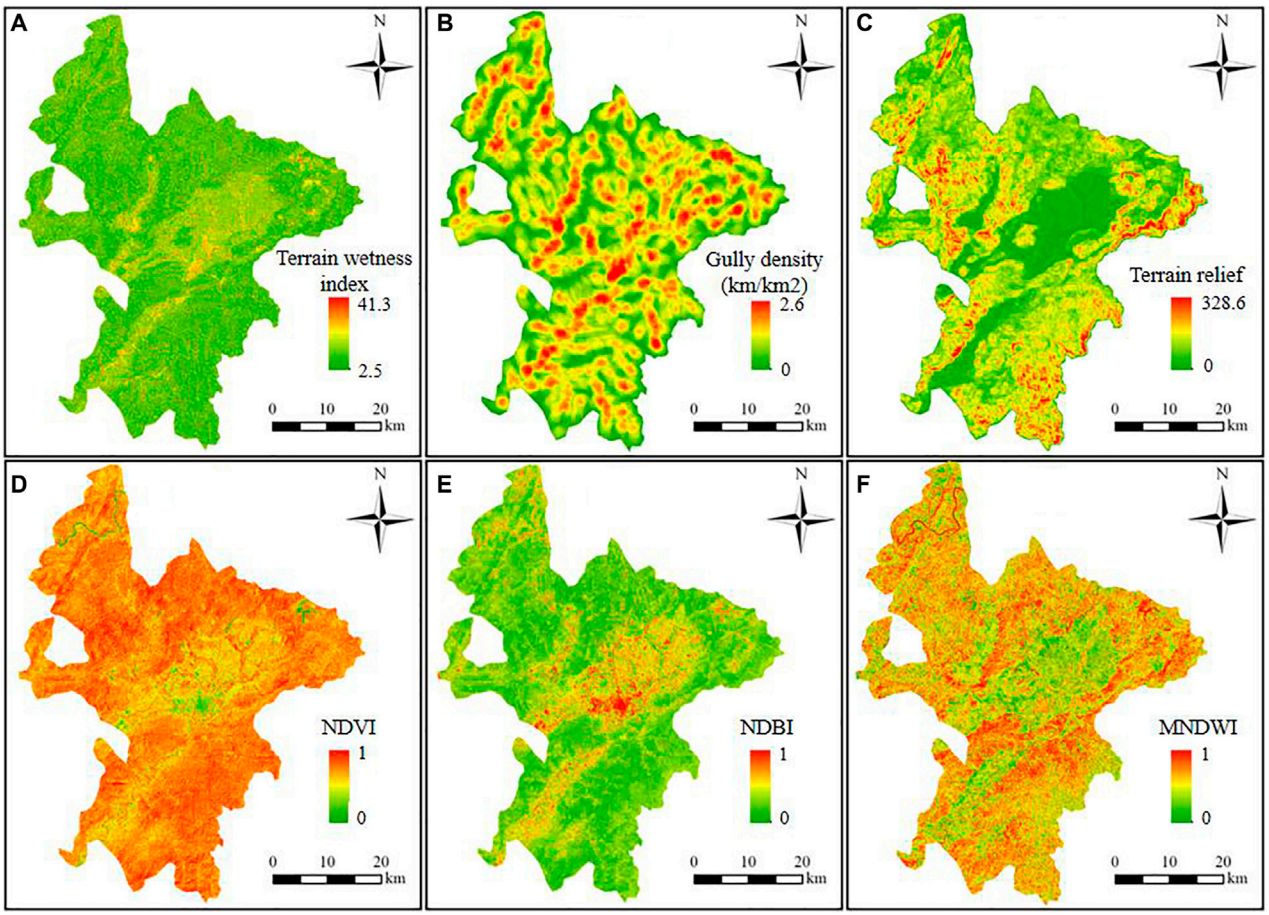

FIGURE 4 | Environmental factors: **(A)** Terrain wetness index, **(B)** Gully density, **(C)** Terrain relief, **(D)** NDVI, **(E)** NDBI, **(F)** MNDWI.

landslides (Guo et al., 2019; Yang et al., 2019; Fu et al., 2020). The MNDWI and the terrain wetness index reflect the characterization of the surface moisture distribution in the study area, which can effectively indicate the influence of hydrological environmental factors on landslide susceptibility (Li Z.-L. et al., 2021). The FR values of MNDWI in nearly 90% of the units are positively correlated with the MNDWI, indicating that the water body has a great influence on the occurrence of landslides. As shown in **Table 1**, when the terrain wetness index is between 2.4 and 6.6, FR values are greater than 1, and the FR values are negatively correlated with the terrain wetness index.

NDVI usually reflects the coverage of local vegetation (Zhang H. et al., 2020), indicating that the occurrence of landslides is affected by vegetation coverage. Studies have shown that the spatial distributions of landslides and other geological hazards are highly correlated with human engineering activities such as road excavation and slope cutting (Zheng et al., 2018; Guo C. et al., 2021). NDBI is used to characterize the surface building density (Ridwan et al., 2021), which reflects the influence of human activities on landslide occurrence. As shown in **Table 1**, when NDVI is within 0.73–0.87 and NDBI is within 0.06–0.28, the FR values are greater than 1, and landslides are more likely to occur.

4. RESULTS OF LANDSLIDE SUSCEPTIBILITY PREDICTION MODEL

4.1 Landslide Susceptibility Predicted by C5.0 Decision Tree and SVM Models

Based on the 30 m resolution, the environmental factors in the study area are divided into 2,750,691 grids. The unit also ranks the main 10 basic environmental factors according to their contribution. The landslide interface will change continuously with the increase of the safety factor, meanwhile, its shear outlet will be directly or indirectly constrained. For complex landslides, directly intercepting the non-landslide area without considering the distribution of potential landslides does not meet the safety regulations for landslide control. Therefore, 366 landslide surfaces and potential landslide area that have occurred are taken and converted into 5,515 grid units.

Further, the susceptibility of the grid units extracted from the landslide area are assigned to 1, which is unstable areas. Meanwhile the same number of non-landslide grid units are randomly selected in the whole study area. The non-landslide grid units are assigned to 0, which are stable area. The assigned landslide and non-landslide susceptibility values are taken as the

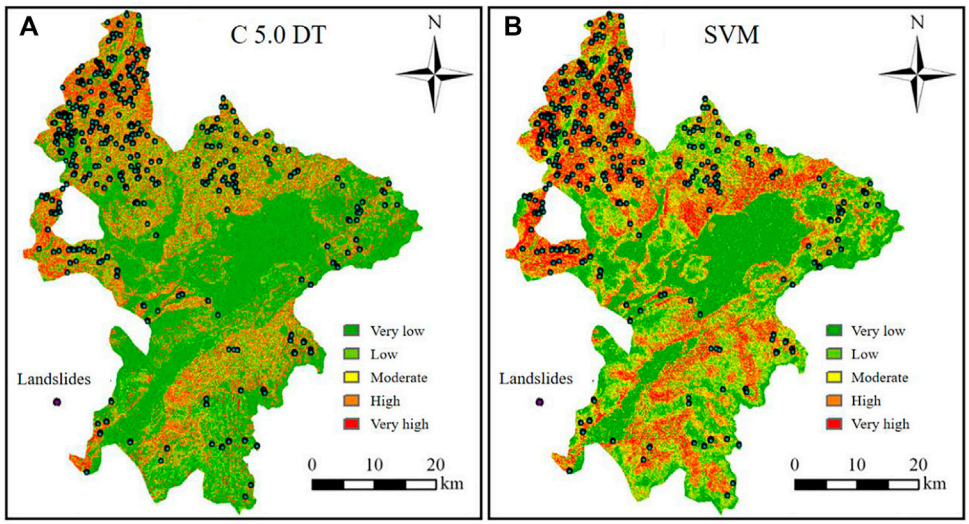

FIGURE 5 | LSM: **(A)** C5.0 DT, **(B)** SVM.

TABLE 2 | FR values of LSP grades in C5.0 DT and SVM models.

Model	Susceptibility levels	Susceptibility indexes	Grid in study area	Proportion of grid (%)	Grids in landslide	Proportion of grid in landslides (%)	FR values
C5.0 DT	Very low	0–0.14	1506219	54.76	210	3.81	0.07
	Low	0.14–0.37	404185	14.69	377	6.84	0.47
	Moderate	0.37–0.59	91926	3.34	169	3.06	0.92
	High	0.59–0.81	505631	18.38	2383	43.21	2.35
	Very high	0.81–1	242730	8.82	2376	43.08	4.88
SVM	Very low	0–0.14	846690	30.78	142	2.57	0.08
	Low	0.14–0.31	590034	21.45	397	7.20	0.34
	Moderate	0.31–0.49	456571	16.60	651	11.80	0.71
	High	0.49–0.67	409805	14.90	1210	21.94	1.47
	Very high	0.67–1	447591	16.27	3115	56.48	3.47

output variables of the LSP model, and then those landslide-non-landslide grid units are divided at a proportion of 7:3 in SPSS software, 70% of which are trained by SVM and C5.0 DT models, 30% are tested on SVM and C5.0 DT models.

Finally, the trained and tested SVM/C5.0 DT models are applied to the 12 environmental factors. Then, the LSM of the whole Ruijin City can be predicted. In ArcGIS 10.3 software, combined with the relationship between each environmental factor and the landslides, the predicted landslide susceptibility indexes are divided into five levels from low to high by using the natural break method (Kaur et al., 2018; Guo Z. et al., 2021).

4.2 Mapping Analysis of Landslide Susceptibility

The LSM based on the C5.0 DT model is shown in **Figure 5A** and **Table 2**. The predicted area proportions of the very low, low, moderate, high and very high landslide-prone area are respectively 54.75, 14.69, 3.34, 18.38, 8.82%. The FR values of very low, low, moderate, high and very high susceptible levels predicted by the C5.0 DT model are 0.07, 0.47, 0.92, 2.35, 4.88, respectively. The very high and high landslide-prone areas only accounted for 27.21% of the whole study area, but their corresponding FR values are contained for 86.29% of the total FR values.

The LSM predicted by the SVM model is shown in **Figure 5B** and **Table 2**, and the predicted area proportions of the very low, low, moderate, high and very high landslide-prone areas are 30.78, 21.45, 16.59, 14.89 and 16.27%, respectively. The FR values of the predicted landslide susceptibility from very low to very high landslide-prone areas are 0.08, 0.34, 0.71, 1.47, and 3.47, respectively. While the very high and high landslide-prone areas only account for 31.17% of the whole study area, their corresponding FR values account for 78.42% of the total FR values.

Comparing the two models, the FR values increase along with the increase of the landslide susceptibility level. However, the proportion of FR values in high and very high susceptibility levels of C5.0 DT model are greater than that of SVM model. It

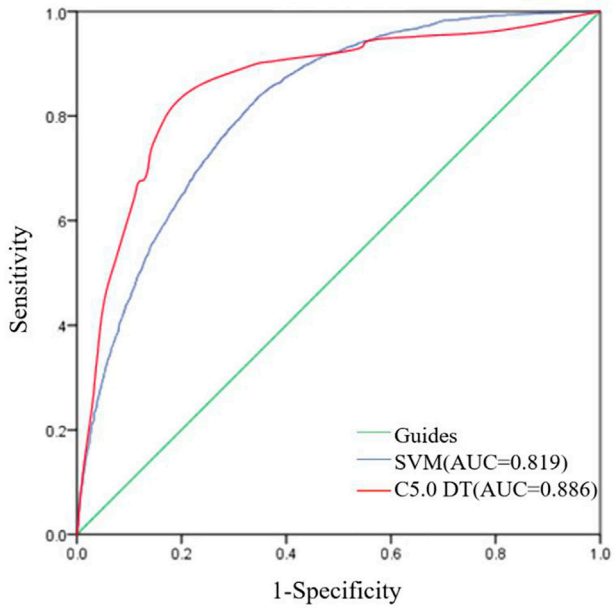

FIGURE 6 | ROC curves for LSP of C5.0 DT and SVM models.

shows that the LSP accuracy of the C5.0 DT model is higher than that of the SVM model, and that the landslide susceptibility indexes predicted by the C5.0 DT model are more consistent with the basic environmental factors of the study area.

As shown in **Figure 5** and **Table 2**, most of Ruijin City is in the low and very low landslide-prone areas. The high and very high landslide-prone areas predicted by the two models are generally similar. But the high and very high landslide-prone areas predicted by the SVM model are significantly larger than C5.0 DT model, as a result, C5.0 DT model is better refined. And the high and very high landslide-prone areas are mainly concentrated in the north of the study area, while the high and very high landslide-prone areas in the south are sparse. The main reason distribution of landslides is that the terrain of Ruijin City is dominated by basins, surrounded by dense hills. The hills on the northern part of the city are the most dense, and the terrain is complex and the river network is concentrated. The weak surface slides down as a whole, which is conducive to the occurrence of landslides.

5 DISCUSSION

This study discusses the LSP accuracy of the C5.0 DT and SVM models, the analysis of the basic environmental factors, and the application prospects of the LSP models.

5.1 ROC Curve for Landslide Susceptibility Predicted Accuracy of C5.0 Decision Tree and SVM Models

The prediction results of 70% of the training samples and 30% of the test samples of the C5.0 DT and SVM models are arranged from small to large, and are further used as the threshold for precision analysis in turn. The sample points greater than or equal to this threshold are defined as landslide points. The proportion of the correct landslide prediction points to the total number of landslide points is the model's sensitivity which reflects the model's ability to detect landslides; the proportion of the wrong landslide prediction points to the total number of non-landslide points is the model's specificity which is reflects the model's ability to correctly identify landslides (Paryani et al., 2021).

FPR is the value of 1-specificity; TPR is the value of sensitivity. The ROC curve mainly uses 1-specificity and sensitivity as the abscissa and ordinate, and its LSP accuracy results are shown in **Figure 6**. The AUC value of C5.0 DT is 0.886, while the AUC value of SVM is 0.819. The larger the AUC value, the better the overall prediction performance of the LSP model (Jiang et al., 2018a; Huang et al., 2021b; Paryani et al., 2021). Both C5.0 DT and SVM models have good LSP accuracy, however, the overall LSP accuracy of the C5.0 DT model is better than that of SVM.

5.2 Analysis of Environmental Factors

As shown in **Figures 3**, **4** and **Table 1**, for the basic environmental factors affecting the landslide susceptibility in Ruijin City. It is conducive to the occurrence of landslides, when the

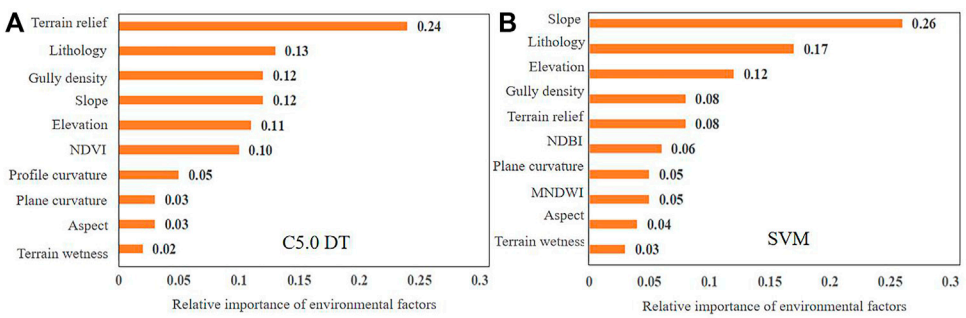

FIGURE 7 | Relative importance of environmental factors, **(A)** C5.0 DT, **(B)** SVM.

environmental factors are in these ranges where, the elevation is 139.7–308.5 m, the slope aspect is smaller than 202.5°, and the slope is high At 7.0°, the terrain wetness index is 2.5–6.6, the MNDWI is 0.39–0.62 or 0.74–0.86, the NDVI is 0.73–0.86, the NDBI is 0.16–0.27, and the lithology are Mesoproterozoic *Pt2 (1)*, Late Paleoproterozoic (*Z*), *Pt3*, Silurian *S*, Triassic *T*, Quaternary *Q*. The influence degree of environmental factors on landslide susceptibility can more intuitively reflect the main environmental factors considered by different models and provide a theoretical reference for the LSP (Wu Y. et al., 2020; Chang et al., 2020; Zhao et al., 2020; Pan et al., 2021).

In this study, SPSS Modeler and R Studio software are used to analyze the main 10 environmental factors in the C5.0 DT and SVM models, and the importance of each factor is ranked. As shown in **Figure 7**, the environmental factors with higher importance in the SVM model are slope, lithology, elevation, gully density, terrain relief, etc. The environmental factors with a higher contribution degree considered by the C5.0 DT model are terrain relief, lithology, gully density, slope, etc. The top five environmental factors are the same for the C5.0 DT and SVM models, but the slope is more important in the SVM model, and the terrain relief is more important in the C5.0 DT model. This also leads to the difference in the LSP between C5.0 DT and SVM models. Comprehensive analysis shows that the LSP accuracy of the C5.0 DT model is greater than the results of the SVM model.

5.3 Landslide Susceptibility Predicted Results of C5.0 Decision Tree and SVM Models and Their Application Prospects

Based on the analysis of the LSM and ROC curve in Ruijin City, the 366 landslides are concentrated in the high and very high susceptibility areas. Furthermore, the high and very high landslide areas are concentrated in the north and west of the study area. There are more landslides in the north and less in the south, more landslides in the edge and less in the middle. In the concentrated area of landslides, the altitude is low, the lithology formation is young, and the slope is relatively high. The obtained 12 types of basic environmental factors are representative. At the same time, the LSP of FR method based SVM and C5.0 DT is accurate, which have strong operability.

The reliability and LSP accuracy of the C5.0 DT model are higher than those of the SVM. The LSP result of C5.0 DT model can effectively give early warning to high landslide-prone area and reduce the occurrence of related safety accidents. Therefore, this study considers the C5.0 DT model to be an accurate and reliable LSP model. With the rapid development of big data platform, cloud computing, GIS and other technologies, machine learning have bright and broad application prospects in landslide susceptibility prediction (Dou et al., 2019; Merghadi et al., 2020). At the same time, C5.0 DT model is simple and clear, and has the advantages of easy learning, good reliability and high LSP accuracy (Abraham et al., 2021; Huang et al., 2021b).

6 CONCLUSION

This study explores the LSP results based on the FR method and C5.0 DT/SVM models in Ruijin City, and draws the following conclusions:

1) Both C5.0 DT and SVM models have high LSP accuracy, and the predicted landslide susceptibility maps are similar to each other on the whole. In addition, the landslides are mainly distributed in ravines and valleys. Especially, the landslides are likely to occur in the areas of moderate slope and large terrain relief.
2) The top contributing environmental factors calculated by the C5.0 DT/SVM models are terrain relief, lithology, gully density, slope and elevation. Factors that have minor effects on landslide susceptibility are the aspect, terrain wetness index, etc.
3) The C5.0 DT is an accurate and reliable LSP model. The LSP accuracy of C5.0 DT model is higher than that of the SVM model in LSP. It is concluded that we can predict accurate landslide susceptibility through combining the FR values and the C5.0 DT model.

DATA AVAILABILITY STATEMENT

The original contributions presented in the study are included in the article/supplementary material, further inquiries can be directed to the corresponding author.

AUTHOR CONTRIBUTIONS

MS, AH, and JZ contributed to conception and design of the study. JZ, XC, and YT collected Ruijin City local landslide inventory. GL performed the statistical analysis. MS and AH wrote the first draft of the manuscript. MS, AH, JZ, and YT wrote sections of the manuscript. All authors contributed to manuscript revision, and approved the submitted version.

FUNDING

This research is funded by the Natural Science Foundation of China (No.52069013 and 52109089).

REFERENCES

Abraham, M. T., Satyam, N., Jain, P., Pradhan, B., and Alamri, A. (2021). Effect of Spatial Resolution and Data Splitting on Landslide Susceptibility Mapping Using Different Machine Learning Algorithms. *Geomatics, Nat. Hazards Risk* 12, 3381–3408. doi:10.1080/19475705.2021.2011791

Akgun, A., Sezer, E. A., Nefeslioglu, H. A., Gokceoglu, C., and Pradhan, B. (2012). An Easy-To-Use MATLAB Program (MamLand) for the Assessment of Landslide Susceptibility Using a Mamdani Fuzzy Algorithm. *Comput. Geosciences* 38, 23–34. doi:10.1016/j.cageo.2011.04.012

Bai, S.-b., Lu, P., and Wang, J. (2015). Landslide Susceptibility Assessment of the Youfang Catchment Using Logistic Regression. *J. Mt. Sci.* 12, 816–827. doi:10.1007/s11629-014-3171-5

Bui, D. T., Tsangaratos, P., Nguyen, V.-T., Liem, N. V., and Trinh, P. T. (2020). Comparing the Prediction Performance of a Deep Learning Neural Network Model with Conventional Machine Learning Models in Landslide Susceptibility Assessment. *CATENA* 188, 104426. doi:10.1016/j.catena.2019.104426

Chang, Z., Du, Z., Zhang, F., Huang, F., Chen, J., Li, W., et al. (2020). Landslide Susceptibility Prediction Based on Remote Sensing Images and GIS: Comparisons of Supervised and Unsupervised Machine Learning Models. *Remote Sens.* 12, 502. doi:10.3390/rs12030502

Conforti, M., and Ietto, F. (2019). Influence of Tectonics and Morphometric Features on the Landslide Distribution: A Case Study from the Mesima Basin (Calabria, South Italy). *J. Earth Sci.* 31, 393–409. doi:10.1007/s12583-019-1231-z

Dai, C., Li, W., Wang, D., Lu, H., Xu, Q., and Jian, J. (2021). Active Landslide Detection Based on Sentinel-1 Data and InSAR Technology in Zhouqu County, Gansu Province, Northwest China. *J. Earth Sci.* 32, 1092–1103. doi:10.1007/s12583-020-1380-0

Dou, J., Yunus, A. P., Tien Bui, D., Merghadi, A., Sahana, M., Zhu, Z., et al. (2019). Assessment of Advanced Random Forest and Decision Tree Algorithms for Modeling Rainfall-Induced Landslide Susceptibility in the Izu-Oshima Volcanic Island, Japan. *Sci. Total Environ.* 662, 332–346. doi:10.1016/j.scitotenv.2019.01.221

Fawcett, T. (2006). An Introduction to ROC Analysis. *Pattern Recognit. Lett.* 27, 861–874. doi:10.1016/j.patrec.2005.10.010

Fu, X., Sheng, Q., Li, G., Zhang, Z., Zhou, Y., and Du, Y. (2020). Analysis of Landslide Stability under Seismic Action and Subsequent Rainfall: a Case Study on the Ganjiazhai Giant Landslide along the Zhaotong-Qiaojia Road during the 2014 Ludian Earthquake, Yunnan, China. *Bull. Eng. Geol. Environ.* 79, 5229–5248. doi:10.1007/s10064-020-01890-z

Fu, X., Sheng, Q., Zhang, Y., Chen, J., Zhang, S., and Zhang, Z. (2017). Computation of the Safety Factor for Slope Stability Using Discontinuous Deformation Analysis and the Vector Sum Method. *Comput. Geotechnics* 92, 68–76. doi:10.1016/j.compgeo.2017.07.026

Gkioulekas, I., and Papageorgiou, L. G. (2021). Tree Regression Models Using Statistical Testing and Mixed Integer Programming. *Comput. Industrial Eng.* 153, 107059. doi:10.1016/j.cie.2020.107059

Guo, C., Xu, Q., Dong, X., Li, W., Zhao, K., Lu, H., et al. (2021a). Geohazard Recognition and Inventory Mapping Using Airborne LiDAR Data in Complex Mountainous Areas. *J. Earth Sci.* 32, 1079–1091. doi:10.1007/s12583-021-1467-2

Guo, Z., Shi, Y., Huang, F., Fan, X., and Huang, J. (2021b). Landslide Susceptibility Zonation Method Based on C5.0 Decision Tree and K-Means Cluster Algorithms to Improve the Efficiency of Risk Management. *Geosci. Front.* 12, 101249. doi:10.1016/j.gsf.2021.101249

Guo, Z., Yin, K., Gui, L., Liu, Q., Huang, F., and Wang, T. (2019). Regional Rainfall Warning System for Landslides with Creep Deformation in Three Gorges Using a Statistical Black Box Model. *Sci. Rep.* 9, 8962. doi:10.1038/s41598-019-45403-9

Hong, H., Liu, J., and Zhu, A.-X. (2019). Landslide Susceptibility Evaluating Using Artificial Intelligence Method in the Youfang District (China). *Environ. Earth Sci.* 78, 8415. doi:10.1007/s12665-019-8415-9

Huang, F., Cao, Z., Guo, J., Jiang, S.-H., Li, S., and Guo, Z. (2020a). Comparisons of Heuristic, General Statistical and Machine Learning Models for Landslide Susceptibility Prediction and Mapping. *Catena* 191, 104580. doi:10.1016/j.catena.2020.104580

Huang, F., Cao, Z., Jiang, S.-H., Zhou, C., Huang, J., and Guo, Z. (2020b). Landslide Susceptibility Prediction Based on a Semi-supervised Multiple-Layer Perceptron Model. *Landslides* 17, 2919–2930. doi:10.1007/s10346-020-01473-9

Huang, F., Chen, J., Du, Z., Yao, C., Huang, J., Jiang, Q., et al. (2020c). Landslide Susceptibility Prediction Considering Regional Soil Erosion Based on Machine-Learning Models. *Int. J. Geo-Info* 9, 377. doi:10.3390/ijgi9060377

Huang, F., Chen, J., Liu, W., Huang, J., Hong, H., and Chen, W. (2022a). Regional Rainfall-Induced Landslide Hazard Warning Based on Landslide Susceptibility Mapping and a Critical Rainfall Threshold. *Geomorphology* 408, 108236. doi:10.1016/j.geomorph.2022.108236

Huang, F., Huang, J., Jiang, S., and Zhou, C. (2017a). Landslide Displacement Prediction Based on Multivariate Chaotic Model and Extreme Learning Machine. *Eng. Geol.* 218, 173–186. doi:10.1016/j.enggeo.2017.01.016

Huang, F. M., Wu, P., and Ziggah, Y. Y. (2016). GPS Monitoring Landslide Deformation Signal Processing Using Time-Series Model. *Ijsip* 9, 321–332. doi:10.14257/ijsip.2016.9.3.28

Huang, F., Pan, L., Fan, X., Jiang, S.-H., Huang, J., and Zhou, C. (2022b). The Uncertainty of Landslide Susceptibility Prediction Modeling: Suitability of Linear Conditioning Factors. *Bull. Eng. Geol. Environ.* 81, 182. doi:10.1007/s10064-022-02672-5

Huang, F., Tao, S., Chang, Z., Huang, J., Fan, X., Jiang, S.-H., et al. (2021a). Efficient and Automatic Extraction of Slope Units Based on Multi-Scale Segmentation Method for Landslide Assessments. *Landslides* 18, 3715–3731. doi:10.1007/s10346-021-01756-9

Huang, F., Yan, J., Fan, X., Yao, C., Huang, J., Chen, W., et al. (2022c). Uncertainty Pattern in Landslide Susceptibility Prediction Modelling: Effects of Different Landslide Boundaries and Spatial Shape Expressions. *Geosci. Front.* 13, 101317. doi:10.1016/j.gsf.2021.101317

Huang, F., Ye, Z., Jiang, S.-H., Huang, J., Chang, Z., and Chen, J. (2021b). Uncertainty Study of Landslide Susceptibility Prediction Considering the Different Attribute Interval Numbers of Environmental Factors and Different Data-Based Models. *Catena* 202, 105250. doi:10.1016/j.catena.2021.105250

Huang, F., Yin, K., Huang, J., Gui, L., and Wang, P. (2017b). Landslide Susceptibility Mapping Based on Self-Organizing-Map Network and Extreme Learning Machine. *Eng. Geol.* 223, 11–22. doi:10.1016/j.enggeo.2017.04.013

Huang, F., Zhang, J., Zhou, C., Wang, Y., Huang, J., and Zhu, L. (2019). A Deep Learning Algorithm Using a Fully Connected Sparse Autoencoder Neural Network for Landslide Susceptibility Prediction. *Landslides* 17, 217–229. doi:10.1007/s10346-019-01274-9

Ismail, E. H., Rogers, J. D., Ahmed, M. F., and Bakar, M. Z. A. (2016). Subsurface Profile Interpretation of Landslides, Examples from Bashilo River Watershed, Ethiopia. *Environ. Earth Sci.* 75, 5964. doi:10.1007/s12665-016-5964-z

Jiang, S.-H., and Huang, J.-S. (2016). Efficient Slope Reliability Analysis at Low-Probability Levels in Spatially Variable Soils. *Comput. Geotechnics* 75, 18–27. doi:10.1016/j.compgeo.2016.01.016

Jiang, S.-H., Huang, J., Huang, F., Yang, J., Yao, C., and Zhou, C.-B. (2018a). Modelling of Spatial Variability of Soil Undrained Shear Strength by Conditional Random Fields for Slope Reliability Analysis. *Appl. Math. Model.* 63, 374–389. doi:10.1016/j.apm.2018.06.030

Jiang, S.-H., Huang, J., Qi, X.-H., and Zhou, C.-B. (2020). Efficient Probabilistic Back Analysis of Spatially Varying Soil Parameters for Slope Reliability Assessment. *Eng. Geol.* 271, 105597. doi:10.1016/j.enggeo.2020.105597

Jiang, S.-H., Huang, J., Yao, C., and Yang, J. (2017). Quantitative Risk Assessment of Slope Failure in 2-D Spatially Variable Soils by Limit Equilibrium Method. *Appl. Math. Model.* 47, 710–725. doi:10.1016/j.apm.2017.03.048

Jiang, S.-H., Papaioannou, I., and Straub, D. (2018b). Bayesian Updating of Slope Reliability in Spatially Variable Soils with In-Situ Measurements. *Eng. Geol.* 239, 310–320. doi:10.1016/j.enggeo.2018.03.021

Kaur, H., Gupta, S., Parkash, S., and Thapa, R. (2018). Application of Geospatial Technologies for Multi-Hazard Mapping and Characterization of Associated Risk at Local Scale. *Ann. GIS* 24, 33–46. doi:10.1080/19475683.2018.1424739

Kouhartsiouk, D., and Perdikou, S. (2021). The Application of DInSAR and Bayesian Statistics for the Assessment of Landslide Susceptibility. *Nat. Hazards* 105, 2957–2985. doi:10.1007/s11069-020-04433-7

Li, W., Fan, X., Huang, F., Chen, W., Hong, H., Huang, J., et al. (2020). Uncertainties Analysis of Collapse Susceptibility Prediction Based on Remote Sensing and GIS: Influences of Different Data-Based Models and Connections between Collapses and Environmental Factors. *Remote Sens.* 12, 4134. doi:10.3390/rs12244134

Li, W., Shi, Y., Huang, F., Hong, H., and Song, G. (2021a). Uncertainties of Collapse Susceptibility Prediction Based on Remote Sensing and GIS: Effects of Different Machine Learning Models. *Front. Earth Sci.* 9, 731058. doi:10.3389/feart.2021.731058

Li, Z.-L., Leng, P., Zhou, C., Chen, K.-S., Zhou, F.-C., and Shang, G.-F. (2021b). Soil Moisture Retrieval from Remote Sensing Measurements: Current Knowledge and Directions for the Future. *Earth-Science Rev.* 218, 103673. doi:10.1016/j.earscirev.2021.103673

Lin, Q., Lima, P., Steger, S., Glade, T., Jiang, T., Zhang, J., et al. (2021). National-scale Data-Driven Rainfall Induced Landslide Susceptibility Mapping for China by Accounting for Incomplete Landslide Data. *Geosci. Front.* 12, 101248. doi:10.1016/j.gsf.2021.101248

Liu, L.-L., Yang, C., Huang, F.-M., and Wang, X.-M. (2021). Landslide Susceptibility Mapping by Attentional Factorization Machines Considering Feature Interactions. *Geomatics, Nat. Hazards Risk* 12, 1837–1861. doi:10.1080/19475705.2021.1950217

Ma, C., Yan, Z., Huang, P., and Gao, L. (2021). Evaluation of Landslide Susceptibility Based on the Occurrence Mechanism of Landslide: a Case Study in Yuan' an County, China. *Environ. Earth Sci.* 80, 9381. doi:10.1007/s12665-021-09381-4

Mao, Y., Zhang, M., Sun, P., and Wang, G. (2017). Landslide Susceptibility Assessment Using Uncertain Decision Tree Model in Loess Areas. *Environ. Earth Sci.* 76, 7096. doi:10.1007/s12665-017-7095-6

Marjanović, M., Kovačević, M., Bajat, B., and Voženílek, V. (2011). Landslide Susceptibility Assessment Using SVM Machine Learning Algorithm. *Eng. Geol.* 123, 225

Merghadi, A., Yunus, A. P., Dou, J., Whiteley, J., ThaiPham, B., Bui, D. T., et al. (2020). Machine Learning Methods for Landslide Susceptibility Studies: A Comparative Overview of Algorithm Performance. *Earth-Science Rev.* 207, 103225. doi:10.1016/j.earscirev.2020.103225

Nanda, A. M., Hassan, Z. u., Ahmed, P., and Kanth, T. A. (2020). Landslide Susceptibility Assessment of National Highway 1D from Sonamarg to Kargil, Jammu and Kashmir, India Using Frequency Ratio Method. *GeoJournal* 86, 2945–2956. doi:10.1007/s10708-020-10235-y

Pan, W., Pan, W., Luo, J., Fan, L., Li, S., and Erdenebileg, U. (2021). Slope Stability of Increasing Height and Expanding Capacity of South Dumping Site of Hesgoula Coal Mine: a Case Study. *Int. J. Coal Sci. Technol.* 8, 427–440. doi:10.1007/s40789-020-00335-y

Panchal, S., and Shrivastava, A. K. (2021). A Comparative Study of Frequency Ratio, Shannon's Entropy and Analytic Hierarchy Process (AHP) Models for Landslide Susceptibility Assessment. *Int. J. Geo-Inf.* 10, 603. doi:10.3390/ijgi10090603

Paryani, S., Neshat, A., and Pradhan, B. (2021). Spatial Landslide Susceptibility Mapping Using Integrating an Adaptive Neuro-Fuzzy Inference System (ANFIS) with Two Multi-Criteria Decision-Making Approaches. *Theor. Appl. Climatol.* 146, 489–509. doi:10.1007/s00704-021-03695-w

Qiu, H., Cui, P., Regmi, A. D., Hu, S., Zhang, Y., and He, Y. (2017). Landslide Distribution and Size versus Relative Relief (Shaanxi Province, China). *Bull. Eng. Geol. Environ.* 77, 1331–1342. doi:10.1007/s10064-017-1121-5

RidwanRasyidi, E. S., SyafriRahman, R., Rahman, R., Jumadil, N., and Ma'rief, A. A. (2021). Assessment of the Relationship between Building Density and Urban Heat Island Using Landsat Images in Makassar City. *IOP Conf. Ser. Earth Environ. Sci.* 802, 012042. doi:10.1088/1755-1315/802/1/012042

Shahabi, H., Hashim, M., and Ahmad, B. B. (2015). Remote Sensing and GIS-Based Landslide Susceptibility Mapping Using Frequency Ratio, Logistic Regression, and Fuzzy Logic Methods at the Central Zab Basin, Iran. *Environ. Earth Sci.* 73, 8647–8668. doi:10.1007/s12665-015-4028-0

Su, Q., Tao, W., Mei, S., Zhang, X., Li, K., Su, X., et al. (2021). Landslide Susceptibility Zoning Using C5.0 Decision Tree, Random Forest, Support Vector Machine and Comparison of Their Performance in a Coal Mine Area. *Front. Earth Sci.* 9, 7814272. doi:10.3389/feart.2021.781472

Sun, D., Xu, J., Wen, H., and Wang, Y. (2020). An Optimized Random Forest Model and its Generalization Ability in Landslide Susceptibility Mapping: Application in Two Areas of Three Gorges Reservoir, China. *J. Earth Sci.* 31, 1068–1086. doi:10.1007/s12583-020-1072-9

Vakhshoori, V., and Zare, M. (2018). Is the ROC Curve a Reliable Tool to Compare the Validity of Landslide Susceptibility Maps? *Geomatics, Nat. Hazards Risk* 9, 249–266. doi:10.1080/19475705.2018.1424043

Wang, M., Liu, M., Yang, S., and Shi, P. (2014). Incorporating Triggering and Environmental Factors in the Analysis of Earthquake-Induced Landslide Hazards. *Int. J. Disaster Risk Sci.* 5, 125–135. doi:10.1007/s13753-014-0020-7

Wang, Y., Tang, H., Huang, J., Wen, T., Ma, J., and Zhang, J. (2022). A Comparative Study of Different Machine Learning Methods for Reservoir Landslide Displacement Prediction. *Eng. Geol.* 298, 106544. doi:10.1016/j.enggeo.2022.106544

Wu, R., Zhang, Y., Guo, C., Yang, Z., Tang, J., and Su, F. (2020a). Landslide Susceptibility Assessment in Mountainous Area: a Case Study of Sichuan-Tibet Railway, China. *Environ. Earth Sci.* 79, 8878. doi:10.1007/s12665-020-8878-8

Wu, Y., Ke, Y., Chen, Z., Liang, S., Zhao, H., and Hong, H. (2020b). Application of Alternating Decision Tree with AdaBoost and Bagging Ensembles for Landslide Susceptibility Mapping. *CATENA* 187, 104396. doi:10.1016/j.catena.2019.104396

Xiao, T., Segoni, S., Chen, L., Yin, K., and Casagli, N. (2020). A Step beyond Landslide Susceptibility Maps: a Simple Method to Investigate and Explain the Different Outcomes Obtained by Different Approaches. *Landslides* 17, 627–640. doi:10.1007/s10346-019-01299-0

Xiao, T., Yu, L., Tian, W., Zhou, C., and Wang, L. (2021). Reducing Local Correlations Among Causal Factor Classifications as a Strategy to Improve Landslide Susceptibility Mapping. *Front. Earth Sci.* 9, 781674. doi:10.3389/feart.2021.781674

Yang, Y., Sun, G., Zheng, H., and Qi, Y. (2019). Investigation of the Sequential Excavation of a Soil-Rock-Mixture Slope Using the Numerical Manifold Method. *Eng. Geol.* 256, 93–109. doi:10.1016/j.enggeo.2019.05.005

Yang, Y., Sun, G., Zheng, H., and Yan, C. (2020a). An Improved Numerical Manifold Method with Multiple Layers of Mathematical Cover Systems for the Stability Analysis of Soil-Rock-Mixture Slopes. *Eng. Geol.* 264, 105373. doi:10.1016/j.enggeo.2019.105373

Yang, Y., Xu, D., Liu, F., and Zheng, H. (2020b). Modeling the Entire Progressive Failure Process of Rock Slopes Using a Strength-Based Criterion. *Comput. Geotechnics* 126, 103726. doi:10.1016/j.compgeo.2020.103726

Yu, D., Lv, L., Meng, F., Gao, F., He, J., Zhang, L., et al. (2021). Landslide Risk Assessment Based on Combination Weighting-Improved TOPSIS. *IOP Conf. Ser. Earth Environ. Sci.* 769, 032022. doi:10.1088/1755-1315/769/3/032022

Zhang, H., Ma, J., Chen, C., and Tian, X. (2020a). NDVI-net: A Fusion Network for Generating High-Resolution Normalized Difference Vegetation Index in Remote Sensing. *ISPRS J. Photogrammetry Remote Sens.* 168, 182–196. doi:10.1016/j.isprsjprs.2020.08.010

Zhang, Y.-X., Lan, H.-X., Li, L.-P., Wu, Y.-M., Chen, J.-H., and Tian, N.-M. (2020b). Optimizing the Frequency Ratio Method for Landslide Susceptibility Assessment: A Case Study of the Caiyuan Basin in the Southeast Mountainous Area of China. *J. Mt. Sci.* 17, 340–357. doi:10.1007/s11629-019-5702-6

Zhao, B., Ge, Y., and Chen, H. (2021a). Landslide Susceptibility Assessment for a Transmission Line in Gansu Province, China by Using a Hybrid Approach of Fractal Theory, Information Value, and Random Forest Models. *Environ. Earth Sci.* 80, 9737. doi:10.1007/s12665-021-09737-w

Zhao, H., Tian, Y., Guo, Q., Li, M., and Wu, J. (2020). The Slope Creep Law for a Soft Rock in an Open-Pit Mine in the Gobi Region of Xinjiang, China. *Int. J. Coal Sci. Technol.* 7, 371–379. doi:10.1007/s40789-020-00305-4

Zhao, Z., Liu, Z. y., and Xu, C. (2021b). Slope Unit-Based Landslide Susceptibility Mapping Using Certainty Factor, Support Vector Machine, Random Forest, CF-SVM and CF-RF Models. *Front. Earth Sci.* 9, 589630. doi:10.3389/feart.2021.589630

Zheng, Y., Chen, C., Liu, T., Song, D., and Meng, F. (2019a). Stability Analysis of Anti-dip Bedding Rock Slopes Locally Reinforced by Rock Bolts. *Eng. Geol.* 251, 228–240. doi:10.1016/j.enggeo.2019.02.002

Zheng, Y., Chen, C., Liu, T., Zhang, H., and Sun, C. (2019b). Theoretical and Numerical Study on the Block-Flexure Toppling Failure of Rock Slopes. *Eng. Geol.* 263, 105309. doi:10.1016/j.enggeo.2019.105309

Zheng, Y., Chen, C., Liu, T., Zhang, H., Xia, K., and Liu, F. (2018). Study on the Mechanisms of Flexural Toppling Failure in Anti-inclined Rock Slopes Using Numerical and Limit Equilibrium Models. *Eng. Geol.* 237, 116–128. doi:10.1016/j.enggeo.2018.02.006

Zheng, Y., Chen, C., Meng, F., Liu, T., and Xia, K. (2020). Assessing the Stability of Rock Slopes with Respect to Flexural Toppling Failure Using a Limit Equilibrium Model and Genetic Algorithm. *Comput. Geotechnics* 124, 103619. doi:10.1016/j.compgeo.2020.103619

Zhou, Y., Sheng, Q., Li, N., and Fu, X. (2022). The Dynamic Mechanical Properties of a Hard Rock under True Triaxial Damage-Controlled Dynamic Cyclic Loading with Different Loading Rates: A Case Study. *Rock Mech. Rock Eng.* 55, 2471–2492. doi:10.1007/s00603-021-02756-w

Zhu, L., Wang, G., Huang, F., Li, Y., Chen, W., and Hong, H. (2022). Landslide Susceptibility Prediction Using Sparse Feature Extraction and Machine Learning Models Based on GIS and Remote Sensing. *IEEE Geosci. Remote Sens. Lett.* 19, 1–5. doi:10.1109/lgrs.2021.3054029

Conflict of Interest: The authors declare that the research was conducted in the absence of any commercial or financial relationships that could be construed as a potential conflict of interest.

Advantages of publishing in Frontiers

OPEN ACCESS
Articles are free to read for greatest visibility and readership

FAST PUBLICATION
Around 90 days from submission to decision

HIGH QUALITY PEER-REVIEW
Rigorous, collaborative, and constructive peer-review

TRANSPARENT PEER-REVIEW
Editors and reviewers acknowledged by name on published articles

Frontiers
Avenue du Tribunal-Fédéral 34
1005 Lausanne | Switzerland

Visit us: www.frontiersin.org
Contact us: frontiersin.org/about/contact

REPRODUCIBILITY OF RESEARCH
Support open data and methods to enhance research reproducibility

DIGITAL PUBLISHING
Articles designed for optimal readership across devices

FOLLOW US
@frontiersin

IMPACT METRICS
Advanced article metrics track visibility across digital media

EXTENSIVE PROMOTION
Marketing and promotion of impactful research

LOOP RESEARCH NETWORK
Our network increases your article's readership